

# **Interplanetary Laser Ranging**

Analysis for Implementation in Planetary Science Missions



# Interplanetary Laser Ranging

Analysis for Implementation in Planetary Science Missions

## Proefschrift

ter verkrijging van de graad van doctor  
aan de Technische Universiteit Delft,  
op gezag van de Rector Magnificus prof. ir. K.C.A.M. Luyben,  
voorzitter van het College voor Promoties,  
in het openbaar te verdedigen op

donderdag 22 oktober 2015 om 12:30 uur

door

Dominic DIRKX

Ingenieur luchtvaart- en ruimtevaarttechniek,  
Technische universiteit Delft, Nederland,  
geboren te Aix-en-Provence, Frankrijk

This dissertation has been approved by the:

promotors: prof. dr. L.L.A. Vermeersen en  
prof. dr. ir. P.N.A.M. Visser

Composition of the doctoral committee:

Rector Magnificus,	voorzitter
prof. dr. L.L.A. Vermeersen,	promotor
prof. dr. ir. P.N.A.M. Visser,	promotor

*Independent members:*

Prof. dr. ir. R.F. Hanssen,	Technische Universiteit Delft
Prof. dr. M. Menenti,	Technische Universiteit Delft
Prof. dr. L.I. Gurvits,	Joint Institute for VLBI in Europe
Prof. dr. J. Oberst,	Technische Universität Berlin/DLR Berlin
Dr. D.E. Smith,	Massachusetts Institute of Technology



The work presented in this dissertation was performed in the context of the FP7 ESPaCE project, financially supported by the EC FP7 Grant Agreement 263466.

*Keywords:* Interplanetary Laser Ranging, Planetary Geodesy, Planetary Missions, Space-based Clocks, Experimental Gravitation

*Printed by:* Ridderprint

*Front & Back:* Schematic representation of a Phobos lander performing laser ranging to Earth. Image courtesy: NASA/JPL-Caltech (Mars image), ESA/DLR/FU Berlin (Phobos image), NASA/Apollo 17 crew (Earth image). Cover design: Nikki Vermeulen/Ridderprint

Copyright © Dominic Dirkx

ISBN 978-94-6299-192-7

An electronic version of this dissertation is available at  
<http://repository.tudelft.nl/>.

All rights reserved. No parts of this publication may be reproduced, stored in a retrieval system, or transmitted, in any form or by any means, electronic, mechanical, photocopying, recording, or otherwise, without the prior written permission of the author.

---

# Contents

---

<b>Preface</b>	<b>iii</b>
<b>Summary</b>	<b>vii</b>
<b>Samenvatting</b>	<b>xi</b>
<b>1 Introduction</b>	<b>1</b>
1.1 Historical Background . . . . .	2
1.2 Research Motivation . . . . .	6
1.3 Dissertation Structure . . . . .	8
<b>2 Tracking of Planetary Missions</b>	<b>11</b>
2.1 Planetary Tracking Data . . . . .	12
2.1.1 Tracking Types . . . . .	12
2.1.2 Radiometric Tracking Data Quality . . . . .	20
2.1.3 Preliminary Comparison of Tracking Types . . . . .	22
2.2 Science Return: Solar System Bodies . . . . .	24
2.2.1 Gravity Fields . . . . .	25
2.2.2 Rotational Dynamics . . . . .	28
2.2.3 Tidal Deformation . . . . .	33
2.2.4 Planetary Ephemerides . . . . .	38
2.3 Science Return: Gravitational Physics . . . . .	40
2.3.1 Theories of Gravitation . . . . .	40
2.3.2 Influence of Gravitation on Planetary Tracking Data . . . . .	44
2.3.3 Experimental Gravitation on Solar System Scales . . . . .	48

<b>3</b>	<b>Laser Ranging</b>	<b>55</b>
3.1	Physical Aspects of Laser Ranging . . . . .	56
3.1.1	Measurement Principle . . . . .	56
3.1.2	Interplanetary Ranging Concepts . . . . .	58
3.1.3	Free Space Propagation . . . . .	62
3.1.4	Media Propagation . . . . .	64
3.1.5	Link Budget . . . . .	66
3.1.6	Hardware Systems . . . . .	70
3.2	Error Sources . . . . .	74
3.2.1	Range Measurement Uncertainty . . . . .	74
3.2.2	Data Analysis Model Errors . . . . .	79
3.3	Current Status of Interplanetary Application . . . . .	83
3.3.1	Experimental and Operational Status of ILR . . . . .	83
3.3.2	Proposed Missions Employing ILR . . . . .	86
3.3.3	Laser Communications . . . . .	89
3.3.4	Laser Time Transfer . . . . .	91
3.3.5	Laser Altimetry . . . . .	93
<b>4</b>	<b>Paper I - Science Return from a Phobos Lander</b>	<b>95</b>
<b>5</b>	<b>Paper II - Atmospheric Turbulence</b>	<b>137</b>
<b>6</b>	<b>Paper III - One- and Two-way Laser Ranging</b>	<b>175</b>
<b>7</b>	<b>Paper IV - Coupled Relativistic Dynamical Effects</b>	<b>211</b>
<b>8</b>	<b>Synthesis and Discussion</b>	<b>239</b>
8.1	Measurements and Data Analysis for ILR . . . . .	239
8.1.1	Influence of Temporal Behaviour of Errors . . . . .	240
8.1.2	Measurement Errors . . . . .	243
8.1.3	Estimation Model Errors . . . . .	246
8.1.4	Limitations in Interpretation of Estimated Parameters . . . . .	250
8.2	Comparison to Conventional Tracking Techniques . . . . .	253
8.2.1	Definition of Comparison Criterion . . . . .	254
8.2.2	Quantitative Comparison for Periodic Signals . . . . .	256
<b>9</b>	<b>Concluding Remarks</b>	<b>261</b>
9.1	Conclusions . . . . .	261
9.2	Recommendations and Outlook . . . . .	266
	<b>Bibliography</b>	<b>270</b>
	<b>Curriculum Vitae</b>	<b>295</b>
	<b>List of Publications</b>	<b>297</b>

---

## Preface

---

As a kid, I was fascinated with all things space, and loved to read books on astronomy in general and the solar system in particular, especially the ones with detailed figures, illustrations and charts showing the myriad of celestial bodies and cosmic objects that our universe possesses. At the time, however, I was often mystified by how the people writing these books could possibly know all these things. The cutaway views of planets showing a core, mantle and crust seemed almost magical to me. Surely nobody had ever actually cut open a planet like that! Now that I understand how we are able to infer all this knowledge (at least much better than my former 9 year old self), I am not sure whether I am less amazed or more amazed by what we know and how we know it.

I am very fortunate to have been able to pursue what was once a boyhood dream: to work in the field of space engineering and planetary science, and contribute to future solar system missions. Right now, this dissertation seems like the final crowning achievement on the past four years of hard work, including all its triumphs, eureka-moments, frustrations and setbacks. However, with any luck it will be quite the opposite, only the beginning of a career in the planetary sciences.

Despite my boyhood fascination, the education and career path that led me to this point have been far from direct. After high school, I decided not to pursue education in space science, but opted to study physics instead. However, I soon realized that, although very interesting, the subject matter was too theoretical for my tastes, and I preferred studying material for which it was more readily apparent what the practical and/or scientific applications would be. As a result, I switched universities and started studying aerospace engineering in Delft. For most of the B.Sc. curriculum, though, I had my mind set on a master's degree in aerodynamics, having been somewhat disillusioned by the prospects of a career in the space sector, and having been fascinated by the more mathematically challenging (or so I thought at the time) field of flow dynamics. However, I serendipitously ended up doing my design synthesis exercise (the aerospace engineering curriculum's equivalent of a bachelor's thesis) on a space-related topic. While working on this project, I attended my first scientific/engineering conference and realized that my passion was in space after all. As a result, I decided to enroll for a master's degree in space engineering. After having completed my master's degree, for which I was very happy to be able to combine work on both aerodynamics and astrodynamics, a position opened up at the Astrodynamics & Space Missions group in Delft on something

called 'Interplanetary Laser Ranging'. Although I had no idea at the time what this would entail, I did some background research and decided that the topic would be both fascinating and very challenging. As a result, I decided to stay in Delft for my Ph.D. degree, the result of which you are reading now.

Doing research in the field of Interplanetary Laser Ranging (ILR) has been a very interesting experience, as very little work in this area has been done so far. Nevertheless, many aspects of ILR are similar to other tracking techniques for both terrestrial and planetary missions. It has been very stimulating to have been able to investigate the current states-of-the-art of various fields and condense the relevant material for my research, applying this material to ILR and extending it where it proved insufficient for my application. Of course, due to both the width and depth of the work that was required of me, I am very happy to have had the support from a great many people, both professionally and personally, in completing this research.

My supervisor Bert has been very enthusiastic from the start of my research and discussions and comments from him have been very valuable as I started doing professional research, writing scientific papers, extending my international network, *etc.* I also very much appreciate the amount of freedom that he allowed me to have in deciding the direction and focus of my research over the past few years. Due to the width of the topics that I have had to cover, I have been very fortunate to have been able to benefit from the expertise in both laser ranging and orbit determination that is present in our group, especially from Ron and Pieter, with whom I have had many discussions on my plans and results, invariably leading to new insight and ideas.

The work for this dissertation was performed in a European Framework Programme 7 (FP7) project called ESPaCE. For any young graduate looking for a research position, I can very much recommend working within the context of such a project. From day one, this collaboration meant that I had a broad network of international colleagues, whose experience and expertise has been crucial in helping me develop myself as a scientist. The discussions and presentations at project meetings strongly influenced many aspects of this research, and I was very happy to find myself developing from a recent graduate trying to keep up, to an active participant as the project progressed and my expertise grew. To all my ESPaCE colleagues: thank you for all your help in the project. The most valuable part of the ESPaCE collaboration, however, has been the in-depth collaboration with Sven Bauer at DLR. His extensive efforts on LRO orbit determination using one-way laser ranging has been crucial for my understanding of the (dis)advantages of one-way data. Especially my one-month visit to DLR in 2013 was very fruitful and I remember it fondly.

My research has been mostly theoretical in nature, relying largely on simulated data and the analysis of future missions. However, I have been very fortunate to have had a glimpse into the reality of Satellite Laser Ranging (SLR) early in my research when visiting the SLR station in Graz, Austria in March 2012. Georg Kirchner and Franz Koidl were most welcoming and took an exceptional amount of time to answer all the questions I had about the practicalities of laser ranging, and potential future issues for interplanetary applications. Furthermore, the laser ranging community as a whole has been very open in welcoming me at the annual workshops that they organize, and discussions and presentations at these events have been crucial in shaping my understanding



---

of the current state-of-the-art and the future direction of the laser ranging community. To everyone in the SLR community: thank you for all your help.

A substantial part of the time that went into the work presented in this dissertation has gone into programming the software used to generate my results. When starting my research, it quickly became clear that existing software packages (at least the ones I had access to) were unsuitable for the work that I wanted to do, leading me to develop my own software. I'm very happy that Bert took a chance on me, and allowed me to spend a lot of time on this before actually starting to generate results. The gamble seems to have paid off. But even more important in this respect were my colleagues who contributed to the software development. The code I have used is based on the TU Delft Astrodynamics Toolbox (Tudat), a software project initiated in 2010 by Kartik Kumar and Jeroen Melman, two Ph.D. students at the A&S section at the time. Since its inception, this project has been contributed to by dozens of M.Sc. students. The extensive work in setting up a sound basis for Tudat, with a strong emphasis on collaborative development and modular design, greatly facilitated the code that I developed for my research. Also, the extensive research that especially Kartik has done on software architecture, the use external libraries, C++ dos and don'ts, *etc.* has been crucial for this dissertation. Without everything I learned due to Tudat, I am quite sure that this dissertation would not be as extensive as it is, nor would I have a versatile software tool at my disposal now that this dissertation is finished.

Furthermore, my colleagues in Delft have been great to work with. Even if working on very different topics, discussions with them on a variety of subjects have been most helpful for my understanding of many things at the edge of, and beyond, my own field of study. And very importantly, the space bars and other after-work social gatherings have often been a great break from the occasional stresses and frustrations of research. And of course, it has been great to have a 'political-correctness-free-zone' with my office-mate Bart over the past few years. We have had many good discussions on all things life, science, the universe and everything, may we continue to have many more!

The main part of this dissertation consists of the journal papers that I have written during my research. I am very relieved to have been able to write this booklet with these papers in the middle, sandwiched between a set of introductory chapters and a discussion, instead of the more typical approach of writing a dedicated booklet from scratch (although I may gotten carried away a bit with the first few chapters). I can recommend this process to any Ph.D. student starting to write their dissertation. Not only does it provide additional confidence that the main results are sound (due to the peer review), it makes the writing of a dissertation much less arduous and repetitive. My co-authors Bert, Ron, Pieter, Ivan, Sven and Leonid have of course been instrumental in preparing and finishing these papers, providing timely expertise, thoughts, constructive criticisms, *etc.* Also, I am very grateful for the detailed feedback that Bert, Leonid, Pieter and Ron provided on the draft introductory and discussion chapters of this dissertation. Finally, I would like to sincerely thank my Ph.D. committee for taking the time to read my dissertation and for being a part of my defense ceremony. I am especially grateful to the members coming from outside the Netherlands specifically for my defense.

Although doing a Ph.D. has absorbed much of my time over the past years, and often preoccupied my mind even when not working, I luckily managed to continue to have a

life outside of work. To all the friends and family whose company I have enjoyed over the last few years, thank you for being considerate and for helping me keep my horizons broader than my work. I am very happy that in my defense ceremony these worlds of personal and professional life can be combined by having my friends Ben and Daniella as paranymphs: thank you for sharing this milestone with me. Also, I am grateful to my parents, who have supported me during my studies, even when I was much more interested in all other aspects of life besides studying. Somehow in the end it all turned out fine.

Most of all I would like to thank Patricia, who has supported me through thick and thin. When I was down and didn't see an end in sight, you were there to listen to me and help me see that I had what it takes to finish. When I got great results and my papers were accepted, you were there to celebrate with me. When I was working long hours at night or in the weekend, you got my head out of the books and computer and kept me grounded in real life. But most of all I am just happy to share my life with you. Thank you for always being there for me.

Delft, the Netherlands, September 2015  
Dominic Dirx

---

## Summary

---

Accurate determination of the trajectories of planetary spacecraft, as well as ephemerides, gravity fields, rotational characteristics and shapes of solar system bodies allow models of these bodies to be constrained. From these models, unique information can be obtained on the formation and evolution of our solar system, and exoplanetary systems by extrapolation. Furthermore, the observation of solar system dynamics and the propagation of electromagnetic signals between Earth and deep-space missions provides key information on the manifestation of relativistic effects, providing excellent opportunities in experimental gravitation.

The precise determination of the dynamics of solar system bodies (both natural and artificial) has typically been derived from radiometric tracking techniques, which are obtained by a radio link between Earth-based ground stations, such as those of the Deep Space Network (DSN), and the space segment (spacecraft or lander). For Earth-orbiting satellites equipped with retroreflectors, Satellite Laser Ranging (SLR) allows range measurements with sub-cm precision and accuracy to be obtained, which is several orders of magnitude more accurate than radiometric range measurements obtained by the DSN at planetary distances. Also, the use of retroreflectors on the Moon's surface has provided Lunar Laser Ranging (LLR) data with an accuracy in the order of centimeters over a period of decades. However, the use of retroreflector technology is infeasible for planetary missions, since the reflected signal strength is too low at such distances. To use laser ranging technology for planetary missions, an active laser system is required on the space segment, capable of detecting (for a one-way system) or detecting and transmitting (for a two-way system) short (10-100 ps) laser pulses. The analysis of this novel technology, termed Interplanetary Laser Ranging (ILR), is the topic of this dissertation.

In this dissertation, the potential of ILR to improve the science return of interplanetary missions is investigated, with a focus on its capability to better address a mission's planetary science objectives. To this end, parameter estimation has been executed using simulated ILR data for selected planetary missions. Furthermore, the influence of a

number of key sources of measurement and modelling uncertainty have been investigated in detail, thereby strengthening the development roadmap for ILR.

Implementation of ILR will rely strongly on existing SLR/LLR experience and ground infrastructure. The development of an active-ranging space segment is also strongly synergistic with ongoing work in laser time transfer, laser communications and laser altimetry, and a system combining these functions with ranging may allow expedited implementation of ILR. A one-way ranging system has been used operationally on the Lunar Reconnaissance Orbiter (LRO) in lunar orbit, while the two-way system has only been experimentally demonstrated using the altimetry system onboard the MESSENGER spacecraft at a distance of 24 million km, while it was en route to Mercury.

Detailed simulations have been performed for this dissertation to assess the science return in terms of characteristics of the Martian system (Mars Love numbers, Phobos librations, Phobos gravity field, *etc.*) from a single Phobos lander performing ILR to Earth-based ground stations. Such an experiment is conceptually similar to measurements that were to be performed with the failed Phobos-Grunt mission, which was to use a radio link between a Phobos lander and Earth-based stations. To differentiate between random (Gaussian) and systematic measurement noise, so-called 'consider covariance analysis' has been applied, thereby including the influence of unadjusted systematic range measurement errors in the estimation. The results indicate that a single mm of systematic error is typically 1-2 orders of magnitude more influential in the error budget of the estimated parameters than 1 mm of random measurement noise. The estimation results show that a Phobos laser ranging mission would be especially strong for estimating Mars tidal Love numbers and quality factors, as well as Phobos librations and deformation Love number. However, improvement of models describing Mars and Phobos interior structure and composition using such data is limited by deficiencies in other models and measurements, such as an accurate Phobos shape model, and an accurate Mars rotational model as well as seismic and magnetic field measurements. This shows that the strong improvement in range measurement accuracy facilitated by ILR must be accompanied by a commensurate improvement in a wider set of models and measurements to be able to fully exploit the data. The upcoming Insight mission will be crucial for providing such data on Mars, indicating the inter-mission synergy.

A substantial part of the error budget of ILR will be similar to that of SLR/LLR, since the ground segment hardware will be very similar, as will data analysis models for ground station position, Earth rotation and deformation, *etc.* The errors introduced by both this hardware and these models are unlikely to be consistently at the sub-mm level in the near-future, making mm-accurate ILR infeasible. Furthermore, the use of active space segment hardware, consisting of a laser detector for one-way systems (such as that used on LRO) or a laser detector and transmitter for two-way systems (as was used during the MESSENGER experiment) will introduce new sources of measurement uncertainty.

Conversely, the absence of the retroreflector signature on the laser pulse will allow for an improved characterization of temporal laser energy density at the receiver, since the temporal pulse shape is left largely unchanged along the signal path. This makes the influence of spatial intensity variation relatively stronger in ILR, compared to SLR/LLR. The influence of atmospheric turbulence on the spatial (and temporal) intensity pattern

---

of a laser pulse has been investigated for this dissertation, combining a set of existing models in a consistent and novel manner. Signal strength variations at the detector will result in accuracy variations, as the leading edge of a laser pulse with more than one detectable photon will be preferentially detected. The analysis shows that this can cause variations of the measurement accuracy at the level of several mm, for the case of a representative Phobos lander mission. However, this effect can be largely mitigated by consistently operating at the single-photon signal intensity level at the detector. Although the required signal strength attenuation will be at the expense of pulse detection rate (and therefore normal-point precision), the much stronger influence of accuracy (compared to precision) on estimated parameter quality more than warrants such an operational mode.

A crucial added source of range measurement error in ILR (compared to SLR/LLR) is the larger influence of clock noise on the range measurements. This is especially true for one-way ranging, in which the ground station and space segment clock independently register transmission and reception time tags, without the means to independently compare the two clocks. In a two-way system, the addition of a downlink allows the clock-induced error to be limited to that which is accumulated at the ground station during the two-way light time, and at the space segment during the retransmission time. The performance of a one- and two-way system has been numerically compared by simulating clock noise realizations and using the resulting noisy range measurements in parameter estimation for both a lunar orbiter and a Phobos lander. For the estimation from one-way data, the estimation of clock parameters is included over a variety of clock arcs to mitigate the influence of clock noise accumulation. The results for the lunar orbiter show that typical levels of dynamical model uncertainty will limit the capabilities of both the one- and two-way system to a similar level, as the measurement error is no longer the dominant source of error for the estimated parameters. Nevertheless, the two-way data are more amenable for use in improving dynamical models, since remaining trends in range residuals can be almost entirely attributed to dynamical mismodelling, with almost negligible observability of clock noise. The simulation results for a Phobos lander show several orders of magnitude improvement in estimation error when using a two-way instead of a one-way system. Furthermore, it has been shown from the Phobos simulations that the estimation of long-periodic effects (with a period much longer than the clock arc duration) correlates almost fully with clock parameter estimation, making a one-way system unsuitable for the estimation of such parameters, barring the use of an exceptionally accurate space-segment clock.

In addition to the inherently stochastic behaviour of clocks, the influence of relativity on clocks causes their behaviour to deviate from a constant rate. For insufficiently accurate *a priori* time ephemerides (due to for instance inaccurate orbital ephemerides, gravitational parameters, *etc.*), this error in the clock comparison process may adversely influence the analysis of one-way range data. Furthermore, when wishing to exploit relativistic clock behaviour to improve parameter estimation quality, this coupling between translational and time dynamics must be included. A concurrent space-time estimation procedure has been developed for this dissertation, essentially extending the orbit determination problem to include proper time behaviour, thereby estimating an initial four-dimensional state. A 0.1-10 % difference is found between formal estimation er-

rors obtained in the classical manner and those using our newly developed approach of coupled initial space-time estimation, using Mars and Mercury landers as test missions. The change in relevant correlation between the parameters is up to 50 % in extreme cases, though. The results for these planetary lander missions show that the use of an iterative update to the time ephemeris during the least squares estimation is sufficiently accurate for data analysis. However, it is likely that the space-time dynamics coupling will be more influential when analyzing data from orbiters with highly accurate clocks.

To determine whether ILR has a place in addition to existing tracking methods, the performance of an ILR system has been compared to that of a radiometric Doppler system. Using a simplified model in which the influence of physical parameters is assumed to be manifested on tracking data in a purely sinusoidal manner, the performance of laser range and radiometric Doppler measurements has been compared. An accuracy of 3-6 mm has been assumed for the laser range measurements, and a 2 and 10  $\mu\text{m/s}$  for Doppler data at 1000 s and 60 s integration time, respectively. This analysis shows that the two data types have similar sensitivity for estimation of parameters with a characteristic period in the range of 0.5-5 hours, with Doppler tracking more suitable for the estimation of shorter-period signals, and laser ranging more suitable for longer-periodic signals. This makes the science case for laser ranging especially strong for application in lander missions, where the short-periodic perturbations in the range measurements are much weaker, compared to orbiter missions. The poorer sensitivity of laser ranging to spacecraft for higher degree gravity field coefficients (beyond 2-6 for an orbital period of 3 hours) will degrade the trajectory reconstruction quality for orbiters around bodies without an accurate *a priori* gravity field, compared to Doppler tracking.

The apparent ubiquity of model errors limiting the capabilities of an ILR system (Phobos shape model, lunar orbit non-conservative force model, space segment time ephemeris, *etc.*) is a direct result of the revolutionary accuracy in range measurements that the system promises to provide. Many current models of planetary environments have not been developed to a degree where they will be able to fully deal with mm-cm level range accuracies, though. Achieving this will require novel modelling approaches, as well as improved measurements by other instruments, to ensure a balanced and synergistic science return from the payload of next-generation planetary missions.

---

## Samenvatting

---

Door de accurate bepaling van de zowel de banen van planetaire ruimtevaartuigen, als de ephemeriden, zwaartekrachtvelden, rotatie-eigenschappen en vormen van de hemellichamen in het zonnestelsel, kunnen modellen van de fysische eigenschappen van deze lichamen worden gemaakt. Uit deze modellen kan unieke informatie over het ontstaan en de evolutie van ons zonnestelsel worden afgeleid, en door extrapolatie die van exoplanetaire systemen. Hiernaast kan de bepaling van de dynamica, en de propagatie van elektromagnetische straling, in ons zonnestelsel gebruikt worden om cruciale informatie over de manifestatie van relativistische effecten te verkrijgen, waardoor het uitzonderlijke kansen biedt voor de experimentele gravitatie.

De precieze bepaling van de dynamica van (natuurlijke en kunstmatige) lichamen in ons zonnestelsel wordt tot op heden veelal afgeleid uit de analyse van radiometrische metingen, die verkregen worden met een radioverbinding tussen Aardse stations, zoals die van het Deep Space Network (DSN), en het ruimtesegment (satelliet of lander). Voor satellieten met retroreflectoren in een Aardse baan kunnen met Satellite Laser Ranging (SLR) afstandsmetingen worden verkregen die precies en accuraat zijn tot op het sub-cm niveau. Hiernaast heeft het gebruik van retroreflectoren op het oppervlak van de Maan (Lunar Laser Ranging, oftewel LLR) data opgeleverd die accuraat zijn tot op een aantal centimeter over een periode van decennia. Deze SLR/LLR metingen zijn een aantal ordes van grootte beter dan de radiometrische afstandsmetingen die met het DSN worden gemaakt over planetaire afstanden. Het gebruik van retroreflectoren is echter niet haalbaar voor planetaire missies, omdat de gereflecteerde signaalsterkte te zwak is op dergelijke afstanden. Om lasertechniek te gebruiken op deze afstanden moet een actief systeem worden gebruikt op het ruimtesegment, waarmee korte (10-100 ps) laserpulsen kunnen worden gedetecteerd (voor een éénrichtingssysteem) of gedetecteerd en verstuurd (voor een tweerichtingssysteem). Dit proefschrift draagt bij aan het analyseren van deze nieuwe techniek, genaamd Interplanetary Laser Ranging (ILR).

In dit proefschrift wordt de potentie van ILR onderzocht om de wetenschappelijke resultaten van interplanetaire missies te versterken, met de nadruk op de mogelijkheid ervan om missiedoelen in de planetaire wetenschappen te behalen. Hiervoor is met gebruik van gesimuleerde ILR data de schatting van fysische parameters voor een aantal planetaire missies uitgevoerd. Bovendien is de invloed van een aantal bronnen van meet- en modelon nauwkeurigheid in detail onderzocht, waardoor de eisen voor de toekomstige

ontwikkeling van ILR verder zijn verduidelijkt.

De implementatie van een ILR systeem zal sterk afhankelijk zijn van zowel de bestaande ervaring en de Aardse infrastructuur van SLR/LLR. Ook vertoont de ontwikkeling van actief systemen in de ruimte voor laser afstandsmetingen een sterke synergie met vooruitgang in laser tijdsoverdracht, laser altimetrie en laser communicatie. Een systeem dat één of meer van deze functies met afstandsmetingen combineert zou de implementatie van ILR kunnen versnellen. Tot op heden is alleen een éénrichtingssysteem operationeel gebruikt, op de Lunar Reconnaissance Orbiter (LRO) in een baan om de Maan, terwijl een tweerichtingssysteem slechts experimenteel is gedemonstreerd met het altimetriesysteem op het MESSENGER ruimtevaarttuig, op een afstand van 24 miljoen kilometer.

Voor dit proefschrift zijn gedetailleerde simulaties uitgevoerd voor een enkele lander op Phobos die ILR metingen uitvoert naar de Aarde, met het doel de haalbare wetenschappelijke resultaten te beoordelen in termen van de eigenschappen van het systeem van de planeet Mars (Mars Love getallen, Phobos libraties, Phobos zwaartekrachtsveld, *etc.*). Een dergelijke missie lijkt conceptueel op de Phobos-Grunt missie, welke een radioverbinding tussen een Phobos lander en Aardse stations had moeten gebruiken. Om een onderscheid te maken tussen willekeurige (Gaussiaans tijdsongecorreleerde) en systematische ruis, is zogeheten 'consider covariance analysis' gebruikt, waarmee de invloed van niet geschatte systematische meetfouten op het algehele schattingsproces wordt berekend. De resultaten geven aan dat, voor het foutenbudget van de geschatte parameters, een enkele mm systematische ruis over het algemeen 1 tot 2 ordes van grootte meer invloed heeft dan 1 mm Gaussiaanse meetfout. De resultaten van de schattingen tonen aan dat een Phobos Laser Ranging missie vooral sterk zal zijn in het bepalen van Love getallen en kwaliteitsfactoren van Mars, alsmede de libraties en het deformatie Love getal van Phobos. Sterke verbeteringen van modellen die het inwendige van Mars en Phobos beschrijven worden echter afgehouden door fouten in andere modellen en metingen, zoals een model van de vorm van Phobos, een accuraat rotatiemodel van Mars, en seismische en magnetisch veld metingen van Mars. Dit toont aan dat de sterke verbetering in de kwaliteit van afstandsmetingen die zal worden gefaciliteerd voor ILR samen zal moeten gaan met verbeteringen in een breder palet aan metingen en modellen om de data maximaal te kunnen benutten. De Insight missie die binnenkort zal worden gelanceerd is cruciaal om dergelijke data van Mars te verzamelen, hetgeen de synergie tussen planetaire missies aangeeft.

Een substantieel gedeelte van het foutenbudget van ILR zal sterk lijken op dat van SLR/LLR, gezien het feit dat de hardware van het grondsegment van ILR op deze bestaande technieken zal zijn gebaseerd. Ook zullen modellen voor de positie van het grondstation, Aardse rotatie, Aardse deformatie *etc.* (vrijwel) hetzelfde zijn voor de analyse van ILR en SLR/LLR data. Voor zowel deze hardware en deze modellen is het onwaarschijnlijk dat ze consistent tot op het sub-mm niveau accuraat zullen zijn in de nabije toekomst, waardoor ILR metingen met een mm-nauwkeurigheid niet haalbaar zullen zijn. Het gebruik van actieve hardware op het ruimtesegment, wat uit een detector bestaat voor een éénrichtingssysteem (zoals die op LRO) en uit een detectie- en transmissiesysteem voor een tweerichtingssysteem (zoals gebruikt tijdens het experiment met MESSENGER), zal ook nieuwe bronnen van meetnauwkeurigheid introduceren.

De afwezigheid van de invloed van de retroreflectoren op de laserpulsen zal er echter



---

voor zorgen dat het tijdsgedrag van de energiedichtheid van de puls beter bepaald kan worden bij ILR (vergeleken met SLR/LLR), gezien het feit dat dit tijdsgedrag praktisch onaangetast is door de propagatiemediën. Hierdoor is de invloed van de ruimtelijke intensiteitsvariatie op de meetkwaliteit, veroorzaakt door bijvoorbeeld atmosferische turbulentie, relatief sterker in ILR dan in SLR/LLR. De invloed van atmosferische turbulentie op het ruimtelijke (en tijds-)gedrag van een laserpuls is voor dit proefschrift onderzocht, waarvoor een aantal bestaande modellen in een consistente en nieuwe manier zijn samengevoegd. De door turbulentie (en geometrie) veroorzaakte variatie van signaalsterkte bij de detector zal zorgen voor variaties in nauwkeurigheid van de metingen, aangezien de voorkant van de laserpuls met meer dan één foton een grotere kans zal hebben om gedetecteerd te worden. De analyse toont aan dat dit effect een variatie in de nauwkeurigheid van de metingen kan veroorzaken op het niveau van een aantal mm, in het geval van een typische Phobos lander missie. Dit effect kan echter grotendeels ongedaan worden door consistent met een signaalintensiteit van een enkele foton bij de detector te werken. De hiervoor benodigde attenuatie van de signaalsterkte zal ten koste gaan van het aantal gedetecteerde pulsen (en daardoor normal-point precisie). Echter, zo'n aanpak is wel degelijk aan te raden, gezien de veel sterkere invloed van nauwkeurigheid (vergelijken met de precisie) van de meting op de kwaliteit van de geschatte parameters.

Een cruciale nieuwe bron van fouten in ILR (vergeleken met SLR/LLR), is de sterkere invloed van klokfouten op de afstandsmetingen. Dit is met name het geval voor éénrichtingsmetingen, waarin het grondstation en het ruimtesegment onafhankelijk van elkaar de tijd registreren, zonder een manier om de twee klokken onafhankelijk met elkaar te vergelijken. In een tweerichtingssysteem zorgt de toevoeging van de downlink ervoor dat de fouten die door de klok worden veroorzaakt gelimiteerd zijn tot de fout die zich op het grondstation opbouwt tijdens de tweerichtings-lichtafstand, en op het ruimtesegment tijdens de hertransmissietijd. De prestaties van een één- en tweerichtingssysteem zijn numeriek vergeleken door realisaties van klokkruis te simuleren, en met de resulterende afstandsmetingen een parameterschatting voor zowel een satelliet in een baan om de Maan en een lander op Phobos te simuleren. Voor de éénrichtingsdata wordt de schatting van klokparameters gedurende een verscheidenheid aan arc lengtes gebruikt om de opbouw van klokkruis tegen te gaan. De resultaten voor de satelliet om de Maan geven aan dat typische onzekerheden in het dynamisch model van deze satelliet de kwaliteit van de resultaten van één- en tweerichtingsmetingen tot hetzelfde niveau zal limiteren, doordat de meetfout niet de dominante bron van fouten in de schatting zal zijn. Desalniettemin zijn de tweerichtingsdata beter geschikt om de dynamische modellen te verbeteren, aangezien residuen tussen de gemeten en gesimuleerde afstandsmetingen van dit type bijna geheel aan fouten in het dynamisch model kunnen worden toegeschreven, met een vrijwel verwaarloosbare invloed van de klokkruis. De simulaties voor de Phobos lander geven aan dat een tweerichtingssysteem voor deze missie één tot twee ordes van grootte beter zal presteren dan een éénrichtingssysteem, in termen van de fout in de parameterschatting. Bovendien is het aangetoond met de simulaties van de Phobos lander dat de schatting van lang-periodieke effecten (met een periode veel langer dan de geschatte klok arc) zeer sterk is gecorreleerd met de schatting van klokparameters, waardoor een éénrichtingssysteem ongeschikt is voor het bepalen van dergelijke parameters

(zonder het gebruik van uitermate accurate klokken).

Naast het inherent stochastische gedrag van de klokken, zorgt de invloed van relativiteit ervoor dat het gedrag van de klokken afwijkt van een constante loopsnelheid. Met onvoldoende accurate *a priori* tijdsephemeriden (bijvoorbeeld door fouten in baanephemeriden, zwaartekrachtsvelden, *etc.*) kan dit ervoor zorgen dat de analyse van de éénrichtingsdata sterk negatief wordt beïnvloed. Bovendien moet de koppeling tussen tijd- en ruimtegedrag meegenomen worden wanneer relativistische klokeffecten worden gebruikt om parameterschatting te verbeteren, voor zowel één- en tweerichtingsdata. Er is voor dit proefschrift een methode voor gelijktijdige ruimte-tijd schatting ontwikkeld, waarin het baanbepalingsprobleem is uitgebreid om de eigentijd op een bepaald epoch mee te nemen, en een vier-dimensionale positie wordt geschat. Er is een verschil van 0.1-10 % gevonden in de formele schattingsfout tussen de resultaten met de klassieke en de nieuw ontwikkelde methode voor de gekoppelde ruimte-tijd schatting, voor het geval van landers op Mars en Mercurius. De invloed op de relevante correlaties kan echter in extreme gevallen oplopen tot 50 %. Resultaten van simulaties voor planetaire landers tonen aan dat een iteratieve update van de tijdsephemeris in een kleinste kwadraten schatting voldoende is voor accurate data analyse. Wel is het waarschijnlijk dat de invloed van de ruimte-tijd koppeling sterker zal zijn tijdens de analyse van data voor satellieten met een zeer accurate klok die in een baan zijn om hemellichamen.

Om te bepalen of laserafstandsbeplating een plek heeft naast bestaande methodes voor plaatsbepaling van interplanetaire missies, zijn de prestaties van radiometrische Dopplermetingen en laserafstandsmetingen in dit proefschrift vergeleken. Deze conceptuele analyse is gedaan met behulp van een versimpeld model van de invloed van fysische parameters op de metingen, waarin deze invloed zich op een puur sinusoidale manier manifesteert. Er is een 3-6 mm nauwkeurigheid van de afstandsmetingen aangenomen, en 2 en 10  $\mu\text{m/s}$  over een integratietijd van 1000 s en 60 s, respectievelijk, voor de Doppler metingen. Deze analyse toont aan dat deze twee soorten data een gelijksoortige gevoeligheid hebben voor de schatting van parameters met een karakteristieke periode van 0.5-5 uur, waar Dopplermetingen geschikter zijn voor de schatting van effecten met een kortere periode, en laser metingen geschikter zijn voor die met een langere periode. Hierdoor is de 'science case' van laser metingen vooral sterk voor landers, waar de kort-periodieke perturbaties veel zwakker zijn (vergeleken met satellieten in een baan om een hemellichaam). De zwakkere gevoeligheid voor zwaartekrachtsveldcoëfficiënten van lasermetingen naar satellieten zal de kwaliteit van de geschatte baan van een satelliet die ILR gebruikt i.p.v. Doppler verslechteren voor missies om lichamen zonder een *a priori* zwaartekrachtsveld van hoge kwaliteit.

De alom aanwezige invloed van modelfouten die de mogelijkheden van een ILR systeem limiteren (Phobos vorm model, model voor niet-conservatieve krachten in een baan om de Maan, tijdsephemeris van het ruimtesegment *etc.*) is een direct gevolg van de revolutionaire kwaliteit van de afstandsmetingen die dit systeem zal bezorgen. Veel huidige modellen van planetaire omgevingen zijn niet ontwikkeld tot op het punt dat ze metingen met een nauwkeurigheid op het mm-cm niveau kunnen verwerken. Het bereiken van dit niveau vereist een nieuwe aanpak van modelleren, en het gebruik van verbeterde metingen van een breed aantal instrumenten, om gebalanceerde, synergetische wetenschappelijke resultaten te bereiken met de volgende generatie planetaire missies.

# CHAPTER 1

---

## Introduction

---

In the advancement of science, technological and intellectual developments go hand-in-hand, with theoretical breakthroughs often driven by the inability of prevailing theories to explain new experimental facts. Examples of such breakthroughs include Kepler's laws describing heliocentric planetary motion to explain detailed observations of their apparent motion (*e.g.* Hawking, 2003) and Einstein's theory of special relativity to explain the observed invariance of the speed of light (Einstein, 1905). As our technology has allowed us to expand beyond our own planet in the past half century, so have our capabilities to obtain new experimental information on a wealth of subjects such as geodesy, climate science and fundamental physics (*e.g.*, Seeber, 2003; Chuvieco, 2008; Turyshev, 2009). As a result, our understanding of our own planet, the solar system, and the universe as a whole has been revolutionized. Future theoretical developments will be greatly facilitated by the development of the next generation of space- and ground-based instrumentation. The analysis of the application of one such type of instrumentation in the field of planetary science is the topic of this dissertation.

In the planetary sciences, a combination of state-of-the-art Earth- and space-based technology is used to improve the characterization of the processes governing the solar system, aiding our understanding of its formation and evolution, (*e.g.*, de Pater and Lissauer, 2001; Bertotti et al., 2003b). Furthermore, by using the solar system as our laboratory, we can use the various moons, planets, asteroids, *etc.* as elements in an experimental setup, allowing us to test various laws of physics, and the physical processes that emerge from them, in a manner that we could not hope to do in terrestrial laboratories. By sending spacecraft to the bodies in our solar system, we can add custom-made components to our 'grand laboratory'. This allows ongoing processes to be measured to much greater detail than is possible in an astronomical setting, where we are limited to distant observations. This puts solar system observations in a unique middle ground, combining the use of *in situ* instrumentation (as is the case in terrestrial laboratories)

with the observation of effects at distances, masses *etc.* much greater than what can be achieved on Earth, as is the case in astronomical observations.

In this dissertation, we analyze several key aspects of an emerging technology that could provide significant improvements in such a set of experimental data obtained from solar system space missions: Interplanetary Laser Ranging (ILR). This technology can facilitate a strongly improved characterization of the dynamics of both natural and next-generation artificial bodies in our solar system (Degnan, 2002; Turyshev et al., 2010). However, its development is partly in its infancy, requiring substantial additional development and analysis before it can be implemented. This dissertation forms part of these developments. In this chapter, we put the technology in a historical context in Section 1.1, followed by a more detailed description for the rationale for investigating interplanetary laser ranging in Section 1.2. Finally, we discuss the structure of the subsequent chapters in this dissertation in Section 1.3.

## 1.1 Historical Background

The start of the space age in the 1950s spurred developments in a wide range of fields in both science and engineering. For the first time in history, global observations of our planet were available, facilitating a quantum leap in our ability to measure, model and understand the Earth. Since that time, observations made by orbiting satellites have been absolutely crucial in monitoring the state of our planet, allowing changes in weather, climate, topography and sea level to be measured on a truly global scale, (*e.g.*, Ohring et al., 2002; Berger et al., 2012). One of the key steps that allowed for the accurate analysis of space-based observations was the development of technologies and methods for the precise determination of the positions of artificial satellites (Vetter, 2007), which could be used for accurate processing of remote-sensing observations. Furthermore, the reconstruction of the orbital dynamics of spacecraft can be used to obtain science products in various branches of (Earth) sciences such as geodesy, (*e.g.*, Kaula, 1966), as it allows for a characterization of the time history of the (gravitational) accelerations that have acted on the spacecraft.

The observation and estimation of orbits of natural solar system bodies was by no means a new science at the beginning of the space age, however. Detailed methods for the determination of orbits of planets, moons, *etc.* from astrometric observations had been developed for several centuries (Boyer and Merzbach, 2011). For instance, one of the first applications of the method of least squares was by Gauss to predict the orbit of Ceres from a short arc of observations, allowing it to be successfully recovered after it became observable again following a solar opposition. In an even greater triumph of dynamical astronomy, the discovery of the planet Neptune in 1846 was a result of unexplained perturbations that were observed in Uranus' orbit. These perturbations led to the postulation of the existence of an eighth planet, which was subsequently found in an orbit very close to that predicted from the observed Uranian orbital perturbations (Grosser, 1962). Despite the width and depth of existing methods for the calculation of (planetary) ephemerides at the start of the space age, the small physical size of artificial satellites posed a variety of challenges in dynamical modelling. Conversely, their potential for being purposely designed for a specific (active or passive) method of

tracking allowed much more accurate orbits to be determined than had been the case for natural solar system bodies, leading to the development of a number of technologies (Seeber, 2003), among them Satellite Laser Ranging (SLR).

The ground segment required for SLR consists of systems for generating and transmitting short laser pulses, as well as detecting laser pulses that are reflected back from a satellite. The space segment must be equipped with retroreflectors that reflect incoming laser pulses (from the ground station) back to their source. By measuring their transmission and reception time, total times-of-flight of these pulses are determined, which yield (raw) two-way range measurements between the spacecraft and the ground station (Degnan, 1993). State-of-the-art attainable range accuracy and precision is at the (sub-)cm level, depending on ground segment hardware quality, as well as the space segment distance and retroreflector array properties. For SLR operations, a ground station must be equipped with a stable detection and timing assembly, and be capable of transmitting and detecting short laser pulses by direct detection of the reflected photons. The concept of SLR was first presented in detail by Plotkin (1964), although it is briefly mentioned in a conceptual manner by Veis (1963). The first successful SLR measurements were performed at NASA Goddard Space Flight Center (GSFC) to the Beacon-B satellite in Low Earth Orbit in 1964. These measurements yielded position determination with several meters accuracy. Compared to microwave radar measurements performed at the time, this was an order of magnitude improvement. By 1967, four retroreflector-equipped satellites had been launched and an international ranging campaign was initiated, culminating in the contribution to an improved Earth gravity field model and station position data. In 1975, the first satellite designed purely for laser ranging, the French STARLETTE, was launched. In 1976, a new type of laser operated at GSFC achieved sub-decimeter single-shot precision, a great improvement compared to that obtained during the first ranging campaign only a decade earlier. In the same year, the Laser Geodynamics Satellite (LAGEOS) was launched (shown in Fig. 1.1(a)), which has arguably been the most prolific satellite for laser ranging purposes over the last decades, (Degnan, 1993; Wood and Appleby, 2004; Plotkin, 2014). The current SLR ground station network consists of about 40 stations, which track more than 50 different satellites<sup>1</sup>.

The coordination of SLR activities falls under the responsibilities of the International Laser Ranging Service (ILRS), which was formed in 1998 to provide an overarching organization that can improve cohesion between various SLR stations and activities and serve as an interface between the SLR community and the science community (Pearlman et al., 2002; Gurtner et al., 2005). Over the last decades, SLR has been instrumental in geodetic observations of the Earth and is one of the four main space-geodetic techniques (along with GNSS, DORIS and VLBI) (Petit et al., 2010). It has contributed to the determination of (variations of) the Earth's gravity field and geocenter, measuring plate motions, improving the terrestrial reference systems, measuring rotational variations of the Earth, *etc.* (Exertier et al., 2006; Altamimi et al., 2011). Additionally, owing to its (nearly) unbiased range measurements, it allows for a crucial form of validation of GNSS-derived spacecraft orbits, (*e.g.*, Urschl et al., 2005). Furthermore, it has recently been demonstrated that high-powered SLR systems can be used for highly accurate tracking

---

<sup>1</sup><http://ilrs.gsfc.nasa.gov/>

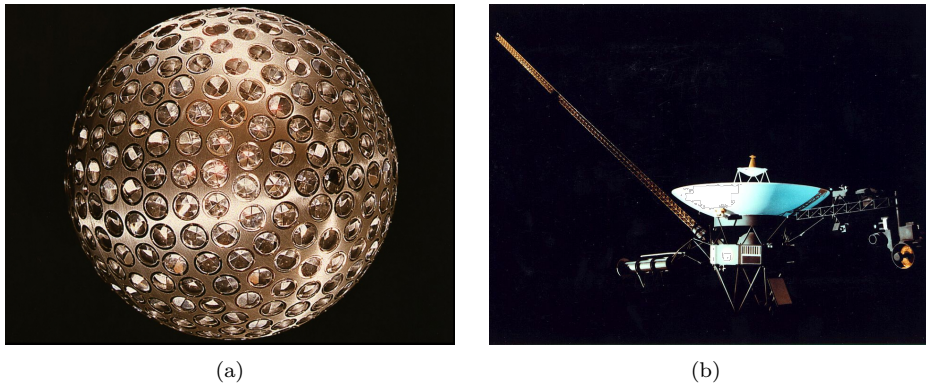


Figure 1.1: Images of a) LAGEOS (photo: NASA) b) Voyager 1 (illustration: NASA). Note the prominence of the HGA on the Voyager spacecraft.

of space debris (Kirchner et al., 2013), allowing for range measurements of about 1 m precision to be obtained for selected large pieces of space debris.

The primary task of the ILRS and the SLR network consists of providing coordinated and systematic range measurements to satellites (equipped with retroreflectors). An additional relatively small but crucial task of the network is Lunar Laser Ranging (LLR), which uses retroreflectors on the lunar surface in the same manner that SLR uses reflectors on satellites. The concept of deploying retroreflectors on the Moon was proposed by Alley et al. (1965), which would allow much greater accuracy at much lower laser power than the proposed passive reflection of laser pulses off the lunar surface (Orszag, 1965). Shortly thereafter, Apollo 11 delivered the first retroreflector to the surface of the Moon in 1969, allowing LLR to be performed (Faller et al., 1969; Alley et al., 1970). Four more retroreflector arrays were to follow, two on Apollo 14 and 15 and two French ones on the Soviet Lunokhod 1 and 2 rovers. Performing LLR is extremely challenging however, due to the very large distance and SLR/LLR's inverse quartic dependency of signal strength on distance (Degnan, 1993). As a result, only very few ground stations are capable of LLR observations. Additionally, the optical properties of the lunar reflectors have degraded over the decades that they have been used (Murphy et al., 2010), further complicating the ranging activities. Nevertheless, LLR has been of exceptional value in a variety of scientific fields, from lunar science and geodesy to fundamental physics, owing to the uniquely long-term and highly accurate range measurements between Earth and another solar system body (Murphy, 2013). Recently, the Apache Point Observatory Lunar Laser-ranging Operation (APOLLO) station has been commissioned (Murphy et al., 2008). The technology of this new station now allows ranging at lunar distance with an accuracy of several millimeters.

While SLR and LLR were being developed (among others) for use in terrestrial and lunar applications, respectively, planetary missions relied almost completely on radiometric techniques for their orbit determination. In planetary missions, signals transmitted between a high gain antenna (HGA) on the satellite (see Fig. 1.1(b) for an image

of the Voyager probe, prominently featuring the HGA) and a large radio antenna on Earth are used for both communication and tracking purposes (Mudgway, 2001). Current missions use radio signals at the X-band, and in certain cases Ka-band, of the radio frequency spectrum, from which higher communications bandwidth and more accurate tracking observables can be obtained than signals in the lower frequency bands, which were used in early missions. Improvements in hardware, for instance the use of multi-wavelength systems (Bertotti et al., 1993), and advances in data analysis techniques (Iess et al., 2014a) have further improved tracking data and processing accuracy over the past decades. The reconstruction of the dynamics of spacecraft and planetary landers has facilitated measurements of *e.g.*, planetary gravity fields, rotational behaviour and tidal deformations, providing the scientific community with valuable information from which the interior of these bodies can be inferred (Section 2.2). Additionally the tracking of planetary missions (including the use of LLR) has resulted in some of the most successful experimental verifications of general relativity (Section 2.3).

Spacecraft tracking by use of radio signals suffers from a number of inherent limitations in precision and accuracy, though, owing to the relatively long wavelength of the electromagnetic signals that are used. Although improvements in tracking data quality are expected from next generation missions (Section 2.1.2), the use of electromagnetic signals with a shorter wavelength, such as the laser pulses used for SLR and LLR, could yield two to three orders of magnitude improvement in the accuracy of the range measurement of planetary missions (Degnan, 2002).

Due to the inverse-quartic signal-strength-to-distance relation of SLR/LLR, this technology is not feasible for use at planetary distance. Instead, an active laser transponder is required on the space segment for the implementation of Interplanetary Laser Ranging (ILR), reducing the signal-strength dependency to inverse square with distance. Such a transponder contains a detector, timer and laser transmitter. A transponder is required at both ends of the link for two-way active laser ranging system. Alternatively, the space segment may contain only a detection system for the implementation of a one-way system (Degnan, 2002). In 2004, the first such measurements using lasers at interplanetary distance were achieved with two-way ranging to the MESSENGER space probe at a distance of 24 million km. This was accomplished by using its altimetry system as a space-based laser ranging system (Smith et al., 2006). For the very first time, this demonstrated the application of laser ranging technology in a planetary mission, opening the door for obtaining mm-cm precise and accurate range measurements at distances on the order of an Astronomical Unit (AU) (Degnan, 2002; Turyshev et al., 2010; Dirksen et al., 2014a). The experiment with MESSENGER, which was an experiment of opportunity performed with non-dedicated hardware, yielded a distance measurement with about 20 cm precision. Although the implementation of the technology is only in its infancy, with the only operational example the one-way laser tracking of the Lunar Reconnaissance Orbiter (LRO) at the Moon (Section 3.3.1), it has the potential to revolutionize the science return of future planetary missions. In this dissertation, these scientific contributions will be investigated and some of the key developments that are needed for its future use are highlighted and discussed.

## 1.2 Research Motivation

With some exceptions, such as LLR and the use of altimetry crossovers, orbit determination of planetary missions (and the science products derived from it) have relied almost exclusively on the use of radiometric tracking types (Section 2.1.1), obtained using a combination of (high gain) radio antennas on the spacecraft and large Earth-based radio dishes, such as those in the Deep Space Network (DSN) (Imbriale, 2002). Despite the significant scientific advances that have been made and the exceptional tracking accuracy that is achievable by means of radio technology, a number of factors limit future improvements in its performance. Due to their relatively long wavelength, radio signals are influenced well beyond a measurable level by propagation media, specifically (non-dispersive) tropospheres and (dispersive) ionospheres and interplanetary plasma (Asmar et al., 2005). Although modelling of the media and the use of multi-wavelength systems can largely mitigate the influence of dispersive media, the influence of the propagation media can limit the future improvement of the accuracy of radio tracking technology (Section 2.1.2). Additionally, at radio wavelengths very large transmitting and receiving systems are required due to the magnitude of the beam divergence angle, with associated difficulties in power and mass budgets, mechanical stability and operational costs. Using a shorter wavelength system for the tracking of planetary satellites is limited by the opacity of Earth's atmosphere at a wide range of frequencies of electromagnetic radiation. However, an atmospheric window at optical frequencies, which allows SLR and LLR to be performed, can be used for both communication and tracking purposes (Bland-Hawthorn et al., 2002). An issue with the usage of the optical atmospheric transmittance window, however, is that signals at optical wavelengths cannot pass through clouds, as opposed to radio signals.

A comparison of a 70 m DSN tracking station and the Next Generation SLR (NGSLR) prototype station is given in Fig. 1.2, showing the dramatic difference in tracking station size. Although the 70 m dish is capable of tracking spacecraft well into the outer solar system, for which the NGSLR station will likely be too small, NGSLR (formerly named SLR2000) will be able to track most planetary spacecraft (McGarry et al., 2006), provided that the space segment is equipped with the suitable instrumentation (Section 1.1).

Although the existing SLR/LLR ground segment is well suited for ILR in most regards, the requirements for an active space segment differ drastically from SLR/LLR, requiring more substantial technology development. However, the required space-based laser technology has matured in a variety of related applications. Prime examples are the use of laser altimetry by a variety of planetary missions such as Mars Global Surveyor (MGS), MESSENGER and LRO (Hussmann, 2014), laser time transfer used by the T2L2 experiment onboard the Jason-2 satellite (Exertier et al., 2010), and laser communications used on the lunar-orbiting LADEE satellite (Borson and Robinson, 2013). These developments can facilitate the faster development of laser ranging technology and operations for interplanetary missions in the near future, by increasing its Technology Readiness Level (TRL), see Sections 3.3.3-3.3.5.

The seminal article by Degnan (2002) presents the proposed measurement concept of ILR in detail, along with a preliminary link budget, showing the feasibility of laser





Figure 1.2: Images of a) a typical DSN tracking dish (photo: NASA) b) the Next Generation SLR (NGSLR) station prototype at the NASA Goddard Geophysical and Astronomical Observatory (photo: NASA).

ranging systems for use in planetary missions, providing accuracy and precision at the mm-cm level. Successful experiments of two-way ranging by MESSANGER (Smith et al., 2006) and one-way detection with MGS (Neumann et al., 2008) demonstrated the first interplanetary laser links. These experiments, however, also showed a variety of operational difficulties associated with ILR. The first operational usage of an ILR concept started in 2009 with one-way laser ranging to the Moon-orbiting LRO satellite (Zuber et al., 2010). Although the distance to LRO is relatively small, the measurement system employs an active space-based detector for the realization of a one-way laser link. However, due to the fact that the quality of the radiometric tracking data for LRO was better than expected, in addition to unforeseen complications with the one-way laser ranging data analysis, the laser ranging data was not included in operational orbit determination (Mazarico et al., 2012). Nevertheless, recent development of expertise in analyzing one-way laser ranging data has led to progress in its use for orbit determination, with laser-only orbit solutions with a quality similar to those from Doppler and altimetry crossover data obtained by Mao et al. (2013); Bauer et al. (2014).

A number of mission proposals has emerged during the past decade which have included an ILR element (a detailed overview is given in Section 3.3.2). In these proposals, ILR is included for a variety of reasons, ranging from primary science instrument (Turyshv et al., 2010) to supporting orbit determination data (Oberst et al., 2012). Although preliminary error estimates for range measurement quality are found in literature, (*e.g.*, Degnan, 2002; Turyshv et al., 2010), a full characterization of the potential contribution of ILR to planetary missions using a detailed error budget has not been performed to date. Additionally, the use of laser ranging in planetary missions has thus far been proposed largely for the improved testing of general relativity, with little analysis of its potential benefits for planetary science goals. Therefore, the goal of this dissertation is twofold. It will address the question of how laser ranging can contribute to achiev-

ing the goals of planetary science missions, by means of quantitative analyses. Also, it will address several key uninvestigated sources of range measurement errors and data analysis shortcomings for ILR. As a result, this dissertation provides vital steps to the future implementation of laser ranging technology in planetary missions, by showing its potential for improving a mission's science return and highlighting some of the main sources of range measurement errors that are distinct from those in SLR/LLR, allowing for a better assessment of hardware development required for an ILR mission.

The work that has led to this dissertation was performed in, and funded by, the European Framework Program 7 (FP7) project called 'European Satellite PARTnership for Computing Ephemerides' (ESPaCE) (Thuillot et al., 2011, 2013). The primary aim of this project is to use a combination of radio science and astrometric observations to improve the ephemerides of small solar system bodies and artificial planetary satellites. In the context of this project, work is also performed on improving reference systems of solar system bodies, such as Phobos and Ganymede, as well as analysis of their rotational behaviour. Additionally, the project includes the investigation of new technologies for future improvements of planetary ephemerides, where the work which led to this dissertation was performed within Work Package (WP) 3: Laser Ranging.

The work that we present in this dissertation is based largely on numerical simulations of laser ranging measurements and subsequent orbit determination and parameter estimation. We opted to develop our own software for this purpose, as discussed in more detail by Dirkx and Vermeersen (2012, 2014), and have set up a generic orbit determination and dynamical space mission analysis framework, based on the Tudat software libraries (Kumar et al., 2012). Our framework is set up in a generic and modular fashion, facilitating its use for the broad range of ILR-related aspects that we investigate here, as well as a wide variety of future applications.

### 1.3 Dissertation Structure

This dissertation addresses the question of whether laser ranging at interplanetary distance has the potential to improve the science return of space missions in the near future, with a focus on planetary science objectives. The core of this dissertation is comprised of Chapters 4-7, each of which contains a journal article in which separate aspects of this aim are investigated. These articles have been peer-reviewed and published (Chapters 4- 6), or are under review at the time of writing of this dissertation (Chapter 7). These four chapters consist of an analysis of the potential scientific contributions that ILR could make to future space missions and contain a quantitative assessment of various sources of error that could limit the quality of the science products. Aspects related to hardware-derived range measurement errors, environment-derived measurement errors and current deficiencies in the models for obtaining scientific parameters from laser range measurements are discussed. To put the contents of these articles into the broader context of existing planetary missions and tracking types, as well as existing SLR and LLR activities and technology, two introductory chapters are included in addition to the current one. In Chapter 2, a description of existing tracking methods for planetary missions is given, as well as a broad discussion of the scientific results that have and can be derived from these data, providing theoretical background for Chapters 4-7 and

detailing the science case for ILR in a general sense. Additionally, we discuss in a qualitative manner how including laser ranging measurements could impact the estimation quality of the various physical parameters from which scientific theories on the interiors of solar system bodies, theories of gravitation, *etc.* can be improved. In Chapter 3, we present the basic operating principle of SLR and LLR and discuss how these technologies can be extended to interplanetary distance. We address technological developments, operational challenges and developments in data analysis that will be required for the successful implementation of ILR.

Chapter 4 is comprised of an article entitled '*Phobos Laser Ranging: Numerical Geodesy Experiments for Martian System Science*' (Dirkx et al., 2014a). In this article, a detailed analysis of the potential science return from the Phobos Laser Ranging (PLR) concept, a Phobos lander mission equipped with a two-way laser ranging system discussed in detail by Turyshev et al. (2010), is presented, in terms of geodetic parameters of Mars, Phobos and Deimos. In this paper, the analysis instead relies on so-called 'consider covariance analysis', instead of using a bottom-up model for the range errors. By using this method, the influence of both random uncorrelated (Gaussian) noise and systematic errors on the range measurements are analyzed. Taking this approach, a parametric analysis of the science return is given in terms of these two types of error sources. This work serves as a demonstration of the potential of scientific breakthroughs that could be facilitated by ILR. Additionally, it shows how different types of errors propagate into the uncertainties of the science observables, providing the context for subsequent analyses of specific error sources.

Both Chapter 5 and Chapter 6 deal with the analysis of such error sources on the quality of ILR science results. In Chapter 5, the article '*Influence of Atmospheric Turbulence on Planetary Transceiver Laser Ranging*' (Dirkx et al., 2014b) is reprinted, in which the influence of both atmospheric turbulence and finite signal strength and pulse length on laser range measurement accuracy and precision is discussed. A general theoretical development of the problem is given, resulting in a more comprehensive theory of the influence of turbulence on the spatio-temporal laser pulse intensity distribution for SLR/LLR/ILR applications than what was heretofore available. The method is illustrated by its application to the PLR concept, providing a quantitative analysis of the influence of atmospheric turbulence and varying laser signal strength on range measurement quality. Additionally, system design aspects that can be used to mitigate the influence of these disturbances are discussed.

Subsequently, a comparative analysis of one- and two-way laser ranging is given in Chapter 6, where the article '*Comparative Analysis of One- and Two-Way Planetary Laser Ranging Concepts*' (Dirkx et al., 2015a) is reprinted. The primary difference between the one- and two-way laser ranging concepts is the influence of clock noise on the laser range measurement error budgets. As such, this chapter contains a detailed analysis of the relation between clock noise and one- and two-way laser ranging measurements and ways in which to mitigate this noise source. The analysis is performed for both a lunar orbiter similar to LRO, and the PLR concept.

In Chapter 7 the article entitled '*Simultaneous Spacetime Dynamics Estimation From Space Mission Tracking Data*' (Dirkx et al., 2015b) is reprinted, where we investigate a potential deficiency in data analysis techniques that can become an important contrib-

utor to the estimation quality of parameters of interest from one-way ILR data, even in the case of perfect (error-free) data. Specifically, we analyze the inherent relativistic coupling between time and space dynamics in the estimation procedure, recognizing the fact that the relativistic influence of estimated parameters on observers' proper times could have a measurable impact on data reduction techniques. Beyond the application to one-way data, our theoretical development can have important consequences for use in (interplanetary) time transfer and relativistic geodesy. Our dynamical approach in this chapter differs from that of the rest of this dissertation in that we apply a fully relativistic model, to consistently represent the gravitational influence of both space and time dynamics.

In Chapter 8, we provide a cohesive discussion of the results given in Chapters 4-7. We present the relative contributions of the various sources of uncertainty in the final science products of a mission employing ILR, as well as methods with which to mitigate them. Subsequently, we present a conceptual comparison to existing tracking techniques and discuss the challenges that remain for the successful implementation of ILR. We summarize the overall conclusions of this dissertation in Chapter 9, where we also present an outlook to the future of interplanetary laser ranging, regarding both the developments in both analyses and hardware that are needed, as well as other issues that will need to be addressed for it to be used in an operational manner in future missions.

---

## Tracking of Planetary Missions

---

For both Earth-orbiting and planetary missions, a wide range of tracking observables is typically available from which the orbit of the spacecraft can be reconstructed, either combined with a dynamical model or in a purely kinematic manner, (*e.g.*, Montenbruck and Gill, 2000; Seeber, 2003; Tapley et al., 2004). The reconstruction of the trajectory of a spacecraft is crucial for a variety of reasons. From an operational point of view, the orbit must be determined and propagated forward in time to optimally plan and execute maneuvers, schedule science observations, *etc.* Also, a precise knowledge of the trajectory is crucial for the processing of data generated by instruments such as cameras, altimeters and radars. For instance, when processing altimetry data from an orbiter, the radial orbit error propagates directly onto the derived altitude measurement. Finally, the determination of the orbit of a spacecraft holds crucial intrinsic value. Specifically, a state history of the spacecraft can be estimated by adjusting a set of model parameters to make the observations best fit a parameterized dynamical and observation model. These parameters can be used to derive properties of the spacecraft's environment, both gravitational and non-gravitational. A number of tracking types, both active and passive, can be used in planetary missions. We give an overview of these techniques and discuss their relative strengths and weaknesses in Section 2.1, focusing on radiometric range and range-rate data.

The gravitational accelerations acting on an orbiter offer the unique possibility to globally measure the gravitational field of a body (and time-variations thereof), from which constraints on a body's interior structure can be derived through the determination of, for instance, gravity field coefficients, rotational variations or Love numbers, (*e.g.*, Konopliv et al., 2011). In addition to being useful for probing gravity fields, orbit reconstruction of (planetary) spacecraft allows for the determination of a variety of non-gravitational forces, primarily atmospheric drag (for spacecraft orbiting bodies with an atmosphere), facilitating an *in situ* determination of atmospheric properties,

(*e.g.*, Mazarico et al., 2008). Additionally, tracking of planetary landers allows the combined measurement of the orbital dynamics, rotational dynamics and tidal deformation of the target body, of which LLR is a prime example (Williams et al., 2001). Although tracking of planetary landers does not allow for the direct determination of gravity field characteristics of the body (barring the use of absolute gravimetry or the exploitation of relativistic clock effects), they provide highly accurate direct measurements of planetary dynamics that are invaluable in the determination of ephemerides. We discuss the various observables in planetary sciences that can be obtained by tracking planetary missions in Section 2.2, including the strengths and weaknesses of various mission and tracking types for their determination.

In addition to being valuable for achieving planetary science objectives, determination of the gravitational acceleration acting on a spacecraft or natural solar system body allows for a wide variety of tests of gravitational physics. Although general relativity has been a highly successful theory of gravity for almost a century, a number of issues lead to postulated alternative theories of gravitational physics. Observing the dynamics of the solar system in general, and the usage of tracking data of planetary missions in particular, offers unique opportunities to test these theories of gravitation, which we discuss in Section 2.3.

## 2.1 Planetary Tracking Data

Tracking data of both artificial and natural solar system bodies can be obtained by a variety of methods, each with its own challenges, advantages and disadvantages. To ascertain whether there is a place for laser ranging in addition to existing methods, we give an overview of existing tracking techniques in Section 2.1.1, where we discuss both typical radiometric techniques, as well as some more exotic methods. In addition to active tracking systems used in space missions, we discuss passive methods which are used for observing solar system bodies, to provide a full and cohesive overview of the measurements currently used in dynamical astronomy of the solar system. Subsequently, we discuss the error budgets of typical radiometric tracking techniques in Section 2.1.2, focussing specifically on the radiometric range and Doppler observations. Finally, we show in Section 2.1.3 the relative strengths of range and range-rate measurements by means of a preliminary analysis.

### 2.1.1 Tracking Types

Radio tracking of spacecraft is typically performed by a set of dedicated Earth-based ground stations, such as NASA's DSN or ESA's ESTRACK system. Orbit determination for most planetary missions relies largely on radiometric Doppler measurements, which encodes the time-averaged range-rate of the space segment w.r.t. the ground station. Essentially, the Doppler observable is obtained by measuring the change in range to the spacecraft over a certain integration time. Typically, the range-rate measurement is integrated over a period of about 60 s, (*e.g.*, Iess et al., 2014a). However, both smaller integration times such as 1-10 s (Lemoine et al., 2013) and larger integration times such as 1000 s (Iess et al., 2009) may be used. Radio tracking of modern space missions

is typically done in X-band ( $\sim 7\text{-}8.5$  GHz) or Ka-band ( $\sim 32\text{-}35$  GHz) (Thornton and Border, 2000), or both simultaneously to account for the influence of the dispersive propagation media (Bertotti et al., 1993). The Doppler data type is often supplemented by radiometric range measurements, which is realized by measuring the light time of a coded radio signal to obtain the direct range between a ground station and the space segment. We discuss the (comparative) data quality of range and Doppler data in more detail in Section 2.1.2.

In addition to the range and range-rate observables, an angular position measurement, realized by Very Long Baseline Interferometry (VLBI) techniques, is routinely used as a supporting radiometric data type. In VLBI, a set of radio telescopes on Earth is simultaneously used to observe the same radio signal originating from the spacecraft. After resolving the cycle ambiguity, *i.e.*, determining the total signal propagation time difference for the different stations, an angular observable may be obtained. The realization of a VLBI angular position observable is made using two similar, but distinct techniques (Lanyi et al., 2007), which differ primarily in the manner in which they resolve the cycle ambiguity. Firstly, the  $\Delta$  Differential One-way Ranging ( $\Delta$ DOR) system uses only one baseline, but requires so-called 'DOR tones' to be present in the signal, resulting in a signal bandwidth on the order of 1 MHz. Using the group delay from the sideband signal, the cycle ambiguity is resolved in  $\Delta$ DOR (Curkendall and Border, 2013). Alternatively, a phase-referencing VLBI method may be used to resolve the cycle ambiguity. Using this approach, many (sometimes  $> 10$ ) ground stations are used, the combined signals received by which can be cross-correlated, allowing the phase delay to be used directly to determine the difference in propagation time between the stations (Duev et al., 2012). By comparing the measurements from the space segment to those from stable astronomical sources such as quasars, the angular position of the spacecraft in the background International Celestial Reference Frame (ICRF) is determined. Both measurement types can yield accuracies at the 1 nrad ( $\approx 0.2$  mas) level, corresponding to an out-of-plane uncertainty of about 150 m per AU of distance to Earth, although the phase-referencing method allows for somewhat better data quality than  $\Delta$ DOR, since the phase delay can be measured to greater accuracy than the group delay.

When comparing ILR with existing tracking methods (Sections 2.1.3 and 8.2), we will focus mostly on the comparison with Doppler measurements. Therefore, we require a mathematical comparison of the two data types. Since a Doppler observable can be modelled as differenced range measurements, we will first describe the model for the range observable, followed by the Doppler observable. We will denote the one-way range observation between station  $A$  (transmitter) and station  $B$  (receiver) by  $s_{BA}^{(1)}$ . From the position functions of these link ends, denoted  $\mathbf{r}_A(t)$  and  $\mathbf{r}_B(t)$ , respectively, the one-way range is calculated as follows:

$$s_{BA}^{(1)}(t_t=t_1) = \left| \mathbf{r}_B \left( t_1 + \frac{s_{BA}^{(1)}}{c} \right) - \mathbf{r}_A(t_1) \right| + \Delta s_{BA}^{(1)}(t_1, t_2) \quad (2.1)$$

$$s_{BA}^{(1)}(t_r=t_2) = \left| \mathbf{r}_B(t_2) - \mathbf{r}_A \left( t_2 - \frac{s_{BA}^{(1)}}{c} \right) \right| + \Delta s_{BA}^{(1)}(t_1, t_2) \quad (2.2)$$

where the first formulation is referenced to the transmission time  $t_t$ , here equal to  $t_1$ ,

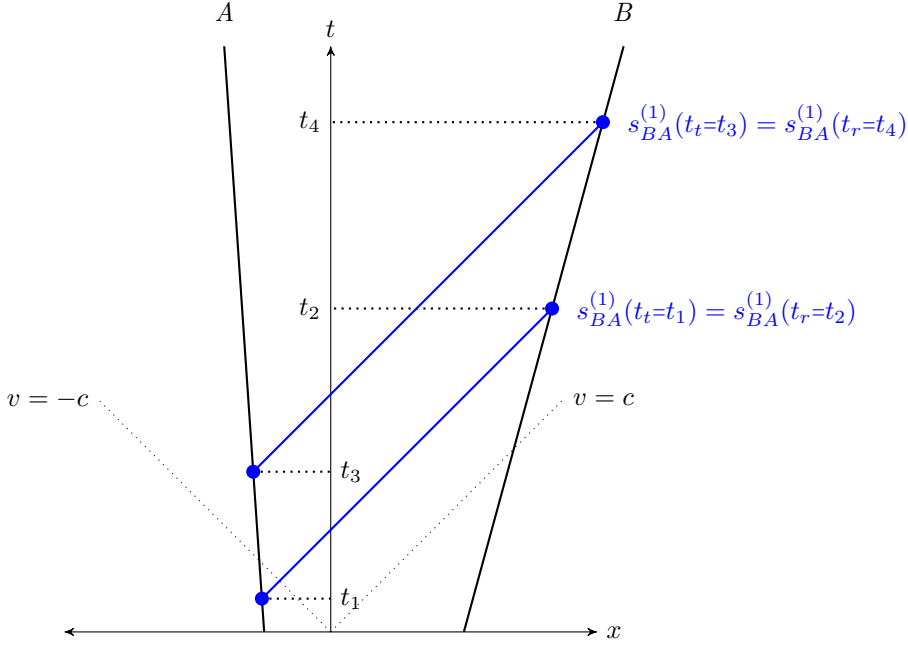


Figure 2.1: Schematic spacetime diagram showing one-dimensional representation one-way range and range-rate observables between link ends  $A$  and  $B$ , which have constant but different velocities (adapted from Fig. 2 of Chapter 6).

and the second one to the reception time  $t_r$ , here equal to  $t_2$ . That is, for the first equation, the transmission time  $t_1$  is assumed to be known, and the reception time and resulting range measurement are calculated from this value. For the second equation, the reception time  $t_2$  is assumed known. The term  $\Delta s_{BA}^{(1)}$  denotes range corrections due to *e.g.*, propagation medium (Sections 2.1.2 and 3.1.4) and relativistic (Section 2.3.2) effects. The two-way range observable is obtained from the combination of the up- and downlink of the signal, including a retransmission time/delay time (Section 3.1.2; Chapter 6).

For a one-way range-rate observable, denoted here as  $\dot{s}_{BA}^{(1)}$ , with an integration time denoted by  $\Delta t_i$  the observable is modelled by (Moyer, 2000):

$$\dot{s}_{BA}^{(1)}(t_r=t_4) = \frac{s_{BA}^{(1)}(t_r=t_4) - s_{BA}^{(1)}(t_r=t_2)}{\Delta t_i} \quad (2.3)$$

$$t_2 = t_4 - \Delta t_i \quad (2.4)$$

$$\dot{s}_{BA}^{(1)}(t_t=t_3) = \frac{s_{BA}^{(1)}(t_t=t_3) - s_{BA}^{(1)}(t_t=t_1)}{\Delta t_i} \quad (2.5)$$

$$t_1 = t_3 - \Delta t_i \quad (2.6)$$

where we have reference the observation to the reception and transmission time (both



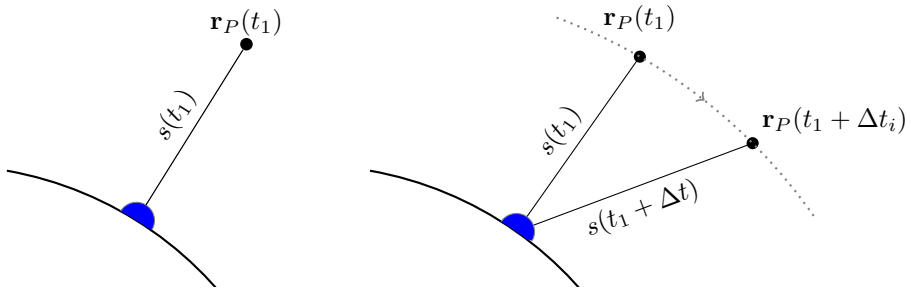


Figure 2.2: Schematic representation of spacecraft tracking observables range (left) and range-rate (right).

of the second range measurement; see Fig. 2.1) in Eqs (2.3) and (2.5), respectively. A schematic comparison of the range and range-rate observable is given in Fig. 2.2. Note that the integration time  $\Delta t_i$  at the two link ends will not be equal due to the relative velocity of  $A$  and  $B$  (see Fig. 2.1). That is, the  $t_4 - t_2 \neq t_3 - t_1$ , as the same number of cycles of the electromagnetic signal are stretch/shrunk due to the Doppler effect. Consequently, the integration time shown in Eq. (2.4) has a different value from that shown in Eq. (2.6) for a given link.

The Doppler data typically provides the strongest information on the orbit of a spacecraft around a planet, as they are in essence local (differential) measurements. The range and angular position observables, however, are absolute position measurements and are currently used largely to determine the position of the orbited planet w.r.t. Earth. This makes these data types crucial for the improvement of planetary ephemerides, (*e.g.*, Fienga et al., 2009; Jones et al., 2015). We discuss these matters in more detail in Section 2.1.3.

Usually, radiometric tracking is performed in a one- or two-way configuration. For a one-way system, only the up- or downlink of the signal is used to obtain the range(-rate) measurement. This setup, however, suffers from the fact that it typically introduces a large error in the processed observable, as it requires the comparison of the clocks onboard the ground and the space segment (Moyer, 2000; Asmar et al., 2005). This difference will be discussed in detail in Chapter 6 for the case of laser ranging systems. A two-way measurement uses both the up- and downlink of the signal to generate a measurement. By combining the up- and downlink, the space- and ground-based clocks no longer need to be compared in an absolute manner, removing a typically dominant source of error in the one-way measurement.

In radio measurements, the two-way observation is obtained by means of signal retransmission on the spacecraft. A radio signal from an Earth-based ground station is amplified, scaled and retransmitted by a transponder on the space segment. This retransmitted signal is then observed by the ground station, allowing a two-way measurement from the combined up- and downlink measurement to be obtained. Since the

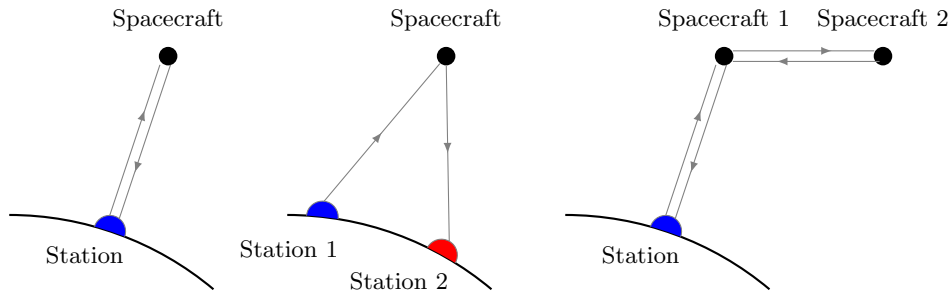


Figure 2.3: Schematic representation of two-way (left), three-way (middle) and four-way (right) data types.

retransmission is not instantaneous, the time delay  $\delta t_B$  is typically measured by the spacecraft and included in the data analysis. The influence of this retransmission delay on the data analysis is analyzed by (Bertone et al., 2013), who speculate that ignoring this retransmission delay may be a solution for a long-standing unexplained phenomenon in spacecraft dynamics: the flyby anomaly (Anderson et al., 2008). The flyby anomaly is an as-yet unexplained difference between the observed and predicted velocity (at the mm/s level) of a number of spacecraft in an interplanetary transfer trajectory as they perform an Earth swingby.

In addition to the one- and two-way range measurement, a so-called three-way measurement is used routinely in spacecraft tracking (Moyer, 2000). The three-way measurement is essentially a two-way measurement in which the transmitting and receiving ground station are different (Fig. 2.3). Such a setup may be needed for observation geometry reasons, especially for missions to the outer solar system with very long light times between the spacecraft and the ground. However, the use of a three-way system has the complication that it requires the comparison of the two Earth-based systems. As a result, the systematic errors that will cancel in a two-way system are not immediately cancelled in a three-way system. Novel calibration methods (Shin et al., 2014) can be used to attain similar data quality as from two-way data. It should be noted that the term 'three-way' is something of a misnomer, since there are still only two signal paths. In SLR systems, a three-way measurement is termed bistatic (Degnan, 1993).

For more exotic mission geometries, tracking data types with more than two signal paths can also be used. For instance, the SELENE mission, which consisted of two lunar orbiters, employed a four-way Doppler tracking technique (Namiki et al., 2009). In this four-way technique, one of the satellites was used as a relay to the other spacecraft, so that a total of four signal paths were used in the full up- and downlinks (Fig. 2.3). In the SELENE mission, the use of the four-way system allowed, for the first time, direct tracking of a satellite at the far side of the Moon, resulting in a global lunar gravity field of much higher spatial resolution compared to previous missions (Goossens et al., 2011).

Although the radiometric Doppler measurements, supplemented by range and angular position observables, are typically the main tracking types used for orbit determination of planetary missions, a number of additional measurements can be used for their

trajectory reconstruction. We summarize the ones that are most relevant in the context of this dissertation here:

- **Altimetry crossovers.** Missions which use an altimetry system (LRO, MGS, MESSENGER, BepiColombo, JUICE, *etc.*) can use the altimetry measurements to improve their orbit determination by means of crossovers (Hussmann, 2014). Crossovers have been used for a number of Earth-orbiting missions and were first applied in a planetary context for MGS (Rowlands et al., 1999; Neumann et al., 2001), improving the satellite’s orbit reconstruction quality and the gravity field determination. The crossover method exploits the fact that multiple altimetry ground tracks will regularly cross one another. At the crossing point of the ground tracks, the body-fixed latitude and longitude of the spacecraft will be (approximately) equal for both ground tracks. The altitude difference at the times at which the two ground tracks pass the crossover point are deduced from the altimetry measurements, resulting in a differential altitude measurement between crossover times  $t_1$  and  $t_2$ . A prime example of the use of altimetry crossovers is the orbit determination of LRO (Mazarico et al., 2012), where an improvement in arc overlaps by a factor of 3 is obtained in certain mission phases. In addition to allowing for an improved orbit determination, crossovers may be used to estimate the deformation Love number  $h_2$  of the body being orbited (see Section 2.2.3), as done for the Moon by LRO (Mazarico et al., 2014a). Currently, this is also the primary method by which JUICE is expected to retrieve the Love number  $h_2$  of Ganymede (Steinbrügge et al., 2014).
- **Same beam interferometry.** Same beam interferometry (SBI) is a radio tracking technique that is based on in-beam phase-referencing VLBI, in which the calibrator and target are visible at the same time, (*e.g.*, Fomalont et al., 1999; Cao et al., 2014). For the planetary tracking application of SBI, two spacecraft at close angular separation are simultaneously tracked by multiple ground stations (Folkner and Border, 1990), instead of simultaneously tracking a target object and reference source. This technique can be used to determine the differential range (to the ground stations) by comparison of the (phase) delays from the two spacecraft, allowing for a differential range to be obtained directly, as well as a differential angular separation following cross-correlation. Due to the very small angular separation between the two targets, the influence of the propagation medium on the observations is reduced, since only the gradient of the medium’s influence over the small separation distance of the two beams influences the observable, allowing for exceptionally accurate differential observations. This technique was demonstrated by the combined tracking of the Magellan and Pioneer spacecraft at Venus (Border et al., 1992), where a measurement accuracy in the differenced range of 10 ps over 60 s integration time was achieved. It was used operationally by the SELENE mission in lunar orbit (Kikuchi et al., 2009), where a sub-ps differential measurement accuracy was demonstrated (also at 60 s integration time). The addition of the SBI data to the orbit determination resulted in an order of magnitude reduction in arc overlap difference and an improved lunar gravity field determination (Goossens et al., 2011). Furthermore, SBI has been used to improve the relative

positioning of the Change'E 3 rover and lander (Liu et al, 2014). SBI has been proposed for usage in lunar landers (Bender, 1994; Gregnanin et al., 2012), where potential differential range measurements with an accuracy of  $<0.1$  mm would allow exceptional refinement of lunar interior structure models.

- Time transfer. Time transfer is a method by which the clocks of separated observers may be synchronized (in the relativistic sense of the term) using the transmission and reception of electromagnetic signals, such as laser pulses or radio signals (Bjerhammar, 1985; Klioner, 1992). In addition to the typical tracking systems (optical or radio), highly stable clocks are required to perform time transfer. Although time transfer is not currently used to improve the orbit determination of spacecraft, the relativistic clock effects (Section 2.3.2), to which the time transfer observable is sensitive, (*e.g.*, Blanchet et al., 2001), could be exploited to improve the geodetic (Müller et al., 2008a) and relativistic (Angéil et al., 2014) measurements. We discuss the time transfer method in more detail in Section 3.3.4 in the context of synergy with active laser ranging systems. Furthermore, the main goal of Chapter 7 is to develop a method by which time transfer can be incorporated into the orbit determination and parameter estimation procedures, by recognizing the fundamental coupling between time and translational dynamics.

Other techniques include the use of accelerometers, (*e.g.*, Flury et al., 2008), optical landmark tracking (*e.g.*, Konopliv et al., 2002), pulsar timing (*e.g.*, Sheikh et al., 2006), gravity gradiometry (*e.g.*, Rummel et al., 2011) and autonomous spacecraft navigation (*e.g.* Wertz, 1992), which are less relevant in the context of this dissertation.

In addition to the active systems described above, which can be used for tracking space missions, passive (*i.e.*, requiring no active systems in space) observations of solar system bodies are used for reconstructing their dynamical behaviour. These data types are the primary input for ephemeris generation of bodies to which no orbiters have been flown yet. Additionally, they are important for the determination of ephemerides over longer time periods, supplementing accurate spacecraft tracking techniques to observationally constrain ephemerides over a longer time span, more than a century in certain cases (Jacobson and Lainey, 2014). As such, we briefly present these techniques here, as their usage is crucial in a complete dynamical characterization of solar system bodies.

- Radar ranging. Radar ranging is a technique that uses very powerful radio signals, reflected off the target body. The detection of these reflected signals are then used to infer the range to that body, as well as a number of its physical characteristics, such as shape and rotational state. Although the measurement accuracy is orders of magnitude worse than that of spacecraft tracking, on the order of 1 km for terrestrial planets (Folkner et al., 2009), it does not require any active systems at the target body. However, just as SLR, radar ranging is limited by an inverse quartic variation of signal strength with distance. Nevertheless, radar ranges out to the Galilean moons have been obtained using the Arecibo antenna, with an accuracy of about 5-15 km (Harmon et al., 1994). A time history of measurements of the reflected waveform can be used to infer a shape and rotation model of the target body (Mitchell et al., 1998) by analyzing the changes over time in

the reflected signal. Additionally, radar ranging can also be used to determine the instantaneous spin rate and spin axis orientation (Margot et al., 2007). By measuring the temporal intensity pattern from the reflected signal at multiple stations, the speckle pattern that the reflecting body imposes on the waveform may be used to correlate the signal detection at the two stations and obtain independent and much more accurate information on the rotation of the body than from typical concurrent analyses of topography and rotation.

- **Astrometry.** Optical observations of celestial bodies such as planets and moons (both by Earth- and space-based instruments) can be used to obtain astrometric measurements of these bodies. An astrometric observation consists of the angular position (right ascension and declination) of the target body in the sky. This observation is obtained by measuring the position of the target body w.r.t. the positions of known stars and resultantly calculating its position, (*e.g.*, Kovalevsky and Seidelmann, 2004). Although astrometric observations are of relatively low quality (at best around 0.1 as) compared to VLBI angular position observables (with sub-mas accuracy), (*e.g.*, Folkner et al., 2014), they can be made without the need for an active transmitter or receiver on the target body, allowing observations of any sufficiently bright body in the solar system. Usable astrometric observations of solar system bodies go back more than a century. Lainey et al. (2007) used observations as far back as 1877 for ephemeris generation of the Martian moons, for instance. The GAIA mission, which is still operational as of the writing of this dissertation, will compile astrometric observations of background stars to an unprecedented level of accuracy (on the order of several  $\mu$ as for strong sources), as well as observe small solar system bodies. Both these types of observations will improve the planetary ephemerides (Fienga, 2012). Firstly, re-reduction of old photographic plates using the new GAIA catalogue will result in more accurate astrometric data from these older plates. Secondly, direct astrometric observations of around 400,000 small solar system bodies such as asteroids will provide additional, highly accurate (about 5 mas), observations for the generation of ephemerides. Historically, optical astrometry has been used as a passive method for the positioning of early (Earth-orbiting) spacecraft, using scattered and reflected sunlight from the spacecraft surface (*e.g.*, Veis, 1963). To enhance the visibility of the spacecraft, the use of stroboscopic beacons on the spacecraft has been applied. Alternatively, for using optical astrometry at larger (for instance lunar) distances, the artificial comet concept was used (Shklovskii et al., 1959), in which a gas was expelled from the spacecraft that greatly enhances the amount of sunlight that is scattered towards Earth from the (vicinity of) the spacecraft.

Using the measurements obtained by both the active and passive techniques described in this section, ephemerides of solar system bodies as well as the trajectories of spacecraft are estimated. To process the measurements, models for both the dynamical environment of the bodies (initial state, gravity field coefficient, empirical correction factors, *etc.*), and a number of environment- and hardware-related corrections to the measurements are used (see Section 3.2 for a more elaborate discussion of such corrections for range measurements). By adjusting various parameters in these models, an

optimum solution of these parameters is computed, which produces a best fit of the measurements, (*e.g.*, Montenbruck and Gill, 2000; Tapley et al., 2004; Fienga et al., 2009; Folkner et al., 2014). This process is discussed in some more detail in Section 5 of Chapter 4.

### 2.1.2 Radiometric Tracking Data Quality

The potential use of ILR is contingent upon its data being able to provide scientific results that are complementary or competitive with existing systems. To support the comparison of ILR data with existing radiometric tracking data, we provide a brief overview of the main sources of error in these data, as well as near-future potential for their improvement. Detailed discussions of sources of systematic and random noise for range and Doppler data are given by Thornton and Border (2000); Asmar et al. (2005); Iess et al. (2014a).

The typical precisions of radiometric tracking techniques, as quantified by the postfit estimation residuals, are currently at the level of 0.02-0.1 mm/s at 60 s integration time for range-rate measurements at X-band (*e.g.*, Thornton and Border, 2000; Marty et al., 2009; Konopliv et al., 2011; Mazarico et al., 2014b; Iess et al., 2014a) and 0.5-5 m for range measurements (*e.g.*, Thornton and Border, 2000; Kuchynka et al., 2012; Folkner et al., 2014; Iess et al., 2014a). In addition to the random noise, systematic errors may be present in the measurements, which are more difficult to quantify in detail than the random noise. For Doppler measurements, the short-periodic systematic errors are typically at a negligible level (Iess et al., 2014a), although small low-frequency systematic errors (periods on the order of 1,000-100,000 s) may be present. Despite the typical absence of short-periodic error source in Doppler tracking, an anomalous signal in the Doppler measurements (at 1 s integration time) of MRO is found by Genova et al. (2015), who obtain an improvement in postfit residual of a factor of 2-3 after filtering this anomalous behaviour. Whether the source of this error is due to a modelling error or an inherent noise source in the data remains to be investigated. In contrast to Doppler data, the level of systematic errors are typically quite large for range measurements, comparable to the random noise at the m level (Thornton and Border, 2000; Iess et al., 2014a). For situations with a small solar separation angle, this value increases to tens of meters and above, as the influence of the interplanetary plasma becomes stronger.

The inherent noise sources can be classified as due to ground- and space-segment hardware instabilities and due to the propagation media. Mechanical instabilities at both the spacecraft and the ground station, as well as clock noise, decrease the quality of the measurements, although not at a dominant level for two- and three-way Doppler tracking (Asmar et al., 2005), where the absolute range bias is not relevant (see Section 2.1.1). For range measurements, however, these effects are important contributors to the systematic noise level (Thornton and Border, 2000; Iess et al., 2014a). The influence of the propagation medium is due to interplanetary plasma, the ionosphere and the troposphere of the Earth (as well as potentially the body being orbited by the spacecraft). The influence of the Earth's ionosphere can be largely removed by using GPS measurements of the total electron count (TEC) and mapping this to the line-of-sight of the interplanetary link (Thornton and Border, 2000). The tropospheric influence can

be modelled at the 0.01-0.03 mm/s level (at 60 s integration time) using typical current meteorological measurements at the ground station (Iess et al., 2014a), a value which can be improved by a factor of about 10 by using additional microwave radiometry measurements at the ground station (Asmar et al., 2005). The influence of interplanetary plasma can be modelled or estimated during data analysis to reduce its influence on the data (Moyer, 2000; Verma et al., 2014). The influence of plasma becomes stronger as the radio signal path passes closer to the Sun, where the plasma density is larger. This is shown by, (*e.g.*, Iess et al., 2014a; Mazarico et al., 2014b), who find that the signal quality degrades significantly for solar separation angles smaller than 30-40°, causing gaps of high quality data during the orbit determination.

A crucial improvement in radiometric tracking data quality can be obtained by simultaneously using multiple wavelengths. Since the dispersive media (interplanetary plasma and ionosphere, but not the troposphere at radio wavelengths) influence the propagation of electromagnetic radiation at different wavelengths in a different but predictable manner, combining observations at multiple wavelengths allows the removal of the majority of the plasma and ionospheric noise. This calibration was performed with ranging measurements at S- and X- band by the Viking landers (Reasenberg et al., 1979) and Voyager spacecraft (Krisher et al., 1991). Bertotti et al. (1993) proposed the use of multi-frequency Doppler measurements, as opposed to previous experiments with dual-frequency range data. This approach was demonstrated using the instrumentation onboard the Cassini spacecraft (Bertotti et al., 2003) obtaining a Doppler noise level close to 1  $\mu\text{m/s}$  level in some cases (when scaled to 1000 s integration time) at small solar separation angles, providing a much improved estimate of the relativistic parameter  $\gamma$  (see Section 2.3.3). Unfortunately, the Ka-band transponder on Cassini suffered a malfunction, preventing plasma noise cancellation on the downlink during the Saturn phase. The use of multiple wavelengths largely mitigates the issue of tracking at small solar separation angles, where the data quality of single-frequency systems degrades due to the larger influence of the Sun's plasma environment. The combined X- and Ka-band approach is also to be used on the BepiColombo (Iess et al., 2009), JUICE (Iess et al., 2013) and Juno (Tommei, et al. 2015) missions, which have tracking data quality requirements of 0.01 mm/s at 60 s integration time and 3  $\mu\text{m/s}$  at 1000 s integration time. However, as discussed above experience with the dual-frequency link on Cassini has shown data noise levels down to 1  $\mu\text{m/s}$  at 1000 s in some cases, making it likely that these future missions will be able to go beyond their required 3  $\mu\text{m/s}$  range-rate requirement. Additionally, upcoming missions such as JUICE and BepiColombo will employ a wideband ranging system (Iess and Boscagli, 2001), allowing two-way range measurements with a predicted accuracy of down to 20 cm.

In addition to these inherent measurement errors, analysis of Doppler data using typical double precision floating-point representation (Goldberg, 1991) introduces substantial so-called numerical noise (Zannoni and Tortora, 2013), since the Doppler observable is obtained by differencing two large values, where only the small difference between the range at the start and end of the integration time represents the observable, as shown in Eqs. (2.3) and (2.3). Furthermore, the representation of time as seconds since J2000 (or some the reference epoch), using a single double-precision variable, will introduce numerical time biases due to round-off errors (Moyer, 2000). Similar issues arise in the

simulation and processing of ILR data, where relative range resolution at the  $10^{-14}$ - $10^{-15}$  level is required, and extremely accurate time representation is crucial. In our software used in Chapters 4-7, we apply a time representation with sub-fs resolution and relative range resolution of  $\approx 10^{-19}$ , translating to a range resolution of 15 nm per AU.

### 2.1.3 Preliminary Comparison of Tracking Types

In orbit determination of planetary spacecraft, Doppler measurements are typically much more valuable than the range or angular position measurements, (*e.g.*, Fienga et al., 2009). This is due to the combination manner in which these observables are generated, and how their data noise levels differ (Section 2.1.2). In this section, we conceptually discuss how these two different data types contain different information content on the behaviour of the spacecraft and the body that it orbits. In Section 8.2, we will elaborate this discussion with a quantitative comparison of radiometric range and Doppler with ILR tracking data.

The reason that Doppler data is generally the data type of choice for estimating the orbits planetary spacecraft becomes clear when comparing the typical noise levels of the techniques (Section 2.1.2). As can be seen from Eq. (2.3), the range rate measurement is obtained from the range difference at a time  $t$  and time  $t + \Delta t_i$ . As a result, a range-rate measurement with a noise level of 0.05 mm/s over an integration time of 60 s is sensitive to a range difference of 3 mm (over this period of 60 s), compared to the absolute range accuracy of 1 m of the direct range measurements.

The large discrepancy between the quality of the two types of observables is due to the differenced range nature of the Doppler observable. This causes the influence of systematic range errors to be removed, since they are not manifested in Eq. (2.3). For range measurements, however, the total range measurement including all its error sources, is used, resulting in a much larger error budget. It should be understood that the method by which the range and range-rate measurements are generated is quite different and a range-rate measurement is not realized by measuring range values at time  $t$  and  $t - \delta t_i$ . Instead, a range-rate measurement is generated by counting the number of cycles of the electromagnetic signal over the integration time, resulting in an observable that can be equivalently modelled by Eqs. (2.3) and (2.5). Therefore, the range-rate measurement is not obtained directly by differencing two realizations of a range measurement.

An advantage of the absolute nature of the range (and angular position) measurements, though, is that they can be used to observe effects that are manifested as very slow variations in range. For instance, a range measurement with a precision of 0.05 mm/s will not be able to properly distinguish a physical effect from the observation noise that causes changes in range of  $<0.05$  mm/s over the integration time  $\Delta t_i$ . Two range measurements with a precision of 1 m spread  $2 \cdot 10^5$  seconds apart, though, will be able to observe such an effect with an accuracy of 10%. As a result, range and angular (VLBI) measurements (which provide an absolute position perpendicular to the line of sight) are more valuable in determining parameters with long-periodic or slow secular influences on the observations.

This makes range and VLBI observations very valuable for use in the creation of



Table 2.1: Examples of relative influence of position and velocity of spacecraft about body and body about Sun.

Case	$ r_{P,I} $ [m]	$ r_{SC,P} $ [m]	$\frac{\mu_P}{\mu_S}$ [-]	$\frac{\dot{r}_{P,I}}{\dot{r}_{SC,P}} \cdot \frac{r_{SC,P}}{r_{P,I}}$ [-]
Mercury (1000 km altitude)	$5.80 \cdot 10^{10}$	$3.44 \cdot 10^6$	$1.66 \cdot 10^{-7}$	$1.12 \cdot 10^{-2}$
Mars (500 km altitude)	$2.28 \cdot 10^{11}$	$3.89 \cdot 10^6$	$3.21 \cdot 10^{-7}$	$1.24 \cdot 10^{-4}$
Jupiter (70,000 km altitude)	$7.80 \cdot 10^{11}$	$1.40 \cdot 10^8$	$9.53 \cdot 10^{-4}$	$7.79 \cdot 10^{-5}$
Saturn (180,000 km altitude)	$1.44 \cdot 10^{12}$	$1.40 \cdot 10^8$	$2.86 \cdot 10^{-4}$	$1.28 \cdot 10^{-4}$

planetary ephemerides (Pitjeva, 2001; Fienga et al., 2009; Jones et al., 2015), as opposed to the value of Doppler in determining the orbit of the spacecraft around the target body, as planetary orbits imprint long-periodic effects on the measurements (on the order of years). Although the range-rate measurement is not insensitive to the spacecraft's absolute position in the solar system, since the body  $P$  which the satellite orbits will have a different barycentric velocity if it is at a different point in the solar system (assuming it to have a roughly circular orbit), the relative influence of the spacecraft's state relative to the body  $P$  on the range rate will be much greater. Examples of various other physical parameters  $q$  which will be exhibited as slow variations in the range will be highlighted throughout Sections 2.2 and 2.3, where we discuss the parameters that are typically estimated from space mission tracking data.

To demonstrate the relative importance of position and velocity in determining the orbit of a spacecraft and the ephemeris of a planet, we decompose the state of a spacecraft  $SC$  orbiting a solar system body  $P$  as follows:

$$\mathbf{r}_{SC,I} = \mathbf{r}_{P,I} + \mathbf{r}_{SC,P} \quad (2.7)$$

where the first component of the subscript denotes the body of which the position  $\mathbf{r}$  is denoted and the second subscript denotes the origin of the frame in which it is expressed, where  $I$  denotes the inertial (*i.e.*, barycentric) frame. To illustrate the relative contributions of range and range rate observations, we assume that the body  $P$  is in a circular orbit about the barycenter, and that the spacecraft is in a circular orbit about the body  $P$ , so that their velocity  $v_c$  w.r.t. the body they orbit becomes:

$$v_c = \sqrt{\frac{\mu}{r}} \quad (2.8)$$

where  $\mu$  denotes the gravitational parameter of the central body and  $r$  denotes the (assumed constant) distance of the orbiting body from the central body  $P$ .

The relative influence of bodycentric and barycentric velocity may be approximated by:

$$\frac{\dot{r}_{P,I}}{\dot{r}_{SC,P}} = \sqrt{\frac{\mu_S}{\mu_P}} \sqrt{\frac{r_{SC,P}}{r_{P,I}}} \quad (2.9)$$

where the subscript  $S$  denotes quantities associated with the Sun. As we illustrate with

several examples in Table 2.1, this will lead to the following for most planetary missions:

$$\frac{\dot{r}_{P,I}}{\dot{r}_{SC,P}} \frac{r_{SC,P}}{r_{P,I}} = \sqrt{\frac{\mu_S}{\mu_P}} \left( \frac{r_{SC,P}}{r_{P,I}} \right)^{3/2} \ll 1 \quad (2.10)$$

As a result, the relative influence of the spacecraft's velocity, and resultantly the range-rate, is more important for determining the state of the spacecraft about the body  $P$  and the relative influence of the spacecraft's position, and resultantly the range, is more important for determining the ephemeris of body  $P$  about the Sun. Since the period of the spacecraft orbit is much smaller than the planet's orbit, the above indicates that (at least conceptually) the range data are better suited to measuring the global dynamics. This comparison is quantitatively linked to the relative quality of the range and Doppler data in Section 8.2. Although we observe a wide range of values of the left hand side of Eq. (2.10) for the various test cases we show, the values clearly verify our statement of the inequality. This shows that much more information content encoded in the range observable comes from the body  $P$  than from the spacecraft  $SC$ . However, it must be understood that these values only hold for the assumptions of circular orbiters and circular planetary orbits. Although the circular planetary orbit assumption is reasonable, highly eccentric orbits, such as those of Juno or MESSENGER, will have a substantial impact on the value of the inequality in Eq. (2.10). Nevertheless, the very low values of its right-hand side shown in Table 2.1 leave ample margin for its validity beyond the circular spacecraft orbit assumption.

## 2.2 Science Return: Solar System Bodies

Science products obtained from the tracking of planetary missions have been invaluable for our understanding of the interiors of the bodies in our solar system, with important implications for their origin and evolution, (*e.g.*, de Pater and Lissauer, 2001). Future missions using laser ranging technology will benefit from improved range measurement accuracy and precision, which may reach values down to 1 mm (Section 1.2), further improving our understanding of bodies in our solar system (and of exoplanetary systems by extrapolation). In this dissertation, Chapter 4 gives a detailed analysis of the potential science return from a Phobos lander performing two-way laser ranging to Earth, providing a simulation demonstration of the potentially revolutionizing influence that ILR could have on space mission science return.

In this section, we provide an overview of the types of characteristics of solar system bodies that tracking of planetary missions has provided information on in the past, and can provide in future missions. We address the various physical phenomena that are measured and how they relate the science goals of space missions. We relate the discussion of the various observables to the discussion in Section 2.1.3, indicating the relative importance of the potential addition of laser ranging technology, compared to existing data types.

For the determination of the interior structure and composition of a body, the combination of the various geodetic parameters, as well as other measurements (magnetic, geological, thermodynamical) can be used. By combining the various data sets, the

best constraints on a wide range of parameters that determine the characteristics of the body can be obtained, as is done by *e.g.*, Konopliv et al. (2011) for Mars, Williams et al. (2014) for the Moon and Baland et al. (2014) for Titan. In this section, we will focus on describing the physical processes that lead to the various observable geodetic parameters. Detailed analysis of the relation between these parameters and the interior structure and evolution of these bodies is outside the scope of this dissertation, though, and is discussed in more detail by *e.g.* Murray and Dermott (1999); de Pater and Lisauer (2001); Bertotti et al. (2003b). We discuss the estimation and interpretation of gravity fields in Section 2.2.1, rotational dynamics in general and librations in particular in Section 2.2.2 and the effects of tidal deformation on both the shape and gravity field of a body in Section 2.2.3. Finally, we give an overview of the creation and application of planetary ephemerides in Section 2.2.4. The contents of this section serve to illustrate the contribution of tracking of space missions to the planetary science community but is not an exhaustive survey of planetary interiors.

## 2.2.1 Gravity Fields

The quintessential product of space geodetic techniques is a body's (static and time-variable) gravity field, which is described by the body's gravitational potential  $U(\mathbf{r}, t)$ . The gravitational potential  $U$  may be calculated from the (matter) density distribution  $\rho$  as follows, (*e.g.*, Torge, 2001)

$$\nabla^2 U(\mathbf{r}, t) = 4\pi G\rho(\mathbf{r}, t) \quad (2.11)$$

where  $G$  represents Newton's gravitational constant. This equation is the (differential form of the) fundamental relation for determining the potential  $U$  in the classical limit. We will show the generalized relativistic version of this law in Section 2.3.1. Gradients in the gravitational potential cause the main accelerations  $\ddot{\mathbf{r}}$  of solar system bodies (both natural and artificial) from:

$$\ddot{\mathbf{r}}(\mathbf{r}, t) = \nabla U(\mathbf{r}, t) \quad (2.12)$$

As a result, reconstructing the dynamics of both solar system bodies and spacecraft is very well suited to the characterization of the gravitational fields of the bodies in our solar system. Typically, gravity fields of solar system bodies are represented as a spherical harmonic expansion of the potential  $U$ , (*e.g.*, Kaula, 1966):

$$U(r, \phi, \lambda) = \frac{GM_P}{r} \sum_{l=0}^{\infty} \left(\frac{R_P}{r}\right)^n \sum_{m=0}^{\infty} (\bar{C}_{nm} \cos(m\lambda) + \bar{S}_{nm} \sin(m\lambda)) \bar{P}_{nm}(\sin(\phi)) \quad (2.13)$$

where  $M_P$  denotes the total mass of the body, and the mass distribution is quantified by the normalized spherical harmonic coefficients  $\bar{C}_{nm}$  and  $\bar{S}_{nm}$  of degree  $n$  and order  $m$ .  $\bar{P}_{nm}$  denotes the normalized associated Legendre polynomials. The parameters  $\phi$  and  $\lambda$  denote the body-fixed latitude and longitude at the point where the gravitational potential is evaluated,  $r$  denotes its distance from the center of body  $P$  and  $R_P$  denotes the equatorial radius of body  $P$ . The series in Eq. (2.13) converges outside the smallest circumscribing sphere of the body  $P$ . A different, but mathematically equivalent

manner in which to represent Eq. (2.13) is with the use of symmetric trace free (STF) tensors (Hartmann et al., 1994). The use of this method is rare in most astrodynamics applications, but prevalent in the field of relativistic celestial mechanics (Kopeikin et al., 2011).

The spherical harmonic expansion may also be written in terms of the unnormalized coefficients  $C_{nm}$  and  $S_{nm}$ , and unnormalized associated Legendre polynomials  $P_{nm}$ , where  $\bar{P}_{nm}\bar{C}_{nm} = P_{nm}C_{nm}$  and  $\bar{P}_{nm}\bar{S}_{nm} = P_{nm}S_{nm}$ , with, (*e.g.*, Montenbruck and Gill, 2000):

$$\begin{Bmatrix} \bar{C}_{nm} \\ \bar{S}_{nm} \end{Bmatrix} = \sqrt{\frac{(n+m)!}{(2-\delta_{0m})(2n+1)(n-m)!}} \begin{Bmatrix} C_{nm} \\ S_{nm} \end{Bmatrix} \quad (2.14)$$

where  $\delta_{nm}$  represents the Kronecker delta. In certain situations, the  $m = 0$  coefficients are represented by  $J_n$ , with:

$$J_n = -C_{n0} \quad (2.15)$$

which are termed the (unnormalized) zonal coefficients.

The spherical harmonic coefficients  $\bar{C}_{nm}$  and  $\bar{S}_{nm}$  are related to the body's internal mass distribution through, (*e.g.*, Lambeck, 1988):

$$\begin{Bmatrix} \bar{C}_{nm} \\ \bar{S}_{nm} \end{Bmatrix} = \frac{1}{M_P(2l+1)} \iiint_P \left(\frac{r}{R_P}\right)^n \bar{P}_{nm}(\sin(\phi)) \begin{Bmatrix} \cos(m\lambda) \\ \sin(m\lambda) \end{Bmatrix} dV \quad (2.16)$$

Since the fraction  $r/R_P$  is always smaller than 1, the higher the degree  $n$  of the gravity field coefficients, the less the coefficients are influenced by the mass distribution of the deep interior of the body (small  $r$ ).

Due to the formulation of the spherical harmonic coefficients, the influence of coefficients of degree  $n$  and order  $m$  on the gravitational potential (and resultantly the acceleration on an orbiting spacecraft) exhibits characteristic wavelengths with a size of  $2\pi R_P/n$  (north-south) and  $2\pi R_P/m$  (east-west). As a result, the higher degree and order effects are manifested in planetary tracking data as signals with a shorter period. Therefore, the local nature of Doppler observables makes this data type much more suited to the determination of especially the higher degrees and orders of planetary gravity fields than range measurements (Section 2.1.3). Nevertheless, exceptionally accurate range measurements that are expected from ILR could have a better sensitivity to gravitational perturbations than current Doppler tracking data, at least for the long wavelength (low  $n$ ) coefficients. Resultantly, our brief overview of planetary gravity field science in this section will be mostly limited to that which relates to the low degrees and orders, without going into detail on the science return from high degree gravity fields.

For the Earth, a number of dedicated missions such as GRACE and GOCE have contributed to the determination of Earth's gravity field to high temporal and spatial resolution. For the  $C_{20}$  field coefficient estimation, however, SLR data from a number of geodetic satellites such as LAGEOS I/II continue to provide the best information (Sośnica, 2014), due to the aliasing of errors in the ocean tide models with gravity field determination from LEO satellites (Chen and Wilson, 2008) and the near polar orbits of GRACE/GOCE.

Table 2.2: Examples of estimated gravity fields of selected solar system bodies, including the value and (formal) uncertainty of  $J_2$  gravity field coefficient; (f) indicates data from flybys; D/O indicates maximum degree and order of static field.

Body	D/O	$J_2$	$\sigma_{J_2}$	Source
Moon	900 (full)	$2.0 \cdot 10^{-4}$	$6.0 \cdot 10^{-10}$	GRAIL, Lemoine et al. (2014)
Mercury	50 (full)	$5.0 \cdot 10^{-5}$	$1.5 \cdot 10^{-9}$	MESSENGER, Mazarico et al. (2014b)
Phobos	$J_2, C_{22}$	$1.1 \cdot 10^{-1}$	$6.7 \cdot 10^{-3}$	MeX (f)/astrometry, Jacobson and Lainey (2014)
Mars	110 (full)	$2.0 \cdot 10^{-3}$	$3.1 \cdot 10^{-11}$	MGS, Mars Odyssey, MRO, Konopliv et al. (2011)
Jupiter	$J_{2-4;6}; C, S_{22}$	$1.5 \cdot 10^{-2}$	$1 \cdot 10^{-6}$	Pioneer/Voyager (f), Campbell and Synnott (1985)
Titan	3 (full)	$3.2 \cdot 10^{-5}$	$5.6 \cdot 10^{-7}$	Cassini (f), Iess et al. (2012)
Ganymede	$J_2, C_{22}$	$1.3 \cdot 10^{-4}$	$2.9 \cdot 10^{-6}$	Galileo (f), Anderson et al. (1996)
Earth	280 (full)	$1.1 \cdot 10^{-3}$	$3.5 \cdot 10^{-13}$	15 spacecraft, Mayer-Guerr et al. (2015)

There is a wide range of accuracies to which planetary gravity fields have been characterized, due to the large variety of mission geometries, tracking types and data quality that have been obtained for them. This can be seen in Table 2.2, which shows a summary of state-of-the-art planetary gravity field data. The determination of the gravity field of the Moon was problematic for a long time, due to the lack of direct tracking data at the lunar far side. This situation was first remedied by the SELENE mission, which used a novel four-way radio link (Namiki et al., 2009) to observe the lunar farside (see Fig. 2.3). Recently, the GRAIL mission, which consisted of two orbiters with an inter-satellite Ka-band range-rate link flying in a trailing formation, has resulted in the estimation of the gravity field up to degree and order 900 (Konopliv et al., 2013; Lemoine et al., 2014) from spacecraft data alone, higher than any other body in the solar system, including the Earth. For Earth, however, higher-degree gravity field models are available, such as EGM2008, which is complete up to degree and order 2159 (Pavlis et al., 2012) and incorporates additional models and data, such as altimetry and surface gravimetry, to estimate the high degree and order coefficients.

For many bodies for which spacecraft tracking data is used to infer gravity field coefficients, this data is only from one or several flybys, limiting the degree and order to which the gravity field can be estimated. Although determinations from flyby missions alone suffer from limitations in data quantity and coverage, flybys of bodies do not require a dedicated mission for the body under consideration. Instead, a single space mission may perform flybys of many different bodies, whereas it typically only has an orbit phase around a single body. An excellent example of this is the Cassini mission, which has performed flybys of a number of Saturn’s moons, (*e.g.*, Anderson and Schubert, 2010; Iess et al., 2012; Iess et al., 2014b). From radio science data gathered during the flybys, the full degree two gravity field, as well as  $J_3$  of Enceladus has been determined (Iess et al., 2014b). For Titan, the full degree-three gravity field, as well as the  $k_2$  Love number (Section 2.2.3) could be determined from tracking during flybys (Iess et al., 2012), which provides crucial constraints on its interior structure (Baland et al., 2014).

For the determination of the gravity field of a body in synchronous rotation from a small number of flybys, such as in the case for the Galilean and major Saturnian moons, a relation between the  $J_2$  and  $C_{22}$  coefficient can be used, which is valid for a synchronously rotating body in hydrostatic equilibrium, (*e.g.*, Murray and Dermott,

1999; Bills and Nimmo, 2008):

$$\frac{J_2}{C_{22}} = \frac{10}{3} \quad (2.17)$$

This equation can be used to reduce the set of estimated parameters during flyby data analysis. Alternatively, estimation of both  $J_2$  and  $C_{22}$  can be used to test the hypothesis of whether a body is indeed in hydrostatic equilibrium. Eq. (2.17) has been applied to (partly) differentiated bodies such as the Galilean satellites (Schubert et al., 2004) and Titan (Iess et al., 2012), as well as (almost) undifferentiated bodies such as Rhea (Anderson and Schubert, 2010).

The degree two gravity field coefficients typically provide the strongest constraints on the overall mass distribution of a body, as they are most easily detectable and provide a quite direct relation to the total (radial) mass distribution, as shown by Eq. (2.16). Since both the gravity field coefficients and moments of inertia (Section 2.2.2) of a body result from its integrated interior mass distribution, they are not independent parameters. In fact, there is a simple relation between the principal moments of inertia and degree two gravity field coefficients, due to the definition of the gravity field coefficients in Eq. (2.16) and the inertia tensor given below by Eq. (2.21). This results in (*e.g.*, Lambeck, 1988):

$$\begin{pmatrix} J_2 \\ C_{22} \end{pmatrix} = \frac{1}{M_P R_P^2} \begin{pmatrix} C - \frac{A+B}{2} \\ \frac{B-A}{4} \end{pmatrix} \quad (2.18)$$

where  $A$ ,  $B$  (equatorial) and  $C$  (polar) denote the principal three moments of inertia of the body  $P$  (with  $A \leq B \leq C$ ) and  $M_P$  and  $R_P$  denote the mass and reference (typically equatorial) radius of body  $P$ , as in Eq. (2.13).

As a result of Eq. (2.18), a combination of relative moments of inertia (such as that inferred from rotational characteristics) and degree two gravity field coefficients can be used to infer the absolute moments of inertia  $A$ ,  $B$  and  $C$ , the implications of which are discussed in Section 2.2.2. The  $C_{21}$  and  $S_{21}$  gravity field coefficients are typically (close to) zero, as they indicate the deviation between the body pole (principal axis) and the rotation pole (axis about which body rotates). Similarly, a non-zero  $S_{22}$  gravity field coefficient denotes an offset between the body equatorial  $x$ - and  $y$ -axes and the equatorial principal moments of inertia.

As an example of the use of degree two planetary gravity fields, Rivoldini and van Hoolst (2013) constrain the core size and density of Mercury using a combination of the  $J_2$  and  $C_{22}$  gravity data of Mercury, as obtained from MESSENGER tracking data by Smith et al. (2012), combined with measurements of its rotational state. However, as they clearly state, combination with other data (magnetic, tidal, *etc.*) is required to get a full characterization of the state and composition of Mercury.

## 2.2.2 Rotational Dynamics

In addition to characterizing a body's gravity field from the translational dynamics of an orbiting satellite, observing or inferring the rotational behaviour of the body can be used to constrain its interior structure. The rotational dynamics of a body

is manifested in a number of different types of measurements of planetary missions. Firstly, tracking data from planetary landers are directly sensitive to (variations in) the rotation of their target body, as its effects result in a direct geometric effect on the range measurement (see Section 5.1 of Chapter 4 for details). A prime example of this is the rotational characterization of the Moon by means of LLR (Williams et al., 2001). Secondly, since the static gravity field is defined in a body-fixed frame, changes in the rotation between the body-fixed and inertial frame will result in variations in the gravitational accelerations acting on an orbiter. An example of this approach is the determination of Mars' rotational behaviour from radio-science observations of multiple Mars orbiters reported by Konopliv et al. (2011). Thirdly, analysis of observations by an altimetry or imaging system, combined with a sufficiently accurate spacecraft orbit, can be used to observe variations in the body's rotation. For examples, the rotational state of Phobos was constrained by Pasewaldt et al. (2012) by using Mars Express High Resolution Stereo Camera (HRSC) data.

For bodies such as icy moons, which may have a strongly rotationally decoupled core and surface, great care must be taken in the combination of these techniques, since lander tracking and imaging are only sensitive to the shell rotational variations, whereas gravity field determination is sensitive to rotational variations of the entire body. Rotational variations are typically manifested as effects at a wide range of time scales, down to the order of the body's rotational period, but up to many years (tens of thousands of years for precession of certain bodies, for instance). However, unlike the influence of (high degree) gravity field parameters (Section 2.2.1), very short-periodic effects will typically not be relevant in the analysis of rotational behaviour, making range measurements to landers well suited to the determination of rotational dynamics. Inferring the rotational characteristics from orbiter tracking data, however, requires observations of signals with the same period as the spacecraft orbit, which is typically (much) shorter than one rotational period of the body. This makes range-rate measurements relatively more suited than range data for extracting characteristics of a body's rotational dynamics from orbiter tracking data.

Various different types of rotational behaviour are observed among the bodies in the solar system, such as tumbling asteroids, tidally locked moons and planetary rotations consisting of precession, nutation and polar motion. Fundamentally, though, the rotational dynamics of a completely rigid body is described by Euler's equation:

$$\frac{d(I\boldsymbol{\omega})}{dt} + \boldsymbol{\omega} \times (I\boldsymbol{\omega}) = \boldsymbol{\Gamma} \quad (2.19)$$

where  $I$  is the body's inertia tensor,  $\boldsymbol{\omega}$  its rotation vector and  $\boldsymbol{\Gamma}$  denotes the sum of all torques acting on it. By modelling the influence of both the environment and the body's interior structure on the torque  $\boldsymbol{\Gamma}$ , as shown by for instance Eq. (2.22), and measuring the (time-variation of) the rotation vector  $\boldsymbol{\omega}$ , constraints may be placed on the body's moment of inertia tensor  $I$ . The situation is complicated by a number of aspects, though. Firstly, the torque on a body can itself depend on its inertia tensor  $I$ , as shown below in Eq. (2.22), which represents the torque due to the body's flattened and elongated shape. Additionally, even for a single monolithic body, both its own rotation and tidal effects cause it to deform, resulting in time-dependency of the inertia tensor  $I$ , (*e.g.*, Williams et al., 2001).

For an arbitrary mass distribution, the moment of inertia is obtained from, (*e.g.*, Dehant and Mathews, 2015):

$$I = \int_V \rho(\mathbf{r}) ((\mathbf{r} \cdot \mathbf{r})^2 \mathbf{1}_{3 \times 3} - \mathbf{r} \cdot \mathbf{r}^T) dV \quad (2.20)$$

where the integral is taken over the complete body with density distribution  $\rho$  as a function of internal position in the body  $\mathbf{r}$ , and  $\mathbf{1}_{3 \times 3}$  denotes the three-dimensional identity matrix.

Typically, the axes in which Eq. (2.19) is evaluated are chosen such that they align with the principal axes of the body, eliminating the products of inertia (off-axis terms of inertia tensor), so that the inertia tensor can be written as:

$$I = \begin{pmatrix} A & 0 & 0 \\ 0 & B & 0 \\ 0 & 0 & C \end{pmatrix} \quad (2.21)$$

where  $C$  is the body's polar moment of inertia and  $A$  and  $B$  its equatorial moments of inertia, where  $A \leq B \leq C$ . The moments of inertia are often normalized by the product  $M_P R_P^2$ , see Eq. (2.18). They provide fundamental information on the radial mass distribution of the body, with large moments of inertia representing bodies with little or no mass concentrations at the center (0.4 for a uniform mass distribution), whereas small moments of inertia indicate a large mass concentration at the body's center (a core).

The primary torque  $\Gamma$  acting on a body is typically that of central body (approximated as a point mass) acting on the elongated shape of the rotating body under consideration and is calculated from (*e.g.*, Williams et al., 2001)

$$\Gamma = \frac{3\mu_c}{r^5} \mathbf{r} \times (I\mathbf{r}) \quad (2.22)$$

where  $\mu_c$  denotes the gravitational parameter of the central body exerting the torque. Nevertheless, additional torques from third bodies and other extended body effects of both the central and the rotating body may significantly complicate the expression for  $\Gamma$  (Bois et al., 1992).

The model of a single rigid body without an atmosphere is valid for certain small bodies, such as Phobos, allowing their rotational dynamics to be related to its internal structure with relatively minor complications (Rambaux et al., 2012). However, most larger bodies in the solar system show a clear radial structure (core, mantle, crust) which may be (partially) rotationally decoupled from one another in the case of a liquid core or subsurface ocean. This requires models for the dynamical coupling between the various layers, such as that given by van Hoolst et al. (2008) for Europa and Williams et al. (2001) for the Moon, complicating both the setup, solution and inversion of the rotational equations of motion. Also taking into account coupling between rotational dynamics, tidal deformation and dissipation, (*e.g.*, Williams et al., 2001; Rambaux et al., 2010; Williams and Boggs, 2015) results in additional information on the interior structure being manifested in its rotational dynamics. Furthermore, atmospheric torques, such



as those described by Richard et al. (2014) for Titan, may complicate the models for rotational dynamics and the interpretation of its observation even more.

Not only the variations in the rotational behaviour, but also the steady-state rotation of a body can be used to infer characteristics of the interior structure of solar system bodies. Determination of the steady-state and long-periodic rotational behaviour can be constrained to relatively high accuracy with (laser) range measurements, compared to Doppler tracking (Section 2.1.3). In general, both the orbital pole and rotational pole will precess about some axis. For tidally damped behaviour, both the orbital and spin pole will precess about the same axis at the same rate, in a manner that the spin axis, orbit axis and the axis about which they precess will be coplanar, a condition termed a Cassini state. In a Cassini state, there is a fixed relation between the inclination  $i$ , obliquity  $\epsilon$ , precession rate and the moment of inertia ratios (Peale, 1969). By measuring the rotational (and orbital) states and assuming a tidally damped configuration, constraints may be placed on the moments of inertia, (*e.g.*, Bills and Nimmo, 2008). Determination of the obliquity of Titan from Cassini radio tracking data has led to improved constraints on its interior structure (Baland et al., 2014). However, a Cassini state represents a mean equilibrium condition, not taking into account short-periodic perturbations or dissipative effects that induce time lags, requiring a characterization of the possible deviations of the rotational behaviour from a Cassini state for a given body, (*e.g.*, Peale, 2006).

The above discussion shows that the rotational dynamics encodes in its steady-state value, as well as in its temporal variations, a wide variety of influences of a body's interior structure. Instead of analyzing the mapping from  $I$  to  $\omega$  directly, a decomposition of the rotational behaviour into various components is typically performed, to at least partially decouple the various physical effects influencing the rotation and thereby facilitate the interpretation of the measurements. For synchronously rotating bodies, such as many of the moons in our solar system (Earth's moon, Phobos, Deimos, Galilean moons, Titan, Enceladus, *etc.*), the rotation motion is to first approximation described by a once-per-orbit rotation about its polar axis, with the body's long axis (*i.e.* principal axis of minimum inertia) pointing towards the central body as a result of tidal despinning, see Section 2.2.3), with the orbital and rotational motion in a Cassini state. Similarly, bodies may be in a higher-order resonance, such as Mercury (which is in a 3:2 spin-orbit resonance).

However, the rotation of such bodies will never be exactly synchronous, due to their (small) orbital eccentricities and inclinations. Assuming that a body rotates exactly once per orbit, with a constant rotation rate, this will cause the long axis to no longer point directly to the center of the central body, since the rotation angle  $\gamma$  and the true anomaly  $\theta$  will not be equal (except at  $\theta = n\pi$  with integer  $n$ ). This will cause a torque to act on the satellite as per Eq. (2.22) and shown schematically in Fig. 2.4. Additionally, other external perturbations, such as those from other solar system bodies, as well as effects of the bodies' interiors, are manifested as deviations of the body's behaviour from purely synchronous rotation. These variations are known as librations and are typically modelled as a frequency decomposition, either obtained (semi-)analytically, or from analysis of the numerical integration of the equations of motion, (*e.g.*, Williams et al., 2001; Rambaux et al., 2012).

Librational motion can consist of a combination of free and forced librations. Forced

librations are due to external torques acting on the body, whereas non-zero free libration requires an internal excitation mechanism (assuming that the damping time of the free libration is sufficiently short). Assuming a rigid body (Phobos or other small moons) the librational motion (in longitude) of a tidally locked body is approximated by the following expression (omitting the effect of tidal dissipation), obtained through linearization of the  $z$ -component of Eq. (2.22) (Rambaux et al., 2010):

$$\gamma = A_0 \sin(\omega_0 t + \phi_0) + \sum_i \frac{\omega_0^2 H_i}{\omega_0^2 - \omega_i^2} \sin(\omega_i t + \alpha_i) \quad (2.23)$$

where the summation over  $i$  represents all periodic variations in its orbit, with  $\omega_i$  the frequency of the excitation,  $\omega_0$  the body's natural (resonant) frequency and  $H_i$  the forcing amplitude. The resonant frequency can be directly related to the ratio of the moments of inertia (Chapront-Touze, 1990). Therefore, determination of the libration amplitudes can be used to determine these ratios (details are provided in Appendix B of Chapter 4). Combination with gravity field measurements, using Eq. (2.18), can then be used to determine the absolute values of the moments of inertia of the body. For small bodies such as Phobos, it is safe to assume that no excitation mechanism is present and the libration consists purely of that due to external torques. This approach is taken in the numerical simulations of Le Maistre et al. (2012) and Dirkx et al. (2014a) to analyze the observability of Phobos' interior structure from radiometric and laser range measurements to a Phobos lander, respectively.

For bodies with a more complicated (*e.g.*, radially stratified) structure, the coupling between the various layers will result in signatures on the rotational variations that can be used to constrain, for instance, the size and shape of a core or ocean layer. As an example, the influence of Mercury's core on its free librational motion is studied by Veasey and Dumberry (2011). They conclude that although current measurements of rotational behaviour do not impose strong additional constraints on the core structure, accurate observations over a period of several years would reveal the influence of the core in Mercury's libration to a point where inferences on the core's size could be made. This is an excellent example of a very slowly changing physical effect for the detection of which laser ranging (to a lander) would be ideally suited. To determine whether such an effect can be distinguished from other effects that are manifested in the tracking data would require more in-depth simulation and analysis, however.

In cases where the rotational variations of the core are decoupled from those of the mantle and crust, observations of shell libration may be used to infer a moment of inertia of the outer layers of a body only (Peale et al., 2002), as is the case for Mercury. Using measurements of the libration amplitude of Mercury, obtained from Earth-based radar ranging (Margot et al., 2012) and MESSENGER gravity field information (Smith et al., 2012), moments of inertia of both the whole planet and its shell were determined, and used by Rivoldini and van Hoolst (2013) to constrain the structure and composition of Mercury.

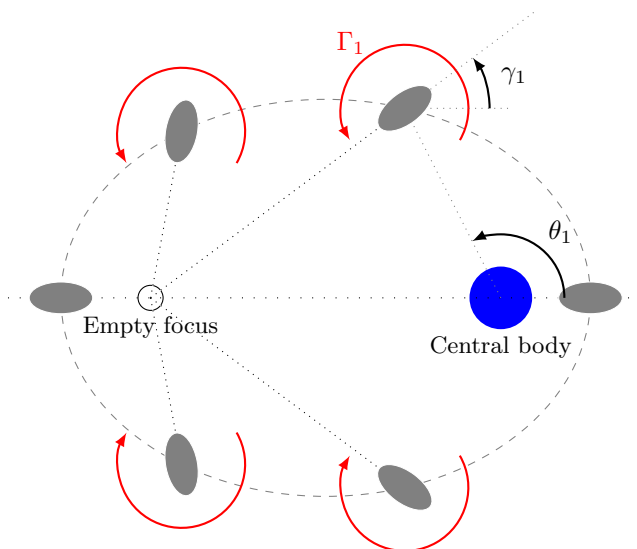


Figure 2.4: Schematic representation of the direction of the torque (red) exerted by a central body (blue) on an oblate body in synchronous rotation (grey). Indicated are the true anomaly  $\theta$  and body rotation angle  $\gamma$  at one position in the orbit. Note that the rotating body's long axis points towards the empty focus of its orbital ellipse in the case of pure synchronous rotation (Murray and Dermott, 1999).

### 2.2.3 Tidal Deformation

Gradients of external gravitational potentials inside solar system bodies induce stress fields that cause tidal deformation of these bodies. The magnitude, as well as the spatial and temporal pattern, of the resulting deformation are dependent on the body's structure, composition and rheology. As a result, the measurement of this deformation can be used to infer visco-elastic characteristics of the body's interior. Tidal deformations manifest themselves in (variations of) the shape, gravity field and rotation (Section 2.2.2) of solar system bodies, which can be measured by means of a variety of methods. In this section we give an overview of the physical effects of tidal deformation, providing examples from previous and upcoming observations and discussing the potential use of ILR for improved future determination of tidal characteristics.

Tidal variations of a body's gravity field are determined by the external potential of the body causing the deformation, denoted  $U'(\mathbf{r})$ , and the tidal Love numbers  $k_{nm}$  of the deformed body, first introduced by Love (1911), albeit without the  $n$  and  $m$  subscripts, which represent the degree and order of the spherical harmonic expansion, respectively, (*e.g.*, Munk and MacDonald, 1975; Petit et al., 2010). It are these Love numbers which contain the information relating the body's interior to the tidally-induced gravity field variations, and therefore encode the physical information that we wish to extract from the observations. Typically variations in  $k_{nm}$  with  $m$  at a given  $n$  are small, so that often a lumped coefficient  $k_n$  is used. For the general case, Love numbers

$k_n$  are complex numbers, where the typically small imaginary part quantifies the tidal lag of the deformation, resulting in tidal dissipation, (*e.g.* Williams and Boggs, 2015), to be discussed in more detail later in this section. The value of the Love number can also be dependent on the period of the forcing frequency of the tide, although typically relatively weakly so.

The induced gravitational potential of spherical harmonic degree and order  $n$  and  $m$ , denoted  $\delta U_{nm}$ , due to the external tidal potential of a body  $j$ , denoted  $U^{(j)}(\mathbf{r})$ , follows from the following, approximating the perturber as a point mass (Munk and MacDonald, 1975):

$$U^{(j)}(\mathbf{r}) = \sum_{n=2}^{\infty} \sum_{m=0}^n U'_{nm}{}^{(j)}(\mathbf{r}) \quad (2.24)$$

$$\delta U_{nm}(\mathbf{r}) = k_{nm} U'_{nm}{}^{(j)}(\mathbf{r}) \quad (2.25)$$

where  $U'(\mathbf{r})$  was expanded into a spherical harmonic series (decomposed into  $U'_{nm}{}^{(j)}$ ) about the origin of the body  $P$  in Eq. (2.24).

The influence of tidal deformation on the gravity field can be obtained by explicit expansion of Eq. (2.25), resulting into the following after combination with Eq. (2.13), (*e.g.*, Petit et al., 2010):

$$\Delta \bar{C}_{nm} - i \Delta \bar{S}_{nm} = \frac{k_{nm}}{2n+1} \sum_j \frac{\mu_j}{\mu_P} \left( \frac{R_P}{r_j} \right)^{n+1} \bar{P}_{nm}(\sin \phi_j) e^{-im\lambda_j} \quad (2.26)$$

where the symbols used are the same as in Eq. (2.13) and the summation in  $j$  runs over all bodies that raise a tide on the body  $P$  (the Sun and the Moon on Earth; the Sun, Phobos and Deimos on Mars, *etc.*).

The degree two Love number  $k_2$  represents the total variation of the degree two gravity field of the deformed body, see Eq. (2.25) and is typically the primary tidal parameter of interest in planetary missions, as it has by far the largest effect on the gravity field variations, with  $k_n \ll k_2$  for  $n > 2$  in most cases. This degree two deformation results in two tidal bulges along the vector from the deformed body and the perturbing body (one on each side of the body, see Fig. 2.5). However, deviations from spherical symmetry can cause small variations between the degree two Love numbers of orders 0 through 2 (Bills et al., 2005). Separate estimation of  $k_{20}$ ,  $k_{21}$  and  $k_{22}$  requires exceptional tracking accuracy, though, as their values are typically very similar and distinguishing the specific signals of the small influence of  $k_{20}$  and  $k_{21}$  from the primary influence of  $k_{22}$  is challenging (Yoder et al., 2003; Konopliv et al., 2011). Love numbers of degree higher than two also require highly accurate measurements, due to the typically very small value of the degree three Love numbers and the small degree three disturbing potential (compared to the degree two effect). However, estimates for the Moon are available from the GRAIL mission (Williams et al., 2014), providing unique input to constrain lunar structure models. Higher-degree Love numbers can be used to further refine interior structure models by providing an additional independent parameter. For instance, Wahr et al. (2013) propose the potential determination of ice shell thickness variations on Europa and Ganymede through determination of higher-degree tidal deformation.

Table 2.3: Examples of estimated  $k_2$  Love numbers for selected solar system bodies. Value for Moon is averaged over  $m = 0, 1, 2$ 

Body	$k_2$	$\sigma_{k_2}$	Source
Moon	0.0241	$2.2 \cdot 10^{-4}$ (realistic)	GRAIL, Williams et al. (2014)
Mercury	0.451	0.014 (preliminary), 0.1 (realistic)	MESSENGER, Mazarico et al. (2014b)
Mars	0.12	0.004 (formal), 0.01 (realistic)	MGS, Mars Odyssey, Marty et al. (2009)
Titan	0.637	0.112 (formal)	Cassini (flybys), Iess et al. (2012)

Tidal effects can be separated into a permanent tide and a time-varying tide. For synchronously rotating bodies, the permanent tide is quite large, compared to the time-varying part, since the body-fixed latitude and longitude of the central body ( $\phi$  and  $\lambda$  in Eq. (2.26)) are constant to first-order approximation. Specifically, for the measurement of the time-variability of tidal effects on synchronously rotating bodies, it are only deviations from the synchronous rotation due to orbital eccentricity (see Fig. 2.4 for schematic representation) and inclination, as well as librations, which result in time-varying gravity field and shape variations. As a result, the measurement of periodic tidal effects on these bodies is more difficult than on non-synchronously rotating bodies. The effect of the permanent tide on the shape of a synchronously rotating body is approximated by Eq. (2.17) for bodies in hydrostatic equilibrium, representing the shape that the body takes when exposed to (approximately) the same tidal potential over long time periods.

Since the measurement of tidal Love numbers is essentially part of the determination of the global gravity field of a body (omitting the possibility of planetary surface gravimeters), Doppler measurements are well suited for its determination. However, since it is typically only the very low degree term(s) which is(are) estimated, laser range measurements may offer competitive performance, depending on the specific situation (period and amplitude of the variation). In addition to being measurable through the dynamics of an orbiting spacecraft, the  $k_2$  Love number also influences the rotational dynamics of a body (see Section 2.2.2; discussion by Williams et al. (2001) for the case of the Moon and van Hoolst et al. (2012) for Mercury). Resultantly,  $k_2$  can be obtained from measurements of rotational dynamics, making range measurements to a suitably located lander valuable for determining it (*e.g.*, LLR). By combining rotational dynamics measurements and orbiter dynamics tracking (LLR and GRAIL data for the Moon), complementary observation techniques can be used to improve the estimation of a body's interior structure, as well as provide independent determinations of the same parameter.

Tidal Love numbers place unique constraints on the interior structures of bodies. Static gravity field and rotational parameters are primarily related to the internal mass distribution of a body (although a variety of additional effects influence rotational variations; Section 2.2.2). The Love numbers, however, are mainly determined by the elasticity and viscosity profile of a body making it very useful in distinguishing between solid and liquid layers, such as a core or subsurface ocean. The effect of  $k_2$  on the orbits of spacecraft is much more subtle than that of the static gravity field (comparing  $\sigma_{J_2}$  in Table 2.2 to  $\sigma_{k_2}$  in Table 2.3 clearly shows that  $\sigma_{J_2}/J_2 \ll \sigma_{k_2}/k_2$ ). Nevertheless, tidal Love numbers play a crucial role in constraining the interior structure of bodies for which estimates are available, as they provide information on the body's material

properties that cannot be resolved using gravity or rotational measurements. It can be seen from Table 2.3 that the value of the  $k_2$  Love number varies by more than an order of magnitude for different bodies, which is indicative of their very different structure, for instance the very small value for the Moon, indicating a high rigidity, and the large value for Titan, which is indicative of a subsurface ocean. For the Earth, the nominal value of the  $k_2$  Love number is about 0.3, with the frequency-dependence for the various forcing frequencies given by Petit et al. (2010).

In addition to its influence on a body's gravity field, tidal deformation also has a direct influence on shape of a body and therefore the location of landers, an effect which is typically quantified by the  $h_{nm}$  and  $l_{nm}$  Love numbers. The  $l_{nm}$  parameters are also termed the Shida number. These parameters quantify the radial and tangential displacement of a surface point in response to a disturbing tidal potential as follows, (*e.g.*, Munk and MacDonald, 1975; Petit et al., 2010):

$$u_r(\mathbf{r}) = \frac{h_{nm}U'_{nm}(\mathbf{r})}{g} \quad (2.27)$$

$$\mathbf{u}_t(\mathbf{r}) = \frac{l_{nm}}{g}\nabla_t U'_{nm}(\mathbf{r}) \quad (2.28)$$

where  $g$  is the local gravitational acceleration,  $\nabla_t$  denotes the gradient operator along the surface of the body and  $U'_{nm}(\mathbf{r})$  is defined in Eq. (2.24). Just as with the  $k_{nm}$  Love numbers, the degree two term has by far the greatest influence and typically the variations of the deformation Love numbers over an order  $m$  are neglected. The  $h_2$  and  $l_2$  Love numbers can be determined by means of tracking of a lander, or altimetry data analysis. An advantage of using altimetry data is that the coverage is typically (near-)global (assuming a polar satellite orbit), so that non-homogeneous deformation can be measured and local behaviour will not be spuriously extrapolated to global scales, as may occur for analysis from lander data (Mazarico et al., 2014a). The determination of the  $l_2$  Love numbers is usually especially difficult, since its value is typically very small.

As with rotational variations (Section 2.2.2), a wide range of different tidal behaviour is observed throughout the solar system. Relating Love numbers to constraints on the interior structure typically requires extensive modelling of the structure of that specific body. Analytical formulations are, however, available for the simplest cases of incompressible homogeneous elastic bodies, (*e.g.*, Lambeck, 1988). However, the presence of a radial stratified structure, especially the presence of fluid layers, can have a dramatic influence on a body's Love numbers, making such an approximation only valid in the simplest of cases. Typically, relating Love number estimates to interior structure constraints is done numerically by calculating the Love numbers for a range of interior structure models to obtain a range of models that are consistent with the observations, (*e.g.*, Rivoldini et al., 2011; van Hoolst et al., 2013; Williams et al., 2014). In addition to complicating the interpretation of the Love number estimates, the use of this approach is contingent upon using a model for the body's properties that correctly represents it, albeit in a simplified manner. For bodies with a subsurface ocean such as Europa or Titan, however, an elegant analytical theory is available which exploits the fact that the surfaces of these worlds can be modelled as a thin membrane floating on an ocean, largely decoupling the deformation of the crust from that of the mantle (Beuthe,

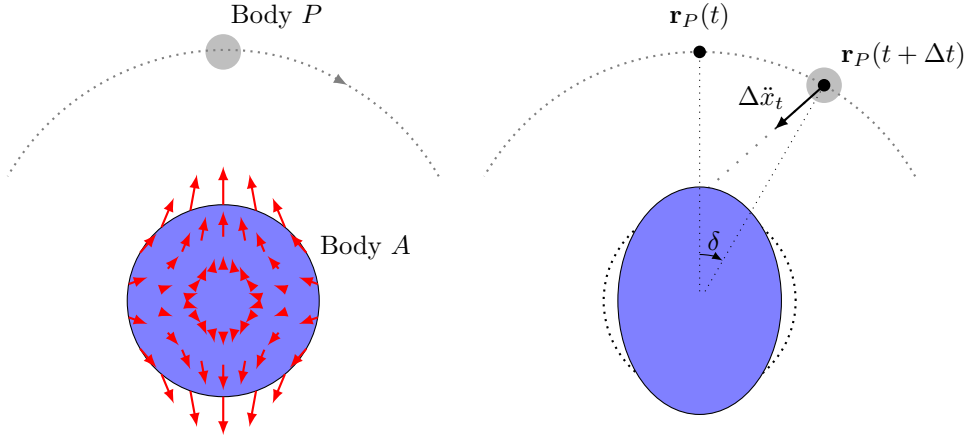


Figure 2.5: Schematic representation (in a frame fixed to body  $A$ ) of the physical effect causing secular tidal acceleration of body  $P$  due to a tide raised on visco-elastic body  $A$  in case of bodies below synchronous orbit. Left: tide-generating body  $P$  at time  $t$ , with tidal forces shown acting on the unperturbed shape of body  $A$ . Right: Deformed body  $A$  at time  $t + \Delta t$ , due to the perturbing potential of body  $P$  at time  $t$ . The additional acceleration at a lag angle  $\delta$  due to the upper tidal bulge is shown as  $\Delta \ddot{x}_t$  (not to scale).

2015). Using this theory for the determination of  $k_2$  does require the manual input of a parameter describing the influence of the sub-ocean interior, though.

Due to the visco-elastic response of the deformed body, the tidal bulge raised by a perturber will never be exactly at the sub-perturber point. Instead, there will be a time lag between the occurrence of the disturbing potential and the tidal response (in the approximate form of a tidal bulge, see Fig. 2.5). This effect is typically quantified by a quality factor  $Q$ , defined as, (*e.g.*, Khan et al., 2004):

$$Q = \frac{|k_2|}{\text{Im}(k_2)} \quad (2.29)$$

where typically the degree and order  $n$  and  $m$  of the quality factor are omitted, implicitly assuming that the degree two (order-independent) quality factor is denoted. The time lag in the raising of the tidal bulge is directly related to the quality factor through (Lainey et al., 2007):

$$\Delta t = \frac{T \sin^{-1}(Q^{-1})}{2\pi} \quad (2.30)$$

where  $T$  is the orbital period. For a perturber whose orbit is below the stationary orbit (so that the orbital period of a body is smaller than the rotation rate of the body it is orbiting), this causes the tidal bulge to be behind the sub-perturber point, whereas for a body above a stationary orbit, the bulge will be in front of the sub-perturber point, causing a secular along-track deceleration and acceleration, respectively. This effect has important implications for the evolution of planetary systems, since the secular effect will

result in long-term secular changes in orbital distance (Mignard, 1981). By measuring these secular effects through the use of long time series of observations, the  $k_2/Q$  ratio of the moons can be determined. Examples of this usage of ephemerides for measuring tidal interactions are given by (Lainey et al., 2007; Jacobson, 2010) for Phobos-Mars and (Lainey et al., 2009) for Io-Jupiter.

As with the Love numbers, the value of the quality factor is not only related to a body's internal structure, but also to the frequency of the tidal forcing. Various methods exist for modelling this frequency dependency, an overview of which is given by Efroimsky and Lainey (2007). They propose a power-law for  $Q$  as follows:

$$Q \sim \chi^\eta \quad (2.31)$$

where  $\chi$  is the tidal frequency, and the exponent  $\eta$ , which is typically between 0.2 and 0.4. Determination of the parameter  $\eta$  for a certain body can be related to its rheology. However, in addition to allowing additional constraints on a body's interior, determination of the frequency-dependence of  $Q$  is important for modelling the evolution of planetary systems, as shown for the Martian system by Efroimsky and Williams (2009). Since Phobos' orbit shrinks over time due to the tidal lag angle, the frequency of its tidal interaction with Mars changes in time, resulting in a change in  $Q$ . Since  $Q$  in turn directly influences the secular deceleration of Mars' orbit, propagating Phobos' orbit either forward or backward in time for a long duration requires an accurate model for  $Q(\chi)$ .

In addition to tidal dissipation, differential rotation of two internal layers can result in dissipation. For instance, dissipation between a fluid outer core and a solid mantle was observed on the Moon through its influence on LLR and GRAIL data (Williams et al., 2001; Williams and Boggs, 2015), specifically by detailed analysis of their influence on lunar rotational variations (see Section 2.2.2). The detection and separation of this effects was facilitated by both the long time-span and exceptional accuracy of the LLR dataset, highlighting the importance of such measurements.

## 2.2.4 Planetary Ephemerides

Ephemerides are models for the time histories of position and velocity of celestial bodies. Spacecraft tracking data provides crucially accurate input for the improvement of planetary ephemerides, where especially the absolute measurements (Section 2.1.3) of range (Pitjeva, 2001; Fienga et al., 2009) and angular position (Jones et al., 2015) are important for reducing their uncertainty. To constrain the ephemerides over long time periods, as well as for the calculation of ephemerides of bodies for which few or no spacecraft tracking data is available, radar ranging and astrometric data provide crucial input (Section 2.1.1).

Currently, there are three main research institutes producing solar system ephemerides. The Jet Propulsion Laboratory (JPL) in the US produces the Developmental Ephemerides (DE) *e.g.* Folkner et al. (2009, 2014). The Institute for Celestial Mechanics and the Calculation of Ephemerides (IMCCE) in France produces the INPOP ephemerides (Fienga et al., 2009; Verma et al., 2013) and the Institute of Applied Astronomy (IAA) in Russia produces the EPM ephemerides, (*e.g.*, Pitjeva, 2013). The



independent generation of these ephemerides, using different (but similar) models and data sets allows for an intercomparison, which can be used to estimate the (true) uncertainty of the ephemerides.

The main dynamical model of planetary ephemerides are the Einstein-Infeld-Hoffman equations derived by Einstein et al. (1938), parametrized by post-Newtonian parameters (see Section 2.3.1), as given by *e.g.*, Moyer (2000). These equations are the first post-Newtonian approximation for the gravitational interaction between a set of  $N$  point masses. By imposing that the solar system is an isolated system, the solar system barycenter is kept fixed, allowing for the combined ephemeris generation of the set of bodies under consideration (provided sufficiently accurate data is available to decorrelate their signatures). In recent planetary ephemerides, the states and masses of many ( $> 300$ ) asteroids are estimated in addition to those of the main planets (with suitable *a priori* constraints), to reduce the influence of unmodelled asteroid gravity on the ephemerides of the planets, which can be an important source of error, especially for Earth and Mars (Standish and Fienga, 2002). To further reduce the influence of mismodelled asteroids, a ring or annulus model is used, which approximates the remaining asteroids by a homogeneous mass distribution throughout the asteroid belt (Kuchynka et al., 2010). During the generation of solar system ephemerides, not only the state of a set of bodies in the solar system is estimated. A large set of additional physical parameters, such as body gravitational parameters, relativistic parameters (see Section 2.3.3), gravity field coefficients (for instance solar  $J_2$ ) and rotational characteristics (for instance lunar rotation properties derived from LLR) are estimated. The parameters that are estimated during the generation of ephemerides are typically those that are manifested over large distance (gravitational parameters of solar system bodies, solar  $J_2$ , post-Newtonian parameters), or those that have relevance for the correct processing of specific sets of highly accurate data, most notably physical parameters of the Moon that are required for the correct analysis of LLR data.

In addition to the analysis of parameters estimated during the creation of an ephemeris, there have been various studies in dynamical astronomy at solar system scales from existing ephemerides. For instance, by analyzing the precession of perihelia of solar system planets, Iorio (2014) was able to place strong constraints on the possible distance and mass of a 'Planet X'. Similarly, such analyses of planetary precessions can be used for a variety of experiments in gravitational physics, as will be discussed in Section 2.3.3. The errors in planetary ephemerides may diverge outside of the domain where accurate tracking observables are available, as shown for, for instance, the case of Mars by Folkner et al. (2009). This effect is indicative of mismodelling in the dynamics and data processing, resulting in errors in the estimation. Specifically, it indicates that the estimation has converged to a certain parameter set that minimizes the residuals during the observation period, where this parameter does not necessarily reflect the physically optimal solution. Recently, it was shown by Verma et al. (2013) that including estimation of solar plasma coefficients improves extrapolation capabilities, indicating an improved correspondence between modelled and actual physical effects in the resulting ephemerides.

## 2.3 Science Return: Gravitational Physics

In addition to its application to planetary science objectives (Section 2.2), planetary tracking data (Section 2.1) are also used for experimental tests in fundamental physics. Primarily, these tests are in the field of gravitational physics for which the currently prevailing theoretical description is general relativity (GR). However, a number of issues, such as the ongoing development of a quantum theory of gravity and the search for dark matter and dark energy (or physical theories leading to equivalent observations), has spurred the development of a variety of alternative theories of gravitation, (*e.g.*, Turyshev, 2009; Capozziello and de Laurentis, 2011; Will, 2014). Some of these theories yield predictions that are testable, or have free parameters that can be constrained, from the analysis of space mission tracking data, both from Earth orbiters and planetary missions.

We first give a broad theoretical overview of relativity and alternative theories of gravitation in Section 2.3.1, in support of the discussion in subsequent sections. In Section 2.3.2, we discuss the physical effects that relativity has on space mission tracking data analysis, in terms of deviations from Newtonian theory. Finally, we provide an overview of current and future progress in applying space mission tracking data in experimental gravitation in Section 2.3.3. This forms an important rationale for the work described in this dissertation, as applications in gravitational physics have typically been the primary reason for the inclusion of ILR in mission proposals (Section 3.3.1). We largely defer mathematical details of gravitational physics and its effects on space missions to Chapter 7, where we discuss in detail a proposed new method for the relativistic analysis of range data. Note that the notation we use in this Section is in line with that given in Section 2 of Chapter 7.

Although planetary tracking could be used for experiments in fundamental physics outside the realm of gravitational physics, (*e.g.*, Damour and Donoghue, 2011), we focus here on GR and its theoretical alternatives, as it is science return in this field for which planetary tracking in general and ILR in particular will be most valuable.

### 2.3.1 Theories of Gravitation

GR is one of the foundations of modern physics, describing the macroscopic framework for the behaviour of physical systems by giving a mathematical description of the background space-time, and its physical interaction with matter and energy (*e.g.*, Misner et al., 1973). GR grew out of efforts to extend the theory of special relativity to systems including gravitational interaction (*e.g.*, Sauer, 2004). Two cornerstones of GR are the principle of relativity and the strong equivalence principle, (*e.g.*, Kopeikin et al., 2011). The relativity principle states that physical behaviour is locally governed by special relativity. The strong equivalence principle states that the outcome of any local experiment (both gravitational and non-gravitational) is independent of the velocity and position of the test apparatus, and of the time at which the experiment is performed. Also, it encompasses the weak equivalence principle, extending it to massive bodies, so that inertial and gravitational mass of any body are equal, regardless of its structure, composition or size (Will, 2014). These postulates lead to the formulation of GR, providing a theoretical description of the interaction of matter and the gravitational field.

GR describes the manner in which matter causes gravity, generalizing Eq. (2.11), and prescribes how the motion of any body (irrespective of whether it is massless, is a point mass, or has some arbitrary mass distribution) under the influence of gravity can be determined, generalizing Newton's law of gravity in Eq. (2.12). Motion under the influence of gravity alone is determined directly from the geometry of the four-dimensional space-time manifold, comprising a single time dimension and three space dimensions. Instead of being flat, as is the case in Newtonian mechanics (3-dimensionally flat) and special relativity (4-dimensionally flat), space-time geometry is curved in GR. This geometry is characterized by the metric tensor  $g_{\mu\nu}$ . Determining the motion of a body (and in general the transport of any vectorial or tensorial quantity) requires the affine connection  $\Gamma_{\mu\nu}^{\sigma}$  on the manifold to be additionally specified, (*e.g.*, Kopeikin et al., 2011). Under the assumptions of GR however,  $\Gamma_{\mu\nu}^{\sigma}$  can be directly derived from  $g_{\mu\nu}$  (and its first space derivatives).

The metric  $g_{\mu\nu}$  can be determined from the stress-energy-momentum tensor  $T_{\mu\nu}$ , which describes the distribution of energy (which includes mass), momentum and stress. The equations relating the  $g_{\mu\nu}$  to  $T_{\mu\nu}$  are the Einstein field equations, first formulated by Einstein (1915b). They read (omitting the putative contribution of the cosmological constant), as follows in modern formulation (*e.g.*, Misner et al., 1973):

$$G_{\mu\nu} = \frac{8\pi G}{c^4} T_{\mu\nu} \quad (2.32)$$

where the Einstein tensor  $G_{\mu\nu}$  can be expressed as a coupled, non-linear combination of the first and second derivatives of the metric (we omit the explicit formulation here). Therefore, the field equations are a second-order set of coupled, non-linear, partial differential equations for  $g_{\mu\nu}$  in terms of  $T_{\mu\nu}$ . They are a generalization of the classical formulation of Eq. (2.11). In fact, a free constant that remains in deriving the Einstein equations is obtained from requiring that the equation reduces to its Newtonian counterpart in the limit case (Kopeikin et al., 2011). Due to the complicated nature in which  $g_{\mu\nu}$  is related to  $T_{\mu\nu}$ , as given by Eq. (2.32), only very few exact solutions are known. Examples are the Schwarzschild and Kerr metric, first obtained by Schwarzschild (1916) and Kerr (1963), which describe the gravitational field of a point mass with and without angular momentum, respectively. Analytical approximations for  $g_{\mu\nu}$  can be found in some more general cases, such as the post-Newtonian metric of gravitationally interacting bodies, including the effect of spin and mass multipoles given by Damour et al. (1991). This metric is applicable for most solar system situations (at least at the current level of measurement and model accuracy), and is recommended by the International Astronomical Union (IAU) (Soffel et al., 2003). A second order expansion (including parameterized deviations from GR, see below) is given by Minazzoli and Chauvineau (2009), with a general higher order formulation given by Kopeikin et al. (2011). An explicit formulation of  $g_{\mu\nu}$  and  $\Gamma_{\mu\nu}^{\sigma}$ , applicable for most solar system situations, is given in Appendices A and B of Chapter 7, respectively.

In the physical interpretation of GR, gravity can no longer be thought of as a force in the classical sense, but as an inherent effect that the shape of space-time has on the motion of particles and bodies moving in it. From the metric, the motion of particles and extended bodies can be determined. The motion of point particles which are only

affected by gravity follows geodesics on the manifold, which are calculated from, (*e.g.*, Misner et al., 1973):

$$\frac{\partial^2 x^\mu}{\partial \tau^2} = -\Gamma_{\alpha\beta}^\mu \frac{\partial x^\alpha}{\partial \tau} \frac{\partial x^\beta}{\partial \tau} \quad (2.33)$$

These geodesics can be thought of as generalizations of straight lines in curved space-time. Both the propagation of massive bodies and massless particles (photons) may be derived from this equation.

The interaction of matter and the gravitational field, as expressed by the Einstein field equations in Eq. (2.32), can be derived from a variational principle requiring that the variation of the so-called Einstein-Hilbert action  $S$ , first formulated by Hilbert (1915), of the interaction between matter and gravity of the physical system under consideration is minimized. Although the theoretical aspects of field theory that lead to this formulation are well beyond the scope of this dissertation, many alternative theories of gravity (Section 2.3.2) that are testable by space mission tracking data (Section 2.3.3) rely on a modification of the action. Therefore, it is instructive to provide it here explicitly, (*e.g.*, Kopeikin et al., 2011):

$$S = \int \left( \frac{c^4}{8\pi G} R + L_M \right) (\sqrt{-g}) d^4x \quad (2.34)$$

where  $g$  is the determinant of the metric tensor and  $R$  the Ricci scalar (which is the only invariant scalar that can be obtained from linear combinations of the metric and its first and second partial derivatives).  $L_M$  is the matter Lagrangian (or more formally the Lagrangian density), which is related to  $T_{\mu\nu}$  and  $g_{\mu\nu}$ . A modification of this formulation of the action  $S$  will result in modification of the field equations and therefore result in a different  $g_{\mu\nu}$  for a given  $T_{\mu\nu}$ . Examples of such modifications include replacing  $R$  with an arbitrary function of  $R$  (termed  $f(R)$  gravity), adding additional fields (scalar, vector and/or tensor fields), or introducing an additional (so-called non-minimal) coupling between the matter Lagrangian and the field variables, (*e.g.*, Capozziello and de Laurentis, 2011; Will, 2014).

Various alternative formulations of the action  $S$  lead to changes in the metric that can be described in terms of the Parameterized Post-Newtonian (PPN) framework (Will, 1981), which is a first-order slow-motion ( $v \ll c$ ), weak-field ( $|g_{\mu\nu} - \eta_{\mu\nu}| \ll 1$ ) approximation of metric theories of gravity, where  $\eta_{\mu\nu}$  denotes the Minkowski metric. The field equations of the PPN framework are parameterized by 10 parameters, which take on different values in different theories of gravitation. By varying the parameters, the contribution of various physical effects to the metric is modified. As a result, estimating the value of these parameters allows us to distinguish between various theories of gravitation.

The full set of PPN parameters were first given by Will and Nordtvedt (1972), and described in extensive detail by Will (1981). The PPN parameters include the so-called Eddington parameters  $\gamma$  and  $\beta$ , first introduced by Eddington (1923), which determine the amount of space-curvature caused by unit rest mass and the degree of non-linearity for gravity superposition, respectively. Additionally, the PPN framework includes parameters describing potential preferred-frame effects ( $\alpha_1$ - $\alpha_3$ ), preferred location effects

( $\xi$ ) and potential violations of energy-momentum conservation ( $\zeta_1$ - $\zeta_4$ ). An overview of a variety of alternative theories of gravitation that can be described in the PPN framework, and how their free parameters relate to the PPN parameters, is given by Will (2014). The Eddington parameters are both equal to unity in GR, with all other parameters equal to zero. The dependence of the metric  $g_{\mu\nu}$  on  $\gamma$  and  $\beta$  is shown explicitly in Appendix A of Chapter 7. For higher order expansions of the metric, additional coefficients can be added. For the second order post-Newtonian metric of the solar system, a Post-PPN (PPPN or 2PN) parameter  $\delta$  can be included for the 2PN contribution on the space-space (*i.e.*,  $g_{ij}$ , with  $i, j = 1, 2, 3$ ) terms of the metric. However, depending on the underlying theory, such additional parameters may not be independent from the original PPN set (Minazzoli, 2012) and can be constrained by the original PPN parameters.

Despite its broad applicability, a variety of postulated theories of gravitation result in modifications of the gravitational interaction that are not covered by the PPN framework (or its higher order extensions) (Hees et al., 2014d). Effects due to the theoretical Yukawa-interaction, for instance, are not covered by the framework. Instead of modifying the relation between the metric and the potentials, as is the case in the PPN formalism, it proposes a modification of the basic Newtonian potential in Eq. (2.13) that GR reduces to in the limit case, due to the existence of a fifth fundamental force of nature. This potential has (in the limiting case of a point mass) the following form, (*e.g.*, Merkowitz, 2010):

$$U = \frac{\mu}{r} \left( 1 + \alpha \exp\left(-\frac{r}{\lambda}\right) \right) \quad (2.35)$$

so that an additional potential of a certain strength  $\alpha$  is present, which drops off with characteristic length  $\lambda$ .

An additional alternative theory of gravitation in which the form of the potential is modified is Modified Newtonian Dynamics (MOND). MOND provides a description of the gravitational interaction which aims to explain the observations currently attributed to the postulated presence of dark matter. In MOND, the strong equivalence principle is violated, as the dynamics of an isolated system (for instance the solar system) depends not only on gradients of the external potential (as is the case in Newtonian and Einsteinian gravity), but also on the absolute value of the potential itself, a phenomenon termed the external field effect (EFE). This theory results in a modified dynamics in the solar system, due to the EFE of the mass of the Milky Way (Blanchet and Novak, 2011). Other parameterized extensions of gravity that have been and could be constrained by space mission tracking data are the Post-Einsteinian Gravity (PEG), in which the Einstein field equations in Eq. (2.32) are modified by replacing the gravitational constant  $G$  by a set of response functions (Jaekel and Reynaud, 2005) and Standard Model Extension (SME), a field theory aiming to unify quantum theory and GR, which allows for Lorentz symmetry breaking beyond that expressed by the PPN framework (Bailey and Kostelecký, 2006).

An alternative formulation of GR stems from the fact that the use of  $\Gamma_{\alpha\beta}^{\mu}$  as the affine connection of the manifold is not a unique choice in its derivation. Alternatively, one can also choose to include a torsion component  $T_{\alpha\beta}^{\mu}$  in the connection. In fact, choosing the theory of gravitation to be curvature-free ( $\Gamma_{\alpha\beta}^{\mu} = 0$ ), instead of torsion-free (as is the case in GR), allows for an equivalent description of the gravitational

interaction (on macroscopic scales), in so-called teleparallel gravity (Aldrovandi and Pereira, 2013). Although this description of gravity is equivalent to GR, a broader spectrum of gravitational theories is obtained when including variations for the coupling between torsion and matter. This class of alternatives, termed  $f(T)$  theories of gravity, is conceptually similar to  $f(R)$  theories of gravity.

### 2.3.2 Influence of Gravitation on Planetary Tracking Data

The influence of relativistic effects on space mission tracking data must be included at several stages in the reduction and analysis process, (*e.g.*, Moyer, 2000; Soffel et al., 2003; Kopeikin et al., 2011; Hees et al., 2014b). Besides being required for a correct interpretation of the data for non-relativistic objectives, these effects may be exploited to test various aspects of gravitational physics, improving the experimental verification of GR or potentially confirming post-Einsteinian theories. In this section, we give a conceptual overview of the relativistic effects on space mission tracking and its data analysis, while we discuss specific applications of these effects for experimental gravitational physics in Section 2.3.3. We distinguish between three different kinds of relativistic effects, each of which must be accounted for in a distinct manner: the influence on translational dynamics, the influence on time dynamics and the influence on electromagnetic signal propagation. We address the first two of these effects in more mathematical detail in Chapter 7. Although relativistic effects also influence rotational dynamics of massive bodies (Damour et al., 1993), these effects are beyond the scope of our applications in planetary missions.

The relativistic equations of motion in Eq. (2.33) differ from the Newtonian ones at the  $c^{-2}$  level. This results in a difference in acceleration at the  $10^{-8} \text{ m}\cdot\text{s}^{-2}$  level for spacecraft in Low Earth Orbit (LEO). The relativistic effects on the translational dynamics may be included by adding a number of corrections to Newtonian theory, which is the approach typically taken for the orbit propagation of spacecraft, (*e.g.*, Damour et al., 1994; Petit et al., 2010). When propagating the orbit of a spacecraft about a solar system body, the correction becomes the following, when approximating this body as a point mass with angular momentum:

$$\begin{aligned} \Delta \ddot{\mathbf{r}} = & \frac{\mu_P}{c^2 r^3} \left( \left( 2(\beta + \gamma) \frac{\mu_P}{r} - \gamma \dot{\mathbf{r}} \cdot \dot{\mathbf{r}} \right) \mathbf{r} + 2(1 + \gamma)(\mathbf{r} \cdot \dot{\mathbf{r}}) \dot{\mathbf{r}} \right) + \dots \\ & \dots + (1 + \gamma) \frac{\mu_P}{c^2 r^3} \left( \frac{3}{r^2} (\mathbf{r} \times \dot{\mathbf{r}}) (\mathbf{r} \cdot \mathbf{J}_P) + (\dot{\mathbf{r}} \times \mathbf{J}_P) \right) - \dots \\ & \dots - (1 + 2\gamma) \frac{\mu_S}{c^2 R^3} \left( (\dot{\mathbf{R}} \times \mathbf{R}) \times \dot{\mathbf{r}} \right) \end{aligned} \quad (2.36)$$

where  $\mathbf{r}$  denotes the position vector from the central body center to the spacecraft,  $\mathbf{J}_P$  denotes the angular momentum vector of the central body (per unit mass),  $R$  denotes the distance from the central body w.r.t. the Sun,  $\mu_P$  and  $\mu_S$  denote the gravitational parameters of the central body and the Sun, respectively and  $\beta$  and  $\gamma$  denote the Edington parameters (Section 2.3.1). The first term is the rcorrection term due to the different gravitational influence of a stationary point mass in GR (Schwarzschild metric, see Section 2.3.1), compared to the Newtonian case. The second term is due to

the rotation of the Earth and is termed the frame-dragging, or Lense-Thirring effect, first identified by Lense and Thirring (1918). The final term is called the de Sitter (or geodetic) precession term, first identified by de Sitter (1916). It originates from the fact that the kinematically non-rotating (where the background stars are fixed) and dynamically non-rotating frames (the frame attached to a freely falling observer) (Klioner, 1993) following the trajectory of the Earth undergo a mutual precession as a result of the relativistic effects.

In general, the contributions depending on stationary mass can be termed gravitoelectric, whereas the contribution depending on the body's angular momentum can be termed the gravitomagnetic term. This terminology stems from the similarity between Maxwell's equations of electromagnetism and the linearization of the Einstein field equations (see Eq. (2.32)) in a flat spacetime background (Clark and Tucker, 2000), where we can distinguish between different physical effects from static charges (or masses) and moving charges (rotating mass or mass in translational motion). An additional gravitomagnetic effect which is not manifested in Eq. (2.36) is the dependence of the relative velocity on a body's gravitational influence on a third body (Murphy et al., 2007), *i.e.*, arising from a translational mass current. However, the magnitude of such terms is frame-dependent and should be interpreted with caution (Kopeikin, 2007).

Instead of adding correction terms to the classical gravitational equation of motion, fully relativistic equations of motion may be used, where the acceleration is calculated directly from the metric  $g_{\mu\nu}$  and the connection  $\Gamma_{\mu\nu}^{\sigma}$  (see Eq. (2.33) and Chapter 7). Such an approach allows for a much more condensed formulation of the governing equations, as can be seen from Eq. (2.36), which represents a first-order correction for a simple test case. By comparison, the full expansion of first-order corrections to the Newtonian equations of motion, with arbitrary mass and multipole moments, can become extremely complex, (*e.g.*, Kopeikin et al., 2011; Xie and Kopeikin, 2014), making their implementation both cumbersome, error-prone and untransparent.

For extended bodies such as moons and planets, local gradients of external potentials cause a difference between the worldline (*i.e.* the curve describing the motion of its center of mass) of a body and a geodesic, as given by Eq. (2.33) (Kopejkin, 1988), introducing an additional term  $Q^{\mu}$ . Additionally, non-gravitational forces  $A^{\mu}$  may act on the body to an observable degree, resulting in the following full equation of motion:

$$\frac{\partial^2 x^{\mu}}{\partial \tau^2} = -\Gamma_{\alpha\beta}^{\mu} \frac{\partial x^{\alpha}}{\partial \tau} \frac{\partial x^{\beta}}{\partial \tau} + Q^{\mu} + A^{\mu} \quad (2.37)$$

Extensive discussion on the formulation of  $Q^{\mu}$  is given by Kopeikin and Vlasov (2004). Since the non-gravitational component  $A^{\mu}$  is typically quite small (Xie and Kopeikin, 2014), the difference between it and the acceleration as measured by an accelerometer will typically be very small (relative difference on the order of  $v^2/c^2$  and  $U/c^2$ ).

As shown in Section 2.1, a range observable (and therefore also the range-rate measurement, due to its realization by means of difference ranges) is obtained from the reception and transmission time  $t$  of an electromagnetic signal, where  $t$  is typically a global time such as Dynamical Barycentric Time (TDB) or Coordinate Barycentric Time (TCB) (Klioner, 2008). However, the observing stations register a proper time  $\tau$ , which must be converted to  $t$  to form the range observable. Both the local strength of the

gravitational field and the velocity of the observer influence the rate of proper time w.r.t. global time, (*e.g.*, Soffel et al., 2003):

$$\dot{\tau} = \sqrt{-g_{\mu\nu} \frac{\dot{x}^\mu \dot{x}^\nu}{c^2}} \quad (2.38)$$

where  $\dot{\tau} = 1$  in the classical, non-relativistic.

As a result of Eq. (2.38), a variety of physical parameters, both classical and (post-) relativistic, influences the proper time rate. During data analysis, the conversion between global and proper time is typically performed by an *a priori* integration of the proper time equation, such as that produced by (Irwin and Fukushima, 1999; Fienga et al., 2009). Primarily, it has been the relativistic effects on translational dynamics and electromagnetic signal propagation that have been used in solar system experimental gravitation. However, the use of time dynamics to probe the gravitational environment is gaining traction with the development of ever more accurate clocks, as will be discussed in Section 2.3.3. We present a unified description of parameter estimation of space and time dynamics in Chapter 7.

Relativistic effects cause a deviation in both the path of an electromagnetic signal and its apparent propagation speed (due to time dilation), resulting in a relativistic light time correction in Eq. (2.1). Like the relativistic effects on translational dynamics, its influence on signal propagation may be included either by the application of correction terms, or the full relativistic determination of the null geodesic. The largest influence in solar system situations is the delay due to a stationary mass monopole, typically the Sun. The use of this effect in experimental relativity was first proposed by Shapiro (1964) and eponymously termed the Shapiro time delay. It is this correction that is routinely applied for radiometric tracking (Moyer, 2000). For a link between observers  $A$  and  $B$ , this correction becomes the following (in harmonic coordinates):

$$\Delta t_{BA} = \frac{\mu(\gamma + 1)}{c^3} \ln \left( \frac{r_A + r_B + R_{AB}}{r_A + r_B - R_{AB}} \right) \quad (2.39)$$

where  $r_A$  and  $r_B$  are the distance from body's  $A$  and  $B$ , respectively, to the perturbing mass monopole, and  $R_{AB}$  is the distance between the two observers. Eq. (2.39) is only dependent on the PPN parameter  $\gamma$ , the parameter  $\beta$  only enters the correction at the second order ( $G^2/c^5$ ) (Richter and Matzner, 1983). This distinct influence of these two parameters has been crucial in obtaining independent estimates of them (Section 2.3.3). In addition to the result shown in Eq. (2.39), analytical results have been found for a number of simplified, but typical, cases, such as the first- and second-order relativistic effects due to a stationary point mass (Richter and Matzner, 1983), the influence of a body's angular momentum (Kopeikin and Mashhoon, 2002) and general multipole moments (Kopeikin, 1997). Although such analytical equations are typically sufficient to calculate the light time between two observers, it will be highly advantageous in the application of ILR to have higher order effects included in the models, if only to verify that they may be neglected for a given situation. An analytical expansion up to second order for solar system situations is derived by Minazzoli and Chauvineau (2011), which is quite elaborate and suffers from similar practical issues as direct expansions for translational equations of motion discussed earlier in this section.



The relativistic light time correction can have a much more complicated structure in ILR than in either SLR or LLR. For existing laser ranging systems, light time corrections due to the static part of the Earth, Sun and Moon are taken into account, with other extended body or gravitomagnetic effects on the light time below the observable level of accuracy. For ILR, however, a much broader range of signal paths is possible, including those that pass much closer by the Sun or the giant planets. The  $J_2$  gravity field coefficients of Saturn and Jupiter are quite high, at around  $1.5 \cdot 10^{-2}$  (Guillot, 1999), compared to the values shown for selected other bodies in Table 2.2. Consequently, Minazzoli and Chauvineau (2011) estimate relativistic mass multipole range corrections of up to 100 due to the  $J_2$  coefficient of both planets (for light-ray paths grazing the planets). Also, the angular momentum of the Sun may influence the light time to an observable level for signal paths with a small solar separation angle, as deduced from relations given by (*e.g.*, Kopeikin and Mashhoon, 2002).

A general framework from which the light-time correction (as well as frequency shift and light-ray bending) may be obtained is the Time Transfer Formalism (TTF) (Linet and Teyssandier, 2002; Le Poncin-Lafitte et al., 2004; Teyssandier and Le Poncin-Lafitte, 2008). In this framework, the relativistic corrections to electromagnetic signal propagation may be obtained at  $n^{\text{th}}$  post-Minkowskian (expansion into powers of  $G$ ) order from integrals taken along the straight line connecting the transmission and reception event. For instance, the first post-Minkowskian correction follows from (Teyssandier and Le Poncin-Lafitte, 2008):

$$\Delta t^{(1)} = \frac{T_{AB}}{2} \int_0^1 \left( g_{(1)}^{00} - 2N_{AB}^i g_{(1)}^{0i} + N_{AB}^i N_{AB}^j g_{(1)}^{ij} \right)_{z_-(\lambda)} d\lambda \quad (2.40)$$

where  $g_{(1)}^{\alpha\beta}$  denotes the first post-Minkowskian term of the metric,  $N_{AB}^i$  denotes the vector from transmitter to receiver and  $z_-(\lambda)$  is the parameterized straight line between them ( $0 < \lambda < 1$ ). The higher-order corrections depend on both the higher-order terms of the metric and the spatial derivatives of the lower-order light time correction terms, thereby including the relativistic influence of light ray curvature on the light time. This formalism allows for the use of an arbitrary metric description and may be used to include, for instance, the effect of the (non-linear) motion of celestial bodies (Hees et al., 2014a) or a spin/mass multipole body (with a constant velocity) (Soffel and Han, 2015) and is extremely valuable for a general description of light propagation and validation of other (numerical) methods (Bertone et al., 2014). The use of this framework could be a powerful tool in the future analysis of laser ranging data, as it may be implemented in a largely general fashion, allowing a rigorous and consistent analysis of a variety of first- and higher-order effects that may become relevant in ILR.

In addition to requiring the relativistic corrections to the light time between two points in a global frame, the position and velocity of the observers in this frame must be known, requiring accurate relativistic conversions between local (body-centered GCRS-like and/or topocentric) frames. These conversions are more complicated than their Newtonian counterparts, requiring conversions of positions, velocities and times between the frames, which depend on their mutual velocities and gravitational potentials. The mathematical procedure for these conversions is described in detail by (*e.g.*, Klioner, 1993; Kopeikin and Vlasov, 2004; Turyshev et al., 2013).

### 2.3.3 Experimental Gravitation on Solar System Scales

In this section, we give an overview of some of the contributions that space mission tracking has made to experimental gravitational physics. By using the solar system as a natural laboratory, reconstructing the dynamics of planets and moons can provide some of the best tests of GR. The prime advantage of the use of solar system bodies over more distant astronomical objects stems from the fact that we can observe their dynamics with much higher accuracy, especially due to the possibility of active tracking of space missions. However, in a relativistic sense the dynamics of the solar system falls into the weak-field, slow-motion regime, so that deviations of measurable physical effects from Newtonian gravity are quite small. For instance, at 1 AU from the Sun,  $|g_{\mu\nu} - \eta_{\mu\nu}|$  is only at the  $10^{-8} \text{ m}\cdot\text{s}^{-2}$  level. As a result, to observe potential deviations from GR, small deviations from a small effect are to be observed, highlighting the challenge of their detection. Nevertheless, some of the strongest experimental confirmations of GR come from solar system experiments, including those performed using SLR and LLR (Turyshev, 2009; Will, 2014).

Although LLR and planetary tracking data provide the bulk of dynamical space-based tests of relativity, SLR has yielded a number of contributions to experimental relativity (Nordtvedt, 2001; Lucchesi and Peron, 2014). The Lense-Thirring effect (term dependent on  $\mathbf{J}$  in Eq. (2.36)) was first determined experimentally (to within 5%) by long time-series data analysis of the LAGEOS I/II satellites (Ciufolini and Pavlis, 2004). A novel linear combination of the precessions of the two satellites was used to largely cancel the influence of uncertainties in the Earth's gravity field. However, the accuracy of this estimate has been hotly debated in a long series of scientific papers, (*e.g.*, Iorio, 2005; Ciufolini et al., 2009). Nevertheless, the LAsER RELativity Satellite (LARES) spacecraft, a passive SLR satellite, was launched in 2012 with the explicitly goal of improving SLR's measurement of gravitomagnetism to better than 1% (Paolozzi and Ciufolini, 2013). In addition to the detection of gravitomagnetism, SLR has for instance contributed to constraining a Yukawa interaction, shown in Eq. (2.35), at Earth-orbit scales (Lucchesi and Peron, 2014).

Due to the combination of almost undetectably low non-conservative forces acting on the Moon, and the long time-series of exceptionally accurate range data, LLR has been one of the most prolific sources of experimental tests of relativity, (*e.g.*, Williams et al., 2006; Müller et al., 2008b; Merkowitz, 2010). For instance, it has been used to constrain the time-variation of the gravitational constant (Müller et al., 2007), put constraints on the SME class of alternatives to GR (Battat et al., 2007), constrain a Yukawa interaction at the length scale of the lunar orbit (Müller et al., 2008a), constrain preferred frame effects through estimation of PPN parameter  $\alpha_1$  (Müller et al., 1996) and provide one of the most stringent tests of the strong equivalence principle (Williams et al., 2009; Müller et al., 2012) (discussed below). A test of GR using a combination of LLR data and interior structure models of the Moon is given by Bartlett and van Buren (1986), who constrain the  $\zeta_3$  PPN parameter by noting that  $\zeta_3 \neq 0$  would result in an observable effect in the dynamics of the Moon due to its asymmetric internal mass distribution. The proposed use of active laser transponders on the Moon (Section 3.3.2), allowing LLR to be supplemented by ILR techniques, could allow for more accurate and more dense observations of lunar dynamics to be obtained, further strengthening the science

return of LLR.

As mentioned in Section 2.3.1, the main parameters of interest in the PPN framework are  $\gamma$  and  $\beta$ , as they take on a value different from that of GR in many alternative theories of gravity, while the other parameters only exhibit deviations in a more limited set of alternatives (Will, 2014). In the analysis of LLR, a combined parameter  $\eta_N$  (the Nordtvedt parameter) is typically estimated. Assuming all other PPN parameters take on their GR value,  $\eta_N$  is expressed by (Dickey et al., 1994):

$$\eta_N = 4\beta - \gamma - 3 \quad (2.41)$$

Deviations of  $\eta_N$  from 0 signify a violation of the equivalence principle, which would manifest itself in the lunar orbit if the difference in mass between the Earth and the Moon would result in a different gravitational interaction with the Sun. The Nordtvedt parameter can be directly related to a difference in inertial mass  $M_I$  and gravitational mass  $M_G$  as (Nordtvedt, 1988):

$$\frac{M_G}{M_I} - 1 = \eta_N \frac{U_G}{Mc^2} \quad (2.42)$$

where  $U_G$  denotes the gravitational self-energy of the body. That is, in the case of a violation of the strong equivalence principle, the Moon and the Earth would sense a Sun of a different mass, resulting in a small influence on the Lunar orbit. Current uncertainties in estimates of  $\eta_N$  are at the level of  $3 - 5 \cdot 10^{-4}$  (Williams et al., 2009; Müller et al., 2012), with the nominal value consistent with the GR-predicted  $\eta_N = 0$ .

Estimating uncorrelated values for the PPN parameters  $\beta$  and  $\gamma$  from orbital motions alone is troublesome, as shown by Eq. (2.36). However, the relativistic light time correction is dependent on only  $\gamma$  at the level of  $c^{-3}$ , shown in Eq. (2.39). Therefore,  $\gamma$  and  $\beta$  can be well separated by including analysis of solar conjunction experiments, where the light time correction, and resultantly the influence of  $\gamma$ , is largest. Such experiments have been performed by the Cassini spacecraft (before its Ka-band transponder failed) from which  $\gamma$  was determined with an uncertainty of  $2.3 \cdot 10^{-5}$  (Bertotti et al., 2003), with a nominal value of  $\gamma = 1$ . The influence of  $\gamma$  on the bending of signal path was used by Lambert and Le Poncin-Lafitte (2009) to estimate  $\gamma$  from VLBI observations, but their estimation failed to improve upon the result obtained from Cassini data. Results from astrometric data obtained by the GAIA satellite, however, are expected to improve the estimation of  $\gamma$  by one or two orders of magnitude (Mignard, 2002).

Both  $\gamma$  and  $\beta$  are estimated in the analysis of planetary ephemerides (Verma et al., 2014; Folkner et al., 2014), using a combination of orbital dynamics and light-time correction effects, where the use of data from the recent MESSENGER mission has greatly improved the accuracy of the orbital model of Mercury. Due to Mercury's proximity to the Sun, and its relatively eccentric orbit ( $e \approx 0.2$ ), its dynamics are exceptionally well suited to constrain relativistic effects on orbital dynamics. A detailed analysis of the realistic error budget of the PPN parameter estimation in the INPOP ephemerides is presented by Fienga et al. (2014), who consider the influence of mutual variations in  $\dot{G}$ ,  $J_{2\odot}$ ,  $\beta$  and  $\gamma$  and obtained a  $1\sigma$ -error bound of  $5 \cdot 10^{-5}$  and  $7 \cdot 10^{-5}$  for  $\gamma$  and  $\beta$ , respectively. Fig. 2.6 shows a summary of the current uncertainty in  $\beta$  and  $\gamma$ . Although LLR has long been the dominant source of experimental constraint on  $\beta$  (combined with

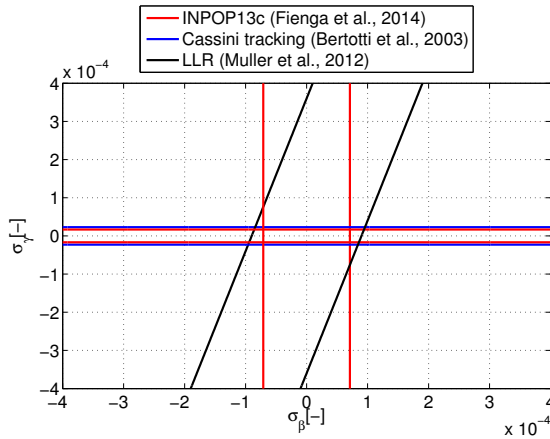


Figure 2.6: Current uncertainties on PPN parameters  $\beta$  and  $\gamma$ , updated from Turyshev and Williams (2007).

determination of  $\gamma$  from a Cassini(-like) experiment), the improvements in planetary ephemerides are providing ever more accurate experimental tests of GR. Future tests of relativity using interplanetary laser ranging promise to increase the accuracy of the measurements by orders of magnitude more (see Section 3.3.1), both from reconstruction of orbital dynamics and mm-level measurement of relativistic light-time corrections.

Postfit analysis of planetary ephemerides (see Section 2.2.4), specifically the analysis of orbital precessions of the planets, has been used to constrain a variety of theoretical alternatives to GR. For the INPOP2010 ephemeris, Fienga et al. (2011) provide estimates for the magnitude and uncertainty of the remaining freedom in the precessions of the perihelia and the longitude of the orbital node, obtained by means of a sensitivity analysis. A similar approach is taken by Pitjev and Pitjeva (2013), who provide values for precessions in the perihelion of the planets, as obtained from the EPM2011 ephemeris. The uncertainty in these precessions are currently at the order of 0.15 to 1.5 mas/century for planets for which accurate ephemerides are available.

The effect of a variety of theoretical extensions to relativity (Section 2.3.1) on the orbital precession can be used to confirm or refute such theories, or to constrain the possible ranges of free parameters in such theories. For instance, (Iorio and Saridakis, 2012) constrain the strength of an  $f(T)$  extension of gravitational physics, in which higher-order dependency on the torsion scalar  $T$  modifies the free space Lagrangian in Eq. (2.34), by calculating the orbital precessions due to such extensions. Similarly, by fitting remaining precessions in the EPM ephemeris, solar system dark matter distribution is constrained by Pitjev and Pitjeva (2013). Theoretical alternatives to both dark matter (MOND) and dark energy (galileon-induced potential) are constrained using this approach of using solar system dynamics by Blanchet and Novak (2011) and Iorio (2012b), respectively, who derive equations relating these putative effects on pericenter precessions.

However, the use of such postfit analyses are less reliable than estimates where the

parameters are fit concurrently with the observations. Firstly, this is due to the fact that during ephemerides generation unmodelled physical effects will be absorbed (partially) into the estimation of other parameters, such as the solar  $J_2$ , due to correlations of this signal with those that are to be fit. Additionally, postfit orbital precessions can result from the combination of any number of physical effects, making it difficult to attribute them to single specific effects. The reason for the nearly ubiquitous occurrence of such correlations are that, due to the near-circular, near-coplanar orbits of the planets, the various effects manifest themselves as very similar influences on the periapsis precessions  $\dot{\omega}$ . For instance, the precessions due to the first-order gravito-electric effect, Lense-Thirring effect and solar  $J_2$ , (*e.g.*, Pireaux and Rozelot, 2003; Ciufolini and Pavlis, 2004) are given by:

$$\dot{\omega}_{PN} = \frac{(2\gamma - \beta + 2)\mu_S}{a(1 - e^2)c^2}n \quad (2.43)$$

$$\dot{\omega}_{LT} = -\frac{6GJ_S \cos i}{c^2 a^3 (1 - e^2)^{3/2}} \quad (2.44)$$

$$\dot{\omega}_{J_2\odot} = -\frac{3}{2} \frac{J_{2,S} R_S^2}{(a(1 - e^2))^2} n (3 \sin^2 i - 1) \quad (2.45)$$

where  $a$ ,  $e$ ,  $i$  and  $n$  represent the semi-major axis, eccentricity, inclination and mean motion of the planet under consideration, respectively, and the subscript  $S$  denotes properties of the Sun, with  $R_S$  the Sun's equatorial radius (other symbols are as in Eq. (2.36)). For Mercury, where these precessions will be largest, the values of  $\dot{\omega}_{PN}$ ,  $\dot{\omega}_{LT}$  and  $\dot{\omega}_{J_2\odot}$  are approximately 43 as/century, 3.2 mas/century and 25 mas/century, respectively. The first order post-Newtonian precession, given by Eq. (2.43), of the planet Mercury was used by Einstein (1915a) as an experimental verification of general relativity.

The complications arising from these similar effects (in behaviour, not magnitude) are recognized by Iorio (2012a), who use the residual orbital precession of Mercury in planetary ephemerides to obtain a solar angular momentum that is incompatible with estimates from helioseismology by a factor of 2, begging the question whether this estimate is reliable. However, it is noted there that the incompatibility is likely due to the fact that the influence of the Sun's angular momentum has been absorbed into for instance the value of the solar  $J_2$  or PPN parameters, showing the weakness inherent in the postfit analysis approach. Similarly, both the INPOP2010 and EPM2011 ephemerides are used by Deng and Xie (2015) to constrain a class of  $f(R)$  extension to general relativity, where they consider the correlations with other parameters such as  $J_{2,S}$  in their analysis. However, not all such parameters that are estimated will show a strong correlation with the existing parameter set. For instance, Hees et al. (2014c) use Cassini tracking data to constrain the MOND-induced EFE, the effect of which is modulated by the preferential direction towards the galactic center, giving it a signature on solar system dynamics that is distinct from effects due to the mass or rotation of the Sun.

Including additional physical effects and parameters directly into the generation of future ephemerides would facilitate an improved consistency between the estimated pa-

rameters, when compared to the postfit analysis approach. Crucially, it would provide insight into the correlations between the various parameters. For instance, Müller and Biskupek (2007) find a correlation of 0.97 between  $\dot{G}/G$  and the tidal lag angle of the Moon. Although this information on the correlation between the estimated parameters is important for a realistic interpretation of the results, it is not obtained from a postfit analysis. However, the inclusion of too many parameters in the estimation, in the absence of sufficiently accurate and diverse data, results in (nearly) fully correlated parameters and an ill-posed estimation problem. Therefore, improvement of planetary ephemerides that would be facilitated by the use of highly accurate ILR measurements would result in both an improved accuracy of parameters currently estimated directly, as well as allow for the inclusion of additional parameters into the estimation. As a result, it would allow for improved and more reliable constraints on possible post-relativistic gravitational effects.

Although the majority of experimental tests of gravitational physics on solar system scales have been performed by exploiting the relativistic influence on the translational dynamics, exploitation of the relativistic effect on signal propagation (Section 2.3.2) has provided crucial information, especially on the parameter  $\gamma$  (see above). In addition to the translational dynamics and light-time experiments, the relativistic influence on clock rates may be exploited to test general relativity. With the advent of highly accurate clocks and time transfer techniques, such experiments are now entering the domain where they can contribute to provide state-of-the-art information on the validity of GR or one of the various alternative theories (Angélil et al., 2014; Schäfer et al., 2014). Mayrhofer and Pail (2012) propose to exploit the relativistic frequency shift in electromagnetic signals to improve the gravity field recovery capabilities of an Earth orbiter. We present a novel manner in which to robustly assess the science return from coupled relativistic translational and time dynamics effects in Chapter 7. Nevertheless, relativistic clock effects are typically very small and their exploitation to a degree where they are competitive with other tests will be challenging. For instance, Deng and Xie (2013a,b) investigate effects of  $f(T)$  gravity and a Yukawa potential, respectively, on an interplanetary time transfer link, and show that the effects of both these types of modifications to GR will be very difficult to detect, with translational dynamics likely providing (much) stronger information.

In addition to performing solar-system-scale experimental gravitation by means of exploiting the observable effects discussed in Section 2.3.2, space-based gravitational wave observatories, such as the proposed LISA (Danzmann et al., 2003), ASTROD-II/ASTROD-GW (Ni, 2008, 2013) and DECIGO (Kawamura et al., 2006) missions could provide new types of experimental information on relativity and cosmology. Furthermore, the influence of gravitational waves on frequency shift of Doppler data of planetary missions (Armstrong et al., 2003) and GPS data (Aoyama et al., 2014) has been used to place constraints on the background gravitational wave level. Using these existing radio links provide model-independent constraints on low-frequency gravitational wave amplitudes ( $10^{-6}$ - $10^{-1}$  Hz), but their accuracy is not competitive with dedicated gravitational wave detection missions. The measurement principle behind these dedicated missions fundamentally different from SLR/LLR/ILR, in that it uses interferometry between a local laser source and the incoming laser signal from other space segments, as opposed

to direct detections of incoming photons. As such, detailed discussion of such missions is beyond the scope of this dissertation both in terms of measurement technology and primary science goals. Furthermore, orbit determination requirements for such missions are relatively loose, with the requirement on relative position between the space segments of 100 m (Hechler and Folkner, 2003). Therefore, typical tracking techniques will be sufficient for the operation of such missions, without need to investigate the potential addition of an ILR system.





Satellite and Lunar Laser Ranging (SLR and LLR, respectively) have been developed for over 50 years and have long been mature techniques (Section 1.1), with well-developed technologies (Degnan, 1985, 1993; Pearlman et al., 2002; Gurtner et al., 2005) and a clear contribution to the science objectives and the operational products of various Earth-orbiting spacecraft (Seeber, 2003; Urschl et al., 2005; Exertier et al., 2006; Turyshev and Williams, 2007; Müller et al., 2007; Altamimi et al., 2011; Sośnica et al., 2015). The implementation of laser ranging to interplanetary distances, however, is still in its infancy with only a few experiments at greater-than-lunar distances successfully performed. Nevertheless, we expect that the much greater attainable accuracy of laser ranging, compared to radiometric range (Section 2.1.1), will allow Interplanetary Laser Ranging (ILR) to be a strongly supplementary, complementary and in some cases even competitive technique for future planetary missions (Section 1.2).

Future development and implementation of ILR will depend strongly on existing technologies, as well as on future developments in SLR/LLR and related fields. Since our goal in this dissertation is to analyze the potential for the scientific use of ILR, it is crucial to have a detailed understanding of the relevant aspects of the current state-of-the-art of SLR/LLR, extrapolating this to the interplanetary situation where possible, which is the goal of the present chapter. First, we discuss the general principle of laser ranging in Section 3.1, including details on the propagation of the laser pulse and associated aspects of the measurement technology. Subsequently, we discuss the primary error sources in both the measurement and analysis of laser ranging data in Section 3.2. Finally, we give an overview of the current and proposed implementations of ILR and related technologies in Section 3.3.

## 3.1 Physical Aspects of Laser Ranging

In this section, we give an overview of the various techniques and models that are applied in SLR/LLR, subsequently extrapolating them to the context of interplanetary applications. First, we give an overview of the measurement principle of laser ranging systems in Section 3.1.1. Subsequently, we discuss the manner in which laser ranging systems can be used in interplanetary applications in Section 3.1.2. Having provided the general concept by which the SLR/LLR/ILR observations are attained, we address the various concepts required to model the laser link in Sections 3.1.3, 3.1.4 and 3.1.5, where we describe the free-space propagation, atmospheric propagation and the calculation of a laser ranging link budget, respectively. Finally, we give an overview of the various hardware systems that are used in laser ranging applications in Section 3.1.6, setting the stage for a discussion and analysis of the technological readiness and limiting factors of ILR (Chapter 8).

### 3.1.1 Measurement Principle

The technology of SLR is based on the transmission and detection of short (typically 10-100 ps) laser pulses by ground stations. These transmitted laser pulses reflect off dedicated retroreflectors placed on Earth-orbiting satellites and the lunar surface (Section 1.1), and return to the ground station to be detected, allowing a two-way range measurement to be obtained (see Fig. 2.3 for a schematic representation) (*e.g.*, Degnan, 1993).

By time-tagging the transmission and reception times ( $t_t$  and  $t_r$ ) of the laser pulse, a two-way range measurement  $s(t_t)$  (where we have referenced the observation to the transmission time; see Section 2.1.1) is obtained. The error-free two-way free-space range measurement follows from:

$$s(t_t) = c(t_r - t_t) \quad (3.1)$$

where  $c$  denotes the speed of light. This measurement of the two-way range is then used in the orbit determination process, where Eq. (2.1) or (2.2) is used (for both the up- and downlink) to reproduce the measured range values.

By adjusting various parameters in the dynamical model of the spacecraft (and the Earth in ILR) and the observation model, such as the spacecraft's initial state, ground station position and characteristics or the various physical parameters discussed in Sections 2.2 and 2.3, a best estimate of the estimated parameters is obtained by, for instance, minimizing the (weighted) squared difference between the modelled and measured ranges. This results in an estimate of the parameters. However, due to errors  $\Delta t_t$  and  $\Delta t_r$  in the timing of the transmission and detection times, as well as a variety of other error sources (Section 3.2.1), the range measurement quality is degraded. As a result, the imperfect realizations  $\tilde{t}_t$  are  $\tilde{t}_r$  (instead of the ideal  $t_t$  and  $t_r$ ), are measured:

$$\tilde{t}_t = t_t + \Delta t_t \quad (3.2)$$

$$\tilde{t}_r = t_r + \Delta t_r \quad (3.3)$$

The resulting raw realization of the range measurement, which we denote  $\tilde{s}$  subsequently becomes:

$$\tilde{s}(\tilde{t}_t) = c(\tilde{t}_r - \tilde{t}_t) \quad (3.4)$$

$$\tilde{s}(\tilde{t}_t) = s(t_t) + \epsilon_s \quad (3.5)$$

where  $\epsilon_s$  is the lumped range error, including errors in the timing of the signal, the influence of the pulse's shape, and the finite pulse length. From Eq. (3.4), it can be seen that constant errors in signal timing  $t_t$  and  $t_r$  will drop out of the two-way range measurement, making it insensitive to absolute timing errors. Nevertheless, a time bias  $\Delta t$  can adversely influence the orbit determination process. For instance, an error in reference time of 10  $\mu\text{s}$  will result in the modelled reflection time at the satellite to be shifted by a similar amount. For a LEO spacecraft, with a speed of approximately 8 km/s, this results in an along-track position difference of about 8 cm, larger than the accuracy of state-of-the-art SLR systems (Section 3.2.1).

A variety of effects at the ground station and on the space segment contribute to  $\epsilon_s$ . Calibration of SLR systems is routinely carried out at the ground stations, (*e.g.*, Kirchner and Koidl, 2014), allowing part of its contribution to  $\epsilon_s$  to be resolved and corrected for before delivering the data (see Sections 3.1.6 and 3.2.1 for details on hardware used in SLR and its contribution to  $\epsilon_s$ , respectively). We denote this *in situ* determination of the range bias as  $\hat{\epsilon}_s$ . This results in the following measurement that is used in the orbit determination, denoted  $\hat{s}(t_t)$ :

$$\hat{s}(\tilde{t}_t) = \tilde{s}(\tilde{t}_t) - \hat{\epsilon}_s \quad (3.6)$$

$$= s(t_t) + (\epsilon_s - \hat{\epsilon}_s) \quad (3.7)$$

so that the remaining range error is the difference between the true and *a priori* estimated value of  $\epsilon_s$ .

The correction term  $\epsilon_s$  in Eq. (3.4) is distinct from the  $\Delta s$  terms in Eqs (2.1) and (2.2). Specifically, the correction  $\epsilon_s$  is applied to convert the measured two-way range to a best estimate of the true two-way range, whereas the  $\Delta s$  terms are corrections that are applied to convert the modelled ideal free-space Cartesian two-way range to the modelled true range (which includes relativistic and atmospheric propagation corrections). However,  $\Delta s$  may contain additional (estimated) corrections to the range measurement, which can capture errors that are not or imperfectly removed by  $\hat{\epsilon}_s$ , such as clock errors (Bauer et al., 2013) or unresolved range biases, (*e.g.*, Coulot et al., 2007; Angermann and Müller, 2009). In SLR and LLR, corrections also need to be applied for the influence of the retroreflectors. The reflection point on the space segment is generally not the center of mass (Otsubo and Appleby, 2003), with the exception of the experimental BLITS retroreflector satellite, (Kucharski et al., 2011)). Therefore, an offset needs to be added to the range measurement. Additionally, since the reflected pulse may consist of the reflections from multiple reflectors (depending on the retroreflector array configuration), the reflected signal consists of a convolution of the pulses reflected off all reflectors. Resultantly, a signal-strength dependent range correction must be applied, which also depends on the ground station characteristics and the target's elevation angle (see Section 3.2.1).

Ideally, the measurement  $\hat{s}(\tilde{t}_t)$  represents the two-way range between a reference point fixed to the ground station  $\mathbf{r}_{gs}(t)$  and the center-of-mass of the satellite  $\mathbf{r}_{sc}(t)$ . However, errors both in the range measurement itself and the models used to process the measurement (including those for  $\mathbf{r}_{gs}(t)$  and  $\mathbf{r}_{sc}(t)$ ) limit the attainable accuracy of both the range measurements (Section 3.2.1) and the data products that may be obtained from them (Section 3.2.2).

### 3.1.2 Interplanetary Ranging Concepts

In ILR, the use of retroreflectors is no longer feasible due to the large distances involved and the technology's inverse quartic dependency of receiver signal strength with distance (Section 3.1.5). To overcome this, an active system must be used on the space segment, the use of which changes the signal strength dependency to inverse square with distance.

Three different types of active laser ranging systems (sometimes termed transponder laser ranging) can be distinguished for use in planetary missions (Degnan, 2002; Birnbaum et al., 2010). These concepts are shown schematically in Fig. 3.1a)-3.1c), with a schematic diagram of the laser range up- and downlink shown in Fig. 3.2. Below, we summarize these concepts:

- **One-way laser ranging.** A laser pulse is transmitted from a ground station and detected by a (satellite-based) receiver. The pulse transmission time  $\tilde{t}_t$  at the ground station and reception time at the space segment  $\tilde{t}_r$  are then used to determine the one-way range from Eq. (3.4). An important issue with this method is that the transmission and reception times are measured by different, unsynchronized, clocks. As a result, offsets and rate differences between transmitter and receiver clocks will introduce an error in the range determination. This error may be mitigated either by the use of an exceptionally high-quality clocks, or the inclusion of the estimation of clock parameters. A detailed analysis of this aspect of the error budget of a one-way laser ranging system is given in Chapter 6. Relatedly, the rate difference between proper and coordinate time (Section 2.3.2) becomes much more important in the correct reduction of one-way range data, as we discuss in more detail in Chapter 7.
- **Two-way echo laser ranging.** In echo laser ranging, the space segment transmits a laser pulse back to the ground station upon reception of a laser pulse. Using a two-way method largely negates the clock offset problem of one-way systems. However, an echo system is incapable of operating in a high noise environment (Section 3.1.5), since each detection (be it signal or noise) will cause the transmission of a laser pulse back to Earth (Degnan, 2002). To mitigate this issue, the detection threshold must either be set very high, requiring high laser power at the receiver (with associated issues of multi-photon detection, see Section 3.2.1), or one must accept longer outages due to the signal being overwhelmed by noise. The two-way echo system is used in radio tracking systems (Thornton and Border, 2000), where there is a more benign noise environment, as the Sun's output in radio wavelengths is much smaller than that in optical frequencies.

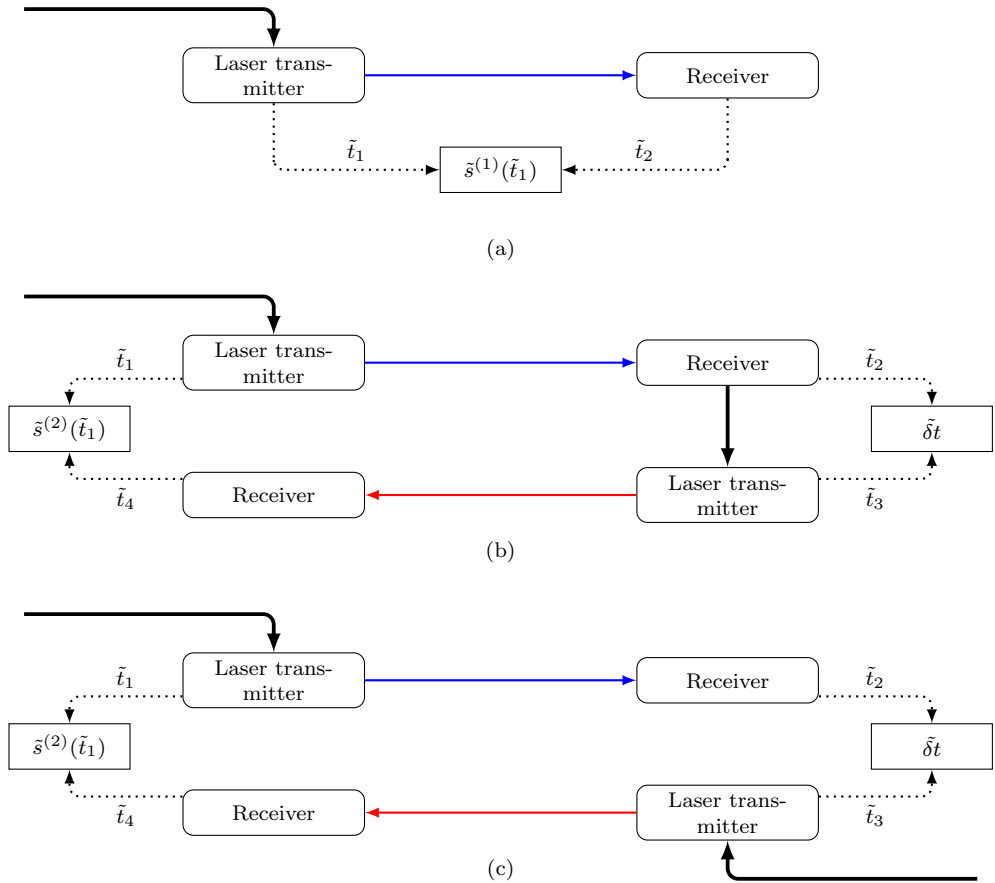


Figure 3.1: Schematic representations of laser ranging concepts, based on figure by Birnbaum et al. (2010). Thick lines indicate signals to trigger the transmission of a laser pulse. a) One-way laser ranging b) Two-way echo laser ranging c) Two-way asynchronous laser ranging.

- Two-way asynchronous laser ranging. In an asynchronous two-way laser ranging concept, both the space and ground segment fire laser pulses towards one another independently (Degnan, 2002). This negates the problem that occurs in the echo laser ranging concept, where laser pulses are sent in response to a noise signal. By pairing a range measurement from the up- and down-link, a two-way range measurement is obtained (Birnbaum et al., 2010), which suffers from neither the large clock error issue of a one-way system, nor the strong noise sensitivity of the echo system.

For the one-way system, a one-way range  $s^{(1)}(t)$  is measured, in which  $t_t = t_1$  and  $t_r = t_2$  in Eq. (3.6). For the two-way systems, it is the two-way range  $s^{(2)}(t)$  that is measured, with  $t_t = t_1$  and  $t_r = t_4$  in Eq. (3.6). For active two-way ranging, the difference between uplink reception time  $t_2$  and downlink transmission time  $t_3$ , denoted

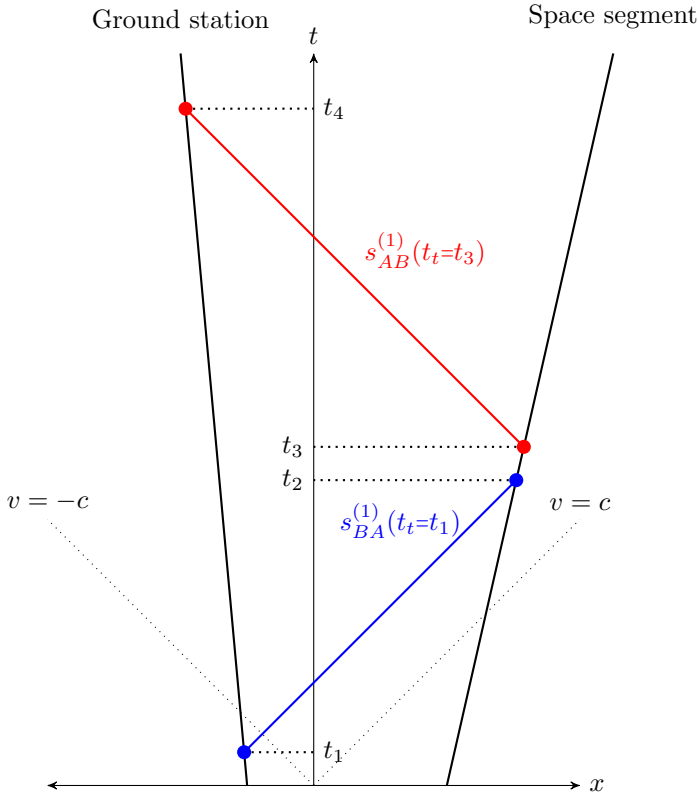


Figure 3.2: Schematic spacetime diagram showing one-dimensional representation of up- and downlink one-way ranges between stations a ground station and space segment (both moving with constant velocity). Adapted from Fig. 2 in Chapter 6.

by  $\delta t$  and termed the retransmission delay in an echo system, is measured by the space segment as:

$$\delta t = t_3 - t_2 \quad (3.8)$$

For typical SLR/LLR operations, the  $\delta t$  term is absorbed into the retroreflector signature, ( *e.g.*, Otsubo and Appleby, 2003). For the two-way transponder concepts, the times  $t_2$  and  $t_3$  are measured and  $\delta t$  is included in the observation model directly. More details on the mathematical formulation of the one- and two-way range observations are given in Section 3.2 of Chapter 6.

For an echo system, the retransmission time will typically be very small, with  $\delta t \ll 1$  s. For an asynchronous system, however, its magnitude will be on the order of the pulse detection frequency of either the ground or space segment (whichever is larger), this value can be anywhere from  $\ll 1$  s to the order of minutes, depending on system and link characteristics. In a situation where much more up- than downlink one-way ranges are obtained (due to an asymmetric link budget), the asynchronous system can

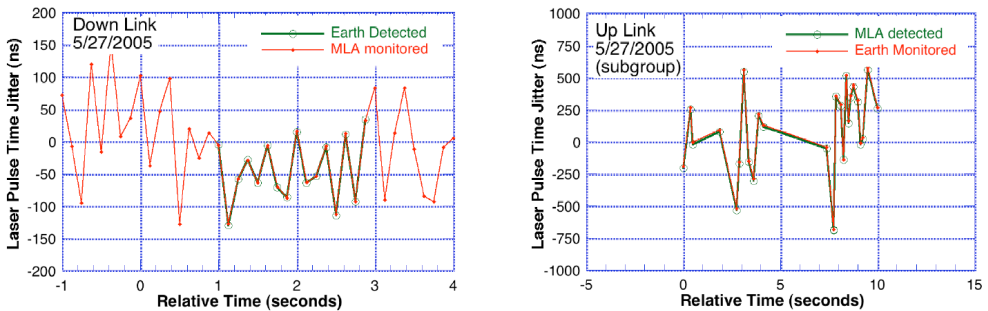


Figure 3.3: Graph indicating the excellent fit between the jitter in transmission and detection time of the laser pulses during the MESSENGER experiment (Neumann et al., 2008).

operate asynchronously not only in an operational sense, but it also in the data analysis process. For instance, a single downlink one-way range  $t_4 - t_3$  may be paired with a number of uplink one-way ranges  $t_2 - t_1$  to obtain a number of asynchronous two-way ranges. In doing so, each of the uplink one-way ranges is used, without the clock noise polluting the range measurement at the level that it would for one-way measurements.

Of the above three concepts, two-way asynchronous laser ranging has been the method of choice in most interplanetary laser ranging mission proposals (Section 3.3.1), at least from a science return point of view, as it has neither the clock synchronization problem of a one-way system, nor the sensitivity to high noise levels of the echo system. However, a one-way system is simpler to operate and potentially cheaper to build and fly, since it does not require a laser generation and transmission system (but does have more stringent requirements on clock stability). A notable example of a one-way system is the LRO spacecraft, for which one-way laser ranging is employed to support precise orbit determination (Section 3.3.1). The absence of a two-way laser ranging capability on LRO was due to mission scheduling constraints, however, not technical requirements (Degnan, 2008). An interesting commonality shared between these three transponder laser ranging systems is that they can all be used to perform laser time transfer (Section 3.3.4) without modifications to the operating principle, since electromagnetic signals are exchanged and accurately time-tagged by different observers. We discuss the use of time transfer, specifically the relativistic clock effects that manifest themselves in the measurements, in Chapter 7.

An important difference between the asynchronous two-way and reflector laser ranging used in SLR/LLR, is that reflection techniques typically have no ambiguity as to which detected pulse corresponds to which transmitted pulse. For space segments with sufficiently accurate state predictions, as is the case for LRO, this *a priori* information can be used to pair the transmitted and received laser pulses with a high degree of confidence (Bauer et al., 2013). If the dynamics of the space segment is not (yet) well characterized, though, pairing a detected pulse at one transponder to a transmitted pulse at the other transponder can become a non-trivial task. A number of different approaches can be taken to overcome this potential measurement ambiguity. In the

laboratory experiment by Chen et al. (2011) a coded sequence was sent between the two link ends, serving to anchor the pairing between the pulses at one point in the experiment, which can then be extrapolated to subsequent pulses. Alternatively, the entire ranging campaign can be done by a coded sequence. Pulsed laser systems, however, tend to be better suited to operate at a constant pulse frequency. For the ranging experiment to the MESSENGER spacecraft (Section 3.3.1) (Smith et al., 2006), inherent pulse transmission time jitter was used as a coding for the signal (Neumann et al., 2008). This jitter was on the order of 100 ns, which is well above the time resolution of the detection systems, allowing this random jitter to be employed as the coded sequence. The correlation of the detected and transmitted pulses is shown in Fig. 3.3. In this figure, the excellent correspondence between the transmitted and detected jitter pattern can be seen. Also, a clear difference between the jitter amplitude can be distinguished between the up- and downlinks, due to the different characteristics of the ground- and space-segment laser systems. When employing a jitter matching technique, a number of system characteristics must be taken into account. Specifically, pulse arrival and transmission time must be measurable to much greater accuracy than the mean jitter in the transmission time. Similarly, the pulse length must be (much) shorter than this jitter, in order to ensure that the transmission jitter pattern can be resolved from random noise.

### 3.1.3 Free Space Propagation

SLR systems use laser pulses which have a spatial (in the direction perpendicular to the direction of signal propagation) intensity profile that closely approximates a Gaussian shape (Degnan, 1993), omitting the effects of aperture diffraction (Klein and Degnan, 1974). The spatial signal intensity  $I$  of a Gaussian beam in the far field can be described by the following (Siegman, 1986):

$$I(r, z) = I_0 \left( \frac{w_0}{w(z)} \right)^2 \exp \left( -2 \frac{r^2}{w(z)^2} \right) \quad (3.9)$$

$$w(z) = w_0 \sqrt{1 + \left( \frac{\lambda z}{\pi w_0^2} \right)^2} \approx \frac{\lambda z}{\pi w_0} \quad (3.10)$$

where the approximation holds if the final term in Eq (3.10) is much larger than 1 (far-field approximation).

Here,  $\lambda$  is the wavelength of the laser pulse and  $I_0$  is the signal intensity at the waist (defined as  $z=0$  here; approximately equal to the transmission system position when  $z \gg 1$ ). The laser spot size is denoted by  $w(z)$ , with the beam waist radius denoted as  $w_0$  and the off-axis distance  $r$ . The off-axis angle  $\theta$  is defined as follows for small angles:

$$\theta = w(z)/z \approx \frac{\lambda}{\pi w_0} \quad (3.11)$$

The beam-divergence half-angle (denoted  $\theta_{1/2}$ ), which is the angle  $\theta$  at which the intensity in Eq. (3.9) drops to  $1/e^2$  of its on-axis value, is determined from Eq. (3.10) to be

---

Section 3.1.3 has been adapted from Section 2.1 of Chapter 5, and is included here as required background information for subsequent sections of this chapter.



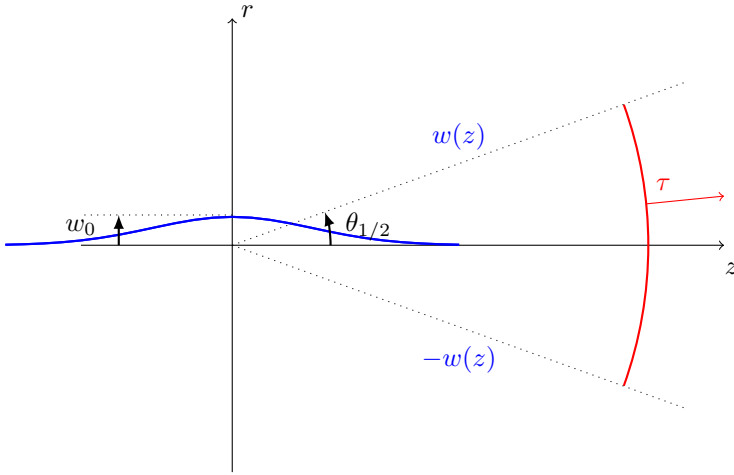


Figure 3.4: Schematic representation of Gaussian beam profile, with a wavefront in the farfield regime indicated in red (with associated local  $\tau$  variable, where  $\tau = 0$  on the wavefront by definition).

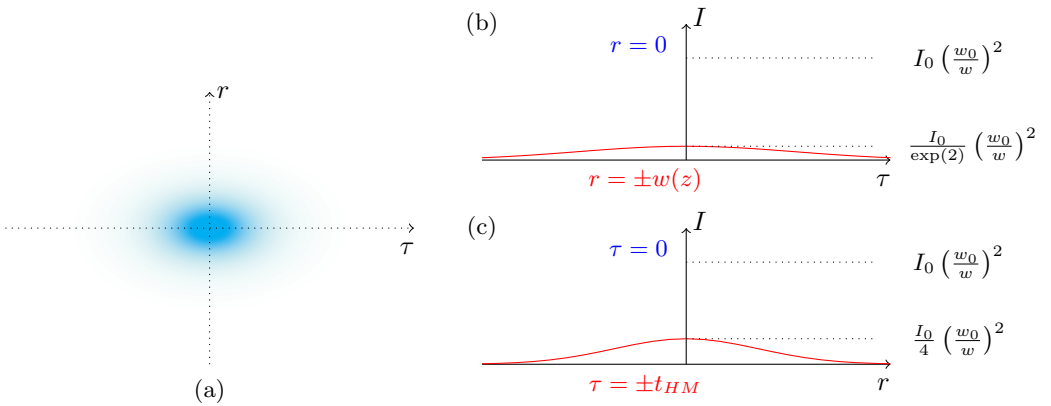


Figure 3.5: Representations of laser pulse intensity as a function of off-axis distance  $r$  and propagation direction time offset  $\tau$ . a) Pulse intensity indicated as shading. b) Intensity profiles for selected constant  $r$ . c) Intensity profiles for selected constant  $\tau$ . Note that the different multipliers for the intensity at  $r = \pm w(z)$  and  $\tau = \pm t_{HM}$  is due to the different formulations of Eqs. (3.9) and (3.13) and the use of  $t_{HM}$  instead of  $\sigma_t$  in this figure.

the following in the far-field:

$$\theta_{1/2} \approx \frac{\lambda}{\pi w_0} \quad (3.12)$$

The half-angle is typically around 50-75  $\mu\text{rad}$  ( $\approx 10\text{-}15''$ ) for SLR systems (Degnan, 1993). A schematic representation of a Gaussian beam profile is shown in Fig. 3.4.

For a laser pulse used in SLR, the temporal profile can also be well approximated by a Gaussian shape (Degnan, 1993). This Gaussian shape is not significantly influenced by atmospheric turbulence (Fante, 1975; Degnan, 1993), except for pulse lengths on the order of picoseconds and shorter. To describe the spatiotemporal intensity pattern of the pulse  $I_p$ , we introduce a time  $\tau$ , which is defined to be zero at the pulse center and obtain:

$$I_p(r, z, \tau) = I(r, z) \exp\left(-\frac{\tau^2}{2\sigma_t^2}\right) \quad (3.13)$$

where  $\sigma_t$  is the pulse-length standard deviation, related to the pulse full-width half-maximum (FWHM)  $t_{HM}$  ( $t_{HM} = 2\sqrt{2\ln 2}\sigma_t$ ), which is typically used to quantify SLR systems (Murphy, 2001).

To illustrate the behaviour of the intensity of a Gaussian pulse, we schematically show the signal intensity as a function of both  $r$  and  $\tau$  in Fig 3.5a). Also, we plot the signal intensity of cutaways at constant  $r$  and constant  $\tau$  in Figs. 3.5b) and 3.5c), respectively.

### 3.1.4 Media Propagation

Since the laser beam propagates through the terrestrial atmosphere (and potentially the atmosphere of another celestial body, *e.g.*, Mars), atmospheric influence on the propagation of the beam must be considered in both the design of the system and during the analysis of laser ranging data. In fact, accounting for atmospheric delays is one of the main challenges in precise laser ranging measurement analysis (Degnan, 1993; Exertier et al., 2006). The influence of the atmosphere on the laser pulse can be divided into a deterministic contribution and a stochastic contribution due to atmospheric turbulence.

The deterministic contribution is due to the influence of a medium's refractive index on the propagation velocity of an electromagnetic signal. Secondly, gradients in the refractive index  $n$  of the atmosphere cause a bending of the signal path. Both these effects cause a delay in a laser pulse's arrival time, which may be quantified by the range correction  $\Delta s_{atm}$  (atmospheric contribution to  $\Delta s$  in Eqs. (2.1) and (2.2)), (*e.g.*, Hulley and Pavlis, 2007):

$$\Delta s_{atm} = \int_{ray} (n - 1)ds + \left( \int_{ray} ds - \int_{vac} ds \right) \quad (3.14)$$

where  $ds$  either runs along the vacuum propagation path or the curved atmospheric propagation path (depending on the integral subscript). The total delay is dominated by the first term, called the excess path delay, which is about 2.5 m at zenith. The term in brackets, called the geometric delay, is typically very small, reaching values of 2 cm at very small elevation angles ( $10^\circ$ ).

Turbulence in the atmosphere influences laser pulse propagation, since it causes temperature fluctuations that, in turn, cause slight variations in the refractive index  $n$  (Andrews and Phillips, 2005). This causes variations in both the travel time and the light intensity at the receiver. In effect, the atmosphere behaves as a series of lenses of stochastic strength and size. We present a detailed analysis of the influence of atmospheric turbulence on laser ranging in Chapter 5.

Both the deterministic and the stochastic influences cause changes in the beam intensity pattern and its travel time. Especially the travel time is crucial for the data processing of ranging measurements, whereas the influence on the beam intensity is important for determining the expected performance of a system (Section 3.1.5). Also, the analysis of beam intensity variations due to atmospheric effects influences the system performance both due to varying signal attenuation and the resulting changes in the detection time Probability Distribution Function (PDF) (Section 3.2.1; Chapter 5).

A first approximation that can be made when modelling the influence of an atmosphere on laser pulse propagation is to assume that it consists of spherical shell layers, i.e., that there is no latitudinal and longitudinal influence on its state. One such model given by Marini and Murray Jr. (1973) has typically been used until recently for the analysis of SLR/LLR data. Although relatively simple, the model has an uncertainty of only about 1 cm in zenith and several cm for low elevations (Schwartz, 1990; Seeber, 2003). For the application of this method, the only required meteorological data are pressure, temperature and water vapour pressure at the ground station, at signal transmission and reception times. New models for both the delay's dependence on zenith angle (Mendes et al., 2002) and the zenith delay itself (Mendes and Pavlis, 2004) have been developed. The combination of these models is the current standard for atmospheric ranges corrections in SLR/LLR data reduction (Petit et al., 2010). Errors due to mismodelled atmospheric propagation correction are estimated to be around 4-6 mm (Exertier et al., 2006).

A new method to calculate the atmospheric correction to laser ranging measurements was proposed by Hulley and Pavlis (2007), who use a ray-tracing method and global meteorological information for the numerical calculation of an atmospheric correction from Eq. (3.14). By using this method, horizontal gradients in the refractive index  $n$  are included, which were neglected in previous models. The influence of horizontal gradients is especially strong at low elevations, but is also dependent on station location, time of year, time of day, azimuth angle, *etc.* The mean influence of horizontal gradients at  $10^\circ$  elevation is at several mm, whereas the standard deviation is at a level of 5-10 mm for typical cases, decreasing by a factor of roughly 3 at  $20^\circ$  elevation. These values indicate the need for the inclusion of the horizontal refractivity gradients for mm-accuracy laser ranging (SLR, LLR and ILR). Such horizontal gradients become less important for small zenith angles, where the propagation is close to vertical. For zenith signal propagation, though, the model of Mendes and Pavlis (2004) shows a difference with ray tracing solutions that is at the 1 mm level. This shows the desirability of ranging near  $90^\circ$  elevation angles, so as to reduce the error in atmospheric correction modelling. However, as discussed in Section 3.2.2, this is often not an option for ILR mission scenarios.

A method that has been proposed to correct for the atmospheric delay is multi-

wavelength (also termed multi-color) laser ranging (Abshire and Gardner, 1985). Since the troposphere is dispersive at optical wavelengths, the atmospheric delay of a laser beam is wavelength-dependent. Therefore, multiple wavelengths could be used simultaneously to allow for a very accurate characterization of the delay. This approach is conceptually similar to the use of multi-wavelength radio tracking of planetary satellites (Bertotti et al., 2003). However, the application for atmospheric correction has not yet reached maturity, since a range precision on the order of  $50 \mu\text{m}$  is required to detect the difference atmospheric influence at two typical SLR frequencies (Wijaya and Brunner, 2011), which is well beyond current state of the art of SLR (Section 3.2.1).

For ILR, the effect of the interplanetary medium and the solar atmosphere needs to be assessed. For radio tracking, these media limit the attainable accuracy at small solar separation angles (Section 2.1.2). No data specifically on the influence of this medium on optical pulse propagation has been found. However, measurements for the influence of solar wind on the time delay of radio signals have been performed with the Mariner 6 and 7 probes (Muhleman et al., 1977), as well as the Viking spacecraft (Muhleman and Anderson, 1981). Muhleman and Anderson (1981) find a relation for  $(n - 1)$  that is linearly dependent on electron density and inverse squared-dependent on signal frequency, valid for frequencies larger than 1 GHz and solar impact parameters larger than two solar radii. The signal frequency requirement clearly holds for laser pulses, where  $f > 100 \text{ THz}$ . Measurements indicate that for an S-band signal (2.2 GHz), the influence of the interplanetary electron density on signal propagation time is in the order  $10 \mu\text{s}$  (3 km signal propagation distance in vacuum) for a solar impact parameter of  $2R_s$ . Since the delay is dominated by the particle environment near the Sun, this value is largely independent of the distance between the Earth and the target, and instead depends on the solar impact parameter of the signal path. For an optical pulse (with a frequency more than  $10^5$  times that of an S-band signal), the S-band delay of  $10 \mu\text{s}$  scales to well below measurable effects, validating the assumption of negligible influence of interplanetary medium on laser pulse propagation.

### 3.1.5 Link Budget

Laser pulse detection in SLR is performed by means of direct detection of the arrival time of one or several photons of a laser pulse (Section 3.1.6). The number of photons  $N_p$  per pulse that can trigger the detector can be determined from the radar link equation, as adapted from (Degnan, 1993):

$$N_p = \eta_q \left( E_T \frac{\lambda}{hc} \right) \eta_t G_t(\theta) \sigma_{cs}^{m-1} \left( \frac{1}{4\pi R^2} \right)^m A_r \eta_r T_a^m \quad (3.15)$$

where  $\eta_q$  is the quantum efficiency of the detector,  $E_T$  the energy of the transmitted laser pulse,  $\lambda$  the laser wavelength, which is typically 532 nm,  $\eta_t$  the transmission optics efficiency,  $G_t$  the transmitter gain as a function of off-axis pointing angle  $\theta$ ,  $\sigma_{cs}$  the satellite optical cross-section,  $R$  the range to the target,  $A_r$  the effective telescope receiver area,  $\eta_r$  the receiver optics efficiency and  $T_a$  is the one-way transmissivity of the atmospheric propagation path. The value of  $m$  is 2 for reflection systems (such as SLR and LLR) and 1 for one-way ranging systems (such as the up- or downlink in a transponder system).

The dependence of the transmitter gain on the off-axis angle  $\theta$  in Eq. (3.15) may be obtained by the approximation of the Gaussian pulse shape (Section 3.1.3). Under this assumption, the gain can be seen to decrease with  $\theta$  as  $\exp(-2\theta^2/\theta_{1/2}^2)$ , see Eqs. (3.9) and (3.12), as illustrated in Fig. 3.5. However, the far-field gain is also influenced by atmospheric turbulence, which is discussed in detail in Chapter 5. For a typical link budget and assuming single-photon detection, a general rule of thumb for the pointing requirement  $\sigma_\theta$  of the system is  $\sigma_\theta < \theta_{1/2}$ .

In addition to photon flux from the laser pulse, noise photons from the environment can also trigger the detector. The noise environment in laser ranging operations can be especially punishing, as the range of operating wavelengths (typical values are 532 and 1064 nm) coincides with the peak of the Sun's radiation output (883 nm). To mitigate the influence of environmental noise, a number of filtering methods are used in SLR, which drastically reduce the noise rate:

- Spectral filtering. Only light of a very limited spectral bandwidth is allowed through a physical filter placed in the reception optical path. Due to the strong monochromaticity of laser light, the spectral filter can be set to a very narrow bandwidth without loss of signal. The spectral bandwidth is typically  $\sim 0.1$ -1 nm, (*e.g.*, Degnan, 1994; Seeber, 2003). The size of the spectral bandwidth is limited by the fact that the wavelength bandwidth of the photons in the laser pulse increases for shorter laser pulses due to dispersion.
- Temporal filtering. A good initial estimate of the target location is required to acquire a return signal in SLR, due to the very small beam divergence angle of the laser (Section 3.1.3). This initial position is calculated from available ephemerides and used for initial pointing. Consequently, the time interval during which the return signal is expected can be determined. The detector is only active during these time intervals, preventing it from picking up noise during the intervening time, an approach termed range gating. Typical range gate durations are 0.1 to 10  $\mu\text{s}$  (Seeber, 2003), dependent on the accuracy of the *a priori* orbit predictions of the target.
- Spatial filtering. Since an initial position estimate of the target is available, the direction from which return photons are expected can be predicted. This yields a solid angle range over which the returns will occur. As such, the direction of the telescope, as well as the solid angle over which light is allowed directly onto the detector, can be set to a limited range.

In addition to environmental noise, the detector itself will have a certain dark noise level, which is the number of spurious detection signals per unit time that the detector produces, even in the absence of external stimuli. For instance, the space-grade SPAD detector (see Section 3.1.6) presented by Prochazka et al. (2007) has a dark noise rate of about 1 kHz at 0° C, increasing by about one order of magnitude per 30 K temperature increase.

In interplanetary laser ranging, the noise photon rate can be much larger than in typical SLR/LLR situations, due to the fact that the receivers are pointed (almost) directly at the Earth or at a target body, such as a moon or planet (for the space-

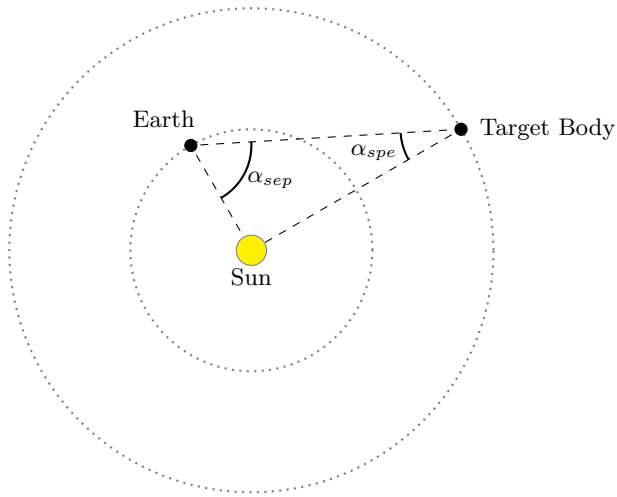


Figure 3.6: Representation of Sun avoidance angle at Earth and target body, denoted  $\alpha_{sep}$  and  $\alpha_{spe}$

Table 3.1: Fraction of days per synodic period with visibility of given target, for given limits on Sun separation angles from both Earth and target planet

(a) Equal limits on $\alpha_{sep}$ and $\alpha_{spe}$					(b) Varying limit on $\alpha_{spe}$ ; limit on $\alpha_{sep}$ fixed to $10^\circ$				
Target body	$10^\circ$	$5^\circ$	$2^\circ$	$1^\circ$	Target body	$10^\circ$	$5^\circ$	$2^\circ$	$1^\circ$
Mercury	0.70	0.87	0.96	0.99	Mercury	0.70	0.70	0.70	0.70
Moon	0.89	0.96	0.99	1.00	Moon	0.89	0.93	0.94	0.95
Mars	0.83	0.91	0.97	0.98	Mars	0.83	0.90	0.91	0.91
Jupiter	0.29	0.70	0.88	0.94	Jupiter	0.29	0.70	0.88	0.91
Saturn	0.00	0.41	0.79	0.90	Saturn	0.00	0.41	0.79	0.89
Uranus	0.00	0.00	0.54	0.79	Uranus	0.00	0.00	0.54	0.79
Neptune	0.00	0.00	0.00	0.65	Neptune	0.00	0.00	0.00	0.65

and ground-segment, respectively). Since planets reflect solar radiation (albedo) and produce their own blackbody radiation, they are sources of noise photons (Degnan, 2002). Additionally, during daylight ranging operations atmospherically scattered light will become an important source of noise photons. Due to the geometry of ILR, ranging will only be possible during daylight for extended periods of time. In fact, for missions closer to the Sun than the Earth, the target will only be visible in daylight. The problem of increased noise rate may be further exacerbated by the fact that temporal filtering can no longer be applied in all cases, due to the asynchronous nature of the typical application, where the signal has to have been acquired before the detection system can start to operate in phase with the transmitted system, allowing temporal filtering to be used. This acquisition is further complicated by the long light time, so that it cannot be immediately verified whether transmitted pulses are detected or not.

An additional source of noise which is very important for ILR is stray light. Stray light occurs due to light outside the direct field of view of the instrument being scattered onto the detector. This can be from intrinsic scattering, due to reflected light from parts of the structure and optics, or contaminated optics (Roberts, 2010). Although the intensity of stray light will, in general cases of laser ranging, be quite low compared to that of other noise sources, it can become very high when the telescope is pointing near the Sun. The problem of stray light is exacerbated by the fact that it is notoriously hard to model robustly (Hemmati, 2006). Reduction of stray light can be achieved by a number of design options, such as baffles, field stops and stringent optical surface quality requirements. Most ILR concepts have targets near the plane of the ecliptic, so the Sun avoidance angles  $\alpha_{sep}$  and  $\alpha_{spe}$  for the ground and space segments (*sep* and *spe* is short for Sun-Earth-Planet and Sun-Planet-Earth, respectively), shown in Fig. 3.6, will become very small once every synodic period of the Earth and the target. This means that for a certain portion of the mission, ranging will be impossible (as is also the case for radio ranging). For gravitational physics experiments, maintaining the link as close to conjunction as possible is crucial (Section 2.3.2), as this increases the gravitational influence of the Sun on the laser pulse propagation. Typical values of limiting angles that are proposed for dedicated systems, in which substantial design effort has been made to reduce stray light, are  $3^\circ$  (Roberts, 2010) or  $2^\circ$  (Hemmati, 2006). For their analyses of science return from Mars and Phobos landers performing ILR, Chandler et al. (2005) and Turyshv et al. (2010) investigate a range of Sun avoidance angle limits of  $0.5^\circ$ - $15^\circ$  and  $2^\circ$ - $2^\circ$ , respectively. For outer planet ranging, the angle remains low throughout the synodic period, making stray light rejection especially important for missions to these planets. We present the visibility fraction of a number of targets for a range of limits on the separation angles in Table 3.1 to highlight and quantify the issue of stray light rejection. To generate the numbers in this table, we have simulated the  $\alpha_{spe}$  and  $\alpha_{sep}$  angles over a full synodic period between Earth and the target planet, and subsequently calculated the number of days in the synodic period where there was a possibility of performing ranging without violating the indicated Sun avoidance angle constraints. It can clearly be seen that for ranging to the outer planets, exceptional stray light rejection (Sun avoidance angles of  $< 2^\circ$  for ranging to Uranus and Neptune) will be required, making the implementation of ILR in such missions technologically challenging.

In typical SLR situations, the signal return rate will be sufficiently large for noise photons to only rarely be spuriously identified as signal photons. In certain situations, however, for instance in LLR, the signal-to-noise ratio can become very low. A method to extract measurement data in these cases is described by Abbot et al. (1973) and Ricklefs and Shelus (1992). The method is based on the fact that background noise will approximately obey Poisson statistics, while laser ranging returns will not, since the arrival times of subsequent pulses are very strongly temporally correlated. Low signal-to-noise situations may occur in a number of situations in ILR, especially for laser ranging at extreme distance, or ranging at small solar separation angles.

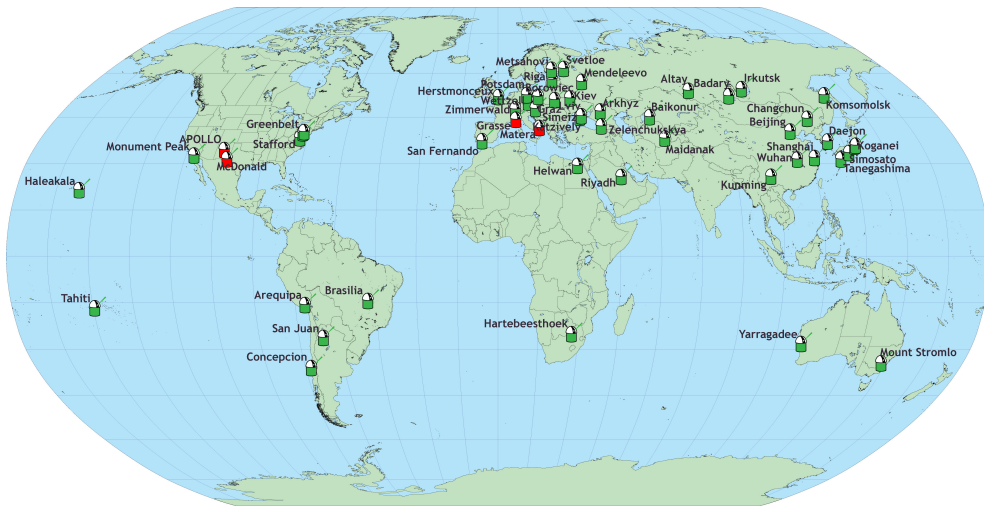


Figure 3.7: Illustration showing global distribution of ILRS stations (NASA/ILRS). Stations routinely performing LLR (as of 2014) shown in red (Murphy, 2014). Note the latitudinal and longitudinal heterogeneity in station distribution.

### 3.1.6 Hardware Systems

Precise, accurate and stable time tagging of laser pulse transmission and reception is crucial for the minimization of errors in the range measurement, as shown by Eq. (3.4). In this section, we give an overview of the hardware that is used to obtain such measurements in SLR/LLR, extrapolating this to ILR where possible. The error sources induced by hardware imperfections are discussed in more detail in Section 3.2.1. Although we are not concerned with the detailed workings of the hardware of either the space or ground segment here, it is crucial to have an overall understanding of the various subsystems involved in the realization of laser ranging measurements. Specifically, we are concerned with how their properties influence the realization of the (interplanetary) range measurements, as hardware-induced effects are an important contributor to the error budget of laser ranging measurements, (*e.g.*, Exertier et al., 2006). Therefore, we discuss the various components of an SLR system here, in preparation for our discussion of error budgets in Section 3.2. The ground segment for ILR will likely be made up largely of existing ILRS stations, the global distribution of which is shown in Fig. 3.7. It can clearly be seen that the global distribution is far from homogeneous, especially for LLR. For ILR, this may have significant consequences beyond those in SLR/LLR, as discussed in Section 3.2.2.

A block diagram of the system for both pulse transmission and detection is shown in Fig. 3.8. We will discuss the main characteristics of the key elements (in the context of this dissertation) of existing hardware in SLR/LLR. These elements are the following:

- Laser generation and transmission system. The laser pulse generator produces a pulsed laser signal, that is passed through the transmission optics to the telescope,



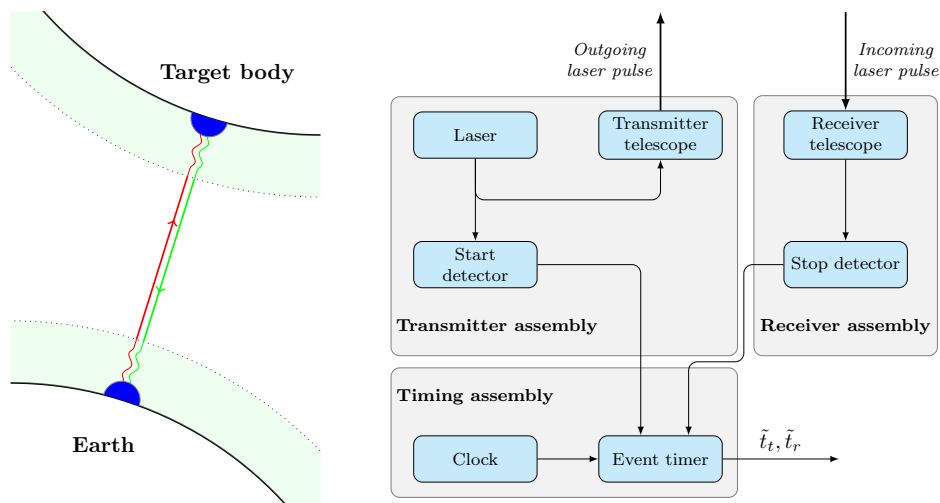


Figure 3.8: Diagrams showing: (left) Up- and downlink of two-way laser operations between an Earth-based and a planetary transponder (both in blue), including atmospheric distortion on both bodies; (right) Transponder subsystems relevant for laser pulse time tagging.

where it is transmitted to the target. The laser medium used in many modern laser ranging systems produces laser light at a fundamental wavelength of 1064 nm, which is typically frequency-doubled to produce a wavelength of 532 nm (green light). Other parameters of the laser system that have significant influence on system performance are the pulse repetition rate, pulse length and pulse energy. The pulse repetition rate has typically been in the order of 10 Hz in SLR/LLR systems. In the past decade, however, a number of laser ranging stations have started operating at 1-2 kHz frequencies, (*e.g.*, Kirchner and Koidl, 2004), which has a number of key advantages. Most notably for ILR, it allows the system to more easily operate at the single-photon signal intensity level, without excessive data volume loss and associated precision reduction (Section 3.2.1). Pulse lengths in the order of 10-100 ps are typically used, with shortening of the pulse length limited to about 10 ps by atmospheric dispersion (Chapter 5). SLR systems may use pulse energies ranging from values on the order of 0.1-1 mJ (for kHz systems), to the order of 1-100 mJ for typical SLR stations, and some LLR stations operating at pulse energies around 1 J<sup>1</sup>. The influence of detected laser pulse energy on the stability and accuracy of the range measurement is discussed in Section 3.2.1.

- **Detector.** The detector is the device that triggers an electronic signal upon the transmission or reception of a laser pulse. For the transmission, a dedicated start detector is used, which is directly linked to the transmission optics to register the transmission time of a laser pulse. The stop detector, which is separate from

<sup>1</sup><http://ilrs.gsfc.nasa.gov/SLV2/network/QueryILRSLogs.action>

the start detector, is triggered when one or more reflected photons (depending on the detector settings and efficiency) of the transmitted pulse successfully impact the detector. In SLR, two different types of detectors are used: Single Photon Avalanche Diodes (SPAD) and Photo-Multiplier Tubes (PMT), (*e.g.*, Wood and Appleby, 2004). The two systems are currently about evenly represented in the ILRS network (Otsubo et al., 2015), with the PMT system preferred by US-managed stations. Although the SPAD is better suited to consistent single-photon operation (Wood and Appleby, 2004), a complication with the system is that its rise time (the time between photon impact and electronic signal trigger) is dependent on the number of photons that triggers the system. This requires a compensation (Compensated SPAD, or C-SPAD) of the detector output, to take into account this signal-strength dependence (Kirchner et al., 1998). A difficulty of such a compensation is that it is dependent on the received temporal pulse shape, and therefore on the target that is ranged to (due to the retroreflector signature), as discussed by Otsubo and Appleby (2003). However, the temporal pulse shapes in ILR are very stable, due to the absence of retroreflectors, allowing for easier compensation.

- **Clock.** The system clock is typically a stable frequency standard which is used to keep the current time at the station. In SLR, the need for a stable clock at the station is twofold. Firstly, any clock instability over the two-way light time propagates directly into the error budget of the measurements (Section 3.2.1). Additionally, any time tag error of the range measurement introduces a time bias into the range measurement processing (Section 3.1.1). An overview of modern frequency standards used in space geodetic stations (including SLR/LLR) is given by Soffel and Langhans (2013). For one-way ILR systems, the clock noise (see Section 3.2.1 and Chapter 6 for some more details on typical noise levels) can accumulate over long time periods, becoming the dominant source of measurement error by orders of magnitude. Additional discussion on near-future developments of space-based clocks, which will be crucial for ILR, are discussed in Chapter 6.
- **Timer.** The timer creates the time tag, based on the current time provided by the clock and the detection signal from the (start or stop) detector, (*e.g.*, Kalisz, 2004). The time between the transmission of the laser pulse and the reception of the reflected photons is the primary raw observable of laser ranging. Consequently, precise, accurate and stable timing is a crucial element in the determination of high-quality range measurements. Two classes of systems may be used for determining the time of flight of photons: Time Interval Units (TIUs) and event timers. In a TIU, the time difference between two events is measured explicitly, whereas in an event timer, the times of separate events are measured, their time difference being obtained in post-processing. The former of these is not suitable for use in high-repetition rate ranging systems (Iqbal et al., 2008) or ILR systems. This excludes stations using TIUs from participating in ILR operations. However, state-of-the-art ILRS stations are now mostly using event timers, a trend that will likely continue into the future. We will discuss some key properties (including typical uncertainty levels) of event timers in Section 3.2.1.

In summary, the detector generates an electrical signal upon the transmission or reception of a laser pulse, which is sent to the event timer to be time tagged. The system clock provides a stable reference time, typically by the production of a signal with (nearly) constant frequency and amplitude. The clock continuously sends the reference time signal to the timer. The event timer then uses the signal from the clock to time tag the signals it receives from the detector.

In addition to the hardware components used in the transmission and detection assembly, an accurate pointing system is required for both the ground and space segments. The beam divergence angle in ILR and SLR will be similar, with  $50 \mu\text{rad}$  a typical value for the divergence half angle (Section 3.1.3). Such a divergence half angle propagates into a laser beam spot size radius of 7,500 km at a distance of 1 AU. For the link budget of the Phobos Laser Ranging (PLR) mission presented by Turyshv et al. (2010), the corresponding uplink laser power at the Phobos lander is about  $40 \text{ aW/m}^2$ , resulting in about 10 photons per second reaching the detection telescope.

As a result of the large laser spot size at the target, it will be feasible for the pulses transmitted by the space segment to be simultaneously received by ground stations across the world, in part mitigating the issue of cloud coverage, since the downlink is not limited to a single station. Although the pointing systems of the current ILRS network are sufficiently accurate for ILR, the long time until target acquisition in ILR complicates the planning of the ranging campaign. In SLR, it can be nearly immediately verified whether a transmitted pulse was successfully reflected off the target spacecraft, or whether a pointing bias or target prediction error must be compensated for. In ILR, however, the ranging may have to be done completely without any feedback (as is the case for LRO one-way ranging), where the laser pulses are transmitted, without any verification during the ranging pass as to whether they were received by the space segment or not. In ILR operations, for instance, a dedicated station or stations could be used for the initial signal acquisition (with feedback from the space segment), which subsequently relay this information to the 'normal' SLR stations involved in the ranging campaign. For the downlink, the ground segment must point its receiving telescope to the target position, based on the *a priori* orbit prediction. To facilitate the acquisition of the space segment signal, it would be advisable for the stations involved to collaborate in real time (during a tracking pass) to update the prediction's range bias, time bias and pointing data as efficiently as possible.

An additional issue related to the pointing operations in ILR is that the transmitter will require a so-called point-ahead (Degnan, 2002), where the system is pointed to the predicted target position at some later time, due to the relatively long light-time of the signal. However, in many ILRS stations, the transmitter and receiver telescopes cannot be independently pointed, either requiring a large receiver field-of-view or a large transmitter beam divergence angle.

Due to the asynchronous nature of a typical two-way ILR system (Section 3.1.2), the space segment requires hardware that fulfills the same functions as those shown in Fig. 3.8 and described above. However, whereas SLR technology has matured over the past decades, the active space-based systems that are required for ILR have not nearly seen as much development. Nevertheless, experience with, and developments for, laser communications, time transfer and altimetry systems (Sections 3.3.3 - 3.3.5,

respectively), which share many system requirements with ILR systems, have facilitated the maturation of much of the required hardware. A recent development in technology that is crucial for ILR is the European Laser Transfer (ELT) project (Schreiber et al., 2009b), which is a laser time transfer system that is to be used on the ISS in conjunction with the Atomic Clock Ensemble in Space (ACES) project (see Section 3.3.4 for more details on these projects). Although the distance to ground stations will be exceptionally small for ELT, the requirement for single-photon detection is met by using extreme signal attenuation, using neutral density filters on the space segment to reduce the energy by about 5 orders of magnitude. The high incident laser energy will allow the ELT system to operate at a very wide acceptable angle (field of view) of  $120^\circ$ , essentially operating without any spatial filtering. Similar approaches may be beneficial for reducing the pointing requirement on the space segment of a (one-way) ILR system.

## 3.2 Error Sources

To characterize the error budget of ILR measurements and the products obtained from them, we can distinguish errors in two different steps of the process. Firstly, inaccuracies in the measurement technology result in a difference between the true range value  $s(t)$  at a given time  $t$ , represented by Eq. (3.1), and its calibrated realization  $\hat{s}(t)$ , represented by Eq. (3.6). We discuss the various sources of this type of error in Section 3.2.1. Secondly, even in the limit of a perfect measurement ( $\hat{s} \rightarrow s$ ), errors in the models to evaluate Eq. (2.1) or (2.2) during the data analysis will result in errors in the final science products. We give an overview of the primary contributors to this error source in Section 3.2.2.

For the design of missions employing ILR, a characterization of both these types of error sources is crucial. Firstly, it is important that data analysis models are developed to a sufficient level that they can make full use of the data that are obtained by a mission employing ILR. Relatedly, possible inherent limitations in data analysis models limit the degree to which improvements in range measurement accuracy will lead to improved science products, which must be taken into account when setting up instrument requirements. Additionally, the various possible mission and system concepts should be traded off with sufficient knowledge on their error sources, both to facilitate an optimum system design and drive design efforts to focus on reducing the dominating sources of uncertainty. In Chapters 5-7 we investigate three crucial and previously unquantified sources of both types of errors. In Chapter 8, we provide a synthesis of these chapters, combining our results on the expected ILR error budget and comparing the attainable science return with that from traditional tracking types.

### 3.2.1 Range Measurement Uncertainty

Ideally, a range measurement is an exact representation of the (one- or two-way) light time between two moving reference points (Section 3.1.1). In practice, however, a variety of effects cause deviations from these ideal measurements, resulting in a range measurement error  $\epsilon_s$ . Although part of this error can be removed by ground station system

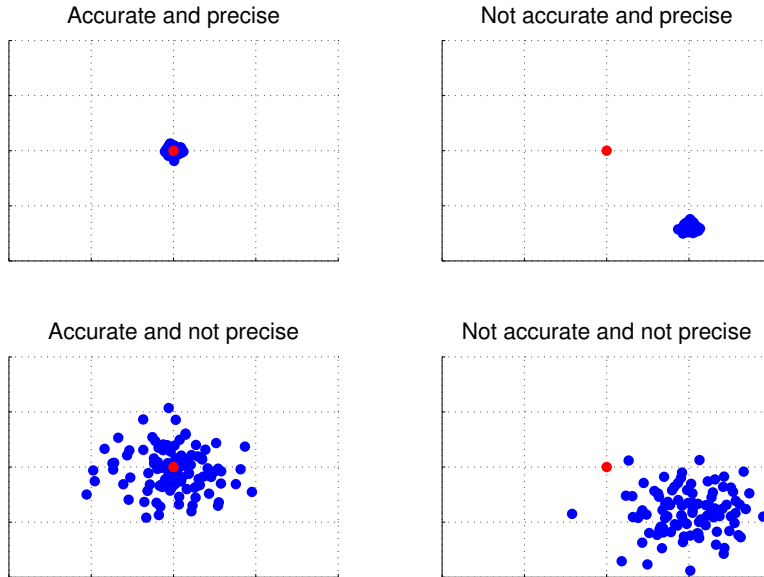


Figure 3.9: Schematic representation of difference between accuracy and precision. The four plots show two-dimensional measurements (blue) on the same, arbitrary, scale. Truth value indicated in red.

calibration (and space segment calibration in ILR), resulting in an estimate of the range error, denoted  $\hat{\epsilon}_s$  (see Eq. (3.6)), uncertainty from various sources remain.

Part of this uncertainty is a result of the inherently stochastic manner in which the range is measured, due to the finite size and energy of a laser pulse. Also, hardware imperfections contribute significantly to the error budget. These uncertainties can be divided into random noise (precision) and systematic errors (accuracy). Note that we use the convention in which accuracy represents *only* the systematic error, in which the mean random noise is removed, as opposed to the convention in which accuracy represents the total measurement error, including the random noise. We show a schematic representation of the difference between the two concepts in Fig. 3.9. In addition to random noise and systematic errors, the time-variation of the systematic errors (stability) is an important characteristic of the laser ranging measurement, as it is a key factor for how well systematic errors can be identified and removed.

Laser pulse detection typically occurs in a regime where only a single, or very few, photons from a transmitted laser pulse actually fall onto the detector. Certain detectors can be set to a certain threshold, so that it triggers a detection signal upon the detection of the  $N^{\text{th}}$  photon (instead of being triggered by the first photon). Ideally, an electrical signal will be sent to the timer upon the detection of this  $N^{\text{th}}$  photon of a laser pulse. In Chapter 5, we provide explicit Probability and Cumulative Distribution Functions for

the ideal (no errors as a result of hardware imperfections) detection time as a function of  $N$  and  $N_p$ , where  $N$  is the detector photon threshold and  $N_p$  is the number of photons from a laser pulse that could trigger the detector, see Eq. (3.15). Due to the finite length of the laser pulse, there is an inherent range measurement random uncertainty, since one can only statistically describe which photon(s) in the laser pulse were detected. This effect limits the single-shot precision that can be attained with a laser ranging system. For a purely Gaussian pulse detected at the single-photon intensity level, this single-shot precision is at the level of  $\sigma_t$ , see Eq. (3.13). The integrated range precision of  $N$  measurements improves as approximately  $1/\sqrt{N}$ , converging to detection at the pulse center (for the single-photon detection case, where only one photon from the laser pulse reaches the detection system, so that  $N_p = 1$  in Eq. (3.15)). The precision of the combined measurement over  $N$  pulses (normal points) is limited by time-correlated error sources, though, such as optical turbulence (Chapter 5) and short-term instrumental instability. However, such uncertainties only become relevant well below the 1 mm level for state-of-the-art SLR systems, (*e.g.*, Blazej et al., 2011), allowing sub-mm normal point precision (but not accuracy) to be routinely achieved.

For cases where more than one detectable photon reaches the detector, the mean pulse detection time will not be equal to the pulse center arrival time at the detector, since photons in the leading edge of the pulse are preferentially detected (Section 2.2 of Chapter 5). Therefore, detections at such signal strength can result in a biased range measurement if this effect is not properly corrected for. At such multi-photon signal detection intensity levels, time-variations in the received signal strength will result in variations of this range bias, reducing the stability of the range measurement. Variations in received signal intensity can be the result of any of a number of causes, including instabilities in the transmission hardware, variabilities in atmospheric conditions at the ground stations, changes in target elevation at the ground station (resulting in a longer atmospheric propagation path and a resultantly greater attenuation) and errors in pointing. To ensure detection at the single-photon level, the signal strength can be attenuated (either at the transmitter or receiver) to a level where  $N_p = 1$  is practically ensured. Such an approach, however, will be at the expense of a reduced pulse detection probability and it is therefore advantageous to use a system operating at a high pulse repetition rate (kHz) for such a situation, where a sufficient data volume can be obtained even in cases where only a (very) small fraction of pulses is detected. Alternatively, a multi-array detector can be used, which allows multiple single-photon detections from a single laser pulse (Murphy et al., 2002), as was also proposed for the Phobos Laser Ranging concept (Turyshchev et al., 2010).

The temporal shape of the laser pulse is typically well described by a Gaussian shape (Section 3.1.3). In SLR/LLR, the retroreflector signature causes significant distortion of this temporal shape (Otsubo and Appleby, 2003). However, this is not the case for ILR. Also, atmospheric effects do not significantly influence the laser pulse temporal energy distribution for pulses in the typical pulse energy and pulse length regime of SLR. As a result, the temporal pulse shape at transmission and detection are approximately the same in ILR (Section 3.1.3). The true generated pulse shape will differ from the Gaussian, though, but a transmission system measurement can be used to characterize these deviations, which will remain approximately constant throughout the pulse's

propagation. As a result, the stability of ILR data may be better than that of SLR (no time-varying accuracies due to time-variations in pulse-shape), as it is much easier to characterize the received pulse temporal intensity distribution, with resulting advantages for data analysis. This is discussed by Kucharski et al. (2011) for analysis of the BLITS SLR satellite, which uses a novel signature-free reflector system.

In addition to the inherently stochastic nature of laser range measurements by direct detection of photon(s) from a finite laser pulse, various sources of error in the measurement hardware (Section 3.1.6) degrade the realization of the range measurement from its ideal value. For ILR, the hardware-derived error sources are similar to those of SLR, summarized by (*e.g.*, Exertier et al., 2006). However, an important difference between the two stems from the fact that part of the active hardware is on the space segment in ILR. For such systems, there is much less experience in the development and use of the various components of the laser ranging system, requiring the development and characterization of dedicated new hardware. Also, the possibility of in-operation system characterization and modification is much more limited than for ground stations. Nevertheless, there have been important developments in the fields of laser time transfer (Section 3.3.3), laser communications (Section 3.3.4) and laser altimetry (Section 3.3.5), all of which use hardware systems with similar characteristics and requirements. Development of these systems, and the characterization of their properties relating to a range measurement error budget, is invaluable in the estimation of near-term ILR hardware-induced errors. However, the application of laser pulse transmission over planetary distances has only been proven a small number of times (Section 3.3.1), and never operationally.

To estimate the inaccuracies in both ground and space segment hardware for ILR, we rely on the extrapolation of existing ground stations and space-based systems. For the characterization of the space segment, we rely strongly on the development of the space-grade single-photon detection system developed for ELT, an overview of the characterization of which is given by Prochazka et al. (2012). We will give a summary of the expected error magnitude of the various hardware-induced measurement uncertainties, discussing both the ground and space segments. Specifically, inaccuracies in the following aspects result in a range measurement of degraded quality.

- Detection time errors. Inaccuracies in both the start and stop detection time directly propagate into the determination of  $t_t$  and  $t_r$ , as they result in an incorrectly timed signal being sent to the timer. Since a different detector is used for the signal transmission and reception, these errors will not automatically cancel out (even in perfectly stable, but inaccurate, detectors). This is especially true in ILR, where the start and stop detector are located far apart and cannot be calibrated independently of the measurements themselves. The time between a photon triggering the detector and the generation of the electrical signal being sent to the event timer can be quite large ( $> 1$  ns), and can depend on a variety of parameters, such as the signal strength and noise level. Nevertheless, this delay can be characterized to very high accuracy. The error budget given by Exertier et al. (2006) gives values of several mm uncertainty for both the start and stop detector (with stop detector errors somewhat smaller). New detectors showing sub-ps stability (Kodet and Prochazka, 2012) and jitter at the 10 ps level (Prochazka et al., 2011) have been developed for the ELT project, providing confidence that space-based pho-

ton detectors are capable of operating at the same level of uncertainty as current ground-based systems.

- **Event timer.** In a laser ranging station, a single event timer is typically used for timing both signal reception and detection. Various types of event timers have been used in SLR stations. A typical SLR event timer is the 'Riga event timer'. A recent version of this system is described by Artyukh et al. (2010) and has sub-mm resolution. Recently, development of a new type of event timer, based on a Surface Acoustic Wave (SAW) is reported by Panek and Prochazka (2007); Panek et al. (2010); Prochazka et al. (2011c). They demonstrate a timer with sub-ps precision and a stability of several fs over a period of minutes to hours. The use of this technology allows the event timer to have an almost negligible contribution to the range measurement accuracy error budget.
- **Clock noise.** The system clock ideally generates a signal directly in keeping with the local proper time  $\tau$ . In actuality, however, it will produce a noisy signal  $\tilde{\tau}$ , representing an imperfect realization of the local proper time. For two-way systems, the clocks only need to be accurate over short periods of time (two-way light time), whereas a one-way range system requires clocks to be stable over longer time periods at both ends of the link (see Chapter 6 for an extensive discussion). For example, for LEO, lunar and planetary targets, which have light times on the order of 1 ms, 1 s and 1000 s, respectively, a clock with a relative stability of  $10^{-14}$  (over these light times), will induce two-way range errors of 3 nm, 3  $\mu\text{m}$  and 3 mm, respectively. A stability of about  $10^{-15}$  over the typical ILR light time of 1000 s is achievable by H-masers (Soffel and Langhans, 2013), providing sub-mm clock-induced range noise.
- **System calibration errors.** Delays in various components of the electrical and optical system of the detection assembly, as well as systematic biases in various parts of the system must be accurately characterized to realize a high quality range measurement. In a typical SLR system, the range to a reference calibration target (for instance attached to the telescope) at a known distance is periodically measured. This allows part of the systematic errors to be removed from the range measurement (Section 3.1.1). Kirchner and Koidl (2014) show that ground station calibration consistency on short time scales is at the several ps level, corresponding well to the laser beam propagation length uncertainty of 3 ps given by Prochazka et al. (2012). Similarly, Exertier et al. (2006) give state-of-the-art systematic uncertainties of 1 mm in both electronic and mechanical range uncertainties. However, a ground-target calibration will not fully reproduce the situation of ranging to space-based targets (for instance due to very different signal strength levels) and will therefore not fully be able to capture the hardware induced systematic range measurement errors.

Based upon these considerations, the two dominant sources of range error will stem from the detection delay instabilities and system calibration uncertainties. Combined instabilities in these systems can reach values at the several mm level. However, this requires that all participating ILRS stations will have clocks that are sufficiently stable



over the two-way light time, which will significantly reduce the number of participating stations. Since the majority of the stations in the network does not have a frequency standard of H-maser quality, we can expect clock-induced range errors at the several mm level for such stations.

Although no data from existing ILR missions can be used to set up a measurement error budget, full two-way links have been demonstrated on laboratory scales by Chen et al. (2011); Chen et al. (2013). They use ultrashort (4 and 5 ps) laser pulses in a two-way setup over a distance of about 1.0 m, varying the distance by about 8 cm during the experiment. They obtain range measurement errors below the 0.2 mm level (averaged over 1000 measurements). Similarly, recent laboratory experiments performed by Blazej et al. (2014) have shown time transfer with an accuracy of 3 ps ( $\approx 1$  mm) using two representative ground segment hardware packages. These experiments show the capabilities of laboratory-scale experiments with well-controlled hardware, indicating the potential for (sub-)mm range accuracy (at least from a hardware point-of-view). However, practical aspects related to system calibration over longer periods of time, comparison of distinct SLR and space segment systems, environmental instabilities, *etc.* may make this infeasible in near-term ILR operations. Also, as we discuss in Section 3.2.2, inaccuracies in the hardware error budgets must be accompanied by similar improvements in data analysis models to bring total ILR error budgets down to the (sub-)mm level.

### 3.2.2 Data Analysis Model Errors

Even in the case of perfect range measurements, the final science products (orbits, gravity fields, rotational parameters, *etc.*; see Sections 2.2 and 2.3) will not be error-free, due to inaccuracies in the models used to map the observations to the estimated parameters. In orbit determination, parameters are estimated by modelling their influence on the observables, described by Eqs. (2.1) and (2.2) for range measurements, and subsequently finding a set of estimated parameter values that minimizes the (weighted) difference between the modelled and measured observations (Montenbruck and Gill, 2000; Tapley et al., 2004), see Section 5.1 of Chapter 4 for additional details. Resultantly, errors in modelling the range observable can lead to degraded science products, as the estimator uses these imperfect models to minimize the difference between measured and modelled observables. This can result in a signal of a parameter  $p_1$  being partly misattributed to a parameter  $p_2$ , skewing the estimation of both parameters. Also, it can limit the model from fully fitting the trend in the measurement residuals to the parameterized model, preventing the data from being fully exploited.

From Eqs. (2.1) and (2.2), it can be seen that errors in the state function of either link end  $\mathbf{r}_A(t)$  and  $\mathbf{r}_B(t)$ , as well as errors in the range corrections  $\Delta_{s_{BA}}$ , may degrade the fidelity of the model used to produce computed range measurements. For SLR and LLR, the errors in the various components of the range calculation primarily stem from the following issues:

- Ground station position errors. A model for the (time-dependent) position of the ground station reference point in the Geocentric Celestial Reference System (GCRS) is used to model a range measurement. This model consists of a position

in an Earth-fixed frame as a function of time and a rotation from this frame to the GCRS. The position of the reference point of the ground station is typically given in the International Terrestrial Reference Frame (ITRF) (Altamimi et al., 2011), and is defined by a position at epoch and a linear velocity. This reference frame is generated from a combined analysis of data from the four main space geodetic techniques (SLR, VLBI, DORIS, GNSS, see Section 1.1), where stations with multiple measurement systems (local ties) are crucial for merging the various techniques. The transformation from ITRS to GCRS consists of precession, nutation and polar motion, which are a combination of theoretical predicted rotations, combined with small measured corrections (Petit et al., 2010). Additionally, for some SLR stations, the measurement reference point is offset from the station's ITRF position by a constant value, a so-called eccentricity. Inaccuracies in each of these models limit the accuracy of the ground station position function at the sub-cm level (Altamimi et al., 2011; Rothacher et al., 2011). Also, inaccuracies of Earth deformation models, both tidal and non-tidal, can limit the accuracy of ground station positions. For instance, such inaccuracies can reach several mm due to errors in the ocean and atmospheric tide models (Sośnica et al., 2013). Each of these errors directly enter Eq. (2.1) as  $\mathbf{r}_A(t)$  or  $\mathbf{r}_B(t)$  (depending on whether the ground station acts as transmitter or receiver), limiting the accuracy of the ground station position function to the several mm level.

- Space segment dynamics. The dynamics of the space segment is typically estimated from the laser ranging data, requiring a (parameterized) dynamical model. The characterization of the dynamics of the space segment can be a limiting factor in the attainable quality of science products of SLR. Typically, inaccuracies in the modelling of non-conservative forces (radiation pressure, anisotropic reradiation, *etc.*), as well as (time-varying) gravity will accumulate over sufficiently long times, requiring the estimation of empirical accelerations and scaling parameters. Also, it requires the cutting of the state estimation of the spacecraft into short segments (arcs), (*e.g.*, Seeber, 2003), which are typically in the order of days to weeks for geodetic SLR satellites (Sośnica, 2014). This increase in the number of estimated parameters, and the reduction of the length of the state arcs, lead to increased correlations between the estimated parameters and a potentially reduced sensitivity to the physical parameters of interest. In certain cases, such as the passive LARES SLR satellite (Ciufolini et al., 2012), the design of the mission and the spacecraft can inherently limit the influence of non-conservative forces, but such an approach is typically hindered by the requirement for large solar panels, antennas, *etc.* on (planetary) spacecraft. Alternatively, the use of accelerometers, (*e.g.*, Flury et al., 2008) or a full drag-free system, (*e.g.*, Kundt, 1974; Theil, 2008) can decrease the influence of non-conservative forces acting on a spacecraft.
- Tropospheric correction errors. As discussed in more detail in Section 3.1.4, atmospheric propagation causes both deterministic and stochastic variations in laser pulse time of flight. Accuracy degradations at the order of 5-8 mm are estimated by Exertier et al. (2006), which can be reduced to the (several) mm level using ray tracing models. Atmospheric propagation model errors may be absorbed by the

(frequent) estimation of range biases, but this can be at the expense of estimation quality of other physical parameters.

The above issues will remain present in missions employing ILR. However, the distinct nature of planetary missions requires some additional considerations on how these aspects influence the error budgets. For instance, the space-segment orbit propagation can no longer be done in an Earth-centered frame (as is the case for SLR), and must instead be performed in, for instance, a barycentric frame. As a result, uncertainties in the *a priori* Earth ephemeris will enter the error budget of the ground station position model. This can introduce a substantial additional source of error, since the ephemeris of the Earth is several orders of magnitude less accurate than ILR measurements are expected to be. Estimates for the uncertainty in planetary ephemerides can be obtained by comparing differently generated ephemerides from similar data sets (Section 2.2.4). By comparing the INPOP10a and DE421 ephemerides, (Fienga et al., 2011) obtain differences for the position of the Earth-Moon Barycenter (EMB) at the level of several meters (in the period where accurate tracking data are available), at the same order of magnitude of the quality of radiometric range data that is currently available. However, as discussed in Section 2.2.4, laser ranging will facilitate a substantial improvement in planetary ephemerides, including that of the Earth, partly mitigating this source of error in the data analysis. However, it does indicate that the Earth's ephemeris must be estimated during ILR data analysis (in addition to the dynamics of the space segment) to prevent its *a priori* errors to reduce the analysis quality.

For the highly accurate dynamical modelling that will be required for ILR, various relativistic effects on the dynamics will become relevant, as discussed by Xie and Kopeikin (2010) for next-generation LLR measurements, complicating the dynamical models. Additionally, the gravitational influence of the asteroid belt will complicate the accurate long-term dynamical modelling of (inner) solar system bodies, (*e.g.*, Fienga et al., 2009; Folkner et al., 2009). We discuss these issues in some more detail in Section 8.1.3.

Tropospheric models used to correct laser ranging measurements are the same for SLR and ILR and therefore at the sub-cm, but not the mm-level (Section 3.1.4). Since inaccuracies in tropospheric delay modelling increase with decreasing elevation angle (as the atmospheric path becomes longer), ranging close to zenith is preferred to minimize this source of modelling error. In ILR, however, this poses a unique challenge due to the typical geometry of such missions. With some notable exceptions such as the Ulysses mission (Wenzel et al., 1992), all interplanetary missions are performed very close to the plane of the ecliptic, as this is where most targets of interest are located. However, targets near the ecliptic will be visible in a limited range of elevation angles at most SLR stations. Additionally, the range of visible angles from a given ground station to a given target will vary with a period of roughly one synodic period. Due to the strong concentration of SLR stations at mid-latitudes (see Fig. 3.7), with only few stations near the equator, there will be a 'seasonal' signature in the accuracy of ILR missions. This variation in accuracy would be on the order of expected uncertainty variations in atmospheric range corrections over a range of elevation angles, amounting to several mm for elevation angles of 20° and lower (Hulley and Pavlis, 2007). To illustrate the variation in elevation angle, we show the daily maximum elevation angle of Mars as seen

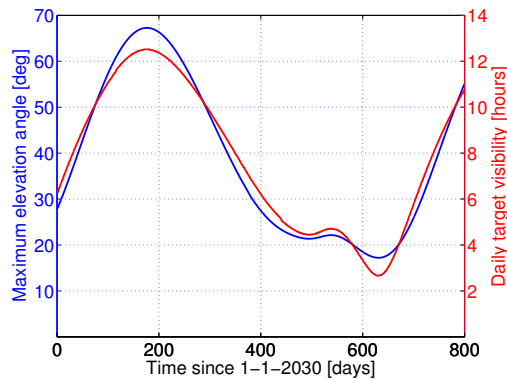


Figure 3.10: Target geometry for Graz-Mars laser link showing both daily maximum target elevation angle at Graz and number of hours per day with suitable target elevation angle ( $> 10^\circ$ ).

from Graz (see Fig. 3.7) SLR station in Fig 3.10. There, it can be seen that for a period of about 300 days, the local elevation angle will stay below  $25^\circ$  at all times, a value which will be similar for most stations in Europe.

To mitigate the atmospheric influence, it is proposed by Hurd et al. (2006) to place the Earth-based transponder for an interplanetary communications link in Earth orbit. This would put the atmospheric influence on the short Earth-orbit-to-Earth link and mitigate the atmospheric influence on the long range link. For tracking purposes, however, this approach will most likely be of limited value, since the problem of atmospheric propagation (as well as issues with orbiter modelling of the Earth-orbiting spacecraft) would now be placed on the orbit determination of this relay satellite, propagating onto the error of the interplanetary target. It would allow the influence of seasonal variations in maximum elevation angle to be mitigated, though.

In addition to the direct errors in the calculation of a range observable, any model inaccuracies in determining the range partial derivative  $\partial s/\partial \mathbf{q}$  for a certain parameter  $\mathbf{q}$  will limit the attainable accuracy for the estimation of this parameter  $\mathbf{q}$ . Such limitations can be caused by imperfect geophysical modelling incomplete or inaccurate parameterization of a model, *etc.* A typical example of this phenomenon in SLR is the mismodelled dynamics of the space segment discussed above. This aspect of the uncertainty in data processing results in a general, but crucial, issue in the analysis of ILR data, since planetary targets and their environments are typically characterized to a much lower degree than the terrestrial environment. As a result, estimation model inaccuracies could be an important issue when processing ILR data. The impact that this will have on the quality of the data analysis will differ per mission, but a characterization of this source of error is crucial during mission definition. We discuss these issues in more detail in Chapter 4 for a Phobos lander and in more general terms in Section 8.1.3.

### 3.3 Current Status of Interplanetary Application

ILR has not yet been used as a tracking method for (inter)planetary missions. However, substantial effort has gone into the development of the concept. Additionally, progress in a number of related fields has improved its technological readiness. We discuss such developments in this section. First, we give an overview of current activities using ILR systems in Section 3.3.1, discussing experimental and operational implementations of laser ranging. In Section 3.3.2 we provide an overview of mission proposals that have included an ILR element, highlighting the improved science return that is expected from its inclusion. In addition to applications for range determination by direct detection of laser pulses, pulsed lasers can be used in space for a variety of applications in planetary space missions. A number of these applications in current and upcoming mission share many system characteristics with ranging systems, potentially making them strongly synergistic, from a development, implementation and operations point of view. These applications are: laser communications (Section 3.3.3), laser time transfer (Section 3.3.4) and laser altimetry (Section 3.3.5). We give an overview of the past, current and future implementations of these technologies, with a focus on interplanetary applications and possible synergies with ILR. We only discuss systems employing direct detection of pulsed lasers, omitting any discussion of the fundamentally different technology of laser interferometry, such as that proposed for use on the Laser Interferometer Space Antenna (LISA) mission (Danzmann et al., 2003) or the follow-on to the GRACE mission (Turyshev et al., 2014).

#### 3.3.1 Experimental and Operational Status of ILR

The concept of ILR dates back to the 1980s (Zuber, 2006). Further development of the concept, and serious consideration of its implementation in the laser ranging community was initiated further by Degnan (1996); Degnan et al. (1998). Due to the emergence of this field, transponder applications of laser ranging systems, most notably time transfer and ILR, are now coordinated by a dedicated working group of the ILRS. Additionally, workshops organized by the ILRS have routinely included presentations on various aspects of the technology since the initial work of Degnan (1996). However, the experimental implementation of the technology in space missions has only been achieved relatively recently. To date, three experiments involving the detection of laser pulses at larger-than-lunar distances have been performed:

- Laser pulses sent to the Galileo spacecraft, en-route to Jupiter, were detected by the spacecraft's camera at a distance of 6 million km during the Galileo Optical Experiment (GOPEX) (Wilson et al., 1993). Although this experiment did not allow any range measurement to be obtained, as the received pulses were not accurately time-tagged, it was the first demonstration of pointing of a laser system at such distances, and validated existing models on the expected performance of such a link.
- A two-way asynchronous laser link was established with the MESSENGER spacecraft en-route to Mercury using its Mercury Laser Altimeter (MLA) instrument,

at a distance of 24 million km (Smith et al., 2006). This experiment represents the first interplanetary two-way laser ranging experiment. Analysis of the data showed a formal range uncertainty of 20 cm. This experiment demonstrated the feasibility of the technique despite the lack of purpose-designed ILR hardware, such as precise laser signal acquisition and tracking capabilities (Degnan, 2008). Attempts prior to the successful experiment with MESSENGER were foiled by scheduling problems, weather issues at the ground sites, and the spacecraft going into safe mode days before the scheduled experiment (Zuber, 2006).

- In 2005, laser pulses from Earth were detected by the laser altimeter instrument onboard the Mars Global Surveyor (MGS) (Abshire et al., 2006; Neumann et al., 2008). No two-way link was possible for MGS, due to failure of the altimeter oscillator and the resulting inability to fire the laser. However, the (crude) detection timing of the pulses from Earth allowed a clock offset of MGS to be determined with a precision of about 10 ms.

All of these were experiments of opportunity, however, facilitated by the chance availability of deep space laser and/or receiver hardware. As such, the space segments were by no means optimized for ILR operations in any of these cases, nor was the ground segment experienced in performing them.

In addition to these laser ranging efforts over larger-than-lunar distances, one-way laser ranging was used for the tracking of LRO (Zuber et al., 2010) until late 2014, when funding for the experiment was discontinued. For LRO, orbit uncertainty is one of the main sources of error for the topographic model and geodetic grid that are produced with data from its Lunar Orbiter Laser Altimeter (LOLA) instrument, (Smith et al., 2010). One-way laser ranging was added to the LRO spacecraft to improve its orbit determination, with a number of ILRS stations serving as transmitters and LOLA as receiver. The altimeter was designed to time both reflected altimetry signals from the lunar surface and laser signals from Earth. Earth ranging was facilitated by using a fiber optic cable connecting the Earth-pointing High-Gain Antenna (HGA) to the altimeter assembly. To measure the laser pulse transmitted from Earth, a 5 ms range gate was opened for terrestrial signal reception prior to the lunar surface range return gate. Using this method, data with a precision of about 10 cm were obtained (Bauer et al., 2013), limited by the design of the altimetry system. The accuracy of the data is degraded, however, by the one-way nature of the data and the resulting accumulation of instabilities in the clocks of both the ground stations and the spacecraft (Section 3.1; Chapter 6). Complications in the analysis of the removal of clock noise from the one-way data (Bauer et al., 2013), combined with the unexpectedly high quality of the (radio) Doppler data, resulted in laser ranging not being included in the operational orbit determination of LRO (Mazarico et al., 2010). Recent progress in one-way data processing and estimation strategies, however, have led to laser ranging-only orbits that are of comparable quality to those produced by combining radiometric and altimetry crossover data (Bauer et al., 2014; Mao et al., 2013).

In addition to the routine one-way range observations, several experiments using two-way laser ranging between ILRS stations and LRO have been performed (Sun et al., 2014), representing an additional demonstration of the two-way asynchronous concept

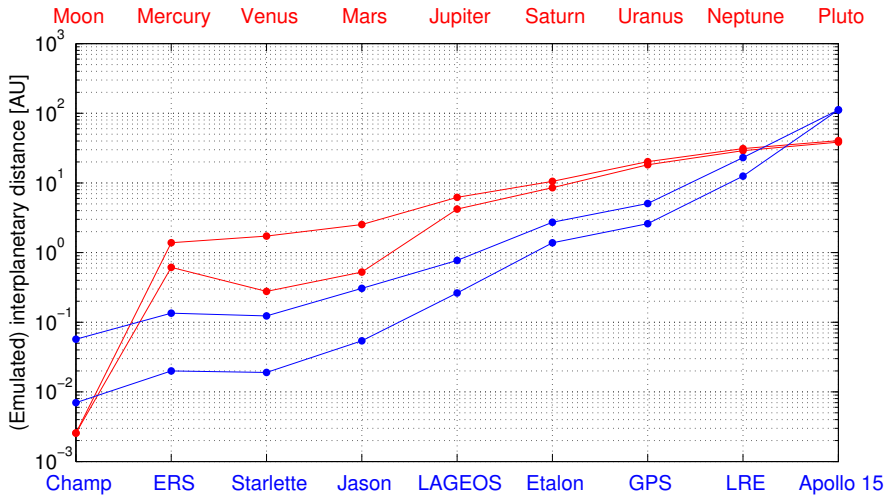


Figure 3.11: Figure showing the capabilities of emulating interplanetary asynchronous laser ranging signal strength by colocated laser ranging to retroreflectors, reproduced from (Degnan, 2006). Minimum and maximum distances to solar system bodies shown in red, interplanetary distance that can be emulated with representative SLR/LLR targets shown in blue. Circular equatorial, Sun-centered (Earth-centered for the Moon) orbits assumed for determining minimum and maximum distance from Earth to other solar system bodies.

beyond that of the MESSENGER spacecraft (although not quite at interplanetary distances). By performing Earth-scans over the area of the target ground station, the far-field diffraction pattern of the altimeter system could be measured directly, allowing for a better calibration of the data from LOLA. Also, this experiment allowed a pointing error in the altimetry system to be identified. This shows the added operational value of (occasional) two-way ranging using an altimetry system, which goes beyond a potential improvement in orbit determination that is obtained from the ILR data.

Performing real ILR experiments requires the rare availability of a deep-space-based pulsed laser system. However, as discussed in Section 3.2.1, laboratory experiments of ILR systems have been performed (Chen et al., 2013; Blazej et al., 2014), achieving (sub-)mm accuracy. An intermediate type of experimental implementation can be achieved with existing SLR infrastructure, which goes beyond laboratory tests, but does not require an interplanetary space segment. Specifically, emulation of asynchronous two-way laser ranging can be performed using two co-located laser ranging sites, by having both sites perform SLR measurements of the same target simultaneously at different wavelengths (Degnan, 2006), thereby simulating an interplanetary link. Due to the inverse quartic signal strength dependency that is inherent in reflector laser ranging (Section 3.1.5), such an experiment simulates the received energy level of an asynchronous two-way system at far greater distances, see Fig. 3.11. Note that the distance that can be emulated is not only dependent on satellite distance, but also the satellite reflection properties (cross-section  $\sigma_{cs}$ ), as shown by Eq. (3.15). Using LAGEOS, ILR distances

of almost up to 1 AU can be emulated. A two-way emulation experiment via LAGEOS was performed at the Wettzell SLR station, where the transponder link at conditions equivalent to a 0.44 AU distance for ILR (Schreiber et al., 2009a) were successfully demonstrated. Although this type of emulation allows expertise in the operation and analysis of a two-way asynchronous link to be obtained, they do not fully simulate the true interplanetary ranging conditions. For instance, it does not properly simulate the long pulse time-of-flight and non-linear relative dynamics of the ground station and target in that time, typically requiring a bistatic receiver/transmitter setup (Degnan, 2002). Also, the error budget of these measurements is essentially that of an SLR measurement, not an ILR measurement (Section 3.2.1).

### 3.3.2 Proposed Missions Employing ILR

Despite the lack of complete maturity of one- and two-way laser ranging over interplanetary distances, there have been a number of mission proposals utilizing ILR. Here, we give an overview of representative efforts in this direction.

Currently, the longest distance over which laser ranging has been performed is to the retroreflectors on the Moon, at a distance of about 400,000 km. Due to the low signal return of lunar reflectors only very few laser ranging stations, with poor geographic coverage, are capable of performing LLR (see Fig. 3.7). Although the recent start of operations of the APOLLO LLR system (Murphy et al., 2008) has substantially improved the quality and quantity of LLR data, it will remain sparse into the foreseeable future. As an additional source of lunar range data with mm-cm accuracy, it is proposed by Müller et al. (2009) to let future lunar landers deploy active laser systems on the Moon. Active laser transponders on the Moon can be used to improve the existing science return of LLR (see Sections 2.2 and 2.3.3) and serve as a stepping stone for implementation of the technology at larger distances, such as Mars (Merkowitz et al., 2007). General analyses for the science return of a Mars lander performing ILR are presented by Chandler et al. (2005) and Turyshev and Williams (2007), who analyse its potential for gravitational physics, as derived from improved planetary ephemerides.

A laser ranging mission to Phobos is analyzed and described in detail by Turyshev et al. (2010), and analyzed further here in Chapter 4. The primary objective of the mission is the accurate determination of PPN parameters, the time dependency of the gravitational constant and constraining a long-distance Yukawa potential (Section 2.3.1). Additionally, the mission would provide valuable data on the orbital and rotational motion of Phobos and the related science products described in Section 2.2 (see Chapter 4 for quantitative analysis). For the selection of Phobos as the location of the space segment, a trade-off was made for different target locations, namely Mercury, Mars, Martian moons and an asteroid. Phobos was deemed the optimal choice, as it has no atmosphere, a much more benign thermal environment than Mercury, and a superior conjunction occurrence compared to asteroids. A schematic representation of the mission concept is shown in Fig. 3.12. A similar ILR mission to the asteroid Icarus is described by Luo et al. (2009), with the goal of using laser ranging for accurate positioning of the asteroid and associated determination of relativistic parameters.

An additional proposed mission concept to the Martian system that includes an ILR



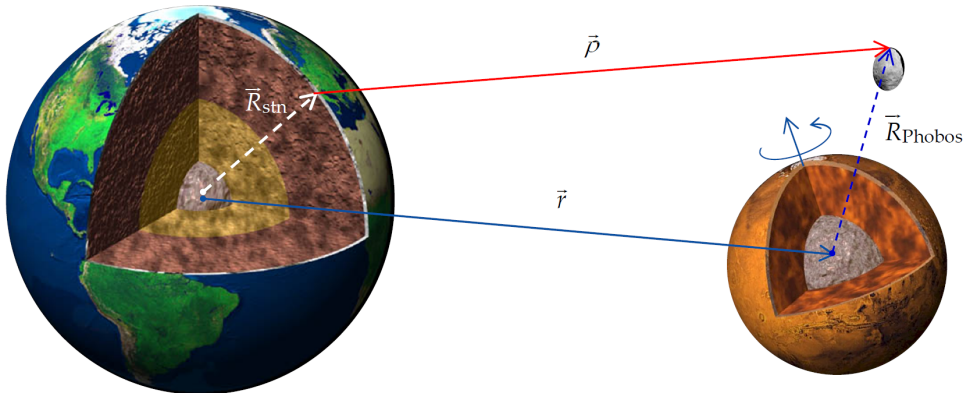


Figure 3.12: Schematic representation of PLR concept with laser transponders on Earth and Phobos surface, from Turyshev et al. (2010).

element is the GETEMME mission proposal (Oberst et al., 2012). For this mission, a spacecraft is to be sent to the Martian system for detailed study of the Martian satellites Phobos and Deimos. Part of the mission calls for the placement of laser retroreflectors on both moons, which can be used by the spacecraft for laser ranging, essentially achieving SLR inside the Martian system. Additionally, the spacecraft is to perform asynchronous laser ranging to Earth. Combined with data from onboard accelerometers, exceptional improvements in ephemerides, gravitational physics parameters and geodetic observables of the Martian system can be obtained. Further upcoming analysis of laser retroreflectors for planetary missions is discussed by Dell’Agnello (2014), who proposes the use of retroreflectors on landers (similar to the GETEMME proposal) on a variety of solar system bodies, including Galilean and Saturnian moons. These reflectors would then be ranged to by an orbiting spacecraft, allowing improved accuracy compared to altimetry measurements (although only locally).

The possibility of including a one-way laser link on the Solar System Odyssey concept is discussed by Christophe et al. (2009). This mission has the primary goal of probing the behaviour of gravitational effects in the outer solar system, motivated by the then-unexplained Pioneer anomaly (Turyshev and Toth, 2010). The inclusion of the laser link mostly benefits an increase in accuracy for the determination of the PPN parameter  $\gamma$  (Section 2.3.1) from occultation experiments. The laser link for this experiment is envisioned to be one-way, based on the Télémétrie InterPlanétaire Optique (TIPO) project, which is a proposed interplanetary extension of the T2L2 project (see Section 3.3.4).

A mission purely designed for fundamental physics objectives is the Laser Astrometric Test of Relativity (LATOR) (Turyshev et al., 2004). Specifically, it is designed to measure the curvature of spacetime to unprecedented accuracy and thereby test GR. It is to use two spacecraft that perform laser ranging to each other, as well as to the ISS. On the ISS, telescopes are to be placed at either end, forming a 100 m baseline optical interferometer. The first incarnation of the LATOR concept was reported by Yu et al.

(1994), which had the interferometric segment of the mission on the surface of the Earth. A covariance analysis of the measurements that are to be performed by this mission was given by Plowman and Hellings (2006), where the attainability of the science goals of LATOR is reaffirmed, with one caveat. For the estimation of the PPN parameter  $\gamma$ , the solar impact parameter (the closest distance between the laser pulse path and the Sun) must be accurately known. They find that the value of this parameter can be measured to higher accuracy by means of drag-free control of the two spacecraft than when using the nominal setup of laser ranging between the two spacecraft. A mission with some similarities to LATOR is proposed by Ashby and Bender (2008). It is to measure the Shapiro time delay (Section 2.3.2) between two drag-free satellites, one in an orbit similar to those in the LATOR concept, and one at the Earth-Sun L1 point.

In addition to the application of the laser link in conjunction experiments, where the influence of gravitation is manifested directly on the light time (as is done in the LATOR concept), laser ranging is well suited to reconstruct (long-period) spacecraft dynamics, and thereby constrain physical parameters (as is done in for instance the PLR concept). Such an approach is also proposed by Iorio (2013), who discusses the design of a mission with a spacecraft in a highly elliptical drag-free heliocentric orbit, which is to perform laser ranging to Earth. Due to the eccentric orbit, various relativistic effects can be decorrelated much better than from planetary ephemerides (Section 2.3.3), allowing the characteristics of the gravity field of the Sun (classical and relativistic) to be probed to improved accuracy.

A set of space missions with the name Astrodynamical Space Test of Relativity (ASTROD) has been proposed by Ni et al. (1997); Ni (2008); Appourchaux et al. (2009); Ni (2013). The proposed missions consist of drag-free spacecraft performing ranging operations, both using an ILR system and using an interferometric system to measure extremely accurate range variations, to other spacecraft in the constellation and/or Earth-based stations. An interferometric system allows changes in the range between two link ends to be measured to an accuracy orders of magnitude greater than is the case in ILR, but does not allow absolute range measurements to be obtained. The first proposed ASTROD mission, termed ASTROD-I, is to have a single spacecraft performing ranging to Earth using an ILR system. This mission has science goals similar to that of the PLR and LATOR mission, focussing on gravitational physics observables ( $\gamma$ ,  $\beta$ ,  $\dot{G}/G$ , *etc.*). Secondary objectives include the improved characterization of solar system dynamics and mass distribution. The followup missions ASTROD-II, ASTROD-GW and Super-ASTROD are to consist of multiple spacecraft, performing interferometric ranging (possibly combined with ILR) to one another, allowing the measurement of gravitational waves, in a similar manner as is to be done by the LISA mission concept (Danzmann et al., 2003). Such missions are beyond the scope of this dissertation, however. Additionally, these advanced ASTROD concepts will be able to measure oscillations of the solar shape by time-variations of its gravitational field, as well as an independent determination of its angular momentum through the Lense-Thirring effect (Section 2.3.2) providing a unique probe of the solar deep interior.

### 3.3.3 Laser Communications

A technology strongly related to that of interplanetary laser ranging is optical deep-space communications (Hemmati, 2006), in which the exchange of laser pulses (using direct detection) is used to transfer data. Due to the low frequency of radio bands when compared to optical wavelengths, the data rate that can be achieved with optical communications systems using a system of a given size can be much greater, with similar advantages and disadvantages w.r.t. the use of a radiometric system as is the case for laser ranging (Section 1.2).

To achieve a high data rate in laser communications, multiple bits of information per single received laser pulse must be attained. A typical encoding to achieve this scheme is the ( $M$ -ary) Pulse Position Modulation (PPM) scheme (Hemmati, 2006). By dividing a given time slot into  $M$  different disjoint intervals and transmitting a pulse into only a single one of these intervals,  $k$  bits of information can be transferred where  $M = 2^k$ . Laser communications at larger-than-geostationary distance was first demonstrated by the lunar orbiter LADEE, which included a laser communications system. It demonstrated a data downlink with a data rate of  $> 500$  Mbps using a transmitted pulse power of 0.25 W (Boroson et al., 2014). Additionally, the laser communications system on the LADEE spacecraft demonstrated two-way light time measurements with an accuracy of 200 ps, corresponding to about 6 cm two-way range accuracy. These data were obtained automatically in post-processing during communications operations, without the need for additional explicit considerations on ranging operations.

Despite the synergy between the two technologies, the requirements on the two show some important differences. Firstly, ultra-precise timing of pulse arrival is not as crucial for laser communications as it is for ILR (Section 3.2.1). That is, with the use of a PPM system, the detection time uncertainty of a laser pulse is only relevant to the point where it is sufficiently accurate to robustly distinguish between detection in different bins. Detection timing improvements in ILR, however, directly improve the quality of the range measurement (to the point where detection timing errors stop being a significant error source, Section 3.2.1). Secondly, the successful detection of a large fraction of the transmitted laser pulses is important for communications operations, whereas the pulse detection probability is much less crucial in ranging operations. Although the use of an error-correcting scheme can allow for data reconstruction in the case where a part of the pulses remains undetected in a communications link, this will only work robustly down to a certain fraction of missed pulses (depending on the correction scheme). For laser ranging operations, however, even an exceptionally small detected pulse fraction ( $< 1\%$ ) can be used to generate useful measurement data. In SLR, this is especially true for a kHz pulse repetition rate system, where many pulses may be lost while retaining a data volume that is comparable to that of a typical SLR system. As a result, single-photon detection is not desirable for a communications system, while pointing requirements become much more stringent, with accuracies down to (sub-) $\mu\text{rad}$  level, (*e.g.*, Lee et al., 2001; Mohan et al., 2014), which is more than an order of magnitude more stringent than typical laser ranging operations. An additional difference between the ranging and communications systems stems from the asymmetry of the link, since communications typically require a downlink with a much higher data volume. Similarly driven by the need for high data rates, communications systems require very high pulse repetition

frequencies, since data rate scales linearly with the number of received pulses, whereas SLR systems typically operate at kHz frequencies at most.

Despite the different system requirements on optical ranging and communications systems, a combined system was already proposed by Folkner and Finger (1990). Recent developments in both communications and ranging applications of laser technology have led to more mature proposals of combined systems (Hemmati et al., 2009; Wolf et al., 2009; Hemmati, 2011). Such systems would have more stringent requirements than either system separately, but by combining both functions into a single instrument (as is currently done with radio systems), the total added value of the system on the spacecraft can be greatly increased with a relatively small increase in cost.

In addition to synergy in the implementation of the technology, research in the field of optical communications over interplanetary distances is of greater volume and detail in a number of aspects than it is for ranging applications. One of the areas where a wealth of research has been done for communications is in the field of pointing, acquisition and tracking, which is highly important for communications purposes, due to the small beam width and requirement for limited link outages, (*e.g.*, Alexander et al., 1999; Lee et al., 2001; Hemmati, 2006; Mohan et al., 2014). Relatedly, there has been extensive analysis of the influence of atmospheric turbulence on link outages of a laser communications system, which our development and discussion in Chapter 5 rely heavily upon.

The synergy between communications and ranging systems is further shown by the experiments in laser communications that have been performed using SLR systems. The SLR station in Graz used their kHz system to transmit data over a 4 km distance (Kirchner et al., 2011), proving the capability of their system to concurrently perform ranging and (low data-rate) communications operations. The NGSLR station demonstrated the use of an SLR system to transmit data to the LRO satellite in lunar orbit (Sun et al., 2013), using PPM on the one-way laser uplink to the spacecraft (Section 3.3.1). Additionally, a station design adapted from the SLR2000 (now called NGSLR) for laser communications is shown by Degnan et al. (2004) to be possible with a relatively low investment in terms of cost and required technological development.

Although truly interplanetary laser communications have not been achieved so far (with the LADEE satellite in lunar orbit being the most distant optical communications target to date), technology demonstration was planned for the Mars Telecommunications Orbiter, (Franklin et al., 2004), which was cancelled in 2005. However, extensive research and technology development has gone into the preparation for this mission, (*e.g.*, Ortiz et al., 2000; Khatri et al., 2004). Implementation of laser communications to Earth orbit, as for instance proposed for the next generation of Tracking and Data Relay Satellites (Edwards and Israel, 2014), will continue to increase the maturity of the technology, facilitating its inclusion on planetary missions. Also, the potential use of cubesatellites and microsattellites at interplanetary distances (Klesh and Castillo-Rogez, 2012) may greatly benefit from the use of optical communications and tracking (Staehele et al., 2011), so as to prevent the use of a heavy and power-consuming radio system, although at the expense of much more stringent pointing requirements.

### 3.3.4 Laser Time Transfer

In addition to applications in ranging and communications, a (laser) link between two distant stations can be used to synchronize the clocks of these stations, (*e.g.*, Klioner, 1992; Blanchet et al., 2001). Such a clock synchronization has interesting applications in experimental relativity (Section 2.3.3), as it allows the proper time rates of two observers, described by Eq. (2.38), to be compared to very high accuracy, facilitating the exploitation of relativistic clock effects for parameter estimation. With the use of highly accurate clocks, time transfer may be used to measure accurate positions of ground stations, contribute to gravity field determination by space missions, (*e.g.*, Müller et al., 2008a; Mayrhofer and Pail, 2012) and improve measurements of relativistic effects (Section 2.3.3).

A laser time transfer system requires a laser pulse transmitter on Earth and a receiver on the space segment in a one- or two-way setup, in an identical manner as a laser ranging setup (Section 3.1.2). When both clocks perfectly reproduce their local proper time, and the dynamics of both ends of the link is perfectly known, the proper time rates of the two observers may be compared to within the laser pulse time-tagging accuracy and precision. However, the degrading influence of clock noise on one-way ranging (Chapter 6) is the same for one-way time transfer, making a two-way link highly desirable, which allows for a strong decoupling of signals from the clock and the state dynamics, although state errors may still propagate into the estimated clock behaviour (Chapter 7). However, even in the case of two-way time transfer, this does not allow relativistic clock effects and clock noise to be distinguished. Therefore, to analyze the long-term behaviour of a clock, even when using two-way data, a highly accurate clock is required. The analysis of the coupling between relativistic clock effects and translational dynamics is the topic of the work described in Chapter 7, where the mathematical details of a time-transfer link are discussed. In addition to ground-to-space time transfer, ground-to-ground time transfer may be performed when multiple ground stations are used for time transfer to the same space segment, (*e.g.*, Exertier et al., 2014). When these ground stations are operating simultaneously, common-view time transfer can be performed, in which the accumulation of clock noise at the ground stations and space segment is minimal (as is the case for two-way ranging). An example for common-view time transfer is shown by Mao et al. (2014), who use one-way data to the LRO spacecraft. In non-common-view time transfer, the ground stations perform time transfer to the same space segment in non-overlapping arcs (for instance because of the lack of simultaneous visibility conditions), causing integrated clock noise to degrade the quality of the time transfer.

For terrestrial satellites, the two-way link may be realized by the placement of retroreflectors on the space segment, using the same laser pulse for an active one-way uplink, as well as a standard SLR two-way range measurement. For planetary missions, though, a two-way link must be realized by means of an active two-way system (Section 3.1.2). Unlike laser communications and laser altimetry, which impose different requirements on the system in a number of key aspects, the system requirements for a laser time transfer and active laser ranging system are largely equal. An important exception is the long-term stability of the space-based clock, which is relevant for time transfer, but not for two-way ranging. In fact, time transfer is a free by-product of both one- and two-way planetary laser ranging.

For a one-way setup, the consideration of the clock behaviour (both in terms of relativistic effects and hardware stability) of both clocks is crucial for a correct analysis of the laser ranging data (Chapters 6 and 7). For a two-way link, the inclusion of a time transfer component need not be considered during the data analysis, as the clock effects do not accumulate in the observations (Section 3.1.2). However, time-transfer data can be extracted from a two-way link by using the up- and/or downlinks separately in addition to the full two-way observable. Doing so introduces a coupling between the clock behaviour analysis and the state dynamics, though, since an uncertainty in the clock's position translates into an uncertainty in its proper time behaviour. Duchayne et al. (2009) conclude, however, that this effect is small for time transfer to typical Earth-orbiting space segments and will not adversely influence the analysis of the data from the ACES project (see below).

The first laser time transfer link was achieved by the LASer Synchronization from Stationary Orbit (LASSO) experiment (Fridelance and Veillet, 1995). LASSO achieved a precision of the time transfer between stations in Texas and France of better than 100 ps. Currently, laser time transfer using the T2L2 experiment onboard the JASON-2 satellite is ongoing, with a number of participating ILRS stations forming the ground segment of the experiment (Exertier et al., 2010). For ground-to-space time transfer, a stability at the ps-level was achieved over integration times of 75 s, at an accuracy of  $< 100$  ps. Data analysis of the T2L2 time-transfer campaigns has yielded both common-view and non-common-view time transfer data. For the common-view time transfer using two systems slaved to the same reference clock (H-maser at the Grasse station) a stability in the order of 10 ps over a single pass was obtained (Exertier et al., 2010).

Another notable time transfer effort is the laser time package on the Chinese Bei-dou satellites (Prochazka and Yang, 2009; Meng et al., 2013), which represents the first demonstration of laser time transfer to navigation satellites. The potential benefit of laser time transfer to navigation satellites is discussed by Prochazka et al. (2011b), with a specific focus on the Galileo constellation. The use of hydrogen masers onboard the Galileo satellites will mitigate the main source of error that is present in the T2L2 experiment (clock noise), thereby facilitating substantially improved time transfer quality. Earth-to-space time transfer also has important applications for VLBI operations, especially space-VLBI, in which (at least) one of the telescopes is in space (typically Earth-orbiting), since the accurate signal correlation requires both accurate characterizations of the orbit of the spacecraft, as well as its clock (HirabayashiEtAl, 1998).

A major upcoming advancement in the accuracy of laser time transfer will be achieved with the Atomic Clock Ensemble in Space (ACES) project (Cacciapuoti et al., 2007) which will contain both a cesium standard atomic clock and a hydrogen maser, and is currently planned for launch to the ISS in 2016. By combining the stability of the two clocks, a very accurate short- and long-term in-space clock assembly is realized. This clock assembly will be combined with both a two-way radio time transfer (Delva et al., 2012) and laser time transfer: the European Laser Time Transfer (ELT) system (Schreiber et al., 2009b), for space-to-ground and ground-to-ground time transfer. In addition to its applicability for, among others, precise measurement of the gravitational redshift, it will demonstrate the use of highly stable clocks in space. Such clocks are crucial for accurate interplanetary laser ranging, especially the implementation of one-

way systems, as discussed in Chapter 6. Development of the ELT system has resulted in a space-qualified ultra-short laser pulse detection package with high accuracy, precision and stability, with important implications for the future implementation of ILR (Section 3.1.6).

### 3.3.5 Laser Altimetry

In addition to ranging to retroreflectors, spaceborne pulsed lasers can be used effectively for ranging directly between a spacecraft and the surface of a planet, moon, asteroid, *etc.* by the use of laser altimetry. In laser altimetry, laser pulses are directed to the surface of a body and the reflected pulse is detected by the altimeter. The reflected pulse intensity, temporal pulse shape and arrival time then provide information on the target body's surface albedo (at the laser wavelength), mean surface roughness and distance between surface and spacecraft, respectively (Gardner, 1982; Hussmann, 2014).

Among the applications of laser technology discussed in this section (altimetry, time transfer, communications), laser altimetry has the longest history, having been implemented in over a dozen planetary missions since the 1970s (Hussmann, 2014), first implemented in the Apollo program (Sjogren and Wollenhaupt, 1973). Resultantly, laser altimetry has led to many developments in space-based lasers which are crucial for the future implementation of ILR. In fact, each of the experiments in transponder laser ranging at interplanetary distances so far (see Section 3.3.1) was performed using an altimeter system.

A complication for the combined use of laser altimetry and two-way ranging with the same system, however, are the different pointing requirements of the two systems. Specifically, the altimetry system needs to point the laser towards the surface body, whereas the ranging system requires Earth-pointing operation. Although the system could be used in an alternating mode, this would complicate mission operations. Alternatively, as demonstrated by the LRO spacecraft, the combined use of an altimetry and one-way ranging system can be achieved by connecting the detector assembly to the HGA by means of a fiber-optic cable (Zuber et al., 2010). Such an approach can complicate the systems engineering of a spacecraft, however, since it creates a hardware connection between two otherwise unrelated instruments.

As is the case with a laser communications system (Section 3.3.3), there are some discrepancies between altimetry and ranging system hardware requirements. In an altimetry system, the signal return rate is expected to be in the strong multi-photon regime, facilitating the reconstruction of the pulse shape. Although this need not be a problem for ranging operations, which will typically need to function into the single-photon regime, the system needs to be capable of providing sufficiently accurate detections in both regimes. Additionally, the pulse-shape distortion by the surface diminishes the accuracy with which an absolute altimetry measurement can be achieved. Therefore, a laser altimeter system is typically not designed for a precision of better than 10 cm, which is about 2 orders of magnitude worse than what is desirable for ranging applications. However, even with such a system, future spacecraft carrying laser altimetry systems, such as the BELA instrument on BepiColombo (Thomas et al., 2007) and the GALA instrument on JUICE (Grasset et al., 2013), may facilitate further experiments

in asynchronous laser ranging, allowing greater operational experience to be gained and demonstrating the use of the technology over multi-AU distances. Additionally, Earth-ranging with an altimetry system can be used for calibration of the onboard clock of the spacecraft and the far-field diffraction pattern of the laser (Section 3.3.1).



## CHAPTER 4

---

### Paper I - Science Return from a Phobos Lander

---

*“We can learn about nature in increments [...]. Physical reality does not have to be understood all at once. Thank you, nature.”*

– Anthony Zee, *Fearful Symmetry (Revised edition)*, (Princeton University Press, 2007)



# Phobos Laser Ranging: Numerical Geodesy Experiments for Martian System Science

*D. Dirkx<sup>a</sup>, L.L.A. Vermeersen<sup>a</sup>, R.Noomen<sup>a</sup>, P.N.A.M. Visser<sup>a</sup>*

Published in *Planetary and Space Science*, Vol. 99, p. 84-102, 2014

**Abstract** Laser ranging is emerging as a technology for use over (inter)planetary distances, having the advantage of high (mm-cm) precision and accuracy and low mass and power consumption. We have performed numerical simulations to assess the science return in terms of geodetic observables of a hypothetical Phobos lander performing active two-way laser ranging with Earth-based stations. We focus our analysis on the estimation of Phobos and Mars gravitational, tidal and rotational parameters. We explicitly include systematic error sources in addition to uncorrelated random observation errors. This is achieved through the use of consider covariance parameters, specifically the ground station position and observation biases. Uncertainties for the consider parameters are set at 5 mm and at 1 mm for the Gaussian uncorrelated observation noise (for an observation integration time of 60 s). We perform the analysis for a mission duration up to 5 years.

It is shown that a Phobos Laser Ranging (PLR) can contribute to a better understanding of the Martian system, opening the possibility for improved determination of a variety of physical parameters of Mars and Phobos. The simulations show that the mission concept is especially suited for estimating Mars tidal deformation parameters, estimating degree 2 Love numbers with absolute uncertainties at the  $10^{-2}$  to  $10^{-4}$  level after 1 and 4 years, respectively and providing separate estimates for the Martian quality factors at Sun and Phobos-forced frequencies. The estimation of Phobos libration amplitudes and gravity field coefficients provides an estimate of Phobos' relative equatorial and polar moments of inertia with an absolute uncertainty of  $10^{-4}$  and  $10^{-7}$ , respectively, after 1 year. The observation of Phobos tidal deformation will be able to differentiate between a rubble pile and monolithic interior within 2 years.

For all parameters, systematic errors have a much stronger influence (per unit uncertainty) than the uncorrelated Gaussian observation noise. This indicates the need for the inclusion of systematic errors in simulation studies and special attention to the mitigation of these errors in mission and system design.

## 1 Introduction

Although there have been various proposed and launched missions targeting Phobos, no *in situ* measurements of it have been performed yet. A number of missions to do so are under investigation such as the Phobos Reconnaissance and International Mars Exploration (PRIME) mission (Lee et al., 2008) consisting of a Phobos lander and orbiter and the Phobos Laser Ranging (PLR) mission (Turyshev et al., 2010), a mission focussed on performing direct-to-Earth laser ranging measurements. Current investigations of

---

(a): Delft University of Technology, The Netherlands

Phobos employ direct observations by spacecraft such as Mars Express (Witasse et al., 2014), as well as Earth-based tracking of past and current Mars orbiters and astrometric observations (Jacobson and Lainey, 2014; Pascu et al., 2014).

In addition to *in situ* investigations, tracking of a Phobos lander would allow for the direct observation of Phobos libration and deformation (Le Maistre et al., 2013). Modelling of Phobos interior and orbital evolution constrained by available data has not provided an undisputed answer on its origin (Rosenblatt, 2011), making further investigation relevant not only for our understanding of the moon itself, but planetary system evolution in general. Additionally, Phobos can be used as a drag-free Mars orbiter, allowing potentially improved estimation of Mars physical parameters through tracking of a lander.

Numerical simulations of tracking of spacecraft around and/or landers on Mars, using various mission architectures (*i.e.* direct-to-Earth, lander-orbiter, etc.) have been performed, for instance focussing on the estimation of Martian rotational parameters and their relation to its interior structure (Yseboodt et al., 2002; Dehant et al., 2009; Le Maistre et al., 2013) and the seasonal gravity field signal (Karatekin et al., 2005). These studies largely rely on the use of classical radiometric tracking methods, although work on new orbit determination methods, such as altimetry crossover (Rosat et al., 2008) and same-beam interferometry (Yseboodt et al., 2012) is also ongoing. Simulations of physical parameter determinations from the combination of Doppler and star tracking observations by a Phobos lander were conducted by Le Maistre et al. (2013), with the goal of constraining Phobos' interior through measurement of its physical librations and tidal deformation.

As an alternative to radiometric methods, interplanetary laser ranging (ILR) is under development as a high-precision tracking technique (mm- to cm-level range) for use on planetary missions, (Degnan, 2002). A number of recent mission concepts use this technology, such as the PLR mission (Turyshev et al., 2010), and the Gravity, Einsteins Theory, and Exploration of the Martian Moons Environment (GETEMME) Martian system spacecraft mission (Oberst et al., 2012). The former of these is a Phobos lander that is to perform mm-precise laser range measurements to Earth with the goal of testing general relativity to unprecedented accuracy.

Here, we analyze the capabilities of a Phobos lander similar to the PLR concept to estimate physical parameters of Mars and Phobos. Due to the high range measurement accuracy, as well as the extremely low non-conservative forces acting on Phobos, it is anticipated that significant improvements in their estimation uncertainties can be achieved. From simulated range measurements, we estimate the tidal Love numbers of Mars, as well as the tidal lag at the frequencies of the three main tide-raising bodies. From these parameters, models for the interior structure of Mars can be constrained, in a similar fashion as is now done with tracking data from Martian orbiters (Yoder et al., 2003; Konopliv et al., 2006; Marty et al., 2009; Konopliv et al., 2011).

For Phobos, we simulate the estimation of the libration amplitudes, which are now constrained to only  $\sim 0.15^\circ$  (Willner et al., 2010), and are related to its relative moments of inertia. We also simulate the estimation of Phobos' degree-two gravity field coefficients, the combination of which with the relative moments of inertia can be used to determine Phobos' absolute moments of inertia. Additionally, we investigate the estima-

tion of the tidal deformation of Phobos (which is currently unobserved) from simulated tracking data, placing further constraints on models for its interior structure by differentiating between a monolithic and rubble pile structure. The composition of Phobos will provide insight into its origin as well as its orbital evolution, through both long-term propagation of its orbital dynamics and by comparing it to expected compositions from various Phobos origin scenarios.

We first present an overview of the technology and operations of ILR in Section 2, where we also discuss the current state of the technology in terms of experimental implementations and provide some details on the PLR mission concept. Subsequently, the models for the dynamics of Phobos and the observations are presented in Section 3. We discuss the relevance and observation signatures of the estimated geodetic parameters in Section 4 and the estimation procedure in Section 5. The estimation results are discussed in Sections 6 and 7 for Mars and Phobos geodetic parameters, respectively. Finally, we present the main conclusions in Section 8.

## 2 Planetary Laser Ranging

Satellite Laser Ranging (SLR) is a space-geodetic technique that is used to directly measure distances from ground stations to Earth-orbiting satellites, *e.g.* (Pearlman et al., 2002). It is, along with Global Navigation Satellite Systems (GNSS), Very Long Baseline Interferometry (VLBI) and Doppler Orbitography and Radiopositioning Integrated by Satellite (DORIS), one of the fundamental space-geodetic techniques used in the creation of terrestrial reference frames, *e.g.* (Altamimi et al., 2011). It has been used for a variety of applications in Earth sciences, summarized by Exertier et al. (2006), such as the determination of Earth rotational parameters, the determination of the behaviour of the geocenter and the estimation of low degree and order terms of the Earth's gravity field. Similarly, data from Lunar Laser Ranging (LLR) has been used in the creation of dm-level ephemerides of the Moon (Folkner et al., 2009) and estimation of the lunar libration amplitudes and tidal deformation, leading to an increased understanding of its interior structure (Williams et al., 2006). Additionally, both SLR and LLR have been used in a number of space-based tests of relativity, summarized by Turyshev and Williams (2007).

In this section, the extension of SLR and LLR to interplanetary distances is discussed. Firstly, a general overview of the technique is presented in Section 2.1, followed by its current status of implementation and experimentation in Section 2.2, and its specific conceived implementation for the current study in Section 2.3.

### 2.1 Overview

The technology of SLR and LLR is based on the reflection of short laser pulses (typically about 10-1000 ps), transmitted from Earth-based stations, by space-based retroreflectors. By measuring the round-trip travel time of the laser pulse and applying corrections for relativistic, tropospheric and hardware effects, the distance to the target can be determined to sub-cm accuracy (Degnan, 1993). Due to the use of retroreflectors, the received laser power falls off with  $R^{-4}$ , where  $R$  is the distance from the ground station

to the target. This aspect puts the Moon near the limit of its feasibility. However, by using active laser transmitters and detectors at both ends of the link (*i.e.* replacing the reflector by an active laser transceiver), the range dependency becomes  $R^{-2}$ , allowing sufficient power to be retained when ranging over interplanetary distances (Degnan, 2002).

Also, due to the absence of retroreflectors in such a two-way active configuration, the uncertainty associated with the signature imposed on the laser pulses by reflectors (Otsubo and Appleby, 2003) is absent in ILR. This could potentially increase the attainable measurement accuracy compared to SLR, since the received pulse shape can be predicted better. However, this comes at the expense of the use of active space-based systems (laser transmitter, detector, optics, pointing system, clock), which complicates both the design and operations of the space segment. Additionally, new types of hardware-induced error sources such as those resulting from the instabilities of the spacecraft clock and optical detector, which are absent in reflector ranging, are introduced.

Using a laser ranging architecture with active systems at both ends of the link, one-, two- and three-way (*i.e.* two-way with different ground stations) interplanetary laser links can be established. In a one-way link, the space segment is typically equipped with only a receiver, which is used to detect laser pulses transmitted from Earth-based ground stations. The transmitted and received signals are then matched and a range measurement is generated. However, since the two measurements are performed by different clocks, the relative behaviour of the two clocks during the entire mission needs to be either known from other independent sources or estimated.

In a two- and three-way laser ranging system, laser pulses are typically fired and detected independently from one another by both ends of the link (Degnan, 2002), a technique termed asynchronous ranging. To match transmitted to received laser pulses, the laser pulse transmission time uncertainty (also termed jitter) inherent in transmitters is employed, by matching the jitter pattern as recorded at both ends of the link (Neumann et al., 2008). Alternatively, active pulse position modulation can be used to create a pseudo-random code on the laser pulse transmission times, allowing the matching of transmitted and received shots (Chen et al., 2013).

By matching the received and transmitted laser pulses, a two-way range measurement is effectively emulated, plus a time delay between reception and transmission by the space segment. In this case, synchronization of the spacecraft and ground clock is not needed (Degnan, 2002). Therefore, in such a setup, the stability of the spacecraft clock does not need to be of the same order as that of the ground station clock (Birnbaum et al., 2010). By pairing up- and downlink range measurements, only the time between successive receptions and transmissions at the spacecraft needs to be accurately measured, whereas the ground-based clock needs to be stable over the sum of the paired up- and down-link times.

Previous analyses of the attainable two-way ILR accuracy estimate that it is at the mm- to cm-level (Degnan, 2002; Turyshev et al., 2010), similar to that of concepts using retroreflectors (Degnan, 1993; Exertier et al., 2006). In addition to the spacecraft clock, highly stable detectors and short laser-pulse transmitters will be needed, with requirements more stringent than for current space-based laser systems, such as altimeters. For instance, the accuracy of the Lunar Reconnaissance Orbiter (LRO) one-way laser

ranging system (see next section) is limited to about 10 cm due to hardware limitations. However, ILR system requirements are within current technological capabilities (Degnan, 2008).

## 2.2 Current status

A one-way laser tracking approach is used in the operations of LRO, using its laser altimeter hardware (Zuber et al., 2010). However, the one-way range concept suffers from the fact that time tags from two different clocks need to be combined, degrading the performance. To characterize the behaviour of the spacecraft clock, concurrent estimation of state and clock parameters is required, which is challenging by using laser ranging data alone due to strong correlations between the two sets of parameters (Bauer et al., 2013). Due to these complications, the laser ranging data was not used for orbit determination of LRO (Mazarico et al., 2012), and only radiometric and altimeter crossover observables were used instead. However, later efforts have shown the feasibility of estimating LRO orbits (of a quality comparable to that derived from Doppler data) using one-way laser ranging data only (Mao et al., 2013).

A two-way laser link was demonstrated by the MESSENGER spacecraft, at a distance of 24 million km (Smith et al., 2006). The short (single pass) experiment of opportunity yielded a formal error (see Section 5) of 20 cm in range, using the non-dedicated laser altimeter hardware onboard the spacecraft. A one-way laser detection experiment from Earth to the Mars Global Surveyor (MGS) laser altimeter detector was performed at  $\sim 80$  million km distance (Abshire et al., 2006). Although no two-way ranging link could be established due to partial failure of the MGS hardware, it demonstrated the feasibility of long-distance laser pointing and reception.

Previous in-flight experiments for ILR were performed using altimeter systems. However, in addition to altimetry systems, the use of laser communications on the Lunar Atmosphere and Dust Environment Explorer (LADEE) satellite (Boroson and Robinson, 2013) and the laser communications demonstration that was planned on the now-cancelled Mars Telecom Orbiter (Boroson et al., 2005) indicate an emerging application of lasers for interplanetary communications purposes. Research in this field, as well as the potential combination with ranging, is ongoing (Hemmati et al., 2009; Hemmati, 2011). The combination of ranging and communication activities has the advantage that both require Earth-pointing operations, as opposed to altimetry which requires nadir pointing operations.

A two-way architecture was simulated at the Wettzell SLR station by using two collocated laser systems ranging to the same target at different wavelengths, effectively emulating an interplanetary laser link (Schreiber et al., 2009a). This system used the reflector technology, so that the total received signal strength was similar to what would be expected for planetary laser ranging. A two-way asynchronous laser ranging system was demonstrated in the laboratory over a distance of about 1 m by Chen et al. (2013), who obtained a measurement accuracy at the 0.1 mm level.

### 2.3 Phobos Laser Ranging Concept

A mission proposal for placing a laser transceiver on Phobos with the primary objective of testing general relativity was described by Turyshev et al. (2010). There, the performance of the system for retrieving relativistic parameters, such as the time-dependency of the gravitational constant  $\dot{G}/G$  and the Parametric Post-Newtonian (PPN) parameters  $\beta$  and  $\gamma$  was analyzed. In addition to the relativistic observables, mm-level ranging to Phobos would allow for the observation of a variety of physical quantities of both Phobos and Mars, the analysis of which is the focus of the current paper. For a laser link from Earth to Phobos, the distance between the terminals is roughly between 55 M and 400 M km. The design of the laser lander included a 40 kg laser payload system, requiring 50 W of power for operations. We use a similar concept for simulating laser ranging measurements for the purpose of estimating geodetic parameters of Mars and Phobos, and use the analysis of Turyshev et al. (2010) for modelling the range precision (see Section 3.3).

Due to the extremely small non-conservative accelerations acting on Phobos (see Section 3.1), compared to a Mars orbiter, it can be seen as a drag-free system orbiting Mars. Therefore, mismodelling of surface forces (primarily radiation pressure and atmospheric drag) will have a negligible influence on quality of the analysis results (see Section 3.1). This is in stark contrast to the tracking data analysis of artificial (planetary) orbiters, where these contributions can dominate the error budget (Konopliv et al., 2006; Marty et al., 2009; Konopliv et al., 2011). This long-term predictability of Phobos' orbit makes it ideally suited for estimating properties of the gravitational fields of Mars and Phobos, such as their spherical harmonic coefficients and tidal variability. Additionally, tracking to a Phobos lander will allow the direct observation of the moon's librations and deformation.

## 3 Simulation models

To assess the capabilities of a PLR concept, simulated two-way (asynchronous) laser measurements are generated, which are subsequently used as input to an orbit determination and parameter estimation model. From this, formal errors of and correlations between the estimated parameters as a function of time are obtained.

The estimation software numerically integrates the equations of motion and variational equations, the result of which is used to simulate observations and the partial derivatives of the observations w.r.t. the estimated parameters. These values are then used as input for the estimation process, which uses the same models as the simulations from which the measurements were generated. The influence of and mitigation strategy for the fact that the estimation and truth models used here are equal are discussed in Section 5.3. A software packaged (Dirkx and Vermeersen, 2013) based on the Tudat astrodynamics toolbox (Kumar et al., 2012) is used to perform all simulations.

The models used for to the dynamics, environment and observations are presented and discussed in Sections 3.1, 3.2 and 3.3, respectively.



### 3.1 Dynamical models

For the dynamical simulations, the equations of motion of Phobos are numerically integrated using a variable step size RKF7(8) integrator (Montenbruck and Gill, 2000), yielding the state (position and velocity) of Phobos as a function of time  $\mathbf{x}_p(t)$ . Concurrently with the equations of motion, the variational equations are integrated by analytically calculating and combining the partial derivatives of the acceleration w.r.t. the state and the estimated parameters, yielding the state transition matrix  $\Phi(t, t_0)$  and sensitivity matrix  $S(t)$  (Montenbruck and Gill, 2000). The vector of estimated parameters is here denoted as  $\mathbf{p}$ , which is divided into initial state parameters  $\mathbf{x}_0$  and remaining (environmental) parameters  $\mathbf{p}_e$  as:

$$\mathbf{p} = \begin{pmatrix} \mathbf{x}_0 \\ \mathbf{p}_e \end{pmatrix} \quad (1)$$

from which the state transition and sensitivity matrices may be expressed as:

$$\Phi(t, t_0) = \frac{\partial \mathbf{x}(t)}{\partial \mathbf{x}_0}; \quad S(t) = \frac{\partial \mathbf{x}(t)}{\partial \mathbf{p}_e} \quad (2)$$

which are used for the setup of the observation partials, as will be discussed in Section 3.3.

For calculating the trajectory, the following accelerations on Phobos are included in the simulations:

- Mutual gravitational attraction between Phobos and Mars. The gravity fields are expressed as spherical harmonics series, with the Mars field expanded to degree and order 12 and the Phobos field expanded to degree and order 2. The gravitational acceleration is modelled as follows, after Lainey et al. (2001):

$$\ddot{\mathbf{r}}_p = -(\mu_m + \mu_p) \left( \frac{\mathbf{r}_p}{r_p^3} - \nabla_p U_{\bar{p}\hat{m}} + \nabla_m U_{\hat{m}\bar{p}} \right) \quad (3)$$

where  $\mu$  denotes a gravitational parameter,  $U$  a gravitational potential,  $\mathbf{r}$  a position vector in a Mars-centered inertial (MCI) frame and the  $m$  and  $p$  subscripts denote quantities associated with Mars and Phobos, respectively. The bar and hat notation on the potential subscripts denote the point mass and extended body contributions, respectively. See Lainey et al. (2001) for a more extensive discussion of this model. The models from which the (time-dependent) spherical harmonic coefficients of Mars and Phobos are derived are presented and discussed in Section 3.2.

- Third-body attraction due to the Sun, Deimos, Earth's Moon and all planets. All third bodies are considered as point masses. Although the influence of the Sun's  $J_2$  coefficient is expected to be observable in the dynamics of Phobos, as shown by Turyshv et al. (2010), we do not include it here, as we will not include their estimation parameters. Similarly, the influence of relativistic effects on the dynamics is omitted. The influence on the estimation results was concluded to be negligible by investigating results from a full simulation including these effects.

Solar radiation pressure on Phobos, although at the limit of observability at  $\sim 10^{-13}$  m/s<sup>2</sup>, as calculated for a spherical Phobos from Montenbruck and Gill (2000), is not included in the dynamical model. A verification run including this acceleration was performed, and it was concluded that it has a negligible influence on the estimation results.

### 3.2 Environment models

In this section, the models that have been used for the characteristics of Mars, Phobos and third bodies will be discussed.

The static spherical harmonics gravity field of Mars that is used was derived by Lemoine et al. (2008). Gravity field variations due to seasonal ice and atmosphere mass distribution, with the theoretical model from Sanchez et al. (2006), are used for the zonal spherical harmonic coefficients  $\bar{J}_i (= -\bar{C}_{i0})$  of degree  $i = 1 \dots 8$ , modelling the changes as a combination of trigonometric terms with integer number of cycles per Martian year.

Tidal variations of Mars' gravity field due to Phobos, Deimos and the Sun are included for degrees two and three. The spherical harmonic coefficients of Mars are modified directly as follows (Petit et al., 2010):

$$\Delta \bar{C}_{n,m}(t) - i \Delta \bar{S}_{n,m}(t) = \frac{k_{nm}}{2n+1} \sum_j \frac{\mu_j}{\mu_m} \left( \frac{R_{eq}}{r_j(\tilde{t}_{n,j})} \right)^{n+1} \cdot \dots$$

$$\dots \cdot \bar{P}_{nm} \left( \sin \phi_j^{(m)}(\tilde{t}_{n,j}) \right) e^{-im\lambda_j^{(m)}(\tilde{t}_{n,j})} \quad (4)$$

$$\tilde{t}_{n,j} = t - \Delta t_{n,j} \quad (5)$$

where  $\bar{C}_{n,m}$  and  $\bar{S}_{n,m}$  are the cosine and sine coefficients of the spherical harmonic gravity field expansion,  $R_{eq}$  the equatorial radius of Mars,  $k_{nm}$  the Love number at degree and order  $n$  and  $m$ , and  $\phi_j^{(m)}$  and  $\lambda_j^{(m)}$  the Mars-fixed latitude and longitude, respectively, of body  $j$ . The time delay  $\Delta t_{n,j}$  of the tide of order  $n$  raised by body  $j$  is due to the viscoelastic response of Mars. From this equation, the tidal influence on Phobos' acceleration is calculated through Eq. (3). A discussion on the influence of Phobos' orbit and geophysical implication of models for Mars tides is presented in Section 4.3. The Mars rotation model by Konopliv et al. (2006) is used.

For Phobos, the gravity field values for  $C_{20}$  and  $C_{22}$  as estimated by Lainey et al. (2007) are used, with other terms nominally set to zero. The rationale for this will be discussed in Section 7.1. The gravity field of Phobos is modelled as being static, since its variations are not expected to produce observable effects given the present measurement accuracies.

We use the Phobos libration model by Rambaux et al. (2012), who numerically integrate its rotational equations of motion, using Lainey's ephemeris solution, and perform a frequency decomposition of the results. We use this libration model, cast in the form of Le Maistre et al. (2013), with additional terms from Rambaux (2013). The model decomposes the rotation into three Euler angles  $\alpha, \delta$  and  $W$  (right ascension, declination and longitude of prime meridian, respectively), from which the rotation matrix from J2000 (Moyer, 2000) to the Phobos-fixed frame, denoted  $R^{P/I}$ , is derived

as follows:

$$R^{P/I} = R_z(W)R_x(\pi/2 - \delta)R_z(\pi/2 + \alpha) \quad (6)$$

The libration contribution to each Euler angle is calculated from the following, with  $\gamma$  used a placeholder notation for any one of the three Euler angles:

$$\Delta\gamma(t) = \sum_j \gamma_{T_j}^c \cos\left(\frac{2\pi}{T_j}t\right) + \gamma_{T_j}^s \sin\left(\frac{2\pi}{T_j}t\right) \quad (7)$$

where  $T_j$  denotes the period of the  $j^{\text{th}}$  term and  $\gamma_{T_j}^c$  and  $\gamma_{T_j}^s$  denote the amplitudes of the cosine and sine contribution of the  $j^{\text{th}}$  term, respectively. In addition to these trigonometric terms, we use the constant and linear terms for the three angles, as well as the quadratic term in  $W$ , taken from Seidelmann et al. (2002).

The degree-two Phobos deformation due to the tidal potential of Mars is included by calculating the resulting Phobos-fixed position change of a surface point  $\Delta\mathbf{r}^p(t)$  from the first-order equation from Petit et al. (2010):

$$\Delta\mathbf{r}^p(t) = h_2 \sum_j \frac{\mu_j R_{eq}^4}{\mu_p r_j^3} \hat{\mathbf{r}}^p \left( \frac{3(\hat{\mathbf{r}}_j \hat{\mathbf{r}}^p) - 1}{2} \right) \quad (8)$$

where  $R_{eq}$  is Phobos' reference (mean equatorial) radius,  $\mathbf{r}_j$  is the vector from the center of Phobos to the body causing tidal deformation (in a Phobos-fixed frame), and  $\mathbf{r}^p$  is the Phobos-fixed point where the deformation is to be modelled. However, since Phobos is tidally locked, the majority of this deformation will be constant and cannot be separated from the nominal lander position by a time history of range measurements. Consequently, the measurable deformation of Phobos is described by the following:

$$\Delta\mathbf{r}_{meas}^p(t) = \Delta\mathbf{r}^p(t) - \overline{\Delta\mathbf{r}^p(t)} \quad (9)$$

where the overbar denotes the average value over the complete simulation time and  $\Delta\mathbf{r}^p(t)$  is evaluated from Eq. (8).

For all third-body effects, we use the ephemeris and gravitational parameters of the DE421 planetary ephemeris (Folkner et al., 2009).

### 3.3 Observation simulations

Range observations between Earth-based stations and the Phobos-based lander will be simulated using the result of the numerical integrations of the equations of motion described in Section 3.1 and the Phobos rotation and deformation models described in Section 3.2. The states of the stations involved in the observation are evaluated in a barycentric frame, with axes oriented along J2000. From this, the light time equation(s) are solved (Moyer, 2000) and range corrections, such as troposphere and relativistic effects are applied.

For the Earth-based stations, a set of 8 SLR stations is selected, the combination of which gives relatively good global coverage. The approximate position of these stations is

---

<sup>2</sup><http://ilrs.gsfc.nasa.gov/>

Table 1: Used SLR ground stations and their approximate geodetic positions<sup>2</sup>

Station name	altitude [m]	latitude [deg]	longitude [deg]
Graz	495	47.07	15.49
McDonald Observatory	2006	30.68	255.98
Yarragadee	244	-29.05	115.35
Hartebeesthoek	1406	-25.89	27.69
Koganei	114	35.71	139.49
Greenbelt	19	39.02	238.18
Arequipa	2489	-16.47	288.51
Matera	537	40.65	16.70

given in Table 1. In the simulations, their positions are taken from the ITRF2008 (Petit et al., 2010). It should be stressed that these stations were chosen as a representative set of tracking station positions and do not represent the required or expected set of stations for the mission, nor do their current systems necessarily reflect required capabilities for ILR. Ground station feasibility and selection would depend on the up- and downlink budget and derived system requirements. The Phobos lander will be assumed to be situated on a tri-axial ellipsoid, with axes as given by Willner et al. (2010). The nominal location of the lander is the same as used by Le Maistre et al. (2013): at a latitude of  $14^\circ$  and a longitude of  $224^\circ$ , which was the approximate position the planned Phobos-Grunt landing site.

Processed laser range observations are typically published as normal points (Degnan, 1993), which are a statistical average from a set of single-shot measurements. We take a similar approach in our simulation to prevent the calculation and processing of an excessive number of observations. We use the following settings for generating range measurements:

- Each ground station performs one 30 minute observation arc per day.
- During each 30 minute arc, a single normal point observation is generated per 60 s.
- Each normal point has a precision  $\sigma_{obs}$  of 1 mm, generated independently from a Gaussian distribution with zero mean and  $\sigma_{obs}$  standard deviation.

The measurement integration time of 60 s and precision of 1 mm for the observations were taken from Turyshev et al. (2010). We omit here the influence of weather conditions, day/night ranging and other system outage events, instead assuming tracking passes from the given 8 stations each day. The influence of the precise choice of ground stations that perform the tracking is expected to be of limited influence, though, assuming a similar global distribution of stations.

All observations are subject to a number of constraints. For each ground station, the first opportunity each day for a contiguous 30 minute arc (or maximum arc duration if no 30 minute arc is feasible) is identified and measurements are simulated. The constraints are the following:

- No observation is possible in case of link occultation by the Moon or Mars.
- No observation is possible for solar separation angles  $\leq 5^\circ$ . This constraint is imposed to prevent inclusion of observations for which the stray light would be too intense to separate the signal from the noise photons.
- Local elevation angle both at the lander and at the ground station must be  $\geq 10^\circ$ .

The first and third constraint will result in short periods in which no observations are possible, whereas the solar separation angle constraint will result in a longer observation outage. For relativistic observables, the estimation precision can be very sensitive to the precise constraint function value of the separation angle, (Turyshv et al., 2010). For our estimated parameters, however, there is no direct dependence on the laser pulse trajectory's solar impact parameter. However, the duration of the link outage could be influential in the estimation of certain parameters. Here, we set the Sun separation angle at  $5^\circ$ , which is a conservative lower bound (Hemmati, 2006; Turyshv et al., 2010). A detailed analysis of mission geometry parameters on interplanetary laser ranging analysis will be presented in future work.

## 4 Mars and Phobos physical parameters

In this section, we give an overview of the relevance of the geodetic parameters of which the estimation is simulated, in terms of understanding the behaviour of the Martian system. Also, matters relating to their signatures on the range data are discussed where applicable. First, the static gravity fields are discussed in Section 4.1, followed by the relation between Mars' precession rate and its moments of inertia in Section 4.2. Subsequently, matters related to Martian tides (*i.e.* Love numbers and quality factors) are discussed in Section 4.3, followed by an overview of Phobos librations and moments of inertia in Sections 4.4 and 4.5, respectively. Finally, Phobos tides are discussed in Section 4.6.

### 4.1 Static gravity fields

Although the orbit of Phobos is near-equatorial and near-circular, it will be possible to retrieve low-degree static coefficients of the gravity field of Mars and Phobos. However, since only tracking to a single target in a (nearly) constant orbit is considered, the full spherical harmonic gravity field cannot be estimated (Yoder et al., 2003; Karatekin et al., 2005), since even- and odd-degree zonal coefficients cannot be decoupled. Instead, lumped even- and odd-degree zonal coefficients are obtained. However, by combining tracking data to Phobos with that to other Mars orbiters, the parameters can be decoupled, although at an uncertainty partially limited by the tracking of the spacecraft. Here, we limit ourselves to the analysis of tracking data from a Phobos lander only.

As with the estimation of the Martian gravity field, it will not be possible to decouple the even and odd gravity field coefficients of Phobos, due to the symmetry of Eq. (3) in the  $p$  and  $m$  subscripts.

The lumped even- and odd-degree zonal gravity field coefficients are primarily due to the  $\bar{J}_2$  and  $\bar{J}_3$  terms, respectively. The influence of higher order terms is quantified in Appendix A. For the Mars gravity field estimation, the degree four and five terms both contribute roughly 0.4 times the primary term to the even and odd lumped coefficients, respectively. For the Phobos even lumped coefficient, the contribution is only at the  $5 \cdot 10^{-10}$  level.

From the degree-two spherical harmonic coefficients, relative values of principal moments of inertia can be obtained. However, for determining the absolute moments of inertia, additional information is required. For Mars, the rotational precession rate is used here (see Section 4.2). For Phobos, the libration amplitudes are used (see Section 4.4).

## 4.2 Mars moments of inertia

By combining the gravity field coefficients estimation with that of the rotational precession rate of Mars  $\dot{\psi}_m$ , its polar moment of inertia can be calculated. Currently, the dominant error term in the calculation of the absolute polar moment of inertia is the uncertainty in  $\dot{\psi}_m$  (Konopliv et al., 2011). The uncertainty in the normalized polar moment of inertia  $C/(M_m R_{eq}^2)$ , which we denote as  $C'$  follows from:

$$\sigma_{C'} = \frac{C'}{\dot{\psi}_m} \sigma_{\dot{\psi}_m} \quad (10)$$

An improvement in the determination of Mars' polar moment of inertia will also result in an improvement of the determination of its mean moment of inertia through combination with other degree-two spherical harmonic gravity coefficients.

For a spherically symmetric Mars interior model, it is the mean moment of inertia that can best be used to constrain its radial mass profile (Khan and Connolly, 2008), putting limits on the density and size of the core and mantle. However, additional constraints will be required to be able to properly distinguish between different core compositions, such as Love numbers (see Section 4.3) and other properties of Mars to which a Phobos lander is not sensitive (see Section 6.3).

## 4.3 Mars tides

As described in Section 3.1, tidal bulges are raised on Mars by other bodies, influencing the dynamics of Phobos due to their influence on the Martian gravity field, described by Eq. (4). Due to Mars' viscoelastic response, the tide raised by Phobos is slightly behind the Martian sub-Phobos point, since Phobos is below areostationary orbit and its orbital period is therefore shorter than Mars' rotational period. As a result, a secular effect on the orbital longitude of Phobos is observed.

The tidal lag can be quantified by the quality factor  $Q$ , a measure for the dissipation of tidal energy (at a given frequency and degree), which is related to the tidal time lag  $\Delta t$ , see Eqs. (4) and (5), as follows:

$$\Delta t = \frac{T \sin^{-1}(1/Q)}{2\pi} \quad (11)$$

where  $T$  is the period of the tide (*i.e.* the synodic period of one Martian day and one orbit of the tide-raising body).

The additional acceleration exerted on Phobos due its own degree-two tidal bulge is calculated from (Lainey et al., 2007):

$$\Delta \ddot{\mathbf{r}}_p = \frac{3k_{2,M}\mu_p R_M^5}{r^8} \left( \mathbf{r} + \Delta t \left( \frac{2\mathbf{r}(\mathbf{r} \cdot \mathbf{v})}{r^2} (\mathbf{r} \times \boldsymbol{\Omega}_M + \mathbf{v}) \right) \right) \quad (12)$$

where the term multiplied by  $\Delta t$  causes the secular perturbation in longitude. Combination with Eq. (11) indicates that the secular effect is approximately proportional to  $k_2/Q$ . Higher-order tidal deformation of Mars, *i.e.* due to  $k_3, k_4, \dots$  will also produce additional secular accelerations on Phobos' longitude, which could be obtained explicitly by generalizing Eq. (12). Here, Eq. (12) is not evaluated directly, but is included indirectly by evaluating Eq. (3) using Eq. (4) for the variations in Mars' potential.

An overview of published estimates of  $Q$  is given by Jacobson and Lainey (2014). The smallest uncertainty of  $Q$  is obtained by Jacobson (2010) at 0.2. However, since the  $Q$  estimations from different sources do not coincide to within their error margins, we assume an *a priori* uncertainty of 1.

The tides of the Sun and Deimos do not cause a secular precession in the longitude of the node of Phobos. Instead, they only cause periodic variations. Currently, the separated Sun- and Deimos-raised tides' tidal lags are unobserved from dynamics of Mars orbiters.

The interior structure of Mars can be parameterized by a variety of models, an extensive overview of which is given by Rivoldini (2012), who uses the current value of  $k_2$ , among others, to constrain the Martian interior. Tidal Love numbers are related to the body's density and elasticity profiles. As a result, they are a strong indicator of the existence, size, composition and current state of the Martian core (Yoder et al., 2003; Rivoldini et al., 2011; Dehant et al., 2011). A possible estimation of  $k_3$  by the PLR mission will provide further information on the Martian interior, as indicated by the numerical examples of Konopliv et al. (2011).

Current estimates of the value of Mars'  $k_2$  from tracking data of Mars orbiters differ substantially, well outside their published error ranges, as summarized by (Konopliv et al., 2011). One the reasons for these differences can be attributed to spacecraft surface force mismodelling and estimation. Also a lack of (or imprecise) corrections for the atmospheric tides on Mars degrade the estimation of  $k_2$ . The first of these aspects is mitigated for a Phobos lander, due to the negligible non-conservative forces acting on it (see Section 3.1). The second, however, will require improved modelling, as well as *in situ* atmospheric observations from current and future Mars landers. Finally, by estimating a lumped value for  $k_2$  instead of the Love numbers per order (*i.e.*  $k_{20}, k_{21}$  and  $k_{22}$  separately), which is a typical approach, different spacecraft will experience a different effective degree-two Love number, so that different combinations of tracking data, or differently weighted data, could produce slightly different estimates even in the ideal case of absence of any mismodelling. This effect is mitigated here by estimating separate Love numbers for each degree (see Section 5.2).

In principle, both the Love numbers and the quality factors can be dependent on the frequency of the raised tide. A variety of models for determining the tidal frequency-

dependence of  $Q$  exist, an overview of which is given by Efroimsky and Lainey (2007). The frequency-dependent quality factor behaviour can be used as a measure for the rheology of the body. An extensive discussion on the implications of the frequency dependence of  $Q$  for the Martian system evolution is given by Efroimsky and Williams (2009).

We model only the quality factors as being frequency dependent, since their frequency dependence is expected to be much stronger than that of the Love numbers (Efroimsky and Lainey, 2007) and no evidence for the frequency dependence of the Martian Love numbers has been found (Konopliv et al., 2011). Also, Bills et al. (2005) conclude that for the expected Martian viscosity range, the Love numbers will be "quite independent" from the tide-forcing frequency.

#### 4.4 Phobos librations

Due to the non-symmetric shape and mass distribution of Phobos and its eccentric orbit around Mars, its physical rotation exhibits librations. The behaviour of these librations can be related to Phobos' internal mass distribution, as discussed in Section 4.5.

The primary libration of Phobos, a once-per-orbit term in longitude, is the only presently observed libration of Phobos. It has been determined independently from both photometric data and dynamical simulations by Willner et al. (2010) and Jacobson (2010), respectively. The two estimates agree within their respective error margins, with the smaller uncertainty that of Willner et al. (2010), at  $\pm 0.14$  degrees.

The Phobos libration model used here is the one generated by Rambaux et al. (2012) (see Section 3.2), which includes librations in both longitude and latitude (which are so far unobserved). Although our estimation will be precise to a level that is beyond the truncation amplitude of the libration model, we restrict ourselves to the given frequency decomposition, but will discuss the results in a general manner in Section 7.3, indicating the influence of observed and potential correlations. To mitigate the influence of the existence of unmodelled libration modes in the mission's data analysis, a frequency decomposition of observed residuals could be used to both recognize unmodelled libration terms and potentially identify model errors of the libration model, as discussed by Le Maistre et al. (2013). Alternatively, the rotational and translational equations of motion could be used concurrently, estimating not the libration amplitudes, but the initial rotational state, the dynamics of which would be derived from its inertia tensor and forcing torques.

#### 4.5 Phobos moments of inertia

The amplitudes and phases of the librations are related to its mass distribution through its moments of inertia and gravity field (Borderies and Yoder, 1990; Rambaux et al., 2012). Therefore, measuring the amplitudes of these librations will, combined with the degree-two spherical harmonic coefficient estimation, allow the improved estimation of Phobos' structure and composition through their relation with the inertia tensor.

Interior structure models of Phobos, constrained by current observational data, show that it possesses a substantial fraction of voids and/or ice (Andert et al., 2010; Rosen-



blatt, 2011). These voids will be manifested in both its response to external forcing torques and its tidal deformation.

The list of amplitudes of the librations, given in Appendix C, can be seen to be a combination of long-period motions, with periods  $\gtrsim 1$  year, and those with short-period motions, with periods  $\lesssim 1$  day. Only the latter category contains useful information on Phobos' interior, as its response at these frequencies is mainly influenced by its inertia tensor (Rambaux et al., 2012). The long-period librations are forced by Mars' long-period and secular rotation variations and their estimation is not strongly related to Phobos' moments of inertia. This can be seen from the following first-order equation (neglecting higher-order feedback effects), which relates a forcing amplitude  $\Gamma_f$  at frequency  $\omega_f$  to a libration amplitude  $\gamma_f$  (using the notation of Eq. (7)) through the proper mode of the given libration angle  $\nu_\gamma$  (Le Maistre et al., 2013):

$$\gamma_f = \frac{\nu_\gamma^2}{\nu_\gamma^2 - \omega_f^2} \Gamma_f \quad (13)$$

which shows that the influence of  $\nu_\gamma$  goes to zero as  $\omega_f \gg \nu_\gamma$ . Also, it shows that, in the first-order approximation, the libration amplitude goes to infinity as the forcing and proper-mode frequencies approach one another.

The libration amplitudes can be directly related to Phobos' relative moments of inertia, denoted by:

$$\zeta = \frac{C - B}{A} \quad \beta = \frac{C - A}{B} \quad \gamma = \frac{B - A}{C} \quad (14)$$

where  $A$ ,  $B$  and  $C$  are Phobos' absolute moments of inertia, in ascending order of magnitude. The relation between (uncertainties in) Phobos' libration amplitudes and its proper modes and subsequently between the proper modes and the relative moments of inertia are discussed in Appendix B. The longitude libration directly constrains the  $\gamma$  ratio, whereas the other two libration components jointly constrain the  $\zeta$  and  $\beta$  ratios.

## 4.6 Phobos tides

The Martian tidal potential causes Phobos to undergo deformation, as discussed in Section 3.2. As a result, periodic variations in the Phobos lander positions may be observed in the range measurements. In our model, the deformation of Phobos is quantified by its second-degree deformation Love number  $h_2$ , as shown by Eq. (8).

Currently, no direct measurement of this parameter is available, but constraints can be placed on it by Phobos interior modelling. An analysis of the observability of  $h_2$  Love number by Doppler tracking was done by Le Maistre et al. (2013). They show that a sufficiently precise estimation of the parameter would allow for differentiation between a rubble pile or monolithic structure of Phobos, as well as estimating its mean rigidity, putting constraints on Phobos' origin (Rosenblatt, 2011).

In addition to the magnitude of the deformation, the time lag of the raised tide may be observed, in a similar fashion as the observed Mars tide (see Section 4.3) The quality factor of Phobos is related to its orbital evolution, and is therefore related to the investigation of theories of its formation and origin scenarios, (Mignard, 1981).

## 5 Parameter estimation

Observations are generated using the models described in Section 3 over a mission duration of 5 years. By taking a long mission duration, we analyze the potential added value of an extended mission for each of the science observables (detailed in Section 5.2).

The simulated data is used as input for a weighted batch least squares estimation. In this process, Gaussian noise with standard deviation  $\sigma_{obs}$  is used to determine the measurement weight  $w_{i,i} = 1/\sigma_{obs}^2$ , where  $w_{i,i}$  denotes entry  $i$  on the diagonal of the weight matrix  $W$ . Also, we use a diagonal *a priori* covariance matrix  $P^{(a.pr.)}$  to regularize the inversion problem. The regularization is required in the initial phase of the mission, where only few observations with very little geometric diversity are available. The *a priori* parameter values are based on their current best estimates. Since the PLR mission is expected to provide strong improvements in most parameters (see Sections 6 and 7), the influence of the regularization diminishes as the mission begins to return substantial parameter improvements. The complete covariance matrix  $P$  is then obtained from Montenbruck and Gill (2000):

$$P^{-1} = \left(P^{(a.pr.)}\right)^{-1} + \left(P^{(0)}\right)^{-1} \quad (15)$$

$$P^{(0)} = \left(H_p^T W H_p\right)^{-1} \quad (16)$$

where  $H_p$  is the matrix of partials of the observations w.r.t. the estimated parameters and  $P^{(0)}$  is the covariance matrix without the *a priori* contribution.

In Section 5.1, the setup of the partial derivatives that make up the matrix  $H_p$  is discussed. Subsequently, in Section 5.2 the list of estimated parameters is given and discussed. Finally, a discussion on the use of consider covariance is given in Section 5.3. Consider covariance is used to analyze the influence of systematic errors, which are not directly included in the observation models presented in Section 3.3.

### 5.1 Observation partials

The partial derivatives of the observations w.r.t. the parameter vector, from which  $H_p$  is constructed, are calculated from the state transition and sensitivity matrices (see Section 3.1) as follows, where  $h$  denotes a single observation:

$$\frac{\partial h}{\partial \mathbf{p}} = \sum_j \left( \left. \frac{\partial h}{\partial \mathbf{x}}(t_j) \right|_{\mathbf{p}=\text{const.}} \frac{\partial \mathbf{x}}{\partial \mathbf{p}}(t_j) \right) + \left. \frac{\partial h}{\partial \mathbf{p}} \right|_{\mathbf{x}=\text{const.}} \quad (17)$$

$$\frac{\partial \mathbf{x}(t)}{\partial \mathbf{p}} = \begin{pmatrix} \Phi(t, t_0) & S(t) \\ 0_{n_{p_e} \times 6n_b} & I_{n_{p_e} \times n_{p_e}} \end{pmatrix} \quad (18)$$

where  $n_{p_e}$  is the size of the vector  $\mathbf{p}_e$  in Eq. (1) and  $n_b$  is the number of bodies for which the initial state is estimated. The summation takes place over all times associated with the observation (reception, transmission, etc.) and  $\mathbf{x}$  here denotes the vector of all numerically integrated states (in this case only Phobos). The Jacobians in

the summation are evaluated at different times allow for any possible significant changes in their values between the start (typically transmission) and end (typically reception) of the observation.

It can be seen that the influence of a model parameter on the observation partial is twofold. Firstly, the influence of the state of Phobos on the observation is included, which is mapped to the influence of the parameter by the Jacobian matrix  $\partial \mathbf{x}(t)/\partial \mathbf{p}$ , effectively coupling the dynamics of the body to the estimation of the parameter. In the second term of Eq. (17), the direct influence on the observation is included, which represents the influence that is independent of changes in the estimated bodies' states.

When estimating the libration amplitudes, both contributions to the observation partial in Eq. (17) are non-zero. The direct contribution follows from a different inertial lander position due to a change in libration amplitude, and is the one used by Le Maistre et al. (2013). The contribution from the dynamic coupling is due to the different latitude and longitude of the sub-Phobos point on Mars, as expressed in a Phobos-fixed frame, resulting in a different acceleration as evaluated from Eq. (3). This contribution was used by Jacobson (2010) when creating an ephemeris of Phobos and estimating the primary libration amplitude in longitude. Since we integrate the equations of motion of Phobos and estimate its initial state, this contribution is also present in our problem definition. The consequences of this will be discussed in Section 7.1.

## 5.2 Estimated parameters

Here, we list and discuss the set of parameters that will be estimated from the simulated observations. The complete set of estimated parameters, as well as their *a priori* covariance, is presented in Table 2.

Firstly, the initial state of Phobos is estimated, from which a Phobos ephemeris is obtained through the state transition matrix  $\Phi(t, t_0)$ . Since many of the estimated parameters are obtained from their influence on the dynamics of Phobos (first term in Eq. (17)), it is important to combine the state and parameter uncertainty to obtain realistic error and correlation estimates. Additionally, separating the dynamical and direct signals (*e.g.* from librations) in the observations can be important for the estimation procedure. Le Maistre et al. (2013) show that the attainable true error of the estimated libration amplitudes is severely degraded by an imprecise Phobos ephemeris, especially at the libration frequencies that are resonant with the orbital period. Due to the highly accurate nature of the measurements that are to be obtained from ILR, it is unlikely that a sufficiently precise ephemeris of Phobos will be available from data gathered by (a) previous mission(s). Additionally, the ephemeris accuracy can degrade significantly when it is used outside the time window of the data used to generate it, as is shown for Mars by Folkner et al. (2009). Consequently, the concurrent estimation of the Phobos orbit with its physical parameters is deemed necessary.

Phobos libration amplitudes, both sine and cosine terms, see Eq. (7), are estimated for all terms listed in Appendix C, increasing the constraints on the relative moments of inertia of Phobos, and providing insight on its internal mass distribution. Combined with the  $\bar{C}_{2,0}^p$  and  $\bar{C}_{2,2}^p$  gravity field coefficients, which are both estimated, we will be able to determine the absolute moments of inertia to greatly improved accuracy (see Section

Table 2: List of estimated parameters with *a priori* standard deviation

Parameter name	symbol	<i>a priori</i> st. dev.	par. size
Phobos initial position	$\mathbf{r}_{0,p}$	$10^3$ m	3
Phobos initial velocity	$\mathbf{v}_{0,p}$	1 m/s	3
Phobos degree 2 spherical harmonic zonal coefficient	$\bar{C}_{2,0}^p$	0.2	1
Phobos degree 2, order 2 spherical harmonic coefficient	$\bar{C}_{2,2}^p$	0.2	1
Phobos degree 2 deformation Love number	$h_2$	0.1	1
Phobos prime meridian libration amplitudes	$W_{T_i}^C, W_{T_i}^S$	0.1 deg	30
Phobos right ascension libration amplitudes	$\alpha_{T_i}^C, \alpha_{T_i}^S$	0.1 deg	18
Phobos declination libration amplitudes	$\delta_{T_i}^C, \delta_{T_i}^S$	0.1 deg	18
Phobos gravitational parameter	$\mu_p$	$1000 \text{ m}^3/\text{s}^2$	1
Deimos gravitational parameter	$\mu_d$	$1000 \text{ m}^3/\text{s}^2$	1
Lander position (in Phobos-fixed frame)	$\mathbf{r}_L^p$	$10^3$ m	3
Mars degree 2 quality factor (Phobos tide frequency)	$Q^p$	1	1
Mars degree 2 quality factor (Sun tide frequency)	$Q^s$	20	1
Mars degree 2 quality factor (Deimos tide frequency)	$Q^d$	20	1
Mars degree 2 love numbers (per order)	$k_{2,0..2}$	0.1	3
Mars degree 3 love number (constant)	$k_3$	0.1	1
Mars degree 2 spherical harmonic coefficients	$(\bar{C}, \bar{S})_{2,0..2}^m$	$10^{-10}$	3
Mars degree 3 spherical harmonic coefficients	$(\bar{C}, \bar{S})_{3,0..3}^m$	$10^{-10}$	4
Mars rotational precession	$\dot{\psi}_M$	10 mas/year	1

7.3). Additionally, we estimate Phobos'  $h_2$  Love number to model its tidal deformation, providing constraints on the rigidity of the body.

We also include the gravitational parameters of both Phobos and Deimos in our estimation. Although neither will introduce a particularly strong signal on Phobos' orbit, their high uncertainties mean that a PLR mission may provide improvements in their uncertainties.

For Mars, the main geodetic observables are its moments of inertia, tidal Love numbers and bulk composition (Rivoldini et al., 2011). We only address the first two of these observables in our simulations, since the limiting factor in the estimation of the bulk density is the uncertainty of its volume, which cannot be constrained by a geodetic Phobos mission, requiring a surface mapping mission instead. We estimate the degree-two and three tidal Love numbers, at separate orders for degree two, providing constraints on the internal elasticity and density profile of Mars. Typical Mars interior models assume a spherical symmetry with core, mantle and crust layers, for which thickness, composition and temperature profiles may be varied (Yoder and Standish, 1997; Rivoldini et al., 2011; Konopliv et al., 2011). Minor deviations from this symmetry could be observed from variations in Love numbers of a given degree but different orders (Bills et al., 2005).

Additionally, quality factors  $Q$  of degree two of Mars will provide constraints on its internal dissipation and rheology models. We estimate quality factors at the forcing frequencies of the three primary tide raising bodies: the two Martian satellites and the Sun.

Although the inertial position of a Phobos lander will be moderately sensitive to Mars' rotational variations through the spherical harmonic gravity influence of Mars, estimation results will not be as precise as results from current and future Mars landers, for which the influence of Martian rotational variations is both more direct and stronger.

Of the Martian rotational parameters, we only estimate the Mars rotational precession  $\dot{\psi}_m$ , since the orbital stability of a Phobos lander could make the effect from this secular term observable beyond present uncertainties. From this precession rate, we can derive Mars' (polar) moment of inertia, making it directly applicable to Mars geodetic studies. Although the Martian gravity field has been estimated to very high precision, *e.g.* (Marty et al., 2009), the long-term stability of Phobos may provide improvements. However, its relatively high orbit (compared to Mars-orbiting spacecraft), will make it sensitive to only the lower degree gravity field coefficients. Therefore, we estimate the spherical harmonic coefficients of Mars' static gravity field at degree and order two and three. We set their *a priori* uncertainties at  $10^{-10}$ , about one order of magnitude above the uncertainties of the gravity field model that is used, to take into account possible discrepancies between the published formal and true errors (see next section).

### 5.3 Consider covariance

The formal errors of the estimated parameters are obtained from the square root of the terms on the diagonal of the covariance matrix, obtained from Eq. (15). When processing tracking data to planetary satellites, the true error (which is then unknown) is typically roughly one order of magnitude larger than the formal error (Konopliv et al., 2006; Marty et al., 2009; Konopliv et al., 2011; Lemoine et al., 2013), due to differences between the estimation model and the actual dynamical and observation model. The deviations of the real observation noise power spectrum from the ideal Gaussian noise model that is typically assumed causes further deviations between the truth and estimation model.

In simulation studies, this difference can be introduced artificially by imposing a difference between the truth and estimation model. By then perturbing the estimated parameters and analyzing how well the simulated estimation procedure retrieves the values of the truth model, this influence can be assessed. However, this process can be time-consuming when using a batch estimator, especially in the case where a body state is estimated, since this requires re-integration of the equations of motion (and potentially variational equations) for each iteration. Also, in such an approach, the obtained true error is only a single realization from the stochastic distribution describing it.

Alternatively, the uncertainties in the estimation model may be included by using consider covariance analysis (Montenbruck and Gill, 2000; Tapley et al., 2004). In consider covariance analysis, a number of extra parameters is added to the estimation procedure, which are not themselves estimated, but the uncertainty of which is included when determining the covariance matrix. By taking this approach, a number of parameters are treated as random variables, of which the realization is constant throughout the simulation. This is distinct from treating the observations themselves as random variables, as in this case a new independent realization of a (Gaussian) random variable is taken for each observation, resulting in the formal error decreasing with increasing number of observations  $N$  as approximately  $1/\sqrt{N}$ .

The consider parameters are included by adding a term to the covariance matrix,

resulting in the consider covariance matrix  $P^{0,c}$ . It is calculated from the following:

$$P^{(0,c)} = P^{(0)} + \left( P^{(0)} H_p^T W \right) \left( H_c C H_c^T \right) \left( P^{(0)} H_p^T W \right)^T \quad (19)$$

where  $H_c$  is the matrix of partials of the observations w.r.t. the consider parameters and  $C$  is the assumed covariance matrix of the consider parameters.

For the case where all observations have the same weight in the estimation, the contribution to the covariance matrix from the consider parameters is completely decoupled. This results in the following covariance matrix  $P^c$ , when substituting Eq. (16) for  $P^{(0)}$  and reincluding the *a priori* covariance contribution:

$$(P^c)^{-1} = \left( P^{(a.pr.)} \right)^{-1} + \left( P^{(0)} + \Delta P^c \right)^{-1} \quad (20)$$

$$\Delta P^c = \left( H_p^T H_p \right)^{-1} \left( H_p^T H_c \right) C \left( H_c^T H_p \right) \left( H_p H_p^T \right)^{-1} \quad (21)$$

As a result, when the contribution from  $P^{(0)}$  is much larger than the contribution from  $P^{(a.pr.)}$ , the contribution to the total formal error from the nominal and consider covariance contribution can be obtained by adding the two components. This allows for a direct analysis of the influence of changing the consider covariance values that are used.

An example of the use of consider parameters is to include the effect of observation biases, as done by Jacobson (2010) for determining the uncertainty of their Phobos ephemeris.

We include two sets of consider parameters in the analysis. Firstly, we impose a range bias for each combination of ground station and Phobos lander. In doing so, uncertainties in the estimation model due to systematic range measurement errors are taken into account, such as laser system, clock and detector biases and instabilities. Secondly, we include the Earth-based ground station positions as consider parameters, since the current ITRF (ITRF2008), including all tidal and non-tidal position corrections, is not accurate to well below the mm-level measurement precision (Zumberge et al., 2009). Additionally, Earth ephemerides are not at the required level of accuracy for range data processing at the mm-level. A PLR mission would likely provide improvements of the Earth ephemeris, but we omit estimation of the Earth state here, since such a process would entail the combination of tracking data from many past, current and future missions and is beyond the scope of this work.

The need for precise ground station positions in planetary exploration was discussed by Zumberge et al. (2009) in the context of current and future radiometric observables. Error budgets for radiometric tracking techniques are given by Iess et al. (2014a), who show that solar plasma and wet tropospheric influences are typically the dominant error sources. For laser ranging, however, environmental error sources are expected to be of similar magnitude as for SLR and LLR, *i.e.* in the order of mm. As such, the errors due to the ground and space segment become relatively much more influential in the error budget, making the use of the applied consider parameters more relevant.

To mitigate the systematic uncertainties in real tracking data analysis, empirical corrections, such as range biases or time biases are often included in the estimation in an arc-wise manner (*i.e.* per day, per orbit, etc.). Taking this into account, we nominally use a 5 mm uncertainty for both sets of parameters, which represents an estimate for the

true uncertainty that would remain after estimation of arc-wise empirical parameters. Hereby, we avoid the need for bottom-up models for the systematic uncertainties and uncorrected effects, instead lumping all of these effects into the 5 mm uncertainty. The bottom-up analysis of ILR measurement precision and accuracy will be investigated in future work. The assumption of 5 mm uncertainty is loosely based on the SLR error budget given by Exertier et al. (2006), modified to take into account the fact that our 5 mm is after a possible step including empirical parameter estimation, the usage of active systems on both ends of the link, no retroreflector signature and moderate improvement in tropospheric correction modelling.

To validate our approach using consider parameters, we have performed estimations without them, instead applying a difference between the truth and estimation model which is equivalent to the consider parameters (*i.e.* 5 mm difference for ground station position and observation bias). We have then perturbed the estimated parameters and let the software estimate their values, resulting in values for the true errors. It was found that the results for the two cases are in good agreement, with no large outliers identified, and it was indeed found that a relatively scatter in true errors exists when using slightly different simulation settings or parameter perturbations, as indicated previously.

## 6 Results and Discussion: Mars interior

In this section, we first present our results on estimation of the Mars gravity field and rotational parameters in Section 6.1, from which the uncertainty in Mars' polar moment of inertia can be deduced, followed by the results on the estimation of tidal parameters (*i.e.* Love numbers and quality factors) in Section 6.2. Finally, we give a qualitative discussion of the synergy of Phobos laser measurements with data derived from current and future Mars missions, specifically landers, such as the Interior Exploration using Seismic Investigations, Geodesy and Heat Transport (InSight) mission<sup>3</sup>, in Section 6.3.

### 6.1 Mars gravity field & rotation

The results of the estimation of the static values of the degree-two and -three spherical harmonic coefficients are shown in Fig. 1. Compared to the present uncertainties of these parameters, which are of order  $\sim 10^{-11}$ , it can be seen that the improvement in the zonal coefficients is marginal with the systematic uncertainty at the level of 5 mm. The improvement for the  $\bar{C}_{2,0}$  coefficient requires about three years of observation time and improvement in  $\bar{C}_{3,0}$  requires about 1.5 years. Due to Phobos' near-equatorial orbit, the signal of the degree-three term is relatively large when compared to the degree-two term, resulting in the faster decrease of the odd term uncertainty.

It can be seen that the systematic uncertainties result in a flattening out of the error with time, providing little additional information after a certain mission time. This effect is especially visible for the  $\bar{C}_{3,0}$  estimation, which levels out after about 2 years. After 5 years, the difference between the solutions with and without systematic errors is about a factor of 50. Since the contribution from the consider parameters scales linearly

---

<sup>3</sup><http://insight.jpl.nasa.gov/>

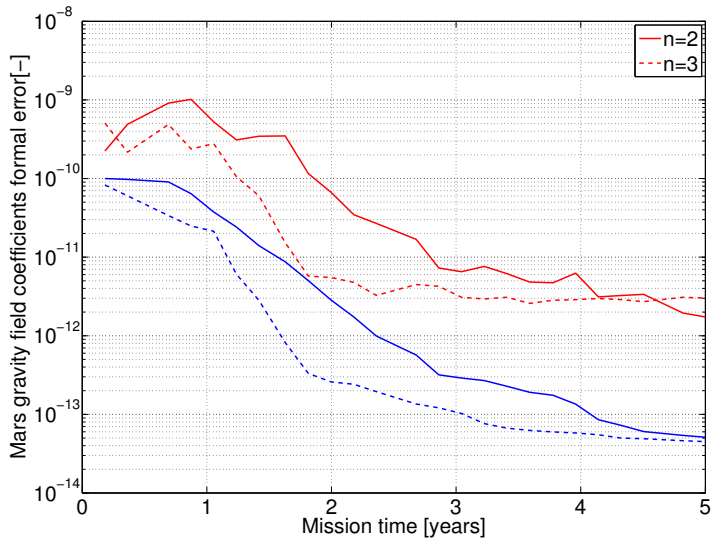


Figure 1: Estimation result of lumped Mars even and odd static gravity field coefficients. Blue: without consider parameters. Red: with consider parameters.

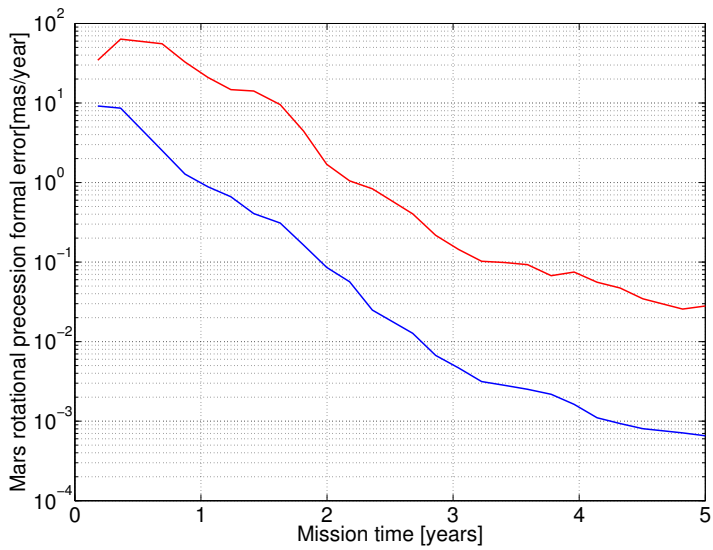


Figure 2: Estimation result of Mars precession rate. Blue: without consider parameters. Red: with consider parameters.



with the consider covariance values (see Section 5.3), the errors in  $\bar{C}_{2,0}$  and  $\bar{C}_{3,0}$  after 5 years of observation increases by about  $4 \cdot 10^{-13}$  and  $6 \cdot 10^{-13}$  per mm of systematic error, respectively. These two points indicate the need for the reduction or mitigation of systematic errors, especially for long-duration missions. Also, they highlight the need for their inclusion in simulation studies to prevent overly optimistic results (i.e. blue curve results as opposed to red curve results in Fig. 1) from being obtained.

For the Mars gravity field that was used, the uncertainty in the non-zonal gravity field coefficients (*i.e.*  $m \neq 0$ ) are roughly two to four times lower than for the zonal terms. As a result, the estimation yields uncertainties which are comparable to their current respective uncertainties, even after a long mission duration. Therefore we do not present the estimation results explicitly, since they will provide little or no science return from the mission. As discussed in Section 4.1, there is a strong influence (about 40 % of the main terms) of the higher degree coefficients in the estimation of the  $\bar{J}_2$  and  $\bar{J}_3$  due to the lumping. Therefore, substantial improvements of the static Martian gravity field from the PLR mission will require a combination with other missions. In such a combination, the added value from this mission is its unusual orbital plane for a gravity field estimation mission (*i.e.* equatorial and relatively high orbit) and long-term stability.

The correlations between the gravity field coefficients themselves, as well as their correlations with other parameters, generally remain very low ( $<0.4$ ). Several moderate correlations (up to 0.7) of the coefficients with libration amplitudes are obtained, all of which can be related to the specific geometry of the spherical harmonic component and Phobos' revisit time of the related effect.

The estimation results of the precession rate of Mars are shown in Fig. 2. Roughly 1.5 years of tracking are required for the estimation to reach the *a priori* uncertainty of 10 mas/year with the applied systematic errors. This improves to about 0.1 mas/year after about 3 years, highlighting the strength of the Phobos orbital stability in the parameter estimation. Since the uncertainties in  $\dot{\psi}_m$  and Mars moment of inertia scale linearly, as shown by Eq. (10) this would constitute a two orders of magnitude improvement in their determination. Due to the nature of the effect of Mars' precession, the estimation does not show strong signs of levelling out at a constant uncertainty, as was the case for the gravity field coefficients. Therefore, as opposed to other, periodic, rotational parameters of Mars, a Phobos lander would be useful for estimating the rotational precession rate of Mars. Substantial improvements will require long mission durations, though (more than 2 years for more than an order of magnitude improvement). Improvements in Earth ephemeris and terrestrial reference frames, as well as reduction of systematic range errors, will allow a reduced mission time to achieve similar estimation results. Synergies of a Phobos lander with a Mars lander, which would be better suited to estimating Mars rotational parameters in general, are described in Section 6.3.

## 6.2 Mars tides

The result of the estimation of the quality factors of Mars is shown in Fig 3. It can be seen from the solid line that the quality factor at the frequency of the Phobos orbit is estimated well beyond the current level of uncertainty of about 1, with a precision

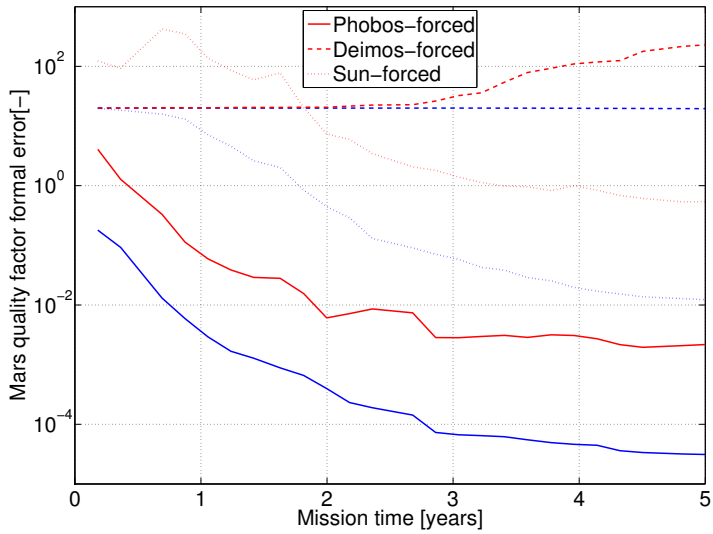


Figure 3: Estimation result of Mars quality factors at forcing frequencies. Blue: without consider parameters. Red: with consider parameters.

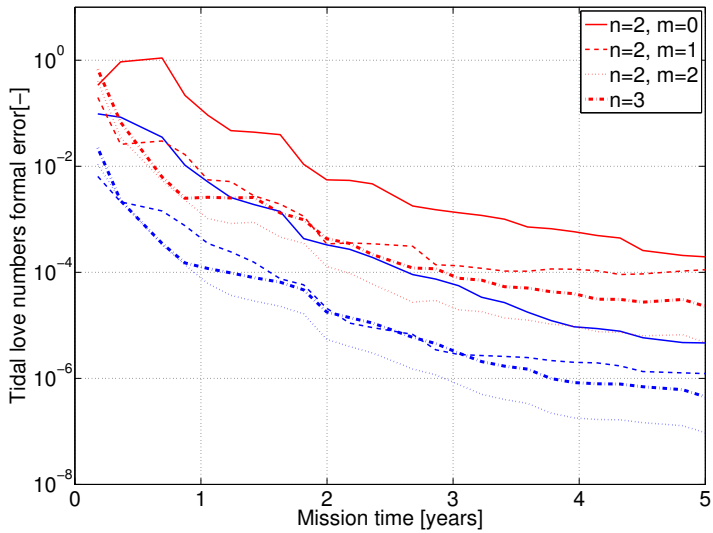


Figure 4: Estimation result of Mars tidal Love numbers. Blue: without consider parameters. Red: with consider parameters.

of  $< 0.1$  after 1 year and  $< 0.01$  after 2 years. The improvement of the solution for a longer mission duration is damped by the inclusion of the consider parameters, with only moderate improvement for a mission duration  $> 2$  years, as was also found in the previous section. The added estimation error due to 1-mm uncertainty increases from 4 times more influential than the random observation noise after 2 years to 15 times after 5 years. This highlights the strong need to include systematic measurement errors in simulation studies, especially for a mission with a longer duration or a very large set of observations. Nevertheless, the 5-mm consider parameter uncertainty allows for in an orders of magnitude improvement in the uncertainty of the value of  $Q^p$ .

The Sun-raised tide delay can be seen from the dotted line in Fig. 3 to require a longer observation time to be determined below the *a priori* uncertainty of 20, unless the systematic errors are kept very low. The observability of this parameter is derived from the long-term stability of Phobos' orbit, where the long-term observation of the periodic effect of the Sun's tidal bulge can be decoupled from other periodic effects. The final uncertainty, which is at the level of about 1 after 3 years will provide an improved observational constraint for Mars interior models.

It can be seen from the dashed lines in Fig. 3 that the delay of the tide raised by Deimos is not observable beyond the level of the *a priori* values with the PLR mission. Even without the consider parameters, which result in an increase in uncertainty as systematic errors go into the  $Q^d$  estimation, no meaningful improvement is observed w.r.t. the *a priori* uncertainty. Including the consider parameters causes an increase in the formal uncertainty with time, due to their addition in Eq. (20), as systematic errors are mistaken for a Deimos tide signal.

Very low correlations are found between the quality factors at different frequencies. However, a relatively high correlation (0.85) is observed between the quality factor at the Phobos frequency and the degree-two Love number, the origin of which can be seen from Eqs. (11) and (12), which shows that the main portion of the acceleration due to the tidal dissipation involves the ratio of  $k_2$  and  $Q$ . The slight decorrelation of the two parameters results from the non- $Q$  dependent term in the equation, which causes periodic variations due to  $k_2$  that are not influenced by  $Q$ .

Since the quality factors themselves are uncorrelated, the results from PLR would for the first time allow for the analysis of the difference of tidal dissipation in Mars at different forcing frequencies. However, since only two data points on the  $Q$ - $f$  curve can be determined using the proposed system (since the Deimos-raised tide delay is unobservable), we cannot test the validity of a specific functional dependency. Assuming the validity of a specific model, though, we can place constraints on their parameters, the precision of which will be limited by the uncertainty in  $Q^s$  and the observed difference between  $Q^s$  and  $Q^p$ . Nevertheless, the two available data points, especially the strong constraint on  $Q^p$ , will provide important information on Mars' internal dissipation due to its two strongest tide-raising bodies.

The results of the tidal Love number estimation are shown in Fig. 4. It can be seen that the results that include the consider parameters estimate the Love numbers roughly at the  $10^{-2}$ - $10^{-3}$  level after 1.5 years of observation time, down to roughly  $10^{-4}$ - $10^{-5}$  after 5 years of operation; levels comparable to those obtained for the Moon by the GRAIL mission (Lemoine et al., 2013). However, it must be noted that at these

levels of precision, the tidal model used here will most likely not be sufficient anymore, since possible frequency-dependence and other deviations from our model of the Love numbers may become observable. As such, the number of estimated parameters will increase, also increasing the potential for correlations between them. This problem may be mitigated by the combination with tracking data from future Mars orbiters, though.

The estimation of  $k_{22}$  yields the smallest uncertainties, as shown by the dotted lines in Fig. 4, with an uncertainty below  $10^{-3}$  after 1 year, reducing to  $10^{-4}$  and  $10^{-5}$  after 2 and 4 years, respectively, compared to current formal uncertainties which are at the  $10^{-2}$  level. This was to be expected, since the tidal bulge causing the secular acceleration is largely caused by the tidal change in Mars'  $\bar{C}_{22}$  value, as quantified by its  $k_{22}$  Love number.

Although the  $k_{21}$  value of Mars seems to converge to very small uncertainty here, better than that of  $k_{20}$ , these simulations do not take into account any variations in the  $\bar{C}_{21}$  and  $\bar{S}_{21}$  coefficients of Mars due to polar motion. Such variations could manifest similarly to variations due to  $k_{21}$  and concurrent estimation of these parameters could yield strong correlations or, alternatively, true errors could be much higher than formal errors when leaving the polar motion model fixed. It was also noted by Yoder et al. (2003) that when performing estimation from orbiter tracking data, Mars'  $k_{20}$  could be decoupled from its  $k_{22}$ , albeit at much lower precision than is expected from the PLR mission, whereas the estimation of  $k_{21}$  proved unstable. However, Mars rotation model uncertainty would benefit greatly from future landers with improved tracking precision, as well as novel mission architectures involving multiple landers and/or orbiters, as described in Section 6.3. With such improved Mars rotation models, the signals due to Mars' rotational variations and its gravity field variations could be better decoupled than with only tracking data from a Mars orbiter (Phobos in this case).

The uncertainty in  $k_3$  can be seen from Fig. 4 to be  $2 \cdot 10^{-3}$  after 1 year, reducing to  $10^{-4}$  after 4 years, whereas there is currently no estimate of this parameter that is derived from observations. Nominal values of  $k_3$  obtained from Mars interior models are about 0.05 (Konopliv et al., 2011). The estimated values represent a relative error of less than 2 and 0.2%, after 1 and 4 years, respectively. This would provide additional constraints on the Mars interior that are now completely absent. However, the estimated values for  $k_{22}$  and  $k_3$  are almost fully correlated (correlation coefficient of about 0.99), indicating that the influence of the two parameters on Phobos' orbit cannot be decoupled. Even though *a priori* constraints on their uncertainties are applied, the estimation results are orders of magnitude better than these values, so that the influence of the *a priori* terms diminishes with increasing mission time. This makes the current estimates for their uncertainties too optimistic and provides only a combined estimate from the secular effect of Love numbers at all degrees on Phobos' orbit, *i.e.* the summation of the effect of Eq. (12) with its higher-order generalizations. This was also noted by Lainey et al. (2007) in the generation of Phobos ephemerides. Although it is not possible to decouple the two effects in the current mission architecture, Mars interior models could still be constrained by a combined effective Love number, including the degree three (and possibly higher) contributions not through an independent value, but instead as a lumped coefficient. Tracking to other spacecraft could be used to decouple the Love numbers, at least to the measurement precision of such missions.

### 6.3 Synergy with Mars lander missions

An extensive study on the influence of Mars interior models on its geodetic observables has been performed by Rivoldini (2012), who conclude that, even with exact determinations of the geodetic observables, substantial errors would remain on Mars' interior structure and composition models, since the chemical composition will not be sufficiently constrained. Rivoldini (2012) also analyzes the influence of seismic and electromagnetic sounding data of Mars and concludes that these observations would be highly complementary to geodetic observables. Also, improved Mars rotation models, for which a Mars lander would be better suited than a Phobos lander, would allow for a better modelling of Mars' gravitational influence on Phobos, which will be required for making optimal use of the data from a PLR mission.

An analysis of the science return of a single Mars lander mission that includes seismometry, heat flow measurements and magnetic field observations was done by Dehant et al. (2012). They show that interior structure model parameters will be further constrained by these non-geodetic observations. These types of observations are expected from the InSight mission, for which Mars surface operations are expected to commence in 2016. Alternatively, by using a network of landers, such as in the NetLander mission concept (Dehant et al., 2004), multiple data points can be used to obtain heat flow and magnetic data. Additionally, the use of multiple stations will improve the science return from the seismometry.

Further constraints on Mars interior structure and composition, as well as its seasonal atmospheric and ice mass cycles, can be obtained by observations of its rotational variations. Nutation resonances of the inner core (Defraigne et al., 2003), which will manifest themselves in the Mars rotational variations, can directly provide constraints on core size, flattening and moments of inertia. Also, variations in Mars rotational parameters due to seasonal mass redistribution would provide additional constraints on the dynamics of its CO<sub>2</sub> cycle, especially when combined with gravity field and altimetry data. We do not estimate these parameters here, as a (dedicated) Mars lander will be much better suited to perform these observations. Analysis of the performance of Doppler tracking systems, both Martian landers and combinations of landers and orbiters has been performed by Yseboodt et al. (2002), Dehant et al. (2009) and Le Maistre et al. (2013).

In summary, although a Phobos lander will be able to provide strongly improved estimates of Martian geodetic observables, especially for Love numbers and quality factors, their interpretation and relation to the Martian interior structure and composition will require additional, independent and improved measurements on Mars rotation, seismic activity, heat flow and magnetic field. This indicates that highly accurate measurements of a specific type can only be used to their full potential when combining them with next generation of measurements of different kinds, such as those expected from the InSight mission. This would prevent the situation where a science bottleneck is created, in which the interpretation of a precise data set is hampered by large uncertainties on parameters to which the existing observations are largely insensitive.

## 7 Results and Discussion: Phobos interior

Here, we first discuss the coupling between the rotational and translational state of Phobos, and the influence of our modelling approach on the estimation procedure in Section 7.1. Subsequently, we discuss the results of the estimation of the gravity field coefficients, libration amplitudes, moments of inertia and tidal deformation in Sections 7.2, 7.3, 7.4 and 7.5, respectively. Little to no improvement in Phobos' and Deimos' gravitational parameters are obtained from the estimation and we therefore do not present the results explicitly in this Section.

### 7.1 Coupling between rotational and translational state

The libration model of Phobos used here was generated by numerical integration of its rotational equations of motion by Rambaux et al. (2012) using the Phobos ephemeris of Lainey et al. (2007) (see Section 3.2). We use the same Phobos ephemeris and settings (*i.e.* Phobos gravity field) as initial input to our numerical integration, resulting in a numerically integrated ephemeris very close to that on which the generation of the rotational model was based. If different integration settings are used without adapting the rotation model, a severe inconsistency can be introduced in the model, since the Phobos rotation may no longer be tidally locked (omitting the deviations due to librations). This would result in the term in Eq (3) from Phobos' gravity field expansion to cause additional secular terms in Phobos' motion, creating a very different signature on the range measurements.

However, the small influence of changes in the orbit on the rotation (and subsequent higher-order effects) is neglected in our model. That is, when estimating the parameters, we do not update the rotational ephemeris by reintegrating the rotational equations of motion and subsequently analyzing the effect of the new rotation model on the orbit. Also, no direct contribution of the rotational equations of motion to the partials from Eq. (17) is used, aside from those arising from the direct partials in the libration amplitudes. Therefore, the model will include a higher-order inconsistency, since spin-orbit coupling is not accounted for at all levels. Although the influence on the observations themselves is expected to be small, as the resulting deviations from the rotation model of Rambaux et al. (2012) will be small, the influence on the partial derivatives, and therefore on the results of the simulation study, could be significant. Here, we choose to keep our dynamical and estimation models consistent with one another in the sense that the coupling in Eq. (17) of translational and rotational state will be omitted in both.

To test the influence of this assumption, we performed the full estimation both with and without the partials due to the dynamical coupling of the Phobos libration amplitudes with the spherical harmonic acceleration. This investigation indicated relatively low differences between the estimations for the two cases, with a number of notable exceptions. Exceptions are the long period librations in  $W$  and  $\delta$ , the Phobos  $\bar{C}_{2,2}$  and the Phobos lander position. The uncertainties of both the aforementioned libration amplitudes and the ground station position decrease by several orders of magnitude. The reason for this is that when including the dynamical coupling in the calculation of the partial derivatives, the effect of a different ground station position can be decoupled from that of a different lander position. This apparent influence, however, is due to the

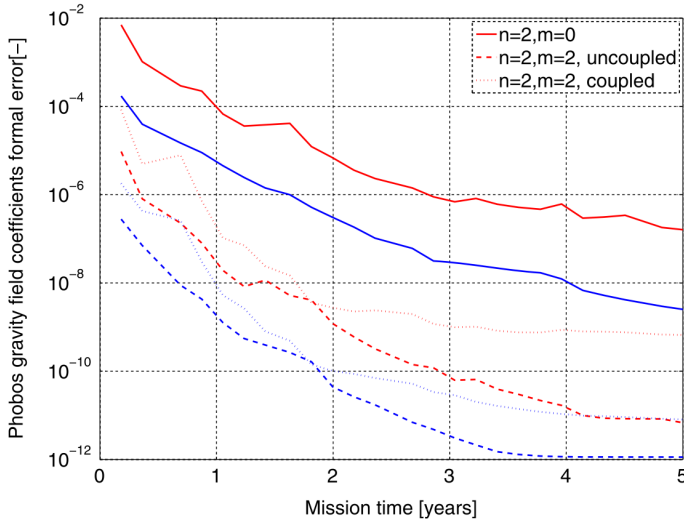


Figure 5: Estimation result of Phobos’ static even-order degree-two gravity field coefficient. Blue: without consider parameters. Red: with consider parameters.

fact that the nominal orientation of Phobos is not estimated, so that the orientation with no libration is assumed to be known perfectly. Since this is not the case, especially since in reality (as is shown from the results in Section 7.3) a (very) long-period libration may look strongly like a different Phobos orientation, this does not indicate a strong influence of the dynamical partial coupling. Similarly, the signal of the  $\bar{C}_{2,2}$  coefficient on Phobos’ orbit will be mismodelled, since its influence on the spin-orbit coupling is not fully included. When discussing the results of Phobos’ gravity field coefficient estimation (Section 7.2), we present the results with and without the dynamical coupling and discuss their differences.

When omitting the affected parameters, the mean ratio of the formal errors for the cases with and without the dynamical coupling in the partials of all parameters after 2 years is 0.97, with a standard deviation of 0.2 and no clear outliers. This indicates a relatively small differences between the two models and verifies the applicability of the equations that are used, at least for the present mission concept study.

## 7.2 Phobos gravity field

As discussed in Section 3.1, the orbit of Phobos will be sensitive to its own spherical harmonic coefficients, allowing for the estimation of Phobos’ gravity field coefficients from observation of its orbital dynamics.

As discussed in Section 7.1, we present the estimation of  $\bar{C}_{2,2}$  with and without the dynamical coupling in the partials and will be conservative in our comparison of the results. As will be discussed in Section 7.4, either the  $\bar{C}_{2,0}$  or the  $\bar{C}_{2,2}$  coefficient will be required to constrain the absolute moments of inertia of Phobos, combined with the results of the libration amplitudes estimation. Related to this, the values of the

two gravity field coefficients constrain the mass distribution of Phobos in terms of the flattening and elongation (w.r.t. a symmetrical and spherical distribution). For instance, by comparing the values to those of a homogeneous composition, mass concentrations and voids can be identified.

The results of the estimation of Phobos' gravity field coefficients are shown in Fig. 5. It can be seen that the estimation of the  $\bar{C}_{2,0}$  is several orders of magnitude weaker than that of the  $\bar{C}_{2,2}$  term. The strong estimation of this term is due to the direct effect of that the libration has on its orbital signal. Due to the primary longitude libration at the orbital period, the Phobos-fixed longitude of Mars  $\phi_m^{(p)}$  will undergo periodic variations. Since the influence of the  $\bar{C}_{2,2}$  term is proportional to  $\sin\left(2\phi_m^{(p)}\right)$ , as obtained when writing out Eq. (3) this will cause a clear signal of the coefficient in the orbital dynamics. The estimation of the zonal term is not modulated as strongly, though, since the short-period librations in  $\alpha$  and  $\delta$  are of a much smaller amplitude (see Appendix C).

It can be seen from the results with and without dynamical coupling shown in Fig. 5 that including the dynamic coupling has a negative effect on the estimation of the  $\bar{C}_{2,2}$  coefficient for mission durations greater than 2 years. with up to two orders of magnitude increase in its uncertainty after 5 years. This effect was found to be caused by additional correlations that are present in the coupled case, between the  $\bar{C}_{2,2}$  and once-per-orbit longitude libration, as well as with the  $\bar{C}_{2,0}$  coefficient, with both correlations around 0.85. Since this correlation is expected to be present in the actual data, due to the similar signals of the parameters in the coupled case, we will use the more conservative asymptotic uncertainty of  $10^{-9}$  for the  $\bar{C}_{2,2}$  coefficient in our subsequent discussion of the moment of inertia determination in Section 7.4.

As discussed in Section 4.1, the  $\bar{C}_{4,0}$  term will contribute about  $5.0 \cdot 10^{-10}$  as strongly to the uncertainty of the degree two zonal term as does the  $\bar{C}_{2,0}$  term itself. To quantify its influence further, we estimate the range of plausible values for  $\bar{C}_{4,0}$  from the relations for a homogeneous triaxial ellipsoid, (Balmino, 1994), from where we derive that in such a case  $\bar{C}_{4,0} \approx (9/7)\bar{C}_{2,0}^2 \approx 0.03$  using the shape model of Willner et al. (2010). Taking a wide uncertainty margin for this coefficient, its nominal uncertainty is assumed to be  $\sigma_{\bar{C}_{4,0}} = 0.05$ . It is concluded that the influence of the degree four term is negligible, since its influence on the estimation of  $\bar{C}_{2,0}$  will be orders of magnitude lower than the uncertainty that is estimated for  $\bar{C}_{2,0}$ .

### 7.3 Phobos librations

The result of the estimation of the total amplitude (*i.e.* uncertainty of sine and cosine term propagated onto uncertainty in total amplitude) of the librational amplitudes is shown in Fig. 6, separately for each libration angle and for the results with and without consider parameters, respectively. It can be seen from panels (c) and (e), as well as (d) and (f), that the estimation errors of the  $\alpha$ - and  $\delta$ -libration amplitudes behave very similarly, as was to be expected since their frequency decompositions are identical and both angles will impose similar signals on the range observables. There is also a rough distinction between three categories of librations in the librations in these two angles, indicated by different colors in the panels of Fig. 6. For the  $W$ -libration, results for



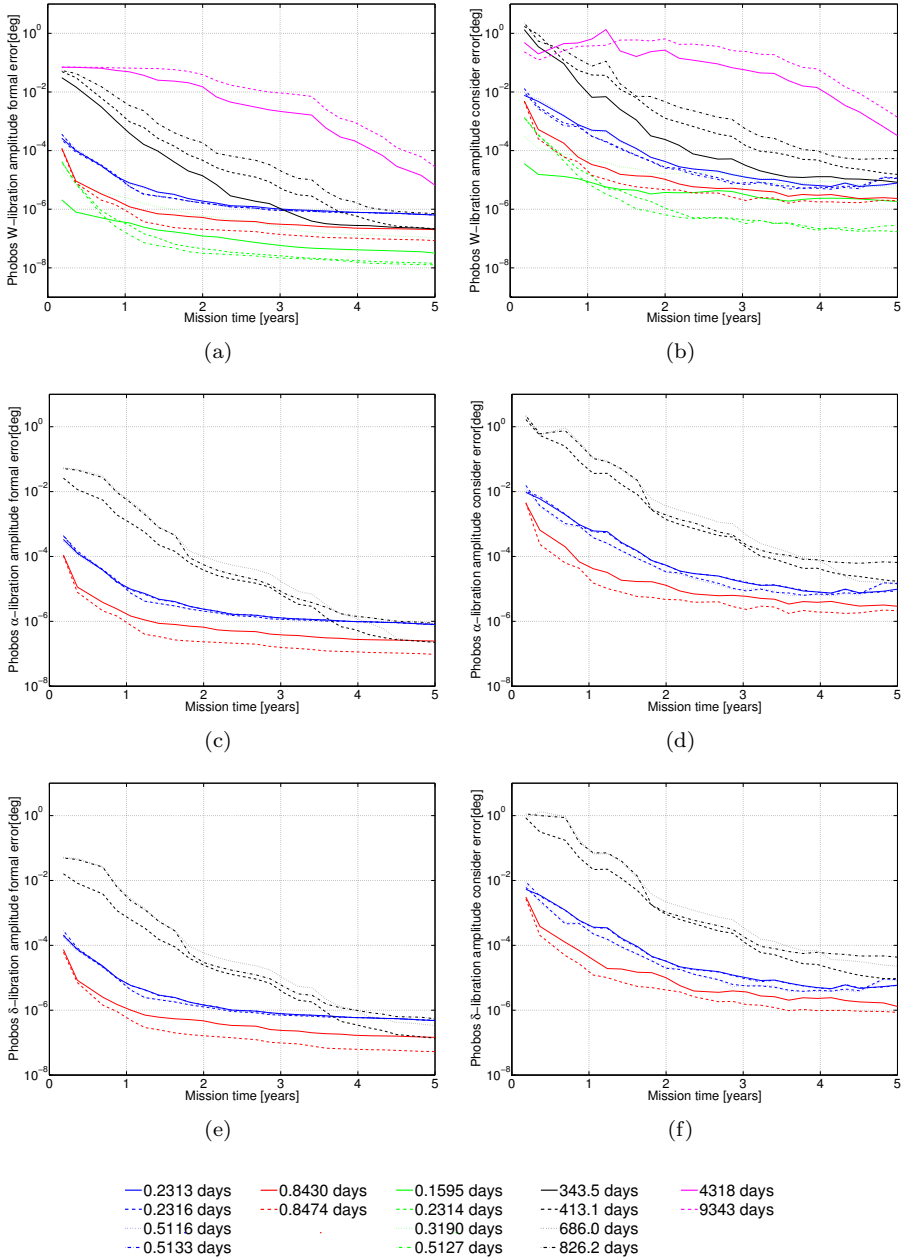


Figure 6: Formal errors of libration amplitudes, without (left) and with (right) taking into account consider parameters of: librations in  $W$  (top), librations in  $\alpha$  (middle), librations in  $\delta$  (bottom)

which are shown in panels (a) and (c) there is a greater spread between the estimation results, although there is still a clustering of a number of modes, some of them in the same groups as the other two libration angles.

The origins of the several categories of librations are due to several causes. Firstly, there are frequencies at which a libration in each of the three components is present (see Appendix C), shown in blue and red in Fig. 6. All short-period  $\delta$ - and  $\alpha$ -librations exhibit this behaviour. The four modes shown in blue have mutual correlations of up to 0.999, whereas the remaining two have correlations of around 0.9. This indicates that a change in one of these parameters may be compensated by an equal change in one of the other parameters and that no robust minimum of the residuals is found in parameter space. The strong correlation is explained by the fact that in principle these three components, estimated by a total of six parameters, represent a decomposition of a single libration mode about an axis defined by the relative amplitudes of the libration in the three angles. In reality, this mode is defined by the (unit) axis in inertial space about which the rotation takes place, its phase, its frequency and its amplitude. Assuming its frequency to be predetermined, the libration mode has four degrees of freedom, instead of the six that are provided by the model that is used. However, the total uncertainty in the estimation of the libration mode is determined by the (overdetermined) combination of the uncertainties of the six components. We have performed reduced simulations which have shown, however, that strong correlations ( $\sim 0.97$ ) still exist when removing two of the six degrees of freedom for these modes, indicating that the observation and estimation method that is used is not well suited for the determination of the rotation axis of the libration in addition to its amplitude and phase. A combination with other measurements (star tracker, Doppler, VLBI) could provide strong independent constraints for decoupling them, though.

Four out of these six libration-mode amplitudes show especially strong correlations, with a reduction in precision up to a factor of 10 compared to the other two modes. Neither of these libration modes correlate strongly with any other parameter ruling out the possibility that their correlation is due to a mutual correlation with a third parameter. Instead, the correlation originates from the relative forcing frequencies of the two sets of modes. Since the observed variation in the range signal is composed of the various sinusoidal signals from the libration frequencies, as well as the nearly sinusoidal once-per-orbit signal, the complete signal will exhibit behaviour in frequencies that arise from the superposition of these signals. For any combination of two signals, the summed signal exhibits periodic behaviour in frequencies both half the sum and half the difference of the two original frequencies. For the two sets of frequencies with the high correlation, the sum of their relative forcing frequencies is half the orbital frequency. This results in the fact that these two modes and orbital frequency cannot be properly decoupled. Very weak decoupling is achieved, since Phobos' orbit is not perfectly circular, so that its orbital eccentricity and orbital perturbations cause slight variations from the precise sinusoidal signal that would be exhibited if Phobos were to have a perfectly circular Kepler orbit. This relation of the libration frequencies with the orbital frequencies is due to the once-per-orbit forcing of Phobos' rotation, which results in this frequency occurring in the libration frequency decomposition. In principle, the correlation could be mitigated by adding star tracker measurements to the mission and data processing

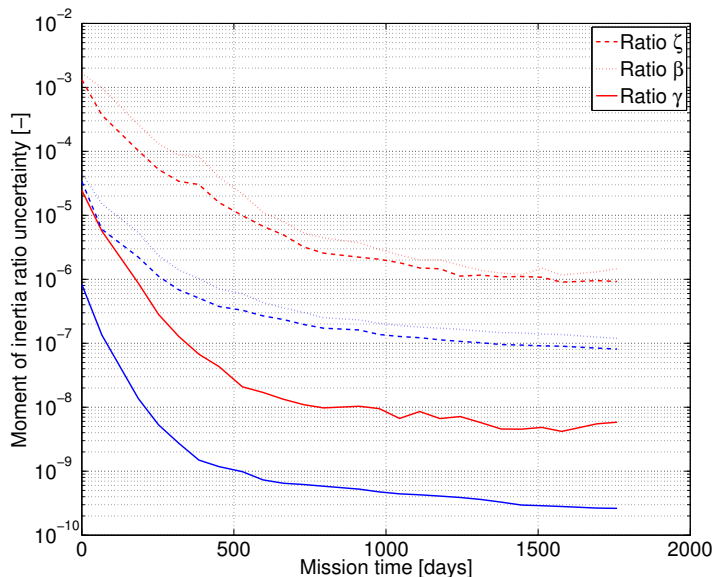


Figure 7: Uncertainty in Phobos relative moments of inertia, as derived from libration amplitude estimation. Blue: without consider parameters. Red: with consider parameters.

scheme, since these measurements will be insensitive to any signals from the orbital motion.

It can be seen from Fig. 6(b) that the very long-period librations in  $W$  (magenta) are not well identified, taking about 2.5 years to be estimated at the *a priori* level of 0.1 degree, when using consider parameters. Additionally, the two modes are almost completely correlated. Their correlation with most other parameters is almost negligible, though, with the exceptions of the ground station position, for which a single component correlates at the  $> 0.9$  level. The reason for this correlation and the poor estimation quality of the very long period librations is that at the time scales of the observations, a change in the amplitudes of these libration modes will provide a signal very similar to a slight constant offset in Phobos' orientation. As a result, the correlation with the Phobos-fixed state of the lander with these librations is very strong, since a constant rotation offset cannot be distinguished from a constant Phobos-fixed position offset. Since these long-period amplitudes provide little information on Phobos' interior, shown by Eq. (13), the direct influence of their rather poor precision is not directly influential for the mission's science return.

Although the influence of the consider parameters is clearly present in the libration amplitude estimation when comparing Figs. 6(a), (c) and (e) with Figs. 6(b), (d) and (f), their influence is not as pronounced as with some other parameters, increasing the uncertainty after 5 years by about a factor of 20 for most parameters. The libration modes which cross-correlate due to the superposition with the orbital signal are estimated at around  $10^{-4}$  after 2 years and around  $10^{-5}$  after 5 years, with the other short-period components having uncertainties 5-10 times lower. The influence of the

consider parameters on the estimation of the long-period librations is roughly an order of magnitude stronger than on the short-period ones, since their signal on the range measurements is more similar to the additional signal from the systematic errors.

## 7.4 Phobos moments of inertia

We now analyze the propagation of the uncertainty in libration amplitudes to uncertainty in moments of inertia. Using the methods discussed in Appendix B, we determine the libration modes which most strongly constrain the uncertainty of the proper modes as a function of time. Subsequently, we propagate this onto an uncertainty in the relative moments of inertia.

Fig. 7 shows the uncertainty in the relative moments of inertia as a function of time. It can clearly be seen that the determination of the  $\gamma$  moment of inertia ratio is consistently about two orders of magnitude more precise than the  $\zeta$  and  $\beta$  ratios. This is due to the higher precision of the longitude librations, which determine the  $\gamma$  ratio, as was discussed previously. The precision that is reached on the moments of inertia will allow for the determination of the degree of heterogeneity of Phobos' interior. For instance, local unsymmetrical voids or other mass anomalies will be manifested in the relative moment of inertia values.

Determination of the absolute moment of inertia uncertainty must take into account the uncertainty in the  $\bar{C}_{2,2}$  coefficient determined in the previous section. It was found that for the entire mission duration, the relative moment of inertia uncertainty is the dominant error term, although narrowly for the  $C$ -term, with  $\sigma_C \approx 20\sigma_\gamma$  and  $\sigma_A \approx \sigma_B \approx 10\sigma_\zeta + 10\sigma_\beta$ , as derived from Le Maistre et al. (2013).

However, the comparison of modelled and measured internal Phobos composition will still be limited by the uncertainty of Phobos' exact volume and shape, which cannot be improved using the PLR mission. Currently, the volume of Phobos has an uncertainty of  $60 \text{ km}^3$ , which is roughly 1% of its total volume, when using the control point network of Willner et al. (2010), propagating onto a 2% uncertainty in the modelled moments of inertia of a homogeneous Phobos (Le Maistre et al., 2013). However, deviations from homogeneity beyond this level, as well as mass or void concentrations, can be strongly constrained by the estimation of Phobos' libration amplitudes.

Similarly to the results for the Mars interior, this indicates that the highly precise ILR measurements will need to be combined with high-precision measurements from other next-generation space missions in order to make full use of the data that is obtained (see Section 6.3).

## 7.5 Phobos tides

The estimation results of Phobos'  $h_2$  Love number are shown in Fig. 8. The estimation without any systematic errors reaches  $\leq 10^{-7}$  after 5 years, corresponding to about  $10^{-2}$  mm surface displacement. This is clearly an overly optimistic estimation with mm-precise measurements, showing the need of the consider parameters (or another approach) for obtaining a realistic determination of the tracking system performance.

However, it can be seen that the  $h_2$  estimation converges to the  $\sim 0.5 \cdot 10^{-5}$  level, with little improvement after 2 years of observation time. Although these results will

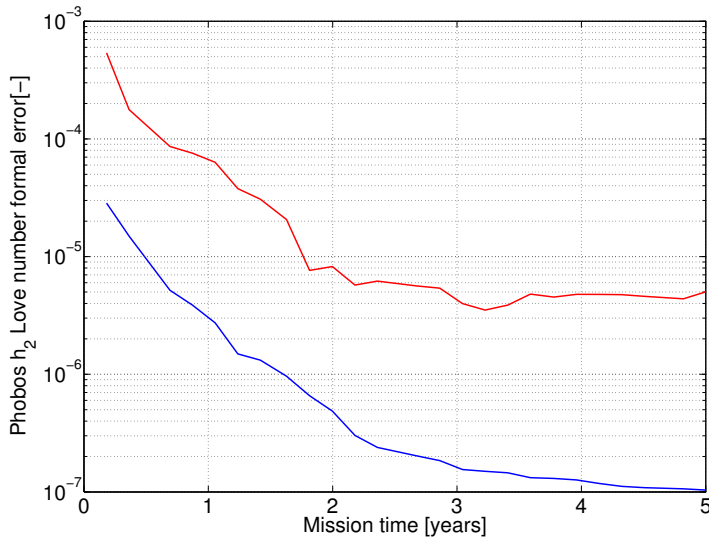


Figure 8: Estimation result of Phobos  $h_2$  Love number. Blue: without consider parameters. Red: with consider parameters.

most likely still be optimistic, due to the simple tidal deformation model used (*i.e.* no latitudinal dependency, no frequency-dependence), the expected lower  $h_2$  values for a rubble-pile Phobos are at the  $10^{-4}$  level (Le Maistre et al., 2013). As a result, a Phobos laser ranging mission will likely be able to distinguish between a Phobos rubble-pile and a monolithic Phobos after about two years of observation time. Additionally, in the case of a rubble pile Phobos, the mean rigidity can be well constrained. By making this distinction, it will be possible to constrain origin theories of Phobos. Additionally, it will provide new insights into its evolution, for instance whether the Stickney impact resulted in compression or fracturization of the Phobos interior.

Although we do not include the Phobos quality factor in our estimation, we can approximate the level of precision that could be attained from  $\sigma_{h_2}$  as follows (Le Maistre et al., 2013):

$$\frac{\sigma_Q}{Q} \approx Q \frac{\sigma_{h_2}}{h_2} \quad (22)$$

Assuming  $Q = 100$  and  $h = 10^{-4}$  (rigid rubble pile), the precision of  $Q$  will be at the 5% level. For  $h_2 = 10^{-3}$ , representing a relatively loose rubble pile however, the uncertainty would be at the level of 50 %, *i.e.* at the limit of observability of the mission.

## 8 Conclusions

We have performed an analysis of the estimation of physical parameters of Mars and Phobos from simulated laser tracking data from Earth-based stations to a Phobos lander. We find that very strong constraints on Phobos librations and degree-two gravity field

coefficients can be determined, resulting in an estimate of its relative moments of inertia at the  $10^{-8}$  level for  $\gamma$  and the  $3 \cdot 10^{-6}$  level for  $\zeta$  and  $\beta$  after 2 years of operation. These values can be directly related to estimates of the absolute moments of inertia which have an uncertainty of one order of magnitude more for  $C$ ,  $B$  and  $A$ , respectively. The contribution of the error in Phobos gravity field coefficients is found to be small, due to the strong constraints on  $\bar{C}_{2,2}$ . However, laser tracking cannot fully decouple all libration modes due to the combined orbit and rotation signal, resulting in high correlations between modes which combine to form signals at the orbital frequency. A combination of laser and star tracker measurements would allow for a much improved decorrelation, though. Additionally, Phobos laser tracking can provide constraints of Phobos  $h_2$  to the  $10^{-4}$  level after 2 years, from which a Phobos rubble pile or monolithic structure can be derived. Comparison of mission results with Phobos interior models are limited by the Phobos shape model uncertainty, though, which is currently at the  $60 \text{ km}^3$ .

Although a Phobos lander is only moderately sensitive to the Mars static gravity field, when compared to results from current Mars orbiters, its orbital stability will allow a strongly improved estimation of both Love numbers and quality factors of Mars. The mission architecture and tracking allows for separate determination of degree-two Love numbers of different orders. The Love numbers at different orders at degree two can be distinguished to the  $10^{-2}$ - $10^{-3}$  level after 2 years. However, due to the combined effect of degree-two and higher-order Love numbers on the orbit of Phobos, the Love numbers at different degrees cannot be decoupled. Mars quality factors at degree two can be decoupled for the Sun- and Phobos-forced frequency. The delay of the Sun-raised tide takes several years to be decoupled from the systematic errors, though, requiring 3 years to attain an uncertainty in  $Q^s$  on the order of 1. The uncertainty in  $Q^p$  reaches 0.01 after 2 years. The effect of the Deimos raised tidal lag is unobservable from the Phobos orbiter, though, preventing the testing of a specific functional form relating quality factor to forcing frequency.

We find a substantial difference between results based on simulated data with Gaussian noise only and with additional systematic errors. Due to the very precise nature of the laser ranging measurements, both observational biases and errors resulting from ground station position and calibration mismodelling are much more influential than what is typically the case for planetary tracking data analysis. We find that the inclusion of systematic errors has a strong damping effect on the decrease of the formal estimation error with time, especially for parameters estimated from periodic effects. Only moderate improvement in parameter uncertainties is obtained after 2-3 years for most parameters. This indicates that, firstly, the reduction or mitigation of systematic errors due to ground station errors will be crucial for future planetary laser ranging mission. Secondly, it shows the need to include them in simulation studies, to prevent averaging out of Gaussian noise from providing overly optimistic simulation results.

Since a Phobos lander is relatively insensitive to Martian rotational variations, combined data analysis of a Phobos and Mars lander would provide strong synergy for investigations relating to the Martian interior, as well as precise modelling of Phobos' dynamics. Additionally, non-geodetic observables of Mars, such as those expected from the InSight mission, as well as *in situ* investigations of Phobos, would allow for stronger

constraints on composition of both Mars and Phobos. This, as well as the limiting influence of Phobos' control point network uncertainty in comparing modelled and measured Phobos interior parameters, shows the need for combining the highly precise laser tracking data with other future high precision measurement types, in both geodetic and non-geodetic studies.

## Acknowledgements

We thank Konrad Willner, Valerie Lainey and Nicolas Rambaux for useful and stimulating discussions on Phobos interior, dynamics and rotation. Nicolas Rambaux is thanked for providing the Spice kernel and model parameters for the Phobos libration model. This work is performed as part of the FP7 ESPaCE project, financially supported by the EC FP7 Grant Agreement 263466.

## Appendix A Lumped gravity field coefficients

The lumped odd and even degree zonal gravity field coefficients are obtained from the following, in the approximation of a negligible Phobos inclination, derived from (Yoder et al., 2003) for normalized coefficients:

$$\bar{J}_{even} = \bar{J}_2 - \frac{7}{5}\sqrt{\frac{9}{5}}\left(\frac{R_{eq}}{a}\right)^2 \bar{J}_4 - \frac{35}{8}\sqrt{\frac{13}{5}}\left(\frac{R_{eq}}{a}\right)^4 \bar{J}_6 + O\left(\left(\frac{R_{eq}}{a}\right)^6\right) \quad (23)$$

$$\bar{J}_{odd} = \bar{J}_3 - \frac{7}{5}\sqrt{\frac{11}{7}}\left(\frac{R_{eq}}{a}\right)^2 \bar{J}_5 + \frac{35}{8}\sqrt{\frac{15}{7}}\left(\frac{R_{eq}}{a}\right)^4 \bar{J}_7 + O\left(\left(\frac{R_{eq}}{a}\right)^6\right) \quad (24)$$

which is valid for determining the lumped contribution of both Mars' and Phobos' higher-order coefficients. Substituting the relevant values for Mars, the following is obtained:

$$\bar{J}_{m,even} \approx \bar{J}_2 - 0.440\bar{J}_4 - 0.121\bar{J}_6 \quad (25)$$

$$\bar{J}_{m,odd} \approx \bar{J}_3 - 0.411\bar{J}_5 + 0.1102\bar{J}_7 \quad (26)$$

Indicating that uncertainties in the even and odd coefficients are dominated by the degree two and three terms, respectively. However, the contribution of the degree 4 and 5 terms are relatively high at approximately 40 % for the even and odd lumped coefficients, respectively.

For Phobos, the contribution to the uncertainty of the lumped even coefficients is given by:

$$\bar{J}_{p,even} \approx \bar{J}_2 - 5 \cdot 10^{-10} \bar{J}_4 \quad (27)$$

indicating that the degree two term of Phobos can be separated much better than of Mars. No estimate from tracking data or astrometry is available for the degree 4 term, however.

## Appendix B Propagating libration to moment of inertia uncertainty

From the first-order equation of Le Maistre et al. (2013) the uncertainty of each proper-mode frequency is related to the uncertainty of the libration amplitude as follows, rearranged to eliminate the dependency on the forcing amplitude:

$$\sigma_{\nu_\gamma} = \frac{(\nu_\gamma^2 - \omega_f^2) \nu_\gamma}{2\gamma_f \omega_f^2} \sigma_{\gamma_f} \quad (28)$$

The possibility of a resonance scenario between the forcing frequency and a proper mode of Phobos was analyzed by Rambaux et al. (2012) and Le Maistre et al. (2013), who conclude that although such a near resonance is possible, current estimates of both the proper modes and the libration frequencies are not precise enough to confirm it. Here, we will take the conservative approach and assume that no strong resonance effect is present, *i.e.* we use the libration amplitudes in Appendix C and do not modify them to include possible resonance influences.

The three proper modes of Phobos in longitude  $\tau$  (corresponding to the  $W$ -libration) and latitude  $L$  and wobble  $w$  (the combination of which corresponds to the combination of  $\alpha$ - and  $\delta$ -librations) are related to the relative moments of inertia by Chapront-Touze (1990), using the values of Willner et al. (2010):

$$\nu_\tau = n\sqrt{3\gamma} \approx 12.2710 \text{ rad/day} \quad (29)$$

$$\nu_L = n\sqrt{\frac{(1 + 3\beta + \zeta\beta) + \sqrt{\Delta}}{2}} \approx 27.2611 \text{ rad/day} \quad (30)$$

$$\nu_w = n\sqrt{\frac{(1 + 3\beta + \zeta\beta) - \sqrt{\Delta}}{2}} \approx 7.4960 \text{ rad/day} \quad (31)$$

$$\Delta = (1 + 3\beta + \zeta\beta)^2 - 16\zeta\beta \quad (32)$$

where  $n$  is Phobos' orbital mean motion. Combining these with Eq. (28), the uncertainty in the librations can be propagated to the uncertainty in the proper modes and subsequently the relative moments of inertia.

## Appendix C Phobos Libration Model

Here, we present the properties of the Phobos libration model that was used, generated by Rambaux et al. (2012), in the form used by Le Maistre et al. (2013), with additional terms from Rambaux (2013). The  $W$ ,  $\alpha$  and  $\delta$  librations are given in Tables 3, 4 and 5, respectively.



Table 3: Properties of  $W$ -libration model used

Period [days]	amplitude [deg]	phase [deg]
0.159516532	0.008682472	108.561
0.231441305	0.005572086	-170.232
0.231647101	0.012518333	-3.058
0.231311789	0.036838974	-47.878
0.319033063	1.099772003	-80.729
0.511653125	0.008180492	-107.311
0.512714439	0.016728058	32.580
0.513296618	0.023916017	-62.498
0.842971242	0.013266486	72.474
0.847441653	0.007862241	116.542
343.483974132	0.006352317	-64.610
413.104129098	0.022824629	111.037
826.207787440	1.427215165	100.518
4318.089673086	0.003817638	-118.818
9343.15863465	0.008515915	-77.828

Table 4: Properties of  $\alpha$ -libration model used

Period [days]	amplitude [deg]	phase [deg]
0.231311789	0.046199156	132.122
0.231647101	0.015699050	176.942
0.511653125	0.010259016	72.689
0.513296620	0.029993200	117.520
0.842971241	0.016637720	-107.525
0.847441653	0.009859994	-63.458
413.103416583	0.022230019	-68.808
686.968929820	0.010681281	69.229
826.209308358	1.788289331	-79.521

Table 5: Properties of  $\delta$ -libration model used

Period [days]	amplitude [deg]	phase [deg]
0.231311789	0.027872555	42.124
0.231647101	0.009471291	86.939
0.511653125	0.006189403	-17.310
0.513296620	0.018094661	27.507
0.847441653	0.005947216	26.620
0.842971248	0.010102656	-18.968
413.099581308	0.006714172	20.832
686.960360505	0.006652784	151.580
826.209789759	1.078116694	10.728



## CHAPTER 5

---

### Paper II - Atmospheric Turbulence

---

*“I am an old man now, and when I die and go to heaven there are two matters on which I hope for enlightenment. One is quantum electrodynamics, and the other is the turbulent motion of fluids. And about the former I am rather optimistic.”*

– Horace Lamb, *An address to the British Association for the Advancement of Science*, (1932)



# Influence of Atmospheric Turbulence on Planetary Transceiver Laser Ranging

*D. Dirka<sup>a</sup>, R. Noomen<sup>a</sup>, I. Prochazka<sup>b</sup>, S. Bauer<sup>c</sup>, L.L.A. Vermeersen<sup>a</sup>*

Published in *Advances in Space Research*, Vol. 54, Issue 11, p. 2349 - 2370, 2014

## Abstract

In this paper we investigate the influence of atmospheric turbulence on the performance of the uplink of a planetary transceiver laser ranging system using a single photon detector. We numerically combine the influence of turbulence in the mean intensity profile variations, scintillation, beam-wander induced pointing errors and stochastic time-of-flight variations, using the Hufnagel-Valley turbulence profile to model the ground turbulence behaviour. We map the intensity variations due to turbulence to variations in the probability distribution of the arrival time of the 1<sup>st</sup> photon in a laser pulse, which influences the range measurement error probability distribution. The turbulence models are applied to assess the influence on single-pass range accuracy and precision statistics, as well as the parameter estimation quality of a Phobos Laser Ranging (PLR) mission.

The difference in range measurement error between weak and strong turbulence is 3-4 mm in a PLR concept. This indicates that turbulence is a potentially important contributor to the error budget of interplanetary laser ranging missions, which aim at mm-level accuracy and precision. The single-shot precision is weakly influenced by turbulence, but strong turbulence is found to cause a strong decrease in detected pulse fraction, reducing normal point precision. We show that a trade-off between range accuracy and precision must be made when selecting laser system parameters, considerations for which are influenced by atmospheric turbulence effects. By consistently operating at the single-photon signal strength level, accuracy variations can be largely removed, at the expense of normal point precision, due to the reduced detection probability. We perform parameter estimation of Phobos initial state and observation biases using simulated measurements with and without turbulence, using a daily periodic turbulence strength model. We show that the parameter estimation quality is degraded significantly below that of the turbulence-free case only in the presence of strong turbulence. This shows the existence of a limit of ground turbulence strength below which its influence on parameter estimation becomes negligible.

## 1 Introduction

The influence of atmospheric turbulence on the performance of free-space communications systems, both terrestrial and Earth-space, has been a topic of active study in recent years. Analyses of the influence of turbulence-induced scintillation and beam wander on link characteristics such as bit rate and signal fades have been performed by *e.g.* Andrews et al. (2000); Hemmati (2006); Farid and Hranilovic (2007); Sandalidis (2011).

---

(a): Delft University of Technology, The Netherlands

(b): Czech Technical University in Prague, Czech Republic

(c): DLR Berlin, Germany

For optical ranging systems, specifically in the field of Satellite Laser Ranging (SLR), the influence of turbulence-induced stochastic time-of-flight variations has been studied by Kral et al. (2005), who verified the validity of the model derived by Gardner (1976) from measurements at the Graz SLR station.

The influence of scintillation on the performance of SLR systems has received more limited attention. The combined influence of scintillation in weak turbulence and retroreflectors on return signal intensity was modelled and measured by Bufton et al. (1977); Bufton (1977). Attenuation of mean signal return strength due to turbulence was studied by *e.g.* Churnside (1993); Degnan (1993); Yaoheng and Hesheng (2003). However, the statistical influence of (time-dependent) turbulence-induced signal-intensity variations on system performance has not been quantified in detail to date.

The fundamental difference between quantifying the influence of turbulence on laser ranging and optical communications is that the exact photon detection time directly influences a range measurement, whereas in optical communications a small error in photon detection time will typically have no effect on the channel performance (Hemmati, 2006). In communications systems, however, a high probability of pulse detection is required to ensure a robust communications channel. In laser ranging systems, the signal return rate may be much lower for the system to still function at a level of performance where it can meet its requirements. This is especially clear in Lunar Laser Ranging (LLR), where stations typically receive returns from very few pulses and operate in a very low signal-to-noise regime (Jefferys and Ries, 1997). Nevertheless, substantial science return is obtained from LLR measurements (Williams et al., 2006).

One- and two-way active transceiver laser ranging systems (Degnan, 2002; Birnbaum et al., 2010; Zuber et al., 2010; Chen et al., 2013) are an emerging technology that is based on existing SLR and LLR technology, modified with an active space segment to allow larger distances to be covered. These technologies have the potential to deliver mm-precise measurements over interplanetary distances, extending the technology of SLR and LLR to Interplanetary Laser Ranging (ILR). The increased range precision and accuracy that can be obtained, compared to current radiometric systems, are expected to yield order(s) of magnitude improvements in the estimation of science parameters related to, for instance, gravitational physics (Turyshv et al., 2010) and planetary interiors (Dirkx et al., 2014a). Also, ILR systems could be combined with long-distance laser communications systems (Hemmati et al., 2009; Hemmati, 2011), such as the laser communications system demonstrated at lunar distances by the LADEE satellite (Boroson and Robinson, 2013).

The measurement error budget breakdown of ILR systems will be different from that of SLR and LLR. For instance, the satellite signature effect on the laser pulse (Otsubo and Appleby, 2003), which is the primary cause of changes in a pulse's temporal shape in SLR, is absent in ILR. For this reason, small intensity fluctuations (such as those caused by turbulence) could play a larger role in the detection-time statistics, uncertainties in which are no longer dominated by retroreflector signature uncertainties. Also, space segment hardware will introduce new sources of errors, such as clock inaccuracies and detector uncertainties (Prochazka et al., 2007). The role of optical turbulence in ILR has not yet been assessed. Quantification of the various error sources of ILR will be crucial in setting up system requirements during conceptual mission design, as well as for assessing

the potential science return from missions using this technology. As opposed to SLR, where ranging data is freely and widely available, no such data exists for ILR, so that we are forced to rely on simulated data for performing analyses of the expected system performance.

In this paper, we investigate the influence of optical turbulence on the range precision and accuracy of the uplink of an ILR system (*i.e.* Earth-to-space). We limit ourselves to the uplink of the system for several reasons. Firstly, aperture averaging is expected to reduce the scintillation effects for the downlink (Degnan, 1993). Secondly, the far-field (as opposed to near-field) turbulence in the case of the downlink cause effects such as beam wander and beam spread to be (nearly) absent.

We simulate laser pulse propagation, including the effects of turbulence, as well as pulse detection times. We map the (turbulence-induced) variations in intensity to variations in the probability distribution of the photon detection times. From these, we statistically quantify the influence of turbulence on the achievable performance of such a system under a variety of atmospheric turbulence conditions, and assess the influence of the non-Gaussian range errors on the orbit determination process.

We use a representative planetary laser ranging system for our simulations, specifically a Phobos lander equipped with a laser transceiver system. The system uses a single photon detector and our analysis in this paper will be restricted to such systems. However, we do not consider a detector array (as is done in the PLR concept), but instead use a single detector element in our simulations. We only consider the receiver system since only the uplink is analyzed here. The feasibility of such a Phobos Laser Ranging (PLR) system was investigated by Turyshev et al. (2010), who performed a preliminary design and analyzed the capabilities of such a system to estimate gravitational-physics parameters. Subsequently, Dirkx et al. (2014a) investigated the potential of such a mission to estimate physical parameters of Mars and Phobos such as moments of inertia and Love numbers. In both these studies, the noise level was quantified by a 1 mm precision averaged over a 1 minute interval. Dirkx et al. (2014a) additionally included systematic errors in their analysis by the use of consider-covariance analysis, distinguishing between the influence of degraded accuracy and precision of the range measurements. There, it is shown that mm-level accuracy uncertainties have an order-of-magnitude higher influence on the estimation than a similar level of uncertainty in (Gaussian) precision. This result indicates that it is crucial to analyze the various error sources in ILR to gain a complete understanding of the potential science return and bottlenecks of this technology.

This paper is structured as follows. We present the models used for the propagation and detection of laser pulses in Section 2 and the influence of turbulence on the pulse intensity variations in Section 3. We simulate the influence of ground turbulence strength on the range measurement errors and parameter estimation procedure and present the results in Sections 4 and 5, respectively. We present our conclusions in Section 6. We present a derivation of a far-field criterion for the Ryotv variance (which described weak-turbulence scintillation statistics) in Appendix A and present and discuss the behaviour of the two integrals given by Eqs. (22) and (25), which are crucial for linking ground turbulence strength to turbuelt effects on the detection statistics, in Appendix B.

## 2 Laser pulse detection

In this section, we summarize the models used for simulating the laser pulses used in SLR and ILR and discuss the statistics of variations in its detection time as a function of received signal intensity. First, in Section 2.1, we briefly review and define our nomenclature for the propagation of a Gaussian laser pulse. Subsequently, we discuss the statistics for single-photon detection in a laser pulse which has a Gaussian intensity pattern in the direction of signal propagation (also termed a temporally Gaussian pulse) in Section 2.2.

### 2.1 Laser pulse model

SLR systems use laser pulses which have, to close approximation, a Gaussian spatial (*i.e.* in the direction perpendicular to the direction of signal propagation) beam profile (Degnan, 1993).

For the spatial signal intensity  $I$  of a Gaussian beam (Siegman, 1986), we use the following notation:

$$I(r, z) = I_0 \left( \frac{w_0}{w(z)} \right)^2 \exp \left( -2 \frac{r^2}{w(z)^2} \right) \quad (1)$$

$$w(z) = w_0 \sqrt{1 + \left( \frac{\lambda z}{\pi w_0^2} \right)^2} \approx \frac{\lambda z}{\pi w_0} \quad (2)$$

where  $\lambda$  is the wavelength of the laser pulse and  $I_0$  is the signal intensity at the waist (defined as  $z = 0$  here). The laser spot size is denoted by  $w(z)$ , with the beam waist radius denoted as  $w_0$  and the off-axis distance  $r$ . The approximation in Eq. (2) is valid for Gaussian beam far-field conditions:

$$z \gg \frac{\pi w_0^2}{\lambda} = \frac{k w_0^2}{2} \quad (3)$$

In the far field, the beam-divergence half-angle  $\theta_{FF}$  follows from Eqs. (1) and (2) as:

$$\theta_{FF} = \frac{\lambda}{\pi w_0} = \frac{2}{k w_0} \quad (4)$$

for which 50-75  $\mu\text{rad}$  ( $\approx 10\text{-}15''$ ) are typical values for SLR systems (Degnan, 1993).

In the context of optical turbulence models, input plane parameters  $\Theta_0$  and  $\Lambda_0$  and output plane parameters  $\Theta$  and  $\Lambda$  are often used to quantify the state of a Gaussian beam, defined by the following for a beam with its waist at  $z = 0$ , (Andrews et al., 2006):

$$\Theta_0 = 1 \quad \Lambda_0 = \frac{2z}{k w_0^2} \quad (5)$$

$$\Theta = \frac{\Theta_0}{\Lambda_0^2 + \Theta_0^2} \quad \Lambda = \frac{\Lambda_0}{\Lambda_0^2 + \Theta_0^2} \quad (6)$$



Here, the  $\Theta$  and  $\Lambda$  parameters are measures for the relative strength of refraction and diffraction, respectively (Andrews and Phillips, 2005). Under the far-field conditions given by Eq. (3), it follows that  $\Lambda_0 \approx w(z)/w_0$ , which is simply the beam expansion factor, a result of diffraction. Additionally, for the far field approximation, the relation  $\Lambda \approx 1/\Lambda_0$  will hold.

For a laser pulse used in SLR, the temporal profile can also be well approximated by a Gaussian shape (Degnan, 1993). This Gaussian shape is not significantly influenced by atmospheric turbulence (Fante, 1975; Degnan, 1993), except for pulse lengths on the order of picoseconds or shorter. Below these pulse lengths, atmospheric dispersion causes the pulse to spread as it propagates through the atmosphere. Therefore, the Gaussian temporal shape is assumed to remain fixed throughout the path of the pulse in ILR, as opposed to SLR, where it is disturbed by the reflection from a (set of) retroreflectors (Otsubo and Appleby, 2003), except when using the novel Blitz-type ball reflectors (Kucharski et al., 2011). For a pulse transmission time (*i.e.* pulse center at  $z = 0$ ) at  $t = 0$ , a time  $\tau$  is introduced by defining:

$$\tau = t - \frac{z}{c_{eff}} \quad (7)$$

where  $c_{eff}$  represents the mean propagation speed of the laser pulse over its trajectory, which may include an atmosphere where its speed is less than  $c$ . The value of  $\tau$  is always zero at the pulse center. This transformed time parameter is used here to define the pulse intensity in the  $z$ -direction in terms of the intensity at the pulse center as follows:

$$I_p(r, z, \tau) = I(r, z) \exp\left(-\frac{\tau^2}{2\sigma_t^2}\right) \quad (8)$$

where  $\sigma_t$  is the pulse-length standard deviation, related to the pulse full-width half-maximum (FWHM)  $t_{HM}$ , which is typically used to quantify SLR systems, (Murphy, 2001):

$$t_{HM} = 2\sqrt{2 \ln 2} \sigma_t \quad (9)$$

In addition to the effects of turbulence, which we describe in Section 3, we take into account a number of additional environmental effects modulating the pulse intensity. Firstly, we include atmospheric attenuation using the models presented by Degnan (1993). Using this method, we map zenith transmittance  $T_a$  to non-zero zenith angles  $\zeta$ . Secondly, the optical efficiency of the transmitter and receiver telescope receiver telescope  $\eta_t$  and  $\eta_r$ , as well as the detector quantum efficiency  $\eta_q$  cause a variation in detected signal strength between subsequent pulses. We discuss the combination of these effects with our turbulence models in Section 3.6.

## 2.2 Detection statistics

In this study, we consider only laser ranging systems operating with a single photon detection systems such as Single Photon Avalanche Diodes (SPADs), which register the arrival of a single photon and the detection of this photon is time-tagged. Detection at the single-photon level is preferred for a number of reasons in SLR, (Otsubo and

Appleby, 2003; Degnan, 2001; Prochazka et al., 2004), such as the superior performance of detectors at the single photon level. We assume a negligible environmental noise regime, so that all detected photons are from the transmitted laser pulses. Due to the finite length of the laser pulses, the detection time of the photon will be different from that of the pulse center, as will be discussed in this section.

The detection time Probability Distribution Function (PDF) of the first photon in a temporally Gaussian pulse, denoted PDF  $p_{first}^{(1)}(\tau)$ , was derived by Murphy (2001). From this, we derive an explicit form of the Cumulative Distribution Function (CDF)  $P_{first}^{(1)}(\tau)$ :

$$p_{first}^{(1)}(\tau) = \frac{N}{\sqrt{2\pi}\sigma_t} e^{-\frac{\tau^2}{2\sigma_t^2}} \left( \frac{1}{2} - \frac{1}{2} \operatorname{erf} \left( \frac{\tau}{\sqrt{2}\sigma} \right) \right)^{N-1} \quad (10)$$

$$P_{first}^{(1)}(\tau) = \int_{-\infty}^{\tau} p_{first}^{(1)}(\bar{\tau}) d\bar{\tau} = 1 - \left( \frac{1 - \operatorname{erf} \left( \frac{\tau}{\sqrt{2}\sigma} \right)}{2} \right)^N \quad (11)$$

$$\operatorname{erf}(x) = \frac{2}{\sqrt{\pi}} \int_0^x e^{-t^2} dt \quad (12)$$

where  $\operatorname{erf}(x)$  denotes the standard error function (Abramowitz and Stegun, 1964) and  $N$  is the number of detectable photons (*i.e.* the number of photons that are incident on the detector and which could potentially be the photon that triggers the system). This PDF is plotted in blue in Fig. 1 for a number of values of  $N$ , where it can be seen that, for increasing  $N$ , the peak of the PDF is shifted and its shape becomes skewed.

Under turbulence-free conditions and no signal attenuation along the beam path, the value of  $N$  is obtained from evaluating Eq. (8) at the detector position to obtain the irradiance  $I(t)$ . In Eqs. (10) and (11), the influence of atmospheric turbulence is manifested in its stochastic influence on the signal intensity  $I$  (discussed in Section 3) and resultant the number of photons  $N$ , so that  $N$  will itself become a random variable.

The result of  $N$  itself being a random variable on the pulse detection time is shown in Fig. 1, where the PDF for the detection time of the first photon is shown for the case where  $N$  is a random variable with a uniform integer distribution in the [1,4] range (values chosen for illustrative purposes). In this case, the resulting PDF can be seen as the average PDF when combining the PDFs for  $N = 1, 2, 3, 4$  from Eq. (10). It can clearly be seen that the deviation from the Gaussian shape increases compared to the constant  $N$  case. Additionally, the time-dependence of the turbulence conditions will cause the PDF to also be time-dependent.

To illustrate the magnitude of the mean detection time error as a function of  $N$ , the expectation value of  $\tau$  from Eq. (10) is plotted in Fig. 2. In this figure, it can be seen that a small change in  $N$  (*i.e.* increase or decrease of 1) causes an especially high change in the expectation value of  $\tau$  for low photon number  $N = 1, 2, 3, 4$ , with changes on the order of the pulse length standard deviation.

To quantify the influence of turbulence, we require a mapping from  $I(t)$  to  $N$ . Assuming that the signal intensity varies negligibly over the detector with radius  $r_d$ , *i.e.*

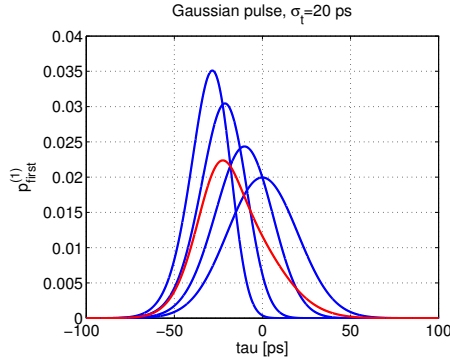


Figure 1: Examples of first photon detection statistics PDF, with  $\tau = 0$  indicating detection of photon at the pulse center, Eq. (10). Blue: for  $N = 1, 2, 5, 10$ , for PDFs with peaks from right to left, respectively. Red: PDF in Eq. (10) with  $N$  a random variable, modelled as a uniformly distributed integer in the  $[1, 4]$  range.

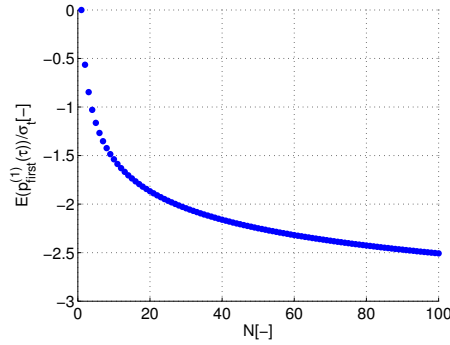


Figure 2: Expectation value for the first photon detection time error, Eq. (10), as a function of  $N$ .

$r_d \ll w(z)$ , the power on the detector  $P(t)$  is calculated to be  $I(t)A_d$ , with  $A_d$  the detector area. The total received energy  $U_{p,r}$  is obtained by integrating the result over the temporal pulse shape from Eq. (8):

$$U_{p,r}(r, z) = A_d \int_{-\infty}^{\infty} I_p(r, z, \tau) d\tau = I(r, z) A_d \sigma_t \sqrt{2\pi} \quad (13)$$

The energy of a single photon  $E_{ph}$  at the given wavelength is determined from:

$$E_{ph} = \frac{hc}{\lambda} \quad (14)$$

Consequently, the mean expected number of detectable photons,  $\langle N \rangle$ , follows from:

$$\langle N \rangle = \frac{U_{p,r}}{E_{ph}} \quad (15)$$

To generate an (integer) value  $N$  for the number of detectable photons, we use Poisson statistics. The probability mass function (PMF) for the number of photons  $N$  that reach the detector plane is described by the following:

$$f_N(N) = \frac{\langle N \rangle^N}{N!} e^{-\langle N \rangle} \quad (16)$$

As a result, even for very low energy levels, with  $\langle N \rangle \ll 1$ , detection will not always occur at the single photon level, since  $P(N > 1) \neq 0$ . For instance, for  $\langle N \rangle = 0.1$ , it follows that  $P(N = 2) \approx 0.005$ . As a result, even for an average detectable energy equal to that contained by  $1/10^{\text{th}}$  of a photon, 2 photons will still be detected for  $\approx 0.5\%$  of all pulses (on average), compared to 1 photon in  $\approx 9\%$  and 0 photons in  $\approx 90\%$  of all pulses. One way in which to mitigate the multi-photon detections is to use a multi-element photon detector, such as that used at the APOLLO LLR station (Murphy, 2013). When using a multi-element detector, the multiple photons may be detected by separate elements. In such a system, the detection statistics discussed in this section do not apply to the detector as a whole, but to each element separately. The influence of this on photon detection statistics is discussed further by Murphy (2001).

### 3 Optical turbulence

In the presence of turbulence, the spatial intensity profile of the laser pulse will be stochastically altered due to a number of physical effects, discussed extensively by Andrews and Phillips (2005).

We seek to statistically quantify the influence of turbulence on the signal intensity and pulse delay at a given value of the off-axis distance  $r$  and propagation distance  $z$  and map these results to statistics for the pulse detection error. To achieve this, we require a model for the atmospheric turbulence strength, specifically the refractive index structure constant  $C_n^2$ , along the beam path. This model is discussed in Section 3.1. We subsequently present the theoretical discussion of the statistics of turbulence-induced signal strength variations. We present the models of turbulence on the mean (time-averaged) irradiance pattern  $\langle I(r, z) \rangle$  in Section 3.2. We present models for the statistical deviations of signal strength from this mean pattern in Section 3.3. Specifically, we describe the model we use for the scintillation index  $\sigma_I^2$  and turbulence-induced pointing error  $\Delta\theta$ . A model for the direct influence of turbulence on the laser pulse time-of-flight is presented in Section 3.4. The probability distribution functions for the various stochastic aspects of the turbulence-induced variations in are given in Section 3.5.

In Section 3.6, we summarize our numerical procedure for combining the various turbulence models and generating range error statistics. Finally, the expected influence of the various turbulence effects on laser range measurement accuracy and precision are qualitatively discussed in Section 3.7.

#### 3.1 Refractive index structure constant

The local strength of the atmospheric turbulence can be quantified by the refractive index structure constant  $C_n^2$ , which is a measure for the turbulence-induced spatial variation

of the atmosphere's refractive index. A wide variety of models for this quantity with altitude, location and time exist (Tunick, 2002). One of the most widely used models in the current context is the Hufnagel-Valley (HV) model (Beland, 1993), as it is relatively simple and provides reasonably accurate results (Andrews and Phillips, 2005), which is well suited for a conceptual study such as this one.

It requires the ground turbulence level of an exponentially decaying term, which we denote as  $C_{n(0)}^2$ , and the mean high-altitude wind velocity  $u$  as input to generate a profile with altitude  $h$  as follows:

$$C_n^2(h) = 0.00594 \left(\frac{u}{27}\right)^2 (10^{-5}h)^{10} \exp\left(-\frac{h}{1000}\right) + \dots \\ \dots + 2.7 \cdot 10^{-16} \exp\left(-\frac{h}{1500}\right) + C_{n(0)}^2 \exp\left(-\frac{h}{100}\right) \quad (17)$$

$$u = \sqrt{\frac{1}{15 \cdot 10^3} \int_{5 \cdot 10^3}^{20 \cdot 10^3} V_u^2(h) dh} \quad (18)$$

with  $V_u(h)$  the wind velocity as a function of altitude  $h$ . Typical values for  $C_n^2(0)$  and  $u$  are  $1.7 \cdot 10^{-14} \text{ m}^{-2/3}$  and 21 m/s, respectively, for which the above is termed the HV<sub>5/7</sub> model (Andrews and Phillips, 2005). However, local values of the parameters can vary strongly, depending on location, time of day and time of year, by orders of magnitude in the case of the  $C_{n(0)}^2$  (Walters and Kunkel, 1981; Tunick, 2002).

We expect that it will be especially the time-dependence of  $C_n^2$  that will influence the performance of the ranging system, due to the fact that a constant bias estimation will not be able to fully compensate for it, as opposed to constant turbulence conditions (see Section 3.7). The HV model allows for variations of the ground-level structure constant  $C_{n(0)}^2$  and rms wind speed  $u$  in the atmosphere to include time-dependent turbulence strength effects in the analysis (see Section 5).

A limitation of the HV model is that it works best for atmospheric profiles starting at sea level ( $h = 0$ ). Although it may be applied for ground station locations above sea level, the expected errors on the turbulence profile will increase, due to the strong decrease in the influence of the term modulated by  $C_{n(0)}^2$ . Kral et al. (2004) compared measured values for the coherence length with those obtained from the HV model for a station at an altitude of 2332 m, arriving at an error of 30%. However, it must be stressed that it is not our goal here to make precise turbulence predictions. Instead, it is our goal to statistically map a range of turbulence strength statistics to a range of range error statistics, to assess the expected influence of turbulence on (planetary) laser links. Nevertheless, since we wish to investigate the influence of the  $C_{n(0)}^2$  term in Sections 4.1 and 5, we only use stations near sea-level and replace  $h/100$  with  $(h - h_0)/100$  in Eq. 17 to include strong observed variability in ground turbulence levels, also for  $h \neq 0$ . When using the models presented in this paper to make precise predictions of the influence of turbulence on SLR/ILR links, a more precise model for  $C_n^2$  with position, altitude and time should be used.

### 3.2 Mean irradiance

The mean irradiance profile (*i.e.* the intensity pattern for a static link as averaged over time) for a Gaussian beam is influenced by both beam wander and beam spread in the presence of atmospheric turbulence (Andrews et al., 2006). Beam wander causes the center (*i.e.* point of maximum intensity) of the beam to move around in the detection plane (Section 3.3). Beam spread increases the instantaneous beam divergence beyond its nominal divergence angle. These effects are known to limit the attainable focusing of the laser pulse in SLR (Degnan, 1993). Both effects contribute to a long-term (*i.e.* averaged over longer periods of time) mean irradiance profile that can in many cases be closely approximated by replacing  $w(z)$  by the long-term spot size  $w_{lt}(z)$  in Eq. (1), (Andrews et al., 2006), so that:

$$\langle I(r, z) \rangle = I(r, z)|_{w(z) \rightarrow w_{lt}(z)} \quad (19)$$

with the following model for  $w_{lt}(z)$  :

$$w_{lt}(z) = w(z) \left( 1 + 2^{5/2} \left( \frac{w_0}{r_0} \right)^{5/3} \right)^{3/5} \quad (20)$$

where  $r_0$  is Fried's parameter, or the atmospheric coherence diameter. This quantity is a measure for the strength of optical turbulence and quantifies the distance over which turbulence-induced wavefront errors accumulate (Andrews and Phillips, 2005). From this equation, it can be seen that the long term spot size has different asymptotic behaviour for  $w_0/r_0 \ll 1$  and  $w_0/r_0 \gg 1$ . For very small  $w_0/r_0$ , the influence of turbulence on the mean irradiance pattern becomes negligible and  $w_{lt}(z)$  reduced to  $w(z)$ . For very large  $w_0/r_0$ , however,  $w_{lt}(z) \sim w_0/r_0$ . with  $r_0$  effectively acting like a diffractive parameter broadening the beam. In essence, atmospheric turbulence acts as a stochastic lens, the time-averaged effect of which we quantify by beam spread.

The quantity  $r_0$  is determined from the following Andrews and Phillips (2005):

$$r_0 = (0.423\mu_{u0}k^2 \sec \zeta)^{-3/5} \quad (21)$$

$$\mu_{u0} \approx \int_{h_0}^H C_n^2(h) dh \quad (22)$$

where  $k$  is the signal's circular wavenumber (*i.e.*  $2\pi/\lambda$ ),  $H$  is the altitude of the observer,  $h_0$  the altitude of the transmitter and  $\zeta$  is the zenith angle of the target at the ground station, so that  $z = H \sec \zeta$ . For the the  $HV_{5/7}$  model (Section 3.1), which represents typical turbulence conditions,  $r_0 = 0.0533$  m and  $\mu_{u0} = 2.2 \cdot 10^{-12} \text{ m}^{-2/3}$ . The approximation for  $\mu_{u0}$  holds when  $h_{max} \ll H$ , with  $h_{max}$  the maximum altitude at which atmospheric turbulence contributes non-negligibly to  $\mu_{u0}$ . The value of  $h_{max}$  can be safely assumed to be 50 km, when inspecting Eq. (17), from which it can be seen that all terms contribute negligibly to  $C_n^2(h)$  at such an altitude. The behaviour of  $\mu_{u0}$  for a wide range of model parameter for the Hufnagel-Valey model (Section 3.1) is presented in Appendix B.

Although the modified Gaussian irradiance profile is a good approximation for most cases, large deviations may occur for relatively large values of  $r$ , as shown for the case of collimated beams by Reclons et al. (2007), where numerical turbulence simulations show large deviations in the tails of the Gaussian distribution, with far higher values of  $\langle I \rangle$  than predicted by Eq. (1), with  $w(z) = w_{lt}(z)$  from Eq. (20). However, these deviations only become pronounced for very large off-axis distances, with  $r > 3\text{-}5w_{lt}$ . As an example, at 1 AU, the turbulence-free spot-size of a typical system is on the order of 5000 km. Such large off-axis distances are expected to occur only very rarely in ILR, due to the quality of target position predictions, as shown by the accuracy of modern planetary and spacecraft ephemerides *e.g.* (Fienga et al., 2009; Folkner et al., 2009). Also at such large values of  $r$  the signal strength is unlikely to be sufficient for a photon detection, with or without turbulence.

### 3.3 Irradiance variations

In this section, we present models for the parameters describing the statistical deviations of the intensity pattern from the mean pattern discussed in the previous section. We first present our model for the scintillation index and subsequently present the model for pointing errors induced by turbulence (beam wander).

The scintillation index  $\sigma_I^2$  is a key parameter in describing the statistics of optical turbulence. It is defined as follows:

$$\sigma_I^2(z, r) = \frac{\langle I^2(r, z) \rangle}{\langle I(r, z) \rangle^2} - 1 \quad (23)$$

and is a measure for the expected level of fluctuations of the signal intensity from the mean pattern described by Eq. (19).

The statistical theory for the influence of weak turbulence on the propagation of Gaussian beams is well-developed. Under such conditions, (*i.e.*  $\sigma_I^2 \ll 1$ ), the on-axis scintillation index  $\sigma_I^2(z, r=0)$  is well approximated by the Rytov variance, denoted by  $\sigma_B^2$  (Andrews and Phillips, 2005):

$$\sigma_B^2 = 8.7\mu_{u1}k^{7/6}z^{5/6}\sec(\zeta) \quad (24)$$

$$\mu_{u1} = \text{Re} \left( \int_{h=h_0}^{h=H} C_n^2(\xi) \left( \xi^{5/6} (\Lambda\xi + i(1 - \bar{\Theta}\xi))^{5/6} - \Lambda^{5/6}\xi^{5/3} \right) d\xi \right) \quad (25)$$

$$\xi = 1 - \frac{h}{H} \quad (26)$$

with  $\Theta$  and  $\Lambda$  from Eq. (6). The behaviour of  $\mu_{u1}$  for a wide range of model parameter for the Hufnagel-Valey model (Section 3.1) is presented in Appendix B.

To extend the scintillation model presented above to strong turbulence conditions, the extended Rytov theory will be used, which was developed by (Andrews et al., 1999, 2000). In this theory, the index of refraction is split into two components, one due to small scale turbulence eddies and one due to large scale turbulence eddies. In weak turbulence, all eddies fall into either of these two categories. In strong turbulence, however, there is a region of 'medium-sized' eddies which do not contribute substantially

to the scintillation. In order to incorporate these concepts into the calculation of  $\sigma_I^2$ , heuristic spatial filter functions are introduced, which limit the eddy sized which are included in the derivation of the scintillation conditions. Using this theory, the on-axis scintillation index is calculated from:

$$\sigma_{\ln x}^2 = \frac{0.49\sigma_B^2}{\left(1 + 0.56(1 + \Theta)\sigma_B^{12/5}\right)^{7/6}} \quad (27)$$

$$\sigma_{\ln y}^2 = \frac{0.51\sigma_B^2}{\left(1 + 0.69\sigma_B^{12/5}\right)^{5/6}} \quad (28)$$

$$\sigma_I^2 = \exp(\sigma_{\ln x}^2 + \sigma_{\ln y}^2) - 1 \quad (29)$$

where  $\sigma_{\ln x}^2$  and  $\sigma_{\ln y}^2$  are the contributions to the (logarithm of the) scintillation index  $\sigma_I^2$  due to the large- and small-scale turbulent atmospheric eddies, respectively. It can be seen from Eqs. (27)-(29) that under weak turbulence conditions (*i.e.*  $\sigma_B^2 \rightarrow 0$ ), the scintillation index tends to  $\sigma_B^2$ . For strong turbulence  $\sigma_I^2$  converges to  $\sim 1$ , instead of increasing without bound, as is the case for  $\sigma_B^2$ . The above method shows close coincidence with results obtained by numerical optics methods (Andrews et al., 2000, 2007) for both terrestrial and space-uplink scenarios, and can be used for a conceptual analysis of scintillation strength.

In Appendix A, it is shown that in the far-field the condition  $\Theta = 0$  may be assumed to evaluate the integral in Eq. (25). In this context, the far-field is defined as follows, assuming the HV turbulence profile:

$$z \gg \left(\frac{kw_0^2}{2}\right)^2 \frac{1}{100} \quad (30)$$

which can be seen to be distinct from Eq. (3). For typical SLR values of  $\lambda = 532$  nm,  $w_0 = 1$  cm, (obtained from Eq. (4) with a relatively large  $\theta_{FF}=150$   $\mu$ rad) this condition imposes a far-field distance of only about 3.5 km. For planetary laser ranging systems, the  $\Theta = 0$  assumption will still be valid for all realistic values of  $w_0$  and typical values of  $k$ , reducing the dependency of the scintillation index on wavelength, distance and waist radius to a single combined parameter  $\Lambda \cdot z$ . However, due to the 4<sup>th</sup> power dependency of Eq. (30) on  $w_0$ , the far-field condition is not necessarily valid for all systems and (LEO) SLR targets.

In addition to the scintillation index for the on-axis conditions calculated from Eqs. (27)-(29), the off-axis scintillation, *i.e.* for  $r \neq 0$ , requires an additional modification. Although we assume ideal pointing of the system hardware in our study, we do include pointing errors induced by turbulence. Specifically, beam wander has an influence on the intensity fluctuation statistics by causing an effective (off-axis) pointing jitter (Baker and Benson, 2004). Here, we adopt the method to account for these effects that was proposed by Andrews et al. (2006) and applied by *e.g.* Sandalidis (2011) in the context of optical communication channel performance.

It is a semi-empirical theory for including the influence of the beam-wander effect. It is derived using similar approach as the derivation of Eqs. (27)-(29) by Andrews et al.



(1999), splitting the turbulent eddies into small and large scales and thereby splitting the effects of beam wander and beam spread. A filter function is used to limit the calculation of beam wander to the influence of eddies of the beam size and larger (Andrews et al., 2006). The method can be used to either modify the scintillation index directly or alternatively to separately model the influence of beam wander as a stochastic pointing error, as will be discussed further in Section 3.5.

Using the theory developed by Andrews et al. (1999), the equation for the effective pointing error variance  $\sigma_{pe}^2$  becomes, for a slant uplink path

$$\langle r_c^2 \rangle = 0.54z^2 \left( \frac{\lambda}{2w_0} \right)^2 \left( \frac{2w_0}{r_0} \right)^{\frac{5}{3}} \quad (31)$$

$$\sigma_{pe}^2 = \langle r_c^2 \rangle \left( 1 - \left( \frac{C_r^2 \left( \frac{w_0}{r_0} \right)^2}{1 + C_r^2 \left( \frac{w_0}{r_0} \right)^2} \right)^{\frac{1}{6}} \right) \quad (32)$$

where  $\langle r_c^2 \rangle$  is the mean large-scale beam wander magnitude and  $C_r$  is an empirical constant set to  $\approx \pi$  in the simulations by Andrews et al. (2006). For moderate turbulence strength ( $w_0/r_0 = 1$ ),  $\lambda = 532$  nm and  $w_0 = 5$  cm,  $\langle r_c^2 \rangle / z \approx 12.5$  rad.

From the above relations, the additional on- and off-axis scintillation index contribution becomes the following:

$$\Delta\sigma_I^2(z, r) = 5.95z^2 \left( \frac{2w_0}{r_0} \right)^{5/3} \cdot \left( \left( \frac{\theta_{pe}}{W} \right)^2 + \left( \frac{\theta_r - \theta_{pe}}{W} \right)^2 U(\theta_r - \theta_{pe}) \right) \quad (33)$$

where  $\theta$  is the off-axis pointing error ( $\theta_{pe} \approx \sigma_{pe}/z$ ;  $\theta_r \approx r/z$ ) and  $U$  denotes the Heaviside function. When setting  $\theta_{pe} = 0$  this equation reduces to the off-axis scintillation index contribution in the absence of beam wander (Andrews et al., 2006). In addition to this signal intensity variation due to  $r \neq 0$ , an increase in  $r$  will decrease the mean irradiance  $\langle I \rangle$  in Eq. (19).

For our numerical simulations, we separate the random variable for the beam-wander induced pointing error  $\Delta\theta$  from  $I$ , combining them geometrically in our model by the stochastic influence of  $\Delta\theta$  on  $r$  and resultantly on  $I$  and  $\sigma_I^2$  through Eqs. (19) and (33), respectively. The variance of  $\Delta\theta$ , denoted  $\sigma_p^2$ , is derived using the relations given by Titterton (1973) and the term  $\gamma$  used by Andrews et al. (2007), assuming a Gaussian distribution of pointing errors:

$$\sigma_p^2 = \frac{w(z)^2}{2z^2\gamma} \quad (34)$$

$$\gamma = \sqrt{1 + \frac{\sigma_I^2 + 1}{\Delta\sigma_I^2}} - 1 \quad (35)$$

By taking this approach we retain more flexibility in our models, since it allows us to combine the beam-wander induced pointing error with an arbitrary pointing error due to for instance hardware errors, *etc.*

As discussed by Andrews et al. (2006), the far-field beam profile, which we seek to statistically model, can be characterized as a function of  $w_0/r_0$ , with the asymptotic regimes  $w_0/r_0 \ll 1$ ,  $w_0/r_0 \sim 1$  and  $w_0/r_0 \gg 1$ . The numerical simulations show that the model that we also apply here is applicable for conceptual studies throughout these regimes. For saturated turbulence,  $w_0/r_0 \gg 1$  and the beam breaks up into a number of smaller spots, an effect termed speckle. Although our models cannot generate a speckle pattern at a given point in time, it can provide a statistical description of the signal intensity through the combined use of the scintillation and beam wander models.

### 3.4 Time-of-flight variations

In addition to the intensity variations, for which models have been presented in the previous section, atmospheric turbulence has a direct influence on the range measurement statistics by causing time-of-flight variations of the laser pulses. These variations are due to the stochastic variations of the atmospheric index of refraction, which lead to variations in the pulse propagation speed. A theoretical model for this behaviour was derived by Gardner (1976):

$$\sigma_t^2 = 26.3L_0^{5/3} \int_0^L C_n^2(\xi) d\xi \approx 26.3L_0^{5/3} \sec \zeta \int_{h_0}^H C_n^2(h) dh \quad (36)$$

$$\approx 26.3L_0^{5/3} \sec \zeta \mu_{u0} \quad (37)$$

where  $L_0$  is the outer scale of the turbulence, *i.e.* the maximum size of the turbulent eddies. The second approximation in the integral is valid when neglecting latitude and longitude dependencies of  $C_n^2$  and making the approximation in Eq. (22). The above relation was verified at the Graz SLR station (Kral et al., 2005), who related the integral to atmospheric seeing conditions and fitted a value for  $L_0$  of roughly 30 m, which we consistently use in our simulations. For the HV<sub>5/7</sub> turbulence model (Section 3.1), this results in  $\sigma_t \approx 0.13$  mm for zenith transmission and  $\sigma_t \approx 0.25$  mm for a 15° elevation angle.

### 3.5 Probability distributions

To describe the statistical influence of turbulence on a laser ranging system, a PDF for the variations of the intensity  $I(r, z)$ , as well as the time-of-arrival fluctuations discussed in Section 3.4, are required.

The intensity fluctuation PDF must take into account both scintillation and beam wander. For scintillation, the lognormal model is known to be a good approximation for weak turbulence and is often applied in conceptual studies (Degnan, 1993; Andrews et al., 2007). However, it fails to model scintillation under moderate or strong turbulence conditions. The gamma and gamma-gamma distributions are shown by Al-Habash et al. (2001); Andrews et al. (2007) to closely model scintillation across all intensity scales. Here, we use the gamma distribution, as it has an analytically tractable CDF and inverse CDF (*i.e.* cumulative probability as a function of random variable value), facilitating its use in numerical simulation studies. The expression for the PDF of the intensity  $I$

becomes:

$$f_I(I) = \frac{1}{\Gamma(m)I} \left( \frac{mI}{\langle I \rangle} \right)^m \exp \left( -\frac{mI}{\langle I \rangle} \right) \quad (38)$$

$$m = \sigma_I^{-2} \quad (39)$$

where  $\Gamma(m)$  represents the standard Gamma function. The above equation represents a gamma-distributed random variable  $I$  with shape factor  $m$  and scale factor  $\langle I \rangle / m$ .

For the inclusion of the beam-wander induced pointing error, we take an approach that is conceptually similar to modulating the gamma-distributed scintillations with additional variations due to beam-wander induced pointing errors that is taken by (Andrews et al., 2007). They model the pointing errors as a beta distribution modulating the intensity fluctuations. This is derived from the assumption of mutually independent random pointing errors in two independent pointing directions under the condition of  $r \ll w$  (Titterton, 1973). We choose to model the pointing errors as separate PDFs: independent Gaussian distributions, with zero mean and variance from Eq. (34). The realizations of the random variables are combined numerically in our simulations, allowing more flexibility in including other effects into the model.

### 3.6 Model synthesis

In this section, we will give a stepwise overview of our numerical procedure to combine the models presented in the previous sections to generate range measurement statistics.

- Calculate from a given pulse transmission time the measurement geometry for an ideal link, calculating the ideal reception time and the state of both the receiver and transmitter at reception and transmission time, respectively, *e.g.* (Moyer, 2000). From the geometry we obtain the link distance  $z$  and zenith angle  $\zeta$ .
- Evaluate the model for  $\sigma_p^2$  in Eq. (34). Use  $\sigma_p^2$  to generate realizations of the Gaussian PDFs for the two pointing errors (Section 3.5), from which we obtain an off-axis target distance  $r$ .
- Calculate  $\langle I(r, z) \rangle$  from Eqs. (1) and (19) by evaluating  $w_{lt}(z)$  from Eq. (20) and using the system parameters and current values of  $r$  and  $z$ . We use zenith angle  $\zeta$  and atmospheric transmittance ( $T_a = 0.7$ ), as well as the transmission system efficiency  $\eta_t$ , to modulate signal intensity through the appropriate decrease in  $I_0$  (see Section 2.1).
- Evaluate the model for the scintillation index  $\sigma_I^2$  from Eq. (29).
- Generate a realization of the intensity at the receiver from the Gamma distribution in Eq. (39) using  $\sigma_I^2$  and  $\langle I(r, z) \rangle$ .
- From the total intensity at the detector and the receiving telescope diameter, obtain the total energy that is incident on the detector using Eq. (13). Generate a realization of the ideal number of detectable photons  $N_{id}$  (*i.e.* with detection efficiency of 1) from the Poisson distribution in Eq. (16).

- Use the binomial distribution with  $N_{id}$  possibly detectable photons with equal and independent possibility of detection  $\eta_r \eta_q$  to determine number of detected photons  $N$ , where  $\eta_r$  is the receiver optical efficiency and  $\eta_q$  is the detector quantum efficiency.
- From  $N$  and the pulse length  $\sigma_t$ , generate a realization of the pulse detection time error from the distribution with CDF given by Eq. (11); add stochastic time of flight variation using Gaussian distribution and variance from Eq. (37).

The primary output of this procedure is the pulse measurement time error  $\tau$ , discussed in Section 2.2. However, we also use the intermediate quantities of the calculation to analyze the results in Sections 4 and 5.

### 3.7 Turbulent effects on range accuracy and precision

To simulate the influence of turbulence on laser range measurements, we generate range errors  $\Delta s (= c\tau)$  numerically and investigate their statistical distribution as a function of turbulence strength. Thereby, we combine the various influences of optical turbulence on  $N$  in Eq. (10), as discussed in Section 3.6, and quantify their influence on range accuracy and precision. In this section, we qualitatively discuss the expected effects of atmospheric turbulence on the accuracy and precision, in preparation for the interpretation of the simulation results presented in Sections 4 and 5.

As discussed in Section 2.2, the mean range error can be directly related to the mean number of detectable photons per pulse  $N$  in Eq. (10). Specifically, for larger  $N$ , larger mean range biases will be present in the observations, shown explicitly in Fig. 2. However, higher mean values of  $N$  will also imply fewer pulses for which  $N \leq 0$ , in the presence of signal strength variations due to (among others) turbulence, *i.e.* higher numbers of detected pulses. Since the normal point precision improves with  $\sqrt{N_d}$  (Sinclair, 1997), where  $N_d$  is the number of detections used for generating a single normal point, high mean values of  $N$  will generally result in a higher normal point precision. Therefore, higher signal strength will result in a higher normal point precision, but lower accuracy. The decrease in accuracy can be mitigated by including an observation bias in the parameter estimation process (Section 5.1). When the PDF describing the statistical behaviour of  $N$  varies in time, however, an observation bias will only remove the time-averaged value of the mean turbulence-induced error and a time-varying range bias will remain in the simulated observations.

Time-dependent signal strength variations are present even in the absence of turbulence, due to varying atmospheric attenuation with both time and zenith angle, varying target distance and hardware inaccuracies.

Scintillation and beam wander will statistically cause a larger variation in pulse detection energy and a smaller number of detection events, thereby reducing the data quantity and reducing the normal point precision over a given time interval. However, for a given turbulence strength, the mean range error will also decrease, but time-variations in turbulence strength will result in time-varying range inaccuracies.

Finally, turbulence causes direct laser pulse time-of-flight variations, discussed in Section 3.4. This influence will consistently reduce the precision of the range measure-

Table 1: Nominal parameters for Earth-Phobos laser link.

$\lambda$	$U_{p,t}$	$t_{FWHM}$	$\theta_{FF}$	$r_d$	$\eta_q \cdot \eta_r$
532 nm	1.0 mJ	50 ps	25 $\mu$ rad	0.25 m	0.12

ments, without reducing the number of measurements, thereby requiring averaging of more measurements to reach a given normal point precision.

## 4 Results: range measurement statistics

In this section, the simulation results for the influence of atmospheric turbulence on the range measurements statistics of a representative mission and system are presented and discussed. We investigate the influence of time-invariant turbulence on the range accuracy and precision statistics over a single pass for a broad range of HV model parameter values  $C_{n(0)}^2$  and  $u$  (see Eq. (17)).

In Section 4.1, we outline our simulation scenario and setup, discussing the mission parameters that we use. Subsequently, we discuss the influence of turbulence on the measurement accuracy and precision in Sections 4.2 and 4.3, respectively. Finally, the effect of variation of laser system settings on the influence of atmospheric turbulence and the associated considerations for link design trade-offs are presented in Section 4.4.

### 4.1 Simulation parameters

We use the uplink of the Phobos Laser Ranging (PLR) system of Turyshev et al. (2010) as the test case for our analysis, and use similar system parameters as nominal input to our simulations, shown here in Table 1. Here  $U_{p,t}$  denotes the transmitted pulse energy, which includes the transmission efficiency  $\eta_t$ . This system is representative for systems nominally operating in the low multi-photon regime. For closer targets, such as the Moon or lunar orbiters, the unattenuated signal strength will be in the high multi-photon regime, leading to less variation in mean range error (see Fig. 2). For systems nominally operating in the single-photon regime, there will be little variation in range accuracy, but extremely large degradations in normal point precision may occur (see Section 3.7). We choose to analyze a system of intermediate signal strength (nominally operating at the low multi-photon levels), as such systems are not overdesigned from a system power point-of-view, while retaining a comfortable margin of allowable signal strength degradation. Also, simulations of such a system provide us with insight into both the degradation in system accuracy due to pulses with multiple detectable photons, which will occur under weak turbulence strength conditions, as well as normal point precision degradation due to a reduction in the number of detections, which will occur under strong turbulence conditions (see Section 3.7).

For the situation without turbulence, several factors modulate the pulse detection statistics (see Section 3.6). Changes in target distance change the energy at the detector, thereby modifying the value of the number of detected photons  $N$ , see Eq. (10). Similarly, a changing zenith angle causes variations in detectable energy through changes in

Table 2: Nominal measurement statistics for turbulence-free Earth-Phobos laser link.

$\overline{\Delta s}$	$\sigma_{\Delta s}$	Detected fraction	$\overline{N}$	$\sigma_N$
-4.93 mm	5.66 mm	94.35 %	3.09	1.87

atmospheric attenuation. Finally, our statistical modelling of detection system efficiency causes pulse-per-pulse variations in  $N$ .

We investigate a broad range of values for  $C_{n(0)}^2$ , with  $0 \text{ m/s} \leq u \leq 50 \text{ m/s}$  and  $2.0 \cdot 10^{-16} \text{ m}^{-2/3} \leq C_{n(0)}^2 \leq 10^{-11} \text{ m}^{-2/3}$ . It should be noted that the  $> 10^{-12} \text{ m}^{-2/3}$  turbulence case represents rather extreme turbulence conditions. Such large ground turbulence values are only expected at daytime. Measurements of ground turbulence strength are given by Walters and Kunkel (1981), who report a mean mid-day ground turbulence value of  $7.7 \cdot 10^{-13} \text{ m}^{-2/3}$ . However, unlike in SLR, daytime ranging cannot be avoided in ILR, since the interplanetary observation geometry changes very slowly in time, with the synodic period of Earth and the target body.

In Sections 4.2-4.4, we present results for measurements made during a single day by the station Yarragadee, located in Australia, with a pulse repetition frequency of 5 Hz. The simulations are made for an entire pass a range of zenith angles of  $0^\circ$ - $75^\circ$ , so the results include the averaged effects of varying zenith angle on signal strength intensity. During the measurements, Phobos is at a distance of about 120 million km ( $\approx 0.8 \text{ AU}$ ) from Earth. For the case without turbulence, which we use as a benchmark, the simulation results are summarized in Table 2, which shows the standard deviation and mean value of the range error and number of detected photons. Note that we use the term 'detected pulse fraction' for the fraction of total pulses for which the number of detected photons  $N > 0$ . In the SLR community, the equivalent term for the two-way ranging is 'return rate'. However, since there is no return in our one-way observable, we choose to use the detected pulse fraction term instead.

## 4.2 Range accuracy

The results for the mean range errors (*i.e.* accuracy) as a function of the HV parameters  $C_{n(0)}^2$  and  $u$  (Section 3.1) are shown in Fig. 3. It can be seen that the range error is mostly influenced by the ground turbulence term  $C_{n(0)}^2$  and much less by the high-altitude wind speed  $u$ , indicating a weak dependence of accuracy on  $\mu_{u1}$  and therefore the scintillation index  $\sigma_I^2$  (Appendix B). This is clear when comparing Fig. 3 to Figs. A.1(a) and A.1(b), where a much stronger resemblance to Fig. A.1(a) than Fig. A.1(b) is observed. When interpreting Fig. 3, it must be stressed that the high turbulence conditions, which lead to a mean  $\Delta s$  of approximately zero, does not represent a better result than those at weaker turbulence conditions. The estimation of range biases, including those resulting from turbulence are typically estimated during data processing. However, time-variabilities of range biases may be difficult to remove during data analysis and can degrade estimation performance, as will be discussed in Section 5.

For strong turbulence conditions, the mean range error reaches values of nearly 0 mm, as shown in Fig. 3. This indicates that nearly all detections occur for cases where

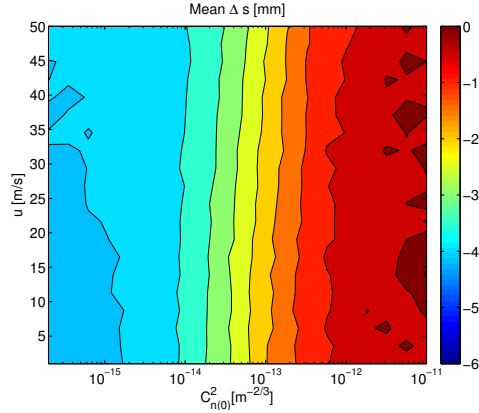


Figure 3: Results for mean range error for nominal mission scenario and varying turbulence conditions.

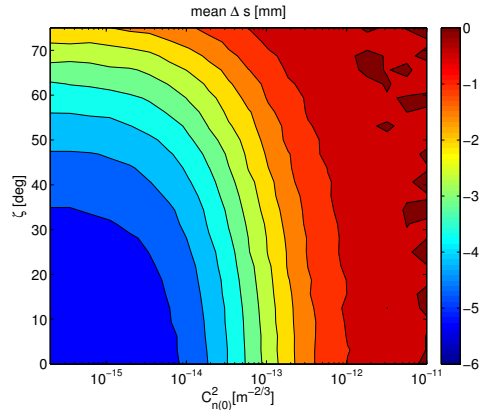


Figure 4: Results for mean range error for nominal mission scenario and varying ground turbulence strength and zenith angle.

only a single photon reaches the detector. However, it is interesting to note that even for very low energy levels, detections still occur for which  $\Delta s \neq 0$ , so where  $N > 1$ . This is due to the Poisson statistics describing the ideal distribution of  $N$ , shown in Eq. 16. The results shown here reinforce the discussion in Section 2.2, showing that true single photon signal strength is not achieved, even for  $\langle N \rangle \ll 1$ .

The lack of smoothness in the plot at large  $C_{n(0)}^2$  is due to the very small number of detected pulses under these strong turbulence conditions. The small number of data points used to numerically calculate the mean of the range error causes deviations from the ideal mean range error. For the low values of  $C_{n(0)}^2$ , the number of pulse detection is substantially higher, leading to a more robust determination of the mean range error.

The mean value of the range error can be seen in Fig. 3 to vary over a range of

roughly 3-4 mm between low ( $< 10^{-15} \text{ m}^{-2/3}$ ) and high ( $> 10^{-12} \text{ m}^{-2/3}$ )  $C_{n(0)}^2$ , with very little variation due to variations in  $u$ . The larger range error for weak turbulence conditions is due to the higher average value of  $N$  in these cases, leading to a detection earlier in the laser pulse (Sections 2.2 and 3.7). The observed range error variations between weak and strong turbulence conditions are well above the sub-mm level that are desired for interplanetary laser ranging. This indicates that time variations in the ground turbulence strength at even the moderate variation of  $10^{-15} - 10^{-13} \text{ m}^{-2/3}$  could cause a noticeable degradation of ILR system performance, which we will investigate further with simulated parameter estimation in Section 5.

The reduction in signal strength at the receiver (*i.e.* smaller value of  $N$ ) due to large  $C_{n(0)}^2$  is primarily a result of the strong increase in pointing error  $\Delta\theta$  for large  $\mu u_0$ . Both the mean value and standard deviation of the pointing error grow above values of  $100 \text{ } \mu\text{rad}$  ( $= 4\theta_{FF}$ , see Table 1) for  $C_{n(0)}^2 > 10^{-12} \text{ m}^{-2/3}$ . This reduces the signal intensity and number of detectable photons due to reduction of the ratio  $r/w(z)$  in Eq. (1). Mitigation strategies for pointing-error induced signal strength reduction will be discussed in Section 4.4. Since the beam-wander induced variations are the dominant source of strong accuracy variations, our approach of analyzing only the uplink of the two-way laser ranging system is a valid one for this conceptual analysis, since beam wander is not present in the downlink.

The results shown thus far have been generated by averaging over an entire pass, with the zenith angle  $\zeta$  between 0 and 75 degrees. Now, we will discuss the influence of the zenith angle on the accuracy by generating range statistics at various separate zenith angles  $\zeta$ . Since it was shown (see Fig. 3) that the accuracy depends only very slightly on  $u$ , we calculate the mean range accuracy as a function of  $C_{n(0)}^2$  and  $\zeta$  only, omitting the influence of  $u$  (which we set at a constant 20 m/s). The results are shown in Fig. 4. Although these results are quantitatively dependent on the zenith transmittance, which we set to 0.7, it allows us to gain general qualitative insight into the dependency of the angle on the influence of turbulence. For low elevation angles (high zenith angles), the values of  $|\Delta s|$  become smaller, as was expected since the signal attenuation reduces the number of detectable photons. The complete range of mean errors increases somewhat, since the effect of zenith angle is no longer averaged out over the entire pass. Also, for any zenith angle, the total variation in range error between low and high ground turbulence is larger than 1 mm. The influence of varying pass zenith angle, including time-correlation of the zenith-angle repeat period and periodicity of the  $C_{n(0)}^2$  variations, will be discussed in Section 5.3.

### 4.3 Range precision

The standard deviation of the pulse detection times (*i.e.* precision) as a function of turbulence strength is shown in Fig. 5(a). This standard deviation represents the variability in pulse detection time about the pulse center time (Section 2.2) and represents the precision of the range measurement from a single pulse, termed the single shot precision. For the nominal pulse length of 50 ps FWHM used here (Table 1), the impact of turbulence on the precision of the measurements is relatively small. We find a variation of about 1-1.5 mm single-shot precision between weak and strong turbulence conditions,



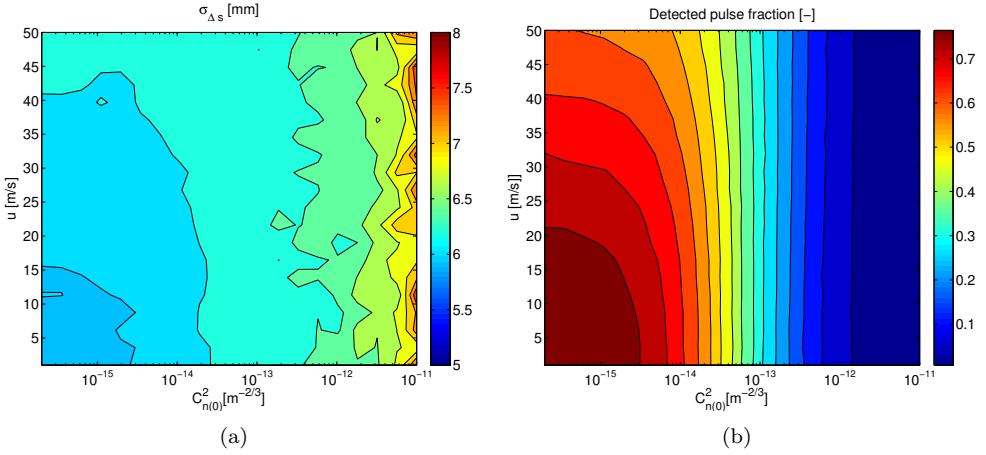


Figure 5: Results for nominal mission scenario and varying turbulence conditions of a) standard deviation of range error and b) number of detected pulses.

compared to a turbulence-free value of about 5.6 mm single-shot precision (Table 2).

The behaviour of the range precision with turbulence parameters in Fig. 5(a) exhibits a moderately stronger dependence on  $u$  than the range accuracy (see Fig. 3). This is due to the influence of scintillation on the range precision, which is determined by the strongly  $u$ -dependent  $\mu_{u0}$  integral (Appendix B). However, for larger values of  $C_{n(0)}^2$ , the variations in range measurement precision are no longer noticeably dependent on  $u$ , and are physically dominated by the strong variations in pointing angle error  $\Delta\theta$ , as was the case for the range accuracy.

Although the influence on single-shot precision is quite small, a very strong decrease in the detected pulse fraction is observed between weak and strong turbulence, as shown in Fig. 5(b). This decrease is due to the large turbulence-induced pointing error in strong turbulence. As a result, although the single-shot precision is left largely unaffected by turbulence, the normal point precision for a given time interval decreases, or alternatively the time to reach a certain normal point precision increases, because fewer pulses are detected per unit time (Section 3.7). Note that the behaviour of the detected pulse fraction in Fig. 5(b) does not show the erratic behaviour of Fig. 5(a), since it includes fewer effects causing variability, measuring only whether  $N > 0$ , not the precise range error.

As with the range accuracy, we also show the influence of the zenith angle on the precision statistics in Fig. 6, again omitting the  $u$  dependency. Although the total range of values for the single shot precision in the figure increases somewhat, when comparing it to Fig. 5(a), variations in single-shot precision for realistic turbulence values remain quite low.

Although the single-shot precision is only weakly influenced by turbulence for our nominal pulse characteristics, this is not the case for shorter pulse lengths. For such systems, the influence of turbulence on the range precision can become a more impor-

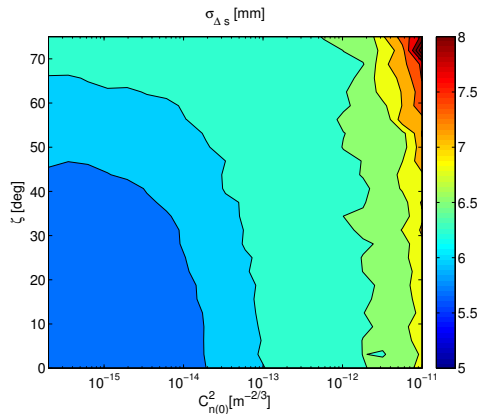


Figure 6: Results for standard deviation of range error for nominal mission scenario and varying ground turbulence strength and zenith angle.

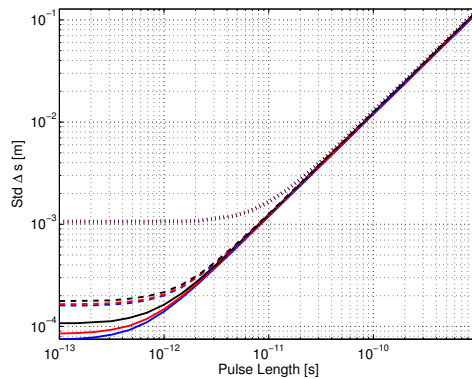


Figure 7: Variation of standard deviation of range error with pulse length, ignoring the influence of dispersion, for various turbulence conditions. Color-coded for  $u$ , blue: 1 m/s, red: 21 m/s, black 45 m/s; Linestyle-coded for  $C_{n(0)}^2$ , solid:  $10^{-16}$  m $^{-2/3}$ , dashed:  $1.7 \cdot 10^{-14}$  m $^{-2/3}$ , dotted:  $10^{-12}$  m $^{-2/3}$ .

tant contributor to the single-shot error budget, limiting the added value of shortening the laser pulse. This is illustrated in Fig. 7, where the single-shot precision is shown for various turbulence conditions as a function of pulse length. There, it is clear that in the case of strong turbulence, the system is limited to about 1 mm single-shot precision, independent of the pulse length. However, the influence of dispersion on the propagation of these ultrashort laser pulses is not included here. Since a shorter laser pulse has a broader spectrum, the atmospheric photon propagation velocity variation with wavelength limits the practical decrease of pulse lengths to the several ps-level Degnan (1993). The (relative) influence of dispersion on ILR system performance under a variety of conditions will be investigated in future research. Nevertheless, the results

shown here indicate that, even in the absence of dispersion, for instance through active compensation (Lee et al., 2011), the influence of turbulence will limit the added value of shortening laser pulses.

#### 4.4 Laser pulse parameter influence

The large pointing error variations under strong turbulence conditions were shown to be the major contributor to variations in range accuracy, range precision and detected photon fraction in Sections 4.2 and 4.3, respectively. Therefore, we will investigate the possibilities of mitigating this influence through variations of the laser pulse parameters.

The strong variations in range accuracy between small and large  $C_{n(0)}^2$  that are observed in Fig. 3 may be mitigated by increasing the beam divergence angle. An increased beam divergence angle will result in lower variations of  $r/w(z)$  in Eq. (1) for given varying turbulence-induced pointing angle errors  $\Delta\theta$ . However, for a given laser pulse energy level and nominal turbulence-free operating conditions, this will also reduce the pulse intensity at the detector, thereby reducing the pulse detection probability.

The variation of mean range error with beam divergence angle (using the nominal pulse energy of 1 mJ) is shown for a number of representative turbulence cases in Fig. 8(a). The decrease in range error difference between small and large beam divergence angles can clearly be observed. The difference is firstly caused by a decrease in the influence of a given pointing error caused by strong turbulence. Secondly, increasing the beam divergence angle without increasing the pulse energy will decrease the intensity at  $r = 0$ . As a result, there will be a decreased intensity at the detector under nominal and weak turbulence conditions, reducing the value of  $N$  and therefore the mean range error. The influence of varying the beam divergence angle on the number of registered detections is shown in Fig 9(a), which shows a strong drop-off in detected pulse fraction for larger beam divergence angles.

The behaviour in Fig. 9(a) shows (although weakly due to the log-scale plot) that for weak turbulence conditions (solid blue and red lines), the detected pulse fractions have a maximum in the 10-20  $\mu\text{rad}$  range. This is due to the fact that for smaller beams, the pointing error becomes larger than the far field divergence angle to the point where it will decrease the number of detected pulses. This behaviour is not observed for stronger turbulence conditions, since beam spread (Section 3.2) limits the beam divergence angle that is actually achieved and the actual beam divergence angle becomes dominated by the  $w_0/r_0$  term in Eq. (20).

From these figures, it is clear that a trade-off between reduced mean error variations (*i.e.* improved accuracy) and number of detections (*i.e.* improved normal point precision) must be made when selecting the divergence angle, and that considerations of turbulence must be taken into account for this. For small (smaller than 20  $\mu\text{rad}$ ) divergence angles, there is little to no increase in the number of detections, whereas for large (larger than 100  $\mu\text{rad}$ ) divergence angles, there is little reduction in mean error variation and a strong decrease in detections. These results indicate an optimal range of turbulence-limited beam divergence angles for the given mission and system.

In addition to increasing the divergence angle, the pulse energy may be reduced to mitigate the range error variations by directly reducing the number of detectable

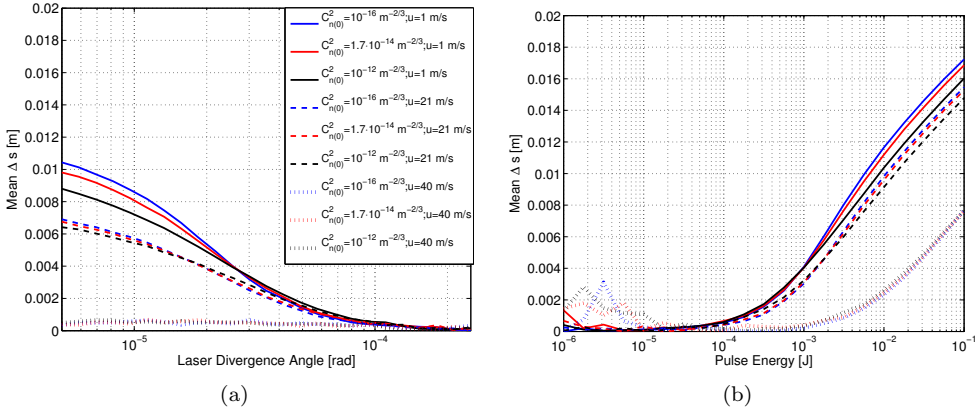


Figure 8: Mean range error for various turbulence conditions; variations with a) laser divergence angle and b) pulse energy. Color-coded for  $u$ , blue: 1 m/s, red: 21 m/s, black 45 m/s; Linestyle-coded for  $C_{n(0)}^2$ , solid:  $10^{-16} \text{ m}^{-2/3}$ , dashed:  $1.7 \cdot 10^{-14} \text{ m}^{-2/3}$ , dotted:  $10^{-12} \text{ m}^{-2/3}$ .

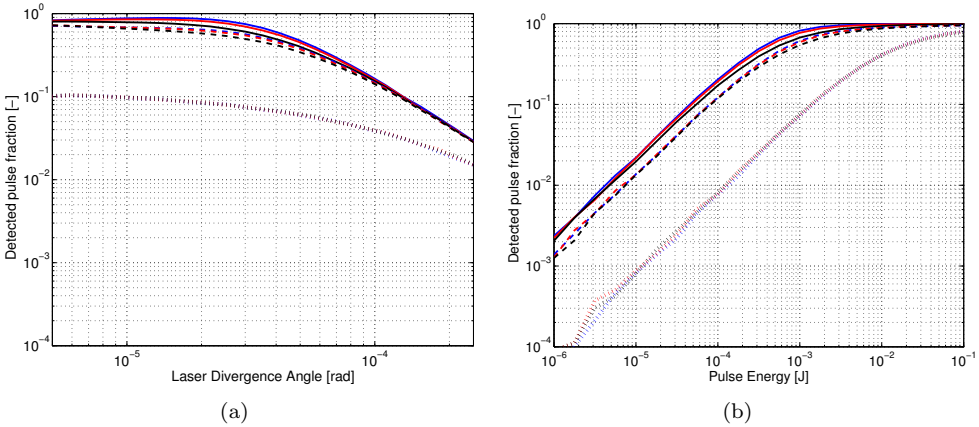


Figure 9: Fraction of detected laser pulses for various turbulence conditions; variations with a) laser divergence angle and b) pulse energy. Color-coded for  $u$ , blue: 1 m/s, red: 21 m/s, black 45 m/s; Linestyle-coded for  $C_{n(0)}^2$ , solid:  $10^{-16} \text{ m}^{-2/3}$ , dashed:  $1.7 \cdot 10^{-14} \text{ m}^{-2/3}$ , dotted:  $10^{-12} \text{ m}^{-2/3}$ .

photons and thereby the variation of the detected pulse intensity. Unlike increasing the divergence angle, it will not mitigate the fundamental reason for the strong variations in the number of detected photons per pulse  $N$ , *i.e.* the relative influence of the strong pointing errors at high values of  $C_{n(0)}^2$ . Instead, by decreasing the value of  $N$  under all conditions, the mean range error is decreased. This decrease is at the expense of a reduction in detection probability for weaker turbulence conditions, where the detection probability is quite high for our nominal scenario, degrading the normal point precision.

The effect of varying pulse energy on the mean range error and detected pulse fractions is shown in Figs. 8(b) and 9(b), respectively. The erratic behaviour for low pulse energy in the figures is again caused by the fact that only very few detections occur in these cases, causing the statistical averaging to exhibit non-smooth behaviour. In the limiting case of very low pulse energy,  $N \leq 1$  under all conditions and the mean range error will reduce to zero in all conditions. For our link conditions, it can be seen in Fig. 8(b) that for a pulse energy of less than 0.1 mJ, the mean error variation are sub-mm at all turbulence conditions, at the expense of a factor of about 5 decrease in pulse detection probability, as shown in Fig. 9(b). For an increase in pulse energy to around 10 mJ, the number of detections tends to the limiting value (detection of all pulses), with an associated mean error variation of more than 1 cm. These results of conflicting requirements for high accuracy and precision again highlight the influence of turbulence on the trade-off that must be made when selecting system parameters.

The trade-off consideration in the selection of system parameters is strongly influenced by the pulse repetition frequency of the transmitter. For a high repetition (*i.e.* kHz) laser ranging system, *e.g.* Kirchner and Koidl (2004), the system typically operates in a low pulse energy regime, for which relatively many pulses go unobserved. However, due to the large number of transmitted pulses, the total data yield is still sufficient to generate a normal point of sufficient precision within a short period of time. Therefore, such systems will more easily be able to successfully operate under conditions with a low mean value of  $N$  under a wide variety of turbulence conditions. In fact, it is shown by Degnan (2001) that distributing a given amount of power over a larger number of pulses of lower energy will result in more pulse detections, although at lower values of  $N$ , thereby improving both accuracy and precision. However, currently only a limited number of SLR stations are capable of operating at kHz repetition rates, whereas changes of pulse energy and divergence angles can be achieved in many of the existing SLR systems. Although the use of kHz systems may increase in coming years, it is likely that ILR missions will still use numerous low repetition rate systems. Similarly, the use of multi-element detectors, discussed in Section 2.2, can mitigate the influence of multiple detectable photons by providing the capability to separately detect different photons from the same pulse.

In reality, noise photons and dark noise will be detected in addition to the signal photons, which need to be filtered when processing the detections (Degnan, 1993). However, at extremely low signal detection levels, noise signals may overwhelm the signal to a point where the two can no longer be separated, providing a certain lower bound to feasible mean signal strength at the target. This will limit the applicability of reduction in pulse energy/increase in pulse frequency.

## 5 Results: parameter estimation influence

Having presented the influence of turbulence on the range accuracy and precision for a single pass of a representative interplanetary laser ranging system in the previous section, we will now present the influence of turbulence on the parameter estimation capabilities of such a mission. Our goal here is to illustrate the influence of turbulence with a specific mission test case and qualitatively discuss the expected influence of

turbulence on parameter estimation in general cases. In Section 5.1, we outline our estimation scenario and time-varying turbulence model. In Section 5.2 we present the estimation results with and without turbulence and discuss the influence of turbulence on the quality of the results. Finally, we discuss the influence of mission geometry on the effect of turbulence in Section 5.3.

## 5.1 Simulation settings

As in the previous section, we use the PLR system for our simulations, using the system parameters given in Table 1. We apply the same dynamical model for Phobos, observation model and estimation procedure as Dirx et al. (2014a), using the same software package (Dirx and Vermeersen, 2013), based on the Tudat library (Kumar et al., 2012). We use the same 8 SLR stations, each operating at a pulse repetition rate of 5 Hz, and a  $15^\circ$  elevation angle cutoff. Each station performs a single 15-minute continuous ranging arc per day, randomly generated from the viable time intervals each day. Instead of the full estimated parameter vector used by Dirx et al. (2014a), we only analyze the estimation of the state of Phobos and range biases, and do not include so-called 'consider parameters'. We take this approach as our goal here is only to obtain insight into the influence of turbulence on the performance of a typical interplanetary laser ranging mission, not to fully reanalyze the PLR mission. Biases will be important in this context to remove the mean effect of multi-photon detections (see Section 3.7). As discussed in Section 4.1, turbulence-free observations will still suffer from signal intensity variations due to changing observation geometry, so that our (per-station constant) estimated biases will not be able to fully remove the non-physical range signals from the measurements, neither in the turbulent nor turbulence-free case.

We use an arc length of 1 month for our estimation of both the state of Phobos and the observation biases, using a different observation bias for each station. We do not make the arc duration for the biases shorter, as this was found to lead to excessive correlations between the biases and the state. Estimating the biases over very long time periods, however, will reduce their capability to absorb the variations in range error due to slowly varying influences, such as the distance between the ground station and the target and possible (small) seasonal effects on Earth.

As a validation, we perform the estimation with perfect measurements, *i.e.* only limited by numerical precision, which results in sub-mm estimation errors for the initial Phobos state. To achieve this, we employ extended numerical precision (Goldberg, 1991) in our software, corresponding to a resolution of  $<0.02 \mu\text{m}$  at 1 AU. In doing so, we prevent numerical errors from being the limiting factor in software performance, which can be a concern for modern interplanetary orbit determination when using double precision floating point representations (Zannoni and Tortora, 2013).

To include the time-variability of the turbulence conditions, we set up a conceptual model for the variation of the Hufnagel-Valley (HV) parameters (Section 3.1). We note from data in *e.g.* Sadot and Kopeika (1992); Tunick (2002) that the largest variations in  $C_n^2$  occur with a daily period. Therefore, we assume only variations with a daily period in the HV parameters. Although this model neglects any shorter- or longer-period variations, our goal here is to assess the expected influence of optical turbulence on

Table 3: Summary of mean and standard deviation of true and formal errors of estimations, all values in mm.

Simulation case	Formal		True			
	$\sigma_x$	$\sigma_y$	$\sigma_x$	$\sigma_y$	$\bar{x}$	$\bar{y}$
No turbulence, bias estimation	4.9	0.5	87.8	11.9	21.6	-6.4
No turbulence, no bias estimation	3.3	0.4	59.4	8.8	202.0	-22.1
Nominal turbulence, bias estimation	6.2	0.7	86.1	12.0	21.1	-6.9
Strong turbulence, bias estimation	9.5	1.0	114.3	16.1	14.3	-9.7

planetary laser ranging links in a general sense, not to provide a quantitatively accurate prediction for a specific station or link.

We use two cases, one for moderate maximum and one for strong maximum turbulence, in which, respectively:

- $10^{-15} \text{ m}^{-2/3} < C_{n(0)}^2 < 10^{-13} \text{ m}^{-2/3}$ ;  $5 \text{ m/s} < u < 25 \text{ m/s}$ .
- $10^{-15} \text{ m}^{-2/3} < C_{n(0)}^2 < 10^{-12} \text{ m}^{-2/3}$ ;  $5 \text{ m/s} < u < 45 \text{ m/s}$ .

with a sinusoidal behaviour where the phase is determined by the local solar time. In addition to these two cases, we also use two cases without turbulence for reference purposes, one with and one without the estimation of range biases, for a total of four simulation cases.

We simulate range measurements for each of these four cases, randomly perturb the initial state of Phobos and use the simulated measurements to estimate its original value, as well as the range biases. We compare the results of the estimation with the real value of the initial Phobos state and compare the true and formal errors of the estimation. The true error is defined as the difference between the parameter value in our truth model (which was used to simulate the laser range measurements) and the parameter value produced by the estimation procedure. The formal error is obtained directly from the covariance matrix (Montenbruck and Gill, 2000). We perform 250 simulations for each case to generate an empirical statistical distribution of the true estimation error and compare it to the formal estimation error that is obtained from the covariance matrix. We use the single shot pulse standard deviation  $\sigma$  to set up the (constant) measurement weight as  $\sigma^{-2}$  for each observation in the estimation.

## 5.2 Estimation errors

The main results for the four simulation cases are summarized in Table 3, where the mean and standard deviation of the true estimation errors of the position of Phobos are shown, as calculated from 250 simulation runs, along with the formal errors obtained from the least squares estimation. Our coordinate frame is the (inertial) Ecliptic J2000 frame, representing the J2000 frame (Vallado and McClain, 2001), reoriented by a constant rotation about its  $x$ -axis, so that the  $xy$ -plane coincides with the ecliptic. Results on the  $z$ -position are omitted from this table due to the strong correlation with the  $x$ -component, as described below. We present the results in terms of Cartesian coordinates.

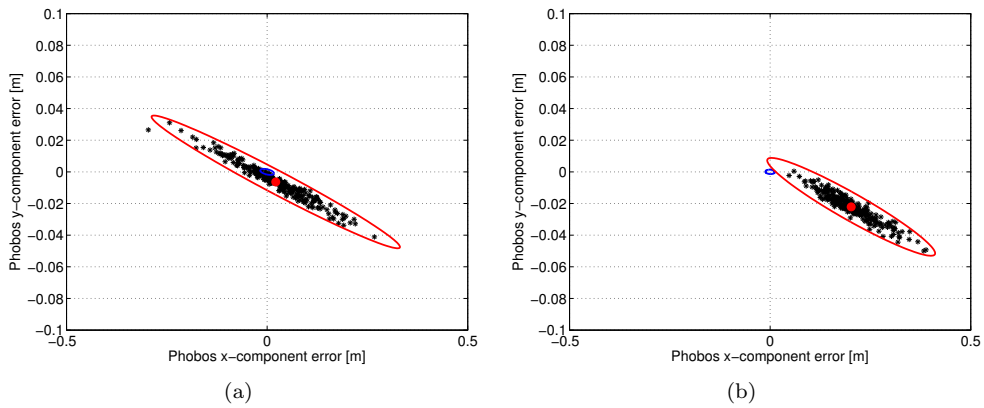


Figure 10: Scatter plot with true errors obtained from simulations without turbulence, formal error ellipse shown in blue, empirical error ellipse in red, mean value of true errors indicated by red dot; variations with a) with range bias estimation and b) without range bias estimation.

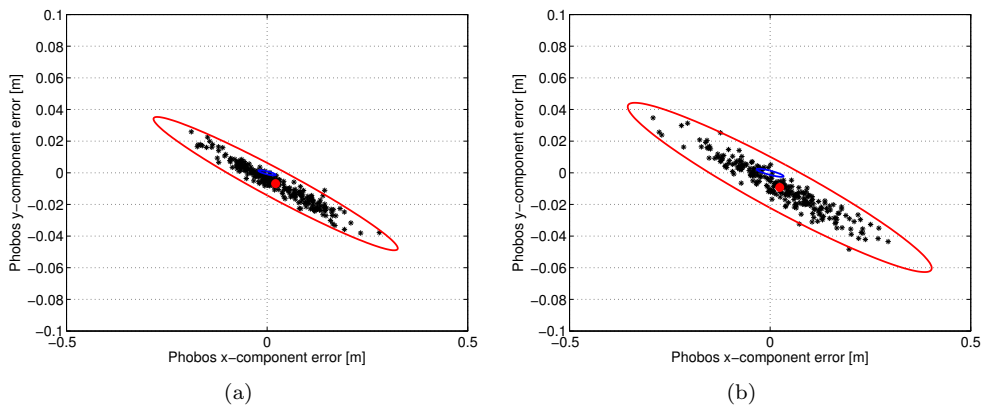


Figure 11: Scatter plot with true errors obtained from simulations with turbulence, formal error ellipse shown in blue, empirical error ellipse in red, mean value of true errors indicated by red dot; variations with a) moderate turbulence and b) strong turbulence.

For all cases, the standard deviation of the observation residual converges to the 5 mm level, which is roughly the pulse length standard deviation (Section 4.3), indicating that the estimator has removed the trends in the residuals by adjusting the estimated parameters. However, comparing the 5 mm residual level to the true accuracy and precision values in Table 3 ( $\bar{x}$ ,  $\bar{y}$  and  $\sigma_x$ ,  $\sigma_y$ , respectively), it can be seen that the true estimation error is much larger than the mean range residual after estimation. This is due to the correlations between the estimated parameters, both between the elements of the initial state and between the initial state and the observation biases. This correlation causes the estimation procedure to have too much freedom in minimizing the residuals



by adjusting parameters, thereby leading to true estimation errors that are much larger than the residuals. This problem of near-singular behaviour in the normal equations of orbit determination for planetary satellites is inherent in its unfavorable observation geometry, as discussed in detail by Bonanno and Milani (2002).

We find that the correlation coefficients between the  $x$ - and  $z$ -components of the initial position are  $> 0.99$ , indicating that these parameters cannot be properly estimated independently from a 1-month arc, but only a weighted combination of the two can be realistically obtained. We will present the estimation errors only in the  $xy$ -plane, omitting the  $z$ -component, but noting that we find  $\sigma_z \approx 2\sigma_x$ .

The formal and true error ellipses for the simulations without turbulence are shown in Fig. 10, with and without the estimation of a bias. It is clear that the true error is at least an order of magnitude larger than the formal error in both cases, as can also be seen in Table 3. This is the result of non-Gaussianity and time-correlation of the true error distribution, which should be understood to be distinct from the parameter correlations discussed earlier. In reality, the differences between the truth and estimation models will result in additional differences between the two errors. However, we keep the dynamical and observation models equal in both cases, to focus on the influence of the non-Gaussian observation errors.

Although the true error ellipse is smaller for the estimation without bias estimation (Fig. 10(b)) than in the case with bias estimation (Fig. 10(a)), the mean estimation error is quite large, at more than 25 cm total, since the observation biases are absorbed and amplified, as also found by Dirkx et al. (2014a), into an erroneous estimation of the initial state. When including the biases, the mean total error reduces, but at the expense of an increase in the size of the error ellipse, induced by the correlations between the biases and the initial state. Nevertheless, these results show that even in the absence of turbulence the inclusion of a bias, either *a priori* or through estimation, is important to prevent observation errors from being interpreted as signals from physical parameters.

The error ellipses for two turbulence cases are shown in Fig. 11. In these figures, the relative difference of the true and formal errors is slightly smaller than for the case without turbulence, which is to be expected, since observations are on average made at a lower signal intensity level and will therefore more closely resemble a Gaussian distribution (Section 2.2). The increased size of the formal error ellipse, when compared to the nominal case, is due to the reduction in number of detected pulses. Therefore, the determination of a formal to true error correction factor that is typically applied in the interpretation of interplanetary orbit determination results, *e.g.* (Marty et al., 2009; Konopliv et al., 2011), should include turbulence effects for ILR data.

Although the results for nominal turbulence conditions shown in Fig. 11(a) indicate a slightly larger spread of estimation errors than for the case without turbulence depicted in Fig. 10(a), the differences remain relatively small. The majority of the estimation errors are caused by the detection time errors inherent in the geometry and hardware characteristics of the mission, *i.e.* those already present in turbulence-free conditions. Also, the correlations between parameters degrades the solution to a level where small variations in range accuracy due to turbulence are not dominant true error sources in the estimation. This indicates that, despite the range accuracy variations which were found in Section 4, turbulence will not be a significant contributor to the estimation error

budget of this scenario for the case where  $C_{n(0)}^2 < 10^{-13} \text{ m}^{-2/3}$  and  $u < 25 \text{ m/s}$ . Firstly, this is due to the fact that non-turbulent effects cause the detection statistics to be non-Gaussian (multi-photon detections) and time-dependent (atmospheric attenuation variations with zenith angle). Additionally, due to strong correlations between the repeat period of the target visibility and the turbulence cycle, potential turbulence-induced effects are moderated, as will be discussed in Section 5.3.

The results of our second case, where the maximum HV parameters are increased, are shown in Fig. 11(b). It can be seen that the spread of the solutions has noticeably increased due to the stronger turbulence, which leads to both fewer measurements and larger accuracy variations. This can also clearly be seen in Table 3, which shows increases up to 50 % in the true error standard deviations compared to moderate turbulence. The strong increase in the relative strength of turbulence due to the increase in the maximum HV model parameters cannot be directly associated with a similarly strong change in range accuracy (Section 4.2). In fact, the change in single pass range accuracy in Fig. 3 is similar when moving from  $10^{-14}$  to  $10^{-13}$  as when moving from  $10^{-13}$  to  $10^{-12}$ . However, the full range in possible ground turbulence strengths is not influential for many ground stations, as will be discussed in more detail in Section 5.3. In essence, although large range accuracy variations are possible, also in the moderate turbulence case, they will occur only on a very irregular basis and the average turbulence strength variations that are influential for the range variations will be accordingly smaller, corresponding on average to the cases of lower  $C_{n(0)}^2$  in Fig. 3, where there is less variation of range error with HV parameters.

We also see in Fig. 11 that the formal error ellipse of Phobos' initial position is larger due to the reduction in the number of detections. When inspecting the error ellipse, it is clear that it is less flattened in the stronger turbulence case. This indicates a lower correlation between the  $x$ - and  $y$ -component that is obtained for the true errors. The reason for this is that, due to the larger range error variations, the estimation needs to compensate for additional fluctuations in the apparent dynamics of Phobos, inducing a non-physical error.

These results indicate that, for the mission analyzed here, turbulence-induced errors will, for  $C_{n(0)}^2 \leq 10^{-13} \text{ m}^{-2/3}$  and  $u < 25 \text{ m/s}$ , be of minor concern compared to inherent sources. However, a substantial increase is observed when increasing the maximum ground-level turbulence to  $10^{-12} \text{ m}^{-2/3}$ . Although these ranges will not hold for all mission and system designs, it indicates the existence of turbulence strength values below which the estimation procedure is not significantly influenced by turbulence. The range of turbulence parameters at which their effects must be taken into account can be varied by changing the mission and system parameters, including ground station location selection. As such, it can again be seen that it can be important to analyze turbulence-induced errors during the system design and include these effects during the design trade-off, thereby potentially modifying it in such a manner that its influence is only a minor contributor to the science return error budget. As discussed in Section 4.4, kHz repetition rate SLR systems can operate at signal levels where the occurrence of multiple detectable photons is much less frequent, providing such systems with a clear advantage of mitigating the influence of signal strength variations on parameter estimation quality. Similarly, multi-element detectors can mitigate the influence of detection at energies for

Table 4: Range error statistics per station per pass for the two turbulence estimation cases.

Station	$\zeta_{\min}$ [deg]	$\zeta_{\max}$ [deg]	Nominal turbulence			Strong turbulence		
			$\overline{\Delta s}$ [mm]	$\sigma_{\Delta s}$ [mm]	$\Delta_{max}$ [mm]	$\overline{\Delta s}$ [mm]	$\sigma_{\Delta s}$ [mm]	$\Delta_{max}$ [mm]
1	8.3	70.3	-2.9	6.1	4.0	-2.4	6.3	5.2
2	71.3	74.7	-1.8	6.3	1.6	-1.3	6.4	2.1
3	63.4	74.3	-1.7	6.3	2.5	-0.7	6.4	2.4
4	0.2	62.4	-4.8	5.9	4.6	-3.6	6.1	6.1
5	60.0	74.0	-1.4	6.4	1.2	-0.4	6.5	0.9
6	65.2	72.5	-2.4	6.3	1.8	-1.8	6.3	2.2
7	55.0	74.6	-2.0	6.3	2.1	-0.7	6.4	1.8
8	4.3	74.4	-2.9	6.2	2.8	-1.3	6.4	3.5

which the number of detectable photons is  $> 1$  by allowing the separate photons to be detected by separate elements.

The case which is tested here is one where the laser pulse detections will regularly occur at the multi-photon level, causing turbulence-induced variations in mean true range error with time, as discussed in Section 4.2. Although there is also a clear increase in the formal error due to the reduction in the number of detections, this effect is not dominant in the change in estimation error. However, for other mission and system parameters, the detections may be inherently single-photon, in which case the range errors will be largely unbiased. In such cases, turbulence will result in fewer photon detections, degrading the system performance directly by a reduction of precision, as discussed in Section 4.3.

### 5.3 Ground station geometry

In the previous section, it was shown that the turbulence-induced range error becomes a significant contributor to the total estimation error budget from a certain turbulence variation amplitude onward. However, this effect proved difficult to relate to the single pass range accuracy variations shown in Section 4.2. In this section, we will analyze and discuss the influence of the specific measurement geometry of each ground station to elucidate the estimation error behaviour.

The measurement statistics per station for the two turbulence cases are shown in Table 4, including the difference in range error between the pass with the largest and that with the smallest mean range error of a single station, denoted here as:

$$\Delta_{max} = (\max - \min) (\overline{\Delta s}_{\text{pass}}) \quad (40)$$

This difference is an indicator of the pass-to-pass range error variations. It is these range error variations that cause fluctuations in the range measurement error that cannot be fully absorbed by the bias estimation. For each station, the range of zenith angles at which observations are made is also shown.

It can be seen from Table 4 that the zenith angle range can be very limited for some stations. This is due to the time of year and the mission type that is analyzed. For stations measuring in (mid-)winter, the angle between the vector from the geocenter to

the stations and the ecliptic can become quite large  $\approx 23.5^\circ + |\phi|$ , with  $\phi$  the station latitude. As a result, these stations cannot observe targets near the plane of the ecliptic at small zenith angles during part of the year. Relatively few SLR stations are located on the equator and the vast majority of interplanetary missions are performed near the plane of the ecliptic. Therefore, the small ranges of zenith angles that we get for a number of stations are rather common for planetary laser tracking.

For the turbulence-free case, zenith angle variations are an important source of signal strength variations, due to their influence on the atmospheric attenuation, whereas turbulence is not directly influenced by the zenith angle. However, when comparing the maximum range error difference between passes in nominal and strong turbulence in Table 4, an effect of station zenith angle range on the influence of turbulence is observed. Specifically, for stations that can only observe at a small range of zenith angles, the increase in maximum pass range error difference is relatively small, at about 0.5 mm. For stations with a full zenith angle range, this difference can be larger than 1 mm. The cause for this lies in the visibility conditions. For the stations which observe Phobos at large zenith angles, there will be a relatively short time interval every day where Phobos is at a sufficiently small zenith angle to be observed, leading to a nearly daily period of observations. However, since the turbulence strength variation cycle is also daily, the majority of the variations in turbulence strength goes unobserved. That is, the stations with small elevation angle ranges will only experience small differences in turbulence-induced measurement statistics variations. For the stations which observe Phobos at a larger variety of zenith angles, the times of day when observations are made are not as restrictive. In essence, the measurement geometry automatically induces a moderation of signal strength variation. However, in reality effects such as atmospheric attenuation variations and non-daily turbulence variations will also result in signal intensity variations that are not modelled here.

## 6 Conclusions

We have presented the results of simulations to analyze the influence of atmospheric turbulence on the performance of planetary laser ranging systems, using a Phobos Laser Ranging mission as representative test case. We have taken mean intensity profile variations, scintillation, beam-wander induced pointing errors and stochastic time-of-flight variations into account. Using the Hufnagel-Valley turbulence profile model, we calculated the influence of turbulence on range accuracy and precision as well as parameter estimation performance.

We find that for our mission test case, turbulence-induced signal strength variations cause a variation in range error of 3-4 mm between weak and strong turbulence conditions. Nearly all strong accuracy variations are due to variations in ground turbulence strength  $C_{n(0)}^2$ , with little to no influence of the mean wind velocity. The magnitude of the turbulence-induced variations are at a level where they could be a significant contributor to an ILR error budget, which aims at sub-mm range accuracy. Influence of turbulence on single-shot precision is relatively small, at about 1 mm increase, compared to a nominal value of 5.6 mm. However, strong turbulence conditions cause a strong decrease in the detected pulse fraction, reducing the number of pulses that can be used

to generate a normal point.

The primary contributor to turbulence-induced accuracy and detected pulse fraction variations is found to be the turbulence-induced pointing error. We have analyzed the influence of increasing the divergence and decreasing the pulse energy to mitigate the variations, leading to an increase in accuracy and a decrease in normal point precision. This indicates the influence of turbulence on the trade-off process of ILR system and mission design, which is strongly influenced by the pulse repetition rates that are available at the ground station. When operating at the single-photon detection energy across all turbulence scales, accuracy variations tend to zero, at the expense of a strong reduction in pulse detection probability. Such an approach would be feasible for kHz laser ranging systems. However, due to the Poisson statistics that govern the number of detected photons, multi-photon detections will even occasionally occur for cases of very low detectable energy levels. The use of a multi-element photon detector would allow for a mitigation of the influence of pulses at a higher than single-photon energy level by spreading the multiple photons over different detector elements.

We have performed the parameter estimation of the PLR mission, estimating Phobos' initial state and a bias for each ground station, under no-turbulence conditions, moderate turbulence conditions and strong turbulence conditions. We find that the difference in true estimation error increases only weakly when including moderate turbulence for the simulated observations. This indicates that it is not a leading contributor to the error budget in such cases. For strong turbulence, however, we find that the true estimation error increases by up to 50 %. This indicates that the influence of turbulence cannot be neglected from a certain turbulence strength onwards, which we have quantified for the PLR mission. However, the precise turbulence strength at which the contributions become significant varies strongly with mission and system parameters.

## Acknowledgements

DD is financed by the FP7 ESPaCE project, financially supported by the EC FP7 Grant Agreement 263466. We thank an anonymous reviewer for detailed comments which helped to improve the clarity and rigour of this manuscript.

## Appendix A Far-field criterion

In this Appendix, we give a derivation of the conditions under which the contributions of a non-zero  $\Theta$  to the integral  $\mu_{ul}$  in Eq. (25) becomes negligible. The dependence of the integral on the target distance is indirect through the dependence on  $z$  of  $\Lambda$  and  $\Theta$ .

In the far-field,  $\Lambda \ll 1$ ,  $\Theta \ll 1$  and  $\Theta/\Lambda \ll 1$ , indicating that  $\Theta$  tends to zero more quickly than  $\Lambda$ . For  $\Theta = 0$ , Eq. (25) correctly predicts the turbulence in the far field. However, for  $\Lambda = 0$ , the integral evaluates to a constant for all  $w_0$ , which is inconsistent with the full results. Therefore, we conclude that we must derive conditions under which the  $\Theta = 0$  assumption is valid when evaluating Eq. (25).

To derive the far-field condition, we note from the functional form of the integral that for the case where the influence of  $\Theta$  becomes small there is very little coupling between

the influences of  $\Lambda$  and  $\Theta$  on  $\mu_{u1}$ . Therefore, the condition under which  $\mu_{u1}(\Lambda, \Theta)$  has a negligible contribution of  $\Theta$  will be approximately equal to that under which  $\mu_{u1}(\Lambda = 0, \Theta)$  has a negligible contribution of  $\Theta$ . Therefore, we set  $\Lambda = 0$  in Eq. (25) and derive a condition where the near field effects of this reduced integral are negligible. For far-field conditions, the Rytov variance  $\sigma_B^2$  reduces to a value that is independent of both  $z$  and  $w_0$ , so we expect (see Eq. 24):

$$\mu_{u1} \sim z^{-5/6} \quad (41)$$

The term  $\mu_{u1}$  from Eq. (25), expressed using Eq. (26), may be written as a combination of terms of the following form, assuming the HV  $C_n^2$  profile from Eq. (17):

$$\mu_{u1} = \Re(i^{5/6}) \int_0^\infty Ah^M \exp\left(\frac{-h}{C_h}\right) (1 - (1 - \Theta)\xi)^{5/6} dh \quad (42)$$

$$= \Re(i^{5/6}) \int_0^\infty Ah^M \exp\left(\frac{-h}{C_h}\right) \Theta^{5/6} \left(1 - \frac{1 - \Theta}{\Theta} \frac{h}{H}\right)^{5/6} dh \quad (43)$$

$$= \Re(i^{5/6}) \Theta^{5/6} \frac{\Theta H}{1 - \Theta} \int_0^\infty Ah'^M \exp\left(\frac{-h'}{C_h} \frac{\Theta H}{1 - \Theta}\right) \cdot \dots \cdot (1 - h')^{5/6} dh' \quad (44)$$

The integral in Eq. (44) is an expression for the confluent hypergeometric function of the second kind, denoted  $U(a; c; z)$ , Abramowitz and Stegun (1964), so that:

$$\mu_{u1} = A \Re(i^{5/6}) \Theta^{5/6} \frac{\Theta H}{1 - \Theta} U\left(M + 1; 17/6 + M; \frac{\Theta H}{C_h(1 - \Theta)}\right) \quad (45)$$

The function  $U(a; c; z)$  has the following asymptotic behaviour:

$$U(a; c; z) \sim \frac{\Gamma(c-1)}{\Gamma(a)} z^{1-c} + O(z^{c-2}), \quad z \ll 1 \quad (46)$$

Assuming the dominant influence of Eq. (17) on determining the far-field criterion is the ground-level turbulence ( $M = 0$ ), the following is obtained:

$$\mu_{u1} \sim \Theta^{5/6} \left(\frac{\Theta H}{C_h(1 - \Theta)}\right)^{-5/6} \quad (47)$$

$$\sim H^{-5/6} \sim z^{-5/6} \quad (48)$$

which is the expected asymptotic behaviour of Eq. (41).

Now, an algebraic criterion can be derived for the region in the  $w_0$ - $h$  plane where the contribution to  $\mu_{u1}$  of the non-zero value of  $\Theta$  is non-negligible. To this end, we set:

$$\frac{\Theta H}{C_h(1 - \Theta)} \ll 1 \quad (49)$$

which can be reduced to the following approximate condition by applying Eqs. (5) and (6):

$$z \gg \left(\frac{kw_0^2}{2}\right)^2 \frac{1}{C_h} \quad (50)$$

which is the far-field criterion that is sought.

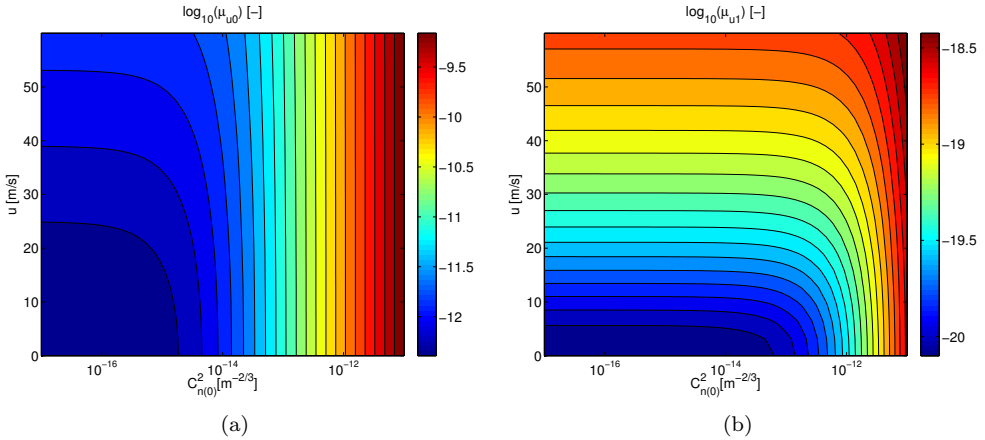


Figure 1: Behaviour of  $\mu_{u0}$  and  $\mu_{u1}$  integrals over a range of HV model parameters. (Note that  $\mu_{u0}$  and  $\mu_{u1}$  have been non-dimensionalized by division with  $1 \text{ m}^{-2/3}$  before taking the logarithm).

## Appendix B Turbulence profile parameter integrals

Using the models presented in this paper, the influence of turbulence strength on the laser range measurement error statistics for given link parameters is determined by the integrals  $\mu_{u0}$  and  $\mu_{u1}$  from Eqs. (22) and (25). Here, we investigate the behaviour of these two integrals with the parameters of the HV model:  $u$  and  $C_{n(0)}^2$  (see Eq. 17). The behaviour of the integrals is plotted in Fig. 1, where it must be noted that even for vanishing  $C_{n(0)}^2$  and  $u$ , the turbulence profile is non-vanishing due to the second term in Eq. (17), which is independent of the model parameters.

In Fig. A.1(a), it can be seen that  $\mu_{u0}$  exhibits a much stronger variation with  $C_{n(0)}^2$  than with  $u$  for moderate to strong ground turbulence ( $C_{n(0)}^2 > 10^{-14}$ ). The parameter  $\mu_{u0}$  is used to determine the beam-wander induced pointing errors (see Section 3.3) and stochastic time-of-flight variations (see Section 3.4), indicating that under strong turbulence conditions these parameters will have little to no dependence on the vertical wind profile.

In Fig. A.1(b) the variation in  $\mu_{u1}$ , from which the scintillation index is derived (see Section 3.3), is shown for a range of HV parameters. It can be seen that the dependence on  $u$  is dominant for moderate to small  $C_{n(0)}^2$ . The dependence on  $C_{n(0)}^2$  only becomes important for  $C_{n(0)}^2 > 10^{-13}$ , *i.e.* in strong ground turbulence conditions.





## CHAPTER 6

---

### Paper III - One- and Two-way Laser Ranging

---

*[T]here was gravity, friction and inertia. The physical world was one vast, tangled obstacle course of pointless, arbitrary restrictions.*

– Greg Egan, *Diaspora*, (Millennium, 1997)



# Comparative Analysis of One- and Two-Way Planetary Laser Ranging Concepts

*D. Dirkx<sup>a</sup>, R. Noomen<sup>a</sup>, P.N.A.M. Visser<sup>a</sup>, S. Bauer<sup>b</sup>, L.L.A. Vermeersen<sup>a</sup>*

Accepted for publication in *Planetary and Space Science*, June 2015

## Abstract

We numerically investigate the performance of one- and two-way active planetary laser ranging systems. We simulate range measurement errors for both types of systems, using clock error time histories generated from Allan variance profiles. We use two test cases: a lunar polar orbiter and a Phobos lander. In the Phobos lander simulations, we include the estimation of Phobos librations and  $\bar{C}_{2,2}$  gravity field coefficient. For the lunar orbiter, we include an empirical force-error model in our truth model. We include the estimation of clock parameters over a variety of arc lengths for one-way range data analysis and use a variety of state arc durations for the lunar orbiter simulations. For the lunar orbiter, performance of the one- and two-way system is similar for sufficiently short clock arcs. This indicates that dynamical-model error, not clock noise, is the dominant source of estimation uncertainty. However, correlations between the clock and state parameters cause an exchange between clock and state signal for the one-way system, making these results less robust. The results for the Phobos lander show superior estimation accuracy of the two-way system. However, knowledge of Phobos' interior mass distribution from both the one- or two-way system would currently be limited to the same level by inaccuracies in our knowledge of Phobos' volume. Both the lunar orbiter and Phobos lander simulations show that the use of two-way planetary laser ranging should be accompanied by improvements in associated measurements and models to allow this data type to be exploited to its full potential.

## 1 Introduction

The determination of the orbits of interplanetary satellites is traditionally done using radiometric tracking techniques (Moyer, 2000; Thornton and Border, 2000; Asmar et al., 2005), in which radio signals, typically in S-, X- and/or Ka-band are transmitted from a ground station to the space segment, (and/or *vice versa*). The primary observable used in planetary spacecraft orbit determination is typically a Doppler measurement, which represents a differenced range rate, *i.e.* the change in range, integrated over a certain time, ranging from 1 s *e.g.* (Mazarico et al., 2012) to more than 1000 s *e.g.* (Iess et al., 2009). Doppler data may be supplemented by range measurements (typical accuracy about 1 m) obtained from a coded radio signal or by  $\Delta$ DOR (Thornton and Border, 2000) or VLBI (Duvet et al., 2012) observations, both of which are angular observables generated by the concurrent observation of the same radiosignals by a (global) set of radio telescopes. Analysis of the tracking data of interplanetary spacecraft and landers

---

(a): Delft University of Technology, The Netherlands

(b): DLR Berlin, Germany

has contributed greatly to achieving the scientific objectives of planetary missions, for instance for deducing gravity fields and their temporal variations (Marty et al., 2009; Lemoine et al., 2014), as well as for measuring rotational variations of solar system bodies (Kuchynka et al., 2014) and experimental gravitational physics (Will, 2014).

The use of laser ranging has been proposed for use over interplanetary distances (Degnan, 2002), extending the use of Satellite Laser Ranging (SLR) and Lunar Laser Ranging (LLR) to Interplanetary Laser Ranging (ILR). This will potentially allow an orders-of-magnitude improvement in the accuracy and precision of interplanetary range measurements (compared to traditional radiometric tracking data). Single shot measurement accuracy could potentially be at the order of several mm for ILR, with attainable single shot precision at or below the mm-level attainable for moderate integration times of one minute (Turyshev et al., 2010). However, the use of reflectors in SLR and LLR is not feasible at planetary distances due to the inverse fourth-power dependency of received signal strength with distance (Degnan, 1993). Instead, an active space segment is required, reducing the signal-strength dependency to inverse square with distance. In a one-way laser range system, only a receiving system is required on the spacecraft and the observable is directly obtained from the uplink light-time. For two-way systems, a transmitter is additionally needed on the space segment, which is used to (asynchronously) fire laser pulses to the ground station(s) (Degnan, 2002; Dirkx et al., 2014a). Using such a system, the two-way range observable is realized through pairing of the up- and downlink light-times (Birnbaum et al., 2010).

The primary difference in error budget between the one- and two-way systems stems from the different influence of clock noise on the observables. For the one-way system, clock noise in both the transmitting and the receiving system accumulates over time, in a similar manner that dynamical model errors accumulate in spacecraft orbit determination. For two-way range systems, this clock noise accumulation only occurs over a limited time, specifically the two-way light-time for the ground station clock noise and the retransmission time for the space segment clock noise.

One-way laser ranging has been used for tracking the Lunar Reconnaissance Orbiter (LRO) spacecraft (Zuber et al., 2010), which used a novel link between receiver optics mounted on the high-gain antenna and its laser altimeter. However, orbit determination of LRO was initially performed using classical radio tracking and altimeter crossovers only, due to the difficulties in processing the one-way laser ranging measurements, as well as the unexpectedly high quality of the radio -science data (Mazarico et al., 2012). Recent progress in including the laser ranging data into LRO orbit determination, as well as efforts to produce laser-only orbits, have shown the feasibility of using this data type for producing high-quality spacecraft trajectories (Mao et al., 2013; Bauer et al., 2014). The concept of two-way laser ranging has been demonstrated by the MESSENGER spacecraft en route to Mercury (Smith et al., 2006) using its laser altimeter system to both detect laser pulses from Earth and transmit pulses to a ground station from a distance of 24M km.

The use of two-way laser ranging has been proposed for ultra-precise tracking in a number of mission concepts, such as Phobos Laser Ranging (PLR) (Turyshev et al., 2010) and GETEMME (Oberst et al., 2012). Analyses of the attainable parameter estimation quality of the PLR mission for relativistic parameters (Turyshev et al., 2010)

and geophysical parameters of the Martian system (Dirkx et al., 2014a) indicate that substantial gains in science return can be made by using this technology, compared to results from radiometric methods.

However, detailed analyses of the error budgets of ILR systems have not been performed to date, whereas such analyses are crucial for understanding the limitations in its applicability, the required technology development for its implementation and its expected science return. Due to the absence of retroreflectors in ILR, and the inclusion of active space segment hardware, the relative contributions of the various sources of range errors will be different than for SLR and LLR. Although mm-level precision over one minute integration-times (Turyshv et al., 2010) are likely feasible, attaining a measurement accuracy at this level will prove to be more difficult. For instance, (Dirkx et al., 2014b) showed that atmospheric turbulence and variable detection energy can already result in accuracy degradations of several mm. It has been shown by Dirkx et al. (2014a) that systematic range errors (accuracy degradation) at or even well below the mm-level can result in a much reduced attainable estimation accuracy, compared to perfectly accurate mm-precise range measurements. That is, range measurements with 0 mm precision and 1 mm systematic error will result in substantially larger estimation uncertainties than measurements with 1 mm precision and 0 mm systematic error. This difference between attainable true error and formal error is well acknowledged in literature on tracking data processing of current planetary missions *e.g.* (Marty et al., 2009). To obtain realistic insight into the potential of planetary laser ranging systems, it is crucial to properly include non-Gaussian errors in both observation models and dynamical models.

In this paper, we investigate the influence of signal timing errors on the performance of both one- and two-way laser ranging systems by quantifying the mapping of uncertainties in the clock stability to parameter estimation accuracy. Using these results, we compare the performance of one- and two-way laser ranging systems, for which the primary difference is in how clock errors accumulate in the range measurements. For our simulations we use both a lunar orbiter and a Phobos lander as test cases. In Section 2, we present models for simulating the timing of the transmission and reception of laser pulses, with a specific emphasis on modelling the influence of stochastic clock noise. Methods for modelling and measuring one- and two-way range measurements are given in Section 3. The settings and assumptions for our simulations of both the lunar orbiter and the Phobos lander are presented in Section 4, and results for the performance of both the one- and two-way range systems are presented in Sections 5 and 6 for the lunar orbiter and the Phobos lander, respectively. Finally, Section 7 will summarize the main conclusions of this study. Mathematical details of the method we use to generate coloured noise time series are provided in Appendix A.

## 2 Signal timing

Both one- and two-way range measurements are obtained directly from time tags of signal transmission and reception on the space and ground segments. By processing and combining these time tags, the observables are formed, as will be described in more detail in Section 3.2. Here, we will discuss the model we use for the clocks registering the

time tags, from which we can (statistically) quantify the difference between actual and observed measurement times and observables. First, we briefly review the conversion between observable (proper) time and global (coordinate) time in Section 2.1. Subsequently, we present the models we use to quantify clock errors in Section 2.2 and our method to generate stochastic clock noise in Section 2.3. Finally, we discuss the use of estimated arc-wise clock parameters to mitigate clock noise in Section 2.4.

## 2.1 Time scales

The clocks carried by the observers ideally register their local proper time, which is the relativistic concept of time experienced by an observer. The rate at which an observer's proper time passes, compared to a global (coordinate) time is different for observers at different relative potentials and velocities due to relativistic effects *e.g.* (Soffel et al., 2003; Kopeikin et al., 2011).

For generating range observables, measured proper times need to be converted to a global time scale, such as Dynamical Barycentric Time (TDB) or Barycentric Coordinate Time (TCB), which are independent variables in which planetary ephemerides are typically expressed *e.g.* (Moyer, 2000; Fienga et al., 2009). It should be noted that although TDB is typically used as a global time, it is *not* a coordinate time, leading to a rescaling of for instance gravitational parameters. The full ramifications of this are discussed in detail by (Klioner, 2008). The conversion from proper time to global time may be performed by precalculated time ephemerides, such as those given by Irwin and Fukushima (1999) or by integration of the proper time equation (Soffel et al., 2003). In this paper, we will assume that the conversion from proper time  $\tau$  to global time  $t$  is known to sufficient accuracy so that its uncertainties contributes only negligibly to the timing error budget.

## 2.2 Clock model

An ideal clock measures the elapsed local proper time  $\tau$  since some reference proper time epoch  $\tau_0$ . However, all clocks suffer from instabilities, desynchronizations, *etc.*. As such, it actually registers a measured proper time  $\tilde{\tau}$ , which differs from the ideal time measurement as follows:

$$\tilde{\tau} = \tau + \Delta\tau \tag{1}$$

$$= \tau + \Delta\tau_s + \Delta\tau_d \tag{2}$$

where we have distinguished between stochastic and deterministic errors,  $\Delta\tau_s$  and  $\Delta\tau_d$ , respectively.

The stochastic error term  $\Delta\tau_s$  consists of oscillator variability which is inherently stochastic and cannot be removed by calibration. We will discuss the models for the stochastic clock noise in Section 2.3. In this context, we consider deterministic terms to be those errors that could, in principle, be removed by calibration of the clock output.

Here, we model the deterministic clock errors as a polynomial series from of  $2^{nd}$

order, *i.e.*:

$$\Delta\tau_d = \sum_{i=0}^2 \Delta\tau_d^{(i)} (\tau - \tau_0)^i \quad (3)$$

representing the combination of clock bias  $\Delta\tau_d^{(0)}$ , drift  $\Delta\tau_d^{(1)}$  (frequency bias) and aging  $\Delta\tau_d^{(2)}$  (frequency drift). This is an approach that is typically taken for data processing of one-way laser ranging data to the LRO satellite (Mao et al., 2013; Bauer et al., 2013). Similar clock error parameterizations are also used in clock calibration during GNSS data analysis *e.g.* (Huang and Zhang, 2012). However, clock parameter estimation for one-way planetary laser ranging missions differs from GNSS clock estimation in a number of crucial points. Firstly, the data volume for laser ranging systems is much lower and less isotropic than for GNSS. Secondly, the measurement geometry of planetary missions is much less favorable than for Earth orbiters, complicating the orbit estimation process. Thirdly, complementary orbit determination data types of comparable accuracy will not be available in planetary missions using laser ranging, since ILR is expected to provide range measurements that are order(s) of magnitude more accurate than existing tracking techniques (Section 1).

For the inclusion of laser ranging data in the LRO orbit determination process (Mao et al., 2013), ground station and satellite clock parameters are included in the estimated parameter set. Typical values for the drift and aging of the LRO clock are  $7 \cdot 10^{-8}$  s/s and  $1 \cdot 10^{-16}$  s/s<sup>2</sup>, respectively, translating into line-of-sight velocity and acceleration biases of 21 m/s and  $3 \cdot 10^{-8}$  m/s<sup>2</sup>, respectively. In particular the value of the direct drift-induced effect is orders of magnitude beyond the required accuracy of the LRO orbit, necessitating the removal of these clock errors from the range data.

### 2.3 Stochastic noise generation

As discussed in the previous section, oscillator behaviour includes a stochastic term  $\Delta\tau_s$ , see Eq. (2). In this study, we aim to analyze the influence of (stochastic) clock noise on the estimation performance of one- and two-way ILR missions. To achieve this, we generate realizations of the stochastic processes governing this error source, which we subsequently use to create realizations of the range-measurement time-history. The clock noise shows time-correlated behaviour, so that we cannot simply generate independent realizations of a single random-number distribution. In this section, we present our models for generating time-correlated clock noise.

An oscillator provides an output signal that is used to keep time. The amplitude  $A(\tau)$  of this signal can be modelled as follows (Barnes et al., 1971):

$$A(\tau) = A_0 \sin(\omega_0\tau + \phi_0 + \Delta\phi(\tau)) \quad (4)$$

$$\omega_0 = 2\pi\nu_0 \quad (5)$$

where  $\nu_0$  represents the mean (ideal) oscillator frequency,  $A_0$  the amplitude of the signal and  $\Delta\phi(\tau)$  the phase variations. Since small variations of the nominal amplitude  $A_0$  do not influence the time measurements, we do not include its variability in our model. We choose to include all uncertainties in the phase variations  $\Delta\phi(\tau)$ , so that frequency

variations  $\Delta\nu(\tau)$  are included as integrated phase errors. The error in registered time of the oscillator then follows from:

$$\Delta\tau(\tau) = \frac{\Delta\phi(\tau)}{2\pi\nu_0} \quad (6)$$

Therefore, to simulate stochastic clock noise, we must generate realizations of the stochastic process describing the phase variations  $\Delta\phi(t)$ .

The behaviour of the stochastic clock error is typically quantified by its so-called Allan variance (Allan, 1966; Asmar et al., 2005), denoted as  $\sigma_y^2(T)$ , where  $T$  denotes a time interval. Alternatively, the Allan deviation  $\sigma_y(T)$  may be provided. It is a measure for the stability of the reference frequency  $\nu$  (*i.e.* the extent to which it deviates from  $\nu_0$ ) over a time interval  $T$ . Taking two subsequent time intervals  $n$  and  $n + 1$  of equal length, the Allan variance of a quantity  $y$  (here the oscillator relative frequency error) is defined statistically as (Allan, 1966):

$$y = \frac{\nu}{\nu_0} - 1 \quad (7)$$

$$\sigma_y^2(T) = \frac{\langle (\bar{y}_{n+1} - \bar{y}_n)^2 \rangle}{2} \quad (8)$$

Examples of Allan variance profiles for deep-space clocks are given by (Prestage and Weaver, 2007) and discussed in some more detail in Section 4.3.

Given an Allan variance profile, we must generate a realization of the stochastic process describing the clock errors. To achieve this, we use the method of Timmer and Koenig (1995) to generate a time-correlated set of data from a given power spectrum. Using this method, a discretized frequency-domain realization of the stochastic process is created from its power spectrum, which is then converted to the time domain to obtain the required data set. A summary of the method is presented in Appendix A.

To apply this method for the simulation of a clock error time history, we require a mapping from the Allan variance  $\sigma_y^2(T)$ , which is usually provided, to the phase noise power spectrum  $S_x^2(f)$  of the phase variations. The Allan variance can typically be approximated by the following polynomial relation:

$$\sigma_y^2(T) = \sum_{\mu=-2}^1 h^{(\mu)} T^\mu \quad (9)$$

where the coefficients  $h^{(\mu)}$  represent the strength of each term  $T^\mu$  at an integration time of 1 s. The Allan variance is related to the phase noise power spectrum by the following integral (Riley, 2008):

$$\sigma_y^2(T) = \frac{8}{T^2} \int_0^\infty S_x^2(f) \sin^4(\pi T f) df \quad (10)$$

From this integral equation, the following solution can be derived for the phase noise



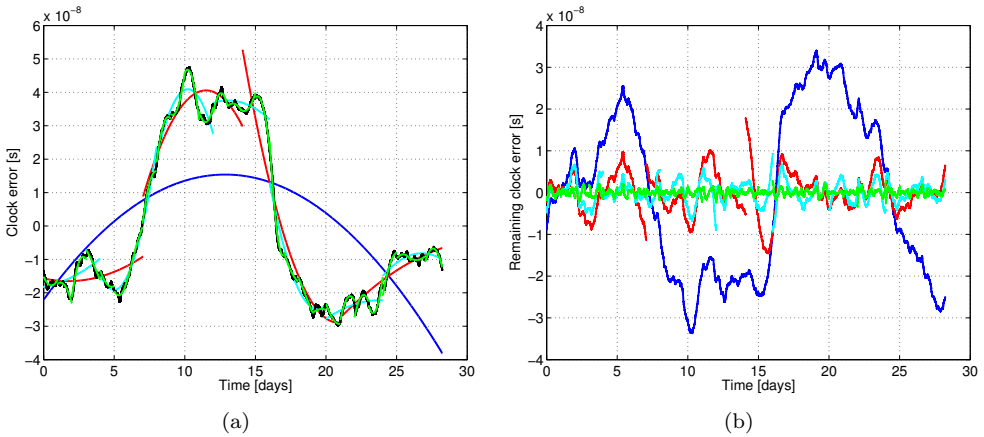


Figure 1: Example of using polynomial clock parameter estimation for removing stochastic clock noise. Black: full error profile, Blue: 1 clock arc, Red: four clock arcs, Cyan: 7 clock arcs, Green: 28 clock arcs. a) Stochastic error profile with estimated clock profiles. b) Remaining clock error after removal of estimated error.

power spectrum, for  $\mu > -2$  (Riley, 2008):

$$S_x^2(f) = K^{(\beta)} f^\beta \quad (11)$$

$$\beta = -\mu - 3 \quad (12)$$

$$h^{(\mu)} = \frac{8K^{(\beta)}}{\pi^{\beta+1}} \int_0^\infty (f')^\beta \sin(f')^4 df' \quad (f' = \pi f'T) \quad (13)$$

where the above integral has analytical solutions for the typical values  $\mu = -1, 0, 1$ . For  $\mu = -2$ , the integral has infinite power at high frequencies, causing the integral to diverge. To solve this issue, a (transformed) cutoff frequency  $f_H$  is substituted for the integral upper bound above which no power is contained in the phase fluctuations. Analytical results for the mappings from  $K^{(\beta)}$  to  $h^{(\mu)}$  for typical integer  $\beta$  are given by (Riley, 2008).

## 2.4 Clock error estimation

During the processing of one-way laser ranging data, the deterministic clock parameters of the space segment (and participating ground stations) may be estimated during the orbit determination process (Bauer et al., 2013). This approach is preferred to *a posteriori* clock calibration, where *post-fit* residuals are attributed to clock errors, since this would obfuscate any correlations between clock parameters and other estimated parameters. As a result, a clock error may be interpreted as a physical signal, resulting in a biased estimation.

However, the estimation of clock parameters may also be used to reduce the influence of stochastic clock errors, in a similar manner that empirical accelerations are often used

in orbit determination to remove errors in the state dynamics model. Similar to the estimation of empirical force parameters, the clock parameters can be estimated over short consecutive arcs instead of one global arc. An example of this is shown in Fig. 1. In this figure, the ideal estimation of a bias, drift and aging over a number of arc durations is used to approximate a stochastic clock error.

It can be seen in Fig. 1 that reducing the arc duration reduces the total remaining clock error, since more parameters are available to remove the clock noise signal. However, when concurrently estimating additional (state, physical, *etc.*) parameters, this may lead to strong correlations, so that the clock parameters absorb part of the physical signal that is to be observed (or *vice versa*).

### 3 Planetary tracking models

In this section, we will review the models linking the dynamics of celestial bodies and spacecraft to the range observables. The inherent difference between one- and two-way range measurements will be discussed. More details for these models are provided by Moyer (2000).

First, we present the models used to simulate range measurements in Section 3.1. Subsequently, we discuss how signal transmission and reception time tags are used to set up range measurements in Section 3.2.

#### 3.1 Range simulation models

In Fig. 2, we show a schematic space-time diagram for two observers, representing a ground ( $A$ ) and space ( $B$ ) segment. Signals are transmitted by the ground segment and received by the space segment (uplink) and *vice versa* (downlink). By combining the signal timing measurements at both link ends, the range observations are generated.

We will denote the one-way range observation between station  $A$  (transmitter) and station  $B$  (receiver), by  $s_{BA}^{(1)}$ . From the position functions  $\mathbf{x}_A(t)$  and  $\mathbf{x}_B(t)$ , the one-way range is calculated as follows:

$$s_{BA}^{(1)}(t_t=t_1) = \left| \mathbf{x}_B \left( t_1 + \frac{s_{BA}^{(1)}}{c} \right) - \mathbf{x}_A(t_1) \right| + \Delta s_{BA}^{(1)}(t_1, t_2) \quad (14)$$

$$s_{BA}^{(1)}(t_r=t_2) = \left| \mathbf{x}_B(t_2) - \mathbf{x}_A \left( t_2 - \frac{s_{BA}^{(1)}}{c} \right) \right| + \Delta s_{BA}^{(1)}(t_1, t_2) \quad (15)$$

where the first formulation is referenced to the transmission time  $t_t$ , here equal to  $t_1$ , and the second to the reception time  $t_r$ , here equal to  $t_2$  (see Fig. 2). The term  $\Delta s_{BA}^{(1)}$  denotes range corrections due to *e.g.* atmospheric and relativistic effects.

The two-way range observation between the same link ends  $A$  and  $B$  is denoted here as  $s_{BA}^{(2)}$ , where link end  $B$  now functions as a reflector/retransmitter. It is calculated by the combined one-way ranges for the up- and downlinks, referenced to either the

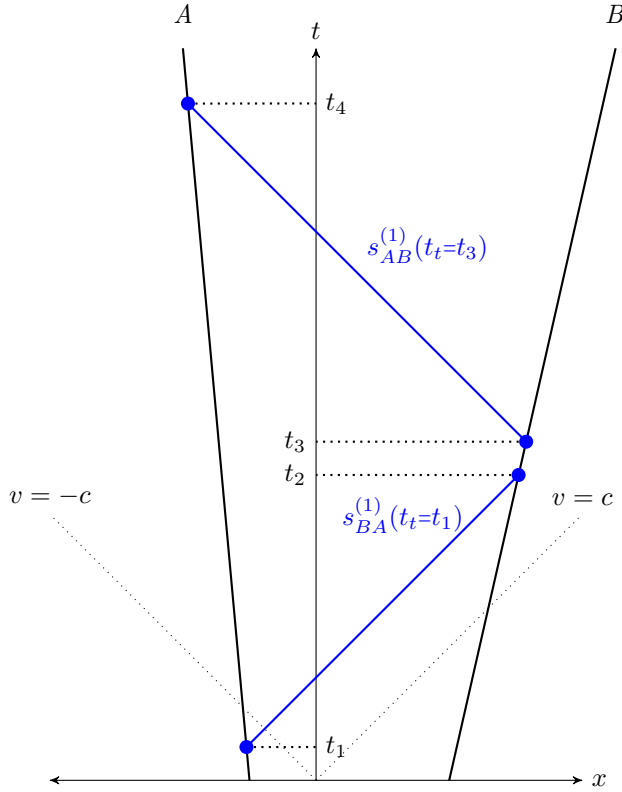


Figure 2: Schematic spacetime diagram showing one-dimensional representation of up- and downlink one-way ranges between stations  $A$  and  $B$  (both moving with constant velocity).

transmission time  $t_1$  or reception time  $t_4$ :

$$s_{BA}^{(2)}(t_t=t_1) = s_{BA}^{(1)}(t_t=t_1) + s_{AB}^{(1)}(t_t=t_3) + c\delta t_B \tag{16}$$

$$t_3 = t_1 + \frac{s_{BA}^{(1)}(t_t=t_1)}{c} + \delta t_B \tag{17}$$

$$s_{BA}^{(2)}(t_r=t_4) = s_{AB}^{(1)}(t_r=t_4) + s_{BA}^{(1)}(t_r=t_2) + c\delta t_B \tag{18}$$

$$t_2 = t_4 - \frac{s_{AB}^{(1)}(t_r=t_4)}{c} - \delta t_B \tag{19}$$

where  $\delta t_B$  represents the delay between the reception and retransmission of the signal at station  $B$  obtained from:

$$\delta t_B = t_3 - t_2 \tag{20}$$

A two-way range measurement can be realized in a number of manners. The differences between these types are in the determination and application of the term  $\delta t_B$ .

For planetary laser ranging systems, the preferred two-way range mode is asynchronous operation (Degnan, 2002). In such a setup, both the space and ground segments independently fire pulses towards one another. That is, the detection of the pulses happens independently of their transmission. In doing so, one-way ranges  $s_{AB}^{(1)}$  and  $s_{BA}^{(1)}$  are generated. By combining two one-way ranges, including the time between a reception and a transmission  $\delta t_B$  a two-way range is obtained (Birnbbaum et al., 2010). Since the range measurement is asynchronous,  $\delta t_B$  may be negative, as it does not represent a physical retransmission time delay. It should be noted that any two one-way ranges may be paired, allowing the selection of the order of magnitude of  $\delta t_B$  in the data analysis (within bounds of the available data).

### 3.2 Range observation models

In Section 3.1, the models for simulating range observables were presented. In this section, we will describe the models used to generate range observables from the signal reception and transmission time tags  $\tilde{\tau}$  (Section 2.2) at the various link ends.

For the one-way range shown schematically in Fig. 2, the measured time tags are combined as follows to determine the observable:

$$s_{BA}^{(1)} = c(t_2 - t_1) + \Delta s_{BA}^{(1)}(t_1, t_2) \quad (21)$$

$$t_i = t_i(\tau_i(\tilde{\tau}_i)) \quad (22)$$

The second equation indicates that the measured proper times  $\tilde{\tau}$  are first converted to the estimate of true proper time (Section 2.4) and subsequently converted to coordinate time.

We will assume for the purposes of our discussion in this section that the proper-to-global time  $t$  conversion is error-free (see Section 2.1). For terrestrial clocks, the rate difference between TCB  $t$  and  $\tau$  is at the order of  $10^{-8}$ , with additional terms orders of magnitude smaller (Kaplan, 2005). Therefore, to simplify our discussion in this section, we will assume that a global time  $\tilde{t}$  is measured, the error of  $t$  is assumed to follow directly from Eq. (2) when replacing  $\tau$  with  $t$ . In doing so, we ignore the conversion errors from proper to global time, as well as the variation in the measurement error  $\Delta t$  due to the time-variability of the conversion. Omitting this effect in our discussion will allow us to more clearly show the influence of the clock error behaviour on the error budgets of one- and two-way range measurements. In our simulations, we do include the full proper-to-global time conversion models (Section 2.1).

Using this simplification, we obtain the following for the one-way range measurement  $\tilde{s}_{BA}^{(1)}$  from the signal transmitted at  $t_1$  (omitting the  $\Delta s_{BA}^{(1)}(t_1, t_2)$  term):

$$\tilde{s}_{BA}^{(1)} = c(\tilde{t}_2 - \tilde{t}_1) + \epsilon_{s_{BA}^{(1)}} \quad (23)$$

$$= c(t_2 - t_1 + \Delta t_B(t_2) - \Delta t_A(t_1)) + \epsilon_{s_{BA}^{(1)}} \quad (24)$$

$$= s_{BA}^{(1)} + c(\Delta t_B(t_2) - \Delta t_A(t_1)) + \epsilon_{s_{BA}^{(1)}} \quad (25)$$

where  $\Delta t_j(t_i)$  represents the time measurement error at station  $j$ , evaluated at global time  $t_i$  and  $\epsilon_Q$  represents the non-clock-induced measurement errors of observable  $Q$ .

For the one-way range measurements, these are due to finite pulse lengths, electronics instabilities, signal strength variations *etc.* Similarly, the two-way range measurement is derived from:

$$\tilde{s}_{BA}^{(2)} = c(\tilde{t}_4 - \tilde{t}_1) + \epsilon_{s_{BA}}^{(2)} \quad (26)$$

$$= \tilde{s}_{BA}^{(1)} + \tilde{s}_{AB}^{(1)} + c(\tilde{t}_3 - \tilde{t}_2) + \epsilon_{s_{BA}}^{(2)} \quad (27)$$

$$= s_{BA}^{(2)} + c(\Delta t_A(t_4) - \Delta t_A(t_1)) - c(\Delta t_B(t_3) - \Delta t_B(t_2)) + \epsilon_{s_{BA}}^{(2)} \quad (28)$$

$$\epsilon_{s_{BA}}^{(2)} = \epsilon_{s_{BA}}^{(1)} + \epsilon_{s_{AB}}^{(1)} \quad (29)$$

Comparing Eqs. (25) and (28), it can be seen that the error term for the one-way range measurement is the difference between the absolute range errors at the transmitter and receiver (at  $t_1$  and  $t_2$  respectively). For the two-way range measurement, however, only the timing error accumulated over a time  $t_4 - t_1$  at the transmitter and time  $t_3 - t_2$  at the retransmitter affect the measurement. As a result, clock errors of station  $A$  are integrated over time  $s_{BA}^{(2)}/c$ , and those of station  $B$  over time  $\delta t_B$ . For the one-way range measurement the clock error terms will accumulate as time increases.

## 4 Simulation settings

In this section, we summarize the models and settings used in our simulations of the performance of one- and two-way ILR systems. First, we summarize our simulated missions (a lunar polar orbiter and a Phobos lander) and provide the rationale for their use in our simulations in Section 4.1. In Section 4.2, we summarize the models we use for the propagation of the dynamics of the lunar orbiter and Phobos. Also, we discuss the manner in which we simulate range measurements and their error profiles. Subsequently, we provide details on the characteristics of the clocks we assume for our test case missions in Section 4.3. In Section 4.4, we discuss the set of Phobos physical characteristics that we include in our estimation. Finally, we discuss the manner in which we generate a force error profile for our lunar orbiter simulation in Section 4.5.

### 4.1 Mission test cases

To assess the relative performance of one- and two-way laser ranging systems, we perform simulations for two distinct types of interplanetary missions. We analyze the performance of a lunar polar orbiter equipped with a laser ranging system over a period of 1 month and that of a Phobos lander equipped with a laser ranging system over a period of 1 year. We choose a relatively short period of 1 month for the lunar orbiter, since neither the state nor the clock is estimated over a longer duration than this (Section 5), and the 1 month orbital period of the Moon about the Earth allows us to sample the full range of observational geometries. For the Phobos lander, we select the longer period of 1 year, to exploit the orbital predictability of Phobos (*i.e.*, lack of strong non-conservative forces). Also, it was found by Dirkx et al. (2014a) that this period of laser range tracking to a Phobos lander allows for the significant improvement

in estimation quality of the primary scientific parameters of interest (Section 4.4). For the lunar orbiter, we assume orbital characteristics similar to LRO (mean lunar altitude  $\approx 50$  km, eccentricity  $\approx 0$ , inclination approx  $90^\circ$ ). For the Phobos mission, we assume the same nominal lander position as Dirkx et al. (2014a).

These two missions differ in several key aspects. Firstly, orbit determination of a lunar orbiter suffers from mismodelled non-gravitational accelerations, necessitating the inclusion of the estimation of empirical force model parameters for optimal orbit reconstruction. The dynamics of Phobos, on the other hand, is hardly affected by non-gravitational forces and the Martian gravitational environment is exceptionally well mapped. Due to the force mismodelling of a lunar orbiter, the estimation of the spacecraft's state must be divided into distinct arcs. For the Phobos dynamics estimation, however, a single state arc can be used for the entire mission. The second important difference between the two missions is in the rationale for performing the Precise Orbit Determination (POD). In the case of the lunar orbiter, the only physical parameter (in addition to empirical force parameters; see Section 4.5) we estimate is the initial state of the spacecraft (per arc). We do not estimate physical parameters of the Moon, since we assume no improvement will be obtained compared to the recent GRAIL results *e.g.* (Lemoine et al., 2014; Konopliv et al., 2013). The requirement for the POD of the lunar orbiter instead stems from the required precise data processing of altimeter, camera data, *etc.*, as is the case for LRO. For a Phobos lander, the primary scientific products of the orbit determination are the physical parameters of Phobos and Mars, which are included in the POD process (Section 4.4).

## 4.2 Observation and dynamical models

In this section, we give an overview of the models that we use for the dynamics of the lunar orbiter and Phobos, as well as the models for the realizations of the range observations.

We propagate the dynamics of the lunar orbiter using a lunar gravity field expanded to degree and order 15, third-body perturbations from the Earth, Sun and all planets, as well as a cannonball radiation pressure model. As will be discussed in more detail in Section 4.5, we also include an empirical model for mismodelled non-conservative forces. Although this model will be insufficient for POD of a low-flying lunar orbiter (which will require a much higher-order gravity field model and better non-conservative force model), the model will capture the overall dynamical behaviour of the satellite, which is the requirement for this simulation work. For the numerical integration of the orbit of Phobos, we use the same models as Dirkx et al. (2014a).

We use six ground stations in our simulations and assume that each ground station will, if geometrically feasible (assumed elevation angle cutoff of  $15^\circ$ ; Sun avoidance angle cutoff of  $5^\circ$ ; occultations by Moon and Mars taken into account, see Dirkx et al. (2014a)) perform one tracking session lasting 20 minutes once every 8 hours in the case of the lunar orbiter and once every day for the Phobos lander.

For the simulations of the Phobos lander, we use a received pulse frequency of 0.4 Hz at the space segment and 0.1 Hz at the ground segment (in the case of two-way simulations). That is, we conservatively assume that a pulse transmitted from the

ground segment is detected once every 2.5 s (on average) by the space segment and a pulse transmitted by the space segment is detected once every 10 s (on average) by the ground segment. For the lunar orbiter, we assume a 1 Hz reception frequency at both the receiver and the transmitter, based on values obtained from LRO one-way laser ranging (Bauer et al., 2013).

To obtain the two-way ranges from the simulated set of up- and downlink one-way ranges, we pair ranges resulting in the smallest values of  $|\delta t_B|$  (Section 3.1). We apply small (mean 10%) random deviations from these pulse frequencies to ensure a continuous range of values of  $\delta t_B$ .

We generate clock error realizations using the approach described in Section 3.2 and the clock settings given in Section 4.3 and use these directly to generate the influence of clock errors on the range measurements. For both the up- and downlink of the system, we assume a 25 ps ( $\approx 7.5$  mm) standard deviation single-shot Gaussian uncertainty in the range measurement as an approximate realization of the terms  $\epsilon_{s_{BA}}^{(1)}$  and  $\epsilon_{s_{AB}}^{(1)}$  (Section 3.2), to capture the effects of *e.g.* finite pulse lengths.

### 4.3 Clock settings

To define the influence of clock errors on the range measurements, we require a definition of the Allan variance (or deviation) of the clocks of both the space segment and the ground segment. Although we expect the influence of the space segment's clock to be dominant in the error budget of one-way range measurement, the ground station clock's influence may be significant for the Phobos lander, since  $\delta t_B \ll s_{BA}^{(2)}$  (Section 3.2).

For one-way range measurements, especially the long-term stability of the (space) clock is important for quantifying the range measurement errors over the longer integration times of days, and even months in the case of the Phobos mission. We do not select a specific existing clock Allan variance for our simulations here, but instead base our Allan variance profiles on a combination of existing clocks and those of space clocks that are currently under development (Cacciapuoti and Salomon, 2011; Ely et al., 2014), conservatively extrapolating the near-term potential of a clock selected and developed specifically for one-way laser ranging missions.

An overview of the Allan deviations of a number of (deep) space clocks is given by Prestage and Weaver (2007). Typical deep-space Ultra-Stable Oscillators (USOs), such as that used by the Cassini mission, have their best Allan variance at an integration time of 10-100 s, increasing with  $\sqrt{\tau}$  afterwards ( $\mu=1$  in Eq. (9)), the use of which here would result in excessive range errors over longer integration times. The Rubidium clocks onboard the GPS block II satellites show much better stability over longer integration times than the Cassini USO does, making a clock of similar capabilities more suitable for one-way laser ranging missions. The highly stable Deep Space Atomic Clock (DSAC) is under development specifically for enabling the use of one-way (radio) ranging over interplanetary distances. However, it has not been tested in space. Also, a highly stable clock will be placed onboard the International Space Station (ISS) in the Atomic Clock Ensemble in Space (ACES) project (Cacciapuoti and Salomon, 2011).

For our simulations of the lunar orbiter, we select a clock with intermediate stability (see Fig. 3), with a stability somewhat worse than that demonstrated by GNSS satellite

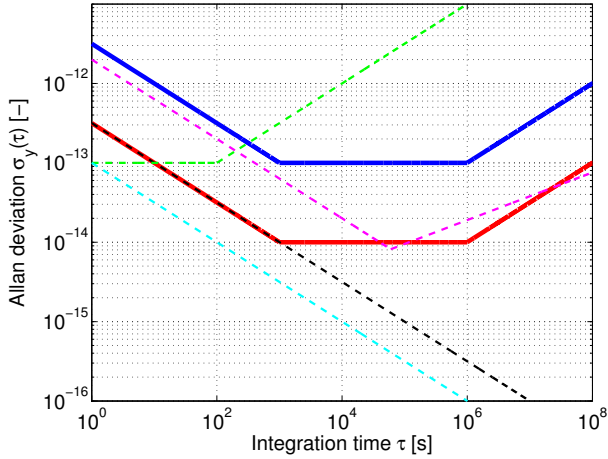


Figure 3: Allan deviations we use for lunar orbiter (blue) and Phobos lander (red) clock simulations. Also shown for reference are the Cassini USO (green), GPS Block 2 (magenta), DSAC (black) (Prestage and Weaver (2007)) and the PHARAO (cyan) (Cacciapuoti and Salomon, 2011) clocks.

clocks (Prestage and Weaver, 2007; Montenbruck et al., 2012). A higher medium-to-long term ( $\tau > 1000\text{s}$ ) stability is used than is the case for, for instance, Cassini. We do not use clocks of the same high stability as GNSS satellites since we assume that less power and mass will be available for the clock on a lunar orbiter. For longer integration times, the Allan variance we use for the lunar orbiter is superior to that currently being used on LRO, for which ground-measured values are  $\sigma_y(\tau) \approx 10^{-13}$  for  $10\text{ s} < \tau < 10^3\text{ s}$ , rising to  $\sigma_y(\tau) \approx 2 \cdot 10^{-13}$  at  $\tau = 10^4\text{ s}$  (Cash et al., 2008). As such, our assumed system represents a meaningful, yet realistic, improvement over existing lunar one-way ranging.

For our Phobos simulation, we use a clock of higher stability than for the lunar orbiter simulations, since the clock will be the crucial instrument for fulfilling the scientific objectives and longer integration times are required than for the lunar orbiter. Also, the use of Phobos as a geodetic observatory is beneficial due to its long-term orbital predictability (compared to artificial satellites), (Dirkx et al., 2014a), warranting additional expenditure on a long-term stable clock. We select a clock with an Allan variance of a factor 10 better than for the lunar orbiter, shown in Fig. 3. For small integration times, its Allan variance is equal to that of the DSAC clock, but we assume less favorable slopes (*i.e.*, exponent  $\mu$  in Eq. (9)) for  $\tau > 10^3\text{ s}$ , using an Allan variance profile which is roughly similar to that in the GPS Block II satellites for  $\tau > 10^4\text{ s}$ .

We present the estimation results using the one-way laser ranging measurements in Sections 5 and 6, where we also estimate polynomial clock errors (Section 2.4) for a variety of arc lengths. When doing so, the Allan variance at integration times on the order of the arc length and longer do not play a role in the range measurement errors. As a result, the random walk frequency noise (for which  $\sigma_y(\tau) \sim \sqrt{\tau}$ , see Fig. 3) that is dominant for large values of  $\tau$  will not be relevant for clock arcs smaller than  $\sim 12$  days. Since we find that an optimal clock arc length is  $\ll 10^6\text{ s}$  for all our simulation



cases, the precise clock profile for long integration times does not significantly influence the results for the laser ranging system performance.

From the selected Allan deviations  $\sigma_y(T)$  and our selected range of values of  $\delta t_B$  (1 s for the lunar orbiter, 2.5 s for the Phobos lander, see Section 4.2), we can see that the contribution of the clock to the range error profile of the two-way range measurements will be quite small. For the lunar orbiter, the Allan deviation  $\sigma_y(\tau)$  at an integration time of 1 s is  $\sqrt{10} \cdot 10^{-12}$ , which leads to a range error of about 1 mm. For the Phobos lander, the Allan deviation  $\sigma_y(\tau)$  at an integration time of 2.5 s is  $2 \cdot 10^{-13}$ , which leads to a range error of about 0.2 mm. For the Phobos lander  $s_{BA}^{(2)}/c \gg \delta t_B$ , whereas for the lunar orbiter  $s_{BA}^{(2)}/c \approx \delta t_B$ . Since the ground station clocks will be substantially better than that of the space segment, we omit the influence of the ground clock for the lunar orbiter. For the Phobos lander, however, we include a realization of the ground station clock noise, for which we assume an Allan deviation a factor 10 better than the Phobos ground station clock. Since the two-way light-time will be on the order of 1000 s, the ground station-clock induced range error due to the Allan deviation  $\sigma_y(\tau = 1000s) = 1 \cdot 10^{-15}$  is around 0.3 mm.

#### 4.4 Estimated Phobos Characteristics

A detailed discussion of the physical parameter estimation from two-way laser ranging data of a Phobos lander is given by Dirkx et al. (2014a). In our simulations here, we use a truncated set of their estimated parameters, since it is not our goal to completely reanalyze the Phobos lander mission performance, but instead to investigate the comparative performance of one- and two-way range systems. Therefore, we only estimate the primary geophysical characteristics of Phobos that are obtainable from the data, as presented by Dirkx et al. (2014a). Specifically, we estimate Phobos'  $\bar{C}_{2,2}$  gravity field coefficient, its primary libration amplitude in longitude, as well as several additional (short-period) libration amplitudes in the Euler angles longitude  $W$ , right ascension  $\alpha$  and declination  $\delta$  selected from the model of Rambaux et al. (2012), cast in the form of Le Maistre et al. (2013). From a combination of the libration amplitudes and  $\bar{C}_{2,2}$  of Phobos, its absolute moments of inertia can be obtained, from which crucial information on Phobos' interior structure and evolution can be derived (Rosenblatt, 2011).

We estimate a limited set of representative libration amplitudes, since it was found by Dirkx et al. (2014a) that there are groups of fully correlated amplitudes that cannot be decoupled by ranging measurements alone. Therefore, we focus on estimating a set of libration parameters that can be independently estimated, implicitly assuming additional observations capable of discerning between translational and rotational motion, such as star trackers.

The components, frequencies and nominal amplitudes of our estimated librations are given in Table 1. The libration contribution to each Euler angle is calculated from the following, with  $\gamma$  used as a placeholder notation for any one of the three Euler angles (Dirkx et al., 2014a):

$$\Delta\gamma(t) = \sum_j \gamma_{T_j}^c \cos\left(\frac{2\pi}{T_j}t\right) + \gamma_{T_j}^s \sin\left(\frac{2\pi}{T_j}t\right) \quad (30)$$

Table 1: List of estimated libration components from the model of Rambaux et al. (2012) included in the estimation.

Euler angle	Period [days]	Amplitude [deg]
$W$ (Longitude)	$T_1 = 0.3190$	1.0998
$W$ (Longitude)	$T_2 = 0.5127$	0.0167
$\alpha$ (Right ascension)	$T_3 = 0.2313$	0.0462
$\alpha$ (Right ascension)	$T_4 = 0.8430$	0.0166
$\delta$ (Declination)	$T_3 = 0.2313$	0.0279
$\delta$ (Declination)	$T_4 = 0.8430$	0.0101

where  $T_j$  denotes the period of the  $j^{th}$  term and  $\gamma_{T_j}^c$  and  $\gamma_{T_j}^s$  denote the amplitudes of the cosine and sine contributions of the  $j^{th}$  term, respectively.

We estimate the  $\bar{C}_{2,2}$  gravity field coefficient of Phobos, as it has a stronger influence on the orbit of Phobos than  $\bar{C}_{2,0}$  or its higher-order gravity field coefficients. We omit any estimation of Mars' physical parameters, or other parameters that are not well observed after only one year. However, we do include the estimation of the Phobos-fixed position of the lander (denoted  $\mathbf{x}_L$ ) in our estimation.

## 4.5 Lunar orbiter force error model

The gravitational environment of the Moon has been mapped to very high accuracy, due to the gravity field solutions generated from data obtained by the GRAIL mission (Lemoine et al., 2014; Konopliv et al., 2013). However, since a variety of imperfectly modelled non-conservative forces (direct and reflected solar radiation pressure, moon IR, thermal reradiation, *etc.*) act on a lunar orbiter, dynamical model errors will be an important source of state estimation errors, especially for longer arcs.

To include the difference between the truth and estimation model in our simulations, we employ an empirical model for the acceleration mismodelling. The model consists of once-per-revolution and constant accelerations in radial, along- and cross-track directions, as well as independent white noise power spectrum acceleration models in these three directions. Although we do not expect this model to be a fully valid representation of the true force model power spectrum, it is sufficient for the purposes of this study, where the primary goal is the inclusion of a realistic mean magnitude of acceleration errors.

To set up our error models, we use the results of Mazarico et al. (2013), who present arc overlap errors for LRO orbit determination with 2.5 day arcs using the GRAIL gravity fields. For the nominal mission, they arrive at  $\sim 8$  m along- and cross-track, and  $\sim 0.6$  m radial overlap error. Additionally, we use information of Mazarico et al. (2012) regarding the magnitude of the estimated LRO along-track empirical accelerations ( $\sim 5 \cdot 10^{-10}$  m/s<sup>2</sup>). We conservatively set the magnitude of the deterministic empirical accelerations to  $10^{-9}$  m/s<sup>2</sup> in each direction. These values lead to orbit errors below those reported by Mazarico et al. (2013), except for the along-track direction. However, since we include along-track empirical accelerations in our estimation, these large orbital differences can be removed in the orbit determination. In addition to the constant

and once-per-revolution signals, we set the (frequency-independent) power spectrum magnitude for the three independent directions to values which result in  $\sim 10$  m total orbit error in along- and cross-track and  $\sim 1$  m total orbit error in radial direction after 2.5 days of propagation.

Typically, errors in the dynamical model are handled in the estimation by including empirical force parameters, such as solar radiation pressure scaling factors and empirical accelerations, on an arc-wise basis. Here, we include the estimation of a radiation pressure scaling coefficient and a constant, as well as a once-per-revolution sine and cosine empirical acceleration in along-track direction. The estimation of along-track-only empirical accelerations is also done in the simulation study of LRO presented by Rowlands et al. (2009), who conclude that estimation of these components results in the best orbit solutions. The estimation of a constant along-track acceleration is also used in the orbit determination of the Lunar Prospector (Mazarico et al., 2010) and LRO (Mazarico et al., 2012).

## 5 Lunar Orbiter Results

In this section, we present the results of the lunar orbiter tracking simulations. The models used in the simulations have been discussed in Section 4. Our goal is to determine the influence of clock noise on the performance of one- and two-way laser ranging systems, and how the performance of these systems compares to one another. To remove accumulated clock noise from the one-way range observations, we include the estimation of clock parameters on a per-arc basis (Section 2.4). We perform the estimation for a range of values of the number of state arcs  $N_s$  and clock arcs  $N_c$ , which we do not impose as being equal to one another. By exploring a range of values of  $N_s$  and  $N_c$ , we investigate the influence of data processing strategies on the quality of the estimation. Our full simulation spans a 28 day duration. All our numerical results are based on a Monte Carlo analysis with 25 independent simulations using different realizations of the observer clock noise processes.

We start by presenting the results of the simulations where there is no error in the dynamical model used during the estimation in Section 5.1. Subsequently, we analyze the performance of the simulations where an error in the dynamical model is included (Section 4.5), the influence of which we attempt to mitigate by means of the estimation of a radiation pressure coefficient  $C_r$  and along-track empirical acceleration  $\mathbf{a}_{e,c}$  on a per-state-arc basis. The results of these simulations are presented in Sections 5.2, 5.3 and 5.4, where the position estimation accuracy, removal of stochastic clock noise and comparison of one- and two-way systems are discussed, respectively.

### 5.1 Preliminary analysis: no dynamics errors

In this section, we present results of the lunar orbiter one-way laser tracking simulations without dynamical model errors. In these simulations, the only uncertainties in the estimation model are the result of the clock noise and Gaussian observation noise (see Section 4.2). The estimation results are shown in Fig. 4, where the mean position error over the one-month period is shown for all combinations of  $N_c$  and  $N_s$  in Fig. 4(a). We

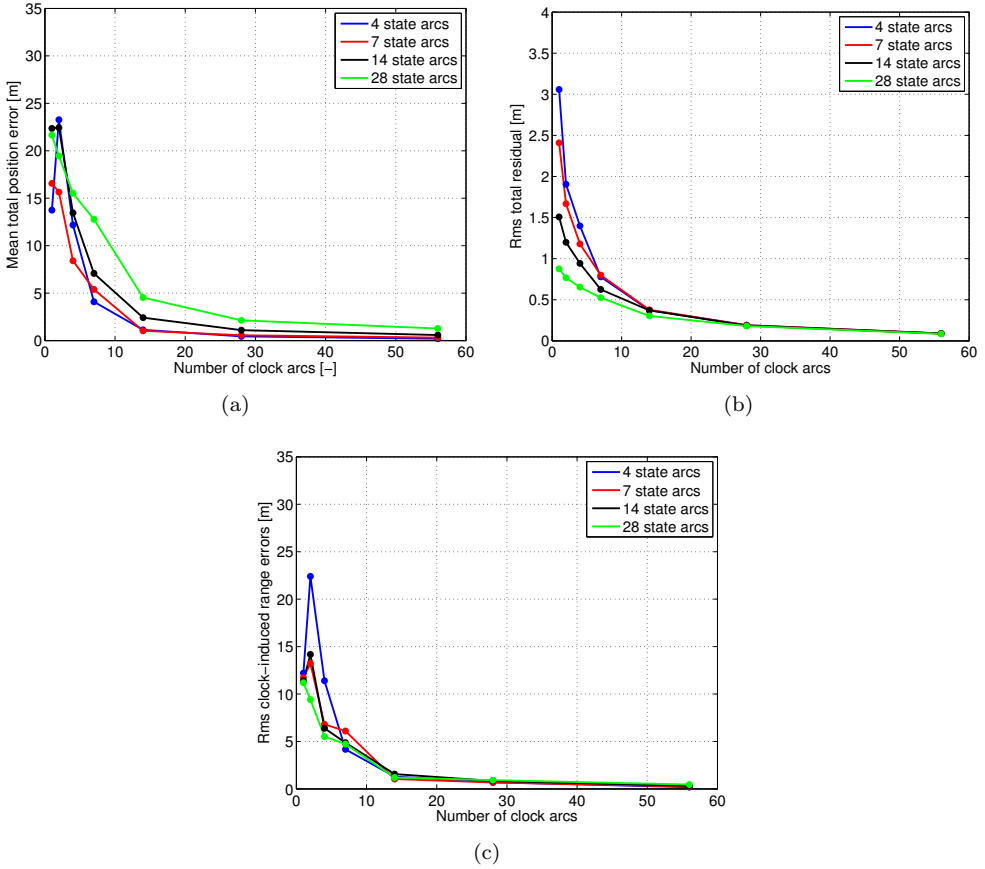


Figure 4: Estimation results for lunar orbiter one-way range observations as a function of number of state arcs and clock arcs, without errors in estimation dynamical model a) Mean position error over full 28-day period b) Observation residual after estimation convergence c) Residual clock noise. Circular dots denote data point for which results were generated by means of Monte Carlo analysis ( $N = 25$ ).

obtain the mean position error by taking the root sum square of the difference between the true state history  $\mathbf{x}(t)$  and the estimated state history  $\hat{\mathbf{x}}(t)$  every 30 s and averaging the result over the full one month period. The observation residual after convergence is shown in Fig. 4(b) and the clock-induced observation error in Fig. 4(c). By clock-induced observation error  $\Delta s_c$ , we denote the remaining clock error after removal of the estimated clock behaviour  $\Delta \hat{t}_d$ , averaged over all observations, so:

$$\Delta s_c(t) = c(\Delta t_d(t) + \Delta t_s(t) - \Delta \hat{t}_d(t)) \quad (31)$$

where we fit a set of polynomials (the estimation clock noise  $\Delta \hat{t}_d$ ) to the combined deterministic and stochastic clock noise, as discussed in Section 2.4.

It can be seen in Fig. 4(a) that for most of the range of the number of clock and state arcs ( $N_c$  and  $N_s$ , respectively), both an increase in  $N_c$  and a decrease in  $N_s$  leads to an improvement in estimation quality. The decrease in clock arc length (increase in  $N_c$ ) allows for a better fit of the clock parameters to the stochastic clock noise error profile, as was discussed in Section 2.4 and illustrated in Fig. 1. For the simulations presented here (without dynamical model errors), an increase in state arc length (decrease in  $N_s$ ) improves the results, since the estimation model could theoretically perfectly reproduce the original state history and no shorter arcs are needed to absorb dynamical model errors. In principle, the estimator can obtain the same (perfect) orbit for any value of  $N_s$ . Nevertheless, increasing the number of state arcs leads to additional freedom for the estimator to fit signals in the observation into the state dynamics without significant changes in the residuals, increasing the spread of the estimated solution.

A number of data points in Fig. 4(a) show clear deviations from the overall trend, however. Most notably, the data points at ( $N_s=4, N_c=2$ ) and ( $N_s=4, N_c=4$ ) show a strong increase in estimation error w.r.t. this trend. This behaviour is not observed in the post-fit residuals (Fig. 4(b)). This is a clear indicator that correlations between the clock and state estimation have a stronger influence on the estimation at these data points, and clock signal is absorbed by state estimation and *vice versa*. The clock-induced errors for  $N_s=4$  shown in Fig. 4(c) clearly behave in a similar manner as the position estimation error in Fig. 4(a), indicating that clock signal is interpreted as state signal and *vice versa*.

The reason that the correlations between clock and state parameters result in a much stronger degradation of estimation quality for the aberrant data points is due the combination of a number of factors. Firstly, in the case of two and four clock arcs, the four state arc estimation is essentially cut into two and four completely separated and decorrelated arcs, respectively. For the  $N_s = 7$  case, by contrast, concurrent clock arcs for  $N_c = 2, 4$  are patched together by the state arcs, since  $N_s$  and  $N_c$  are then not integer multiples of one another. Having non-coinciding state and clock arcs allows the perfect state model knowledge to be optimally exploited. That is, since the dynamical model has no imperfections in this set of simulations, connecting multiple state arcs by overlapping clock arcs connects the full 28-day period in the estimation procedure. Secondly, for a small number of clock arcs, the clock estimation model is a relatively poor representation of the actual clock behaviour (Fig. 1), since much of the short-period errors cannot be properly captured by the patched polynomial approach. For cases with higher  $N_s$ , there is more freedom in the state estimation, so that the estimation freedom in the clock estimation becomes lower relative to the estimation freedom in the state, preventing an excessive interchange of clock and state errors. That is, the correspondence between the true correlation and modelled correlation between clock and state behaviour is better for large  $N_s$  and small  $N_c$  than it is for small  $N_s$  and small  $N_c$ , leading to estimation results that show a better correspondence to reality. Therefore, the relative attribution of residual signal in the range observations becomes skewed towards clock parameters when both  $N_c$  and  $N_s$  are small, contributing to the occurrence of the peaks in Figs. 4(a) and 4(c).

We have also performed simulations of the lunar mission orbit determination without dynamical model errors using two-way laser ranging measurements. The results of these

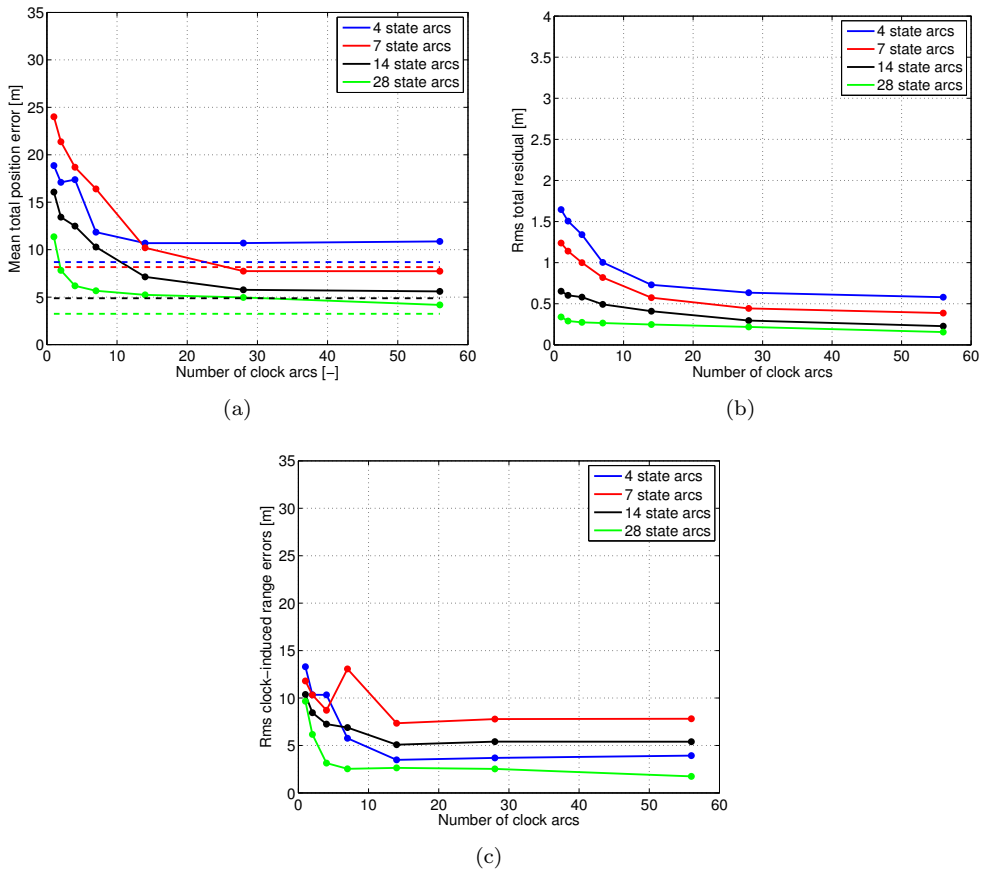


Figure 5: Estimation results for lunar orbiter one-way range observations as a function of number of state arcs and clock arcs, with errors in estimation dynamical model a) Mean position error over full 28-day period (dotted line indicates results for two-way system, for which  $N_c=0$ ) b) Observation residual after estimation convergence c) Residual clock noise. Circular dots denote data point for which results were generated by means of Monte Carlo analysis ( $N = 25$ ).

simulations show a mean position error on the order of several cm for all  $N_s$ . The extremely high quality of the resulting orbits is to be expected, since measurement errors, both the Gaussian components and the time-correlated components, are at the mm- to cm-level in these simulations and there is no buildup of either clock error or dynamical model errors, allowing an extremely good reconstruction of the orbit from these data. It should be stressed, though, that these results do not represent the expected physical performance of the two-way system, since dynamical model errors will degrade the real solution, as will be discussed in the next section.

## 5.2 Orbit reconstruction accuracy

We now investigate the influence of the addition of dynamical model errors on the estimation, starting with the capabilities of the estimator to reconstruct the orbit of the spacecraft. Compared to the preliminary results discussed in Section 5.1, the results we present here and in the subsequent sections (5.3 and 5.4) do include the dynamical model errors discussed in Section 4.5 as well as the estimation of a once-per-state-arc radiation pressure coefficient  $C_r$  and along-track empirical acceleration  $\mathbf{a}_{\mathbf{e},c}$  (constant, sine and cosine once-per-orbit terms).

The results for the position error, averaged over the full 28-day period, are shown in Fig. 5(a) as a function of the number of state arcs  $N_s$  and clock arcs  $N_c$ . Each data point has again been obtained from 25 numerical simulations with independent realizations of the stochastic clock error. In this figure, both the one- and two-way range results are shown. In this section we will focus on the one-way results. The comparative performance of the one- and two-way systems will be discussed in Section 5.4.

Several clear differences are observed between Figs. 4 and 5. Firstly, the improvement of the solution with increasing  $N_c$  is much smaller for the simulation that includes dynamical model errors (Fig. 5), an effect which is observed in the mean position error, the residual and the remaining clock errors. Also, little to no substantial improvement is observed for the position error results in Fig. 5(a) when  $N_c > 14$  (for  $N_s = 4, 28$ ) and  $N_c > 28$  (for  $N_s = 7, 14$ ). The solutions shown in Fig. 4(a), however, continue to improve up until  $N_c = 56$ . This effect is a combination of two aspects. Firstly, it shows that force model errors cannot be fully absorbed into the empirical force parameters, resulting in residual unmodelled state behaviour. Secondly, it indicates that the two sources of imperfectly modelled error sources that we include here (stochastic clock noise and dynamical model imperfections) cannot be properly distinguished from one another beyond a certain point.

In Fig. 5(a), an improvement in estimation quality with increasing number of state arcs is generally observed, the inverse result from what was observed in the case without dynamical model errors in Section 5.1. This is due to the accumulation of dynamical model errors, which occurs more strongly for longer state arcs. We observe behaviour in Fig. 5(a) that differs from the general trend, for  $N_c \leq 7$  and  $N_s = 4$ , however, where superior performance is observed compared to the  $N_s = 7$  case, as opposed to the expected increase in performance with increased  $N_s$ .

The reason for this aberrant behaviour is the following. In Fig. 5(a), the total position error over the entire 28-day period is plotted, which is our measure of quality of the estimated trajectory. The estimator does not produce this quantity directly, however, but produces estimates of the initial state, empirical force parameters and clock parameters. The estimates of the initial state and empirical force parameters are used to determine the actual reconstructed orbit, which we then compare to the (known) true orbit to produce Fig. 5(a). The empirical force parameters are correlated with both the initial state and the clock parameters, although differently for the various combinations of  $N_c$  and  $N_s$ . For our results, the correlations between empirical parameters and initial states are of little concern for the quality of the results, since we are not interested in either of these individual sets of parameters themselves, but instead in the resulting

trajectory of the spacecraft. Since it is this trajectory that is relevant for the quality of the results, estimation errors in both the initial state and empirical acceleration that are such that they largely cancel one another in the resulting trajectory will not lead to a lower quality solution. However, it is important for the quality of the results that range variations that are induced by the orbital dynamics are properly distinguished from those that are induced by the clock noise. The specific behaviour of the mapping from estimated parameters to mean position error are the primary cause of the observed aberrant behaviour at  $N_c \leq 7$  and  $N_s = 7$ . We find that the initial state estimation error is actually larger for  $N_s = 4$  than for  $N_s = 7$ , but this error propagates differently for the different state arc lengths, resulting in the observed behaviour. This behaviour is a result of the specific dynamics used here and not a general result. It does highlight, however, the sensitivity of the estimation performance to the specific characteristics of the problem under consideration.

Comparing Figs. 4(a) and 5(a), it can be seen that for small  $N_c$  and  $N_s = 14, 28$ , the position error is actually larger for the case without dynamical model errors (Fig. 4(a)) than for the estimation that includes such an error model (Fig. 5(a)). This result is quite counter-intuitive, since it seems as though the introduction of additional error sources has actually improved the solution. This effect is also observed in the clock-induced range errors, indicating that the improved state estimation is accompanied by an improvement in clock parameter estimation and therefore, a reduction in clock signal being interpreted as state signal and *vice versa*. This shows that there is a decreased exchange between clock and state behaviour estimation for large  $N_s$  and small  $N_c$  when including the dynamical model parameter estimation. This exchange between clock and state signal was the key aspect degrading the results of the no-dynamics error simulations (Section 5.1). With the additional empirical force parameter estimation, there are mutual (strong) correlations between the clock, initial state and empirical force parameters. The added correlation with the empirical force parameters causes more of the observational signal to be interpreted as state, instead of clock, behaviour. That is, adding the estimation of empirical accelerations drives the estimator to put more of the residual signal into state dynamics (combined initial state and empirical force parameters). This mitigates the effect of the poor clock modelling that occurs for small  $N_c$ , which was highlighted in Section 5.1. The performance of the clock parameter estimation will be discussed further in Section 5.3.

Due to the use of the empirical forces as additional estimated parameters, which provide additional freedom in adjusting the spacecraft state, the estimation quality during the periods of poor orbital observability is further degraded. We define poor observability as conditions where the orbital plane of the lunar orbiter is approximately perpendicular to the vector from Earth to the orbiter. In these cases, the orbital reconstruction from range data is more difficult, both with and without the empirical force estimation. However, the addition of the  $C_r$  and  $\mathbf{a}_{e,c}$  estimation results in even greater variability of the estimated orbit, with little change in residuals during periods of poor observational geometry. This effect is manifested in the estimation of the empirical force parameter for  $N_s = 14$  and especially  $N_s = 28$ , where isolated state arcs of largely poor geometry occur twice in one month. During the state arcs with such geometry, we see a sharp increase in both the mean and standard deviation of the estimated values of  $C_r$  and  $\mathbf{a}_{e,c}$  when



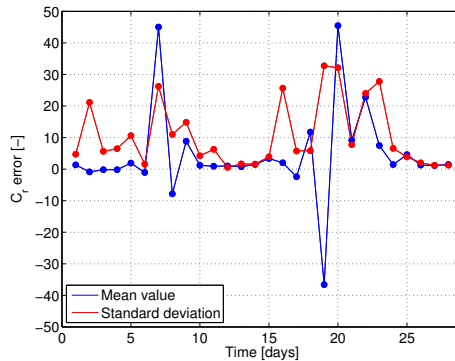


Figure 6: Mean and standard deviation of  $C_r$  estimation (true value = 1.2) for  $N_s = 28$  and  $N_c = 14$  (averaged from 25 independent simulations).

going from a state arc with good geometry to one with bad geometry. This is illustrated in Fig. 6, where the per-state-arc results of both the mean and standard deviation of  $C_r$  are given for a representative  $(N_c, N_s)$  data point. The associated increase in mean position error is less pronounced, at about a factor of 2-4 for  $N_s = 28$ . This effect of poor geometry is not clearly manifested in Fig. 5(a), since the durations of poor geometry comprise only relatively short periods (about 4 days out of 28), so that the mean error, as averaged over the full month, is not very influential. Nevertheless, when requiring a consistent quality of the orbiter state, longer state arcs should be used during periods of poor observational geometry. The resulting quality of the orbit in these periods will still be degraded compared to that of periods of good geometry, though, since the use of longer state arcs will result in a larger accumulation of unmodelled force errors.

### 5.3 Clock parameter estimation

Comparing Figs. 4(c) and 5(c) it is clear that there are substantial differences in the capabilities of the estimation to accurately characterize the stochastic clock noise with and without the inclusion of dynamical model errors. For the simulations without errors in the dynamical model (Fig. 4(c)), increasing the number of clock arcs continues to improve the removal of clock noise for our full range of  $N_c$ , as is the case for the state estimation. For 56 clock arcs, the majority of the clock error is removed from the observations, with a remaining r.m.s. clock error better than 0.5 m. The residual clock error decreases for a decreasing number of state arcs  $N_s$ , as expected (Section 5.1). For the results shown in Fig. 5(c), which do include the dynamical model error and empirical parameter estimation, though, little improvement in clock parameter estimation is observed for  $N_c > 14$ . Also, the values of the remaining clock-induced error at large  $N_c$  depend on the number of state arcs in a more erratic manner than is the case in Fig. 4(c). Additionally, the residual clock error is an order of magnitude larger than in the simulations without dynamical model errors. The cause for these differences is twofold. Firstly, due to the quasi-random nature of the empirical force model, there will be a non-zero part of the dynamical model error which cannot be properly absorbed by

the estimated  $C_r$  and  $\mathbf{a}_{e,c}$  parameters, but which can be (incorrectly) absorbed by clock parameters. This effect is not due to correlations between the estimated parameters, but instead a result of the true dynamical model having a different influence on the range measurement than that which is modelled during the estimation. Essentially, the difference between the true correlation between state and clock noise and the modelled correlation causes a relative misidentification of the residual signal. Secondly, the increased number of estimated parameters for the case with  $C_r$  and  $\mathbf{a}_{e,c}$  estimation causes additional degrees of freedom for the estimator which cause a degradation in the quality of the results for large  $N_c$  due to the additional correlations between the parameters. For small  $N_c$ , where clock arcs are quite long and the capabilities of the clock parameters to properly absorb stochastic clock noise is quite poor, this improves the degree to which the estimator can distinguish between clock and state signal (Section 5.2). For large  $N_c$ , however, this effect degrades the identification of clock noise, since the clock would in principle also be capable of removing a substantial portion of state-error induced range residual.

## 5.4 One- and two-way comparison

Finally, we come to the comparison of the performance of the one- and two-way laser ranging systems for the lunar orbiter mission. The mean position estimation error of the two-way system (in which no clock parameter estimation is performed) is shown by the dotted lines in Fig. 5(a). Comparing the two-way range to the one-way range results in this figure, it can be seen that the two-way range simulations mostly produce slightly better results than the one-way range simulations. The magnitude of the difference is quite small, with the one-way solution even slightly better for  $N_s = 7$ . This indicates that the clock-induced range errors are not the primary source of error in the parameter estimation, and the influence of errors in the dynamical model are dominant instead. Nevertheless, for the one-way range simulations to reach an estimation quality that is similar to the two-way system, clock parameters must be estimated over sufficiently short arcs ( $\lesssim 1$  day) to remove sufficient clock-induced range errors.

Although our simulations here are only for a specific mission and system test case, they indicate that in an environment with even a reasonably low force model uncertainty (the lunar gravity field is exceptionally well mapped), the added value of a two-way system over a one-way system may be marginal, since for our assumed clock stability and dynamical model errors it is the dynamics error, not the clock-induced error, which dominates the position estimation error budget. However, it must be noted that, depending on the type of (non-conservative) forces that dominate the dynamics error budget, a two-way system can improve the force modelling much better than a one-way system, since small unmodelled dynamical signatures can be extracted from the two-way observation residuals more easily. For the one-way system, the correlations between clock and state parameters will limit the capability to properly identify unmodelled dynamical effects, since such effects may be interpreted as clock noise instead. This problem may be partially mitigated by applying *a priori* constraint to the clock parameter estimation, based upon the expected stability of the clock.

An additional important advantage of the two-way system over its one-way counter-

part is the better robustness and reliability of the estimation results. As discussed in Section 5.2 and 5.3, the addition of the clock parameter estimation in the data processing of the one-way data results in clock and state signal potentially being misinterpreted in the estimation. This behaviour is hard to quantify properly without detailed numerical simulations, as shown by the sometimes erratic and unexpected results of the one-way range simulations discussed here. The behaviour of the two-way range simulations, however, is unaffected by correlations between clock and state parameters. Also, the quantitative influence of a clock noise realization on one-way system performance that occurs for a given time interval is a stochastic quantity, for which the data points we show in Figs. 4 and 5 are the average from 25 realizations (with the standard deviation similar to the average in all cases, *i.e.* no observed outliers). As a result, to meet a given positioning requirement over the entire mission, a more stringent mean positioning requirement is needed for the one-way than for the two-way system. However, the predictability of the estimation quality is still dependent on the force model error profile for both the one- and two-way system results.

## 6 Phobos Lander Results

We now present the results for the Phobos lander one- and two-way laser tracking simulations. The settings for the observation and dynamical models are summarized in Section 4.2; the estimated parameter set is discussed in Section 4.4. The Allan variance we use for simulating clock noise is shown by the red curve in Fig. 3. In Sections 6.1 and 6.2 we discuss the behaviour of the results for the one- and two-way laser ranging simulations, respectively. In Section 6.3, the implications of the estimation accuracy of the libration amplitudes and Phobos'  $\tilde{C}_{2,2}$  gravity field coefficient for our knowledge of Phobos' interior are discussed, including a discussion of the comparative science return from a one- and two-way laser ranging mission. In Section 6.4, the estimation quality of long-periodic effects is discussed

### 6.1 One-way ranging simulations

The estimation error of Phobos' position, as obtained from one-way range measurements, averaged over the entire one-year arc, is shown in Fig. 7(a) as a function of the number of estimated clock arcs  $N_c$ . From this figure, it can be seen that the estimation error initially decreases with increasing number of clock arcs, a result of the estimation having more possibilities to remove clock noise from the measurements, similar to the results discussed in Section 5. However, for large number of clock arcs, the position error again increases, albeit slightly. Also, we find that the formal initial position estimation error increases continuously as  $N_c$  increases, since the formal error does not take into account the improvement in the estimated clock profile's capability to correctly represent the true clock behaviour. The true error increase we observe for  $N_c > 100$  in Fig. 7(a) is not accompanied by an increase in estimation residual, which indicates that the increase in position error is due to the dynamical signal being absorbed by other parameters, in this case the increasing number of clock parameters. Resultantly, there is a limit in how well clock errors can be removed from the range error profiles before the correlations

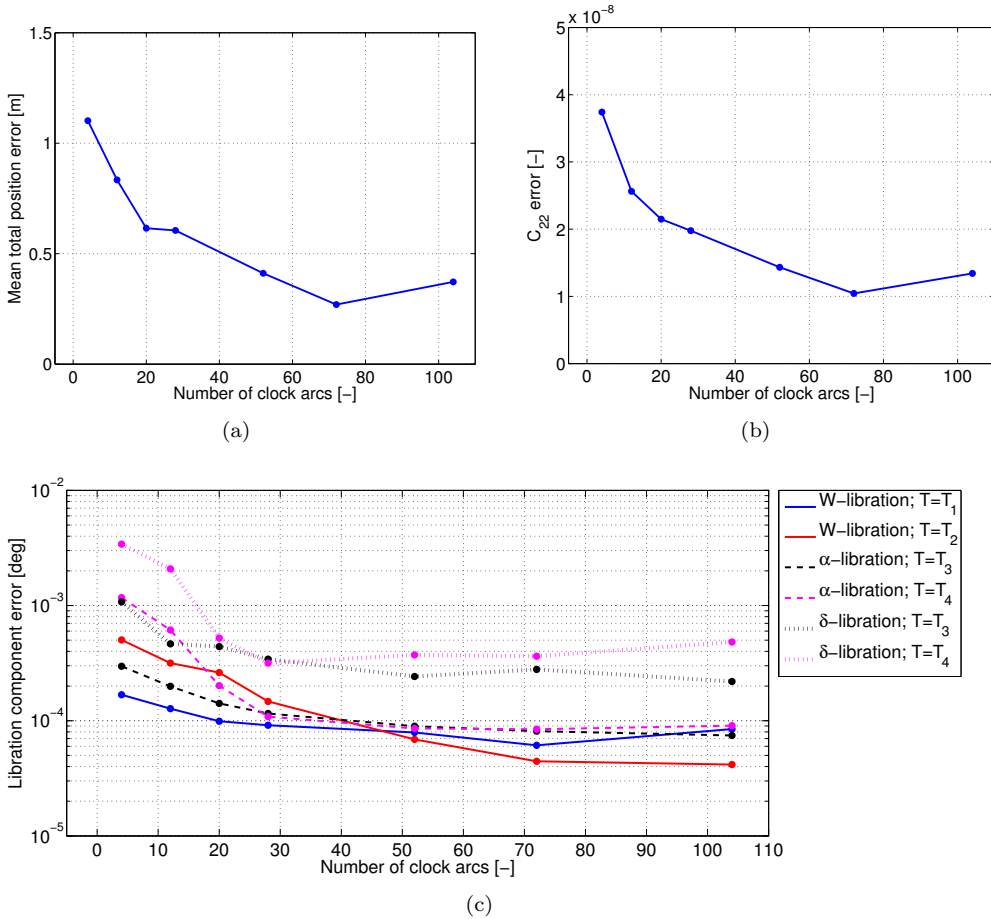


Figure 7: Plot of the estimation error as a function of number of clock estimation arcs of a) Phobos position, averaged over full one year arc b) Phobos  $\bar{C}_{2,2}$  gravity field coefficient c) Phobos libration amplitudes (see Table 1).

between clock parameters and other parameters begin to degrade the position estimates. For our clock noise profile, this effect limits the position estimation accuracy of Phobos to about 30 cm.

The estimation results of the libration components is shown in Fig. 7(c). The mean total libration amplitude error has been plotted, as derived from its estimated sine and cosine component errors,  $\gamma_{T_j}^S$  and  $\gamma_{T_j}^C$ , see Eq. (30). An initially very strong trend of improved estimation accuracy with increasing  $N_c$  is observed for most libration components in Fig. 7(c). The primary libration longitude amplitude estimation (W libration with period  $T_1$ ), however, shows anomalous behaviour when compared to the other components, having a much less steep slope with increasing  $N_c$  and a comparatively small

uncertainty at low  $N_c$ . The reason is that this component is by far the most strongly coupled to the orbital dynamics, since its amplitude is largest by several orders of magnitudes (see Table 1). Therefore, it modulates the influence of Phobos' degree 2 gravity field much more strongly than the smaller librations. As a result, its estimation shows a large correlation with both the initial state components and  $\bar{C}_{2,2}$ . These correlations range from 0.94 to 0.96 with  $\bar{C}_{2,2}$  and 0.99 to 0.995 with the initial state, when varying the number of clock arcs from 4 to 104. For the other libration components, the orbital signal is not dominant when determining the partial derivative of the observation w.r.t. the parameter. As a result, their estimation is largely determined by the direct observation partial, *i.e.* the change in range due to the different instantaneous rotation matrix from a Phobos-fixed to an inertial frame, as discussed in more detail by Dirkx et al. (2014a). The fact that the primary libration amplitude is strongly coupled to the orbital dynamics results in an increase in time of the partial derivatives of the range w.r.t. this libration, as its signature on the orbit accumulates. For the remaining libration components these partial derivatives are largely periodic, since their behaviour is largely the result of geometry, not orbital dynamics. As a result, these libration amplitudes are more sensitive to the presence of clock noise in the observations. The reason for this is that the total fraction of the clock error that can be removed is limited by the correlations between clock parameters and the remaining parameters. There will always be some remaining (trend-free) clock errors, a part of which can be interpreted as a libration signal without a meaningful increase in observation residual.

We observe a clear distinction between the estimation quality of the  $\delta$ - and  $\alpha$ -librations in Fig. 7(c), with the  $\alpha$ -librations estimated to about three times greater accuracy. This effect is due to the geometry of the problem, which causes a unit change in amplitude of the  $\alpha$ -librations to have a larger signature on the range measurements than the same unit change in amplitude of  $\delta$ -libration does. The comparative accuracy of the right ascension and declination libration amplitudes conflicts with the results presented by Dirkx et al. (2014a), where the  $\alpha$ - and  $\delta$ -libration estimation results are almost equal. This conflict is due to the removal of the correlations between these components that results from reducing the estimated parameter set, as discussed in Section 4.4.

As is the case with the primary longitudinal libration, the estimation of Phobos'  $\bar{C}_{2,2}$  shows much weaker improvement in accuracy with increasing number of clock arcs than the small libration amplitudes, as shown in Fig. 7(b). We again observe the small degradation of solution accuracy at  $N_c > 100$ , due to the stonger correlations between state, and resultantly  $\bar{C}_{2,2}$ , and clock parameters. The implications of the libration amplitude and  $\bar{C}_{2,2}$  estimation quality for improving the knowledge of Phobos' interior will be discussed in Section 6.3.

## 6.2 Two-way ranging simulations

The estimation results for the simulation of the Phobos lander tracking using two-way ranging are shown in Table 2, where the mean absolute estimation error of each of the parameters is given. Also given is the mean observation residual after estimator convergence, which can be seen to be close to the single-shot Gaussian measurement error (1.5 cm), indicating that the time-correlated errors are not of strong influence

Table 2: List of estimated parameter errors for Phobos two-way range simulations; mean observation residual = 2.28 cm

Parameter	Rms estimation error
$ \mathbf{x}_{P,0} $	0.0266 m
$ \dot{\mathbf{x}}_{P,0} $	$5.5 \cdot 10^{-6}$ m/s
$\bar{C}_{2,2}^P$	$5.14 \cdot 10^{-9}$
$W_{T_1}$	$1.36 \cdot 10^{-5}$ deg
$W_{T_2}$	$1.90 \cdot 10^{-6}$ deg
$\alpha_{T_3}$	$5.35 \cdot 10^{-6}$ deg
$\alpha_{T_4}$	$1.04 \cdot 10^{-6}$ deg
$\delta_{T_3}$	$2.59 \cdot 10^{-5}$ deg
$\delta_{T_4}$	$2.47 \cdot 10^{-5}$ deg
$ \mathbf{x}_L $	0.497 m

in the estimation. This was expected from the discussion in Section 3.2, due to the combination of small retransmission time  $\delta t_B$  (see Eqs. (16) and (18)) and highly stable ground clock. It should be noted that the results shown here (as well as in the previous section) are contingent upon highly accurate gravitational models of Phobos' orbit, both classical and relativistic.

The mean position estimation error of the two-way system can be seen in Table 2 to be on the order of the observation residual. For an estimation problem with purely white noise and completely uncorrelated parameters, one would expect the estimation error to reduce with  $N_{obs}^{-1/2}$ , where  $N_{obs}$  is the number of observations, which would have resulted in an initial position estimation error that is orders of magnitude smaller than the observation residual (as shown by the formal errors given by Dirx et al. (2014a)). One reason for the lack of such behaviour is the clock noise, which causes a time-correlated component in the observation errors, limiting the reduction of the estimation error with the number of observations. For the space- and ground-clocks used here, though, the combined clock error induced by the stochastic clock errors is at most 0.5-1 mm (Section 4.3), with values several times smaller for short Earth-Phobos distances and, to a lesser degree here, a shorter retransmission delay. Although this time-correlated error imposes a limit beyond which our least-squares approach cannot filter out observational noise, the small clock-induced error indicates that strong correlations between the estimated parameters additionally degrade the results. Inspection of the correlation matrix indeed shows large correlation between initial state components, as well as the primary libration amplitude and  $\bar{C}_{2,2}$  (Section 6.1), so that these parameters may be varied substantially without affecting the observation residual. Nevertheless, the mean initial position error is, at several cm, orders of magnitude more precise than current Phobos ephemerides *e.g.* Lainey et al. (2007). However, the attainability of this value is contingent upon the highly precise mapping of the (time-varying) gravitational environment of Phobos. Although estimating Mars gravity field components is shown by Dirx et al. (2014a) to be feasible using a Phobos lander, they conclude that (next-generation) Mars-orbiting spacecraft are more suitable for characterizing the static part of Mars' gravity field.

Comparing the estimation accuracy of the libration components for the two-way system (Table 2) to those obtained with the one-way system (Fig. 7(c)), there is again a clear difference between the behaviour of the primary libration component  $W_{T_1}$  and the other, smaller, libration components. Specifically, the estimation quality improvement for the small libration amplitudes is much greater than for the primary libration when going from a one- to a two-way system. This indicates that the small libration amplitudes are much more sensitive to the presence of clock noise than the larger libration, as was already hypothesized in Section 6.1. The estimation accuracy of  $\bar{C}_{2,2}$  is relatively close to that which can be obtained from the one-way system (a factor two), as seen when comparing Table 2 and Fig. 7(b). We will discuss the comparative implications for improved Phobos interior structure knowledge in Section 6.3.

### 6.3 Phobos physical parameters

In Sections 6.1 and 6.2, the estimation accuracy for Phobos physical characteristics, specifically its  $\bar{C}_{22}$  gravity field coefficient and selected libration amplitudes, has been presented for one- and two-way ranging systems, respectively. In this section, we will discuss the implications that these estimation accuracies have for the improvements of models of Phobos' internal structure, allowing us to assess the influence that the choice of laser ranging system type has on mission science return.

The combination of libration and degree-two gravity field estimation can be used to determine Phobos' principal moments of inertia, as discussed by *e.g.* Le Maistre et al. (2013); Dirkx et al. (2014a). A total libration amplitude estimate  $\hat{\gamma}_f$  is derived from the estimates of the sine and cosine components (see Eq. (30)). The libration amplitude estimates (combined with their frequencies  $\omega_f$ ) are used to obtain estimates of the proper mode frequencies  $\hat{\nu}_\gamma$  about Phobos' three principal moments of inertia  $A$ ,  $B$  and  $C$ , where  $A$  and  $B$  denote the equatorial components and  $C$  the polar moment of inertia.

From the proper mode frequencies, its relative moments of inertia are obtained, from which estimates of the absolute moments of inertia are obtained through combination with either  $\bar{C}_{2,2}$  or  $\bar{C}_{2,0}$ . It was found by Dirkx et al. (2014a) that laser ranging to a Phobos lander is better able to estimate  $\bar{C}_{2,2}$ . The combination of  $\bar{C}_{2,2}$  and longitude libration constrain  $C$ , whereas  $\bar{C}_{2,2}$  and the combined estimated of the  $\delta$ - and  $\alpha$ -librations jointly constrain  $A$  and  $B$ .

A libration amplitude uncertainty  $\sigma_{\gamma_f}$  propagates to proper mode frequency  $\sigma_{\nu_\gamma}$  (about the same axis) as follows (Dirkx et al., 2014a):

$$\sigma_{\nu_\gamma} = \frac{(\nu_\gamma^2 - \omega_f^2) \nu_\gamma}{2\gamma_f \omega_f^2} \sigma_{\gamma_f} \quad (32)$$

so that the ratio  $\sigma_{\gamma_f}/\gamma_f$  determines the proper mode uncertainty. As a result, to determine the  $C$  moment of inertia, the primary libration amplitude ( $W_{T_1}$ ) provides the strongest constraints, since its total amplitude is about two orders of magnitude larger than the other librations. Similarly, the small amplitudes of the  $\alpha$ - and  $\delta$ -librations (see Table 2) cause the estimation uncertainty of  $A$  and  $B$  to be several orders of magnitude

higher than that of  $C$ . The discrepancy between the accuracy of the equatorial and polar moment of inertia becomes even greater for the one-way range system, where the small libration amplitudes are estimated to a relatively poorer accuracy than that of the primary libration. Comparing Fig. 7 and Table 2, it seems that the science return from the two-way range system would be substantially greater than for the one-way system, since the constraints on Phobos' moments of inertia would be much weaker for a one-way system, especially so for the equatorial moments of inertia.

However, as highlighted by both Le Maistre et al. (2013) and Dirkx et al. (2014a), geophysical interpretation of improved estimated of Phobos' moments of inertia at the level discussed here is currently limited by uncertainty in Phobos' volume. To compare estimated values of Phobos' moments of inertia to values that are obtained from models of Phobos interior structure with various degrees and types of heterogeneities, such as is done by Rosenblatt (2011), an accurate shape model of Phobos is needed. However, the currently best estimate for Phobos' volume (Willner et al., 2014) has an uncertainty of 35 km<sup>3</sup>, which translates into a homogeneous moment of inertia error on the order of  $\approx 1\%$ . As such, both the one- and two-way range systems are capable of providing geophysical parameter estimates, but they cannot be used to their fullest potential in analyzing Phobos' interior structure without improved Phobos shape models. Additionally, it highlights that, although the one-way range estimation is clearly inferior to the two-way range system's performance in terms of estimated parameter accuracy, both systems may result in similar science return for Phobos interior, unless strong improved estimates of additional physical parameters are made available through the use of synergistic next-generation missions and instrumentation.

## 6.4 Long-period signal identification

We did not include the estimation of the long-period librations of Phobos in our simulations, since the results presented by Dirkx et al. (2014a) indicate that they will not be observable for the short 1-year mission we analyze here. Also they have little relevance for analyzing Phobos' internal mass distribution (Rambaux et al., 2012).

Additionally, we find that such long-period signals are impossible to decorrelate from clock parameters in the case of one-way ranging data analysis, making them intrinsically unobservable for these systems. The reason for this correlation is that the piecewise polynomials can very closely represent a long-period sinusoidal signal, allowing much freedom to interchange long-periodic signal for suitable modifications of the clock parameters. Since no clock parameters are estimated during the analysis of the two-way data, the two-way range system does not suffer from this issue.

Although we do not estimate the long-periodic librations, the lander's position is included in our parameter set. The Phobos-fixed component of the lander position perpendicular to the plane of the ecliptic imprints a signal on the range measurements that is mostly periodic, with a period determined by the observation geometry. As a result, we observe very large errors (up to 500 m) in the position estimation of the lander from one-way range measurements for low number of clock arcs, as shown in Fig. 8. For shorter clock arcs, the estimation accuracy reduces to  $\sim 20$  m, compared to  $\sim 0.3$  m for the ecliptic-in plane component. Although the precise ( $< 20$  m) lander position holds



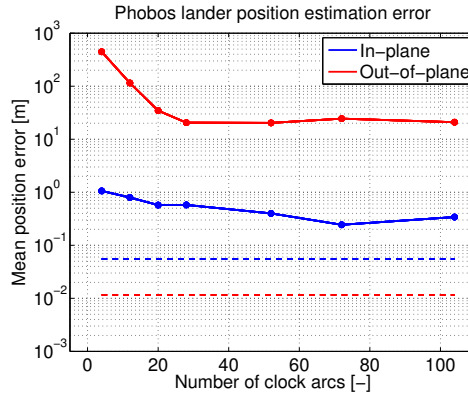


Figure 8: Plot of the estimation error in the out-of-plane (approximately perpendicular to ecliptic) and in-plane position of the Phobos-fixed lander position. One-way results shows as a function of  $N_c$ ; dashed lines show 2-way results.

little intrinsic scientific value, an accurate positioning could be advantageous for the improvement of control point networks, when combined with surface observations by both the lander itself, as well as additional (quasi-orbiting) spacecraft. More importantly, though, the strong correlation with the clock parameters makes it difficult to perform a detailed analysis of the clock behaviour, since it is effectively impossible to decorrelate the signal of the ground station position (and all other long-period signals in general) from that of the clock. Although the estimation of the ground station position when using the two-way system is also substantially worse than that of Phobos' orbit itself (see Table 2), this is instead the result of the inherent geometric difficulty of estimating its out-of-plane component, also without the added complication of the clock parameter estimation.

The influence of this deficiency in the capabilities of the one-way system does not result in substantial degradation of the mission's science return in this particular case. However, a long-period sinusoidal signal may hold crucial information for parameter estimation in other cases. For instance, a once-per-year (relativistic) signal in the dynamics of planets cannot be properly exploited by a one-way system. This again indicates the need for critical evaluation of comparative performance of one- and two-way systems in mission design selection.

## 7 Conclusions

We have simulated one- and two-way laser ranging measurements for both a lunar polar orbiter and a Phobos lander and have used these synthetic measurements as input for orbit determination and parameter estimation. By doing so, we have quantified the influence of clock noise on one-way laser ranging performance and compared the performance of both types of laser ranging systems.

For the lunar orbiter, we find that the one- and two-way laser ranging systems provide

similar mean position estimation errors, at about 5 m for a 1 day state arc duration and a clock arc duration of less than one day (for the one-way system). This result is due to the fact that the dynamical model errors, and not the observation errors, are the dominant source of error in the estimation. Nevertheless, the two-way system has the advantage of being more robust, since it is not influenced by the specific vagaries of the spacecraft clock. We find such effects in the one-way data analysis, manifested as a number of deviations from the expected trend of the results with number of clock arcs  $N_c$  and number of state arcs  $N_s$ . Additionally, the absence of the clock parameters in the estimation procedure both simplifies the data analysis and allows for better force model improvement. In conclusion, although the use of a two-way laser ranging system has a number of definite advantages compared to the one-way system, dynamical model errors prevent the full utilization of both data types. This has stronger consequences for the more accurate two-way system.

Our simulations of the Phobos lander tracking show large differences between the one- and two-way laser ranging system's performance. The correlations between clock and state parameters result in an optimal clock arc length of about one week for our one-year simulation period, for which a mean Phobos position estimation error of 0.3 m is obtained. The two-way system results in a mean position estimation error of 2.5 cm. These results are contingent upon highly accurate dynamical models of Phobos, though. We find that the estimation of small libration amplitudes, which are largely decoupled from Phobos' dynamics, are much more sensitive to the presence of clock noise in the one-way range measurements. This is due to the purely periodic influence that they have on the range measurements. The strong correlations between clock parameters and physical parameters that are manifested in the range measurements as long-periodic trend-free signals (such as the out-of-plane component of the ground station position) prevent an accurate estimation of either of these sets of parameters from one-way ranging data. However, for the case of a Phobos lander, for which the science return from tracking data would largely stem from improved estimates on Phobos' interior and evolution, geodetic parameter estimates (such as libration amplitudes and gravity field coefficients) must be mapped to a space of Phobos interior compositions. In this mapping, the dominant error source at the levels of accuracy that we get for both the one- and two-way systems is Phobos' volume error, not the uncertainty in our estimated parameters. This shows that, although the parameter estimates of a Phobos lander utilizing a two-way system are of higher quality than those of a one-way system, the mission's science return (in terms of Phobos origin and evolution) need not be of higher quality as well.

The two missions that we have analyzed differ in a number of key aspects. Nevertheless, it is interesting to note that the general conclusion that we draw on the comparative performance of the one- and two-way systems is similar. Specifically, although the two-way system has the potential to facilitate superior mission performance, as was to be expected, this potential cannot be fully exploited due to the uncertainties in other models used to process the tracking data. For the lunar orbiter, the limiting factor is the dynamical model errors, whereas the Phobos volume uncertainty dominates the Phobos lander mission's performance. To make full use of the two-way data, the final parameter estimation error induced by measurement uncertainty should be at the same order as that of other error sources. To achieve this, a variety of models used in the tracking

analysis of planetary missions must be improved. This will require the use of synergistic next-generation instrumentation, improving not only the tracking data accuracy, but all relevant scientific measurements (ground-based, space-based and *in situ*) which are required to obtain a balanced error budget of scientific quantities obtained from future planetary missions.

## Acknowledgements

This work is performed as part of the FP7 ESPaCE project, financially supported by the EC FP7 Grant Agreement 263466.

## Appendix A Coloured noise signal generation

We use a coloured noise power spectral density for both the unmodelled segment of the non-gravitational accelerations and the stochastic errors of the oscillator signal. Here, we present the model used to generate a coloured noise signal in time domain from its power spectral density, based on (Timmer and Koenig, 1995).

Starting from the power spectral density of a quantity  $x$ , denoted  $S_x^2(\omega)$ , or its amplitude spectral density  $S_x(\omega)$ , we generate a realization of the signal in frequency domain, using the following relation for the continuous Fourier transform of  $f(t)$ , denoted  $F(\omega)$ :

$$F(\omega) = K \left( \mathcal{N} \left( 0, \frac{1}{2} S_x^2(\omega) \right) + i \mathcal{N} \left( 0, \frac{1}{2} S_x^2(\omega) \right) \right) \quad (33)$$

where  $K$  is a normalization constant depending on the convention of the Fourier transform that is used and  $\mathcal{N}(\mu, \sigma^2)$  denotes a univariate Gaussian random number with mean  $\mu$  and variance  $\sigma^2$ .

To generate the discrete realizations  $f(t_k)$  in time domain, we first discretize the power spectrum into  $n_f$  equisized bins of size  $\Delta\omega$ . We denote the power in each bin as  $(S_x)_i^2$ . Approximating the power across each bin to be constant at the value of its midpoint, we obtain:

$$(S_x)_i^2 \approx S_x^2 \left( \omega_i + \frac{\Delta\omega}{2} \right) \Delta\omega \quad (34)$$

Subsequently, we set up its discrete Fourier transform  $F_n = F(\omega_n)$  of the time domain realization  $f_k = f(t_k)$  from the discretized power spectrum. Our convention for DFT and IDFT are the following:

$$F_n = \sum_{k=0}^{N-1} f_k \exp \left( \frac{-in2\pi k}{N} \right) \quad (35)$$

$$f_k = \frac{1}{N} \sum_{n=0}^{N-1} F_n \exp \left( \frac{ik2\pi n}{N} \right) \quad (36)$$

so that  $K = N$  in Eq. (33).

Since our time domain realization  $f_k$  has no complex part, the following condition is imposed on the components  $F_n$ :

$$F_{N-n} = F_n^* \quad (37)$$

where the asterisk denotes complex conjugation. Additionally, since we assume zero power at zero frequency, *i.e.* the time-average of the realization in time domain will tend to zero as  $t$  tends to infinity, we set:

$$F_0 = F_N = 0 \quad (38)$$

Assuming  $N$  to be odd, we must calculate  $n_f - 1 = (N + 1)/2 - 1$  values for  $F_n$  from the discretized power spectral density. However, we note that due to Eq. (37), the power in a single bin  $i$  is spread out over two values of  $F_n$ , so that we introduce the halved power  $(\tilde{S}_x)_n^2 = (S_x)_n^2 / 2$

We then directly obtain the discrete Fourier transform of our realization in time domain from:

$$F_n = N \left( \mathcal{N} \left( 0, \frac{1}{2} (\tilde{S}_x)_n^2 \right) + i \mathcal{N} \left( 0, \frac{1}{2} (\tilde{S}_x)_n^2 \right) \right) \quad (39)$$

By evaluating the discretized power spectral density and generating realizations of the Gaussian random variables, we generate a frequency domain realization  $F_n$ . By using a Fast Fourier Transform (FFT) of  $F_n$ , we obtain our realization  $f_k$ .

## CHAPTER 7

---

### Paper IV - Coupled Relativistic Dynamical Effects

---

*“Our ultimate analysis of space leads us not to a here and a there, but to an extension such as that which relates here and there. To put the conclusion rather crudely - space is not a lot of points close together; it is a lot of distances interlocked.”*

– Sir Arthur Stanley Eddington, *The Mathematical Theory of Relativity* (Cambridge University Press, 1923)



# Simultaneous Spacetime Dynamics Estimation From Space Mission Tracking Data

*D. Dirka<sup>a</sup>, R. Noomen<sup>a</sup>, P.N.A.M. Visser<sup>a</sup>, L. Gurvits<sup>b,a</sup>, L.L.A. Vermeersen<sup>a</sup>*

To be submitted to *Astronomy and Astrophysics*, September 2015

## Abstract

Many physical parameters that can be estimated from space mission tracking data, *e.g.*, classical gravity field parameters, planetary ephemerides, Parametrized Post-Newtonian (PPN) parameters, *etc.*, influence both the translational dynamics and proper time rate of observers. The different proper time rates of observers cause a variability of the time transfer observable beyond that caused by their translational (and rotational) dynamics. With the near-future implementation of interplanetary laser ranging, these effects will become increasingly important, possibly requiring a re-evaluation of common data analysis practice of using *a priori* time ephemerides. In this article, we present a framework for the simultaneous estimation of initial translational state and initial proper time to facilitate robust tracking data analysis from next generation space missions carrying highly accurate clocks and tracking equipment.

We perform a covariance analysis using our proposed method with simulated laser data from Earth-based stations to both a Mars and Mercury lander. For the Mars lander simulations, 4 years of tracking data results in a difference in results between our simultaneous estimation and classical analysis techniques (with an *a priori* time ephemeris) of around 0.1 % in formal errors and correlation coefficients. For a Mercury lander this rises to around 1% for a 1-month mission and 10 % for a 4-year mission. We find by means of Monte Carlo simulation that using an *a priori* time ephemeris of representative accuracy to process highly accurate laser time transfer data will result in estimation errors that are orders of magnitude above the formal error.

## 1 Introduction

The accurate processing and interpretation of data from modern (interplanetary) space missions requires the consideration of a number of physical effects induced by general relativity. Firstly, spacecraft tracking observations such as range, range rate and astrometric measurements are influenced by relativistic effects well above their measurement accuracy, *e.g.* (Klioner, 2003; Moyer, 2000; Hees et al., 2014b) due to for instance the Shapiro time delay. Secondly, the equations of motion in general relativity differ from their Newtonian counterparts, influencing the dynamics of spacecraft and celestial bodies, *e.g.* (Brumberg, 1991; Damour et al., 1994; Kopeikin et al., 2011). Finally, the influence of time dilation must be included when comparing the clock rates of different observers *e.g.* (Soffel et al., 2003; Müller et al., 2008a).

Due to the effects of gravitation on these aspects of space mission data processing, these data can be used to test general relativity by comparing the observed effects

---

(a): Delft University of Technology, The Netherlands

(b): Joint Institute for VLBI in Europe, The Netherlands

with those predicted by it and certain alternative theories of gravity (*e.g.* Turyshev, 2009; Hees et al., 2012; Will, 2014). A near-future improvement in tracking data quality that will require the use of more sophisticated relativistic data analysis is interplanetary laser ranging. This technology could be used for orbit determination and time transfer over solar system distances to unprecedented accuracy, at the 1 mm to 1 cm level (Degnan, 2002; Turyshev et al., 2010; Dirkx et al., 2014a), compared to a typical current radiometric range measurement accuracy of 1 m (Thornton and Border, 2000) and near-future radiometric range accuracy of 20 cm (Iess et al., 2014a). A variety of missions using this technology has been proposed *e.g.* (Samain, 2002; Turyshev et al., 2004; Christophe et al., 2009; Wolf et al., 2009; Turyshev et al., 2010; Oberst et al., 2012), opening up new possibilities in experimental relativity, requiring highly precise modelling of relativistic effects. Also, to properly estimate non-relativistic parameters from measurements made by such missions (Dirkx et al., 2014a), relativistic effects well below the mm-level should be modelled correctly and consistently. Especially in the case of one-way (interplanetary) laser ranging and time transfer, which should employ a highly precise clock at the space segment for optimal usage (Bauer et al., 2013; Dirkx et al., 2015a), detailed relativistic modelling of clocks in the solar system will be required, as one cannot use this data to directly decouple the signature of translational dynamics and clock effects.

The introduction of next-generation highly precise space-based clocks, combined with time-transfer techniques, *e.g.* (Bjerhammar, 1985; Klioner, 1992; Petit and Wolf, 1994; Blanchet et al., 2001; Müller et al., 2008a) will allow relativistic clock effects to be used for improving both geodetic measurements and experimental tests of general relativity, as is planned for the ACES mission (Delva et al., 2012). Such projects will build on experience with past and current time transfer experiments such as T2L2 (Exertier et al., 2010), in which time transfer from Earth to the Jason 2 satellite was achieved. The exploitation of relativistic clock effects was analyzed by *e.g.* (Angélil et al., 2014; Schärer et al., 2014), specifically for time transfer to Earth-orbiting satellites, who conclude that an improvement in the determination of PPN parameters  $\beta$  and  $\gamma$  is possible with this approach.

Complicating the time transfer data analysis, however, is the fact that it is contingent upon accurate knowledge of the state history of the transmitter and receiver, since an error in these states will propagate into an error in proper time rate. For instance, it is found by Delva et al. (2015) that orbital errors of the Galileo GNSS satellites clearly manifest itself in the use of these satellites' clocks for experimental verification of the gravitational redshift, albeit for short integration times. It was found by Duchayne et al. (2009), though, that the influence of orbital errors on the achievable accuracy of time transfer is acceptably small for the case of the ACES project, validating the decoupling of time and state dynamics estimation for that project.

However, this decoupling of translational and time dynamics may no longer be valid for certain future missions, especially when using the same data types for orbit determination and time transfer. As opposed to current tracking systems, this will be the case for missions employing interplanetary laser ranging. In such cases, the exploitation of space-based clocks for testing general relativity will require the ability to distinguish the influence of orbital errors and relativistic clock effects in a robust manner. Here, we



propose a novel general analysis framework in which the estimation of both translational dynamics and proper time dynamics are simultaneously performed, along with the estimation of physical parameters of interest. To achieve this, we extend the typical orbit determination procedure (*e.g.*, Montenbruck and Gill, 2000), performing it in a fully relativistic setting, taking into account the fundamental physical reality that an object's behaviour in time and space are intimately coupled. In doing so, we extend the classical orbit determination approach (with only translational dynamics estimation) to include the estimation of an observer's initial proper time in addition to its initial translational state. As such, we include the coupling between an observer's translational and time dynamics into the estimation, allowing the coupling between the two to be identified and exploited in tracking data analysis.

Such a concurrent estimation will allow for a more robust analysis of time transfer data, preventing signal from relativistic clock effects to be interpreted as translational dynamics or *vice versa*. Similarly, it will allow a direct quantification of the correlation between the signal of translational and time dynamics, which is key in interpreting the estimation results (*e.g.* Iorio, 2012b; Verma et al., 2014; Fienga et al., 2014; Deng and Xie, 2015).

Our motivation for this work is to analyze the importance of these effects for missions using interplanetary laser ranging as a primary tracking system. However, our approach can be applied equally well to Earth-orbiting missions in which relativistic clock effects become relevant (Müller et al., 2008a). Our approach may be used in the same framework as that of Mayrhofer and Pail (2012), who propose to use post-Newtonian effects to enhance range rate data analysis, and four-dimensional positioning systems *e.g.* (Delva et al., 2011).

We apply our framework to two interplanetary missions: the tracking of a lander on Mars and on Mercury. The goal of our simulations is to demonstrate the application of our proposed methodology, not to provide a detailed analysis of the scientific performance of such mission, as is done by *e.g.* Hees et al. (2012) for a range of missions and relativistic parameters. We investigate whether relativistic clock effects are manifested in planetary mission range/time transfer data at a sufficient level such that the concurrent analysis of relativistic time and translational dynamics effects is required when processing one-way range data, or wishing to exploit relativistic clock effects for improved science return from two-way data. That is, the goal of our test case missions is to investigate whether *a priori* or *a posteriori* relativistic clock calibration is a feasible approach in these cases, or whether they unduly bias the parameter estimation and the combined four-dimensional state estimation is required. Conversely, we investigate whether the physical signal encoded in clock-rate variations leads to a significant change in the estimation quality of a number of physical parameters. In doing so, we further analyze the error budgets of future interplanetary laser ranging missions.

We start by reviewing the relevant details of relativistic celestial mechanics, time dynamics and the formulation of the time-transfer observable in Section 2. Our new derivation of the extended variational equations and the partial derivatives of the time-transfer observable, including the coupling between translational and time dynamics, is given in Section 3. The results of this section comprise the key novel theoretical aspects of this paper. We demonstrate our methodology with numerical simulations of both a

Mars and a Mercury lander in Section 4, followed by our overall conclusions in Section 5. The metric and Christoffel symbols we use in our simulations are given explicitly in Appendix A and Appendix B, respectively. We provide a brief overview of least squares orbit determination and parameter estimation in Appendix C.

## 2 Dynamics and observable modelling

In this section, we define our notation and conventions in Section 2.1 and review the required models for the translational dynamics, time dynamics and range/time transfer observable in a relativistic setting in Sections 2.2, 2.3 and 2.4, respectively.

### 2.1 Notation and conventions

We will use the  $(-+++)$  metric signature, the Einstein summation convention and use Latin indices  $i, j, k = 1, 2, 3$  to denote space indices and Greek indices  $\mu, \nu, \sigma = 0, 1, 2, 3$  to denote space-time indices (with 0 the time index). A subscript of  $_{,\mu}$  will denote partial differentiation w.r.t.  $x^\mu$ .

We will often appeal to the post-Newtonian assumption of slow-motion ( $v \ll c$ ) and weak fields ( $|g_{\mu\nu} - \eta_{\mu\nu}| \ll 1$ ), since our application of orbit determination is limited to solar system situations. As a result, the metric  $g_{\mu\nu}$  can be written in terms of the metric perturbation  $h_{\mu\nu}$  as follows (Kopeikin et al., 2011):

$$g_{\mu\nu} = \eta_{\mu\nu} + h_{\mu\nu} \quad (1)$$

with  $\eta_{\mu\nu}$  the Minkowski metric. We perform our analysis in the Barycentric Celestial Reference System (BCRS), which is kinematically non-rotating, as its orientation is fixed w.r.t. distant objects (*e.g.*, quasars), so that the entries of  $h_{\mu\nu}$  are of order  $1/c^2$  or smaller (Kopeikin and Vlasov, 2004).

A metric to be used for the solar system up to first post-Newtonian order is recommended by the IAU and discussed by Soffel et al. (2003). The development of a metric of scalar-tensor gravity in the solar system has been a topic of active investigation, with an expansion up to second post-Newtonian order given by (Minazzoli and Chauvineau, 2011) and a general expansion to higher order by (Kopeikin et al., 2011). Here, we will use the first-order metric, parameterized with PPN parameters, which we provide explicitly in Appendix A. However, we stress that our approach laid out in Section 3 is not limited to this particular choice of metric, or even to metric theories of gravity.

### 2.2 Relativistic celestial mechanics

In this section we will review the concepts and equations of celestial mechanics in a relativistic framework necessary for our subsequent discussion of relativistic orbit determination. Further extensive discussion of relativistic celestial mechanics can be found in *e.g.* Brumberg (1972); Soffel (1989); Brumberg (1991); Kopeikin and Vlasov (2004); Kopeikin et al. (2011).

The general four-dimensional equation of motion of a point mass is the following:

$$\frac{d^2 x^\mu}{d\tau^2} = -\Gamma_{\alpha\beta}^\mu \frac{dx^\alpha}{d\tau} \frac{dx^\beta}{d\tau} + A^\mu \quad (2)$$

$$\Gamma_{\alpha\beta}^\mu = \frac{1}{2} g^{\mu\nu} (g_{\nu\alpha,\beta} + g_{\nu\beta,\alpha} - g_{\alpha\beta,\nu}) \quad (3)$$

where  $x^\mu$  denotes the four-position  $\{ct, x, y, z\}$ ,  $\tau$  denotes the proper time of an observer co-moving with the test body,  $\Gamma_{\alpha\beta}^\mu$  denotes the Christoffel symbols of the metric connection and  $A^\mu$  denotes the four-acceleration which encodes the non-gravitational forces. Note that in certain alternative theories of gravity, the assumptions that the connection contains no torsion ( $\Gamma_{\alpha\beta}^\mu = \Gamma_{\beta\alpha}^\mu$ ) and no non-metricity ( $\nabla_\alpha g_{\mu\nu} = 0$ ) will no longer hold, resulting in a modification of Eqs. (2) and (3) (Kopeikin et al., 2011). The inclusion of such terms would result in a modification of the equations of motion, light propagation, *etc.* that we use and derive in this section. However, it would not change the general methodology that is derived in Section 3

We will omit the presence of non-gravitational forces in the remainder of this paper and instead focus on trajectories purely described by gravitation, neglecting  $A^\mu$  in Eq. (2), obtaining the following (*e.g.*, Misner et al., 1973):

$$\frac{d^2 x^\mu}{d\tau^2} = -\Gamma_{\alpha\beta}^\mu \frac{dx^\alpha}{d\tau} \frac{dx^\beta}{d\tau} \quad (4)$$

In doing so, we focus on describing our general methodology in a clear and transparent manner. Our framework is easily extended to cases where  $A^\mu$  is not negligible, though. Neglecting  $A^\mu$  is valid for larger solar system bodies such as planets and major moons (at current modelling and measurement accuracy). For artificial satellites and smaller bodies such as asteroids and comets, non-gravitational forces are an important contributor to the dynamics, though.

We note that, in general, the centers of mass of extended bodies will not obey the geodesic equation exactly due to the interaction of the structure of the body with external potentials (Kopeikin, 1988). However, the correction to the equations of motion are at the  $c^{-2}$  level (Soffel et al., 2003; Kopeikin and Vlasov, 2004) and we neglect them in the current presentation. Their inclusion would be similar to the inclusion of the  $A^\mu$  term.

The equations of motion given by Eq. (4) may be written in terms of a coordinate time  $t$  (such as Barycentric Coordinate Time TCB) instead of proper time  $\tau$ . This yields equations of motion expressed in a time scale more closely related to that typically used in orbit propagation and determination *e.g.* (Kopeikin et al., 2011):

$$\ddot{x}^i = -\Gamma_{\alpha\beta}^i \dot{x}^\alpha \dot{x}^\beta + \frac{1}{c} \Gamma_{\alpha\beta}^0 \dot{x}^\alpha \dot{x}^\beta \dot{x}^i \quad (5)$$

$$\begin{aligned} &= -c^2 \Gamma_{00}^i - 2c \Gamma_{0j}^i \dot{x}^j - \Gamma_{jk}^i \dot{x}^j \dot{x}^k + \dot{x}^i \cdot \dots \\ &\dots \cdot \left( c \Gamma_{00}^0 + 2 \Gamma_{0j}^0 \dot{x}^j + \frac{1}{c} \Gamma_{jk}^0 \dot{x}^j \dot{x}^k \right) \end{aligned} \quad (6)$$

where the overdot denotes a derivative w.r.t. coordinate time  $t$ . The first term in Eq. (6) reduces to Newton's law of gravitation in the first Post-Newtonian limit (*i.e.* expanding  $\Gamma_{00}^i$  to terms of  $c^{-2}$ ).

In numerical ephemerides of solar system bodies, the independent variable is typically Dynamical Barycentric Time (TDB), which is a scaled version of Barycentric Coordinate Time (TCB) and not a coordinate time itself. TCB is the coordinate time of a frame centered on the Solar system barycenter, omitting the influence of all gravitating bodies. Detailed discussion of the influences of the transformation between the two various time scales is given by Brumberg and Kopejkin (1990); Klioner (2008). Recent INPOP ephemerides (Fienga et al., 2009) have been published with both TCB and TDB as independent variable, as well as associated TCG-TCB time ephemerides (where TCG is the Geocentric Coordinate Time). In the remainder of this paper, we will assume that the independent variable  $t$  is the coordinate time TCB.

### 2.3 Proper time dynamics

Eq. (4) describes the evolution of the four-velocity of an observer, with the first equation ( $\mu = 0$ ) describing the evolution of the time component and the other three equations ( $\mu = 1, 2, 3$ ) describing the translational dynamics. The norm of the four-velocity is constant by definition, *e.g.* (Misner et al., 1973), a condition that can be expressed as the following condition on the proper time rate:

$$\frac{d\tau}{dt} = \sqrt{-g_{\mu\nu} \frac{\dot{x}^\mu \dot{x}^\nu}{c^2}} \quad (7)$$

The post-Newtonian expansion for solar system situations of this equation is given explicitly by *e.g.* Soffel et al. (2003). Here, we will not restrict ourselves to a specific metric, keeping our formulation as general as possible. However, since our development is in the framework of solar system experiments, we do expand Eq. (7) using the metric perturbation in Eq. (1), obtaining the following:

$$\frac{d\tau}{dt} = \sqrt{1 - \frac{v^2}{c^2} - h_{\mu\nu} \frac{\dot{x}^\mu \dot{x}^\nu}{c^2}} = 1 + O(c^{-2}) \quad (8)$$

Since the leading-order difference between proper time rate and coordinate time rate is at the  $c^{-2}$  level, we will propagate the proper time difference  $\Delta\tau$ :

$$\Delta\tau = \tau - t \quad (9)$$

To evaluate the derivative w.r.t.  $t$  of Eq. (9) using Eq. (8), we expand it using a Taylor-series, thereby canceling the terms of  $O(1)$ , preventing rounding errors from limiting the precision of our results. The order of this expansion may be chosen such that the error that it introduces is below numerical precision, ensuring that it does not influence numerical results. For a first order expansion:

$$\frac{d\Delta\tau}{dt} = -\frac{1}{2} \left( \frac{v^2}{c^2} + h_{\mu\nu} \frac{\dot{x}^\mu \dot{x}^\nu}{c^2} \right) \quad (10)$$

By numerically integrating Eqs. (6) and (10), we obtain a numerical solution for the space-time behaviour of a given observer. This is equivalent to the approach taken in generation of the INPOP ephemerides (Fienga et al., 2009).

## 2.4 Time-transfer observable

To include time dynamics in our estimation procedure, we require measurements of the relative proper time rates of separated clocks. Observations of the proper time difference between two observers may be realized by time transfer. In this section, we summarize the models we use for simulating time-transfer observables, with extensive details provided by *e.g.* (Klioner, 1992; Petit and Wolf, 1994; Blanchet et al., 2001).

We consider two clocks between which time transfer is performed by means of electromagnetic signal transmission, such as a laser pulse. The signal is transmitted by the transmitter (station  $A$ ) at the proper time  $\tau^{(A)}(t_1)$  at coordinate time  $t_1$  and received by the receiver (station  $B$ ) at its proper time  $\tau^{(B)}(t_2)$ , at coordinate time  $t_2$  (Blanchet et al., 2001). In the following, we shall denote  $\tau^{(x)}(t_i)$  as  $\tau_i^{(x)}$ . The time-transfer observable  $h_\tau$  is then the difference between the two proper times, *e.g.*, (Duchayne et al., 2009):

$$h_\tau^{(1)} = \tau_2^{(B)} - \tau_1^{(A)} \quad (11)$$

The proper time rate, given by Eq. (7), will differ between the observers  $A$  and  $B$ , causing variability of the observable  $h_\tau^{(1)}$  beyond that caused by the translational (and rotational) dynamics of the receiver and transmitter that is observed in the one-way range observable.

For conventional range (rate) observables, the observation is referenced to the coordinate time at either the receiver or the transmitter (Moyer, 2000). However, since the information contained in the conversions from proper time to coordinate time is to be included in the analysis, we change this approach to reference the observation  $h_\tau^{(1)}$  to one of the *proper* times, not the *coordinate* times, (Hees et al., 2012). Consequently, when modelling the  $h_\tau^{(1)}$  observable, we reproduce  $\tau_2^{(B)}$  from a fixed  $\tau_1^{(A)}$  or *vice versa*. Our derivation here will show the case where the transmission proper time  $\tau_1^{(A)}$  is fixed. However, due to the symmetry of the governing equations, the inverse result (*i.e.*, keeping reception proper time fixed) may be obtained equivalently.

To model the time-transfer observable, we require three steps. First, we convert the transmission proper time to transmission coordinate time, using the result of the (numerical) integration of Eq. (7) for  $\Delta\tau_A$ . Second, models for the positions of the transmitter and receiver (denoted  $\mathbf{x}_A$  and  $\mathbf{x}_B$ , respectively) are used to calculate the (coordinate) light time  $T_{21} = t_2 - t_1$  between the two as follows:

$$T_{21}(t_1) = \frac{|\mathbf{x}_B(t_1 + T_{21}) - \mathbf{x}_A(t_1)|}{c} + \Delta T_{21}(t_1, t_2, \mathbf{x}_1, \mathbf{x}_2) \quad (12)$$

where the  $\Delta T_{21}$  term denotes light time corrections due to atmospheric and relativistic effects (Seeber, 2003; Moyer, 2000). Eq. (12) is implicit, requiring an iterative solution strategy (Moyer, 2000). To complete the time-transfer observable, we can calculate the reception proper time from the reception coordinate time, using the integration result

of Eq. (7) for  $\Delta\tau_B$ . Summarizing, the time-transfer observable is modelled by:

$$h_\tau^{(1)}(\tau_1^{(A)}) = \tau_2^{(B)} - \tau_1^{(A)} \quad (13)$$

$$t_1 = t_1(\tau_1^{(A)}) \quad (14)$$

$$t_2 = t_1 + T_{21}(t_1; \mathbf{x}_t(t), \mathbf{x}_r(t)) \quad (15)$$

$$\tau_2^{(B)} = \tau_2^{(B)}(t_2) \quad (16)$$

The step in Eq. (15) is the relation for a one-way range observable, which is given by  $cT_{21}$ . The observable  $h_\tau^{(1)}$  may be related to the one-way light time as:

$$h_\tau^{(1)} = T_{21}(t_1(\tau_1^{(A)})) - \int_{t_0}^{t_1} \frac{d\Delta\tau^{(A)}}{dt} dt + \int_{t_0}^{t_2} \frac{d\Delta\tau^{(B)}}{dt} dt \quad (17)$$

so that the integrated value of  $\Delta\tau$  at both the transmitter and receiver influences the observable.

When using both an up- and downlink one-way range measurement to construct a two-way observable, for instance using an asynchronous active laser ranging system (Degnan, 2002; Birnbaum et al., 2010), the influence of relativistic clock effects is substantially reduced, in the same manner that the influence of clock noise at both link ends is substantially reduced (Dirkx et al., 2015a). The downlink of a two-way measurement from the space segment to the ground station consists of a signal transmitted by the space segment at coordinate time  $t_3$ , where  $t_3 = t_2 + \delta t$ , with  $\delta t$  typically at most on the order of seconds. This signal is then received by the ground station at coordinate time  $t_4$ . The raw two-way light time, as measured by the ground station, then becomes:

$$h_\tau^{(2)} = \tau_4^{(A)} - \tau_1^{(A)} \quad (18)$$

$$= T_{21}(t_1(\tau_1^{(A)})) + T_{43}(t_3) + \int_{t_1}^{t_4} \frac{d\Delta\tau^{(A)}}{dt} dt + \delta t \quad (19)$$

$$t_3 = t_1(\tau_1^{(A)}) + T_{21}(t_1(\tau_1^{(A)})) + \delta t \quad (20)$$

Since the retransmission time at the space segment is small, the influence of the proper time rate of the space segment on  $h_\tau^{(2)}$  is almost completely removed. However, the conversion from  $h_\tau^{(2)}$  to the two-way coordinate light time  $t_4 - t_1$  remains sensitive to the difference in rates between  $t$  and  $\tau^{(A)}$ , but only as integrated over  $t_4 - t_1$ . Comparing Eqs. (17) and (19), it is clear that the one-way observable is sensitive to clock effects accumulated over long periods of time, whereas the two-way observable is largely insensitive to relativistic clock variations.

Nevertheless, since an (asynchronous) two-way observable simply consists of two one-way observables, it can be used to exploit relativistic clock effects during the estimation by including one or both of the one-way time transfer observables separately to the estimation

Since our purpose in this work is to present a model for the space-time dynamics estimation, we do not provide detailed models for relativistic effects on the  $\Delta T_{21}$  component of time transfer. Such models have been developed for a variety of contexts and applications *e.g.* (Klioner, 1992; Kopeikin and Schäfer, 1999; Linet and Teysandier, 2002), but

their inclusion does not alter the formulation of our estimation framework. Recently, a formalism of Time Transfer Function (TTF) models for relativistic influence on electromagnetic signal propagation (including light time corrections) has been developed (Le Poncin-Lafitte et al., 2004; Teyssandier and Le Poncin-Lafitte, 2008) and applied by *e.g.* Hees et al. (2012), based on the post-Minkowskian expansion of Synge’s world function. This approach does not require the integration of the null geodesic equation and can be used to set up a framework for the relativistic influence on light time, provided that a global post-Minkowskian metric to sufficient order can be defined.

### 3 Coupled space-time estimation

In this section, we present our proposed coupled space-time dynamics estimation procedure, and show how to apply it to the analysis of time-transfer data. We reiterate that this approach may become important for near-future situations where the same data are used for the estimation of the translational dynamics and the characterization of relativistic clock effects. We start by briefly outlining the problem in Section 3.1. Subsequently, we derive variational equations for the coupled estimation in Section 3.2 and the complete partial derivatives of the time transfer observables in Section 3.3. For reference purposes, we describe the details of orbit determination and parameter estimation using a least squares algorithm in Appendix C.

#### 3.1 Proper time estimation

To estimate the orbit of a celestial body or artificial satellite in a dynamical manner from tracking data, the initial state of that body is adjusted so as to result in a minimum (weighted) residual w.r.t. the measurements (*e.g.* Montenbruck and Gill, 2000). Additionally, parameters that influence the force models and/or observation models may be concurrently estimated.

By extending this approach to the coupled space-time dynamics case, we include the estimation of the initial proper time difference(s) of one or more observers w.r.t. some reference (coordinate) time  $\Delta\tau$ , see Eq. (9). When processing time-transfer observables (see Eq. (11)), proper time rates of both the transmitter and receiver are required.

By using the proper time differential equation Eq. (7), an initial proper time difference  $\Delta\tau_0 = \tau(t_0) - t_0$  can be mapped to a time difference at any later epoch. The value of  $\Delta\tau_0$  can then be estimated by minimizing the residuals between the modelled and measured value of the proper time difference through the variation of  $\Delta\tau_0$ , as well as any other parameters that influence the solution of  $\Delta\tau(t)$  in the same manner as is done in translational orbit determination, *e.g.* (Montenbruck and Gill, 2000). By doing so, the conventional data processing of space geodesy techniques is extended to the field of relativistic geodesy, since the influence of gravity fields on the space-time trajectory of an observer is now considered. Crucially, the adjustment of the time behaviour estimation is done concurrently with that of the translational state behaviour, allowing correlations between the two to be identified and preventing a misidentification of a signal of time behaviour as translational behaviour, or *vice versa*.

### 3.2 Relativistic variational equations

We derive a set of equations to dynamically estimate the initial state of  $N$  bodies and the proper time differences of  $M$  observers. We denote the translational state of a single body  $n$  as  $\mathbf{y}_n = (\mathbf{x}_n; \dot{\mathbf{x}}_n)$ , with  $\mathbf{x}_n$  the current position of body  $n$ , and  $\dot{\mathbf{x}}_n$  its velocity). The concatenated vector of all states is denoted as  $\mathbf{Y}$ , so that  $\mathbf{Y} = (\mathbf{y}_1; \dots; \mathbf{y}_N)$ . The concatenated vector of all proper time differences is denoted as  $\mathbf{T}$ , so that  $\mathbf{T} = (\Delta\tau_1; \dots; \Delta\tau_M)$ . Finally, we construct our full state vector  $\mathbf{X}$  as follows:

$$\mathbf{X} = \begin{pmatrix} \mathbf{Y} \\ \mathbf{T} \end{pmatrix} = \begin{pmatrix} \mathbf{y}_1 \\ \vdots \\ \mathbf{y}_N \\ \tau_1 \\ \vdots \\ \tau_M \end{pmatrix} \quad (21)$$

Our goal in this section is to derive equations for determining the (linearized) change in  $\mathbf{X}$ , due to a change in its initial value  $\mathbf{X}(t_0)$ , denoted  $\mathbf{X}_0$ , and a change in the model parameter vector  $\mathbf{p}$ . This is in contrast to the typical approach to orbit determination and time transfer, where the adjustment of  $\mathbf{Y}_0$  to the data is performed using an *a priori*  $\mathbf{T}_0$ .

In orbit determination, these changes are encoded in the state transition matrix  $\Phi(t; t_0)$  and sensitivity matrix  $S(t)$  (Montenbruck and Gill, 2000). Extending these matrices to our case using Eq. (21) as a state vector, we obtain the following.

$$\Phi(t; t_0) = \frac{\partial \mathbf{X}(t)}{\partial \mathbf{X}_0} = \begin{pmatrix} \frac{\partial \mathbf{Y}(t)}{\partial \mathbf{Y}_0} & \frac{\partial \mathbf{Y}(t)}{\partial \mathbf{T}_0} \\ \frac{\partial \mathbf{T}(t)}{\partial \mathbf{Y}_0} & \frac{\partial \mathbf{T}(t)}{\partial \mathbf{T}_0} \end{pmatrix} \quad (22)$$

$$S(t) = \frac{\partial \mathbf{X}(t)}{\partial \mathbf{p}} = \begin{pmatrix} \frac{\partial \mathbf{Y}(t)}{\partial \mathbf{p}} \\ \frac{\partial \mathbf{T}(t)}{\partial \mathbf{p}} \end{pmatrix} \quad (23)$$

These partial derivatives denote the change in the state that would occur if an initial state or model parameter is changed.

The first-order differential equation for the case of the estimation of the position and velocity of a single body is given by (Montenbruck and Gill, 2000). Here, we generalize their result to the estimation of  $N$  body states and  $M$  observer proper times. This results in the following formulation for the variational equations:

$$\begin{aligned} \frac{d}{dt} (\Phi(t; t_0), S(t)) &= \begin{pmatrix} \frac{\partial \dot{\mathbf{Y}}(t)}{\partial \mathbf{Y}} & \frac{\partial \dot{\mathbf{Y}}(t)}{\partial \mathbf{T}} \\ \frac{\partial \dot{\mathbf{T}}(t)}{\partial \mathbf{Y}} & \frac{\partial \dot{\mathbf{T}}(t)}{\partial \mathbf{T}} \end{pmatrix} (\Phi(t, t_0), S(t)) + \dots \\ &\dots + \begin{pmatrix} 0_{6N \times (6N+M)} & \frac{\partial \dot{\mathbf{Y}}(t)}{\partial \mathbf{p}} \\ 0_{M \times (6N+M)} & \frac{\partial \dot{\mathbf{T}}(t)}{\partial \mathbf{p}} \end{pmatrix} \end{aligned} \quad (24)$$

$$= A(\mathbf{X}, \dot{\mathbf{X}}, t) (\Phi(t, t_0), S(t)) + B(\mathbf{X}, \dot{\mathbf{X}}, t) \quad (25)$$

$$\Phi(t_0, t_0) = \mathbf{1}_{(6N+M) \times (6N+M)} \quad (26)$$

$$S(t_0) = \mathbf{0}_{(6N+M) \times N_P} \quad (27)$$



where  $N_P$  denotes the length of the estimated parameter vector  $\mathbf{p}$ .

There is no explicit dependency of  $\dot{\mathbf{Y}}$  on any of the observer's specific proper times  $\mathbf{T}$ , only on the coordinate time  $t$ . Similarly, the metric in the global coordinates does not depend explicitly on the proper time of a specific observer (Appendix A), so that there is also no explicit dependency of  $\dot{\mathbf{T}}$  on  $\mathbf{T}$ . As a result the matrix  $A(\mathbf{X}, \dot{\mathbf{X}}, t)$  reduces to:

$$A(\mathbf{X}, \dot{\mathbf{X}}, t) = \begin{pmatrix} \frac{\partial \dot{\mathbf{Y}}(t)}{\partial \dot{\mathbf{Y}}} & 0 \\ \frac{\partial \dot{\mathbf{T}}(t)}{\partial \dot{\mathbf{Y}}} & 0 \end{pmatrix} \quad (28)$$

An adjustment in  $\mathbf{T}_0$  will only result in a change in  $\mathbf{T}(t)$ , not of  $\mathbf{Y}(t)$ . However, an adjustment of  $\mathbf{Y}_0$  influences both  $\mathbf{Y}(t)$  and  $\mathbf{T}(t)$ , introducing the space-time-dynamics coupling into the estimation.

The expression for the top-left matrix block of  $A(\mathbf{X}, \dot{\mathbf{X}}, t)$ , *i.e.* the position and velocity derivatives w.r.t. the positions and velocities, is composed of the blocks of the state derivative of body  $m$  w.r.t. the state of body  $n$  as follows:

$$\frac{\partial \dot{\mathbf{Y}}_m(t)}{\partial \mathbf{Y}_n(t)} = \begin{pmatrix} 0_{3 \times 3} & \delta_{mn} 1_{3 \times 3} \\ \frac{\partial \dot{\mathbf{x}}_m}{\partial \mathbf{x}_n} & \frac{\partial \dot{\mathbf{x}}_m}{\partial \dot{\mathbf{x}}_n} \end{pmatrix} \quad (29)$$

To evaluate the components of the variational equations, the partial derivatives of the accelerations and proper time rate w.r.t. the full parameter vector  $\mathbf{q}(= (\mathbf{X}_0; \mathbf{p}))$  must be evaluated. For the equations of motion in the form of Eq. (5), this results in the following general formulation:

$$\begin{aligned} \frac{\partial \ddot{x}^i}{\partial \mathbf{q}} &= -\frac{\partial \Gamma_{\alpha\beta}^i}{\partial \mathbf{q}} \dot{x}^\alpha \dot{x}^\beta + \frac{1}{c} \frac{\partial \Gamma_{\alpha\beta}^0}{\partial \mathbf{q}} \dot{x}^\alpha \dot{x}^\beta \dot{x}^i - 2\Gamma_{\alpha\beta}^i \frac{\partial \dot{x}^\alpha}{\partial \mathbf{q}} \dot{x}^\beta + \dots \\ &\dots + \frac{1}{c} \Gamma_{\alpha\beta}^0 \left( \dot{x}^\alpha \dot{x}^\beta \frac{\partial \dot{x}^i}{\partial \mathbf{q}} + 2 \frac{\partial \dot{x}^\alpha}{\partial \mathbf{q}} \dot{x}^\beta \dot{x}^i \right) \end{aligned} \quad (30)$$

where the symmetry of the Christoffel symbols in the indices  $\alpha\beta$  has been exploited. Note that since  $x^0 = ct$ ,  $\dot{x}^0 = c$  and  $\ddot{x}^0 = 0$  (except in more exotic cases where variations of the vacuum speed of light  $c$  are allowed).

Estimation of the initial proper time difference requires the calculation of the proper time rate  $d\tau/dt$  w.r.t. position, velocity and model parameter vector. The partial derivatives of  $\dot{\tau}$  w.r.t. an arbitrary parameter  $\mathbf{q}$  are derived from Eq. (7) to be:

$$\frac{\partial \dot{\tau}}{\partial \mathbf{q}} = \frac{1}{2\dot{\tau}} \left( \frac{\partial g_{\mu\nu}}{\partial \mathbf{q}} \dot{x}^\mu \dot{x}^\nu + 2g_{\mu\nu} \dot{x}^\mu \frac{\partial \dot{x}^\nu}{\partial \mathbf{q}} \right) \quad (31)$$

The partial derivatives of the Christoffel symbols, required for the evaluation of Eq. (30), may be obtained numerically or analytically, either directly or from partial derivatives of the metric tensor (perturbations) from Eq. (3) through:

$$\begin{aligned} \frac{\partial \Gamma_{\alpha\beta}^\mu}{\partial \mathbf{q}} &= \frac{1}{2} \left( -\frac{\partial h^{\mu\nu}}{\partial \mathbf{q}} (h_{\nu\alpha,\beta} + h_{\nu\beta,\alpha} - h_{\alpha\beta,\nu}) + \dots \right. \\ &\left. \dots + g^{\mu\nu} \left( \frac{\partial h_{\nu\alpha,\beta}}{\partial \mathbf{q}} + \frac{\partial h_{\nu\beta,\alpha}}{\partial \mathbf{q}} - \frac{\partial h_{\alpha\beta,\nu}}{\partial \mathbf{q}} \right) \right) \end{aligned} \quad (32)$$

so that the variational equations may be evaluated analytically or numerically from only (first and second) derivatives of the metric (perturbation), in addition to the current state  $\mathbf{Y}(t)$ .

### 3.3 Time-transfer observable partials

To incorporate the time-transfer observables into the orbit determination, we require the partial derivatives of the  $h_\tau^{(1)}$  observables, given in Eq. (11), w.r.t. the current proper times vector  $\mathbf{T}$ , the current state vector  $\mathbf{X}$  and the model parameters  $\mathbf{p}$ . Denoting (an arbitrary combination of entries of) these vectors by  $\mathbf{q}$ , we require the following:

$$\frac{\partial h_\tau^{(1)}}{\partial \mathbf{q}} = \frac{\partial \tau_2^{(B)}}{\partial \mathbf{q}} - \frac{\partial \tau_1^{(A)}}{\partial \mathbf{q}} \quad (33)$$

As discussed in Section 2.4, we reference the time transfer to either the transmission or reception proper time, fixing its value in our model and using it to reproduce the second value and set up our time-transfer observable. Here, we will again show the case where we reference the observation to the transmission time, so that  $h_\tau^{(1)} = h_\tau^{(1)}(\tau_1^{(A)})$ , with a fixed  $\tau_1^{(A)}$ , making the second term on the right-hand side of Eq. (33) equal to zero. The first term on the right-hand side we derive to be:

$$\frac{\partial \tau_2^{(B)}}{\partial \mathbf{q}} = \dot{\tau}_2^{(B)} \frac{\partial t_2}{\partial \mathbf{q}} + \left. \frac{\partial \tau_2^{(B)}}{\partial \mathbf{q}} \right|_{t_2=\text{const}} \quad (34)$$

$$= \dot{\tau}_2^{(B)} \frac{\partial t_2}{\partial \mathbf{q}} + \frac{\partial \Delta \tau_2^{(B)}}{\partial \mathbf{q}} \quad (35)$$

where the first term on the right-hand side represents the change in reception proper time due to a change in reception coordinate time, and the second term represents the inherent change in the receiver proper time, *i.e.* the direct influence on the integrated result of Eq. (10). The reception coordinate time partial is expanded as follows from Eq. (15):

$$\frac{\partial t_2}{\partial \mathbf{q}} = \frac{\partial t_1}{\partial \mathbf{q}} + \frac{\partial T_{21}}{\partial \mathbf{q}} + \frac{\partial T_{21}}{\partial t} \frac{\partial t_1}{\partial \mathbf{q}} \quad (36)$$

which is equivalent to the one-way range partial as given by *e.g.* Moyer (2000). The partial derivative of the transmission coordinate time  $t_i$  is obtained from Eq. (9), since  $\tau_1^{(A)}$  is kept fixed:

$$\frac{\partial t_1}{\partial \mathbf{q}} = - \frac{\partial \Delta \tau_1^{(A)}}{\partial \mathbf{q}} \quad (37)$$

Combining these results yields:

$$\left. \frac{\partial h_\tau^{(1)}}{\partial \mathbf{q}} \right|_{\tau_1^{(A)}=\text{const.}} = \frac{\partial \Delta \tau_2^{(B)}}{\partial \mathbf{q}} - \frac{\partial \Delta \tau_1^{(A)}}{\partial \mathbf{q}} \left( 1 + \dot{T}_{21} \right) \dot{\tau}_2^{(B)} + \frac{\partial T_{21}}{\partial \mathbf{q}} \dot{\tau}_2^{(B)} \quad (38)$$

The final term of this equation,  $\frac{\partial T_{21}}{\partial \mathbf{q}}$ , is the one-way range partial, as expanded explicitly by *e.g.* Moyer (2000). The first two terms on the right-hand side are the (scaled) terms of the extended state transition matrix, as obtained by (numerical) integration of Eq. (24). It is these terms which our derivation has shown need to be added to the estimation to exploit the coupling between the space and time dynamics in the estimation process.

As a result of the formulation of Eq. (38) and the independence of  $\dot{\mathbf{X}}$  on  $\mathbf{T}$ , the partial derivatives of the observations w.r.t. the initial proper times behave largely as those of range biases. Deviations from unity of the partial derivatives  $\frac{\partial h}{\partial \mathbf{T}}$  instead follow from the  $(1 + \dot{T}_{21})\dot{\tau}_r$  term in Eq. (38).

Eq. (38) may be used to determine the direct part of the sensitivity to  $\mathbf{p}$  or the sensitivity to the current space-time state  $\mathbf{Y}$ . To compute the total sensitivity to  $\mathbf{Y}_0$  and  $\mathbf{p}$ , the state transition and sensitivity matrices that are obtained by (numerical) integration of Eq. (24) are used and the full partial derivatives of the observable w.r.t. the estimated quantities are calculated from:

$$\frac{\partial h(t)}{\partial \mathbf{X}_0} = \frac{\partial h}{\partial \mathbf{X}} \Phi(t, t_0) \quad (39)$$

$$\frac{\partial h(t)}{\partial \mathbf{p}} = \left. \frac{\partial h}{\partial \mathbf{p}} \right|_{\mathbf{x}=\text{const.}} + \frac{\partial h}{\partial \mathbf{X}} S(t) \quad (40)$$

These partial derivatives are calculated for each of the observations, from which the least squares parameter adjustment can be performed, as discussed in more detail in Appendix C.

## 4 Test cases: Mars and Mercury lander

We illustrate the methodology we have described in Section 3 with numerical simulations of Mars and Mercury lander missions performing laser ranging and time transfer to Earth. Our simulations here are not an in-depth analysis of the estimation performance, as is performed by (*e.g.* Turyshev et al., 2010; Hees et al., 2012). They are included here to show the potential influence of the relativistic clock effects on the estimation procedure for representative planetary lander concepts using planetary laser ranging. We analyze both Mars and Mercury lander missions to assess the influence of the depth of the space segment inside the gravity well of the Sun. Simulations of tracking data to planetary landers have been performed for a wide variety of mission and tracking data types, *e.g.* (Turyshev et al., 2010; Dehant et al., 2011; Dirkx et al., 2014a). Also, models and analyses of time transfer at interplanetary distances have been performed by *e.g.* (Degnan, 2002; Nelson, 2011; Pan and Xie, 2015). However, none of these simulations have included the coupled translational dynamics and relativistic clock effects. It is the goal of the present paper to present the influence of this coupling. For an Earth-orbiting mission, though, a sensitivity analysis of this coupling was performed by (Duchayne et al., 2009), using an approach different from the one derived here.

In Section 4.1 we discuss the settings of our simulations. Subsequently, we present a covariance analysis of the performance of both lander missions in Section 4.2, considering both the cases with and without the space-time dynamics coupling. Finally, we compare

the inclusion of proper time in the estimation with the influence of *a priori* and iterative *a posteriori* clock (re)calibration in Section 4.3.

## 4.1 Simulation settings

The settings for our simulation are the following. During one year of operations, we simulate one 30-minute arc of tracking data per day from four Earth-based International Laser Ranging Service (ILRS) stations (Pearlman et al., 2002) each. From this simulated data, we estimate the following parameters using a least-squares approach (Appendix C):

- PPN parameters  $\beta$  and  $\gamma$ . Nominal values equal to 1 in general relativity.
- Solar  $J_2$  gravity field coefficient  $J_{2\odot}$  (quadrupole moment). Nominal value  $\approx 2.2 \cdot 10^{-7}$  (Mecheri et al., 2004).
- Mars/Mercury initial translational state  $\mathbf{y}_{M,0}$ , nominal values taken from DE430 ephemeris (Folkner et al., 2014).
- Initial proper time difference between space segment and each Earth station  $i$ , denoted  $\Delta\tau^{SC}(t_0) - \Delta\tau^{(E,i)}(t_0)$ .
- Mars/Mercury-fixed lander position  $\mathbf{r}_L^{(M)}$  (both placed equatorially).

The first three sets of parameters ( $\beta$ ,  $\gamma$ ,  $J_{2\odot}$  and  $\mathbf{y}_{M,0}$ ) influence both the translational and the time dynamics of the observers.

To decorrelate the PPN parameter  $\gamma$  from the other parameters, its influence on the light time is crucial. Although we do not derive relativistic light-time corrections directly from the metric (see Section 2.4), we include the Sun's first-order effect (in harmonic coordinates) as (Moyer, 2000):

$$\Delta T_{21} = \frac{\mu_S(\gamma + 1)}{c^3} \ln \left( \frac{r_A + r_B + R_{AB}}{r_A + r_B - R_{AB}} \right) \quad (41)$$

The influence of the solar  $J_2$  on light time is very small (Minazzoli and Chauvineau, 2011), owing to the very small solar flattening and we do not include it in the light time calculations. Similarly, since  $\beta$  enters the light time correction at second post-Newtonian order (Richter and Matzner, 1983), we omit its influence on the light time.

In our simulations, we use simulated data of an uplink one-way time-transfer observable only. When exploiting relativistic clock effects over a long duration from a time-series of two-way observables, the inclusion of relativistic clock effects into the estimation would be done by considering separately one or both of the one-way observable that make up the two-way measurement (Section 2.4).

We do not estimate clock parameters, as is done by Dirx et al. (2015a), as we assume that the systems are equipped with highly accurate clocks for which the stochastic clock noise is minimal. Nevertheless, it should be understood that the detection of especially long-periodic signals requires highly stable clocks. To be able to observe a clock effect which manifests itself as a 1 cm change in  $c \cdot h_\tau^{(1)}$  over a period of 1 day requires an

Allan deviation of about  $4 \cdot 10^{-16}$  over such an integration time, which is about a factor of 2 better than that of the proposed deep space atomic clock (DSAC) (Prestage and Weaver, 2007). For a similar 1-cm change over a period of 1 year, an Allan deviation of the clock of  $10^{-18}$  over a similar period is required, which may be facilitated in the future by optical clocks *e.g.*, (Bloom et al., 2014).

Summarizing, our simulations are performed as follows:

- The translational and time dynamics for each observer is concurrently numerically integrated using Eqs. (5) and (10), with the full metric and associated Christoffel symbols given in Appendix A. We include the point-mass potential of the Earth and Mars/Mercury and the Sun's gravity field including its  $J_2$  term. The first partial derivatives of the metric, which are required for evaluating Eqs. (3), are obtained through the partial derivatives of the scalar and vector potentials given in Appendix B.
- From the simulated space-time dynamics, we use Eq. (11) to simulate the observables between the space segment and a number of Earth-based ground stations. We simulate range measurements from four ILRS ground stations to a lander over a period of 4 years. In total we use  $\approx 7.5 \cdot 10^4$  range measurements from each ground station, with these observations constrained by a  $15^\circ$  minimum elevation angle and a  $5^\circ$  Sun avoidance angle.
- We numerically integrate the state transition and sensitivity matrices using Eq. (24) over the same period as the space-time dynamics. We obtain the partial derivatives of the Christoffel symbols, which are required for evaluating Eqs. (32), by means of numerical differentiation.
- Using Eq. (38), we calculate the direct contribution of the partial derivatives of the observations w.r.t. the estimated parameters. Subsequently, we use the numerically integrated  $\Phi(t, t_0)$  and  $S(t)$  matrices to calculate the complete partial derivative of each observation w.r.t. each of the estimated parameters with Eqs. (39) and (40).
- From the partial derivatives of the observations, we set up the information matrix  $H$ , from which we calculate the covariance matrix (see Appendix C).

For the Mercury lander, we evaluate two different mission lengths. Since Mercury's rotation is in a 3:2 resonance with its orbit, a Mercury lander experiences periods of complete darkness and intense sunlight. Therefore, a four-year Mercury lander mission is highly challenging with current technological and budgetary constraints. A 30-day mission, however, would be easier to realize, as it is possible to keep the lander under the same illumination conditions for this amount of time while retaining constant visibility to the Earth. Nevertheless, the depth of Mercury in the Sun's gravity well makes it an attractive test case for exploiting relativistic effects. Since our primary goal in this section is to get a broad overview of the potential effect of space-time dynamics coupling on range data inversion, we will analyze both a 30-day and a 4-year mission, acknowledging the technological difficulties associated with a 4-year mission.

## 4.2 Covariance analysis results

We perform a covariance analysis to investigate the effect of the addition of the  $\Delta\tau$  terms in Eq. (38), as well as the addition of the estimation of  $\Delta\tau^{SC}(t_0) - \Delta\tau^{E,i}(t_0)$  on the formal error and correlation statistics (Appendix C). We present the results of the covariance analyses of the Mars and Mercury lander estimations with the settings defined in Section 4.1. Implicitly, we assume that our truth and estimation models are equal, and that our observations have errors that are identically and independently distributed with a zero-mean Gaussian distribution, omitting the influence of time-correlated (clock) noise on the measurements.

We compare the estimation where we take into account the proper times estimation with the estimation where we use the classical (no initial proper time estimation) approach, but add the estimation of range biases. As discussed in Section 3.3, the behaviour of the observation partials w.r.t. the biases will be similar to that of the initial proper times. The estimation of range biases is typically done in the analysis of satellite laser ranging (SLR) data analysis, although usually over shorter arcs. In our analysis where we include the estimation of the proper time differences, any existing range biases will be absorbed by the proper time difference estimation, so we do not explicitly include the range bias estimation in those simulations. Note that this will perturb the estimated values of the initial proper time values from their true values. However, since none of the estimated parameters is directly sensitive to this, it will not weaken the parameter estimation.

The formal error that we obtain will be more optimistic than the true error that will be obtained from real data, *e.g.* (Marty et al., 2009; Konopliv et al., 2011; Dirkx et al., 2014a). However, by comparing the formal error with and without the contribution of the space-time coupling terms, we identify the sensitivity of the solution to the presence of these terms. Furthermore, our covariance analysis will produce the change in the correlations between the estimation of the parameters due to the inclusion of the space-time coupling. A realistic assessment of the correlation between estimated parameters is crucial when interpreting the results of an estimation from tracking data, as it quantifies how well parameters can be determined in an independent manner. This issue has been crucial in interpreting the physical significance of post-fit residuals in planetary ephemerides (*e.g.*, Iorio, 2012b; Verma et al., 2014), where the signature of the influence of the Sun's  $J_2$  and angular momentum are strongly correlated with, for instance, the signature of alternative theories of gravity (Deng and Xie, 2015).

The changes in the entries of this correlation matrix between the time transfer simulations and range simulations will be presented relative to one minus the absolute value of the original (range-only) correlation matrix  $\mathbf{C}_r$ , so:

$$\Delta C_{ij} = \frac{|(C_t)_{ij}| - |(C_r)_{ij}|}{1 - |(C_r)_{ij}|} \quad (42)$$

where we implicitly set  $\Delta C_{ii}$  to 0 and  $\mathbf{C}_t$  denotes the correlation matrix of the time transfer simulations that include the proper time difference estimation. In this comparison criterion, we divide by  $1 - |(C_r)_{ij}|$  instead of  $|(C_r)_{ij}|$ , since it is not only important to ascertain the absolute changes in the correlation values, but especially its influence

Table 1: Change in formal errors (in %) between estimation from range data to landers with estimated initial proper time difference and estimated bias.

	Mars (4-years)	Mercury (1 month)	Mercury (4-years)
$\mathbf{r}_0$	-0.0138	-3.51	2.56
$\mathbf{v}_0$	-0.158	-2.31	6.31
$\gamma$	0.0480	2.93	-9.65
$\beta$	-0.236	-3.68	15.3
$J_{2,\odot}$	-0.255	-3.29	9.93
$\mathbf{r}_L$	0.0125	-1.75	3.27

in the ability of the estimation to decouple two parameters. That is, a change in correlation of 0.01 is crucial if it changes from 0.99 to 1.0 (or *vice versa*) since it makes the difference between being completely unable and slightly able to decouple the two parameters. Conversely, it is if it changes from 0 to 0.01 (or *vice versa*) largely irrelevant since the parameters remain almost completely decoupled. Therefore, the practical change in information on the estimation of the two parameters is much greater in the first case (0.99 to 1.0) than in the second case (0 to 0.01).

The formal error differences of the estimated parameters with and without the use of the initial proper time difference estimation are shown in Table 1. For the Mars lander, it can clearly be seen that none of the formal errors are significantly affected by the addition of the initial proper time difference estimation, with all relative differences smaller than 1%. The relative difference between (the modulus of) the correlation matrices of the classical and relativistic estimation is shown in Fig. 1. For the Mars simulation, the difference between the correlation matrices of the two estimations is marginal, as shown in Fig. 7.1(a), with differences around and well below the 1% level. Although these differences are larger than for the formal error, it still signifies the extremely limited influence of the addition of the relativistic clock effects on the estimation.

The difference in formal error statistics for both the short- and long-duration Mercury lander mission is also given in Table 1. Even for the short Mercury mission, the influence of the space-time dynamics coupling on the formal error statistics is more than an order of magnitude larger than for the Mars lander. For the 4-year Mercury mission, the formal error of  $\beta$  changes by 15 %. The formal estimation errors of  $\gamma$  and  $J_{2,\odot}$  both change by about 10 %. These values show that also for a long-duration mission relatively deep in the gravity well of the Sun, the differences in formal error will be limited. Nevertheless, the observed differences at the 10 % level may warrant the use of the combined initial space-time dynamics estimation, but depend on the degree and manner in which non-Gaussian observation uncertainties and model errors propagate into the estimation error budget. In Section 4.3, we will investigate how excluding the initial proper time difference from the estimation influences the estimation procedure, when using one-way data.

We show the difference in the correlation matrices for the Mercury mission, as quantified by  $\Delta\mathbf{C}$  from Eq. (42) in Figs. 7.1(b) and 7.1(c) for the 30-day and 4-year Mercury mission, respectively. As can be seen when comparing these figures to Table 1, the max-

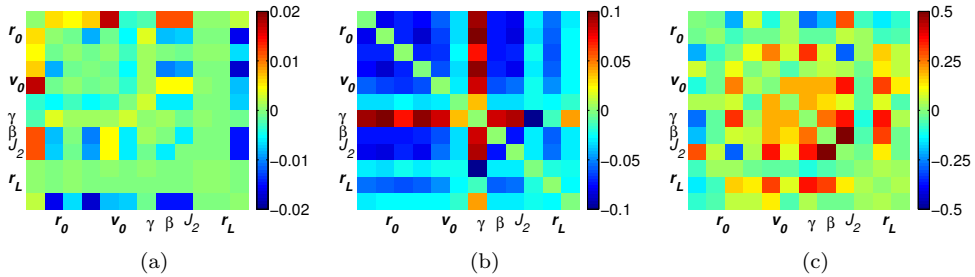


Figure 1: Relative difference  $\Delta\mathbf{C}$  between correlation matrices (omitting bias entries) of estimation incorporating initial proper time estimation and bias-only estimation, defined in Eq. (42) a) 4-year Mars mission b) 1-month Mercury mission c) 4-year Mercury mission.

imum values of  $\Delta\mathbf{C}$  are substantially larger than the changes in the formal error (as was the case for the Mars mission simulations), by a factor of about three for both the 30-day and 4-year mission. This difference is due to the  $1 - (C_r)_{ij}$  term in Eq. (42), which causes larger relative changes for correlations which are closer to 1 (or -1). For the 4-year mission, relatively large relative changes of up to 0.5 and down to -0.25 are observed, where positive values can be seen from Eq. (42) to signify cases where the time transfer simulations have larger absolute correlations and negative values signify those of the classical range simulations, without proper time estimation, are larger. The largest relative change in correlation occurs between  $\beta$  and  $J_{2,\odot}$  for the 4-year mission, where we observe a change in correlation coefficient from -0.74 to -0.87. This shows that the actual correlation between the signals of these two parameters is significantly larger than that which is obtained from the classical approach (without proper time estimation). This shows that, if the space-time dynamics coupling is omitted in the data analysis process, the correlation between the two parameters that one obtains from the estimation will be substantially more optimistic than the true correlation between the signals from these parameters.

The differences between  $\partial h_\tau^{(1)}/\partial\mathbf{q}$  and  $\partial T_{21}/\partial\mathbf{q}$  are at a similar level as the differences in the formal errors shown in Table 1, indicating that the addition of the time transfer to the one-way range observable changes the sensitivity to the estimation by about 0.1 and 10 % for the 4-year Mars and Mercury landers, respectively. This does not imply that the relativistic clock effects are too weak to be of use for parameter estimation. It instead shows that when using the same data (laser range in these simulations) for orbit determination and time transfer, the resulting orbital accuracy will put stronger constraints on the parameters of interest than the relativistic clock effects. However, this may not be the case for missions where time transfer is only sporadically performed, and orbit determination is also performed using other data types such as Doppler tracking. In these cases, the time-transfer observable may be relatively more accurate than the orbital accuracy, potentially increasing the relative strength of the time-transfer observables in the estimation. Also, highly accurate clocks carried by orbiting spacecraft can be used for long-arc comparison of ground- and space-based clocks, whereas their orbits are typically



estimated over relatively short arcs (hours to days) to prevent the accumulation of (non-conservative) force model errors. As such, the longer duration over which the proper time behaviour could potentially be estimated (depending on the clock's stability), compared to the duration over which the state behaviour can be estimated, may increase the relative importance of the inclusion of the proper time into the estimation, as it could possibly be used to better decorrelate long-periodic and secular effects.

### 4.3 Influence of *a priori* and *a posteriori* calibration

Having analyzed the influence of the space-time dynamics coupling on the estimation's formal errors in Section 4.2, we now investigate by direct numerical simulation the influence of omitting this coupling and performing *a priori* or iterative *a posteriori* clock calibration. To do so, we perform the estimation using the simulation settings defined in Section 4.1 and the estimation algorithm given in Appendix C. We estimate a range bias in addition to the physical parameters listed in Section 4.1, as discussed in Section 4.2. We perturb the parameters at their current level of uncertainty and use an iterative least-squares method to estimate the parameters. We perform three sets of simulations for both the Mars and Mercury mission:

1. Estimation in which the true  $t(\tau)$  conversion for each observer is known perfectly.
2. Estimation in which a  $t(\tau)$  conversion is recomputed following each iteration of the estimation (*a posteriori* clock calibration).
3. Estimation in which a  $t(\tau)$  conversion based upon the *a priori* parameter estimate is used.

From these simulations, we will be able to determine the parameter estimation error that is made due to mismodelled relativistic clock effects, when using the typical orbit determination method.

We find no difference in our results for the 1-month Mercury lander mission between the three cases, due to the fact that the estimation errors of even the ideal case are larger than the initial perturbation in the parameter set. That is, for the short Mercury mission, the tracking data inversion does not result in an improved parameter estimation compared to the *a priori* uncertainty.

For both the Mars and Mercury 4-year tracking simulations, the resulting uncertainties for 100 simulations are shown in Figs. 2 and 3, respectively. The error clouds of both initial position of Mars/Mercury and the parameters  $\gamma$ ,  $\beta$  and  $J_{2,\odot}$  are shown. In these figures, the projections of these clouds onto the three planes are also shown. We note that our results for  $\gamma$  for the 4-year Mars simulation are similar to the estimation results obtained by Turyshev et al. (2010) (error of  $1.4 \cdot 10^{-7}$  after 3 years;  $7.9 \cdot 10^{-8}$  after 6 years), who perform simulations of laser ranging to Phobos. Our results for  $\beta$  and  $J_2$  are about an order of magnitude more optimistic, most likely due to our smaller set of estimated parameters and resultantly reduced correlations. However, our goal here is not to provide highly accurate absolute estimates for attainable estimation accuracy, but to compare different data analysis techniques.

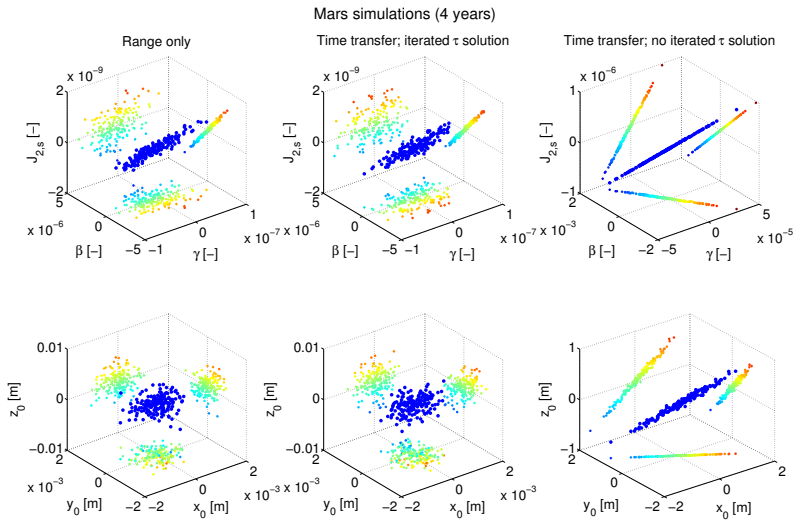


Figure 2: Estimation errors obtained from numerical simulations for 4-year Mars mission. Panels show estimation error clouds for ideal  $t(\tau)$  conversion, iterated  $t(\tau)$  conversion and unupdated *a priori*  $t(\tau)$  conversion. Projections of estimations errors onto the three subplanes are also shown, coloured by error in  $J_{2,\odot}$  (top) and initial  $z$ -position (bottom).

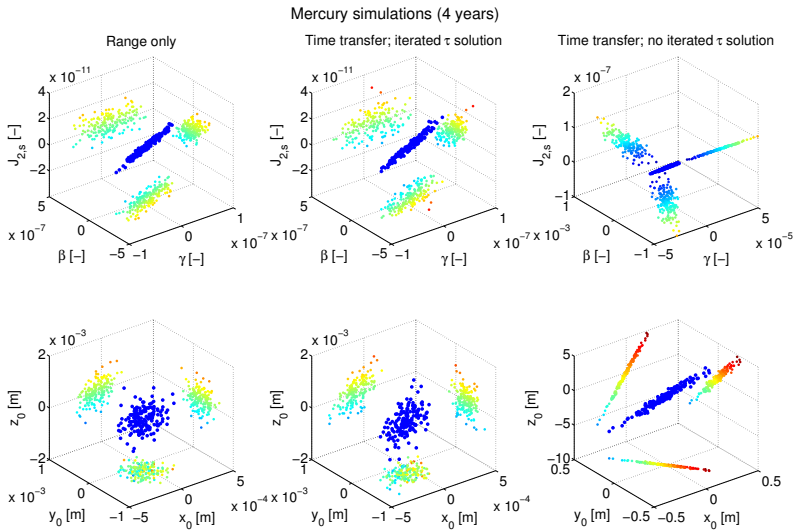


Figure 3: Estimation errors obtained from numerical simulations for 4-year Mercury mission. Panels show estimation error clouds for ideal  $t(\tau)$  conversion, iterated  $t(\tau)$  conversion and unupdated *a priori*  $t(\tau)$  conversion. Projections of estimations errors onto the three subplanes are also shown, coloured by error in  $J_{2,\odot}$  (top) and initial  $z$ -position (bottom).

We observe orders of magnitude differences between cases 2 and case 3. That is, the errors in the *a priori*  $t(\tau)$  conversion are sufficiently large to drive the estimation to erroneous results. This influence was not observed in the previous section, where the truth and estimation model were assumed to be equal. This indicates that the use of *a priori* time ephemerides, for instance those of (Irwin and Fukushima, 1999; Fienga et al., 2009), for the data analysis of planetary laser ranging missions can result in substantial degradations of the estimation quality. In general, this will be true if the *a priori* orbital and parameter uncertainty is much greater than the range measurement uncertainty. It must be noted, however, that the simulations shown here are performed using purely Gaussian noise on the observations. As a result, the estimation accuracy shown here for cases 1 and 2 is substantially better than will be obtainable from real tracking data, which will include time-correlated and non-Gaussian noise. Differences between true and formal errors for interplanetary (radiometric) tracking data inversion are typically around a factor 5-10 (*e.g.* Marty et al., 2009; Konopliv et al., 2011).

The difference between cases 1 and 2 is insignificant for the 4-year Mars mission. This is consistent with the fact that we found formal error differences at the 0.1 % level in Section 4.2. For the 4-year Mercury mission, we find small but statistically significant differences between the error distributions of cases 1 and 2, with around 10 % degradation in estimation error for case 2, compared to case 1. Again, this is consistent with the results presented in the previous section, which showed differences in formal errors of around 5 – 10 % for simulations with and without the inclusion of the coupling.

## 5 Conclusions

We have successfully derived an estimation framework with which the influence of relativistic clock effects on (interplanetary) range and time transfer data analysis can be included on an equal footing with relativistic influence on translational dynamics, with the main theoretical results of our development being Eqs. (24) and (38), which are extended versions of the classical equations used in orbit determination. This approach allows for consistent data processing of high accuracy one-way range data that is expected from future interplanetary laser ranging missions. Similarly, it will allow for a robust analysis of combined two-way range and time transfer data, creating a solid framework to simultaneously extract physical signals from time and space dynamics.

We have simulated data to a Mars and Mercury lander and used the simulated data for a covariance analysis, assessing the possibilities to use these data for the determination of  $\gamma$ ,  $\beta$  and  $J_{2\odot}$ . We analyze the use of both range measurements (including the estimation of range biases) and time transfer (including the estimation of an initial proper time difference). The inclusion of the estimation of the proper time difference between Earth stations and a Mars lander has a negligible influence on both the correlations between the estimated parameters and their formal errors, with differences in the formal errors of around 0.1 % observed. For a Mercury lander this formal error difference rises to 1% for a 1-month mission and 10 % for a 4-year mission. However, we find a significantly greater relevant degree of change in the correlation matrix (as quantified by  $\Delta\mathbf{C}$ ) than for the formal errors, which can be of importance for the interpretation of the robustness of the results, as well as any statistical analysis of postfit residuals.

These results indicate that the influence of our estimated parameter set on the translational dynamics is (much) stronger than on the proper time rate. For spacecraft state estimation, where the translational state is typically determined over short arcs, a highly stable clock may allow substantially modified parameter estimation quality.

We have shown by direct numerical simulation that using an *a priori* time ephemeris with sufficiently low accuracy, can result in orders of magnitude degradation of the true error distribution compared to the formal errors. Recomputing the proper-to-coordinate time conversion for each observer after each iteration of the least-squares estimation results in a degradation similar to the changes observed in the formal errors.

## Acknowledgements

DD is financed by the FP7 ESPaCE project, financially supported by the EC FP7 Grant Agreement 263466. The authors thank Alexander Polnarev of the Queen Mary University of London and Sergei Kopeikin of the University of Missouri for their insightful input, which improved the clarity and quality of the manuscript.

## Appendix A Solar system metric

We use the post-Newtonian solar system metric in harmonic gauge given by Soffel et al. (2003), parametrized by the PPN parameters  $\gamma$  and  $\beta$ , as given by *e.g.* (Minazzoli and Chauvineau, 2009):

$$h_{00}(\mathbf{x}, t) = 2\frac{w(\mathbf{x}, t)}{c^2} - 2\beta\frac{w(\mathbf{x}, t)^2}{c^4} + O(c^{-5}) \quad (43)$$

$$h_{0i}(\mathbf{x}, t) = -(\gamma + 1)\frac{w^i(\mathbf{x}, t)}{c^3} + O(c^{-4}) \quad (44)$$

$$h_{ij}(\mathbf{x}, t) = 2\gamma\frac{w(\mathbf{x}, t)}{c^2}\delta_{ij} + O(c^{-3}) \quad (45)$$

where  $w$  and  $w^i$  denote the scalar and vector potentials. These potentials are calculated from (Soffel et al., 2003):

$$w(\mathbf{x}, t) = \sum_A w_A(\mathbf{x}, t) \quad (46)$$

$$w_A(\mathbf{x}, t) = (w_A)_0(\mathbf{x}, t) + \Delta_A(\mathbf{x}, t)/c^2 \quad (47)$$

$$\Delta_A(\mathbf{x}, t) = \frac{\mu_A}{r_A} \left( -2v_A^2 + \bar{w}_A + \frac{(\mathbf{v}_A \cdot \mathbf{r}_A)^2}{2r_A^2} + \frac{\mathbf{a}_A \cdot \mathbf{r}_A}{2} \right) \quad (48)$$

$$w^i(\mathbf{x}, t) = \sum_A w_A^i(\mathbf{x}, t) \quad (49)$$

$$w_A^i(\mathbf{x}, t) = \frac{G(\mathbf{S}_A \times \mathbf{r}_A)^i}{2r_A^3} + w_A(\mathbf{x}, t)v_A^i \quad (50)$$

where  $\mathbf{x}_A$ ,  $\mathbf{v}_A$ ,  $\mathbf{a}_A$ ,  $\mu_A$  denote the barycentric position, velocity and acceleration and the gravitational parameter, respectively, of body  $A$ . The vector  $\mathbf{r}_A$  denotes the vector from body  $A$  to the point  $\mathbf{x}$  where the metric is evaluated. The external potential  $\bar{w}_A$  represents the potential at  $\mathbf{x}_A$ , due to all other bodies. The nominal potential  $(w_A)_0$  may be approximated by the non-relativistic spherical harmonic gravitational potential of body  $A$  (Soffel et al., 2003), as given by *e.g.* Montenbruck and Gill (2000):

$$(w_A)_0(\mathbf{x}, t) = \frac{\mu_A}{r_A} \sum_{l=0}^{\infty} \sum_{m=0}^l \left( \frac{R_{eq,A}}{r_A} \right)^l \cdot \dots \\ \dots \cdot (\bar{C}_{lm} \cos(m\lambda_A) + \bar{S}_{lm} \sin(m\lambda_A)) \bar{P}_{lm}(\sin(\phi_A)) \quad (51)$$

where  $R_{eq,A}$  denotes the equatorial radius of body  $A$ ,  $\bar{C}_{lm}$  and  $\bar{S}_{lm}$  denote the normalized spherical harmonic coefficients of its gravity field,  $\bar{P}_{lm}$  denotes the associated Legendre polynomial of degree  $l$  and order  $m$ , and  $\phi_A$  and  $\lambda_A$  denote the body-fixed latitude and longitude, respectively, at the point where the potential is evaluated.

We note that each term in the equation for  $\Delta_A/c^2$  contains either  $v_S^2/c^2$ ,  $r_S^k a_S^k/c^2$ ,  $\mu_A/(c^2 r)$  or smaller terms, where  $A \neq S$  and  $S$  denotes properties of the Sun. Since all of these terms are sufficiently small due to the small velocity and acceleration of the Sun, or the weak mass monopoles of the planets are small and only enter into the final metric at the second Post-Newtonian order ( $\Delta_A/c^4$ ), we set  $\Delta_A$  to zero in our simulations. Additionally, we omit the angular momentum term  $\mathbf{S}_A$  if  $w_A^i$  in Eq. (50), thereby neglecting the Lense-Thirring effect.

## Appendix B Christoffel symbols

Here, we provide direct expressions for the Christoffel symbols of the metric given by Eqs. (43)-(45). We set  $\epsilon = 1/c$  and use general derivation given by Kopeikin et al. (2011). We deviate from their notation in that  $\cdot_0$  denotes partial differentiation w.r.t.  $ct$ , not  $t$ . We note that we have no terms of  $O(\epsilon)$  in  $h_{0i}$ , no terms of  $O(\epsilon^4)$  in  $h_{ij}$  and that the  $O(\epsilon^2)$  term in  $h_{ij}$  is diagonal, which results in the following (where we omit the  $(\mathbf{x}, t)$  evaluation point for brevity):

$$\Gamma_{00}^0 = -\epsilon^2 w_{,0} + O(\epsilon^4) \quad (52)$$

$$\Gamma_{0i}^0 = -\epsilon^2 w_{,i} + O(\epsilon^3) \quad (53)$$

$$\Gamma_{00}^i = -\epsilon^2 w_{,i} - 2\epsilon^3(\gamma + 1)w_{,0}^i + 2\epsilon^4(\gamma + \beta)w \cdot w_{,i} + O(\epsilon^5) \quad (54)$$

$$\Gamma_{0k}^i = \epsilon^2 \gamma \delta_{ik} w_{,0} - \epsilon^3(\gamma + 1)(w_{,k}^i - w_{,i}^k) + O(\epsilon^4) \quad (55)$$

$$\Gamma_{ik}^0 = \epsilon^2 \gamma \delta_{ik} w_{,0} + \epsilon^3(\gamma + 1)(w_{,k}^i + w_{,i}^k) + O(\epsilon^4) \quad (56)$$

$$\Gamma_{jk}^i = \epsilon^2 \gamma (\delta_{ij} w_{,k} + \delta_{ik} w_{,j} - \delta_{jk} w_{,i}) + O(\epsilon^3) \quad (57)$$

The partial derivatives of  $w^i$  are given explicitly by:

$$w_{,0}^i = \sum_A \left( \frac{w_A a_A^i}{c} + w_{A,0} v_A^i \right) \quad (58)$$

$$w_{,j}^i = \sum_A w_{A,j} v_A^i \quad (59)$$

where each element of the term  $v_{A,j}^i$  equals 0 if the observer position is independent of body  $A$  (*i.e.* if it is not located on body  $A$ ).

We note that the  $w_{,j}$  terms in the above are equal to the Newtonian gravitational acceleration at position  $x_j$  due to a gravitational potential  $w$ . We calculate the  $w_{,0}$  term as follows for a point mass:

$$w_{A,0} = w_{A,i} \frac{v_A^i}{c} \quad (60)$$

For bodies with mass multipoles, the rotation of these bodies cause the metric to be non-static even in the case that all bodies have zero translational velocity, since the rotation of the bodies will cause variability of the potential at a given evaluation point. For this case, the scalar potential time derivative has the additional term:

$$\Delta w_{A,0} = \frac{1}{c} \frac{\partial w_A}{\partial \mathbf{r}_A} (R^{(I/A)}) (\dot{R}^{(A/I)}) \mathbf{r}_A \quad (61)$$

where  $\mathbf{r}_A$  is evaluated in the global frame  $I$  (not corotating with body  $A$ ).  $R^{(B/C)}$  denotes the rotation matrix from frame  $C$  to frame  $B$ .

## Appendix C Least-Squares Orbit Determination

In this Appendix, we provide a brief overview of batch-least-squares orbit determination and parameter estimation from space mission tracking data (*e.g.* Montenbruck and Gill, 2000). Let  $\mathbf{h}$  denote the set of modelled observations used as input to the estimation and  $\mathbf{q}$  the set of parameters that is to be estimated. The design matrix  $H$  is then formed by computing:

$$H = \frac{\partial \mathbf{h}}{\partial \mathbf{q}} \quad (62)$$

Now, let  $\Delta \mathbf{h}$  denote the residual between the modelled and measured values of the observations  $\mathbf{h}$ , the correction to the set of estimated parameters, denoted  $\Delta \mathbf{q}$  follows from:

$$\Delta \mathbf{q} = K (H^T W \Delta \mathbf{h}) \quad (63)$$

$$K = (H^T W H)^{-1} \quad (64)$$

where  $W$  is the weight matrix of the observations, which is typically set as a diagonal matrix with  $W_{ii} = \sigma_{h,i}^{-2}$ , where  $\sigma_{h,i}$  denotes the uncertainty of observation  $i$ . Using the

parameter correction  $\Delta \mathbf{q}$ , the relevant dynamics is recomputed, from which updated modelled observation values are recomputed. This iterative process is continued until some convergence criterion is reached, such as the relative change in observation residual between subsequent iterations reaching some tolerance  $\epsilon$ .

In the above,  $K$  denotes the covariance matrix, from which the formal errors  $\sigma_{q,i}$  of the estimated parameters are computed as:

$$\sigma_{q,i} = \sqrt{K_{ii}} \quad (65)$$

The entries correlation matrix  $C$  are then computed from:

$$C_{ij} = \frac{K_{ij}}{\sigma_i \sigma_j} \quad (66)$$

The covariance analysis is based on the formal errors and correlations, which denote the potential sensitivity of the observations to the estimation parameters and the capability of the estimation to decouple the signatures of the various parameters.





---

## Synthesis and Discussion

---

In Chapter 2, we presented the science rationale behind the implementation of Interplanetary Laser Ranging (ILR), followed by the current state-of-the-art of SLR technology in Chapter 3, extrapolating this to near-future implementation of ILR where possible. Based on the considerations presented there, we analyzed various aspects of the science return, data analysis strategies, environmental error sources and hardware error sources in Chapters 4-7. These chapters form the main scientific contributions of the work presented in this dissertation. In this chapter, we synthesize and discuss the information in the previous chapters, with the objective of addressing the research goals defined in Chapter 1.

Our presentation here is split into two sections. First, we present a synthesis of the various error sources of ILR, addressing uncertainties in the full data processing and analysis chain, from measurement to interpretation, in Section 8.1. Subsequently, we use the synthesized estimate of a near-future ILR mission's error budget to compare the capabilities of a Doppler tracking system with that from an ILR system in Section 8.2. Resultantly, we discuss the types of missions and science goals for which an ILR system will be complementary or competitive, compared to existing tracking techniques.

### 8.1 Measurements and Data Analysis for ILR

As discussed in Section 3.2, a variety of error sources in both the laser range measurements themselves, as well as inaccuracies in the models used to process these measurements to obtain scientific parameters of interest, limit the performance of an ILR system. In Chapters 4-7 we have investigated a number of these error sources, as well as the potential influence that they can have on ILR data analysis quality. In this section, we provide a synthesis of both the known error sources discussed in Section 3.2, as well

as the new aspects that we investigated in this dissertation.

To provide context for the importance of the various types of errors we start by discussing, in a general sense, the influence of uncorrelated, time-correlated and systematic errors in Section 8.1.1. Subsequently, we discuss in detail the various specific sources of both measurement and modelling uncertainty that limit the performance of an ILR system and the quality of the resulting science products. To structure this discussion, we present them in the order in which they occur in the measurement and analysis process, shown schematically in Fig. 8.1. First, we discuss in Section 8.1.2 the errors in the measurements themselves. We address the various sources of differences between the true and measured transmission and reception times of the pulse centroids, as well as the resulting influence on the measured range  $\hat{s}$  (see Section 3.1.1). We consider the following errors:

- Errors due to the inherently stochastic nature of range measurements by direct detection of photons from a laser pulse (Section 3.2.1 and Chapter 5).
- Error due to detection and transmission system instabilities (Section 3.2.1).
- Errors due to clock noise (Chapter 6).

Subsequently, we discuss in Section 8.1.3 the errors in the data analysis, distinguishing the following steps:

- Errors due to inaccuracies in *a priori* models that are not adjusted during the estimation (Section 3.2.2 and Chapter 7).
- Errors in the estimation models, *i.e.*, mismodelled influence of a parameter  $q$  on an observable  $h$  (Chapters 6, 7).

Finally, we discuss in Section 8.1.4 the limitations in the interpretation of the estimated parameters and the resulting impact on the design of future missions with an ILR component, distinguishing two limitations:

- Limitations in the available analysis models (Chapter 4) to use the estimated parameters to address the scientific objectives of a mission.
- The uncertainty in the true estimation error of the estimated parameters. A lack of knowledge of the true uncertainty of the physical parameters that are estimated limits the degree to which they can be robustly interpreted (Chapters 4-7).

### 8.1.1 Influence of Temporal Behaviour of Errors

Before describing in more detail the various sources of uncertainty in the science products that can be obtained from ILR (Sections 8.1.2-8.1.4), we discuss different types of temporal behaviour of error sources, and how they impact the analysis process. Thereby, we provide context for the relevance of the discussion in subsequent sections.

One of the simplest distribution for measurement and/or estimation errors is that of identically and independently distributed (IID) Gaussian errors, (*e.g.*, Tapley et al.,

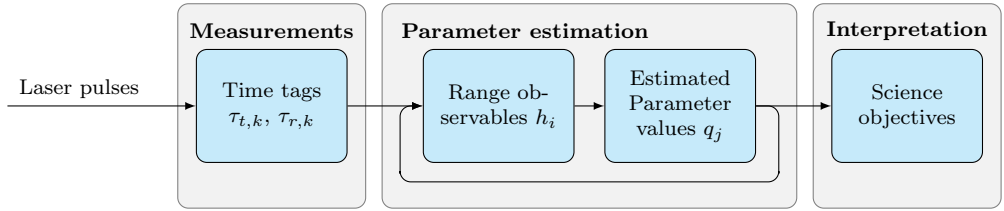


Figure 8.1: Block diagram showing top-level data flow from measurements (pulse transmission and reception time tags  $\tau_t$  and  $\tau_r$ ) to estimation and interpretation. Note the iterative estimation, in which the pre-processing of the time tags into the observables is re-performed after each update of the estimated parameters.

2004). For laser ranging measurement precision, the IID assumption is valid to very close approximation for data from a single station during a single pass, at least when operating in the single-photon signal intensity regime (Section 3.2.1). As a result, the combined precision of  $N$  consecutive measurements scales as  $1/\sqrt{N}$  down to values of  $\ll 1$  mm (Section 3.2.1). By removing the trend in the measurement residuals, the measurement precision can be accurately determined, as it only represents the scatter of the measurements about their running average, without any reference to the ideal measurement. Although this indicates the stability of a range measurement system over short time intervals, it is not a correct indicator for the stability of the systematic error over longer durations, nor does it provide information on the degree to which range measurement systematics from various stations compare to one another. The accuracy of a measurement is much more difficult to quantify, as it represents the mean difference w.r.t. the ideal (error-free) measurement values. Systematic errors can be partially removed by comparing time series of data with those from other techniques, as done by *e.g.*, Urschl et al. (2005), who validate GNSS derived orbits using SLR data. Such an approach is not feasible for ILR, however, since no such complementary tracking type is available capable of validating ILR-derived orbits at the required level of accuracy. Alternatively, systematic errors can be assessed by comparing tracking data from multiple (colocated) stations, (*e.g.*, Noomen, 2001), or by performing internal system calibration, (*e.g.*, Kirchner and Koidl, 2014). A time-correlated source of measurement errors (such as clock noise, see Chapter 6) is more difficult to quantify in an *a priori* manner, though. In the subsequent sections, we discuss a number of such measurement errors, presenting how they are expected to affect ILR measurements in a statistical sense.

For the estimation, a probability distribution of the measurement errors must be (implicitly) assumed, (*e.g.*, Tapley et al., 2004). In a least-squares estimation with a diagonal weight matrix, which is the typical approach in (interplanetary) spacecraft tracking data analysis, (*e.g.*, Moyer, 2000; Konopliv et al., 2011; Lemoine et al., 2013; Mazarico et al., 2014b), the underlying assumption is that all measurements are independently distributed by a Gaussian distribution with zero mean. In fact, a weighted least squares estimator is the best linear unbiased estimator for data with such error properties, as a specific case of the Gauss-Markov theorem, (*e.g.*, Zyskind and Martin, 1969). Under this assumption, the formal estimation uncertainty goes down as  $1/\sqrt{N}$

(where  $N$  is the number of observations), for constant sensitivity of the observations to the estimated parameters (Section 8.1.4). As a result, the formal error that is obtained from a least-squares estimation is typically too optimistic, as it assumes error properties of the measurements that are too benign, neglecting any time correlation (Section 2.1.3; Chapters 5 and 6). The influence of time-correlated errors with increasing data volume and coverage can also decrease, but the manner in which it does so is dependent on how well the estimator can decorrelate the signature of such errors from the expected signature of a particular estimated parameter (discussed in more detail in Section 8.1.3).

For the complete analysis of the influence of time-correlated errors, a bottom-up model of the behaviour of the various error sources would be required (Dirkx and Vermeersen, 2013). However, for a more conceptual analysis we can make this analysis more tractable by assuming that the time-correlation of the errors is that of a systematic error. A systematic error has a specific type of time-correlation, since for an error  $\sigma(t)$ , the time correlation of  $\sigma$  at times  $t_1$  and  $t_2$  is such that  $\sigma(t_1) = \sigma(t_2)$  (for all  $t_1$  and  $t_2$ ). Under this assumption, we can make a general first-order comparison between the influence of Gaussian uncorrelated and time-correlated noise. We have performed this combined analysis of the influence of random and systematic errors (as a specific case of general time-correlated errors) by using consider-covariance analysis (Bierman, 1977; Tapley et al., 2004). In applying this method, we include a constant uncertainty in a set of parameters that are not adjusted in the least squares estimation. This method is used in the context of space mission tracking data analysis by, *e.g.*, Cheng et al. (1989); Wu et al. (2001); Jacobson (2009); Konopliv et al. (2011) for Earth gravity field temporal variation estimation from SLR data, simulations of a Europa orbiter, ephemeris generation of the main Neptunian satellites and tracking data analysis from the Mars Reconnaissance Orbiter (MRO), respectively. In Chapter 4, we applied this method by imposing systematic errors on the range biases for a Phobos lander mission, thereby capturing the true influence of systematic measurement errors without the need for a detailed bottom-up error model.

Our results showed, for the case of a Phobos lander performing ILR, that the influence of random (Gaussian and uncorrelated) and systematic range measurement errors propagate into the error budget of the estimated parameters in a dramatically different fashion. Specifically, we found that the influence on the error budget of the estimated parameters of 1 mm Gaussian uncorrelated range measurement noise is 1-2 orders of magnitude less than the 1 mm systematic range error. That is, for perfectly accurate range measurements with a purely Gaussian observation noise of 1 mm amplitude, and no estimation model errors or uncertainties, the estimation results have an uncertainty that is 1-2 orders of magnitude better than the estimation results from perfectly precise measurements with a consistent 1 mm range error. Although our analysis in Chapter 4 does not quantify directly the influence of an arbitrary time-correlated measurement error, it is indicative of the strong influence of non-Gaussian errors, motivating the detailed investigation of these types of errors in ILR.

The results of the consider-covariance analysis in Chapter 4 show the need to correctly characterize and mitigate systematic error sources, and time-correlated error sources by extension. In Chapters 5-7, we have investigated a variety of such error sources, both in the measurements and in the models used to process the measurements. However, the

results shown in Chapter 4 also indicate that there is little need to improve the precision of laser ranging measurements, which could be achieved by for instance moving to higher pulse repetition frequencies or shorter pulse lengths. Based upon the results shown here, however, even a tenfold increase in pulse length would not degrade the estimation quality as long as systematic errors are not also substantially reduced. This benefits the potential combination of a laser ranging system with either a communications or altimetry system (Sections 3.3.3 and 3.3.5, respectively), where the pulse lengths are typically longer than in typical SLR operations.

### 8.1.2 Measurement Errors

As discussed in Section 3.2.1, measurement errors can occur both due to the inherently stochastic nature of laser ranging detection, as well as due to the influence of imperfect measurement equipment. As discussed in Section 8.1.1, (single-shot) measurement precision will likely not be a limiting factor in ILR data analysis. Instead, the various sources of systematic or otherwise time-correlated errors dominate the influence of the measurement errors on the quality of the final products. Resultantly, we focus our discussion in this section on these types of error sources, providing only limited further discussion on the precision of ILR measurements.

We start by discussing the influence of inherent stochasticity of laser ranging measurements. Both the finite pulse length in a laser ranging measurement and the influence of atmospheric turbulence contribute to the stochastic behaviour of the measurement precision and accuracy of the measurement. As discussed in Section 3.2.1, variations in measurement accuracy will result from variations in the number of photons in a laser pulse that can be detected (as a result of variations in pulse detectable energy), as calculated from Eq. (3.15). The potential problem of such time-correlated accuracy variations was the prime rationale behind the theoretical development of turbulence-induced signal-strength variations presented in Chapter 5. In our work presented there, we synthesized various existing models for the influence of turbulence on the propagation of laser pulses, forming a coherent description for the far-field intensity variations as a function of turbulence strength, combining the influence of a number of stochastic effects, including the inherent (turbulence-independent) effect of the finite pulse length. Our simulations included a constant atmospheric transmittance, but a varying zenith angle, thereby including an additional (physically deterministic) source of signal strength variations, in addition to that caused by atmospheric turbulence. The results showed that accuracy variations of up to 5 mm could occur in a representative laser ranging system, caused by signal-strength variations due to changes in both zenith angle and turbulence strength.

Further analysis indicated, however, that the total turbulence-induced accuracy variations may be reduced due to the observational geometry of planetary missions. Specifically, there will be a part of the year that the time interval during the day and zenith angles at which ranging can be performed will not change much, at least for stations at higher (absolute) latitudes, as is also shown in Fig. 3.10. During such periods, the day-to-day signal strength (and as a result accuracy) variations will be reduced, making the range measurement error more stable on short-medium timescales. Our simulations

in Chapter 5 showed that this effect reduces the accuracy variations to about 1.5-3 mm (depending on turbulence strength) for stations with limited elevation angle possibilities. Although this effect may improve the stability of the range measurements in the medium term of weeks-months (for parts of the year with a limited ranging window per day), it can cause problems for the long-term stability of the range measurements. Specifically, it could cause a periodic signal in the range measurement with an amplitude of several mm and a repeat time of approximately one synodic period of Earth and the target. Since the absolute range between Earth and the target will vary with a similar period as the visibility conditions, the estimation of ephemerides (Section 2.2.4) could be degraded by such an effect, as a periodic signal of several mm due to periodic range measurement errors (and tropospheric correction errors, Section 3.1.4) may be interpreted by the estimator as a signal due to the dynamics of both the Earth and the target body.

The influence of variable detection energy on the measurement accuracy variability, be it caused by turbulence, varying path absorption, transmitted pulse-energy instabilities, *etc.*, may be (nearly) completely mitigated by a number of approaches. Primarily, as also discussed in Section 3.2.1 and Chapter 5, the use of a system by which detection at the single-photon level is ensured will allow signal strength variations to be completely inconsequential for the accuracy of the measurement, facilitating the realization of an unbiased measurement. This is in contrast to single-photon detection in SLR/LLR, where the received signal temporal profile consists of the convolution of the (ideally Gaussian) transmitted pulse shape and the transfer function of the retroreflector, requiring a model for the transfer function (Section 3.2.1). Since this transfer function can be dependent on polarization, pulse reflection orientation, system temperature, dust cover (in the case of lunar reflectors), *etc.*, (*e.g.*, Arnold, 1979; Otsubo and Appleby, 2003; Degnan, 2012), it is exceptionally challenging to obtain mm-accurate range measurements from a retroreflector target, even in the case of perfect measurement equipment and single-photon detection. For systems operating in the kHz pulse repetition frequency regime, though, pulse returns from individual reflectors can be distinguished for certain targets (*e.g.*, Kucharski et al., 2010), partly mitigating the effect. In ILR, though, the detected pulse temporal intensity distribution is nearly the same as the transmitted (Gaussian) pulse shape, allowing the measured photons to be statistically referenced to the pulse centroid without the need for such a retroreflector model. Operation at the single-photon level is at the expense of integrated measurement precision, though, as a result of a decreased pulse detection probability. However, since the results in Chapter 4 unambiguously show that systematic errors are much more influential than (Gaussian) measurement precision, a reduction of a measurement precision will be more than outweighed by an improvement in accuracy (Section 8.1.1). Also, detection at the single-photon level can be achieved in low (but not single) photon detection energy regimes by using a multi-array detector, such as that used by the APOLLO LLR station (Chapter 5). In a multi-array system, multiple photons from a single laser pulse trigger separate detectors, and are separately time tagged, effectively removing the multi-photon measurement accuracy degradation.

However, even for detection of pulse transmission and reception at the exact pulse centers, the realizations of the range measurements are degraded by imperfections in the measurement hardware. As discussed in more detail in Section 3.2.1, many of the

hardware-induced quality degradations will be similar in ILR and SLR, although ILR suffers from a lower TRL due to the use of active space-based systems that have not been previously applied for use in interplanetary ranging applications. Nevertheless, developments in laser communications time transfer and altimetry (Sections 3.3.3, 3.3.4 and 3.3.5, respectively) have shown the feasibility of the required subsystems, although not necessarily in the context of a planetary mission. This will allow ILR to be implemented in the near-future, from a space-segment systems design point-of-view. There have been extensive analyses of both SLR systems and existing space-based laser detectors for shorter-distance applications (altimetry, time transfer, communications), which we have summarized in Section 3.2.1. The measurement errors presented there are largely representative of what is to be expected for ILR (with the notable exception of the influence of clock noise). Resultantly, hardware-induced accuracy variations can be expected to be at the several mm-level. However, laboratory experiments have shown sub-mm range accuracies, but calibration issues due to the difficulties in comparing the hardware characteristics of the various ground and space segment(s) involved will make it difficult to achieve such a quality in (the first generation of) ILR systems. Moreover, limitations in analysis models will be at the several-mm level (Section 8.1.3), so that improvements in measurement accuracy will not necessarily immediately result in substantially improved science products.

A crucial difference in the error budget of an ILR system (compared to that from systems used for sub-planetary distances) stems from the influence of the clock noise, especially for a one-way range system. In Chapter 6, we analyzed this error source in detail, providing a quantitative comparison of one- and two-way laser ranging data. In that chapter, we developed a generic analysis framework for these data types and applied these models to the analysis of two missions employing ILR (Phobos lander and lunar orbiter). In doing so, we quantified the influence of clock noise on both the measurement errors and the estimation process. For two-way systems, moderate requirements on the space-segment clock and reasonably accurate ground station clocks ( $\approx 10^{-15}$  Allan deviation over two-way light time, see Section 2.3 of Chapter 6) cause instabilities in the range accuracy at the sub-mm level (barring missions to the outer solar system with exceptionally large light-times). Due to the small retransmission time  $\delta t$  at the space segment in setting up a two-way measurement, the clock of the space segment only needs to be stable at the level of better than  $3 \cdot 10^{-12}$  or  $3 \cdot 10^{-13}$  over an integration time of 1s or 10 s, respectively, to cause a sub-mm error in the range measurements, which is within the level of accuracy of state-of-the-art systems. In a one-way system, however, the accumulation of clock noise can cause errors in the raw range observations of tens to hundreds of meters, depending on arc length and clock quality. The mitigation of clock noise is typically done in the orbit determination process, by the inclusion of additional estimated clock. We discuss this approach, and associated difficulties in data analysis, in more detail in Section 8.1.3.

Summarizing, variations in pulse energy at the detector (due to a variety of physical causes) can cause variations in measurement accuracy at the level of several mm (Chapter 5). However, consistent operation at single-photon detection energy levels (or few-photon detection energy levels when using a detector array) can largely mitigate this error source. However, hardware imperfections, as they are deduced from current SLR and

space-based laser transmitter and detector systems, will likely remain at the several mm level in the near future (although improvements have been demonstrated at laboratory scales), preventing consistent mm-accurate ILR from being achieved (Section 3.2.1). Furthermore, the influence of clock noise can cause accuracy degradations of many orders of magnitude in the use of one-way ranging data (Chapter 6), provided that this is not corrected for during the estimation process (Section 8.1.3).

### 8.1.3 Estimation Model Errors

As discussed in Section 3.2.2, even in the case of perfectly accurate range measurements, the estimated parameters will not be error-free, due to errors in models used during the post-processing and estimation process.

We distinguish two types of errors that occur in this stage of the data analysis process: those in *a priori* models that are not adjusted during the estimation and those in the models used to adjust the estimated parameters. We have presented a number of errors in *a priori* models for the analysis of both SLR and ILR data in Section 3.2.2. Two of these error sources in SLR will transfer directly to ILR: the uncertainty of the ground station position (in GCRS) and the uncertainty in the tropospheric correction. In the near future, both of these sources of error will likely be at the level of several mm, assuming moderate improvements in both (Section 3.2.2). Both these effects are unlikely to be at the sub-mm level in the near future, making mm-accurate ILR data infeasible, even in the case of perfect measurement equipment and further analysis models.

Additionally, the dynamical modelling of both Earth and the space segment will not be accurate to the measurement accuracy, over the periods of time that the dynamics is integrated (in most cases). This issue is especially strong for spacecraft dynamical modelling, due to the much stronger influence of non-conservative forces (Section 3.2.2; Chapter 6). For the dynamics of natural solar system bodies, however, barycentric dynamical modelling at the mm- or cm-level will require a degree of characterization of the mass distribution in the solar system that is currently not available, when considering the level of model error in current planetary ephemerides (see Sections 2.2.4 and 3.2.2). This is now also apparent in the analysis of accurate LLR data from the APOLLO station (Section 1.1), which yields close to mm-precise (normal point) range measurements, as opposed to the current cm-level dynamical model accuracy (Murphy, 2013).

For the dynamical modelling of planetary orbits, it is especially the uncertainty in mass distribution of the asteroid belt may limit the accuracy of the dynamical model (Standish and Fienga, 2002), although the estimation of additional parameters (facilitated by ILR data) will substantially improve the quality of planetary ephemerides. Crucially, the influence of long-periodic perturbations by other solar system bodies will show only limited correlations with many other physical parameters that are estimated, especially those with a short period (on the order of one rotation of the target body, as opposed to one synodic period), as their characteristic periods will be quite distinct. Still, these combined uncertainties will cause a 'background noise' in the dynamical model that will limit the accuracy to which especially planetary ephemerides (Section 2.2.4) and related parameters with a long-periodic signal can be estimated (Section 2.3.3).



Nevertheless, a substantial improvement in ephemeris accuracy will be attainable from the implementation of laser ranging measurements. For instance, our results in Chapters 4 and 6 show that the accuracy of the Phobos ephemeris could be at the cm-level in the absence of dynamical model errors. As discussed in Section 2.2.4, the current uncertainty of planetary ephemerides is roughly at the same order of magnitude as the accuracy of the range data used as input for these ephemerides (although somewhat larger). However, this rule of thumb will likely no longer be valid in the initial analysis of ILR data. As we discussed in Section 3.2.2, the processing of ILR will require a re-estimation of the ephemerides of all solar system bodies involved in the measurements, including the Earth, since the *a priori* ephemeris of the Earth will be too inaccurate by several orders of magnitude to fully exploit the data. Due to the scarcity of ILR data when it will be first implemented, there will be an additional imbalance of several orders of magnitude between the measurements used for the generation of various solar system bodies. For instance, when analyzing ILR data from an Earth-Mars link in the future, we will have mm-level range measurements for Earth and Mars, m-level (radiometric) range measurements for other solar system bodies with orbiters similar to recent, current and near-term missions (such as Venus Express, MESSENGER and Juno) and km-level range measurements to bodies where little or no data from active tracking techniques is available. Due to the dynamical coupling between the bodies in the solar system, uncertainties in the dynamics of many bodies will degrade the fidelity of the dynamical modelling of the bodies between which an ILR link is set up, for which mismodelled asteroid mass distribution is a prime example. However, the inverse of the problem is also true: due to the dynamical coupling, ILR data will be able to improve the dynamical models beyond those of the bodies which are directly involved in the laser link. Considering the current accuracy of planetary ephemerides (several meters in best cases, see Section 3.2.2), we estimate that at least dm-level planetary ephemerides will likely be attainable from ILR data, representing a substantial improvement to current state of the art. An accurate quantitative assessment of the improvements in planetary ephemerides from ILR data, in the presence of dynamical model errors, remains to be performed, though.

Our analysis of the orbit determination of a lunar orbiter in Chapter 6 included an empirical model for the uncertainty in the non-conservative forces, which is representative of the uncertainty in dynamical modelling of planetary spacecraft. Our simulations showed that uncertainties in this model, not the measurement uncertainty of either the one- or two-way range measurements, limit the attainable orbit accuracy of the lunar mission (to about 5 m r.m.s. when estimating clock and state parameters over sufficiently short clock arcs). However, the use of two-way range data will allow the dynamical models to be improved substantially, improving the attainable orbital accuracy. The use of one-way data is limited in this respect, though, since it is not possible to separate dynamical model errors and clock-induced measurement errors in a model-independent manner (Chapter 6). The issue of spacecraft dynamical modelling is much more influential in the dynamical reconstruction of planetary spacecraft orbits than it is for terrestrial orbits for two reasons. Firstly, the tracking data coverage for planetary spacecraft is typically much sparser than for terrestrial spacecraft, where coverage may be (near-)continuous and may include multiple complementary techniques (GNSS,

SLR, DORIS). As a result, empirical accelerations can be estimated with much higher frequency without causing ill-posedness in the inversion. As an example, Montenbruck et al. (2005) find that the quality of the orbit determination of the GRACE-B spacecraft is best when estimating empirical accelerations (piecewise constant for three orthogonal components) every 600 s. By comparison, Mazarico et al. (2012) use a single constant empirical acceleration component estimated every 2.5 days in the orbit determination of LRO. Secondly, the measurement geometry of planetary spacecraft is quite unfavorable, as all observations are made from almost the same direction (Earth), as shown in detail by Bonanno and Milani (2002). Although the addition of angular observables, such as VLBI observations, can partly mitigate this issue, the limited linear accuracy of these observations (about 4 orders of magnitude difference per AU target distance compared to ILR, see Section 2.1.1) makes this contribution of limited value for characterizing the short-term (hours-days) dynamics of spacecraft (Section 2.1.3).

In addition to mismodelling of the dynamics of both the space segment and the Earth, the influence of clock noise (Section 8.1.2) must be mitigated during the estimation process, at least for data from a one-way ranging system, by the estimation of clock corrections (Chapter 6). This approach of correcting for a measurement error is distinct from calibrations for *e.g.*, tropospheric effects, relativistic effects, or on-site measured system biases, which are applied *a priori* (potentially in an iterative manner during the estimation, as is done for case 2 in Section 5.3 of Chapter 7). Similar to estimated range biases, the clock parameters are included to obtain a best estimate of the range measurement errors (potentially with the use of *a priori* constraints, as is done by Bauer et al. (2014)). Conceptually, this approach is akin to the use of empirical accelerations in spacecraft orbit determination to remove mismodelled dynamics errors.

In general, the degree to which such empirical parameters, including the clock parameters we are concerned with here, can improve the quality of the estimation is dependent on a number of factors (Chapter 6). Firstly, such models depend on a particular parameterization of the correction to the range measurement, which will only be an approximation of the true behaviour of the error source (clock noise) that is to be removed. Therefore, even for an optimal estimation of the clock parameters, remaining clock noise will continue to pollute the measurements (as shown clearly in Section 2.4 of Chapter 6). Secondly, correlations between the additional clock parameters and the physical parameters that are to be estimated can reduce the quality of the final estimation products. Furthermore, the modelled correlation may be different from the true correlation between the clock noise and the signal of the estimated physical parameters, resulting in a skewed estimation.

We found that the difference between the true and modelled effect of clock noise is especially strong for longer clock arcs, where the stochastic clock noise is modelled as relatively smooth in time, as opposed to the inherently erratic clock behaviour. As a result, not only do the correlations between clock and state parameters reduce the quality of the results, a substantial difference between the modelled and true correlation between the state and clock resulted in further estimation errors. These additional errors were caused by the estimator over-attributing range signal to clock noise. The effect of this mismodelled correlation between clock and state signal is difficult to quantify in a general manner, as it depends strongly on the behaviour of the dynamics and

the specific realization of the clock noise, requiring the use of the kind of numerical simulations that we performed. Nevertheless, such simulations will only be able to provide statistical information on the influence of clock noise and require an accurate statistical characterization of the clock noise (in terms of Allan variance, power spectrum, or related quantities). As we concluded in Chapter 6, this lack of robustness in one-way laser ranging data will require a measurement system that is overdesigned for most cases, if a certain positioning requirement is to be met during the mission, since the positioning must be sufficiently accurate even in the worst likely relative behaviour of clock noise and dynamics.

As mentioned above, the addition of clock correction parameters can degrade the estimation quality of the physical parameters, since excessive correlations can cause physical signals to be absorbed by these extra parameters. For our simulations of ranging to a lunar orbiter (in which we estimate no geophysical parameters), we found that the inclusion of a sufficient number of clock arcs could continue to reduce the influence of the clock noise down to several decimeters for 12 hour clock arcs (assuming no mismodelled dynamics). For the simulation of the Phobos lander, however, which includes a larger set of estimated parameters, correlations between clock parameters and other parameters, especially those which are manifested as long-periodic signals, limited the degree to which clock arcs can be shortened to obtain an improved parameter estimate. This shows clearly that the option to add more clock parameters to reduce the influence of stochastic clock noise diminishes for larger sets of estimated parameters. Furthermore, we found that long-periodic effects cannot be properly estimated with one-way range data, as clock parameters correlate almost fully with such parameters.

In addition to the clock noise due to hardware imperfections, we analyzed a previously unconsidered source of clock model error in Chapter 7, specifically errors in the conversions from proper time to coordinate time. The setup of a range measurement typically requires the transmission and reception coordinate times (or a related time scale such as TDB), see Section 3.1.1. However, the ground station clocks register a noisy realization of the local proper time, which differs in rate from this coordinate time in a manner dependent upon a variety of classical and relativistic parameters. When using two-way measurements (especially in the short-range SLR), these errors in proper-to-coordinate time conversion will not propagate into a substantial range error, for the same reason that clock noise does not accumulate for a two-way system. For a one-way range system, however, we showed that errors in the proper-to-coordinate time conversion (if they are not adjusted during the estimation) will result in an orders-of-magnitude discrepancy between the true and formal errors of the estimated parameters. Fundamentally, the cause of this is that the *a priori* uncertainty of planetary ephemerides (and other parameters which influence proper time rates such as gravitational parameters) is orders of magnitude worse than the measurement uncertainty of ILR.

In summary, existing model errors in tropospheric correction and ground station positioning will limit ILR data modelling to the several mm level (Section 3.2.2). Additionally, dynamical model errors of both the space segment and the Earth will limit the accuracy to which the data can be interpreted, although this is of limited influence in the estimation of short-periodic effects (Section 3.2.2; Chapter 6). However, it is fair to assume that the use of ILR measurements will substantially improve the accuracy

of planetary ephemerides (for target bodies to which laser ranging is performed). For spacecraft dynamics, however, the dynamical mismodelling is especially troublesome, as a result of the non-conservative forces acting on them. However, the use of two-way data could be used to improve these dynamical models, as opposed to one-way range, for which the detangling of clock noise and dynamical model errors is not straightforward (Chapter 6). Furthermore, the use of one-way data is limited by the influence of both clock noise and mismodelled proper-to-coordinate time conversions (although the latter may be largely mitigated by iterative updates in the estimation), as shown in Chapters 6 and 7. Clock parameters may be estimated during data inversion, but this can be at the expense of the estimation quality of other physical parameters, especially those with a period much longer than the duration of the clock arcs, which will correlate very strongly. As a result, one-way ranging (except when using systems with exceptionally stable clocks that do not require the frequent removal of clock noise) is not suitable for the determination of parameters which are manifested as long-periodic effects.

#### 8.1.4 Limitations in Interpretation of Estimated Parameters

In Sections 8.1.2 and 8.1.3 we have discussed a number of sources of error that are expected to influence the uncertainty of ILR measurements and data analysis. Although the consistently 1 mm accurate range measurements will likely not be feasible in the near future, a combined accuracy of 3-6 mm total error in measurements and models will likely be feasible for a two-way range system. As a result, highly accurate estimates of (geophysical, relativistic, *etc.*) scientific parameters of interest can be obtained from such missions (as shown most elaborately here in Chapter 4). As discussed in Sections 2.2 and 2.3, though, estimated quantities such as ephemerides, Love numbers, gravity field coefficients and rotational parameters are not the final science products of space missions. Instead, these parameters can be used to constrain physical characteristics and relatedly the origin and evolution scenarios of celestial bodies.

To fully characterize the science return of space missions, it must be determined how the parameters that have been estimated from the (tracking) data can be used to address the science objectives of the mission. For planetary science objectives, this will require a mapping from these measured quantities to physical characteristics describing a body's interior structure, composition, *etc.*, as is done by for instance Rivoldini et al. (2011) for Mars, Baland et al. (2014) for Titan and Williams et al. (2014) for the Moon. Uncertainties in this mapping may limit the capabilities of a mission to complete its scientific objectives. Additionally, science requirements typically specify an accuracy to which the final scientific parameters are to be determined, requiring robust proof that this accuracy can be (before the mission) and has been (following data analysis) attained. To achieve this, a determination of the uncertainties in the various steps of the analysis process is needed.

For the case of the Phobos lander we investigated in Chapter 4, the quantitative analysis did not include any errors in the models used during the estimation (see Section 3.2.2). As a result, our truth model and estimation model were assumed to be equal (although with an imposed uncertainty in range biases). Nevertheless, our results in that chapter (and again in Chapter 6) highlighted a crucial limitation of the laser rang-

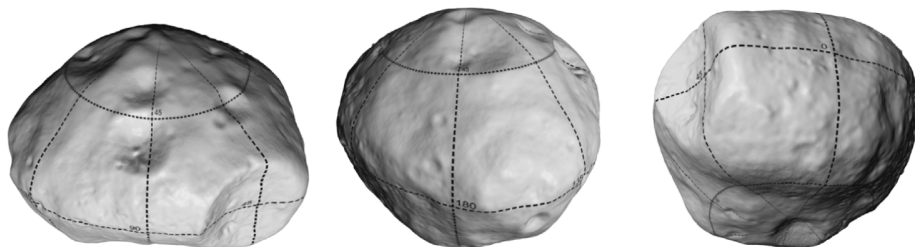


Figure 8.2: Visualization of the Phobos digital terrain model created by Willner et al. (2014), indicating the level of detail that is currently available for the Phobos shape models (volume uncertainty of about 0.6 %).

ing data, which was previously recognized for the case of Doppler tracking of a Phobos lander by Le Maistre et al. (2013). Specifically, it showed that even in the case where the models used to map the range measurements to the orbital dynamics, rotational dynamics and tidal deformation are free of any errors, the mission’s science return can still be limited by uncertainties in models used to further process the estimated parameters. Specifically, the estimated libration amplitudes and gravity field coefficients can be used to determine Phobos’ moments of inertia and thereby constrain the presence of internal heterogeneities such as voids or ice enclosures, allowing Phobos’ origins to be constrained. It is shown by Rosenblatt et al. (2011) that the gravity field and primary libration amplitude (and therefore its moments of inertia) may differ only very slightly from the homogeneous case, making accurate determinations of these quantities crucial for characterizing Phobos’ interior composition. However, Phobos’ shape also enters into the mapping from estimated gravity field and libration to moments of inertia, and for our extremely accurate measurements to Phobos and resultant high quality parameter estimation, it is the shape model uncertainty that limits the knowledge on Phobos’ interior structure, *not* the parameters that are estimated from the tracking data. To illustrate this fact, we show the best current shape model of Phobos in Fig. 8.2 to indicate the level of detail of the best current shape model, which has an inaccuracy of about 0.6 %, (Willner et al., 2014). We have discussed a similar situation for the analysis of highly accurate geodetic parameter estimation of Mars in Section 6.3 of Chapter 4.

This issue is by no means unique to Phobos or Mars and will be a challenge for any mission employing ILR. In fact, the limitation in estimation quality due to the non-conservative force model uncertainty of the lunar orbiter discussed in Chapter 6 is essentially a similar issue, in which the local environment models, as well as spacecraft models, are insufficiently developed to make full use of the data. Furthermore, the dramatic influence of the error in the proper-to-coordinate time conversion we presented in Chapter 7 also stems from the insufficiently characterized dynamics of solar system bodies. Fundamentally, the reason that these issues appear to occur ubiquitously for ILR data analysis is that current models of solar system bodies and environments (except perhaps the Earth and the Moon) are not at the level where they can predict effects at

the same level of accuracy as the range measurements (mm-cm). There are two root causes for this. Firstly, parameters that are required for analyzing the data and achieving the scientific objectives, but which cannot be estimated from tracking data (such as the volume of Phobos) may be of insufficient accuracy due to the lack of sufficiently high quality data from other scientific instruments. Secondly, as highlighted especially for the case of rotational behaviour in Section 2.2.2, body-specific models must often be developed to describe the behaviour of various planets, moons, *etc.* For many bodies, such models are not yet developed to a level where they would be sufficient to facilitate the data analysis for an ILR mission to its fullest, even if there is no fundamental limitation in developing these models. For the Moon, the development of such models has been strongly driven by the long history of LLR, (*e.g.*, Williams et al., 2001). Although such models are typically developed over the course of the design of a mission, it is important to investigate the feasibility of setting up sufficiently accurate models without any accurate *a priori* or complementary measurements.

For the interpretation of scientific results, robust knowledge of the uncertainty of the estimated parameters is important. For instance, an uncertainty in a  $k_2$  Love number or libration amplitude may propagate directly into an uncertainty on the thickness (and existence) of a subsurface ocean or ice shell, (*e.g.*, van Hoolst et al., 2013). Similarly, a sufficiently accurate estimate of the moment of inertia may be used to determine whether a body is (partly) differentiated or not (*e.g.*, Schubert et al., 2004). In general, the combined uncertainties of the various geodetic and non-geodetic parameters will propagate into uncertainties of the parameterized interior of a body, such as layer thicknesses or phase and fraction of a certain compositional element. Generally, only a limited number of parameters is estimated, whereas the interior of a body may be parameterized by many more values, resulting in a (strongly) underdetermined problem. For the numerical simulations we performed in this dissertation, the truth model is (either deterministically or stochastically) known, allowing us to quantify the influence of the various physical range measurement errors and modelling errors. In the analysis of actual data, however, the influence of these errors will remain unconsidered during the analysis if their existence is not known. As shown in each of the Chapters 4-7, the formal error provides uncertainties that can be orders of magnitude too optimistic, making the consideration of other error sources crucial, for instance by the use of consider-covariance analysis.

The fact that formal errors represent estimates of the uncertainty that are far too optimistic, as discussed in Section 8.1.1 is well known for planetary tracking data analysis, (*e.g.*, Konopliv et al., 2006; Marty et al., 2009; Andert et al., 2010; Dehant et al., 2011; Mazarico et al., 2014b). In our work, this is made especially clear in the estimation results of the  $h_2$  Love number and libration amplitudes of Phobos that are presented in Chapter 4. Since the influence of these parameters is mostly a result of geometry, not orbital dynamics (with the exception of the primary libration amplitude), their estimation uncertainty can be directly related to a range uncertainty. For the Love number and libration amplitude uncertainties, using the formal error as an indicator of their estimation quality results in systematic range measurement uncertainties at the 10-100  $\mu\text{m}$  level. This level of uncertainty is clearly far too optimistic. When adding the systematic range errors, this uncertainty increases to the mm-level, which is a more realistic value

considering the 5 mm single shot precision and 5 mm systematic range error.

An example of a more subtle unquantified true error source, is the periodic range accuracy variation due to varying observation geometry found in Chapter 5 and discussed in Section 8.1.2. These variations will, if not modelled (stochastically or otherwise), go unobserved in any gauge of estimation error that is available in the data analysis, where a (scaled) formal error is often used as a measure of quality. The lack of suitability of using the formal error as a measure of observation quality was again highlighted in Chapter 6, where we initially found, for the Phobos lander simulations, a decrease in true error with increasing number of clock arcs  $N_c$ , followed by an increase in the true error beyond a certain point. The formal error, however, continuously increased with  $N_c$ . Finally, we showed in Chapter 7 that the error propagation of position errors onto clock calibration errors (due to the proper time rate's dependence on the translational dynamics) is important for a correct characterization of the error budget of (one-way) ranging data. In that chapter, we presented a model which introduces this coupling into the estimation, thereby allowing the formal errors to capture this coupling.

In summary, although ILR data will allow substantial improvements in parameter estimation from space mission tracking data, it is crucial to analyze the full analysis chain from raw measurements to final science products. Errors in models which cannot be constrained from tracking data may limit the final science return, which requires careful consideration of the relation between the requirements imposed on various instruments on a scientific mission, as well as the relation with *a priori* information. Similarly, the error analysis that is used to assess the quality of the final science products must not be based purely on the formal errors. This can be accomplished by, for instance, including the dominant time correlated sources of error in the error propagation.

## 8.2 Comparison to Conventional Tracking Techniques

In Section 8.1, we have synthesized our discussion on range measurement error sources from Section 3.2 and the core of this dissertation presented in Chapter 4-7, where we have presented a number of novel methods and considerations regarding the error budget of ILR missions. Summarizing, both our analysis in Chapters 4-7 and data from literature presented in Section 3.2 (for instance the  $> 1$  mm inaccuracies in the tropospheric correction model and instabilities in the hardware), lead us to conclude that a 1 mm accurate interplanetary laser range measurement will not be consistently attainable by the network of ILRS stations in the coming years. Values of 3-6 mm accuracy are likely to be more realistic, with the precise values dependent on a score of parameters related to the hardware of the ground and space segments, environmental conditions and various other aspects of the mission under consideration. Sub-mm precision (averaged over a sufficient number of subsequent shots) is possible, though, but of limited value to the science return of the system (Section 8.1.1).

In this section, we use our estimated ILR measurement accuracy values to compare attainable science return from an ILR mission to that from a mission employing standard radiometric tracking techniques, building upon our preliminary comparison in Section 2.1.3. To this end, we derive a quantitative criterion for comparative quality of range and range rate measurements in Section 8.2.1. Subsequently, we use a simplified, purely

periodic, model for the influence of physical signals on both range and range-rate measurements. The application of this model using current and near-future tracking data accuracy values is presented in Section 8.2.2, where we discuss the implications for the competitiveness of ILR as a technology for achieving science goals of planetary missions, such as those discussed in Sections 2.2 and 2.3.

### 8.2.1 Definition of Comparison Criterion

To properly compare the range and range-rate observables, it should be evaluated how their total measurement value, and time-variations of these values, relate to the influence of a parameter  $q$  that is to be estimated. In this section we derive a criterion based upon which the contribution of the range and range-rate observables to the estimation of physical parameters can be quantitatively compared.

The sensitivity of an observable  $h$  to a parameter  $q$  is determined by its associated partial derivative  $\partial h/\partial q$ , (*e.g.*, Montenbruck and Gill, 2000; Tapley et al., 2004). Since the range-rate observable  $\dot{s}$  is calculated from time differenced range observables, as shown by Eqs. (2.1) and (2.3), the partial derivative of the range rate observable can be expressed in terms of range observable  $s$  as follows:

$$\frac{\partial \dot{s}(t)}{\partial q} = \frac{1}{\Delta t_i} \left( \frac{\partial s(t + \Delta t_i)}{\partial q} - \frac{\partial s(t)}{\partial q} \right) \quad (8.1)$$

This relation shows that the range-rate observable will be completely insensitive to parameters  $q$  which have a constant influence on the range measurement ( $\partial s/\partial q = \text{constant}$ ). Similarly, the range rate observable will be only weakly sensitive to periodic signals of a parameter  $q$  for which the period  $T$  is much larger than  $\Delta t_i$ .

To quantitatively compare the data types, we define a criterion that describes the influence of a unit change in  $q$  on bothn range and range-rate by comparing it to the noise levels of  $s$  and  $\dot{s}$  (which we denote  $\sigma_s$  and  $\sigma_{\dot{s}}$ , respectively). Essentially, this criterion is a signal-to-noise (SNR) criterion, comparing signal from a parameter  $q$  to a measurement noise level  $\sigma_h$ . For any observable  $h$ , the  $\text{SNR}_{h,q}$  for measuring a parameter  $q$  may then be defined as:

$$\text{SNR}_{h,q} = \left| \frac{1}{\sigma_h} \frac{\partial h}{\partial q} \right| \quad (8.2)$$

which is a first-order estimate of the relative sensitivity of an observable  $h$  to a parameter set  $q$ .

Using Eq. (8.2) we can define the following criterion to determine when a range observable becomes more sensitive to a parameter  $q$  than the range rate observable:

$$\text{SNR}_{s,q} > \text{SNR}_{\dot{s},q} \quad (8.3)$$

Using this criterion, the qualitative comparative discussion of range and range rate in Section 2.1.3 can be quantified, which we present and discuss for a simplified behaviour of the parameter  $q$  in Section 8.2.2.

With the criterion defined by Eqs. (8.2) and (8.3), we are in a position to make a conceptual comparison between the capabilities of an ILR system and a radiometric



Doppler system of representative current and near-future capabilities. Specifically, for current radiometric systems, we use accuracies of 1 m in range and 0.04 mm/s over an integration time  $\Delta t_i$  of 60 s in range rate (Section 2.1.2). As a result of a number of modifications, such as the use of a multi-wavelength system (Bertotti et al., 2003), these values are expected to improve for future missions. In our analysis, we assume 0.2 m accuracy in radiometric range, and both 0.01 mm/s at 60 s integration time and 0.002 mm/s at 1000 s integration time, values which we extrapolate both from required Doppler noise levels of next-generation space missions, and experience with the Cassini dual-wavelength system (Section 2.1.2). We use the methods described in Section 8.2.1 to investigate the types of effects that can be measured more accurately by laser ranging measurements, when compared to existing and near-future Doppler tracking capabilities.

For our comparison, we use a simplified model for the behaviour of the parameters  $q$ . Specifically, we assume that a variation of a parameter  $q$  is manifested in the range measurements as a purely sinusoidal signal of amplitude  $A$  and angular frequency  $\omega$ , so that:

$$\frac{\partial s}{\partial q} = A \sin(\omega t) \quad (8.4)$$

and it subsequently follows from Eqs. (8.1) and (8.4) that:

$$\frac{\partial \dot{s}}{\partial q} = \frac{1}{\Delta t_i} \left( A \sin(\omega(t + \Delta t_i)) - A \sin(\omega t) \right) \quad (8.5)$$

$$= \frac{A}{\Delta t_i} \left( (\cos(\omega \Delta t_i) - 1) \sin(\omega t) + \sin(\omega \Delta t_i) \cos(\omega t) \right) \quad (8.6)$$

From these equations, it can be seen that the signal of a parameter  $q$  on the range and range-rate measurement will be a sinusoid of equal period. However, they will exhibit a phase and amplitude difference that varies with  $\omega \Delta t_i$ . The phase difference will converge to  $\pi/2$  in the limit of  $\omega \Delta t_i \rightarrow 0$ , though, as follows from the limit ratio of the multipliers of the  $\sin(\omega t)$  and  $\cos(\omega t)$  terms in Eq. (8.6):

$$\lim_{\omega \Delta t_i \rightarrow 0} \frac{\cos(\omega \Delta t_i) - 1}{\sin(\omega \Delta t_i)} = 0 \quad (8.7)$$

and the contribution of the  $\sin(\omega t)$  term in Eq. (8.6) becomes negligible for  $\omega \Delta t_i \rightarrow 0$ . Consequently, the range rate sensitivity limit case is derived from Eq. (8.6) as:

$$\lim_{\omega \Delta t_i \rightarrow 0} \left( \max_t \left( \frac{\partial \dot{s}}{\partial q} \right) \right) = \frac{2\pi A}{T} = \omega A \quad (8.8)$$

which is independent of  $\Delta t_i$ . Since the range-rate noise level decreases with integration time (Asmar et al., 2005), a range rate observation with a longer integration time is inherently better suited for estimating parameters for which  $T > \Delta t_i$  (for similar environment and hardware conditions). For  $T < \Delta t_i$ , however, a  $2\pi$  ambiguity arises in the estimation of purely periodic signals, requiring the use of a smaller integration time. Range measurements can be used for the estimation of such high-periodic signals, although with a generally reduced sensitivity compared to short integration time range-rate measurements, since  $\frac{\partial s}{\partial q}$  does not increase with decreasing  $T$ , as opposed to  $\frac{\partial \dot{s}}{\partial q}$ .

## 8.2.2 Quantitative Comparison for Periodic Signals

Using our representative values of the laser range accuracy and radiometric data accuracy and integration time given in Section 8.2.1, we use Eq. (8.2) to evaluate the sensitivities of these observables to our periodic signals. To compare the performance of range and range-rate systems, we calculate the maximum values of Eqs. (8.4) and (8.5) over a single period to determine the maximum observable signal of the parameter  $q$  on both  $s$  and  $\dot{s}$ , respectively. Subsequently, we use Eq. (8.3) to determine for which periods  $\omega$  of the signal  $q$  the range measurements become superior to Doppler measurement (in terms of  $\text{SNR}_{h;q}$ ), for our assumption of purely periodic signals. Since Eqs. (8.4) and (8.5) are both linearly related to the amplitude of the signal  $A$ , we set  $A = 1$  in our analysis without loss of generality.

The results of our analysis are shown in Fig. 8.3 where the sensitivity of a number of range (laser and radiometric) and range-rate systems to periodic signals are shown. If laser ranging systems are to be implemented in the future, it should be shown that it has a clear scientific advantage over next-generation Doppler systems. From the figure we see that, depending on the integration time of the range-rate and the precise assumption on the laser ranging accuracy, the Doppler and laser range curves cross in the range of 0.5–5 hours. Consequently, physical parameters with periods longer than these values are better estimated using laser ranging than radiometric Doppler systems (under the assumptions of the model we use here). For current typical radiometric range and range-rate measurements, the curves cross at a period of about 40 hours, indicating the relative weakness of current range measurements for use in estimating short-periodic effects (Section 2.1.3). Note that our approach neglects the different influence of mutual correlations between multiple estimated parameters, which may be different for range and range-rate measurements, as well as any the influence of any non-(purely) periodic effects of the parameters  $q$  on the measurements. Furthermore, it omits the influence of measurement frequency (*i.e.*, how many measurements are taken per unit time) on the estimation, quality, as it is assumed that the measurements can fully sample the peak-to-peak behaviour of Eqs. (8.4) and (8.5), respectively.

An overview of the various scientific applications of planetary tracking data was given in Sections 2.2 and 2.3, where we also qualitatively discussed the potential value of laser ranging technology. Based upon the results shown in Fig. 8.3, we are now in a position to draw preliminary quantitative conclusions on the comparative performance of an ILR system. Despite the fact that our approach will only be valid as a first-order approximation (as discussed above), it provides a good initial estimate of the physical parameters and associated science goals for which the use of laser ranging can offer competitive performance.

In Section 2.2.1, it was discussed that range measurements are poorly suited to estimating planetary gravity fields of higher degrees and orders. Considering the results shown here in Fig. 8.3 and typical orbital periods of planetary missions, this conclusion can be seen to be justified. For JUICE, for instance, the orbital period around Ganymede during the 500 km circular orbit phase will be about 3 hours (Grasset et al., 2013). The main BepiColombo spacecraft (Benkhoff et al., 2010) will have a similar orbital period around Mercury (about 2.6 hours at a moderate eccentricity of about 0.16). From Fig. 8.3, we see that Doppler tracking will become superior to the 3 mm accurate

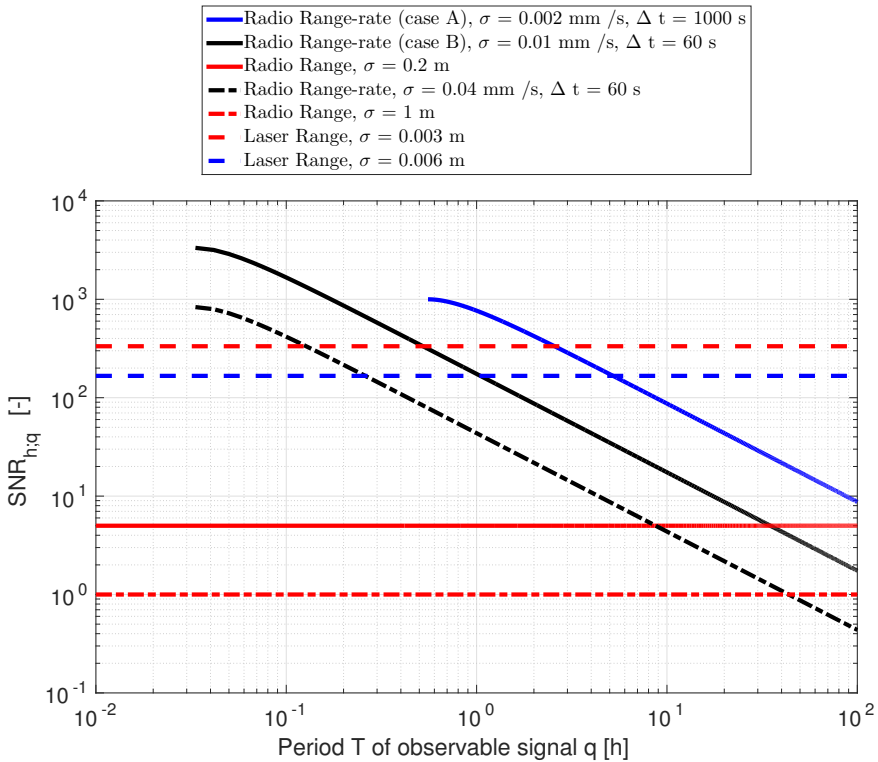


Figure 8.3: Comparison of range and range-rate observable to purely periodic signals of amplitude  $\omega$  (dashed line represents ILR, thick lines next-generation radiometric, dashed-dotted current radiometric).

laser ranging measurement at 2.5 and 0.5 hours for Doppler cases *A* and *B*, respectively. For the 6 mm range accuracy, these crossing points are 1 hour and 5 hour. Consequently, for orbital periods such as those of JUICE and BepiColombi, laser ranging can be competitive for the estimation of the very low degree gravity field coefficients and/or Love number. Assuming an orbital period of 3 hours, the 3 mm range measurement has similar sensitivity as Doppler case *A* at degree 2, and the same or higher sensitivity up to 6 for Doppler case *B*. For the 6 mm range measurement, Doppler case *A* is clearly superior even at degree 2, whereas Doppler case *B* has the same sensitivity at degree 3. For higher degrees, the reduction in gravity field signal wavelength means that the Doppler measurement will likely yield superior results. For spacecraft orbiting larger bodies the orbital period will be longer, increasing the potential value of laser ranging. The period of the science orbit of Juno around Jupiter will be approximately 10 days at an eccentricity of 0.95, for instance (Matousek, 2007). Consequently, laser ranging could offer superior performance for signals up to moderate gravity field coefficients. However, these estimates only hold for circular orbits, omitting the influence of the eccentricity

of these missions (which is substantial for Juno, for instance). The signal of the gravity fields will be especially strong at periapsis, where the velocity of the spacecraft is larger and the (pseudo-)period of the measurable effect resultantly smaller, further reducing the relative value of range measurements for gravimetric purposes, especially for higher degrees and orders.

For the extraction of rotational parameters of solar system bodies (Section 2.2.2) from tracking data of landers, the strongest signals will typically be those with a once-per-revolution signal. The full spectrum of relevant rotational variations spans a wide range of periods, but significant variations are typically not much smaller than the rotational period, (*e.g.*, Williams et al., 2001; Konopliv et al., 2006; Petit et al., 2010). Rotational variations with much larger periods (such as the precession) may be used to deduce valuable information on a body's interior, though. Considering the typical rotational periods of bodies in our solar system, we can confidently state that laser range measurements to landers will be better suited for the estimation of such parameters than Doppler measurements will be. For some fast-rotating bodies such as Phobos, the ratio  $\text{SNR}_s/\text{SNR}_{\dot{s}}$  at the rotational period will be relatively low: around 3.5 for range-rate case *A*, and around 15 for range-rate case *B* (assuming  $\sigma_s=3$  mm). For landers on bodies with much slower rotational periods, such as Ganymede and Mercury, the SNR ratio is about 70 and 1,000, respectively. However, as we found to be the case for simulated data to a Phobos lander (Chapter 4), at these levels of observational accuracy, many models will need to be improved to make full use of the data quality that would be available (Section 8.1.4), making it doubtful that the quality of the final science products from a laser ranging mission to Ganymede or Mercury would be 70 and 1,000 times that from a system using Doppler tracking. Nevertheless, it does illustrate the exceptional strength that laser ranging technology can have in characterizing rotational motion in the solar system. Similarly, tidal deformation of bodies will in most cases manifest itself most strongly as an approximately once-per-revolution effect on the range to a lander, making laser ranging exceptionally well suited for the determination of  $h_2$  and  $l_2$  Love numbers (and possible  $k_2$ , due to its influence on rotational dynamics, see Section 2.2.2). It should be noted, though, that the use of (radiometric) same-beam interferometry (Section 2.1.1) could provide even greater estimation accuracy for these parameters, although it will require a network of (at least two) landers on the target body.

A number of physical effects, such as the influence of a tidal lag angle on the orbital dynamics of natural satellites (Section 2.2.3), are primarily secular in nature. These effects, however, will not propagate into a secular change in the amplitude of the observable sensitivity  $\partial h/\partial q$ . Instead, since effects causing secular orbital acceleration/deceleration result in an increase/decrease in the orbital period, respectively, they will result in variations  $\delta\omega$  of  $\omega$  (and associated variations  $\delta T$  of the period  $T$ ) of the measurement signal, leading to a range sensitivity of the form:

$$\frac{\partial s}{\partial q} = A \sin(\omega t + (\delta\omega)t) \quad (8.9)$$

so that a secular effect on the orbit will manifest itself as a secular effect on the phase of the partial derivative for the range observable. Assuming  $\delta\omega \ll \omega$ , the phase shift will be approximately constant over a single period  $T$  of the signal. Consequently, in

the presence of such a secular effect, the range-rate partial will undergo a phase shift of the same magnitude as the range partial in Eq. (8.9). Also, the period of the signal of a parameter  $q$  on the range and range-rate partials is equal. Therefore, we can compare their sensitivity to a secular effect by comparing their sensitivities at the parameter's basic frequency  $\omega$ , which will be the orbital period in the case of the influence of tidal dissipation.

For the determination of planetary ephemerides (Section 2.2.4), radiometric range and VLBI measurements are currently the primary sources of spacecraft-based data, due to the very long periodic signals that must be resolved for their estimation. Laser range measurements will be about a factor 150-300 more accurate than current planetary range measurements, and about 30-60 times more accurate than range measurements from next-generation radio tracking systems. However, the use of laser ranging will not improve the angular position observations of spacecraft, which are obtained by VLBI measurements. For VLBI observations, the state-of-the-art measurement accuracy of 1 nrad leads to an approximate position accuracy of 150 m for every AU of distance between Earth and the target. Although the VLBI measurements provide much looser constraints in the estimation of ephemerides than laser ranging will, its unique sensitivity to the out-of-plane component will continue to be an important asset for anchoring planetary ephemerides, especially over longer time scales. We discussed the potential of ILR measurements to improve planetary ephemerides in a more general sense in Section 8.1.3.

As discussed in Section 2.3.3, many of the current experimental contributions that planetary tracking has made to gravitational physics have been obtained from planetary ephemerides, either directly during the estimation or indirectly through postfit analysis. Although we have not explicitly included the estimation of gravitational physics parameters (as is done by *e.g.*, Turyshev et al. (2010)) in most of our analyses in Chapters 4-7, our discussion both in this chapter and also in Chapter 4 highlights and partially quantifies the influence that laser ranging could have on experimental gravitational physics, through its improvement in planetary ephemerides. Additionally, although our analysis in Chapter 7 showed that relativistic clock effects will not do much to improve the science return of planetary landers, the use of the framework that we developed there could be helpful in achieving longer-term stability of planetary orbiter dynamics estimation, providing more stringent constraints on gravitational physics parameters. As discussed in Section 2.3.3 and shown by Eqs. (2.43)-(2.45), a number of physical parameters (both relativistic and classical) are strongly correlated due to the nearly circular and equatorial orbits of the planets. Therefore, highly accurate ephemerides of multiple bodies will be highly beneficial to decouple these parameters, and ILR tracking data from a single body will be only limitedly capable of decorrelating various parameters beyond their current level of uncertainty (Section 8.1.3).

In this section, we have focussed largely on the analysis of two-way ILR data. The use of one-way data, which suffers from the influence of clock noise (Chapter 6), will most likely not be able to compete with two-way radiometric data, which is expected to reach 0.2 m accuracy for next-generation missions. Furthermore, one-way range requires the estimation of clock parameters, which correlate strongly with long-periodic effects (see Chapter 6; Section 8.1.3). Therefore, even if the measurement accuracy of one-

way laser ranging could be reduced to below the expected error level of radiometric systems, the combined estimation of both clock parameters with arc length  $T_c$  and physical parameters with periodic signals of period  $T_p$  will reduce the physical reliability of both sets of parameters by orders of magnitude if  $T_c \ll T_p$ . This is detrimental for the science case of such a system, since it is especially the long-periodic effects where the strength of laser ranging can be exploited (as discussed above and shown in Fig. 8.3). As such, to make the use of one-way laser ranging systems competitive in *e.g.*, gravitational physics experiments, an exceptionally stable space-based clock will be required. When using such clocks, the clock arc length can be increased to a point where its correlation with the signals from the estimated physical parameters diminishes, and clock noise can be removed to well below that of a radiometric system. Such a development may be facilitated by both ground- and space-based optical clocks, (*e.g.*, Bloom et al., 2014), potentially providing a competitive implementation for one-way laser ranging in the coming decades.

Our discussion in this section may lead one to the conclusion that laser ranging will be the superior tracking method for most missions, as only gravity field estimation seems to be superior with Doppler tracking (using our first-order model), due to the short wavelength of the signals that are to be measured. However, gravity field determination is a crucial part of planetary geodesy, as discussed in Section 2.2.1. Additionally, the very short periodic perturbations that higher degree gravity field coefficients have on the orbit of a spacecraft makes the accurate knowledge of these parameters important for an accurate orbit reconstruction of the space segment. This is illustrated very clearly by Mazarico et al. (2013), who compare the orbit determination of lunar orbiters before and after the availability of the lunar gravity field computed from GRAIL data (Section 2.2.1). Although gravity field coefficients of low degrees and orders will be estimatable with laser ranging systems to an accuracy that is competitive with state-of-the-art Doppler systems, Doppler will likely remain the method of choice for the estimation of moderately low-to-high degree gravity fields. For use on landers on solar system bodies, however, the case from the science return point of view seems clear, with laser ranging the preferred technology. Nevertheless, as discussed in this dissertation and summarized in Chapter 9, a variety of issues remain for the implementation of laser ranging technology, despite its potential for revolutionizing various aspects of the science return from planetary missions.

---

## Concluding Remarks

---

Having synthesized our results of Chapters 4-7 in Chapter 8, taking into consideration our previous discussion of the theoretical and technological background of ILR of Chapters 2 and 3, we can now offer several overarching conclusions on the use of ILR in planetary missions. In Section 9.1, we address the main research questions discussed in Chapter 1. Finally, we provide an outlook to future research and implementation of ILR in space missions in Section 9.2.

### 9.1 Conclusions

Our goal in this dissertation was to analyze the potential for future scientific application of ILR, with a focus on planetary science objectives (Section 1.2). Specifically, the goal was to understand the quantitative scientific contributions that ILR could make to achieving a mission's planetary science objectives, as well as to understand the main limitations in the accuracy and implementation of the technology. To this end, we have analyzed a variety of sources of uncertainty in the measurement and analysis process (Chapters 4-7; Section 8.1) and have simulated the potential science return for representative ILR missions (Chapters 4, 6 and 7). To guide the selection of a specific type of tracking system, we have investigated the comparative performance of different types of ILR systems and, finally, have made a first-order comparison of the science return from a mission employing ILR to that from typical radiometric Doppler and range measurements (Section 8.2).

#### **Error sources and mitigation**

Due to the lack of current missions employing ILR, we cannot yet create an estimate of ILR measurement and analysis uncertainties based on existing data sets (Section 3.3.1).

Instead, we have relied on both numerical simulations and extrapolation from existing systems, especially those used in SLR and laser time transfer. We have provided a detailed discussion of the various error sources in measurements and data analysis in Section 8.1. Here, we summarize the key issues regarding error sources in ILR, forming a crucial part of the analysis of its potential use.

For ILR, hardware and operational developments of both the ground and space segments will build strongly upon existing and near-future activities of the SLR community. For the ground segment, this means that ILR will rely on the use of the existing ILRS station network (Section 3.1.6). For the development of the active space segment of ILR, hardware developments that are ongoing for laser time transfer and communications (and to a lesser degree altimetry) provide strong synergy (Sections 3.3.3-3.3.5).

One key factor in the operational design of such a system is the requirement of single-photon signal intensity detection (Section 3.2.1, Chapter 5). In ILR, the temporal pulse shape can be modelled to exceptionally high accuracy, due to the absence of retroreflectors. Therefore, operating at the single-photon detection energy levels allows the transmitted temporal pulse shape to be directly sampled, with little ambiguity in how the mean single-photon detection time compares to the pulse centroid's arrival time at the detector. Resultantly, nearly all inherent stochasticity in the pulse detection time, including turbulence-induced signal strength variations, can be removed. Furthermore, laser ranging operations could be extended into the few-photon detection regime without significant loss of accuracy by the use of multi-array detector systems. However, a variety of errors due to both the hardware and analysis model uncertainties (Sections 8.1.2 and 8.1.3) will likely prevent mm-level ILR from being performed in the near future.

A number of the current limitations in the realization and analysis of SLR data will carry over to ILR. Specifically, the uncertainty in tropospheric range corrections, terrestrial reference frame, (non-)tidal loading and rotational variations of the Earth will limit the accuracy of data analysis to the level of at best several mm (Section 3.2.2). Inaccuracies due to hardware imperfections will likely be at a similar level, although the absence of retroreflectors in ILR, and the development of stable (space-grade) detection, timing and calibration systems may allow mm-level hardware-induced inaccuracies in the future (assuming single-photon detection). Such accuracy has already been demonstrated on laboratory scales for a two-way asynchronous system. An important difference between the error budgets of SLR and ILR, though, is the influence of clock noise. This is especially true for the use of a one-way range system, where clock noise can cause large range errors (tens to hundreds of meters) if not mitigated by either the use of an extremely stable clock or the estimation of clock parameters (with resulting difficulties, as discussed below), see Chapter 6. For a two-way system, ground stations will require an H-maser quality clock (or better) for typical planetary target light times to prevent the clock noise at the ground station from introducing >mm-level errors in the (two-way) measurements.

As a specific test case of a planetary mission employing ILR, we analyzed in depth the science return from a Phobos lander equipped with a laser ranging system, focussing on the estimation of geodetic characteristics of the Martian system (Chapter 4). Our analysis has shown that systematic range measurement errors will be 1-2 orders of magnitude more influential in the final error budget of the estimated parameters than the



measurement precision will be. This makes the mitigation of Gaussian uncorrelated measurement noise (for instance by means of using a shorter laser pulse) of limited interest. The specific influence of a general time-correlated error source, of which a systematic error is but one example, depends on how its behaviour compares to that of the estimated parameters.

One of the measurement error sources we investigated in detail here is the non-Gaussian range error due to variable signal strength caused by varying turbulence strength, zenith angle, atmospheric transmittance, target distance, *etc.* (when not operating at the single-photon level), see Chapter 5. We found that this error source can induce variations in the range measurement at the several mm-level for typical ILR systems. Furthermore, such variations will show a periodic signature with a period approximately equal to the synodic period between the Earth and the target body. Such variations could be absorbed into the ephemerides estimation, potentially diminishing their quality, as well as complicating the determination of their accuracy (Section 8.1.2).

### **Influence of ILR system type**

In the selection of an ILR system, mission designers are faced with a range of choices in the type of laser ranging system. Primarily, this concerns the choice of a one-way or two-way system, but also the choice of space segment hardware and ground segment requirements, potentially limiting the set of ILRS stations that can contribute to the tracking campaign.

In this dissertation, we have for the first time made a detailed analysis of the comparative performance of a one- and two-way laser ranging system (Chapter 6). The error budgets of these systems differ primarily in how the clock noise influences the measurements, which accumulates with time for a one-way system, and only over the light time for a two-way system. Due to the impossibility of *a priori* separation of accumulated clock noise from other measurement and model errors in a one-way system, it provides inferior performance in terms of parameter estimation quality compared to that of the two-way system. Nevertheless, a one-way system only requires a detector on the space segment, not an active laser system, thereby reducing the system's mass and power requirements. Although the complexity of a one-way system is lower, making it a lower-risk solution, a two-way system could be repurposed to function as a one-way system in the event of failure of part of the space segment hardware.

In the analysis of one-way data, the influence of clock noise can be reduced with the estimation of clock parameters. This approach is currently taken in the orbit determination of LRO from laser ranging data (Bauer et al., 2014). However, correlations with other parameters, as well as the typically non-continuous coverage of laser ranging data, prevent the use of very short clock arcs. We observed this effect clearly in our simulated estimation of the state of Phobos using one-way range data. There, the increasing influence of correlations with an increasing number of clock arcs prevents the use of clock arcs shorter than about 5 days, resulting in an error of Phobos' state that is 2 orders of magnitude larger than that which is obtained from the two-way data simulations. Furthermore, our numerical analyses show that the estimation of clock parameters to mitigate the accumulated clock noise in a one-way system will correlate strongly with parameters that are manifested as long-periodic signals in the range data, such as lan-

der positions, once-per-orbit planetary dynamics effects, *etc.* Consequently, missions for which the estimation of such parameters is crucial for attaining the (primary) science goals should not use a one-way system that requires the estimation of even moderately short clock arcs. This is problematic for the science case of a one-way system, since range measurements are especially competitive with existing tracking techniques in the estimation of long-periodic effects (Sections 2.1.3 and 8.2.2). The estimation of clock parameters can be prevented by the use of an extremely accurate clock on both the ground and space segments, which can largely undo the influence of clock noise altogether. However, the mass and power requirements of such a timing system may completely undo the advantage of the relative simplicity of a one-way system (compared to a two-way system).

Similar to the influence of clock noise on one-way data, the coupling between translational dynamics and clock rates can cause substantial one-way range errors in the data analysis, when using an *a priori* time ephemeris (Chapter 7). Updating the time ephemeris during each iteration of the estimation can largely mitigate this problem, provided that the parameters that are relevant for computing the time ephemeris are included in the estimation and can be improved to a sufficient degree with the available data. However, to fully quantify the influence of this effect on the estimation uncertainty, the time dynamics and orbital dynamics should be concurrently estimated. We have developed the framework for such an approach in this dissertation.

Despite the apparently clear advantage of a two-way system in terms of parameter estimation uncertainty, the quality of the analysis of both one- and two-way data may be limited by uncertainties in other models, as we found in the case of orbit determination of a lunar orbiter, where dynamical model uncertainty limits the attainable position uncertainty (Chapter 6). As a result, the quality of the orbits estimated from the one- and two-way data was similar. However, two-way data may be used to improve (non-conservative) force models, whereas it is difficult to fully distinguish mismodelled dynamics from clock noise in the residuals of one-way data. As a result, determining the added value of using a two-way system in a specific mission (compared to a one-way or radiometric system) will require an analysis of the full chain of measurement and model errors, including the potential for the measurement data to improve such models.

### **Comparison and synergy with other science instruments**

For ILR to be implemented as a tracking system for planetary missions, considerations of either scientific or programmatic (cost, mass, power, *etc.*) nature should show its inclusion to be the optimal design choice for the mission under consideration. From a science return point of view, it should be shown to be either a superior choice compared to existing (radiometric) tracking techniques, or to provide valuable data in addition to typical tracking techniques. As we have shown in Section 8.2.2, Doppler tracking data is strongest for observing short-periodic effects, since their sensitivity decreases with increasing period of the effects that is to be observed, making them more suitable for estimating the spacecraft's local dynamics. Range measurements, on the other hand, are equally sensitive to effects at any period, making them well suited to observing the global dynamics. We have quantified the comparison of radio Doppler with laser ranging by assuming purely periodic effects on the range measurements due to estimated

parameters. We find that, depending on the precise quality of the next generation of Doppler and laser range systems under consideration, an ILR system can provide competitive estimation quality for parameters which are manifested in the data as signals with a period of longer than 0.5 to 5.0 hours. These values indicate similar or superior estimation performance from ILR for most parameters that are typically estimated from planetary tracking data, with the important exception of all but the lowest orders of a body's gravity field coefficients. The weakness of ILR in gravity field estimation may limit its capabilities as a tracking tool for planetary orbiters, since uncertainty in the planetary gravity field will propagate into uncertainty in the spacecraft's orbit, and the associated science products. For the case of landers on solar system bodies, however, the science return from an ILR system is in most cases clearly superior to that from a radiometric Doppler system, at least in the first-order comparison model that we employ.

The analysis of ILR data poses important challenges beyond the estimation of geodetic (Section 2.2) and relativistic (Section 2.3) parameters, which are typically the two classes of science parameters that are estimated from tracking data. Due to the revolutionarily accurate range measurements that ILR will be able to deliver, improvements in the various models entering the analysis and interpretation of the data must be brought to a level where it can be used to its full potential (Chapter 4; Section 8.1.4). Not only will this require significant modelling efforts (for instance for detailed rotational, tidal or relativistic models), but interpretation of the data will require more accurate knowledge of various quantities that cannot be obtained from tracking data alone. Examples of such synergistic data are magnetic field, heat flow, geological and seismic measurements, which will be important for the full characterization of a body's interior structure and composition. We discussed this effect in detail for our simulations of a Phobos lander in Chapter 4, for which the shape model's uncertainty limits the degree to which the estimated gravity field and rotational characteristics can be mapped to interior structure and composition models. Similarly, due to the difficulty in decorrelating various classical and relativistic effects from planetary orbital dynamics, ILR data for multiple bodies would be highly advantageous in the estimation of parameters that quantify such effects (such as the solar  $J_2$  and the PPN parameter  $\beta$ ), see Section 2.3.3.

Similar results on the limitations of highly accurate two-way data were found in the analysis of simulations for a lunar orbiter (Chapter 6), in which the dynamical model uncertainty, not the measurement errors, limited the orbit estimation quality. Additionally, for our analysis of the coupling between time and translational dynamics (Chapter 7), our results indicated that the uncertainty of *a priori* orbital solutions can dramatically reduce the quality of the analysis of (one-way) range data, if no suitable corrective action is taken during the estimation process. The fact that significant influence of model errors appears in various, unrelated, aspects of ILR data analysis is inherent in the unprecedented measurement accuracy. Resultantly, its application will require not only development of the technique itself, but also the development of related next-generation models and instruments, to ensure a balanced science return from future planetary missions, in which the various instruments complement each other to a level where each of them can be exploited to its full potential.

## 9.2 Recommendations and Outlook

The first implementation of ILR as an operational tracking technique may very well occur some time in the next decades. Considering the high cost and resulting relative scarcity of planetary missions, however, a more precise timeframe for the first operational ILR system is impossible to define. Moreover, the use of ILR is strongly contingent upon the capabilities of such a system to strengthen the science case of a specific mission. In the case of lander missions for which the accurate estimation of rotational, orbital and/or tidal characteristics is crucial to attaining the mission's science goals, this case is the strongest, as we have shown in this dissertation (Section 8.2.2). However, before the technology is implemented, a variety of aspects needs to be investigated further. For instance, the space-segment systems will need to be developed in more detail. Also, ground station operations and systems, specifically the clock quality and bistatic pointing capabilities, will require additional attention for the implementation of ILR (Sections 3.1.6 and 3.2.1; Chapter 6). As such, this dissertation only forms one of the first steps in the path to its implementation in planetary science missions.

The High Gain Antenna and associated systems on planetary missions fulfil two core functions: tracking and communications. In principle, both functions can also be performed by a laser system. Even so, the limitations of a laser ranging system in observing short-periodic effects in the tracking data may prevent an optical system from replacing radiometric systems in future missions. Moreover, there is decades worth of experience with the design, operations and analysis of radiometric systems, making them the logical default choice in mission design. As such, it seems unlikely that the first missions employing ILR will rely entirely on it for their tracking data. Instead, the first operational use of two-way ILR will likely be in combined use with a radiometric system, where the laser system is possibly multi-purposed as a communications or altimetry system, as was the case for LRO (Section 3.3.1). However, as has been shown extensively in both theoretical work and recently in practice by the LADEE mission, a laser communications system can offer extremely high data rates at low mass and power requirements (Section 3.3.3). Therefore, for missions in which the quantification of short-periodic orbital effects is not crucial, using a laser system instead of a radio system may already be a competitive system design choice. Based on these considerations, an optical system could especially facilitate the tracking and communications of planetary microsattellites or cubesatellites, which have much more stringent mass and power requirements. However, a crucial design issue of any space segment performing ILR (especially spacecraft) is the pointing accuracy and stability that is required, which is in the order of  $50 \mu\text{rad}$  ( $\approx 10$  arcseconds) (Section 3.1.3), orders of magnitude more stringent than for radiometric tracking. Development of a pointing system for the laser transmission and detection assembly (potentially bistatic) will be an important part of the required technology development and operational implementation that falls outside the scope of typical SLR operations. However, developments in the field of optical communications (which has more stringent pointing requirements than ILR) are of significant value in this respect.

We have clearly shown throughout this dissertation (Chapters 4-7; Section 8.1.4) that the true error distribution behaves rather differently from the formal error distribution that is obtained from the least squares estimation. Crucially, the formal error can

often be order(s) of magnitude more optimistic than the true estimation error. The use of (scaled) formal errors, as obtained from a weighted least squares estimation, remains common practice in (planetary) tracking data analysis. However, the inclusion of detailed error descriptions directly in the estimation will both streamline the analysis process and allow for the robust processing and interpretation of future ILR data. This could be achieved by including *a priori* knowledge on the magnitude and statistical behaviour of non-Gaussian and time-correlated error sources in both the measurements and analysis models, by applying more elaborate estimation schemes than the typical least squares approach, such as an extended Kalman filter, (*e.g.*, Tapley et al., 2004), in which measurement and model uncertainty distributions can be directly incorporated. Setting up a generic simulation and analysis framework that incorporates such techniques will facilitate the rapid analysis of tracking architectures of future planetary missions, thereby allowing the value of ILR to be analyzed and traded off against other tracking techniques in an early phase of the mission concept development.

Furthermore, such analysis of the performance of an ILR system, including the crucial quantification of differences between true and formal errors, will benefit greatly from a bottom-up measurement error model, efforts towards which have been performed for this dissertation. Using such a bottom-up model, a time series of measurement errors can be generated from hardware and environmental characteristics. These measurement errors can then be used in a simulation/estimation framework, allowing for a realistic mapping from hardware, mission and environment properties to science return. Such models should include the simulation of noise levels and the subsequent data filtering, which will allow for a better quantification of limiting geometric configurations of a mission (such as the Sun avoidance angle) based on models for, for instance, the stray light in a laser detection system, atmospheric scattering, *etc.*

ILR operations will most likely rely largely or entirely on the existing ground infrastructure of the ILRS. Although it is possible that only a selected set of ground stations will contribute to interplanetary ranging campaigns (as was the case for LRO), it is unrealistic to expect that all stations will operate in such a manner that single-photon signal intensity detection is always ensured. In all likelihood, ILRS stations will continue to consider SLR/LLR as their primary goal, and invest their resources to upgrade and optimize their systems accordingly. Nonetheless, current developments in the ground station hardware to achieve mm-accuracy SLR measurements will mostly benefit the improvement of ILR data quality equally well. However, ILR will also require H-maser quality clocks to minimize their error budgets (Section 3.2.1; Chapter 6). Additionally, the required point-ahead of the transmitter (due to the large light times in ILR) will complicate the operations at the ground station, since bistatic pointing will most likely be required, in which the detection and transmission telescope can be independently directed. For both the development of ground station operations and space-grade hardware developments, previous experience with LADEE (Section 3.3.3), current developments on the European Laser Time transfer (ELT) project (Sections 3.2.1 and 3.3.4), and other future developments in laser time transfer, communications and altimetry systems will improve the Technological Readiness Level (TRL) of ILR.

In addition to the need to improve the accuracy and operational readiness of the technology, models for the analysis of ILR data will need to be improved to fully exploit

the information content encoded in the data, as shown at multiple points in this dissertation (Chapters 4, 6 and 7; Section 3.2.2 and 8.1.3). Such improvements include those which are relevant for existing space geodetic techniques, for instance the improvement of the accuracy of the terrestrial reference frame, models for loading effects on station position and models for Earth rotation, each of which currently prevents sub-mm accurate modelling of ground station positions. With the implementation of ILR, such mm-level effects that have plagued the analysis of terrestrial satellite geodesy data will also strongly enter the error budgets of planetary missions. Similarly, sub-mm accurate tropospheric range corrections will be required for the laser data, which could be facilitated by the routine use of ray-tracing models. However, mm-level modelling of ILR data will require substantial developments beyond the terrestrial realm. For instance, dynamical models for the solar system will need to be brought to a new level for ILR data analysis, requiring not only the development of new models, but also the implementation of various physical effects into existing codes, which were mostly developed in an era when mm-level interplanetary range measurements were not deemed to be realistic. One of the key issues is the asteroid and Kuiper belt's perturbations on planetary motions, which will be especially crucial for the accurate ephemerides of the terrestrial planets (Section 2.2.4). Mitigating this perturbation may require the estimation of a very large number of individual asteroid masses and orbits, in addition to the typical estimation of a ring-shaped mass distribution. Furthermore, relativistic modelling issues, such as deviations of a body's geodesic from the worldline of its center of mass and second-order post-Newtonian dynamics and frame transformation effects (Section 2.3.2) will need to be developed and implemented in existing ephemeris generation codes for laser ranging data analysis. At the mm-level, non-gravitational forces, most notably radiation pressure, will begin to be relevant for an increasing number of bodies, such as the Martian moons. Also, the influence of higher order gravitational interactions (between  $J_2$  terms for instance) on the translational dynamics of bodies in close orbits, such as Phobos and Mars, may become relevant in ILR data analysis. Finally, as we showed in Section 7.1 of Chapter 4 the decoupled analysis for translational and rotational motion will no longer be sufficient for such close bodies, requiring the concurrent modelling and estimation of both types of dynamics (in addition to the time dynamics that we discuss in Chapter 7). In such an approach, the estimation of rotational dynamics could be done on an equal footing with that of translational dynamics. The estimated parameters would be the initial rotational state and relevant physical characteristics (inertia tensor, tidal properties), as opposed to the estimation of a wide spectrum of libration amplitudes (Section 2.2.2), which was shown to be an issue for ILR tracking data of a Phobos lander. Such a development of coupled translational-rotational dynamics estimation would be in line with the unification of the estimation of initial translational state and proper time that we have developed here in Chapter 7.

In this dissertation, we have mostly focussed on Phobos as a scientific target of interest, as it forms both a very suitable target for ILR from a mission design perspective and an interesting target from a planetary science as well as a fundamental physics point of view. However, the science case for other mission architectures will require specific attention, as the results for a Phobos lander cannot be directly quantitatively carried over to other missions. Such analyses will be best performed in the context

---

of a complete mission design, be it for a mission call, such as ESA's M- or L-class missions, or a mission design study such as that performed by JPL's Team X, which resulted in the study of Turyshev et al. (2010), or ESA's Concurrent Design Facility (CDF). By performing the analysis within a larger framework, the synergy with other instruments, and interdependencies of their system and science requirements will be more easily identified, which we have shown is crucial in the design of an ILR mission.





---

## Bibliography

---

- Abbot, R. I., Shelus, P. J., Mulholland, J. D., and Silverberg, E. C. (1973). Laser observations of the Moon: Identification and construction of normal points for 1969-1971. *The Astronomical Journal*, 78:784.
- Abramowitz, M. and Stegun, I. (1964). *Handbook of Mathematical Functions with Formulas, Graphs, and Mathematical Tables*. Dover Publications.
- Abshire, J. and Gardner, C. (1985). Atmospheric Refractivity Corrections in Satellite Laser Ranging. *IEEE Transactions on Geoscience and Remote Sensing*, GE-23:414–425.
- Abshire, J., Sun, X., Neumann, G., McGarry, J., Zagwodzki, T., Jester, P., Riris, H., Zuber, M., and Smith, D. (2006). Laser pulses from earth detected at Mars. In *Conference on Lasers and Electro-Optics*.
- Al-Habash, M. A., Andrews, L. C., and Phillips, R. L. (2001). Mathematical model for the irradiance probability density function of a laser beam propagating through turbulent media. *Optical Engineering*, 40:1554–1562.
- Aldrovandi, R. and Pereira, J. (2013). Why to study teleparallel gravity. In *Teleparallel Gravity*, Vol. 173 of *Fundamental Theories of Physics*, pp. 179–186. Springer.
- Alexander, J., Lee, S., and Chen, C.-C. (1999). Pointing and tracking concepts for deep-space missions. In *Free-Space Laser Communication Technologies XI*, Vol. 3615 of *SPIE Conference Series*, pp. 230–249.
- Alley, C. O., Bender, P. L., Dicke, R. H., Faller, J. E., Franken, P. A., Plotkin, H. H., and Wilkinson, D. T. (1965). Optical Radar Using a Corner Reflector on the Moon. *Journal of Geophysical Research*, 70:2267–2269.
- Alley, C. O., Chang, R. F., Currie, D. G., Mulholland, J., Poultney, S. K., Rayner, J. D., Silverberg, E. C., Steggerda, C. A., Plotkin, H. H., Williams, W., Warner, B., Richardson, H. and Bopp, B. (1970). Apollo 11 Laser Ranging Retro-Reflector: Initial Measurements from the McDonald Observatory. *Science*, 167(3917):368–370.
- Allan, D. (1966). Statistics of atomic frequency standards. *Proceedings of the IEEE*, 54(2):221–230.
- Altamimi, Z., Collilieux, X., and Métivier, L. (2011). ITRF2008: an improved solution of the international terrestrial reference frame. *Journal of Geodesy*, 85:457–473.
- Anderson, J. D., Lau, E. L., Sjogren, W. L., Schubert, G., and Moore, W. B. (1996). Gravitational constraints on the internal structure of Ganymede. *Nature*, 384:541–543.
- Anderson, J. D., Campbell, J. K., Ekelund, J. E., Ellis, J., and Jordan, J. F. (2008). Anomalous Orbital-Energy Changes Observed during Spacecraft Flybys of Earth. *Physical Review Letters*, 100:091102.
- Anderson, J. D. and Schubert, G. (2010). Rhea’s gravitational field and interior structure inferred

- from archival data files of the 2005 Cassini flyby. *Physics of the Earth and Planetary Interiors*, 178:176-192.
- Andert, T. P., Rosenblatt, P., Pätzold, M., Häusler, B., Dehant, V., Tyler, G. L., and Marty, J. C. (2010). Precise mass determination and the nature of Phobos. *Geophysical Research Letters*, 37:9202.
- Andrews, L. C., Phillips, R. L., Hopen, C. Y., and Al-Habash, M. A. (1999). Theory of optical scintillation. *Journal of the Optical Society of America A*, 16:1417-1429.
- Andrews, L. C., Phillips, R. L., and Hopen, C. Y. (2000). Scintillation model for a satellite communication link at large zenith angles. *Optical Engineering*, 39:3272-3280.
- Andrews, L. and Phillips, R. (2005). *Laser Beam Propagation through Random Media*. SPIE - The International Society for Optical Engineering, 2<sup>nd</sup> edition.
- Andrews, L. C., Phillips, R. L., Sasiela, R. J., and Parenti, R. R. (2006). Strehl ratio and scintillation theory for uplink Gaussian-beam waves: beam wander effects. *Optical Engineering*, 45(7):076001.
- Andrews, L. C., Phillips, R. L., Sasiela, R. J., and Parenti, R. (2007). PDF models for uplink to space in the presence of beam wander. In *Atmospheric Propagation IV*, Vol. 6551 of *SPIE Conference Series*, No. 655109.
- Angéilil, R., Saha, P., Bondaescu, R., Jetzer, P., Schäfer, A., and Lundgren, A. (2014). Spacecraft clocks and relativity: Prospects for future satellite missions. *Physical Review D*, 89(6):064067.
- Angermann, D. and Müller, H. (2009). On the strength of SLR observations to realize the scale and origin of the terrestrial reference system. In: Sideris, M., (editor), *Observing our Changing Earth*, Vol. 133 of *International Association of Geodesy Symposia*, pp. 21-29. Springer.
- Aoyama, S., Tazai, R. and Ichiki, K. (2014). Upper limit on the amplitude of gravitational waves around 0.1 Hz from the Global Positioning System. *Physical Review D*, 89(6):067101.
- Appourchaux, T., Burston, R., Chen, Y., Cruise, M., Dittus, H., Foulon, B., Gill, P., Gizon, L., Klein, H., Klioner, S., Kopeikin, S., Krüger, H., Lämmerzahl, C., Lobo, A., Luo, X., Margolis, H., Ni, W.-T., Patón, A. P., Peng, Q., Peters, A., Rasel, E., Rüdiger, A., Samain, É., Selig, H., Shaul, D., Sumner, T., Theil, S., Touboul, P., Turyshev, S., Wang, H., Wang, L., Wen, L., Wicht, A., Wu, J., Zhang, X. and Zhao, C. (2009). Astrodynamical Space Test of Relativity Using Optical Devices I (ASTROD I) - A class-M fundamental physics mission proposal for Cosmic Vision 2015-2025. *Experimental Astronomy*, 23:491-527.
- Armstrong, J. W., Iess, L., Tortora, P. and Bertotti, B. (2003). Stochastic Gravitational Wave Background: Upper Limits in the  $10^{-6}$  to  $10^{-3}$  Hz Band. *The Astrophysical Journal*, 599:806-813.
- Arnold, D.A. (1979). Method of Calculating Retroreflector-Array Transfer Functions. *SAO Special Report*, 382.
- Artyukh, Yu., Bespal'ko V., Boole E and Vedin V. (2010). Event Timer A033-ET: Current State and Typical Performance Characteristics. In *17<sup>th</sup> International Workshop on Laser Ranging*.
- Ashby, N. and Bender, P. L. (2008). Measurement of the Shapiro Time Delay Between Drag-Free Spacecraft. In: Dittus, H., Lämmerzahl, C., and Turyshev, S., (editors), *Lasers, Clocks and Drag-Free Control: Exploration of Relativistic Gravity in Space*, Vol. 349 of *Astrophysics and Space Science Library*, pp. 219-230. Springer.
- Asmar, S. W., Armstrong, J. W., Iess, L., and Tortora, P. (2005). Spacecraft Doppler tracking: Noise budget and accuracy achievable in precision radio science observations. *Radio Science*, 40:2001.
- Bailey, Q. G. and Kostelecký, V. A. (2006). Signals for Lorentz violation in post-Newtonian gravity. *Physical Review D*, 74(4):045001.
- Baker, G. J. and Benson, R. S. (2004). Gaussian beam scintillation on ground-to-space paths: the importance of beam wander. In *Free-Space Laser Communications IV*, Vol. 5550 of *SPIE Conference Series*, pp. 225-235.
- Baland, R.-M., Tobie, G., Lefèvre, A., and van Hoolst, T. (2014). Titan's internal structure inferred from its gravity field, shape, and rotation state. *Icarus*, 237:29-41.
- Balmino, G. (1994). Gravitational potential harmonics from the shape of an homogeneous body. *Celestial Mechanics and Dynamical Astronomy*, 60:331-364.

- Barnes, J. A., Chi, A. R., Cutler, L. S., Healey, D. J., Leeson, D. B., McGunigal, T. E., Mullen, J. A., Smith, W. L., Sydnor, R. L., Vessot, R. F., and Winkler, G. M. (1971). Characterization of frequency stability. *IEEE transactions on Instrumentation and Measurement*, 1001(2):105–120.
- Bartlett, D. F. and van Buren, D. (1986). Equivalence of active and passive gravitational mass using the moon. *Physical Review Letters*, 57:21–24.
- Battat, J. B. R., Chandler, J. F., and Stubbs, C. W. (2007). Testing for Lorentz Violation: Constraints on Standard-Model-Extension Parameters via Lunar Laser Ranging. *Physical Review Letters*, 99(24):241103.
- Bauer, S., Dirx, D., Oberst, J., Hussmann, H., Gläser, P., Schreiber, U. Mao, D., Neumann, G., Mazarico, E., Torrence, M., McGarry, J., Smith, D., and Zuber, M. (2013). Analysis and application of one-way laser ranging data from ILRS ground stations to LRO. In *18<sup>th</sup> International Workshop on Laser Ranging*.
- Bauer, S., Dirx, D., Hussmann, H., Oberst, J., Mao, D., Neumann, G., Mazarico, E., Torrence, M., McGarry, J., Smith, D., and Zuber, M. (2014). Application of one-way laser ranging data to LRO into orbit determination. In *19<sup>th</sup> International Workshop on Laser Ranging*, No. 3124.
- Beland, R. R. (1993). Propagation through atmospheric optical turbulence. *Atmospheric Propagation of Radiation*, 2:157–232.
- Bender, P. L. (1994). Proposed microwave transponders for early lunar robotic landers. *Advances in Space Research*, 14(6):233–242.
- Benkhoff, J., van Casteren, J., Hayakawa, H., Fujimoto, M., Laakso, H., Novara, M., Ferri, P., Middleton, H. R., and Ziethe, R. (2010). Bepi-Colombo - Comprehensive exploration of Mercury: Mission overview and science goals. *Planetary and Space Science*, 58:2–20.
- Berger, M., Moreno, J., Johannessen, J.A., Levelt, P.F. and Hanssen, R.F. (2012). ESA’s sentinel missions in support of Earth system science. *Remote Sensing of Environment*, 120:84–90.
- Bertone, S., Le Poncin-Lafitte, C., Lainey, V., and Angonin, M.-C. (2013). Transponder delay effect in light time calculations for deep space navigation. *ArXiv e-print 1305.1950*.
- Bertone, S., Minazzoli, O., Crosta, M., Le Poncin-Lafitte, C., Vecchiato, A., and Angonin, M.-C. (2014). Time transfer functions as a way to validate light propagation solutions for space astrometry. *Classical and Quantum Gravity*, 31(1):015021.
- Bertotti, B., Comoretto, G., and Iess, L. (1993). Doppler tracking of spacecraft with multi-frequency links. *Astronomy and Astrophysics*, 269:608–616.
- Bertotti, B., Iess, L., and Tortora, P. (2003). A test of general relativity using radio links with the Cassini spacecraft. *Nature*, 425:374–376.
- Bertotti, B., Farinella, P. and Vokrouhlick, D. (2003b) Physics of the Solar System - Dynamics and Evolution, Space Physics, and Spacetime Structure. Vol. 293 of *Astrophysics and Space Science Library*. Springer.
- Beuthe, M. (2015). Tides on Europa: the membrane paradigm. *Icarus*, 248:109–134.
- Bierman, G.J. (1977). *Factorization Methods for Discrete Sequential Estimation*. New York Academic Press.
- Bills, B. G., Neumann, G. A., Smith, D. E., and Zuber, M. T. (2005). Improved estimate of tidal dissipation within Mars from MOLA observations of the shadow of Phobos. *Journal of Geophysical Research (Planets)*, 110:7004.
- Bills, B. G. and Nimmo, F. (2008). Forced obliquity and moments of inertia of Titan. *Icarus*, 196:293–297.
- Birnbaum, K. M., Chen, Y., and Hemmati, H. (2010). Precision optical ranging by paired one-way time of flight. In *Free-Space Laser Communication Technologies XXII*, Vol. 7587 of *SPIE Conference Series*, No. 75870A.
- Bjerhammar, A. (1985). On a relativistic geodesy. *Bulletin Geodesique*, 59:207–220.
- Blanchet, L., Salomon, C., Teyssandier, P., and Wolf, P. (2001). Relativistic theory for time and frequency transfer to order  $c^{-3}$ . *Astronomy and Astrophysics*, 370:320–329.
- Blanchet, L. and Novak, J. (2011). External field effect of modified Newtonian dynamics in the Solar system. *Monthly Notices of the Royal Astronomical Society*, 412:2530–2542.
- Bland-Hawthorn, J., Harwit, A., and Harwit, M. (2002). Laser Telemetry from Space. *Science*, 297:523.

- Blazej, J., Prochazka, I., Kodet, J., and Panek, P. (2011). New technologies for submillimeter laser ranging. *Advanced Materials Research*, 301:397–401.
- Blazej, J., Prochazka, I., Kodet, J., and Linhart, P. (2014). Indoor demonstration of free-space picosecond two-way time transfer on single photon level. In *Laser Communication and Propagation through the Atmosphere and Oceans III*, Vol. 9224 of *SPIE Conference Series*, No. 92241E.
- Bloom, B. J., Nicholson, T. L., Williams, J. R., Campbell, S. L., Bishof, M., Zhang, X., Zhang, W., Bromley, S. L., and Ye, J. (2014). An optical lattice clock with accuracy and stability at the  $10^{-18}$  level. *Nature*, 506:71–75.
- Bois, E., Wytryszczak, I., and Journet, A. (1992). Planetary and figure-figure effects on the Moon's rotational motion. *Celestial Mechanics and Dynamical Astronomy*, 53:185–201.
- Bonanno, C. and Milani, A. (2002). Symmetries and Rank Deficiency in the Orbit Determination Around Another Planet. *Celestial Mechanics and Dynamical Astronomy*, 83:17–33.
- Border, J. S., Folkner, W. M., Kahn, R. D., and Zukor, K. S. (1992). Precise Tracking of the Magellan and Pioneer Venus Orbiters by Same-Beam Interferometry Part I: Data Accuracy Analysis. *Telecommunications and Data Acquisition Progress Report*, 110:1–20.
- Borderies, N. and Yoder, C. F. (1990). Phobos' gravity field and its influence on its orbit and physical librations. *Astronomy and Astrophysics*, 233:235–251.
- Borson, D., Chen, C.-C., and Edwards, B. (2005). Overview of the Mars laser communications demonstration project. In *Digest of the LEOS Summer Topical Meetings*, pp. 5–7. IEEE.
- Borson, D. and Robinson, B. (2013). Status of the lunar laser communication demonstration. In *Free-Space Laser Communication and Atmospheric Propagation XXV*, Vol. 8610 of *SPIE Conference Series*, No. 861002.
- Borson, D. M., Robinson, B. S., Murphy, D. V., Burianek, D. A., Khatri, F., Kovalik, J. M., Sodnik, Z., and Cornwell, D. M. (2014). Overview and results of the Lunar Laser Communication Demonstration. In *Free-Space Laser Communication and Atmospheric Propagation XXVI*, Vol. 8971 of *SPIE Conference Series*, No. 89710S.
- Boyer, C. and Merzbach, U. (2011). *A History of Mathematics*. Wiley, 3<sup>rd</sup> edition.
- Brumberg, V. A. (1972). *Relativistic Celestial Mechanics (in Russian)*. Nauka.
- Brumberg, V. A. and Kopejkin, S. M. (1990). Relativistic time scales in the solar system. *Celestial Mechanics and Dynamical Astronomy*, 48:23–44.
- Brumberg, V. A. (1991). *Essential relativistic celestial mechanics*. CRC Press.
- Buften, J. L. (1977). Scintillation statistics measured in an earth-space-earth retroreflector link. *Applied Optics*, 16:2654–2660.
- Buften, J. L., Iyer, R. S., and Taylor, L. S. (1977). Scintillation statistics caused by atmospheric turbulence and speckle in satellite laser ranging. *Applied Optics*, 16:2408–2413.
- Cacciapuoti, L., Dimarcq, N., Santarelli, G., Laurent, P., Lemonde, P., Clairon, A., Berthoud, P., Jornod, A., Reina, F., Feltham, S., and Salomon, C. (2007). Atomic Clock Ensemble in Space: Scientific Objectives and Mission Status. *Nuclear Physics B Proceedings Supplements*, 166:303–306.
- Cacciapuoti, L. and Salomon, C. (2011). Atomic clock ensemble in space. *Journal of Physics: Conference Series*, 327(1):012049.
- Campbell, J. K. and Synnott, S. P. (1985). Gravity field of the Jovian system from Pioneer and Voyager tracking data. *Astronomical Journal*, 90:364–372.
- Cao, H.-M., Frey, S., Gurvits, L. I., Yang, J., Hong, X.-Y., Paragi, Z., Deller, A. T. and Ivezić, Ž. (2014). VLBI observations of the radio quasar J2228+0110 at  $z = 5.95$  and other field sources in multiple-phase-centre mode. *Astronomy and Astrophysics*, 563:A111,
- Capozziello, S. and de Laurentis, M. (2011). Extended Theories of Gravity. *Physics Reports*, 509:167–321.
- Cash, P., Emmons, D., and Welgemoed, J. (2008). Ultrastable oscillators for space applications. In *40<sup>th</sup> Annual Precise Time and Time Interval (PTTI) Meeting*, pp. 51–56.
- Chandler, J., Pearlman, M., Reasenberg, R., and Degnan, J. (2005). Solar-system dynamics and tests of general relativity with planetary laser ranging. In *14<sup>th</sup> International Workshop on Laser Ranging*.

- Chapront-Touze, M. (1990). Orbits of the Martian satellites from ESAPHO and ESADE theories. *Astronomy and Astrophysics*, 240:159–172.
- Chen, J. L. and Wilson, C. R. (2008). Low degree gravity changes from GRACE, Earth rotation, geophysical models, and satellite laser ranging. *Journal of Geophysical Research (Solid Earth)*, 113:B06402.
- Chen, Y., Birnbaum, K. M., and Hemmati, H. (2011). Field demonstrations of active laser ranging with sub-mm precision. In *Free-Space Laser Communication Technologies XXIII*, Vol. 7923 of *SPIE Conference Series*, No. 79230S.
- Chen, Y., Birnbaum, K. M., and Hemmati, H. (2013). Active laser ranging over planetary distances with millimeter accuracy. *Applied Physics Letters*, 102(24):241107.
- Cheng, M. K., Eanes, R. J., Shum, C. K., Schutz, B. E. and Tapley, B. D. (1989). Temporal variations in low degree zonal harmonics from Starlette orbit analysis. *Geophysical Research Letters*, 16:393–396.
- Christophe, B., Andersen, P. H., Anderson, J. D., Asmar, S., B erio, P., Bertolami, O., Bingham, R., Bondu, F., Bouyer, P., Bremer, S., Courty, J.-M., Dittus, H., Foulon, B., Gil, P., Johann, U., Jordan, J. F., Kent, B., L ammerzahl, C., L evy, A., M etris, G., Olsen, O., P aramos, J., Prestage, J. D., Progrebenko, S. V., Rasel, E., Rathke, A., Reynaud, S., Rievers, B., Samain, E., Sumner, T. J., Theil, S., Touboul, P., Turyshev, S., Vrancken, P., Wolf, P., and Yu, N. (2009). Odyssey: a solar system mission. *Experimental Astronomy*, 23:529–547.
- Churnside, J. H. (1993). Effects of turbulence on the geodynamic laser ranging system. In *8th International Workshop on Laser Ranging Instrumentation*.
- Chuvieco, E. (editor), (2008). *Earth Observation of Global Change - The Role of Satellite Remote Sensing in Monitoring the Global Environment*. Springer.
- Ciufolini, I. and Pavlis, E. (2004). A confirmation of the general relativistic prediction of the Lense-Thirring effect. *Nature*, 431:958–960.
- Ciufolini, I., Paolozzi, A., Pavlis, E. C., Ries, J. C., Koenig, R., Matzner, R. A., Sindoni, G. and Neumayer, H. (2009). Towards a One Percent Measurement of Frame Dragging by Spin with Satellite Laser Ranging to LAGEOS, LAGEOS 2 and LARES and GRACE Gravity Models. *Space Science Reviews*, 148:71–104.
- Ciufolini, I., Paolozzi, A., Pavlis, E., Ries, J., Gurzadyan, V., Koenig, R., Matzner, R., Penrose, R., and Sindoni, G. (2012). Testing General Relativity and gravitational physics using the LARES satellite. *European Physical Journal Plus*, 127:133.
- Clark, S. J. and Tucker, R. W. (2000). Gauge symmetry and gravito-electromagnetism. *Classical and Quantum Gravity*, 17:4125–4157.
- Coulot, D., Berio, P., Biancale, R., Loyer, S., Soudarin, L., and Gontier, A.-M. (2007). Toward a direct combination of space-geodetic techniques at the measurement level: Methodology and main issues. *Journal of Geophysical Research (Solid Earth)*, 112(B11):B2214.
- Curkendall, D. W. and Border, J. S. (2013). Delta-DOR: The One-Nanoradian Navigation Measurement System of the Deep Space Network — History, Architecture, and Componentry. *Interplanetary Network Progress Report*, 42(193):D1.
- Damour, T., Soffel, M., and Xu, C. (1991). General-relativistic celestial mechanics. I. Method and definition of reference systems. *Physical Review D*, 43(10):3273–3307.
- Damour, T., Soffel, M., and Xu, C. (1993). General-relativistic celestial mechanics. III. Rotational equations of motion. *Physical Review D*, 47:3124–3135.
- Damour, T., Soffel, M., and Xu, C. (1994). General-relativistic celestial mechanics. IV. Theory of satellite motion. *Physical Review D*, 49:618–635.
- Damour, T. and Donoghue, J. F. (2011). Spatial variation of fundamental couplings and Lunar Laser Ranging. *Classical and Quantum Gravity*, 28(16):162001.
- Danzmann, K., and LISA Study Team (2003). LISA - An ESA Cornerstone Mission for the Detection and Observation of Gravitational Waves. *Advances in Space Research*, 32(7):1233–1242.
- Defraigne, P., Rivoldini, A., van Hoolst, T., and Dehant, V. (2003). Mars nutation resonance due to Free Inner Core Nutation. *Journal of Geophysical Research (Planets)*, 108:5128.
- Degnan, J. (1985). Satellite laser ranging: current status and future prospects. *IEEE Transactions on Geoscience and Remote Sensing*, 23:398–413.

- Degnan, J. (1993). Millimeter Accuracy Satellite Laser Ranging: A Review. In: Smith, D. and Turcotte, D., (editors), *Contributions of Space Geodesy to Geodynamics*, Vol. 25 of *Geodynamics Series*, pp. 133–162. American Geophysical Union.
- Degnan, J. (1994). SLR2000: An autonomous and eyesafe satellite laser ranging station. In *9<sup>th</sup> International Conference on Laser Ranging*.
- Degnan, J. (1996). Compact Laser Ranging Transponders for Interplanetary Laser and Time Transfer. In *10<sup>th</sup> International Workshop on Laser Ranging*, pp. 24–31.
- Degnan, J., McGarry, J., Dabnet, P., Zagwodzki, T., Tierney, M., and Weatherly, M. (1998). Design and Test of a Breadboard Interplanetary Laser Transponder. In *11<sup>th</sup> International Workshop on Laser Ranging*.
- Degnan, J. (2001). Unified Approach to Photon-Counting Microlaser Rangers, Transponders, and Altimeters. *Surveys in Geophysics*, 22:431–447.
- Degnan, J. (2002). Asynchronous laser transponders for precise interplanetary ranging and time transfer. *Journal of Geodynamics*, 34:551–594.
- Degnan, J., Seas, A., Donovan, H., and Zagwodzki, T. (2004). SLR2000C: An Autonomous Satellite Laser Ranging and Space-to-Ground Optical Communications Facility. In *14<sup>th</sup> International Workshop on Laser Ranging*.
- Degnan, J. (2006). Simulating Interplanetary Transponder and Laser Communications Experiments Via Dual Station Ranging To SLR Satellites. In *15<sup>th</sup> International Workshop on Laser Ranging*.
- Degnan, J. (2008). Laser Transponders for High-Accuracy Interplanetary Laser Ranging and Time Transfer. In: Dittus, H., Lammerzahn, C., and Turyshev, S. G., (editors), *Lasers, Clocks and Drag-Free Control: Exploration of Relativistic Gravity in Space*, Vol. 349 of *Astrophysics and Space Science Library*, pp. 231–242. Springer.
- Degnan, J. (2012). A Tutorial on Retroreflectors and Arrays for SLR. In *International Technical Laser Workshop 2012*.
- Dehant, V., Lognonné, P., and Sotin, C. (2004). Network science, NetLander: a European mission to study the planet Mars. *Planetary and Space Science*, 52:977–985.
- Dehant, V., Folkner, W., Renotte, E., Orban, D., Asmar, S., Balmino, G., Barriot, J.-P., Benoist, J., Biancale, R., Biele, J., Budnik, F., Burger, S., de Viron, O., Häusler, B., Karatekin, Ö., Le Maistre, S., Lognonné, P., Menvielle, M., Mitrovic, M., Pätzold, M., Rivoldini, A., Rosenblatt, P., Schubert, G., Spohn, T., Tortora, P., van Hoolst, T., Witasse, O., and Yseboodt, M. (2009). Lander radioscience for obtaining the rotation and orientation of Mars. *Planetary and Space Science*, 57:1050–1067.
- Dehant, V., Le Maistre, S., Rivoldini, A., Yseboodt, M., Rosenblatt, P., van Hoolst, T., Mitrovic, M., Karatekin, Ö., Marty, J. C., and Chicarro, A. (2011). Revealing Mars' deep interior: Future geodesy missions using radio links between landers, orbiters, and the Earth. *Planetary and Space Science*, 59:1069–1081.
- Dehant, V., Banerdt, B., Lognonné, P., Grott, M., Asmar, S., Biele, J., Breuer, D., Forget, F., Jaumann, R., Johnson, C., Knapmeyer, M., Langlais, B., Le Feuvre, M., Mimoun, D., Mocquet, A., Read, P., Rivoldini, A., Romberg, O., Schubert, G., Smrekar, S., Spohn, T., Tortora, P., Ulamec, S., and Vennerstrøm, S. (2012). Future Mars geophysical observatories for understanding its internal structure, rotation, and evolution. *Planetary and Space Science*, 68:123–145.
- Dehant V. and Mathews, P.M. (2015). *Precession, Nutation and Wobble of the Earth*. Cambridge University Press.
- Dell'Agnello, S. (2014). NASA-SSERVI and INFN Partnership "Springlets": Solar system Payloads of laser Retroreflectors of INFN for General reLativity, Exploration and planeTary Science. In *19<sup>th</sup> International Workshop on Laser Ranging*, No. 3100.
- Delva, P., Kostić, U., and Čadež, A. (2011). Numerical modeling of a Global Navigation Satellite System in a general relativistic framework. *Advances in Space Research*, 47(2):370–379.
- Delva, P., Meynadier, F., Le Poncin-Lafitte, C., Laurent, P., and Wolf, P. (2012). Time and frequency transfer with a microwave link in the ACES/Pharao mission. In *European Frequency and Time Forum (EFTF)*, pp. 28–35.
- Delva, P., Hees, A., Bertone, S., Richard, E. and Wolf, P., (2015). Test of the gravitational redshift with stable clocks in eccentric orbits: application to Galileo satellites 5 and 6. *ArXiv e-print 1409.4932*.

- Deng, X.-M. and Xie, Y. (2013a). The effect of  $f(T)$  gravity on an interplanetary clock and its time transfer link. *Research in Astronomy and Astrophysics*, 13:1225–1230.
- Deng, X.-M. and Xie, Y. (2013b). Yukawa effects on the clock onboard a drag-free satellite. *Monthly Notices of the Royal Astronomical Society*, 431:3236–3239.
- Deng, X.-M. and Xie, Y. (2015). New upper limits on the power of general relativity from Solar system dynamics. *New Astronomy*, 35:36–39.
- Dickey, J., Bender, P., Faller, J., Newhall, X., Ricklefs, R., Ries, J., Shelus, P., Veillet, C., Whipple, A., Wiant, J., Williams, J., and Yoder, C. (1994). Lunar Laser Ranging: A Continuing Legacy of the Apollo Program. *Science*, 265:482–490.
- Dirkx, D. and Vermeersen, L. (2012). WP3: Interplanetary Laser Ranging - Software requirements and packages. *FP7 ESPaCE Project Deliverable 3.2 (available upon request)*.
- Dirkx, D. and Vermeersen, L. (2013). Simulation of Interplanetary Laser Links. In *European Planetary Science Congress Abstracts*, Vol. 8, No. 481
- Dirkx, D. and Vermeersen, L. (2014). WP3: Interplanetary Laser Ranging - Selected Software package/Selected Software Modifications. *FP7 ESPaCE Project Deliverable 3.3 (available upon request)*.
- Dirkx, D., Vermeersen, L., Noomen, R., and Visser, P. (2014a). Phobos Laser Ranging: Numerical Geodesy Experiments for Martian System Science. *Planetary and Space Science*, 99:84–102.
- Dirkx, D., Noomen, R., Prochazka, I., Bauer, S., and Vermeersen, L. (2014b). Influence of atmospheric turbulence on planetary transceiver laser ranging. *Advances in Space Research*, 54(11):2349–2370.
- Dirkx, D., Noomen, R., Visser, P., Bauer, S., and Vermeersen, L. (2015a). Comparative Analysis of one- and two-way planetary laser ranging concepts. *Planetary and Space Science (in press)*.
- Dirkx, D., Noomen, R., Visser, P., Gurvits, L., and Vermeersen, L. (2015b). Simultaneous Space-time Dynamics Estimation from Space Mission Tracking Data. *Astronomy and Astrophysics (to be submitted)*.
- Duchayne, L., Mercier, F., and Wolf, P. (2009). Orbit determination for next generation space clocks. *Astronomy and Astrophysics*, 504:653–661.
- Duev, D. A., Molera Calvés, G., Pogrebenko, S. V., Gurvits, L. I., Cimó, G., and Bocanegra Bahamon, T. (2012). Spacecraft VLBI and Doppler tracking: algorithms and implementation. *Astronomy and Astrophysics*, 541:A43.
- Eddington, A.S. (1923). *The Mathematical Theory of Relativity*. Cambridge University Press.
- Edwards, B. and Israel, D. (2014). A geosynchronous orbit optical communications relay architecture. In *IEEE Aerospace Conference*.
- Efroimsky, M. and Lainey, V. (2007). Physics of bodily tides in terrestrial planets and the appropriate scales of dynamical evolution. *Journal of Geophysical Research (Planets)*, 112:12003.
- Efroimsky, M. and Williams, J. G. (2009). Tidal torques: a critical review of some techniques. *Celestial Mechanics and Dynamical Astronomy*, 104:257–289.
- Einstein, A. (1905). Zur Elektrodynamik bewegter Körper. *Annalen der Physik*, 322(10):891–921
- Einstein, A. (1915a). Erklärung der Perihelbewegung des Merkur aus der allgemeinen Relativitätstheorie. *Sitzungsberichte der Königlich Preussischen Akademie der Wissenschaften (Berlin)*, pp. 831–839.
- Einstein, A. (1915b). Die Feldgleichungen der Gravitation. *Sitzungsberichte der Königlich Preussischen Akademie der Wissenschaften (Berlin)*, pp. 844–847.
- Einstein, A., Infeld, L. and Hoffmann, B. (1938). The Gravitational Equations and the Problem of Motion. *Annals of Mathematics*, 39(1):65–100.
- Ely, T., Seubert, J., and Bell, J. (2014). Advancing Navigation, Timing, and Science with the Deep Space Atomic Clock. In *SpaceOps Conference*, No. AIAA2014-1856.
- Exertier, P., Bonnefond, P., Deleflie, F., Barlier, F., Kasser, M., Biancale, R., and Menard, Y. (2006). Contribution of laser ranging to Earth's sciences. *Comptes Rendus Geoscience*, 338:958–967.

- Exertier, P., Samain, E., Bonnefond, P., and Guillemot, P. (2010). Status of the T2L2/Jason2 experiment. *Advances in Space Research*, 46(12):1559–1565.
- Exertier, P., Samain, E., Martin, N., Courde, C., Laas-Bourez, M., Foussard, C., and Guillemot, P. (2014). Time Transfer by Laser Link: Data analysis and validation to the ps level. *Advances in Space Research*, 54(11):2371–2385.
- Faller, J., Winer, I., Carrion, W., Johnson, T. S., Spadin, P., Robinson, L., Wampler, E. J. and Wieber, D. (1969). Laser Beam Directed at the Lunar Retro-Reflector Array: Observations of the First Returns. *Science*, 166(3901):99–102.
- Faller, J. (2014). Lunar Laser Ranging. In *19<sup>th</sup> International Workshop on Laser Ranging*, No. 3127.
- Fante, R. (1975). Electromagnetic beam propagation in turbulent media. *IEEE Proceedings*, 63:1669–1692.
- Farid, A. A. and Hranilovic, S. (2007). Outage Capacity Optimization for Free-Space Optical Links With Pointing Errors. *Journal of Light-wave Technology*, 25:1702–1710.
- Fienga, A., Laskar, J., Morley, T., Manche, H., Kuchynka, P., Le Poncin-Lafitte, C., Budnik, F., Gastineau, M., and Somenzi, L. (2009). INPOP08, a 4-D planetary ephemeris: from asteroid and time-scale computations to ESA Mars Express and Venus Express contributions. *Astronomy Astrophysics*, 507:1675–1686.
- Fienga, A., Laskar, J., Kuchynka, P., Manche, H., Desvignes, G., Gastineau, M., Cognard, I., and Theureau, G. (2011). The INPOP10a planetary ephemeris and its applications in fundamental physics. *Celestial Mechanics and Dynamical Astronomy*, 111:363–385.
- Fienga, A. (2012). How GAIA can improve planetary ephemerides? *Planetary and Space Science*, 73:44–46.
- Fienga, A., Laskar, J., Exertier, P., Manche, H., and Gastineau, M. (2014). Tests of General relativity with planetary orbits and Monte Carlo simulations. *ArXiv e-print 1409.4932*.
- Flury, J., Bettadpur, S., and Tapley, B. D. (2008). Precise accelerometry onboard the GRACE gravity field satellite mission. *Advances in Space Research*, 42(8):1414–1423.
- Folkner, W. and Finger, M. (1990). Preliminary Error Budget for an Optical Ranging System: Range, Range Rate and Differenced Range Observables. *Interplanetary Network Progress Report*, 42(101):121–135.
- Folkner, W. M. and Border, J. S. (1990). Orbiter-orbiter and orbiter-lander tracking using same-beam interferometry. *Telecommunications and Data Acquisition Progress Report*, 42(109):74–86.
- Folkner, W. M., Williams, J. G., and Boggs, D. H. (2009). The Planetary and Lunar Ephemeris DE 421. *Interplanetary Network Progress Report*, 42(178):C1.
- Folkner, W. M., Williams, J. G., Boggs, D. H., Park, R. S., and Kuchynka, P. (2014). The Planetary and Lunar Ephemerides DE430 and DE431. *Interplanetary Network Progress Report*, 42(196):C1.
- Fomalont, E. B., Goss, W. M., Beasley, A. J. and Chatterjee, S. (1999). Sub-Milliarcsecond Precision of Pulsar Motions: Using In-Beam Calibrators with the VLBA. *The Astronomical Journal*, 117:3025–3030.
- Franklin, S., Slonski, J., Kerridge, S., Noreena, G., Townes, S., Schwartzbaum, E., Synnott, S., Deutsch, M., Edwards, C., Devereaux, A., Austin, R., Edwards, B., Scozzafav, J., Borson, D., Roberts, W., Biswas, A., Pillsbury, A., Khatri, F., Sharma, J., and Komarek, T. (2004). The 2009 Mars Telecom Orbiter mission. In *IEEE Aerospace Conference*, pp. 437–456.
- Fridelance, P. and Veillet, C. (1995). Operation and data analysis in the LASSO experiment. *Metrologia*, 32:27–33.
- Gardner, C. (1976). Effects of Random Path Fluctuations on the Accuracy of Laser Ranging Systems. *Applied Optics*, 15:2539–2545.
- Gardner, C. S. (1982). Target signatures for laser altimeters - An analysis. *Applied Optics*, 21:448–453.
- Genova, A., Goossens, S., Lemoine, F.G., Mazarico, E., Fricke, S.K., Smith, D.E. and Zuber, M.T. (2015). Long-term variability of CO<sub>2</sub> and O in the Mars upper atmosphere from MRO radio science data. *Journal of Geophysical Research: Planets*, (in press)
- Goldberg, D. (1991). What every computer scientist should know about floating-point arithmetic. *ACM Computing Surveys (CSUR)*, 23(1):5–48.



- Goossens, S., Matsumoto, K., Liu, Q., Kikuchi, F., Sato, K., Hanada, H., Ishihara, Y., Noda, H., Kawano, N., Namiki, N., Iwata, T., Lemoine, F. G., Rowlands, D. D., Harada, Y., and Chen, M. (2011). Lunar gravity field determination using SELENE same-beam differential VLBI tracking data. *Journal of Geodesy*, 85:205–228.
- Grasset, O., Dougherty, M. K., Coustenis, A., Bunce, E. J., Erd, C., Titov, D., Blanc, M., Coates, A., Drossart, P., Fletcher, L. N., Hussmann, H., Jaumann, R., Krupp, N., Lebreton, J.-P., Prieto-Ballesteros, O., Tortora, P., Tosi, F., and van Hoolst, T. (2013). JUPITER ICY moons Explorer (JUICE): An ESA mission to orbit Ganymede and to characterise the Jupiter system. *Planetary and Space Science*, 78:1–21.
- Gregnanin, M., Bertotti, B., Chersich, M., Fermi, M., Iess, L., Simone, L., Tortora, P., and Williams, J. G. (2012). Same beam interferometry as a tool for the investigation of the lunar interior. *Planetary and Space Science*, 74:194–201.
- Grosser, M. (1962). *The discovery of Neptune*. Harvard University Press.
- Guillot, T. (2012). A comparison of the interiors of Jupiter and Saturn. *Planetary and Space Science*, 47:1183–1200.
- Gurtner, W., Noomen, R., and Pearlman, M. R. (2005). The International Laser Ranging Service: current status and future developments. *Advances in Space Research*, 36(3):327–332.
- Harmon, J. K., Ostro, S. J., Chandler, J. F., and Hudson, R. S. (1994). Radar ranging to Ganymede and Callisto. *The Astronomical Journal*, 107:1175–1181.
- Hawking, S.W. (editor), (2003). *On the Shoulders of Giants: The Great Works of Physics and Astronomy*. Running Press.
- Hartmann, T., Soffel, M. H., and Kioustelidis, T. (1994). On the use of STF-tensors in celestial mechanics. *Celestial Mechanics and Dynamical Astronomy*, 60:139–159.
- Hechler, F. and Folkner, W.M. (2003). Mission Analysis for the Laser Interferometer Space Antenna (LISA) Mission. *Advances in Space Research*, 32(7):131227–1282.
- Hees, A., Lamine, B., Reynaud, S., Jaekel, M.-T., Le Poncin-Lafitte, C., Lainey, V., Füzfa, A., Courty, J.-M., Dehant, V., Wolf, P., (2012). Radioscience simulations in general relativity and in alternative theories of gravity. *Classical and Quantum Gravity*, 29(23), 235027.
- Hees, A., Bertone, S., and Le Poncin-Lafitte, C. (2014a). Light propagation in the field of a moving axisymmetric body: Theory and applications to the Juno mission. *Physical Review D*, 90(8):084020.
- Hees, A., Bertone, S., and Le Poncin-Lafitte, C. (2014b). Relativistic formulation of coordinate light time, Doppler, and astrometric observables up to the second post-Minkowskian order. *Physical Review D*, 89(6):064045.
- Hees, A., Folkner, W. M., Jacobson, R. A., and Park, R. S. (2014c). Constraints on modified Newtonian dynamics theories from radio tracking data of the Cassini spacecraft. *Physical Review D*, 89(10):102002.
- Hees, A., Folkner, W. M., Jacobson, R. A., Park, R. S., Lamine, B., Le Poncin-Lafitte, C., and Wolf, P. (2014d). Tests of Gravitation at Solar System scales beyond the PPN formalism. *ArXiv e-prints 1403.1365*.
- Hemmati, H. (2006). *Deep Space Optical Communications*, Vol. 7 of *JPL Deep-Space Optical Communications and Navigation Series*. John Wiley & Sons.
- Hemmati, H., Birnbaum, K. M., Farr, W. H., Turyshev, S., and Biswas, A. (2009). Combined laser communications and laser ranging transponder for Moon and Mars. In *Free-Space Laser Communication Technologies XXI*, Vol. 7199 of *SPIE Conference Series*, No. 71990N.
- Hemmati, H. (2011). Interplanetary laser communications and precision ranging. *Laser and Photonics Reviews*, 5(5):697710.
- Hilbert, H. (1915). Die Grundlagen der Physik. *Gesellschaft der Wissenschaften zu Göttingen. Mathematisch-physikalische Klasse. Nachrichten*, pp. 395–407
- Hirabayashi, H., Hirose, H., Kobayashi, H., Murata, Y., Edwards, P. G., Fomalont, E. B., Fujisawa, K., Ichikawa, T., Kii, T., Lovell, J. E. J., Moellenbrock, G. A., Okayasu, R., Inoue, M., Kawaguchi, N., Kameno, S., Shibata, K. M., Asaki, Y., Bushimata, T., Enome, S., Horiuchi, S., Miyajima, T., Umemoto, T., Migenes, V., Wajima, K., Nakajima, J., Morimoto, M.,

- Ellis, J., Meier, D. L., Murphy, D. W., Preston, R. A., Smith, J. G., Tingay, S. J., Traub, D. L., Wietfeldt, R. D., Benson, J. M., Claussen, M. J., Flatters, C., Romney, J. D., Ulvestad, J. S., D'Addario, L. R., Langston, G. I., Minter, A. H., Carlson, B. R., Dewdney, P. E., Jauncey, D. L., Reynolds, J. E., Taylor, A. R., McCulloch, P. M., Cannon, W. H., Gurvits, L. I., Mioduszewski, A. J., Schilizzi, R. T. and Booth, R. S. (1998). Overview and Initial Results of the Very Long Baseline Interferometry Space Observatory Programme. *Science*, pp. 1825–1829.
- van Hoolst, T., Rambaux, N., Karatekin, Ö., Dehant, V., and Rivoldini, A. (2008). The librations, shape, and icy shell of Europa. *Icarus*, 195:386–399.
- van Hoolst, T., Rivoldini, A., Baland, R.-M., and Yseboodt, M. (2012). The effect of tides and an inner core on the forced longitudinal libration of Mercury. *Earth and Planetary Science Letters*, 333:83–90.
- van Hoolst, T., Baland, R.-M., and Trinh, A. (2013). On the librations and tides of large icy satellites. *Icarus*, 226:299–315.
- Huang, G. and Zhang, Q. (2012). Real-time estimation of satellite clock offset using adaptively robust Kalman filter with classified adaptive factors. *GPS solutions*, 16(4):531–539.
- Hulley, G. and Pavlis, E. (2007). A ray-tracing technique for improving Satellite Laser Ranging atmospheric delay corrections, including the effects of horizontal refractivity gradients. *Journal of Geophysical Research (Solid Earth)*, 112(B11):B06417.
- Hurd, W., MacNeal, B., Ortiz, G., Moe, R., Walker, J., Dennis, M., Cheng, E., Fairbrother, D., Eegholm, B., and Kasunic, K. (2006). Exo-atmospheric telescopes for deep space optical communications. In *IEEE Aerospace Conference*.
- Hussmann, H. (2014). Laser Altimetry and Its Applications in Planetary Science. In: Shuanggen, J., (editor), *Planetary Geodesy and Remote Sensing*, pp. 51–75. CRC Press.
- Iess, L. and Boscagli, G. (2001). Advanced radio science instrumentation for the mission Bepi-Colombo to Mercury. *Planetary and Space Science*, 49:1597–1608.
- Iess, L., Asmar, S., and Tortora, P. (2009). MORE: An advanced tracking experiment for the exploration of Mercury with the mission Bepi-Colombo. *Acta Astronautica*, 65:666–675.
- Iess, L., Jacobson, R. A., Ducci, M., Stevenson, D. J., Lunine, J. I., Armstrong, J. W., Asmar, S. W., Racioppa, P., Rappaport, N. J., and Tortora, P. (2012). The tides of Titan. *Science*, 337(6093):457–459.
- Iess, L. and 3GM Team (2013). 3GM: Gravity and Geophysics of Jupiter and the Galilean Moons. In *European Planetary Science Congress Abstracts*, Vol. 8, No. 491
- Iess, L., Benedetto, M. D., James, N., Mercolino, M., Simone, L., and Tortora, P. (2014a). Astra: Interdisciplinary study on enhancement of the end-to-end accuracy for spacecraft tracking techniques. *Acta Astronautica*, 94(2):699 – 707.
- Iess, L., Stevenson, D. J., Parisi, M., Hemingway, D., Jacobson, R. A., Lunine, J. I., Nimmo, F., Armstrong, J. W., Asmar, S. W., Ducci, M., and Tortora, P. (2014b). The Gravity Field and Interior Structure of Enceladus. *Science*, 344:78–80.
- Imbriale, W. (2002). *Large Antennas of the Deep Space Network*, Vol. 4 of *JPL Deep-Space Communications and Navigation Series*. John Wiley & Sons.
- Iorio, L. (2005). On the reliability of the so-far performed tests for measuring the Lense Thirring effect with the LAGEOS satellites. *New Astronomy*, 10:603–615.
- Iorio, L. and Saridakis, E. N. (2012). Solar system constraints on  $f(T)$  gravity. *Monthly Notices of the Royal Astronomical Society*, 427:1555–1561.
- Iorio, L. (2012a). Constraining the Angular Momentum of the Sun with Planetary Orbital Motions and General Relativity. *Solar Physics*, 281:815–826.
- Iorio, L. (2012b). Constraints on Galileo-induced precessions from solar system orbital motions. *Journal of Cosmology and Astroparticle Physics*, 7:1.
- Iorio, L. (2013). LETSGO: A spacecraft-based mission to accurately measure the solar angular momentum with frame-dragging. *Acta Astronautica*, 86:149–157.

- Iorio, L. (2014). Planet X revamped after the discovery of the Sedna-like object 2012 VP<sub>113</sub>? *Monthly Notices of the Royal Astronomical Society*, 444:L78–L79.
- Iqbal, F., Kirchner, G., and Koidl, F. (2008). Fast Response, Medium Resolution Digital Event Timer and Range Gate Generator for Satellite Laser Ranging. *Artificial Satellites*, 43:143–149.
- Irwin, A. W. and Fukushima, T. (1999). A numerical time ephemeris of the Earth. *Astronomy and Astrophysics*, 348:642–652.
- Jacobson, R. A. (20089). The Orbits of the Neptunian Satellites and the Orientation of the Pole of Neptune. *The Astronomical Journal*, 37:4322–4329.
- Jacobson, R. A. (2010). The Orbits and Masses of the Martian Satellites and the Libration of Phobos. *The Astronomical Journal*, 139:668–679.
- Jacobson, R. A. and Lainey, V. (2014). Martian satellite orbits and ephemerides. *Planetary and Space Science*, 102:35–44.
- Jaekel, M.-T. and Reynaud, S. (2005). Post-Einsteinian tests of linearized gravitation. *Classical and Quantum Gravity*, 22:2135–2157.
- Jefferys, W. H. and Ries, J. (1997). Bayesian Analysis of Lunar Laser Ranging Data. In: Babu, G. J. and Feigelson, E. D., (editors), *Statistical Challenges in Modern Astronomy II*.
- Jones, D. L., Folkner, W. M., Jacobson, R. A., Jacobs, C. S., Dhawan, V., Romney, J., and Fomalont, E. (2015). Astrometry of Cassini With the VLBA to Improve the Saturn Ephemeris. *Astronomical Journal*, 149:28.
- Kalisz, J. (2004). Review of methods for time interval measurements with picosecond resolution. *Metrologia*, 41:17–32.
- Kaplan, G. H. (2005). The IAU resolutions on astronomical reference systems, time scales, and earth rotation models: explanation and implementation. *U.S. Naval Observatory Circulars*, 179.
- Karatekin, Ö., Duron, J., Rosenblatt, P., an Hoolst, T., Dehant, V., and Barriot, J.-P. (2005). Mars' time-variable gravity and its determination: Simulated geodesy experiments. *Journal of Geophysical Research (Planets)*, 110:6001.
- Kaula, W. (1966). *Theory of Satellite Geodesy - Applications of Satellite to Geodesy*. Dover Publications.
- Kawamura, S. et al. (102 co-authors) (2006). The Japanese space gravitational wave antenna - DECIGO. *Classical and Quantum Gravity*, 23:S125–S131.
- Kerr, R.P. (1963). Gravitational Field of a Spinning Mass as an Example of Algebraically Special Metrics. *Physical Review Letters*, 11(5):237–238.
- Khan, A. and Connolly, J. A. D. (2008). Constraining the composition and thermal state of Mars from inversion of geophysical data. *Journal of Geophysical Research (Planets)*, 113:7003.
- Khan, A., Mosegaard, K., Williams, J. G., and Lognonné, P. (2004). Does the Moon possess a molten core? Probing the deep lunar interior using results from LLR and Lunar Prospector. *Journal of Geophysical Research (Planets)*, 109:9007.
- Khatri, F. I., Boroson, D. M., Murphy, D. V., and Sharma, J. (2004). Link analysis of Mars-Earth optical communications system. In *Laser Radar Technology for Remote Sensing*, Vol. 5338 of *SPIE Conference Series*, pp. 143–150.
- Kikuchi, F., Liu, Q., Hanada, H., Kawano, N., Matsumoto, K., Iwata, T., Goossens, S., Asari, K., Ishihara, Y., Tsuruta, S., Ishikawa, T., Noda, H., Namiki, N., Petrova, N., Harada, Y., Ping, J., and Sasaki, S. (2009). Picosecond accuracy VLBI of the two subsatellites of SELENE (KAGUYA) using multifrequency and same beam methods. *Radio Science*, 44:2008.
- Kirchner, G., Koidl, F., Prochazka, I., and Hamal, K. (1998). SPAD Time Walk Compensation and Return Energy Dependent Ranging. In *11<sup>th</sup> International Workshop on Laser Ranging*.
- Kirchner, G. and Koidl, F. (2004). Graz kHz SLR system: design, experiences and results. In *14<sup>th</sup> International Workshop on Laser Ranging*.
- Kirchner, G., Koidl, F., Kucharski, D., Steinegger, W., and Leitgeb, E. (2011). Using Pulse Position Modulation in SLR stations to transmit data to satellites. In *11<sup>th</sup> International Conference on Telecommunications*, pp. 447–450.
- Kirchner, G., Koidl, F., Friederich, F., Buske, I., Völker, U., and Riede, W. (2013). Laser measurements to space debris from Graz SLR station. *Advances in Space Research*, 51(1):21–24.

- Kirchner, G. and Koidl, F. (2014). SLR Calibration Issues - Example: Graz. In *19<sup>th</sup> International Workshop on Laser Ranging*, No. 3154.
- Klein, B. and Degnan, J. (1974). Optical antenna gain. 1: Transmitting antennas. *Applied Optics*, 13(9):2134–2141.
- Klesh, A.T. and Castillo-Rogez, J.C. (2012). Applications of NanoSats to Planetary Exploration. In *SPACE 2012 Conference & Exposition*, No. AIAA2012-5326.
- Klioner, S. A. (1992). The problem of clock synchronization - A relativistic approach. *Celestial Mechanics and Dynamical Astronomy*, 53:81–109.
- Klioner, S. A. (1993). On the hierarchy of relativistic kinematically nonrotating reference systems. *Astronomy and Astrophysics*, 279:273–277.
- Klioner, S. A. (2003). A Practical Relativistic Model for Microarcsecond Astrometry in Space. *The Astronomical Journal*, 125:1580–1597.
- Klioner, S. A. (2008). Relativistic scaling of astronomical quantities and the system of astronomical units. *Astronomy and Astrophysics*, 478:951–958.
- Kodet, J. and Prochazka, I. (2012). Note: Optical trigger device with sub-picosecond timing jitter and stability. *Review of Scientific Instruments*, 83(3):036101.
- Konopliv, A. S., Miller, J. K., Owen, W. M., Yeomans, D. K., and Giorgini, J. D. (2006). A Global Solution for the Gravity Field, Rotation, Landmarks, and Ephemeris of Eros. *Icarus*, 160:289–299.
- Konopliv, A. S., Yoder, C. F., Standish, E. M., Yuan, D.-N., and Sjogren, W. L. (2006). A global solution for the Mars static and seasonal gravity, Mars orientation, Phobos and Deimos masses, and Mars ephemeris. *Icarus*, 182:23–50.
- Konopliv, A. S., Asmar, S. W., Folkner, W. M., Karatekin, Ö., Nunes, D. C., Smrekar, S. E., Yoder, C. F., and Zuber, M. T. (2011). Mars high resolution gravity fields from MRO, Mars seasonal gravity, and other dynamical parameters. *Icarus*, 211:401–428.
- Konopliv, A. S., Park, R. S., Yuan, D.-N., Asmar, S. W., Watkins, M. M., Williams, J. G., Fahnestock, E., Kruizinga, G., Paik, M., Strelakov, D., Harvey, N., Smith, D. E., and Zuber, M. T. (2013). The JPL lunar gravity field to spherical harmonic degree 660 from the GRAIL Primary Mission. *Journal of Geophysical Research (Planets)*, 118:1415–1434.
- Kopejkin, S. M. (1988). Celestial coordinate reference systems in curved space-time. *Celestial Mechanics*, 44:87–115.
- Kopejkin, S. M. (1997). Propagation of light in the stationary field of multipole gravitational lens. *Journal of Mathematical Physics*, 38:2587–2601.
- Kopejkin, S. M. and Schäfer, G. (1999). Lorentz covariant theory of light propagation in gravitational fields of arbitrary-moving bodies. *Physical Review D*, 60(12):124002.
- Kopejkin, S. and Mashhoon, B. (2002). Gravitomagnetic effects in the propagation of electromagnetic waves in variable gravitational fields of arbitrary-moving and spinning bodies. *Physical Review D*, 65(6):064025.
- Kopejkin, S. and Vlasov, I. (2004). Parametrized post-Newtonian theory of reference frames, multipolar expansions and equations of motion in the N-body problem. *Physics Reports*, 400:209–318.
- Kopejkin, S. M. (2007). Comment on “Gravitomagnetic Influence on Gyroscopes and on the Lunar Orbit”. *Physical Review Letters*, 98(22):229001.
- Kopejkin, S., Efroimsky, M., and Kaplan, G. (2011). *Relativistic Celestial Mechanics of the Solar System*. Wiley VCH.
- Kopejkin, S. M. and Petrov, A. N. (2013). Post-Newtonian celestial dynamics in cosmology: Field equations. *Physical Review D*, 87(4):044029.
- Kovalevsky, J. and Seidelmann, P. (2004). *Fundamentals of Astrometry*. Cambridge University Press.
- Kral, L., Prochazka, I., Blazej, J., and Hamal, K. (2004). Satellite Laser Ranging Precision Ultimate Limit. In *Laser Radar Technology for Remote Sensing*, Vol. 5240 of *SPIE Conference Series*, pp. 26–30.
- Kral, K., Prochazka, I., and Hamal, K. (2005). Optical signal path delay fluctuations caused by atmospheric turbulence. *Optics Letters*, 30(14):1767–1769.

- Krishner, T. P., Anderson, J. D. and Taylor, A. H. (1991). Voyager 2 test of the radar time-delay effect. *The Astrophysical Journal*, 373:665–670.
- Kucharski, D., Otsubo, T., Kirchner, and Koidl, F. (2011). Spin axis orientation of Ajisai determined from Graz 2 kHz SLR data. *Advances in Space Research*, 46(3):251–256.
- Kucharski, D., Kirchner, G., Lim, H.-C., and Koidl, F. (2011). Optical response of nanosatellite BLITS measured by the Graz 2 kHz SLR system. *Advances in Space Research*, 48(8):1335–1340.
- Kuchynka, P., Laskar, J., Fienga, A., and Manche, H. (2010). A ring as a model of the main belt in planetary ephemerides. *Astronomy and Astrophysics*, 514:A96.
- Kuchynka, P., Folkner, W., and Konopliv, A. (2012). Station-Specific Errors in Mars Ranging Measurements. *Interplanetary Network Progress Report*, 42(180):C1.
- Kuchynka, P., Folkner, W. M., Konopliv, A. S., Parker, T. J., Park, R. S., Maistre, S. L., and Dehant, V. (2014). New constraints on Mars rotation determined from radiometric tracking of the Opportunity Mars Exploration Rover. *Icarus*, 229:340–347.
- Kumar, K., Abdulkadir, Y., van Barneveld, P., Belien, F., Billemont, S., Brandon, E., Dijkstra, M., Dirks, D., Engelen, F., Gondelach, D., van der Ham, L., Heeren, E., Iorfida, E., Leloux, J., Melman, J., Mooij, E., Musegaas, P., Noomen, R., Römgens, B., Ronse, A., Leite Pinto Secretin, T., Tong Minh, B., Vandamme, J., and and, Persson, S. (2012). Tudat: a modular and robust astrodynamics toolbox. In *5<sup>th</sup> International Conference on Astrodynamics Tools and Techniques (ICATT)*, ESA.
- Kundt, W. (1974). Dragfree spaceprobe. *Astrophysics and Space Science*, 30:455–461.
- Lainey, V., Vienne, A., and Duriez, L. (2001). New estimation of usually neglected forces acting on Galilean system. *Celestial Mechanics and Dynamical Astronomy*, 81:115–122.
- Lainey, V., Dehant, V., and Pätzold, M. (2007). First numerical ephemerides of the Martian moons. *Astronomy and Astrophysics*, 465:1075–1084.
- Lainey, V., Arlot, J.-E., Karatekin, Ö., and van Hoolst, T. (2009). Strong tidal dissipation in Io and Jupiter from astrometric observations. *Nature*, 459:957–959.
- Lambeck, K. (1988). *Geophysical Geodesy: The Slow Deformations of the Earth*. Oxford science publications. Clarendon Press.
- Lambert, S. B. and Le Poncin-Lafitte, C. (2009). Determining the relativistic parameter  $\gamma$  using very long baseline interferometry. *Astronomy and Astrophysics*, 499:331–335.
- Lanyi, G., Bagri, D. S., and Border, J. (2007). Angular Position Determination of Spacecraft by Radio Interferometry. *IEEE Proceedings*, 95(11):2193–2201.
- Le Maistre, S., Rosenblatt, P., Rivoldini, A., Dehant, V., Marty, J.-C., and Karatekin, O. (2012). Lander radio science experiment with a direct link between Mars and the Earth. *Planetary and Space Science*, 68:105–122.
- Le Maistre, S., Rosenblatt, P., Rambaux, N., Castillo-Rogez, J. C., Dehant, V., and Marty, J.-C. (2013). Phobos interior from librations determination using Doppler and star tracker measurements. *Planetary and Space Science*, 85:106–122.
- Le Poncin-Lafitte, C., Linet, B., and Teyssandier, P. (2004). World function and time transfer: general post-Minkowskian expansions. *Classical and Quantum Gravity*, 21:4463–4483.
- Lee, S., Alexander, J., and Ortiz, G. (2001). Sub-microradian pointing system design for deep-space optical communications. In *Free-Space Laser Communication Technologies XIII*, Vol. 4272 of *SPIE Conference Series*, pp. 104–111.
- Lee, P., Hildebrand, A. R., Richards, R., and Prime Mission Team (2008). The PRIME (Phobos Reconnaissance and International Mars Exploration) Mission and Mars Sample Return. In *39<sup>th</sup> Lunar and Planetary Science Conference*, No. 7045.
- Lee, S.-H., Lee, J., Kim, Y.-J., Lee, K., and Kim, S.-W. (2011). Active compensation of large dispersion of femtosecond pulses for precision laser ranging. *Optics Express*, 19(5):4002–4008.
- Lemoine, F. G., Mazarico, E., Neumann, G. A., and Chinn, D. S. (2008). New Solutions for the Mars Static and Temporal Gravity Field using the Mars Reconnaissance Orbiter. *AGU Fall Meeting Abstracts*, No. B1376.

- Lemoine, F. G., Goossens, S., Sabaka, T. J., Nicholas, J. B., Mazarico, E., Rowlands, D. D., Loomis, B. D., Chinn, D. S., Caprette, D. S., Neumann, G. A., Smith, D. E., and Zuber, M. T. (2013). High-degree gravity models from GRAIL primary mission data. *Journal of Geophysical Research (Planets)*, 118:1676–1698.
- Lemoine, F. G., Goossens, S., Sabaka, T. J., Nicholas, J. B., Mazarico, E., Rowlands, D. D., Loomis, B. D., Chinn, D. S., Neumann, G. A., Smith, D. E., and Zuber, M. T. (2014). GRGM900C: A degree 900 lunar gravity model from GRAIL primary and extended mission data. *Geophysical Research Letters*, 41(10):3382–3389.
- Lense, J. and Thirring, H. (1918) Über den Einfluss der Eigenrotation der Zentralkörper auf die Bewegung der Planeten und Monde nach der Einsteinschen Gravitationstheorie. In *Physikalische Zeitschrift*, 19:156
- Linet, B. and Teyssandier, P. (2002). Time transfer and frequency shift to the order  $1/c^4$  in the field of an axisymmetric rotating body. *Physical Review D*, 66(2):024045.
- Liu, Q., Zheng, X., Huang, Y., Li, P., He, Q., Wu, Y., Guo, L. and Tang, M. (2014). Monitoring motion and measuring relative position of the Chang'E-3 rover. *Radio Science*, 49:1080–1086.
- Love, A.E.H. (1911). *Some Problems of Geodynamics*. Cambridge University Press.
- Luchesi, D. M. and Peron, R. (2014). LAGEOS II pericenter general relativistic precession (1993–2005): Error budget and constraints in gravitational physics. *Physical Review D*, 89(8):082002.
- Luo, Y.-J., Xia, Y., and Li, G.-Y. (2009). Scientific Value of the Laser Ranging of Asteroid Icarus. *Chinese Astronomy and Astrophysics*, 33:440–449.
- Mao, D., Torrence, M., Mazarico, E., Sun, X., Rowlands, D., McGarry, J., Neumann, G., Barker, M., Golder, J., Smith, D., and Zuber, M. (2013). LRO Orbit Determination with Laser Ranging Data. In *18<sup>th</sup> International Workshop on Laser Ranging*.
- Mao, D., Sun, X., Skillman, D., McGarry, J., Hoffman, E., Neumann, G., Torrence, M., Smith, D., and Zuber, M. (2014). Time-transfer Experiments between Satellite Laser Ranging Stations via One-way Laser Ranging to the Lunar Reconnaissance Orbiter. In *19<sup>th</sup> International Workshop on Laser Ranging*, No. 3060.
- Margot, J. L., Peale, S. J., Jurgens, R. F., Slade, M. A., and Holin, I. V. (2007). Large Longitude Libration of Mercury Reveals a Molten Core. *Science*, 316:710–.
- Margot, J.-L., Peale, S. J., Solomon, S. C., Hauck, II, S. A., Ghigo, F. D., Jurgens, R. F., Yseboodt, M., Giorgini, J. D., Padovan, S., and Campbell, D. B. (2012). Mercury's moment of inertia from spin and gravity data. *Journal of Geophysical Research (Planets)*, 117:E00L09.
- Marini, J. W. and Murray Jr., C. W. (1973). Correction of Laser Range Tracking Data for Atmospheric Refraction at Elevation Angles Above 10 Degrees. Technical Report X-591-73-351, NASA.
- Marty, J. C., Balmino, G., Duron, J., Rosenblatt, P., Le Maistre, S., Rivoldini, A., Dehant, V., and van Hoolst, T. (2009). Martian gravity field model and its time variations from MGS and Odyssey data. *Planetary and Space Science*, 57:350–363.
- Matousek, S. (2007). The Juno New Frontiers mission. *Acta Astronautica*, 61:932–939.
- Mayer-Guerr, T. and the GOCO Team (2015). The combined satellite gravity field model GOCO05s. In *Geophysical Research Abstracts, EGU General Assembly*, Vol. 17, EGU2015-12364.
- Mayrhofer, R. and Pail, R. (2012). Future satellite gravity field missions: Feasibility study of post-newtonian method. In *Geodesy for Planet Earth*, pp. 231–238. Springer.
- Mazarico, E., Zuber, M. T., Lemoine, F. G., and Smith, D. E. (2008). Observation of atmospheric tides in the Martian exosphere using Mars Reconnaissance Orbiter radio tracking data. *Geophysical Research Letters*, 35:9202.
- Mazarico, E., Lemoine, F. G., Han, S.-C., and Smith, D. E. (2010). GLGM-3: A degree-150 lunar gravity model from the historical tracking data of NASA Moon orbiters. *Journal of Geophysical Research (Planets)*, 115:E5001.
- Mazarico, E., Rowlands, D. D., Neumann, G. A., Smith, D. E., Torrence, M. H., Lemoine, F. G., and Zuber, M. T. (2012). Orbit determination of the Lunar Reconnaissance Orbiter. *Journal of Geodesy*, 86:193–207.

- Mazarico, E., Goossens, S., Lemoine, F., Neumann, G., Torrence, M., Rowlands, D., Smith, D., and Zuber, M. (2013). Improved Orbit Determination of Lunar Orbiters with Lunar Gravity Fields Obtained by the GRAIL Mission. In *44<sup>th</sup> Lunar and Planetary Science Conference*, No. 2414.
- Mazarico, E., Barker, M. K., Neumann, G. A., Zuber, M. T., and Smith, D. E. (2014a). Detection of the lunar body tide by the Lunar Orbiter Laser Altimeter. *Geophysical Research Letters*, 41:2282–2288.
- Mazarico, E., Genova, A., Goossens, S., Lemoine, F. G., Neumann, G. A., Zuber, M. T., Smith, D. E. and Solomon, S. C. (2014b) The gravity field, orientation, and ephemeris of Mercury from MESSENGER observations after three years in orbit. *Journal of Geophysical Research (Planets)*, 119:2417–2436.
- McGarry, J., Zagwodzki, T., Dabney, P., Dunn, P., and Cheek, J. (2006). Laser ranging at planetary distances from SLR2000. In *15<sup>th</sup> International Workshop on Laser Ranging*, pp. 463–467.
- Mecheri, R., Abdelatif, T., Irbah, A., Provost, J., and Berthomieu, G. (2004). New values of gravitational moments  $J_2$  and  $J_4$  deduced from helioseismology. *Solar Physics*, 222:191–197.
- Mendes, V., Prates, G., Pavlis, E., Pavlis, D., and Langley, R. (2002). Improved mapping functions for atmospheric refraction correction in SLR. *Geophysical Research Letters*, 29(10):1414.
- Mendes, V. and Pavlis, E. (2004). High-accuracy zenith delay prediction at optical wavelengths. *Geophysical Research Letters*, 31:L14602.
- Meng, W., Zhang, H., Huang, P., Wang, J., Zhang, Z., Liao, Y., Ye, Y., Hu, W., Wang, Y., Chen, W., Yang, F., and Prochazka, I. (2013). Design and experiment of onboard laser time transfer in Chinese Beidou navigation satellites. *Advances in Space Research*, 51(6):951–958.
- Merkowitz, S., Dabney, P., Livas, J., McGarry, J., Neumann, G., and Zagwodzki, T. (2007). Laser Ranging for Gravitational, Lunar and Planetary Science. *International Journal of Modern Physics D*, 16:2151–2164.
- Merkowitz, S. (2010). Tests of Gravity Using Lunar Laser Ranging. *Living Reviews in Relativity*, 13(7).
- Mignard, F. (1981). Evolution of the Martian satellites. *Monthly Notices of the Royal Astronomical Society*, 194:365–379.
- Mignard, F. (2002). Fundamental Physics with GAIA. *GAIA: A European Space Project*, Vol. 2 of *EAS Publications Series*, pp. 107–121.
- Minazzoli, O. and Chauvineau, B. (2009). Post-Newtonian metric of general relativity including all the  $c^{-4}$  terms in the continuity of the IAU2000 resolutions. *Physical Review D*, 79(8):084027.
- Minazzoli, O. and Chauvineau, B. (2011). Scalar-tensor propagation of light in the inner solar system including relevant  $c^{-4}$  contributions for ranging and time transfer. *Classical and Quantum Gravity*, 28(8):085010.
- Minazzoli, O. (2012). 2PN/RM gauge invariance in Brans-Dicke-like scalar-tensor theories. *Classical and Quantum Gravity*, 29(23):237002.
- Misner, C., Thorne, K., and Wheeler, J. (1973). *Gravitation*. W. H. Freeman.
- Mitchell, D. L., Hudson, R. S., Ostro, S. J., and Rosema, K. D. (1998). Shape of Asteroid 433 Eros from Inversion of Goldstone Radar Doppler Spectra. *Icarus*, 131:4–14.
- Mohan, S., Alvarez-Salazar, O., Birnbaum, K., Biswas, A., Farr, W., Hemmati, H., Johnson, S., Ortiz, G., Quirk, K., Rahman, Z., Regher, M., Rizvi, F., Shields, J., and Srinivasan, M. (2014). Pointing, acquisition, and tracking architecture tools for deep-space optical communications. In *Free-Space Laser Communication and Atmospheric Propagation XXVI*, Vol. 8971 of *SPIE Conference Series*, No. 89710H.
- Montenbruck, O. and Gill, E. (2000). *Satellite Orbits: Models, Methods, and Applications*. Physics and Astronomy Online Library. Springer.
- Montenbruck, O., van Helleputte, T., Kroes, R. and Gill, E. (2005). Reduced dynamic orbit determination using GPS code and carrier measurements. *Aerospace Science and Technology*, 9:261–271
- Montenbruck, O., Steigenberger, P., Schönemann, E., Hauschild, A., Hugentobler, U., Dach, R., and Becker, M. (2012). Flight characterization of new generation GNSS satellite clocks. *Navigation*, 59(4):291–302.

- Moyer, T. (2000). *Formulation for Observed and Computed Values of Deep Space Network Data Types for Navigation*, Vol. 2 of *JPL Deep-Space Communications and Navigation Series*. John Wiley & Sons.
- Mudgway, D. (2001). *Uplink-downlink: a history of the Deep Space Network, 1957-1997*. The Nasa History Series, NASA SP-2001-4227. National Aeronautics and Space Administration.
- Muhleman, D. O., Esposito, P. B., and Anderson, J. D. (1977). The electron density profile of the outer corona and the interplanetary medium from Mariner-6 and Mariner-7 time-delay measurements. *Astrophysical Journal Part 1*, 211:943–957.
- Muhleman, D. O. and Anderson, J. D. (1981). Solar wind electron densities from Viking dual-frequency radio measurements. *Astrophysical Journal Part 1*, 247:1093–1101.
- Müller, J., Nordtvedt, K., and Vokrouhlický, D. (1996). Improved constraint on the  $\alpha_1$  PPN parameter from lunar motion. *Physical Review D*, 54:5927.
- Müller, J. and Biskupek, L. (2007). Variations of the gravitational constant from lunar laser ranging data. *Classical and Quantum Gravity*, 24(17):4533.
- Müller, J., Williams, J., Turyshev, S., and Shelus, P. (2007). Potential Capabilities of Lunar Laser Ranging for Geodesy and Relativity. In: Tregoning, P. and Rizos, C. (editors) *Dynamic Planet*, Vol. 130 of *International Association of Geodesy Symposia*, pp. 903–909. Springer.
- Müller, J., Soffel, M., and Klioner, S. A. (2008a). Geodesy and relativity. *Journal of Geodesy*, 82:133–145.
- Müller, J., Williams, J. G., and Turyshev, S. G. (2008b). Lunar Laser Ranging Contributions to Relativity and Geodesy. In: Dittus, H., Lammerzahn, C., and Turyshev, S., (editors), *Lasers, Clocks and Drag-Free Control: Exploration of Relativistic Gravity in Space*, Vol. 349 of *Astrophysics and Space Science Library*, pp. 457–472. Springer.
- Müller, J., Biskupek, L., Oberst, J., and Schreiber, U. (2009). Contribution of Lunar Laser Ranging to Realise Geodetic Reference Systems. In: Drewes, H., (editor), *Geodetic Reference Frames*, Vol. 134 of *International Association of Geodesy Symposia*, pp. 55–59. Springer.
- Müller, J., Hofmann, F., and Biskupek, L. (2012). Testing various facets of the equivalence principle using lunar laser ranging. *Classical and Quantum Gravity*, 29(18):184006.
- Munk, W. and MacDonald, G. (1975). *The Rotation of the Earth: A Geophysical Discussion (revised edition)*. Cambridge monographs on mechanics and applied mathematics. University Press.
- Murphy, T. (2001). Statistics of photon arrival time. Technical report, <http://physics.ucsd.edu/~tmurphy/apollo/doc/>. Last accessed 24/03/2014.
- Murphy, T. W., Adelberger, E. G., Strasburg, J. D., and Stubbs, C. W. (2002). APOLLO: Multiplexed Lunar Laser Ranging. In *13<sup>th</sup> International Laser Ranging Workshop*.
- Murphy, Jr., T. W., Nordtvedt, K., and Turyshev, S. G. (2007). Gravitomagnetic Influence on Gyroscopes and on the Lunar Orbit. *Physical Review Letters*, 98(7):071102.
- Murphy, T., Adelberger, E., Battat, J., Carey, L., Hoyle, C., Leblanc, P., Michelsen, E., Nordtvedt, K., Orin, A., Strasburg, J., Stubbs, C., Swanson, H., and Williams, E. (2008). The Apache Point Observatory Lunar Laser-ranging Operation: Instrument Description and First Detections. *Publications of the Astronomical Society of the Pacific*, 120:20–37.
- Murphy, T. W., Adelberger, E. G., Battat, J. B. R., Hoyle, C. D., McMillan, R. J., Michelsen, E. L., Samad, R. L., Stubbs, C. W., and Swanson, H. E. (2010). Long-term degradation of optical devices on the Moon. *Icarus*, 208:31–35.
- Murphy, T. W. (2013). Lunar laser ranging: the millimeter challenge. *Reports on Progress in Physics*, 76(7):076901.
- Murphy, T. W. (2014). Lunar Laser Ranging: Science and Status. In *19<sup>th</sup> International Workshop on Laser Ranging*, No. 3057.
- Murray, C. and Dermott, S. (1999). *Solar System Dynamics*. Cambridge University Press.
- Namiki, N., Iwata, T., Matsumoto, K., Hanada, H., Noda, H., Goossens, S., Ogawa, M., Kawano, N., Asari, K., Tsuruta, S.-i., Ishihara, Y., Liu, Q., Kikuchi, F., Ishikawa, T., Sasaki, S., Aoshima, C., Kurosawa, K., Sugita, S., and Takano, T. (2009). Farside Gravity Field of the Moon from Four-Way Doppler Measurements of SELENE (Kaguya). *Science*, 323:900–905.



- Nelson, R. A. (2011). Relativistic time transfer in the vicinity of the Earth and in the solar system. *Metrologia*, 48:171.
- Neumann, G. A., Rowlands, D. D., Lemoine, F. G., Smith, D. E., and Zuber, M. T. (2001). Crossover analysis of Mars Orbiter Laser Altimeter data. *Journal of Geophysical Research*, 106(E10):23753–23768.
- Neumann, G. A., Cavanaugh, J. F., Coyle, D. B., McGarry, J., Smith, D. E., Sun, X., Torrence, M., Zagwodski, T. W., and Zuber, M. T. (2008). Laser Ranging at Interplanetary Distances. In *16<sup>th</sup> International Workshop on Laser Ranging*.
- Ni, W.-T., Shy, J.-T., Tseng, S.-M., Xu, X., Yeh, H.-C., Hsu, W.-Y., Liu, W.-L., Tzeng, S.-D., Fridelance, P., Samain, E., Lee, D., Su, Z.-Y. and Wu, A.-M. (1997). Progress in mission concept study and laboratory development for the ASTROD (Astrodynamical Space Test of Relativity using Optical Devices). In *Small Spacecraft, Space Environments, and Instrumentation Technologies*, Vol. 3116 of *SPIE Conference Series*, pp. 103–114
- Ni, W.T. (2008). ASTROD and ASTROD I - Overview and Progress. *International Journal of Modern Physics D*, 17(7):921–940
- Ni, W.T. (2013). ASTROD-GW: Overview and Progress. *International Journal of Modern Physics D*, 22(1):1341004
- Noomen, R. (2001). Precise Orbit Determination With SLR: Setting The Standard. *Surveys in Geophysics*, 22:473–480.
- Nordtvedt, K. (1988). Lunar laser ranging and laboratory Eötvös-type experiments. *Physical Review D*, 37:1070–1071.
- Nordtvedt, K. (2001). SLR Contributions To Fundamental Physics. *Surveys in Geophysics*, 22:597–602.
- Oberst, J., Lainey, V., Le Poncin-Lafitte, C., Dehant, V., Rosenblatt, P., Ulamec, S., Biele, J., Spurrmann, J., Kahle, R., Klein, V., Schreiber, U., Schlicht, A., Rambaux, N., Laurent, P., Noyelles, B., Foulon, B., Zakharov, A., Gurvits, L., Uchaev, D., Murchie, S., Reed, C., Turyshiev, S. G., Gil, J., Graziano, M., Willner, K., Wickhusen, K., Pasewaldt, A., Wählisch, M., and Hoffmann, H. (2012). GETEMME - a mission to explore the Martian satellites and the fundamentals of solar system physics. *Experimental Astronomy*, 34:243–271.
- Ohring, G., Lord, S., Derber, J., Mitchell, K. and Ji, M. (2002). Applications of satellite remote sensing in numerical weather and climate prediction. *Advances in Space Research*, 30(11):2433–2439
- Orszag, A. (1965). Moon Distance Measurement by Laser. In *Symposium on Planetary Atmospheres and Surfaces*, No. 69D12-623.
- Ortiz, G. G., Sandusky, J. V., and Biswas, A. (2000). Design of the optoelectronic receiver for deep-space optical communications. In *Free-Space Laser Communication Technologies XII*, Vol. 3932 of *SPIE Conference Series*, pp. 127–138.
- Otsubo, T. and Appleby, G. M. (2003). System-dependent center-of-mass correction for spherical geodetic satellites. *Journal of Geophysical Research (Solid Earth)*, 108:2201.
- Otsubo, T., Sherwood, R. A., Appleby, G. M., and Neubert, R. (2015). Center-of-mass corrections for sub-cm-precision laser-ranging targets: Starlette, Stella and LARES. *Journal of Geodesy*, 89(4):303–312.
- Pan, J.-Y. and Xie, Y. (2015). Relativistic algorithm for time transfer in Mars missions under IAU Resolutions: an analytic approach. *Research in Astronomy and Astrophysics*, 15:281–292.
- Panek, P. and Prochazka, I. (2007). Time interval measurement device based on surface acoustic wave filter excitation, providing 1 ps precision and stability. *Review of Scientific Instruments*, 78(9):094701.
- Panek, P., Prochazka, I., and Kodet, J. (2010). Time measurement device with four femtosecond stability. *Metrologia*, 47:L13–L16.
- Paolozzi, A. and Ciufolini, I. (2013). LARES successfully launched in orbit: Satellite and mission description. *Acta Astronautica*, 91:313–321.
- Pascu, D., Erard, S., Thuillot, W., and Lainey, V. (2014). History of telescopic observations of the Martian satellites. *Planetary and Space Science*, 102:2–8.
- Pasewaldt, A., Oberst, J., Willner, K., Wählisch, M., Hoffmann, H., Matz, K.-D., Roatsch, T., Hussmann, H., and Lupovka, V. (2012). New astrometric observations of Deimos with the SRC on Mars Express. *Astronomy and Astrophysics*, 545:A144.

- Pavlis, N. K., Holmes, S. A., Kenyon, S. C. and Factor, J. K.. (2012). The development and evaluation of the Earth Gravitational Model 2008 (EGM2008). *Journal of Geophysical Research (Solid Earth)*, 117:B04406.
- de Pater, I. and Lissauer, J. (2001). *Planetary Sciences*. Cambridge University Press.
- Peale, S. J. (1969). Generalized Cassini's Laws. *Astronomical Journal*, 74:483.
- Peale, S. J., Phillips, R. J., Solomon, S. C., Smith, D. E., and Zuber, M. T. (2002). A procedure for determining the nature of Mercury's core. *Meteoritics and Planetary Science*, 37:1269–1283.
- Peale, S. J. (2006). The proximity of Mercury's spin to Cassini state 1 from adiabatic invariance. *Icarus*, 181:338–347.
- Pearlman, M. R., Degnan, J. J., and Bosworth, J. M. (2002). The International Laser Ranging Service. *Advances in Space Research*, 30(2):135–143.
- Petit, G. and Wolf, P. (1994). Relativistic theory for picosecond time transfer in the vicinity of the Earth. *Astronomy and Astrophysics*, 286:971–977.
- Petit, G., Luzum, B., and et al. (2010). IERS Conventions (2010). *IERS Technical Note*, No. 36.
- Pireaux, S. and Rozelot, J.-P. (2003). Solar quadrupole moment and purely relativistic gravitation contributions to Mercury's perihelion advance. *Astrophysics and Space Science*, 284:1159–1194.
- Pireaux, S., Barriot, J.-P., and Rosenblatt, P. (2006). (SC) RMI: A (S)emi-(C)lassical (R)elativistic (M)otion (I)ntegrator, to model the orbits of space probes around the Earth and other planets. *Acta Astronautica*, 59:517–523.
- Pitjev, N. P. and Pitjeva, E. V. (2013). Constraints on dark matter in the solar system. *Astronomy Letters*, 39:141–149.
- Pitjeva, E. V. (2001). Modern Numerical Ephemerides of Planets and the Importance of Ranging Observations for Their Creation. *Celestial Mechanics and Dynamical Astronomy*, 80:249–271.
- Pitjeva, E. V. (2013). Updated IAA RAS planetary ephemerides-EPM2011 and their use in scientific research. *Solar System Research*, 47:386–402.
- Plotkin, H. (1964). S66 laser satellite tracking experiment. In *Proceedings of the Quantum Electronics III Conference*, pp. 1319–1332. Columbia University Press.
- Plotkin, H. (2014). Genesis of Laser Satellite Tracking at the NASA Goddard Space Flight Center. In *19<sup>th</sup> International Workshop on Laser Ranging*, No. 3128.
- Plowman, J. E. and Hellings, R. W. (2006). LATOR covariance analysis. *Classical and Quantum Gravity*, 23:309–318.
- Prestage, J. and Weaver, G. (2007). Atomic clocks and oscillators for deep-space navigation and radio science. *Proceedings of the IEEE*, 95(11):2235–2247.
- Prochazka, I., Hamal, K., and Sopko, B. (2004). Recent achievements in single photon detectors and their applications. *Journal of Modern Optics*, 51:1289–1313.
- Prochazka, I., Hamal, K., and Kral, L. (2007). Single photon counting module for space applications. *Journal of Modern Optics*, 54:151–161.
- Prochazka, I. and Yang, F. (2009). Photon counting module for laser time transfer via Earth orbiting satellite. *Journal of Modern Optics*, 56:253–260.
- Prochazka, I., Blazej, J., and Kodet, J. (2011). Measurement of the optical to electrical detection delay in the detector for ground-to-space laser time transfer. *Metrologia*, 48:L13–L16.
- Prochazka, I., Schreiber, U., and Schäfer, W. (2011b). Laser time transfer and its application in the Galileo programme. *Advances in Space Research*, 47(2):239–246.
- Prochazka, I., Kodet, J., Panek, P., and Schreiber, U. (2011c). Novel concept of sub-picosecond timing system and its applications in fundamental metrology. In *Frequency Control and the European Frequency and Time Forum*.
- Prochazka, I., Blazej, J., and Kodet, J. (2012). New technologies for time transfer with picoseconds precision and accuracy. In *IEEE International Frequency Control Symposium*.
- Rambaux, N., Castillo-Rogez, J. C., Williams, J. G., and Karatekin, Ö. (2010). Librational response of Enceladus. *Geophysical Research Letters*, 37:4202.

- Rambaux, N., Castillo-Rogez, J. C., Le Maistre, S., and Rosenblatt, P. (2012). Rotational motion of Phobos. *Astronomy and Astrophysics*, 548:A14.
- Rambaux, N. (2013). Rotational motion of phobos in the earth equatorial reference frame. Technical Note IMCCE.
- Reasenberg, R. D., Shapiro, I. I., MacNeil, P. E., Goldstein, R. B., Breidenthal, J. C., Brenkle, J. P., Cain, D. L., Kaufman, T. M., Komarek, T. A., Zygielbaum, A. I. (1979). Viking relativity experiment - Verification of signal retardation by solar gravity. *The Astrophysical Journal*, 234:L219–L221.
- Recolons, J., Andrews, L. C., and Phillips, R. L. (2007). Analysis of beam wander effects for a horizontal-path propagating Gaussian-beam wave: focused beam case. *Optical Engineering*, 46(8):086002–086002–11.
- Richard, A., Rambaux, N., and Charnay, B. (2014). Librational response of a deformed 3-layer Titan perturbed by non-Keplerian orbit and atmospheric couplings. *Planetary and Space Science*, 93:22–34.
- Richter, G. W. and Matzner, R. A. (1983). Second-order contributions to relativistic time delay in the parametrized post-Newtonian formalism. *Physical Review D*, 28:3007–3012.
- Ricklefs, R. and Shelus, P. (1992). Poisson Filtering of Laser Ranging Data. In *8<sup>th</sup> International Workshop on Laser Ranging*, pp. (9–26) – (9–32).
- Riley, W. (2008). *Handbook of frequency stability analysis*. US Department of Commerce, National Institute of Standards and Technology.
- Rivoldini, A., van Hoolst, T., Verhoeven, O., Mocquet, A., and Dehant, V. (2011). Geodesy constraints on the interior structure and composition of Mars. *Icarus*, 213:451–472.
- Rivoldini, A. (2012). *The interior structure of terrestrial planets - An application to Mars*. PhD thesis, Université Catholique de Louvain.
- Rivoldini, A. and van Hoolst, T. (2013). The interior structure of Mercury constrained by the low-degree gravity field and the rotation of Mercury. *Earth and Planetary Science Letters*, 377:62–72.
- Roberts, W. (2010). Stray light modeling and performance of the 15cm deep space optical communications transceiver (DSOCT). In *Free-Space Laser Communication Technologies XXII*, Vol. 7587 of *SPIE Conference Series*, No. 75870V.
- Rosat, S., Rosenblatt, P., Trinh, A., and Dehant, V. (2008). Mars and Mercury rotation variations from altimetry crossover data: Feasibility study. *Journal of Geophysical Research (Planets)*, 113(E12):12014.
- Rosenblatt, P. (2011). The origin of the Martian moons revisited. *Astronomy and Astrophysics*, 19:44.
- Rosenblatt, P. Rivoldini, A. and Dehant, V. (2011). Modelling the internal mass distribution inside Phobos. In *2<sup>nd</sup> International Conference on the exploration of Phobos and Deimos*.
- Rothacher, M., Angermann, D., Artz, T., Bosch, W., Drewes, H., Gerstl, M., Kelm, R., König, D., König, R., Meisel, B., Müller, H., Nothnagel, A., Panafidina, N., Richter, B., Rudenko, S., Schwegmann, W., Seitz, M., Steigenberger, P., Tesmer, S., Tesmer, V., and Thaller, D. (2011). GGOS-D: homogeneous reprocessing and rigorous combination of space geodetic observations. *Journal of Geodesy*, 85:679–705.
- Rowlands, D. D., Pavlis, D. E., Lemoine, F. G., Neumann, G. A., and Luthcke, S. B. (1999). The use of laser altimetry in the orbit and attitude determination of Mars Global Surveyor. *Geophysical Research Letters*, 26:1191–1194.
- Rowlands, D. D., Lemoine, F. G., Chinn, D. S., and Luthcke, S. B. (2009). A simulation study of multi-beam altimetry for lunar reconnaissance orbiter and other planetary missions. *Journal of Geodesy*, 83:709–721.
- Rummel, R., Yi, W. and Stummer, C. (2011). GOCE gravitational gradiometry. *Journal of Geodesy*, 85:777–790.
- Sadot, D. and Kopeika, N. S. (1992). Forecasting optical turbulence strength on the basis of macroscale meteorology and aerosols: models and validation. *Optical Engineering*, 31:200–212.
- Samain, E. (2002). One Way Laser Ranging In The Solar System: TIPO. In *EGS General Assembly Conference Abstracts*, Vol. 27, No. 5808.

- Sanchez, B. V., Rowlands, D. D., and Haberle, R. M. (2006). Variations of Mars gravitational field based on the NASA/Ames general circulation model. *Journal of Geophysical Research (Planets)*, 111:6010.
- Sandalidis, H. G. (2011). Performance of a laser Earth-to-satellite link over turbulence and beam wander using the modulated gamma-gamma irradiance distribution. *Applied Optics*, 50:952–961.
- Sauer, T., (2004). Albert Einstein's 1916 Review Article on General Relativity. *ArXiv e-print 0405066*.
- Schärer, A., Angélik, R., Bondarescu, R., Jetzer, P., and Lundgren, A. (2014). Testing scalar-tensor theories and parametrized post-Newtonian parameters in earth orbit. *Physical Review D*, 90:123005.
- Schreiber, K. U., Hiener, M., Holzapfel, B., Michaelis, H., Brandl, N., Haufe, K.-H., Lauber, P., and Neidhardt, A. (2009a). Altimetry and transponder ground simulation experiment. *Planetary and Space Science*, 57:1485–1490.
- Schreiber, U., Prochazka, I., Lauber, P., Hugentobler, U., Schafer, W., Cacciapuoti, L., and Nasca, R. (2009b). The European laser timing (ELT) experiment on-board ACES. In *IEEE International Frequency Control Symposium, Joint with the 22nd European Frequency and Time forum*, pp. 594–599.
- Schubert, G., Anderson, J.D., Spohn, T. and McKinnon, W (2004). Interior composition, structure and dynamics of the Galilean satellites. In: Bagenal, F., Downling, T.E., and McKinnon, W.B., (editors), *Jupiter: The planet, satellites and magnetosphere*, pp. 281–306. Cambridge University Press.
- Schwartz, J. (1990). Laser ranging error budget for the TOPEX/POSEIDON satellite. *Applied Optics*, 29:3597–3602.
- Schwarzschild, K. (1916). Über das Gravitationsfeld eines Massenpunktes nach der Einsteinschen Theorie. *Sitzungsberichte der Königlich Preußischen Akademie der Wissenschaften (Berlin)*, pp. 189–196
- Seeber, G. (2003). *Satellite Geodesy*. Walter de Gruyter, 2<sup>nd</sup> edition.
- Seidelmann, P. K., Abalakin, V. K., Bursa, M., Davies, M. E., de Bergh, C., Lieske, J. H., Oberst, J., Simon, J. L., Standish, E. M., Stooke, P., and Thomas, P. C. (2002). Report of the IAU/IAG Working Group on Cartographic Coordinates and Rotational Elements of the Planets and Satellites: 2000. *Celestial Mechanics and Dynamical Astronomy*, 82:83–111.
- Shapiro, I.I. (1964). Fourth Test of General Relativity. *Physical Review Letters*, 13(26):789–791.
- Sheikh, S. I., Pines, D. J., Ray, P. S., Wood, K. S., Lovellette, M. N., and Wolff, M. T. (2006). Spacecraft Navigation Using X-Ray Pulsars. *Journal of Guidance, Control and Dynamics*, 29:49–63.
- Shin, D., Bagri, D., and Border, J. (2014). Advanced Calibration Technique for Accurate Three-Way Spacecraft Ranging. *Interplanetary Network Progress Report*, 42(199):C1.
- Shklovskii, I. S., Esipov, V. F., Kurt, V. G., Moroz, V. I. and Shcheglov, P. V. (1959). An Artificial Comet. *Soviet Astronomy*, 3:986–991.
- Siegman, A. E. (1986). *Lasers*. University Science Books.
- Sinclair, A. (1997). Data Screening and Normal Point Formation - Re-Statement of Herstmonceux Normal Point Recommendation. [http://ilrs.gsfc.nasa.gov/data\\_and\\_products/data/npt/npt\\_algorithm.html](http://ilrs.gsfc.nasa.gov/data_and_products/data/npt/npt_algorithm.html), last accessed 01/03/2014.
- de Sitter, W. (1916). On Einstein's theory of gravitation and its astronomical consequences. Second paper. *Monthly Notices of the Royal Astronomical Society*, 77:155–184.
- Sjogren, W. L. and Wollenhaupt, W. R. (1973). Lunar Shape via the Apollo Laser Altimeter. *Science*, 179:275–278.
- Smith, D., Zuber, M., Sun, X., Neumann, G., Cavanaugh, J., McGarry, J., and Zagwodzki, T. (2006). Two-way Laser Link over Interplanetary Distance. *Science*, 311:53–53.
- Smith, D. E., Zuber, M. T., Neumann, G. A., Lemoine, F. G., Mazarico, E., Torrence, M. H., McGarry, J. F., Rowlands, D. D., Head, J. W., Duxbury, T. H., Aharonson, O., Lucey, P. G., Robinson, M. S., Barnouin, O. S., Cavanaugh, J. F., Sun, X., Liiva, P., Mao, D.-d., Smith, J. C., and Bartels, A. E. (2010). Initial observations from the Lunar Orbiter Laser Altimeter (LOLA). *Geophysical Research Letters*, 37:18204.

- Smith, D. E., Zuber, M. T., Phillips, R. J., Solomon, S. C., Hauck, S. A., Lemoine, F. G., Mazarico, E., Neumann, G. A., Peale, S. J., Margot, J.-L., Johnson, C. L., Torrence, M. H., Perry, M. E., Rowlands, D. D., Goossens, S., Head, J. W., and Taylor, A. H. (2012). Gravity Field and Internal Structure of Mercury from MESSENGER. *Science*, 336:214–217.
- Soffel, M. H. (1989). *Relativity in Astrometry, Celestial Mechanics and Geodesy*. Springer.
- Soffel, M., Klioner, S. A., Petit, G., Wolf, P., Kopeikin, S. M., Bretagnon, P., Brumberg, V. A., Capitaine, N., Damour, T., Fukushima, T., Guinot, B., Huang, T.-Y., Lindgren, L., Ma, C., Nordtvedt, K., Ries, J. C., Seidelmann, P. K., Vokrouhlický, D., Will, C. M., and Xu, C. (2003). The IAU 2000 Resolutions for Astrometry, Celestial Mechanics, and Metrology in the Relativistic Framework: Explanatory Supplement. *The Astronomical Journal*, 126:2687–2706.
- Soffel, M. and Langhans, R. (2013). *Space-Time Reference Systems*. Astronomy and Astrophysics Library. Springer.
- Soffel, M. H. and Han, W.-B. (2015). The gravitational time delay in the field of a slowly moving body with arbitrary multipoles. *Physics Letters A*, 379:233–236.
- Sośnica, K., Thaller, D., Dach, R., Jäggi, A., and Beutler, G. (2013). Impact of loading displacements on SLR-derived parameters and on the consistency between GNSS and SLR results. *Journal of Geodesy*, 87:751–769.
- Sośnica, K. (2014). *Determination of Precise Satellite Orbits and Geodetic Parameters using Satellite Laser Ranging*. PhD thesis, University of Bern.
- Sośnica, K., Thaller, D., Dach, R., and Steigenberger, P., Beutler, G., Arnold, D. and Jäggi, A. (2015). Satellite laser ranging to GPS and GLONASS. *Journal of Geodesy (in press)*.
- Staehele, R., Blaney, D., Hemmati, H., Lo, M., Mouroulis, P., Pingree, P., Wilson, T., Puig-Suari, J., Williams, A., Betts, B., et al. (2011). Interplanetary cubesats: Opening the solar system to a broad community at lower cost. In *CubeSat Workshop*.
- Standish, E. M. and Fienga, A. (2002). Accuracy limit of modern ephemerides imposed by the uncertainties in asteroid masses. *Astronomy and Astrophysics*, 384:322–328.
- Steinbrügge, G., Hussmann, H., Stark, A. and Oberst, J. (2014). Measuring Ganymedes tidal deformation by laser altimetry: application to the GALA Experiment. In *Geophysical Research Abstract, EGU General Assembly*, Vol.16, EGU2014-3761.
- Sun, X., Skillman, D. R., Hoffman, E. D., Mao, D., McGarry, J. F., McIntire, L., Zellar, R. S., Davidson, F. M., Fong, W. H., Krainak, M. A., Neumann, G. A., Zuber, M. T., and Smith, D. E. (2013). Free space laser communication experiments from Earth to the Lunar Reconnaissance Orbiter in lunar orbit. *Optics Express*, 21:1865.
- Sun, X., Barker, M. K., Mao, D., Marzarico, E., Neumann, G. A., Skillman, D. R., Zagwodzki, T. W., Torrence, M. H., McGarry, J., and Smith, David E. and Zuber, M. T. (2014). In-orbit calibration of the lunar orbiter laser altimeter via two-way laser ranging with an earth station. In *AGU Fall Meeting*.
- Tapley, B., Schutz, B., and Born, G. (2004). *Statistical Orbit Determination*. Elsevier Science.
- Teyssandier, P. and Le Poncin-Lafitte, C. (2008). General post-Minkowskian expansion of time transfer functions. *Classical and Quantum Gravity*, 25(14):145020.
- Theil, S. (2008). Drag-Free Satellite Control. In: Dittus, H., Lammerzähl, C., and Turyshev, S. G., (editors), *Lasers, Clocks and Drag-Free Control: Exploration of Relativistic Gravity in Space*, Vol. 349 of *Astrophysics and Space Science Library*, pp. 341–359. Springer.
- Thomas, N., Spohn, T., Barriot, J.-P., Benz, W., Beutler, G., Christensen, U., Dehant, V., Fallnich, C., Giardini, D., Groussin, O., Gundersen, K., Hauber, E., Hilchenbach, M., Iess, L., Lamy, P., Lara, L.-M., Lognonné, P., Lopez-Moreno, J. J., Michaelis, H., Oberst, J., Resendes, D., Reynaud, J.-L., Rodrigo, R., Sasaki, S., Seiferlin, K., Wieczorek, M., and Whitby, J. (2007). The BepiColombo Laser Altimeter (BELA): Concept and baseline design. *Planetary and Space Science*, 55:1398–1413.
- Thornton, C. and Border, J. (2000). *Radiometric tracking techniques for deep-space navigation*, Vol. 1 of *JPL Deep-Space Communications and Navigation Series*. John Wiley & Sons.

- Thuillot, W., Lainey, V., Dehant, V., Arlot, J., de Cuyper, J., Gurvits, L., Hussmann, H., Oberst, J., Rosenblatt, P., Marty, J., and Vermeersen, B. (2011). ESPACE, European Satellite Partnership. In *EPSC-DPS Joint Meeting, European Planetary Science Congress Abstracts*, Vol. 6, No. 833.
- Thuillot, W., Lainey, V., Dehant, V., Arlot, J.-E., Gurvits, L., Hussmann, H., Oberst, J., Rosenblatt, P., Marty, J. C., Vermeersen, B., Bauer, S., de Cuyper, J.-P., Dirx, D., Hestroffer, D., Kudryashova, M., Meunier, L. E., Pasewaldt, A., Rambaux, N., Robert, V., Tajeddine, R., Willner, K. (2013). Recent activities of the FP7-ESPACE consortium. In *Journées Systèmes de référence spatio-temporels*, pp. 277-279
- Timmer, J. and Koenig, M. (1995). On generating power law noise. *Astronomy and Astrophysics*, 300:707.
- Titterton, P. (1973). Power Reduction and Fluctuations Caused by Narrow Laser Beam Motion in the Far Field. *Applied Optics*, 12:423-425.
- Tommei, G., Dimare, L., Serra, D. and Milani, A. (2015). On the Juno radio science experiment: models, algorithms and sensitivity analysis. *Monthly Notices of the Royal Astronomical Society*, (in press).
- Torge, W. (2001). *Geodesy*. Walter de Gruyter, 3<sup>rd</sup> edition.
- Tunick, A. (2002). A Critical Assessment of Selected Past Research on Optical Turbulence Information in Diverse Microclimates. Army Research Laboratory, Technical Report ARL-MR-521.
- Turyshev, S. G., Shao, M., and Nordtvedt, K. L. (2004). Experimental Design for the Lator Mission. *International Journal of Modern Physics D*, 13:2035-2063.
- Turyshev, S. G. and Williams, J. G. (2007). Space-Based Tests of Gravity with Laser Ranging. *International Journal of Modern Physics D*, 16:2165-2179.
- Turyshev, S. G. (editor), (2009). *From Quantum to Cosmos: Fundamental Physics Research in Space*. World Scientific Publishing Company.
- Turyshev, S. and Toth, V. (2010). The Pioneer anomaly. *Living Reviews in Relativity*, 13(4).
- Turyshev, S. G., Farr, W., Folkner, W. M., Girerd, A. R., Hemmati, H., Murphy, T. W., Williams, J. G., and Degnan, J. J. (2010). Advancing tests of relativistic gravity via laser ranging to Phobos. *Experimental Astronomy*, 28:209-249.
- Turyshev, S. G., Toth, V. T., and Sazhin, M. V. (2013). General relativistic observables of the GRAIL mission. *Physical Review D*, 87(2):024020.
- Turyshev, S. G., Sazhin, M. V., and Toth, V. T. (2014). General relativistic laser interferometric observables of the GRACE-Follow-On mission. *Physical Review D*, 89(10):105029.
- Urschl, C., Gurtner, W., Hugentobler, U., Schaer, S., and Beutler, G. (2005). Validation of GNSS orbits using SLR observations. *Advances in Space Research*, 36(3):412-417.
- Vallado, D. and McClain, W. (2001). *Fundamentals of Astrodynamics and Applications*. Springer.
- Veasey, M. and Dumberry, M. (2011). The influence of Mercury's inner core on its physical libration. *Icarus*, 214:265-274.
- Veis, G. (1963). Optical tracking of artificial satellites. *Space Science Reviews*, 2(2):250-296.
- Verma, A. K., Fienga, A., Laskar, J., Issautier, K., Manche, H., and Gastineau, M. (2013). Electron density distribution and solar plasma correction of radio signals using MGS, MEX, and VEX spacecraft navigation data and its application to planetary ephemerides. *Astronomy and Astrophysics*, 550:A124.
- Verma, A. K., Fienga, A., Laskar, J., Manche, H., and Gastineau, M. (2014). Use of MESSENGER radioscience data to improve planetary ephemeris and to test general relativity. *Astronomy and Astrophysics*, 561:A115.
- Vetter, J. (2007). Fifty Years of Orbit Determination: Development of Modern Astrodynamics Methods. *Johns Hopkins APL Technical Digest*, 27(3):239-252.
- Wahr, J. M., A, G., and Zhong, S. (2013). The effects of laterally varying icy shell structure on the tidal response of Europa and Ganymede. *AGU Fall Meeting Abstracts*, No. A1827.
- Walters, D. L. and Kunkel, K. E. (1981). Atmospheric modulation transfer function for desert and mountain locations: the atmospheric effects on  $r_0$ . *Journal of the Optical Society of America*, 71:397.

- Wenzel, K. P., Marsden, R. G., Page, D. E., and Smith, E. J. (1992). The ULYSSES Mission. *Astronomy and Astrophysics Supplement*, 92:207.
- Wertz, J.R. (1992). Autonomous spacecraft navigation system. *U.S. Patent*, 5,109,346.
- Wijaya, D. and Brunner, F. (2011). Atmospheric range correction for two-frequency SLR measurements. *Journal of Geodesy*, 85:623–635.
- Will, C. and Nordtvedt, Jr., K. (1972). Conservation Laws and Preferred Frames in Relativistic Gravity. I. Preferred-Frame Theories and an Extended PPN Formalism. *The Astrophysical Journal*, 177:757–774.
- Will, C. (1981). *Theory and Experiment in Gravitational Physics*. Cambridge University Press.
- Will, C. (2014). The Confrontation between General Relativity and Experiment. *Living Reviews in Relativity*, 17(4).
- Williams, J. G., Boggs, D. H., Yoder, C. F., Ratcliff, J. T., and Dickey, J. O. (2001). Lunar rotational dissipation in solid body and molten core. *Journal of Geophysical Research*, 106:27933–27968.
- Williams, J. G., Turyshev, S. G., Boggs, D. H., and Ratcliff, J. T. (2006). Lunar laser ranging science: Gravitational physics and lunar interior and geodesy. *Advances in Space Research*, 37(1):67–71.
- Williams, J. G., Turyshev, S. G., and Boggs, D. H. (2009). Lunar Laser Ranging Tests of the Equivalence Principle with the Earth and Moon. *International Journal of Modern Physics D*, 18:1129–1175.
- Williams, J. G., Konopliv, A. S., Boggs, D. H., Park, R. S., Yuan, D.-N., Lemoine, F. G., Goossens, S., Mazarico, E., Nimmo, F., Weber, R. C., Asmar, S. W., Melosh, H. J., Neumann, G. A., Phillips, R. J., Smith, D. E., Solomon, S. C., Watkins, M. M., Wieczorek, M. A., Andrews-Hanna, J. C., Head, J. W., Kiefer, W. S., Matsuyama, I., McGovern, P. J., Taylor, G. J., and Zuber, M. T. (2014). Lunar interior properties from the GRAIL mission. *Journal of Geophysical Research (Planets)*, 119:1546–1578.
- Williams, J. G. and Boggs, D. (2015). Tides on the Moon: Theory and determination of dissipation. *Journal of Geophysical Research: Planets*, (in press).
- Willner, K., Oberst, J., Hussmann, H., Giese, B., Hoffmann, H., Matz, K.-D., Roatsch, T., and Duxbury, T. (2010). Phobos control point network, rotation, and shape. *Earth and Planetary Science Letters*, 294:541–546.
- Willner, K., Shi, X., and Oberst, J. (2014). Phobos’ shape and topography models. *Planetary and Space Science*, 102(1):51–59.
- Wilson, K., Lesh, J., and Yan, T.-Y. (1993). GOPEX: a laser uplink to the Galileo spacecraft on its way to Jupiter. In *Free-Space Laser Communication Technologies V*, Vol. 1866 of *SPIE Conference Series*, pp. 138–146.
- Witasse, O., Duxbury, T., Chicarro, A., Altobelli, N., Andert, T., Aronica, A., Barabash, S., Bertaux, J.-L., Bibring, J.-P., Cardesin-Moinelo, A., Cichetti, A., Companys, V., Dehant, V., Denis, M., Formisano, V., Futaana, Y., Giuranna, M., Gondet, B., Heather, D., Hoffmann, H., Holmström, M., Manaud, N., Martin, P., Matz, K.-D., Montmessin, F., Morley, T., Mueller, M., Neukum, G., Oberst, J., Orosei, R., Pätzold, M., Picardi, G., Pischel, R., Plaut, J. J., Reberac, A., Pardo Voss, P., Roatsch, T., Rosenblatt, P., Remus, S., Schmedemann, N., Willner, K., and Zegers, T. (2014). Mars Express investigations of Phobos and Deimos. *Planetary and Space Science*, 102:18–34.
- Wolf, P., Bordé, C. J., Clairon, A., Duchayne, L., Landragin, A., Lemonde, P., Santarelli, G., Ertmer, W., Rasel, E., Cataliotti, F. S., Inguscio, M., Tino, G. M., Gill, P., Klein, H., Reynaud, S., Salomon, C., Peik, E., Bertolami, O., Gil, P., Páramos, J., Jentsch, C., Johann, U., Rathke, A., Bouyer, P., Cacciapuoti, L., Izzo, D., de Natale, P., Christophe, B., Touboul, P., Turyshev, S. G., Anderson, J., Tobar, M. E., Schmidt-Kaler, F., Vigué, J., Madej, A. A., Marmet, L., Angonin, M.-C., Delva, P., Tournenc, P., Metris, G., Müller, H., Walsworth, R., Lu, Z. H., Wang, L. J., Bongs, K., Toncelli, A., Tonelli, M., Dittus, H., Lämmerzahl, C., Galzerano, G., Laporta, P., Laskar, J., Fienga, A., Roques, F. and Sengstock, K. (2009). Quantum physics exploring gravity in the outer solar system: The SAGAS project. *Experimental Astronomy*, 23(2):651–687.
- Wu, X., Bar-Sever, Y. E., Folkner, W. M., Williams, J. G. and Zumberge, J. F. (2001). Probing Europa’s hidden ocean from tidal effects on orbital dynamics. *Geophysical Research Letters*, 28:2245–2248.

- Wood, R. and Appleby, G. (2004). Satellite laser ranging. In: Jones, J. and Webb, C., (editors), *Handbook of Laser Technology and Applications*, pp. 2531–2562. Institute of Physics.
- Xie, Y. and Kopeikin, S. (2010). Post-Newtonian Reference Frames for Advanced Theory of the Lunar Motion and a New Generation of Lunar Laser Ranging. *Acta Physica Slovaca*, 60:393–495.
- Xie, Y. and Kopeikin, S. (2014). Covariant Theory of Post-Newtonian Equations of Motion of Extended Bodies. In: Kopeikin, S.M., (editor), *Frontiers in Relativistic Celestial Mechanics, Volume 1: Theory*, Vol. 21 of *Studies in Mathematical Physics*, pp. 65–154. Walter de Gruyter.
- Yaoheng, X. and Hesheng, F. (2003). Modification of Laser Ranging Equation. In *13th International Workshop on Laser Ranging Instrumentation*.
- Yoder, C. F. and Standish, E. M. (1997). Martian precession and rotation from Viking lander range data. *Journal of Geophysical Research*, 102, E2:4065–4080.
- Yoder, C. F., Konopliv, A. S., Yuan, D. N., Standish, E. M., and Folkner, W. M. (2003). Fluid Core Size of Mars from Detection of the Solar Tide. *Science*, 300:299–303.
- Yseboodt, M., Rosenblatt, P., Dehant, V., Barriot, J. P., and van Hoolst, T. (2002). Mars geodesy with NEIGE: simulation of the Martian orientation parameters estimation. In: Foing, B. H. and Battrick, B., (editors), *Earth-like Planets and Moons*, Vol. 514 of *ESA Special Publication*, pp. 145–149.
- Yseboodt, M., Dehant, V., Iess, L., Mitrovic, M., and Gregnanin, M. (2012). Same Beam Interferometry on Mars for obtaining information on the interior. In *European Planetary Science Congress Abstracts*, Vol. 7, No. 522
- Yu, J. W., Shao, M., Gursel, Y., and Hellings, R. (1994). LATOR: laser astrometric test of relativity. In *Amplitude and Intensity Spatial Interferometry II*, Vol. 2200 of *SPIE Conference Series*, pp. 325–334.
- Zannoni, M. and Tortora, P. (2013). Numerical Error in Interplanetary Orbit Determination Software. *Journal of Guidance Control and Dynamics*, 36:1008–1018.
- Zschocke, S. and Soffel, M. H. (2014). Gravitational field of one uniformly moving extended body and  $N$  arbitrarily moving pointlike bodies in post-Minkowskian approximation. *Classical and Quantum Gravity*, 31(17):175001.
- Zuber, M. (2006). Seconds of Data... Years of Trying. *Photonics Spectra*, May 2006.
- Zuber, M. T., Smith, D. E., Zellar, R. S., Neumann, G. A., Sun, X., Katz, R. B., Kleyner, I., Matuszeski, A., McGarry, J. F., Ott, M. N., Ramos-Izquierdo, L. A., Rowlands, D. D., Torrence, M. H., and Zagwodzki, T. W. (2010). The Lunar Reconnaissance Orbiter Laser Ranging Investigation. *Space Science Reviews*, 150:63–80.
- Zumberge, J., Border, J., Dehant, V., Folkner, W., Jones, D., Martin-Mur, T., Oberst, J., Williams, J., and Wu, X. (2009). Geodesy: Foundation for exploring the planets, the solar system and beyond. In: Plag, H.-P. and Pearlman, M., (editors), *Global Geodetic Observing System*, pp. 197–207. Springer.
- Zyskind, G. and Martin, F.B. (1969). On best linear estimation and general Gauss-Markov theorem in linear models with arbitrary nonnegative covariance structure. *SIAM Journal on Applied Mathematics*, 17(6):1190–1202.



---

## Curriculum Vitae

---

Dominic Dirkx was born in Aix-en-Provence, France, on August 9, 1985. He attended secondary school at the *Stedelijk Gymnasium* in Leiden, the Netherlands, graduating in 2003 with a focus on science and technology. After studying physics at Leiden university for 1 year, he started his university studies at the Delft University of Technology, Aerospace Engineering faculty in 2004, obtaining his BSc degree *cum laude* in 2008 and his MSc degree *cum laude* in 2011, with a thesis entitled *Conceptual Shape Optimization of Entry Vehicles - Applied to Capsules and Winged Fuselage Vehicles*. As part of his MSc studies, he worked at ESA/ESTEC in Noordwijk, the Netherlands, for 4 months to develop a hypersonic aerodynamics module for a space trajectory analysis software project.

In 2011, he joined the Astrodynamics and Space Missions group at the Aerospace Engineering faculty, Delft University of Technology, as a research associate, appointed to perform work on the European Framework Programme 7 project entitled *European Satellite Partnership for the Calculation of Ephemerides* (ESPaCE). The work on this project consisted of analyzing the potential contributions of interplanetary laser ranging to the science return of future space missions, with a focus on planetary science objectives. The research performed in this project has led to the preparation of this dissertation. During this period, he visited DLR Berlin for one month in October 2013, to collaborate on Lunar Reconnaissance Orbiter orbit determination using one-way laser ranging data. He has been involved in the use, development and management of the TU Delft Astrodynamics Toolbox (Tudat) since mid-2010, shortly after its inception.



---

## List of Publications

---

### Journal Articles

- Bauer, S., Hussmann, H., Oberst, J., **Dirkx, D.**, Mao, D., Neumann, G., Mazarico, E., Torrence, M., McGarry, J., Smith, D. and Zuber, M. (2015), Analysis of oneway laser ranging data to LRO: performance and calibration of spacecraft and ground station clocks, *Icarus* (submitted)
- Root, B.C., Novák, P., **Dirkx, D.** and Kaban, M.K. (2015), On forward gravity field modelling *Geophysical Journal International* (submitted)
- **Dirkx, D.**, Noomen, R., Visser, P.N.A.M., Gurvits, L.I. and Vermeersen, L.L.A. (2015), Simultaneous Spacetime Dynamics Estimation from Space Mission Tracking Data, *Astronomy and Astrophysics* (to be submitted)\*
- **Dirkx, D.**, Noomen, R., Visser, P.N.A.M, Bauer, S. and Vermeersen, L.L.A (2015), Comparative Analysis of one- and two-way planetary laser ranging concepts, *Planetary and Space Science* (in press)\*
- Bocanegra-Bahamón, T., Bracken, C., Costa Sitjà, M., **Dirkx, D.**, Gerth, I., Konstantinidis, K., Labrianidis, C., Laneuville, M., Luntzer, A., MacArthur, J.L., Maier, A., Morschhauser, A., Nordheim, T.A., Sallantin, R. and Tlustos, R. (2015), MUSE - Mission to the Uranian system: Unveiling the evolution and formation of ice giants, *Advances in Space Research*, 55(9):2190-2216
- Arridge, C.S. et al. (120 co-authors, including **Dirkx, D.**) (2014), The science case for an orbital mission to Uranus: Exploring the origins and evolution of ice giant planets, *Planetary and Space Science*, 104:122-140
- **Dirkx, D.**, Noomen, R., Prochazka, I., Bauer, S. and Vermeersen, L. (2014), Influence of atmospheric turbulence on planetary transceiver laser ranging, *Advances in Space Research*, 54(11):2349-2370\*
- **Dirkx, D.**, Vermeersen, L.L.A., Noomen, R. and Visser, P.N.A.M. (2014), Phobos Laser Ranging: Numerical Geodesy Experiments for Martian System Science, *Planetary and Space Science*, 99:84-102\*
- **Dirkx, D.** and Mooij, E. (2014), Optimization of entry-vehicle shapes during conceptual design, *Acta Astronautica*, 94(1):198-214

\*: Articles included in this dissertation

### Selected Conference Contributions

- **Dirkx, D.**, Bauer, S., Noomen, R., Vermeersen, L.L.A and Visser, P.N.A.M (2014), Comparative analysis of planetary laser ranging concepts. In *American Geophysical Union Fall Meeting, 15-19 December, San Francisco, CA, USA*, abstract number P31A-3975
- **Dirkx, D.**, Bauer, S., Noomen, R., Vermeersen, L.L.A and Visser, P.N.A.M (2014), Simulated comparative analysis of one-and two-way planetary laser ranging systems. In *19<sup>th</sup> international laser ranging workshop, 27-31 October, Annapolis, MD, USA*, paper number 3101
- **Dirkx, D.**, Noomen, R., Prochazka, I., Bauer, S. and Vermeersen, L.L.A (2014), Influence of Atmospheric Turbulence on Planetary Transceiver Laser Ranging. In *ibid.*, paper number 3087
- Bauer, S., **Dirkx, D.**, Hussmann, H., Oberst, J., Mao, D., Neumann, G., Mazarico, E., Torrence, M., McGarry, J., Smith, D. and Zuber, M. (2014), Application of one-way laser ranging data to LRO into orbit determination. In *ibid.*, paper number 3124
- **Dirkx, D.**, Vermeersen, L.L.A., Noomen, R. and Visser, P.N.A.M. (2013), Numerical Geodesy Experiments for a Phobos Laser Ranging Mission Concept. In *18<sup>th</sup> international laser ranging workshop, 11-15 November, Fujiyoshida, Japan*, paper number 13-0407
- Bauer, S., **Dirkx, D.**, Oberst, J., Hussmann, H., Gläser, P., Schreiber, U. Mao, D., Neumann, G., Mazarico, E., Torrence, M., McGarry, J., Smith, D., and Zuber, M. (2013), Analysis and application of one-way laser ranging data from ILRS ground stations to LRO. In *ibid.*, paper number 13-0404
- Thuillot, W., Lainey, V., Arlot, J.-E., Dehant, V., Gurvits, L., Hussmann, H., Oberst, J., Rosenblatt, P., Marty, J. C., Vermeersen, B., de Cuyper, J.-P., **Dirkx, D.**, Cimò, G., Duev, D. Kudryashova, M., Meunier, L. E., Pasewaldt, A., Rambaux, N., Robert, V., Willner, K. (2013). Recent activities of the FP7-ESPaCE consortium. In *Journées Systèmes de référence spatio-temporels, 16-18 September, Paris, France*, p. 277-279
- **Dirkx, D.** and Vermeersen, L.L.A. (2013), Simulation of interplanetary laser ranging. In *European Planetary Science Congress, 8-13 September, London, UK*, abstract number 2013-481
- **Dirkx, D.**, Bocanegra-Bahamón, T., Bracken, C., Costa Sitjà, M., Gerth, I., Konstantinidis, K., Labrianidis, C., Laneuville, M., Luntzer, A., MacArthur, J.L., Maier, A., Morschhauser, A., Nordheim, T.A., Sallantin, R. and Tlustos, R. (2013), Unveiling the evolution and formation of icy giants. In *ibid.*, abstract number 2013-745-2
- Thuillot, W., Lainey, V., Dehant, V., de Cuyper, J.-P., Arlot, J.-E., Gurvits, L., Hussmann, H., Oberst, J., Rosenblatt, P., Marty, J. C., Vermeersen, B., Robert, V., **Dirkx, D.**, Kudryashova, M. and Le Maistre, S. (2012). ESaPaCE: European Satellite Partnership for Computing Ephemerides. In *Let's embrace space - FP7 Space Conference, 15-16 November, Larnaca, Cyprus*, Chapter 25
- **Dirkx, D.**, Noomen, R., Vermeersen, L.L.A and Visser, P.N.A.M (2012), Quantification of interplanetary laser ranging system requirements through bottom-up link simulations. In *International Technical Laser Workshop, 5-9 November, Frascati, Italy*.
- **Dirkx, D.** and Vermeersen, L.L.A. (2012), Interplanetary laser ranging-an emerging technology for planetary science missions. In *European Planetary Science Congress, 23-28 September, Madrid, Spain*, abstract number 2012-117
- Kumar, K., Abdulkadir, Y., van Barneveld, P.W.L., Belien, F., Billemont, S. Brandon, E., Dijkstra, M. **Dirkx, D.**, Engelen, F., Gondelach, D., van der Ham, L., Heeren, E. Iorfida, E., Leloux, J., Melman, J., Mooij, E., Musegaas, P., Noomen, R., Persson, S.M., Römgens, B., Ronse, A., Leite Pinto Secretin, T.A., Tong Minh, B. and Vandamme, J. (2012), Tudat: a modular and robust astrodynamics toolbox. In *Fifth International Conference on Astrodynamics Tools and Techniques, 29 May - 1 June, Noordwijk, the Netherlands*

### Non-peer reviewed articles

- **Dirkx, D.** (2012) Interplanetary Laser Ranging - An emerging technology for planetary science missions, *Leonardo Times*, 16(4):38-42